UNIVERSIDAD DE CHILE
FACULTAD DE CIENCIAS FÍSICAS Y MATEMÁTICAS
DEPARTAMENTO DE GEOLOGÍA

EVOLUTION AND DYNAMICS OF THE 3.6 KA BP PUCÓN ERUPTION OF VILLARRICA VOLCANO, CHILE

TESIS PARA OPTAR AL GRADO DE DOCTOR EN CIENCIAS, MENCION GEOLOGÍA

EN COTUTELA CON LA UNIVERSITÉ BLAISE PASCAL – CLERMONT-FERRAND II

CAROLINA ANDREA SILVA PAREJAS

PROFESORES GUÍA:
TIMOTHY DRUITT
ALFREDO LAHSEN AZAR

MIEMBROS DE LA COMISIÓN:
CLAUDE ROBIN
FRANCISCO HERVÉ ALLAMAND
OLIVIER ROCHE
MARIO VERGARA MARTÍNEZ
JORGE CLAVERO RIBES
JEAN-LOUIS BOURDIER

SANTIAGO DE CHILE
SEPTIEMBRE 2008

ABSTRACT

The Pucón Ignimbrite (3.6 ka BP, 3.3 km^3, 1.8 km^3 DRE) is a well preserved and complicated sequence of mostly pyroclastic current deposits with basaltic andesitic juvenile composition (54-56% SiO_2) emitted by the largest Holocene eruption of Villarrica Volcano (Chile). Fieldwork, together with the determination of physical and chemical parameters (grain-size, counting, density measurements, textural analysis, microlite content estimations, radiocarbon dating, whole-rock major and trace element analyses, and matrix glass composition of major elements and S, Cl and F), allowed to reconstruct the facies architecture of the deposit and to understand the dynamics of the eruption.

Prior to the Pucón eruption, the volcano summit was covered by an extensive ice cap and subglacial basaltic-andesitic to rhyolitic lava domes and/or flows of unknown age were present near or at the summit. They were fragmented at the onset of the Pucón eruption generating abundant dense prismatically-jointed clasts and dense ash shards that were incorporated by the subsequent Pucón products.

Following a maximum repose period of ~400 years, the Pucón eruption started with a violent strombolian or subplinian fallout (0.1 km^3 of magma, VEI=3-4) which rapidly evolved towards a hazardous ignimbrite-forming mechanism (P1). Multiple pyroclastic flows (20% of the total volume) covered ~180 km^2 of the western and northern flanks of the volcano up to 15 km from the present-day summit. A small base surge was then followed by about ten powerful vulcanian explosions. A progressive deepening of the fragmentation level accompanied P1. Lithic-rich pyroclastic flows were mostly valley-confined with subordinate surges and followed by the emission in rapid succession (degassing pipes traverse the contacts) of at least eight highly-concentrated mostly juvenile-rich pyroclastic flows. During a pause in eruptive activity (several weeks to months?) the P1 deposits cooled below the temperature necessary for charcoalization of wood (~200°C) and reservoir replenishment by a more basic magma batch occurred. Vent erosion and widening in different and more extensive areas than during P1 phase, provided the P2 flows of a new assemblage of basaltic-andesitic to rhyolitic lava fragments.

During the second phase (P2, less than a few days?) voluminous pyroclastic flows and minor surges were deposited all around the volcano (80% of the total volume), covering ~530 km^2 up to 21 km from the present-day summit. This increase in the eruptive intensity is characterised by the abrupt appeareance of a significant proportion of basement granitoids as free clasts and inclusions in scoria (vesicle-bearing and partially-melted granitoid inclusions, but also angular, non-melted ones), suggesting that very rapidly after the start of this phase, a high magma discharge rate caused the fragmentation level to fall within the granitoid basement, probably accompanied by the climactic phase of caldera collapse and stoping of granitoid roof material into a magma reservoir. The turbulent, blast-like leading edge of these flows was followed by three or more high-energy pyroclastic flows followed in rapid succession, forming thick valley ponds and a complete interfluve record. The unsteady flows of high- to intermediate-concentration (diffuse stratification and huge bed forms) formed angular unconformities, shearing and thrusting the underlying strata. Then, black juvenile-rich pyroclastic flows to the southeast of the volcano were rapidly followed by at least two lithic-rich surges (degassing pipes traverse the contact) distributed all around the volcano with important slope deposition. During a final waning phase, three lithic-rich pyroclastic flows were emitted on the northern flank, immediately inundated by several lahar waves.

A new cycle of vigorous strombolian to subplinian eruptions and phreatic/phreatomagmatic explosions started no more than a few rain seasons after the discharge of the final pyroclastic flow.

Pucón magma was probably sufficiently rich in volatiles at depth to exsolve and drive magmatic fragmentation. Low-pressure degassing and rapid microlite crystallization could explain the dense clasts, rather than quenching by external water which may have played a role in pulverizing abundant rock from the conduit margins progressively widening the conduit. This effect could have been the greatest early on P1 and P2, and then decreased because most of the summit glacier and snow had then melted.

Even infrequent on a human timescale, if a Pucón-sized eruption (VEI=5) occurred today, approximately 15,000-40,000 people would be directly threatened by pyroclastic currents and even more by associated lahars and ash falls. The evolution of the Pucón eruption shows that a violent ignimbrite-type episode (P2), of short duration but large magnitude, catastrophic on a regional scale, can occur after a pause of several weeks to months following a period of already important pyroclastic activity (P1). This pause marked an adjustment phase of the plumbing system, rather than the end of the eruption, as could be assumed during monitoring of a similar event today.

RESUMEN

La Ignimbrita Pucón (3.6 ka BP, 3.3 km^3, 1.8 km^3 DRE) es una secuencia complicada y bien preservada de depósitos de corrientes de densidad piroclástica en su mayoría, de composición juvenil basáltico-andesítica (54-56% SiO_2), emitida por la mayor erupción Holocena del Volcán Villarrica (Chile). Trabajo de terreno, junto con la determinación de parámetros físicos y químicos (tamaño y conteo de granos, medidas de densidad, análisis textural, estimaciones de contenido de microlitos, dataciones ^{14}C, análisis de elementos mayores y en trazas por roca total, y análisis de elementos mayores, S, Cl and F del vidrio de la matriz), nos permitieron reconstruir la arquitectura de facies del depósito y entender la dinámica de la erupción.

Previo a la erupción Pucón, lavas y/o domos basáltico-andesíticos a riolíticos, subglaciales y de edad desconocida, estaban presentes cerca o en la cumbre. Fueron fragmentados al comienzo de la erupción Pucón, proporcionando abundantes clastos densos con disyunción prismática y esquirlas de ceniza densa a la Ignimbrita Pucón.

Luego de un período de reposo máximo ~400 años, la erupción Pucón comenzó con una caída estromboliana o subpliniana violenta (0.1 km^3 de magma, VEI=3-4) la cual evolucionó rápidamente hacia un peligroso mecanismo generador de ignimbrita (P1). Múltiples flujos piroclásticos (20% del volumen total) cubrieron ~180 km^2 de los flancos oeste y norte del volcán hasta 15 km de la cima actual. Una pequeña oleada de base fue seguida por cerca de diez fuertes explosiones vulcanianas. Una profundización progresiva del nivel de fragmentación acompañó P1. Flujos piroclásticos ricos en líticos fueron principalmente confinados a los valles con oleadas subordinadas, y seguidos por la emisión en rápida sucesión (pipas de desgasificación atraviesan los contactos) de al menos ocho flujos piroclásticos altamente concentrados y en su mayoría ricos en material juvenil. Durante una pausa en la actividad eruptiva (¿varias semanas a meses?), los depósitos de P1 se enfriaron bajo la temperatura necesaria para la carbonización de la madera (~200°C) y el reservorio fue recargado por un nuevo pulso de magma más básico. Erosión y ensanchamiento del conducto en áreas diferentes y más extensas que durante la fase P1, proporcionaron a los flujos piroclásticos de P2, una nueva asociación de fragmentos de lava basáltico-andesíticos a riolíticos.

Durante la segunda fase P2 (¿unos pocos días?), voluminosos flujos piroclásticos y oleadas menores fueron depositados alrededor de todo el volcán (80% del volumen total), cubriendo ~530 km^2 hasta 21 km de la cima actual. Este incremento en la intensidad eruptiva estuvo caracterizado por la abrupta aparición de abundantes granitoides del basamento como clastos libres y como inclusiones en las escorias (inclusiones de granitoides parcialmente fundidos con vesículas, pero también variedades angulosas de granitoides no fundidos). Esto sugiere que rápidamente después del comienzo de esta fase, una alta velocidad de descarga de magma hizo bajar el nivel de fragmentación dentro del basamento de granitoides, probablemente acompañado por la fase culminante de colapso caldérico y hundimiento del techo de granitoides dentro del reservorio de magma. La parte turbulenta frontal de estos flujos, de tipo onda expansiva, fue seguida por al menos tres flujos piroclásticos de alta energía emitidos en sucesión rápida, formando espesos rellenos en los valles y un registro completo en los interfluvios. Los flujos inestables de concentración alta a intermedia (estratificación difusa y enormes marcas de fondo), cizallaron y sobreescurrieron los estratos subyacentes, formando discordancias angulares. Entonces, flujos piroclásticos negros ricos en juveniles, emitidos al sureste del volcán, fueron rápidamente seguidos por al menos dos oleadas ricas en líticos (pipas de desgasificación atraviesan el contacto). Estas se distribuyeron alrededor de todo el volcán con una importante depositación en los interfluvios. Durante la fase final declinante, tres flujos piroclásticos fueron emitidos hacia el flanco norte e inmediatamente inundados por varias olas de lahares.

Un nuevo ciclo de erupciones estrombolianas vigorosas a subplinianas y explosiones freáticas/freatomagmáticas, comenzó luego de pocas temporadas de lluvia después de la descarga del último flujo piroclástico de la erupción Pucón.

El magma de Pucón fue probablemente lo suficientemente rico en volátiles en profundidad como para exsolver e impulsar fragmentación magmática. Desgasificación de baja presión y rápida cristalización de microlitos podrían explicar los clastos densos, más que enfriamiento instantáneo por agua externa, la cual a su vez pudo jugar un rol en pulverizar abundante roca de los márgenes del conducto progresivamente

ensanchándolo. Este efecto pudo haber sido mayor al comienzo de P1 y P2, y luego decrecer, debido al derretimiento progresivo del glaciar.

A pesar de ser poco frecuente a escala humana, de ocurrir hoy, una erupción del tamaño de Pucón (IEV=5) amenazaría ~15,000-40,000 personas directamente por corrientes de densidad piroclástica e incluso más por lahares y caídas de ceniza asociados. La evolución de la erupción Pucón muestra que un violento episodio de tipo ignimbrítico (P2), de corta duración pero gran magnitud, catastrófico a escala regional, puede ocurrir después de una pausa de varias semanas a meses, luego de un período de importante actividad piroclástica (P1). En el caso de la erupción Pucón, esta pausa marcó una fase de ajuste en los conductos en profundidad más que el fin de la erupción, lo cual debiera considerarse durante el monitoreo de un evento similar hoy.

RÉSUMÉ

L'Ignimbrite Pucón (3.6 ka BP, 3.3 km^3, 1.8 km^3 DRE) est une séquence complexe et bien préservée dans sa majorité composée de dépôts d'écoulements pyroclastiques, de composition juvénile basaltique andésitique (54-56% SiO_2), émise par la majeur éruption Holocène du Volcan Villarrica (Chili). Le travail de terrain conjoint avec la détermination de paramètres physiques et chimiques (taille y comptage des grains, mesures de densité, analyse texturale, estimations de teneurs en microlites, datations ^{14}C, analyse d'éléments majeurs et en traces par roche total, et analyse d'éléments majeurs, S, Cl et F du verre de la matrice), nous ont permis de reconstruire l'architecture de faciès du dépôt et de comprendre la dynamique de l'éruption.

Avant l'éruption Pucón, des écoulements de lave et/ou des dômes sub-glaciaires de composition basaltique andésitique à rhyolitique et d'âge inconnu, étaient présents proche du sommet. Ils ont été fragmentés au début de l'éruption Pucón, en apportant d'abondants fragments denses avec fracturation prismatique et des éclats de cendre dense à l'Ignimbrite Pucón.

Après une période maximum de repos de ~400 ans, l'éruption Pucón a commencé avec une retombée strombolienne violente ou subplinienne (0.1 km^3 de magma, IEV=3-4) laquelle a évolué rapidement vers un mécanisme générateur d'ignimbrites d'aléa volcanique majeur (P1). De nombreux écoulements pyroclastiques (20% du volume total) ont couvert ~180 km^2 des flancs ouest et nord du volcan jusqu'à 15 km du sommet actuel. Une petite déferlante de base a été suivie par près de dix explosions vulcaniennes fortes. Un approfondissement progressif du niveau de fragmentation a accompagné la phase P1. Des écoulements pyroclastiques riches en lithiques ont été principalement confinés aux vallées avec des déferlantes subordonnées, et suivis par l'émission en succession rapide (des tubes de dégazage traversent les contacts) d'au moins huit écoulements pyroclastiques fortement concentrés et dans sa majorité riches en matériel juvénile. Pendant une pause dans l'activité éruptive (de plusieurs semaines à plusieurs mois?), les dépôts de la phase P1 se sont refroidis au-dessous de la température nécessaire pour la carbonisation du bois (~200°C), et le réservoir a été rechargé par une nouvelle remontée de magma plus basique. L'érosion et l'élargissement du conduit, affectant des zones différentes et plus étendues que la phase P1, ont apporté aux écoulements pyroclastiques de la phase P2 une nouvelle association de fragments de lave basaltique andésitiques à rhyolitiques.

Pendant la deuxième phase P2 (de seulement quelques jours ?), de volumineux écoulements pyroclastiques et déferlants mineurs ont été déposées tout autour du volcan (80% du volume total), en couvrant ~530 km^2 atteignant jusqu'à 21 km du sommet actuel. Cette augmentation de l'intensité éruptive a été caractérisée par l'abrupte arrivée d'abondants granitoïdes provenant du socle, comme des fragments libres et des inclusions dans les scories (granitoïdes partiellement fondus contenant des vésicules et des variétés anguleuses de granitoïdes non fondus). Cela suggère que rapidement après le début de cette phase, une décharge de magma de majeure vitesse a fait descendre le niveau de fragmentation dans le socle de granitoïdes, probablement tout ceci accompagné par la phase culminante d'effondrement de caldera et du toit de granitoïdes dans le réservoir du magma. La partie turbulente frontale de ces écoulements, de type onde expansive, a été suivie par au moins trois écoulements pyroclastiques de haute énergie, émises en succession rapide. Ces écoulements ont formé des dépôts épais dans les vallées et une complète séquence dans les interfluves. Les écoulements instables de haute à moyenne concentration (stratification diffuse et des énormes formes du fond du lit) ont cisaillé les couches sous-jacentes en formant des discordances angulaires. Puis, des écoulements pyroclastiques noirs, riches en juvéniles émises au sud-est du volcan, ont été rapidement suivis par au moins deux déferlantes riches en lithiques (tubes de dégazage traversent le contact). Ces déferlantes se sont distribué tout autour du volcan formant un important dépôt sur les interfluves. Pendant la phase finale déclinante, trois écoulements pyroclastiques ont été émis vers le flanc nord et immédiatement inondés par plusieurs vagues de lahars.

Un nouveau cycle d'éruptions stromboliennes vigoureuses à subpliniennes et d'explosions phréatiques/phréatomagmatiques, a commencé après quelques saisons de pluie suivant la décharge du dernier écoulement pyroclastique de l'éruption Pucón.

Le magma de Pucón a été probablement assez riche en volatils en profondeur pour pouvoir produire exsolution et fragmentation magmatique. Le dégazage de basse pression et la cristallisation rapide de microlites pourraient mieux expliquer les fragments denses, plutôt que le refroidissement instantané par l'eau externe, cependant celle-ci aurait pu jouer un rôle dans la pulvérisation d'abondante roche des

marges du conduit en l'élargissant progressivement. Cet effet a pu avoir été plus important au début des phases P1 et P2, et puis décroître, dû à la fonte progressive du glacier.

Même si une éruption de ce type n'est pas fréquente à l'échelle humaine, si une éruption de la taille de Pucón (IEV=5) avait lieu aujourd'hui, elle menacerait ~15,000-40,000 personnes directement à cause des écoulements pyroclastiques et, voir plus, par des lahars et des retombées de cendre associés. L'évolution de l'éruption Pucón montre qu'un épisode violent de type ignimbritique (P2), de courte durée mais grande magnitude, catastrophique a l'échelle régionale, peut intervenir après une pause de plusieurs semaines jusqu'à des mois, à la fin d'un période d'activité pyroclastique déjà importante (P1). Dans le cas de l'éruption Pucón, cette pause a marqué une phase d'ajustement dans les conduits en profondeur plutôt que la fin de l'éruption, ce qui devrait être pris en compte dans la surveillance d'un événement similaire aujourd'hui.

ACKNOWLEDGEMENTS

- ECOS/CONICYT Project N°C01U03 *"Relaciones entre procesos magmáticos y dinámica eruptiva en volcanes de composición basáltica de la provincia central de los Andes del Sur (37°-42°S)",* cooperation between IRD / Instituto de Geología Aplicada (IGEA, Universidad de Concepción, Chile) / Servicio Nacional de Geología y Minería (SERNAGEOMIN, Chile). 2002-2005
- Unité IRD *" Processus et Aléas Volcaniques"* UR 031, Laboratoire Magmas et Volcans (LMV), Université Blaise-Pascal (Clermont-Ferrand, France)
- PhD fund from the Programa MECE EDUCACION SUPERIOR, Departamento de Geología, Universidad de Chile (Santiago, Chile)
- IRD fund for PhD thesis "Bourse de Soutien de thèse de Doctorat"
- Servicio Nacional de Geología y Minería (SERNAGEOMIN, Chile)
- *Hans Van der Plicht* from the Centre for Isotope Research, Radiocarbon Laboratory (University of Groningen, The Netherlands) for the radiocarbon analyses and calibrations
- *Jo Cotten* from the Laboratoire de Pétrologie, Université de Brest Occidental (UBO, Brest, France) for the ICP-AES whole-rock analyses

Coté français

Je voudrais remercier *Olivier Merle* et *Pierre Schiano* du *Laboratoire Magmas et Volcans* (LMV) ainsi que *Pierre Henrard* et *Eliane Passemard* de l'*Université Blaise-Pascal*, pour m'avoir accueilli pendant trois ans avec toutes les facilités, la logistique et le plus important, avec ses gens… chercheurs, professionnels et personnel qui m'ont donné leur temps, disponibilité, connaissances et amitié. Je voudrais remercier spécialement à…

Jean Luc deVidal pour son aide technique avec les analyses à la microsonde électronique et dans la théorie et calculs des erreurs. *François Fauré* et *Jean Marque*, pour son aide technique au MEB. A *Christophe* pour la confection des lames minces. A *Pierre-Jean Gauthier*, pour sa disponibilité avec le matériel et la logistique des ateliers de scie et séparation, ainsi qu'à *Mireille* et *Mohammed* pour faciliter le matériel des labos. A *Didier Laporte* pour m'avoir accueilli dans le Labo de Pétrologie pour la confection des résines et les intéressantes discussions sur la vesiculation des magmas. A *Laurence Girolami* pour sa compagnie et aide sur le terrain au Villarrica. A *Nicholas Cluzel*, pour m'expliquer la confection des résines, les analyses d'images pour les déterminations de vesicularités et teneurs en microlites, pour les intéressantes discussions et son amitié.

A tout le cours *DEA 2003-2004* pour l'inoubliable séjour aux volcans d'Italie. A tous mes copains et copines du labo (*Stéphanie*, *Perrine*, *Silvana, Erwan, Séverine M., Yo, Pierre, Marc Alban, Bergrun, Yvonne, Muriel*, *Séverine J., Géraldine, Daniel, ETC.*) pour tous les petits services de tous les jours, pour sa bonne disposition et amitié de tous ces années en faisant tellement agréable mon séjour à Clermont.

A *Hervé Martin,* pour m'accueillir au sein du LMV et me donner les facilités pour les démarches administratives avec bonne disposition et énorme qualité humaine. A *Alain Gourgaud,* pour son soutien et les intéressantes discussions sur le terrain. A *Benjamin Van Wyk de Vries,* pour m'avoir accueilli dans l'équipe de volcanologie avec bonne disposition et amitié.

A *Olivier Roche,* pour accepter faire parti du jury et pour tout son aide au labo de volcanologie physique. A *Jean-Louis Bourdier,* pour accepter faire parti du jury et pour son critique et constructif rapport qui a aidé à améliorer cette thèse.

A mon professeur *Claude Robin,* pour avoir cru en moi pendant tant d'années et pour son énorme soutien pendant tout ce temps, sans lequel, cette thèse n'aurait pas pu se réaliser. Pour ses enseignements, commentaires et critiques au labo et sur le terrain.

To my proffessor *Tim Druitt*, for accepting me as his student, for giving me a huge amount of knowledge about pyroclastic density currents and volcanology in the field and in the lab, always with enormous generosity, for teaching me the Bard's language and the scientific writing style, for allowing me the fantastic stays on Italian volcanoes and Montagne Noire.

A mes amis *Aissa*, *Catherine*, *Jean-Marque*, *Natalie*, *Ben* et *Nourdinne*, pour son amitié qui m'a beaucoup touchée. Vous êtes pour toujours dans ma mémoire, ainsi que l'aimé *Soleil* qui m'a accueilli généreusement à Clermont-Ferrand.

Lado chileno

Agradezco especialmente a mi profesor *Alfredo Lahsen* por aceptar co-guiar esta tesis, apoyarme y por sus valiosos e interesantes comentarios y críticas. A *Miguel Angel Parada*, *Carlos Palacios*, *Diego Morata* y *Reynaldo Charrier* por permitirme la realización de esta tesis en el Departamento de Geología. A *Cristina Maureira* por toda su ayuda con la parte administrativa, con su cariño siempre presente aún en las dificultades. A *María Rosa Rocco*, por su amor incondicional de verdadera madre.

A *Gerard Hérail* del IRD Chile por apoyar esta tesis con todas las facilidades logísiticas y humanas. Agradezco a *Nelda* por su diligencia y buena disposición con toda la logística y especialmente a *Sergio* por ayudarme y compartir largas campañas de terreno en el Villarrica, siempre con buena disposición, entusiasmo, humor y amistad. A *Hugo Moreno* y *José Antonio Naranjo* del SERNAGEOMIN por la colaboración científica especialmente en la enseñanza de la geología del volcán Villarrica, base sobre la cual fui capaz de reconocer la Ignimbrita Pucón, por facilitar las largas estadías en el Centro Volcanólogico Villarrica. A la señora *Alicia* por recibirnos en este centro, siempre con cariño de madre. A *Leopoldo López-Escobar*, por integrarme en el proyecto ECOS-CONICYT a través del cual fue posible echar a andar esta tesis.

A *Silke Lohmar,* por su compañía y colaboración en tantas jornadas de terreno, y en todas las oficinas por donde pasamos en Chile y en Francia, por las discusiones y por su amistad. *A Jorge Clavero* por aceptar ser parte del jurado, por darme la posibilidad de hacerme participar como co-guía de dos excursiones en la IAVCEI 2004, experiencia de valor incalculable para quien se forma en volcanología, por todas las interesantes discusiones y aportes volcanológicos en el Villarrica y en Santiago, por darme las facilidades con la finalización de esta tesis, y por sus críticas y constructivas correcciones del texto.

A todos los participantes de las salidas a terreno al Villarrica en el marco de la IAVCEI 2004 (intra- y post-meeting fieldtrips), especialmente a Michael García, Michael McCurry, Armin Freundt y Michael Branney, por sus interesantes comentarios, críticas y aportes a mi trabajo, siempre en ánimo constructivo, entusiasta y con la sincera intención de colaborar.

A *Mario Vergara* por aceptar ser parte del jurado y su constante apoyo con la realización de la tesis. A *Francisco Hervé*, por interesarse nuevamente en mi trabajo y por creer en mí durante tantos años, por su amistad y su sabiduría que me ayudan a cada momento.

A todos mis compañeros de doctorado y amigos, *Fabián, Negro, Cecilia, Poti, Christian, Mauri, Felipe,* por su amistad y apoyo de tantos años. A mis amigas de siempre, *Paula, Carie, Pele, Macas y Ceci* por su apoyo incondicional. A *Bruno* por su ayuda con el francés y su amistad. A mis primas, *Xime y Pauli*, por ayudarme con la impresión de las numerosas copias de la tesis y por su cariño de hermanas.

A toda la gente que habita en las faldas y alrededores de Villarrica, en las ciudades de Pucón, Villarrica, Licanray y Coñaripe, pero especialmente a la gente que habita a lo largo de cada valle que desciende del Villarrica: Palguín-Chinay, Voipir, Correntoso, Pedregoso, Chaillupén, Melilahuén, Cajón Negro, Zanjón Seco-Refugio por facilitar los accesos y por compartime sus experiencias de la vida diaria.

Debo olvidar a tanta gente… Mis disculpas…

Desde mucho antes de entrar en este proyecto, había quedado, al igual que muchos geólogos, prendada por el fascinante depósito de la Ignimbrita Pucón. Ya en mi magíster, demostré interés en las rocas más básicas y los depósitos de erupciones explosivas, luego la metodología tipo *Sherlock Holmes* de buscar pistas en el depósito de una erupción que ocurrió hace casi 4000 años con el fin de reconstruirla y volver a narrarla, terminó por devenir lo que me parece uno de los temas de estudio más hermosos y apasionantes que jamás haya conocido. En efecto y aun considerando todas las dificultades, puedo aseverar que se trata del tema de tesis que soñé para mí.

Agradezco profundamente a mi familia, hermanas, sobrinos, sobrinonieto y cuñados, y especialmente a mi padre Juan y mi madre Jovina, no por seguir el protocolo de los agradecimientos de una tesis sino porque en verdad, ellos han sido y son la fuerza motora de todo en mi vida. Este trabajo ha sido realizado con todo mi amor hacia ellos.

CONTENTS

FIGURES

TABLES

APPENDIXES

CHAPTER 1 Introduction

1.1 GENERAL BACKGROUND AND OBJECTIFS

Basic volcanism most typically produces effusion of lava and is not particularly explosive, the most explosive manifestations ranging from violent strombolian to hawaiian. However, some scarce, but highly explosive basic eruptions have been recognised (e.g., prehistoric eruptions at Masaya caldera (Nicaragua), 122 BC Etna eruption (Sicily, Italy), 1790 AD Kilauea eruption (Hawaii, USA), 1886 Tarawera eruption (New Zealand)), and the mechanisms of such activity remain poorly understood. This makes such events a very interesting subject to study. Moreover, the rapid ascent rates of basic magma means that the warning time between the onset of unrest and explosive eruption may be as short as a few hours (Houghton *et al*., 2004). Because such eruptions are atypical at most basic volcanoes, tourism and surrounding inhabitation bring increasing number of people onto them.

Villarrica Volcano (39°25'S, Chile, Figure 2.1) is an extremely active (more than 49 eruptions from 1558; Petit-Breuilh, 1994; Lara, 2004a) mainly basaltic to andesitic stratovolcano located in an increasingly inhabitated zone. Similar to other volcanoes of the central volcanic province of the Southern Andes (37°-42°S, e.g. Stern, 2004; Figure 2.1), Villarrica Volcano has shown recurrent postglacial explosive activity, interspersed with the more usual effusive activity (e.g. Moreno, 1974; Lopez-Escobar, 1995). These explosive eruptions have produced large-volume pyroclastic density currents and caused the formation of calderas. The largest Holocene eruption of Villarrica Volcano produced the Pucón Ignimbrite (3.6 ka BP, 3 km^3), a complicated sequence of massive and stratified pyroclastic current deposits up to several tens of meters thick, which extend up to 21 km from the present-day summit. The Pucón Ignimbrite was first recognised by Moreno (1993), then studied in detail and mapped by Clavero (1996) (Figure 2.3). This very well preserved deposit is an ideal target for studying the eruptive dynamics, transport and emplacement mechanisms of large-volume pyroclastic currents of basic to intermediate composition, and to better understanding hazards associated with the emission of voluminous pyroclastic currents at this stratovolcano.

By applying the concepts and techniques of modern volcanology, this thesis aims to provide a detailed reconstitution of the 3.6 ka eruption that produced the *Pucón Ignimbrite* and to better understand the processes that led up to, and drove, the eruption. It is founded on previous studies of the general geology of the volcano (Moreno, 1993; Moreno *et al*., 1994; Moreno, 2000; Lara & Clavero, 2004; Moreno & Clavero, 2006) and of the deposits of the Pucón eruption (Clavero & Moreno, 1994; Moreno *et al*., 1994; Clavero, 1996).

More specifically, the two main goals of this study are: (1) to reconstruct the facies architecture of the Pucón Ignimbrite (definition of the main stratigraphic units; vertical analysis of units to provide information on the temporal evolution of the eruption; circumpherential or sectorial distribution of units;

radial variation of units in the different valleys; cross-valley variation of units; (2) to understand the dynamics of the eruption (eruptive style, intensity, number of eruptions or eruptive phases, eruptive duration and timing, triggering factors, etc).

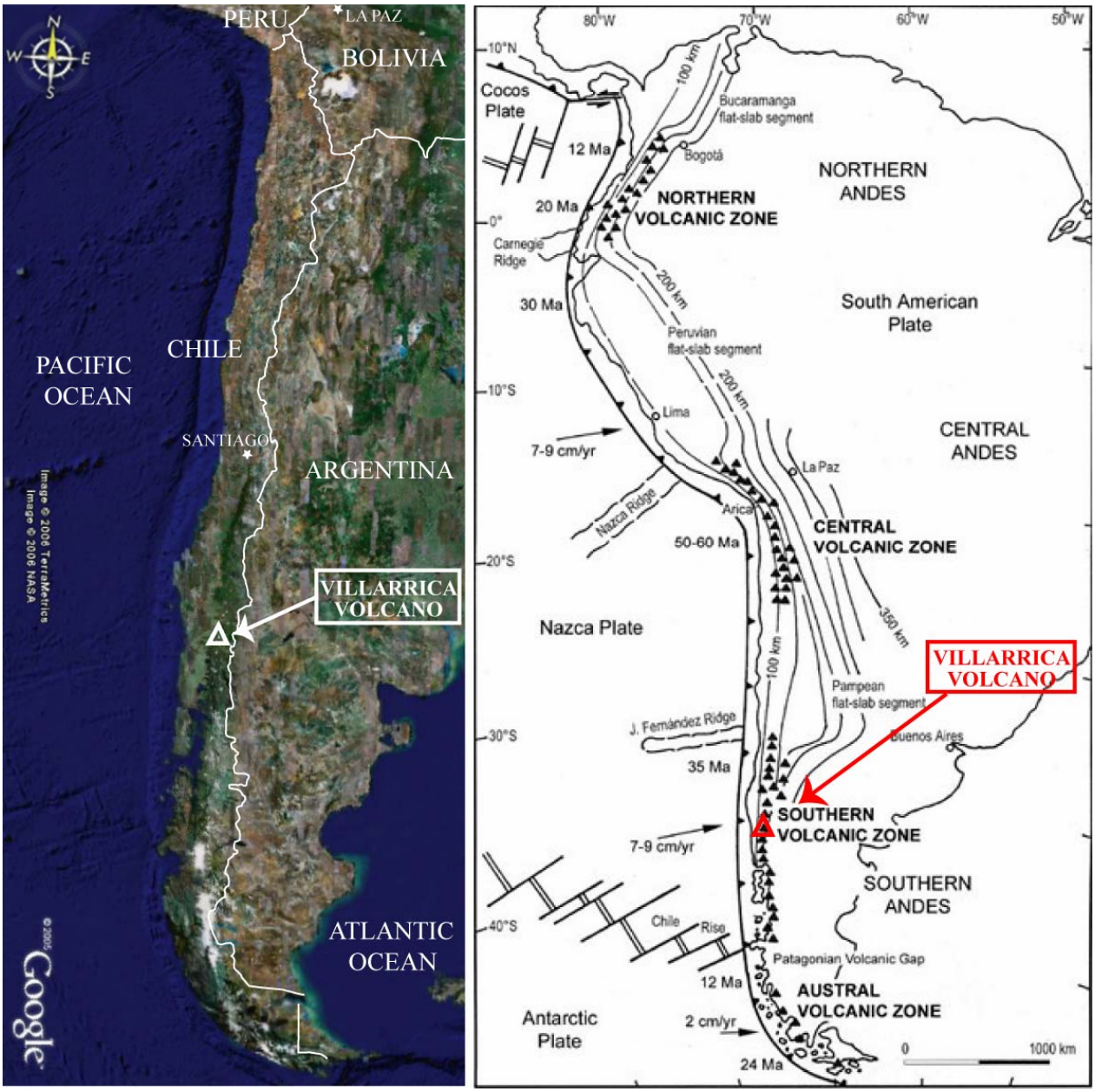

Figure 2.1: Satellite image (left) showing the location of Villarrica Volcano. Schematic tectonic map (right) of South America and the Pacific oceanic plates, showing the four volcanically active segments of the Andes, subduction geometry as indicated by depth in kilometers to the Benioff zone, oceanic ridges, ages of the oceanic plates close to the Perú-Chile trench, and convergence rates and directions along the length of the Andes (modified from Stern, 2004 and references therein).

1.2 METHODOLOGIES

1.2.1 Field work

Four field missions to Villarrica Volcano between 2003 and 2005 (about 120 days) involved detailed stratigraphic logging of about 70 outcrops, thickness measurements (for volume estimation), textural analyses and maximum particles size measurements, lithological counting, structural analysis of the different units of the deposit, including measurements of flow directions, dimensions of bed forms, etc., and study of the boundaries between the layers, with the aim of constraining some eruptive parameters such as timing and intensity.

Sampling in the field was carried out (1) for physical analysis (matrices of the deposits for grain size and lithological counting analyses; selected juvenile scoria for density measurements and SEM analyses), (2) for geochemical (whole-rock and glass composition) and textural analyses (microscope and SEM) of juvenile and accidental components, and (3) for ^{14}C dating of carbonised wood.

1.2.2 Laboratory work

Between 2003 and 2006, the following analyses were performed at the Laboratoire Magmas et Volcans (LMV), Université Blaise Pascal-CNRS-IRD, Clermont-Ferrand, over selected samples from key sections of the Pucón Ignimbrite.

- Grain-size analysis (drying, sieving, weighting) of 26 samples from 8 mm to 64 µm
- Lithological counting of about 40,000 fragments under binocular microscope for determining the scoria and lithic classes in 8 mm, 4 mm, 2 mm, 500 µm and 250 µm fractions
- Density measurements of 50 samples and another 16 samples analysed by the student M.Mercier
- Textural observations of 20 samples of juvenile lapilli and bombs by scanning electron microscope (SEM)
- Microlite content determination by SEM image treatment of 10 samples of juvenile lapilli
- Textural analyses of 10 thin sections of juvenile lapilli fragments by petrographic microscope
- Glass composition of major elements by electron microprobe analyses (CAMECA SX 100) of 31 juvenile and lithic clastsA specific petrologic technique was used in this study to precise the role of external fluids in the trigger of the eruption and the explosivity and quenching of the magma. The most vesicular expanded juvenile scoria and the densest juvenile clast of each of five different stratigraphic levels comprising the whole sequence were chosen for direct measurements of S, Cl and F contents in the matrix glasses using the electron microprobe (CAMECA SX 100). This allowed us to

test whether the dense clasts have higher volatile contents than the more vesiculated ones, suggesting quenching at depth by ground water.

Samples were also sent to other laboratories for the following analyses:

- Whole-rock composition (major and trace elements) of 84 juvenile and lithic clasts by Inductively Coupled Plasma-Atomic Emission Spectrometry (ICP-AES; Laboratoire de Pétrologie, Université de Brest Occidental UBO, Brest, France)
- Radiocarbon dating (^{14}C) of 4 samples of carbonised wood (Laboratory of Gronigen, Netherlands).

1.3 STRUCTURE OF THE THESIS

This thesis is organised into four main chapters. Abstracts in French and Spanish are added at the beginning of every chapter. In this first chapter, a general review is presented of the literature on ignimbrite-forming eruptions, especially basaltic to andesitic ignimbrites relevant to the Pucón Ignimbrite.

Under the title: *"Reconstruction of the basaltic andesitic 3.6 ka BP Pucón eruption, Villarrica Volcano, Southern Andes, Chile"*, the second chapter is the longest of the thesis. It includes the complete set of field data resulting from four field missions to Villarrica Volcano between 2003 and 2005, and uses these data to place constraints on (1) the number and intensities of the eruptive phases that compose the eruption, (2) extension of the different currents emitted, and as a consequence (3) threats posed by a similar eruption to the different sectors around the volcano.

In the third chapter: *« Dynamics of the basaltic andesitic Pucón eruption (3.6 ka BP, Villarrica Volcano, Chile)*", different physical and chemical data (component data, macro and microscopic scoria textures (by optical microscope and SEM) and whole-rock of juvenile and juvenile-suspected fragments), were used to (1) determine the juvenile components of the ignimbrite and accidental components related to the eruption, and (2) to constrain some characteristics of the fragmentation level, magma body and ascent.

The fourth chapter "*The role of fluids in the basaltic andesitic Pucón eruption (3.6 ka BP, Villarrica Volcano, Chile)*" attempts to clarify the role of external fluids in the explosivity of the magma and in the triggering of the eruption, based on microlite content data (by SEM imagery), density/vesicularity data and glass composition.

The second, third and fourth chapter follow the format of articles to be submitted to international journals.

1.4 REVIEW ON IGNIMBRITES AND PYROCLASTIC DENSITY CURRENTS

Explosive fragmentation of gas-rich magma and its ejection into the atmosphere is one of the most violent manifestations of terrestrial volcanism. Such events commonly involve the formation of pyroclastic density currents. After the dramatic death toll of 29,000 in the town of St. Pierre (Martinique, Lesser Antilles, France) in 1902 by the devastating pyroclastic density currents from Montagne Pelée, this phenomenon was perceived as highly dangerous and studies of this and other historical eruptions allowed the recognition of abundant ignimbrites in the geological record, many of them orders of magnitude larger in volume (Freundt *et al.*, 2000). However, a few volcanic products have been misinterpreted for so long and the acceptation of welded ignimbrites as pyroclastic flow deposits took until the 1960s (Cas & Wright, 1987; Freundt *et al.*, 2000). The 1980 eruption of Mount St Helens (Washington, USA) provided volcanologists with abundant new data (Fisher & Schmincke, 1984).

This section is mainly focused in general features of pyroclastic density currents or particularly about those produced during "dry" (i.e. purely magmatic) eruptions. A special section about phreatomagmatism is presented in Chapter 4.

1.4.1 Explosive fragmentation

(Cas & Wright, 1987 and references therein)

Dissolved magmatic volatiles affect the nature of volcanic eruptions in terms of whether they are explosive or non-explosive. The dominant volatile component is water; carbon dioxide is also an important early exsolving volatile phase in basalts. The solubility of volatiles in magma is partly controlled by confining pressure, thus their solubility decreases as the magma rises to shallower crustal levels. At a certain depth, the solubility will decrease sufficiently for volatiles to begin exsolving from the magma and form a separate fluid phase. The depth at which this occurs depends on the magma type, the actual volatile content and the vapour pressure of the dissolved volatiles relative to the confining pressure. The higher the magmatic volatile content, the higher the vapour phase exerted and the greater the depth at which exsolution will begin. This exsolved phase has a vapour pressure which has the potential to explosively disrupt the magma if it continues to increase. The term **pyroclastic** describe explosive eruptions and products.

Prominent explosive eruptions of the last two centuries include those of Tambora (east of Java, Indonesia) in 1815, Krakatau (west of Java, Indonesia) in 1883, Katmai (Alaska, USA) in 1912, Mount St Helens (Washington, USA) in 1980, El Chichón (Chiapas, Mexico) in 1982 and Mt Pinatubo (Phillipines) in 1991.

1.4.2 Definitions

Pyroclastic density current is general term for hot, inhomogeneous mixtures of volcanic particles and gas (with or without free water) that flow across the ground under the influence of gravity (Druitt, 1998; Branney & Kolelaar, 2002). Pyroclastic density currents probably encompass the continuous spectrum of pyroclastic flows and surges, having any concentration up to about 45 vol. % solids (Branney & Kokelaar, 2002).

A ***pyroclastic flow*** forms a predominantly massive, poorly sorted ash-rich pyroclastic density current deposit that thicken markedly into depressions (Fisher & Schmincke, 1984; Druitt, 1998; Freundt *et al*., 2000; Branney & Kokelaar, 2002). It is used as the general term (similar to pyroclastic density current) by some authors (Fisher & Schmincke, 1984) and as the high-concentration, non-turbulent end-member of pyroclastic density currents spectrum by others (Druitt, 1998; Branney & Kokelaar, 2002).

A ***scoria flow*** is a type of pyroclastic flow formed by column collapse and rich in moderately vesicular components. A ***pumice flow*** is a type of pyroclastic flow formed by column collapse and rich in highly vesicular components.

Pyroclastic surges are low-concentration (dilute) currents in which clast support is by fluid turbulence and clast interactions are negligible (Branney & Kokelaar, 2002). A pyroclastic surge forms a well stratified (parallel and low-angle cross-stratified), typically small-volume and topography-draping deposit that is better sorted than a pyroclastic flow deposit (Druitt, 1998; Freundt *et al*., 2000; Branney & Kokelaar, 2002). Surge deposits can also contain massive facies (Branney & Kokelaar, 2002).

The term ***ignimbrite*** was **i**ntroduced by Marshall (1935) and since used in many ways. This term refers to the rock or deposit formed from pumiceous pyroclastic flows (Sparks *et al.*, 1973; Druitt, 1998; Freundt *et al.*, 2000, Branney & Kokelaar, 2002). Ignimbrites are called ***ash flow tuffs*** in the U.S. literature due to their dominance of ash. They are vast, landscape-modifying and form by sedimentation from catastrophic pyroclastic density currents (Branney & Kokelaar, 2002). Ignimbrites are more generally considered as all deposits formed by the emplacement of pyroclastic flows (Fisher & Schmincke, 1984) or large volume pyroclastic flows (Sparks *et al*., 1997).

More commonly, but not necessarily, dominated by poorly-sorted massive lapilli tuff, an ignimbrite comprises various massive and stratified pumiceous lithofacies, as well as subordinate pumice-poor lithofacies, e.g. lithic breccias and massive agglomerates (Branney & Kokelaar, 2002).

Block and ash flows generally form small-volume pyroclastic flow deposit characterized by a large fraction of dense to moderately vesicular juvenile blocks in a medium to coarse ash matrix of the same composition (Fisher & Schmincke, 1984; Freundt *et al*., 2000; Branney & Kokelaar, 2002). The term ***nuée ardente*** was used in the 1902 eruption of Montagne Pelée (Martinique, Lesser Antilles, France) and refers to small-volume block and ash flows produced by the collapse of an active lava flow or dome (Cas & Wright, 1987).

1.4.3 Generation mechanisms, types and settings of pyroclastic density currents

Pyroclastic density currents may be short-lived (highly unsteady) or relatively long-lived (sustained unsteady to quasi-steady) phenomena and according to their origin, they have been categorized into the follwing types (Druitt 1998; Branney & Kokelaar 2002).

(i) Fallback or sustained fountaining of eruption columns (Fisher & Schmincke, 1984; Cas & Wright, 1987; Druitt, 1998; Freundt *et al.*, 2000; Branney & Kokelaar, 2002 and references therein)

This mechanism generates scoria flows, pumice flows or ignimbrites and can be subdivided into:

Short-lived vulcanian columns: The products are restricted in volume and extent. Examples: St Vincent 1902 (Lesser Antilles, Saint Vincent and the Grenadines), Ngaurohoe 1975 (New Zealand), Mount St Helens 1986 (Washington, USA), Montserrat 1997 (Lesser Antilles, UK).

High plinian columns: Moderate- to large-volume ignimbrites are believed to form by the partial or total collapse of high columns during plinian eruptions (Walker, 1981). If the gas-thrust jet leaving the vent with a bulk density of about 10 kg/m^3 becomes sufficiently dilute by air entrainment to become buoyant, it forms a subplinian or plinian eruption column. If, however, the rate of entrainment is insufficient (wider vent diameter, lower magma water content) the particulate dispersion becomes gravitationally unstable and collapses as a fountain, generating pyroclastic density currents. Evidence for the column collapse mechanism is provided both by theoretical modelling and by the high observed mobility of ignimbrite-forming pyroclastic flows. Eruptions that terminate before column collapse conditions are reached will only produce plinian fall deposits.

Even if a common sequence of activity (Sparks *et al*., 1973) includes a plinian fallout phase followed by a pyroclastic flow-phase, a number lines of evidence show that column collapse is not irreversible and that buoyant plinian plumes and fountain collapse can take place together from the same vent (e.g. Laacher See, 1912 (Germany); Novarupta, 1980 (Alaska, USA); Mount St Helens, 1991; Pinatubo, 1800 yr BP (Philippines); Taupo (New Zealand) and 0.76 Ma Bishop Tuff (California, USA)). This includes geologic evidence of multiple flow units intercalated within fallout beds,

historical evidence for simultaneous plinian and ignimbrite-producing activity and recent results from numerical modelling. It therefore appears that substantial volumes of ignimbrite can be generated synchronously with a sustained high plinian column (Wilson & Hildreth, 1997).

Pyroclastic surge deposits are a common subordinate lithofacies in ignimbrite successions. Pyroclastic surges can be generated at the leading edges of pyroclastic flows (**ground surges**) and by the billowing ash clouds overriding pyroclastic flows (**ash cloud surges**). These associated surges can be deposited as veneer facies in some landscape-mantling ignimbrites.

Boil-over and plinian-fall-absent ignimbrites: An eruption in which plinian fallout occurred during pyroclastic fountaining could produce ignimbrites that apparently lack associated plinian pumice-fall layers. However, a low, sustained fountaining without development of a tall well defined eruption column could also produce ignimbrites lacking associated plinian fallout if the eruptive mixture is too dense ("boil over" eruptions, e.g. possibly Cerro Galán ignimbrite in the Central Andes, Argentina).

(ii) Lateral blast (Druitt, 1998; Branney & Kokelaar, 2002 and references therein)

A pyroclastic surge called a lateral blast is generated by sudden decompression of highly pressurised magma, which can be strongly directed due to the flank collapse of a stratovolcano (such as Mount St Helens or Bezimiany (Kamchatka, Russia)), or lava dome (such as Soufrière Hills, Lesser Antilles). Run out distances can achieve 25 km. Lateral blasts have short durations and they do not produce large-volume deposits.

(iii) Collapse of lava domes or flows (Fisher & Schmincke, 1984; Druitt, 1998; Freundt *et al*., 2000; Branney & Kokelaar, 2002 and references therein)

Block-and-ash flows form by partial or total collapse of lava domes. Collapse can be gravitational, explosive or both. The low mechanical strength of hot microvesicular lava provokes its rapid transformation into dusty block-and-ash flows. Block and ash flows can also form by collapse of vulcanian eruption columns. They tend to develop overriding low-concentration dispersions (ash cloud surges) by rapid generation and segregation of relatively fine pyroclasts from underlying relatively high-concentration debris falls and granular flows. Examples: Santiaguito (Guatemala), Merapi (Java, Indonesia), Mount Unzen (Japan), Montserrat (Lesser Antilles, UK).

(iv) Collapse of lava lakes

Pyroclastic flows during the 1993 eruption of Arenal volcano (Costa Rica) formed by the collapse and rapid drainage of a lava lake (Alvarado & Soto, 2002).

1.4.4 Physical parameters of pyroclastic density currents

Velocities (Fisher & Schmincke, 1984; Druitt, 1998 and references therein)

Pyroclastic dispersions are compressible fluids that can exit the vent as sonic to supersonic overpressured jets (Branney & Kokelaar, 2002). The front of the 1980 Mount St Helens (Washington, USA) lateral blast travelled at up to 540 km/h, but the internal speed may have reached 846 km/h. Small pyroclastic flows travel at speeds up to a few hundreds of kilometres per hour (measurements of 108 km/h in Mount St Helens 1986, 216 km/h in Montserrat 1997 (Lesser Antilles, UK) but 36 km/h near their distal limits, up to 110 km/h in Merapi (Java, Indonesia) and up to 160 km/h or more in Mt St Pelée (Lesser Antilles, France)).

Run out (Fisher & Schmincke, 1984; Cas & Wright, 1987; Druitt, 1998; Freundt *et al*., 2000 and references therein)

Ignimbrite-forming pyroclastic currents travel large distances (up to *ca.* 200 km) over gentle slopes as small as a few degrees and they can traverse high topographic barriers (up to 1500 m) at tens of kilometres from the vent. On the other hand, small pyroclastic flows (block and ash flows or small pumice flows) typically travel from a few hundred metres up to 10 km from source and across a plain can confine themselves by forming lateral levées and terminate in lobes with steep flow fronts (e.g. Mount St Helens post-19 May flows). In density-stratified currents, dense underflows or pyroclastic flows *ss.* may travel further than the suspension current itself.

The Mount St Helens lateral blast surge travelled up to 25 km before becoming buoyant to form a large umbrella cloud. Some of the 1991 preclimactic surges at Pinatubo (Philippines) travelled as far as 14 km. The runout distance of base surges rarely exceeds a few kilometres.

The high velocities and ability of pyroclastic flows to move on low slopes and over obstacles are indication of their high mobility. One measure of the flow mobility is the ratio of vertical height (H) to horizontal distance (L) travelled.

Areas, thickness and volumes (Fisher & Schmincke, 1984; Cas & Wright, 1987; Freundt *et al*., 2000; Branney & Kokelaar, 2002 and references therein)

According to volumes emitted, pyroclastic density currents can be subdivided into three groups:

- Small volume (0.001 - 1 km^3) currents (typically rhyolitic to basaltic in composition), in all settings but typical of magmatic arc systems such as 1902 Mt. Pelée, 1968 Mount Mayon (Philippines), 1976 Augustine volcano (Alaska, USA), 1980 Mount St. Helens and 1982 El Chichón (Chiapas, Mexico). They tend to form valley-fill deposits. Block-and-ash flow deposits are about 1-10 m thick and thin to 1-2 m at their lobate fronts. Ash cloud surge deposits are typically <1 m thick. Accompanying ash

cloud surges can reach a wider areal distribution compared to the valley-confined block-and-ash flows.

- Medium volume (1 - 100 km^3) current deposits (typically rhyolitic to basaltic), from larger stratovolcanoes such as Taupo Ignimbrite (30 km^3, New Zealand), Minoan Ignimbrite (30 km^3, Greece), 1815 Tambora (25 km^3, Indonesia), 1883 Krakatau (12 km^3, Indonesia) and AD 79 Vesuvius (4 km^3, Italy).
- Large volume (100 - 5000 km^3) ignimbrites, typically calc-alkaline rhyolitic to dacitic and alkaline and compositionally zoned, are normally restricted to continents and large islands and associated with large calderas (see below). Conspicuous examples of large volume ignimbrites are Fish Canyon Tuff (3000 km^3; Colorado, USA), Toba Tuff (2000 km^3; Sumatra, Indonesia) and Cerro Galan ignimbrite (1000 km^3; Central Andes, Argentina). They tend to form extensive sheets, shields or fans covering up to 45,000 km^2.

In most plinian ignimbrite-forming eruptions, the resulting ignimbrite exceeds the plinian deposit in volume, examples being Crater Lake (Oregon, USA) and Bandelier Tuff (New Mexico, USA; Walker, 1981).

Temperatures and cooling

Dense pyroclastic flows conserve heat very efficiently (Fisher & Schmincke, 1984). Owing to the low thermal conductivity of ash (Ryan *et al.*, 1981) and because only the surface of the flow mixes with cold air during flowage (Boyd, 1961 in Fisher & Schminke, 1984), pyroclastic flow deposits can remain at near-magmatic temperatures for long times. Cooling from emplacement to ambient temperature may take many years, depending on the thickness of the deposit and the emplacement temperature (Fisher & Schmincke, 1984). Premature cooling of surface layers can occur if subjected to strong rain (Hoblitt *et al*. 1985).

Emplacement temperatures of pyroclastic density currents have been directly measured both shortly and some years after the eruption and some examples are shown in Table 1.1.

For older deposits, temperatures are inferred from:

- Thermoremanent magnetization: For example, deposition temperatures in excess of 450°C determined in the submarine facies of the 1883 Krakatau ignimbrite (Indonesia; Freundt *et al.*, 2000).
- Charring of wood: Charcoalization of wood takes place by chemical transformation and volatile loss in the absence of oxygen. The temperature necessary for charcoalization has been estimated in ~200 °C (Scott and Glasspool, 2005). Charred wood within and at the base of the 79 AD pyroclastic flow deposits from Vesuvius (Italy) indicates that they were at ~300°C (Maury, 1973 in Fisher & Schmicke, 1984).

- Charcoal reflectance: This is useful as a temperature proxy for ancient pyroclastic flow deposits, as demonstrated recently by Scott & Glasspool (2005) on block-and-ash-flow deposits from Soufrière Hills. This is particularly useful where magnetic or mineral data are absent and also in reworked deposits; however, only a minimum temperature can be inferred where the heating duration of the deposit is unknown (Scott & Glasspool, 2005).
- Presence of degassing pipes: Even if gas pipes are usually interpreted as indication of high-temperature emplacement, they are also described in lahars emplaced at temperatures of <400°C and in other lahars which seem to have been cold (Fisher & Schmincke, 1984).
- Softening and welding of glass shards and pumice (Fisher & Schmincke, 1984).

Temperatures of up to 250°C have been estimated for the Mount St Helens blast surge deposits (Banks & Hoblitt, 1981).

Table 1.1: Some examples of measured temperatures of pyroclastic flow deposits

DEPOSIT	VOLCANO	TEMPERATURE MEASURED (°C)	TIME AFTER EVENT	REFERENCE
pyroclastic flow	St Augustine (Alaska, USA)	up to 600°C at 5 m depth	a few weeks	Kienle & Swanson, 1980 in Fisher & Schmincke, 1984
1997 block-and-ash flows	Soufrière Hills (Montserrat, UK)	up to 640 °C	20 days	Cole *et al*., 2002
1980 pyroclastic flows	Mount St Helens (Washington, USA)	750-850°C near the vent 300-730°C farther away	up to five months	Banks & Hoblitt, 1981 in Fisher & Schmincke, 1984
1991 pyroclastic flows	Mount Pinatubo (Philipines)	390°C, 1 m below surface	1.5 years	Torres *et al.*, 1996
1912 ash flows	Novarupta (Alaska, USA)	up to 645°C	7 years	Allen & Zies, 1923 in Fisher & Schminke, 1984

Duration

Nine historical plinian eruptions (with or without ignimbrite formation) lasted from a few hours to 4 days, typically about a day and rarely shorter than an hour or longer than two days (Walker, 1981 and references therein). A plinian column can develop within minutes of the commencement of the eruption (Hekla, 1947, 1970), in other cases the eruption may proceed at a moderate intensity for about one hour (Tarawera 1886, New Zealand) or some weeks (Krakatau 1883, Indonesia) before becoming plinian (Walker, 1981). In about 30% of plinian pumice occurrences, the pumice is immediately overlain by an ignimbrite with no evidence for any significant time interval between their formation, examples being Crater Lake (Oregon, USA), Granadilla (Tenerife, Canary Islands, Spain) and Taupo in New Zealand (Sparks *et al.*, 1973; Walker, 1981). Column collapse during ignimbrite-forming eruptions could last just a few minutes such as Taupo (Wilson 1985; Dade & Huppert 1996) up to several hours such as Katmai (Alaska, USA; Fierstein & Hildreth 1992) or Pinatubo (Philippines; Scott *et al*. 1996). It should be emphasised, however, that not all ignimbrites are preceded by a plinian pumice and in some cases the

ignimbrite-forming conditions are preceded by a phreatomagmatic phase (Waimihia (New Zealand), Minoan (Greece) and Rabaul (Papua New Guinea) ignimbrites; Walker, 1981).

The length of a prehistoric plinian eruption can be estimated by studying the distribution of finer beds and this approach yields 6 to 17 hours for the Taupo plinian pumice (Walker, 1980). Knowing the total discharge, the study of explosive eruption dynamics allows estimation of eruption duration which yields times of the same order as those observed in historical eruptions (Walker, 1981). To estimate the duration of prehistoric ignimbrite-forming eruptions is often difficult unless the ignimbrite is interbedded with fall deposits, in which case the relative timing of events can be determined by the method used by Wilson & Hildreth (1997). The method uses fallout isopleths to infer the eruption column height following Carey & Sparks (1986), which is then compared with plinian deposits having known volumes, discharged rates and duration. In the case of the Bishop Tuff (California, USA), a high plinian plume was sustained and fall and flow activity proceeded together throughout the emplacement of hundreds of cubic kilometres of tuff; the method yields an eruptive duration of about 4 days, including an eruptive break (Wilson & Hildreth, 1997).

Models developed by Bursik & Woods (1996) suggest that many extensive ignimbrite sheets derive from eruptions with mass fluxes of 1-10 million tonnes per second for up to 28 hours. Eruption durations for the Bishop and Bandelier (New Mexico, USA) tuffs are estimated at about 28 hours by this method, whereas the 30 km^3 of the Taupo ignimbrite is supposed to have erupted over 20-30 minutes with steady-state flow at 150-200 m/s.

When interbedded fall deposits are absent, the relative timing of successive flow units in ignimbrites can be inferred by careful observation of the contacts. Some examples include:

- The base of an ignimbrite flow unit can exhibit welding where it overlies a previous still-hot unit (Wilson & Hildreth, 1997).
- A flow unit emplaced above another thick densely-welded unit can be vapour-phase-altered and recristallized. In contrast, the same flow unit emplaced above thin moderately- to non-welded flow unit or fall deposits can remain glassy. This implies that degassing of the thick welded flow unit during its cooling and devitrification also altered the overlying flow unit (Wilson & Hildreth, 1997).
- The systematic sharp truncation of degassing pipes at the base of a flow unit which are rooted in the underlying unit shows that the temperature of the lower deposits dropped below that necessary for charcoalization (~200 °C; e.g., Scott and Glasspool, 2005), thus implying an eruptive pause. Considering the time of cooling of pyroclastic flows (Table 1.1), a minimal estimation of the eruptive pause time can be supplied. Inversely, degassing pipes systematically traversing contacts is an

indication of emplacement of successive flow units on a timescale too short for significant surface cooling.

1.4.5 Geometry, facies variations, structures and textures of pyroclastic density currents

Aspect ratio and response to topography

Pyroclastic flow deposits and ignimbrites spread out in fan-like lobes. They typically pond to great thickness in valleys and topographic lows and disappear on topographic highs or grade into thin veneers that drape interfluves and upland plateaus (Fisher & Schmincke, 1984; Druitt, 1998; Freundt *et al*., 2000). The 1991 ignimbrite at Pinatubo (Philippines) infilled and deeply buried incised slopes and pre-existing river valleys; peaks of the former highlands were left protruding out of the ignimbrite fans like isolated islands (Torres *et al*., 1996).

Large, widespread and topographically unconfined ignimbrites normally associated with calderas can form extensive radial sheets that completely bury and smooth out the pre-eruptive topography (Fisher & Schmincke, 1984; Druitt, 1998; Freundt *et al*., 2000). The top is usually flat and either horizontal or inclined downstream at a few degrees (Fisher & Schminke, 1984; Druitt, 1998). Ignimbrite sheets gradually thin toward their distal edges and can be later dissected by erosion to form upstanding plateaus (Fisher & Schmincke, 1984).

A quantitative description of ignimbrite geometry is provided by its **aspect ratio** (Walker *et al.* 1980; Walker 1983 in Druitt, 1998), defined as the ratio of the average thickness to the diameter of a circle equal in area to the deposit. Low-aspect-ratio ($<10^{-5}$) ignimbrites (e.g. Taupo) are thin and widespread with extensive veneer facies that drape upland regions, whereas high-aspect-ratio ($>10^{-2}$) ignimbrites (e.g. VTTS and Pinatubo) are thick and not widespread, being largely confined to valleys and open plains (Druitt, 1998; Freundt *et al*., 2000).

Pyroclastic surges spread to a greater degree over topography than pyroclastic flows. Their deposits thicken and coarsen into topographic lows and thin toward valley margins (Fisher & Schmincke, 1984).

Facies variations

A **facies** or **lithofacies** is a body or interval of rock or deposit which has a unique definable character according to some combination of stratification, grain size, grain shape, sorting, fabric and composition, and which is the product of a unique set of conditions in the depositional environment (Cas & Wright, 1987; Branney & Kokelaar, 2002). Branney & Kokelaar (2002) present an exhaustive review of the wide spectrum of lithofacies found in ignimbrites and their interpretations, using the term lithofacies in a non-genetic sense.

Being mostly massive, ignimbrites can contain variably bedded, tractionally formed deposits close to the vent (e.g. Roccamonfina (Italy), Laacher See (Germany), Taupo (New Zealand), Novarupta 1912 (Alaska, USA), Pinatubo 1991 (Philippines)) or on steep flow paths (Mount St Helens 1980 (USA) and Neapolitan Yellow Tuff (Italy); Freundt *et al.*, 2000).

Where an ignimbrite-forming current was able to surmount interfluves, two main facies that can merge into each other are usually seen (e.g. Taupo, Laacher See):

- Landscape-modifying valley-ponded ignimbrite facies with thick massive poorly-sorted lapilli- and lithic-rich beds such as Laacher See (Fisher & Schmincke, 1984; Freundt *et al.*, 2000).
- Landscape-mantling **ignimbrite veneer** facies with thin lapilli- and lithic-poor beds traceable into ponded thick beds as a "tail" deposit left in the wake of a pyroclastic flow (Walker *et al.* 1980 in Fisher & Schmincke, 1984) or left by the upper, more dilute levels of the current. For example, the initial blast of Mount St Helens surmounted barriers up to 600 m and left debris-mantled slopes (Hoblitt *et al.*, 1981 in Fisher & Schmincke, 1984). A carpet of lag-pumice blocks can occur (e.g. Laacher See, Mount St Helens, Freundt *et al.*, 2000). Ash layers can be elutriated and deposited as overbank ash layers overlying the valley-fill ignimbrite (e.g. Mount St Helens, Freundt *et al.*, 2000).

Correlation between both channel-fill and overbank facies becomes almost impossible with increasing distance from the vent where this segregation does not occur (Freundt *et al.*, 2000).

Flow units can be bounded by steep pumice-block levées distally (e.g. Laacher See, Mount St Helens, Freundt *et al.*, 2000), on upper slopes or along the outer edge of sinuous channels (Fisher & Schmincke, 1984).

Internal stratigraphy

The basal contact of a pyroclastic flow deposit can be unconformable where the currents was able to erode its substrate, e.g. close to the vent, on steep slopes, on soft substrate, through narrow channels or where the flow contains abundant lithic blocks (Freundt *et al.*, 2000).

Most pyroclastic flow deposits are poorly sorted and massive but may show subtle grading, alignment bedding or imbrication of particles. Layering can be defined by graded basal zones, discontinuous trains of large fragments, alternating coarse- to fine-grained layers, crude orientation of elongated or platy particles and by color or compositional changes (Fisher & Schmincke, 1984).

Most pyroclastic surge deposits are thinner, finer-grained and better sorted than pyroclastic flow deposits (Fisher & Schmincke, 1984). Surge deposits commonly exhibit planar, wavy, lenticular and low-angle cross-stratification, while others are massive, inverse or normally graded (Fisher & Schmincke, 1984; Druitt, 1998). For example, the blast surge deposit of Mount St Helens is massive in depressions

and stratified on ridge tops (Druitt, 1998). Surge deposits have a characteristic bipartite layering with a coarse, fines-poor layer overlain by a thinner fines-rich one. They exhibit a variety of bedforms, commonly low-angle downstream or upstream migrating sandwaves that decrease in size away from the vent (Druitt, 1998).

In the case of non-aggradational ignimbrites (see section 8 below) grading textures allow subdividing them into **flow units** defined as depositional units that represent a single or discrete current deposited in one lobe that may follow one another within minutes or hours (Fisher & Schmincke, 1984; Branney & Kokelaar, 2002). Ignimbrites are often composed of flow unit packages whose recognition should be done carefully because (Freundt *et al.*, 2000):

(i) Single flow units can split into two or more thinner ones laterally, due to splitting into lobes or pulsatory motion of the pyroclastic flow. It is useful therefore to distinguish between *vent-derived* flow units and *locally-derived* flow units.

(ii) Breaks or bedding surfaces may just record impersistent or unsteady deposition during the passage of a sustained current that has aggraded progressively (Branney & Kokelaar, 2002).

(iii) Welding compaction and rheomorphic deformation can obliterate depositional contacts.

The **standard ignimbrite flow unit** (Sparks *et al.*, 1973) comprises three layers which represent different regions within a pyroclastic density current:

Layer 1 is interpreted as the deposit laid down at the highly dynamic flow front or head where intense mixing with ambient air occurs (Fisher & Schmincke, 1984; Freundt *et al.*, 2000). The most common are the **lithic-rich ground layers** (or layer 1(H)) which are enriched in segregated heavy components (lithics, crystals), ranging from fines-depleted lithic breccias to thin lithic-rich ash beds. **Pumice-rich ground layers** (e.g. Taupo ignimbrite) are rich in pumice and fine ash, and are thought to be deposited from material jetted ahead of the advancing flow. **Ground surges** lay down fines-poor, laminated, cross-bedded and lithic- or pumice-rich deposits ahead of the current (Freundt *et al.*, 2000).

Layer 2 is interpreted as the deposit of the main body of the flow, and it is composed of a basal boundary layer formed by interaction of the flow with the substratum (**layer 2a**) overlain by the main body of the flow unit (**layer 2b**). Layer 2a is often reversely graded ash in sharp contact or gradational transition with layer 2b. Layer 2b is characterised by reverse coarse-tail grading and upward enrichment of pumices and normal coarse-tail grading and downward enrichment of lithics (Fisher & Schmincke, 1984; Freundt *et al.*, 2000).

Layer 3 is an ash fall deposit interpreted to have settled from the overriding dilute ash cloud. If the emplacement of successive flow units is faster than the rate of ash fallout, layer 3 is not associated with

each flow unit and is present only on top of the entire ignimbrite. If the ash cloud has plinian-like dimensions (phoenix cloud), layer 3 becomes a very extensive **co-ignimbrite ash** deposit (Freundt *et al.*, 2000).

In flow units of block-and-ash flow deposits a block-free basal layer and normal or reverse coarse-tail grading of blocks can be present. Levées and flow fronts enriched in pumice boulders are commonly present in flow units laid down by pumice flows (Freundt *et al.*, 2000).

Lag breccias

A **lag breccia** (Druitt, 1998), **co-ignimbrite lag-fall deposit** (Wright & Walker, 1977), **co-ignimbrite lag breccia** (Druitt & Sparks, 1982), **lithic breccia** (Scott *et al.*, 1996), **co-ignimbrite lithic breccia** (Allen & Cas, 1998), **lithic lag breccia** (Freundt *et al.*, 2000) or **proximal lithic breccia** (Branney & Kokelaar, 2002) is a proximal, commonly clast-supported bed of lithic blocks with a matrix variably depleted in fine ash. Lithic blocks can be rounded and fragile, and dominated by vent-derived wall rocks (Freundt *et al.*, 2000). Lithic breccias can persist far from source and show clast alignment, imbrication, large segregation pipes, bedforms and irregular piles probably dumped in a disorganized manner by flow instabilities (Druitt & Sparks, 1982; Druitt & Bacon, 1986).

Lag breccias are commonly separated from ignimbrites by erosional unconformities (Freundt *et al.*, 2000) or longitudinally grade into the lithic-rich bases of layer 2b (Cas & Wright, 1987), the ground layer (Taupo Ignimbrite (New Zealand), Walker *et al.*, 1981), matrix-supported breccias and coarse pumiceous ignimbrite with complex stratigraphic interrelationships (Santorini (Greece), Druitt & Sparks, 1982) or are deposited near the top of the ignimbrite (Pinatubo (Philippines), Scott *et al.*, 1996). Similar compositional zoning proves that lag breccia and ignimbrite accumulated simultaneously, each batch depositing first lag breccia, then ignimbrite (Wright & Walker, 1977; Druitt & Bacon 1986).

A lithic breccia is composed of lithic clasts too coarse or too dense to be transported by the pyroclastic flows (Wright & Walker, 1977; Druitt & Sparks, 1982; Druitt & Bacon, 1986; Mellors & Sparks, 1991; Rosi *et al.*, 1996; Druitt, 1998). More specifically, the origin could be by fall (Acatlán ignimbrite (Mexico), Wright & Walker, 1977) or flow processes (Santorini, Druitt & Sparks, 1982).

Lapilli pipes

Lapilli pipes are mostly subvertical, narrow, vitric-ash-depleted, lithic- and crystal-rich channels preferentially formed in the upper part of layer 2, above wet ground or charcoalised wood. They form after flow emplacement by the localised gas escape that elutriates fine vitric ash from the settling debris during compaction, forming fumaroles and in some cases, fumarolic mounds, ridges and vapour-phase mineralization (e.g. Valley of Ten Thousand Smokes (Alaska, USA), Bishop Tuff (California, USA)). Lapilli pipes are occasionally deformed to sigmoidal, lenticular and curvilinear shapes by shearing during

emplacement or differential compaction (Druitt & Sparks, 1982; Fisher & Schmincke, 1984; Freundt *et al.*, 2000). They may cut through several flow units, providing timing constraints (see section *Duration*).

Welding

Welding is the cohesion, deformation and eventual coalescence of pyroclasts and glass shards in response to the high emplacement temperatures and retained volatiles under loading stress of ignimbrites (Freundt *et al.*, 2000). The main control of welding compaction is the amount of time that temperature remain above the critical threshold for welding, i.e. the glass transition temperature that depends on the chemical composition of the glass (Fisher & Schmincke, 1984; Paquereau, 2006 and references therein). Typical minimum temperatures for welding are between 500 and 650°C for calcalkaline compositions (Freundt *et al.*, 2000). Glass transition temperature decreases strongly with increasing water content (Giordano *et al.*, 2005 in Paquereau, 2006) and welding intensity increases with increasing temperature, pressure and time (Grunder *et al.*, 2005 in Paquereau, 2006). Post-depositional strongly flowage of welded ignimbrite as a coherent viscous liquid can occur in the most extreme cases, and is called **rheomorphism**. Ignimbrites emplaced at temperatures sufficient to weld commonly cool slowly enough for juvenile glass to devitrify (Fisher & Schmincke, 1984; Freundt *et al.*, 2000).

When several very hot flow units pile up so rapidly one on top of one another that negligible cooling occurs, an ignimbrite may cool as a **single cooling unit,** which is marked by a series of (more or less systematic) zones within the deposit of welding, rock density, strain, devitrification and vapour phase crystallization (Smith, 1960 in Fisher & Schmincke, 1984; Freundt *et al.*, 2000). **Compound cooling units** show irregular vertical gradients in bulk density and strain ratio which reflect prolonged emplacement and consequent partial cooling between successive units (Freundt *et al.*, 2000).

1.4.6 Composition, componentry and grain-size of pyroclastic density currents

(Fisher & Schmincke, 1984; Freundt et al., 2000 and references therein)

Ignimbrites and pyroclastic flow deposits are usually poorly sorted (commonly sorting coefficients $\sigma_{ø}$ > 2) and rich in ash (small median size Mdø = 0 to 2) with size distribution curves that tend to approximate a Gaussian distribution. With increasing distance from source, median grain size generally decreases, the content of fine ash increases, sorting improves and maximum sizes of vent-derived lithics decrease exponentially. Pyroclastic flow and surge deposits are more poorly sorted than fallout deposits, although there is considerable overlap. Pyroclastic surge deposits are better sorted and commonly enriched in crystals and lithics than associated pyroclastic flow deposits, although median diameters may be either larger or smaller.

Ignimbrites are composed of moderately to highly vesicular pumice or scoria bombs and lapilli (juvenile clasts) in a matrix of ash glass shards and commonly-broken crystals, together with lithic fragments derived from the conduit walls or ground surface. Preferential concentration of crystals during transport can produce higher crystal content in the ignimbrite matrix than in juvenile pyroclasts, and the corresponding glass fraction can be concentrated in co-ignimbrite ash.

Block-and-ash flow deposits are poorly-sorted, generally massive and clast- or matrix-supported. They are usually monolithologic and differ from ignimbrites by containing less fine ash and a larger fraction of dense to moderately vesicular, rarely pumiceous, blocks. Associated ash cloud surge deposits consist of sand-sized and finer ash and are relatively well sorted.

1.4.7 Experimental and numerical modelling on pyroclastic density currents and some constraints about their transport, sedimentation and emplacement mechanisms

First, some useful concepts are defined:

Deflation: Progressive decrease in the thickness of a moving pyroclastic flow due to densification that accompanies loss of gas and kinetic energy (Branney & Kokelaar, 2002).

Flow-boundary zone: A loosely delineated zone that includes the lowermost part of the current and the uppermost part of the forming deposit, which rises as the deposit aggrades (Branney & Kokelaar, 2002).

Fluidization: A granular material is fluidised if the vertical drag force exerted by the gas is equal to the weight of the particles. Interparticle friction is greatly reduced and the material takes on a fluid-like behaviour. Fluidization is believed to be an important particle-support mechanism particularly in slow, small-volume ($<<1$ km^3) pyroclastic flows, or in the dense flow-boundary zones of density-stratified, ignimbrite-forming currents (Druitt, 1998; Branney & Kokelaar, 2002).

Considering that a single current deposit can be both stratified and massive, Branney & Kokelaar (2002) proposed a new two-fold classification of pyroclastic currents according to conditions in the flow boundary and not by absolute particle concentration. **Granular fluid-based pyroclastic density currents** are dominated by collisional momentum transfer between the abundant clasts at the flow boundary and turbulence may dominate above the flow-boundary. They predominate in massive lapilli tuff lithofacies of ignimbrites. **Fully dilute pyroclastic density currents** are dominated by turbulence at all levels, except in a basal traction layer.

Ignimbrite-forming currents constitute a spectrum of hyperconcentrated currents in which both clast interaction and instersticial fluid are important, being transitional between dilute and high-concentration currents (Branney & Kokelaar, 2002).

Ignimbrite-forming currents have a remarkable ability to traverse high topographic barriers, e.g. up to 1500 m more than 45 km from vent in the case of the Taupo ignimbrite (New Zealand; Walker, 1980) in contrast with small pyroclastic flows which are more valley confined (Druitt, 1998). The high velocities and ability to move over and around obstacles testify to the great mobility of ignimbrite-forming currents (Fisher & Schminke, 1984).

Ignimbrites can be emplaced:

(i) Layer by layer (flow unit by flow unit) from a number of short-lived flows (Fisher, 1979, 1990b). This model is based on the **standard ignimbrite flow unit** concept (Sparks *et al*., 1973, see above), in which a high-concentration granular flow has an inflated fluidised head and a denser, laminar body that deflate and the massive layer forms when the flow finally came to halt en masse.

(ii) By progressive or incremental aggradation (grain by grain) from a maintained density-stratified current (Fisher, 1966; Branney & Kokelaar, 2002). Massive layers aggrade progressively from the base upwards and depositional processes and deposit textures are governed by conditions in the flow boundary zone, irrespective of the concentration and transport mechanism in overriding parts of the current (Branney & Kokelaar, 1992, 2002). In this case, even a thick compositionally-zoned ignimbrite may not reveal any clear internal depositional boundaries.

Ignimbrites generated on land can travel considerable distances over water, e.g. Koya ignimbrite (40 km, Japan), Campanian ignimbrite (Italy), Krakatau ignimbrite (80 km, Indonesia) and Kos Plateau Tuff (Greece). This indicates that substantial parts of the current were less dense than water, although dense parts may have entered the sea near the proximal shoreline (Druitt, 1998; Branney & Kokelaar, 2002).

The ability of dense pyroclastic flows to travel on slopes as low as few degrees implies low friction which has been attributed in part to fluidization caused by excess gas pore pressure, supplemented by interparticle collisions and buoyancy effects from the fine-grained matrix (Sparks, 1976; Druitt, 1998). Air entrapment at the flow front and gas release by exsolution or particle abrasion during transport may generate additional sources of gas (Fisher & Schmincke, 1984; Wilson, 1980; Formenti & Druitt, 2003). Finer-grained pyroclastic flows are expected to retain gas longer and hence to have higher apparent mobilities than coarser-grained ones (Druitt *et al.*, 2007),

Decoupling between a basal dense layer and an upper dilute layer of fine particles elutriated from the lower part is common during flow propagation (Druitt *et al*., 2002). In some cases, a current may become completely buoyant at the distal flow margins and rise into the atmosphere producing a major mushroom-like ash plume which may be the source of very large volumes of co-ignimbrite air-fall deposits (e.g.

Mount St Helens 1980 blast (USA); Cas & Wright, 1987). Also, the dilute upper cloud may sediment quickly to form a secondary, surge-derived pyroclastic flow (Druitt *et al*., 2002).

1.4.8 Calderas and association of pyroclastic density currents with fissures and faults

Circular depressions named **pit craters**, **collapsed craters**, **subsided craters** or **calderas**, from several metres to several tens of kilometres in diameter, are common structures on the summit of basaltic shield volcanoes and basaltic to silicic stratovolcanoes. Flank eruption often precedes the formation of pit craters or calderas at basaltic shield volcanoes (Geshi *et al*., 2002).

Some volcanoes show changes in eruption style and petrological character after caldera formation, implying an intimate relationship between caldera formation and evolution of the shallow magma system (Geshi *et al*., 2002). Moreover, the shape and diameter of a caldera often approximates that of the magma chamber, and a widely accepted idea is that the escape of magma from the shallow reservoir causes caldera collapse when the lithostatic pressure on the chamber roof exceeds the chamber pressure (Druitt & Sparks, 1984; Cas & Wright, 1987; Geshi *et al*., 2002).

Moderate- to large-volume ignimbrites are commonly associated with caldera collapse, e.g. Long Valley, Valles, Crater Lake, San Juan Mountains and Yellowstone (all western USA), Aira caldera (Japan), Toba (Sumatra, Indonesia), Koya (Japan), Taupo (New Zealand), Peach Springs (USA), Aso-4 (Japan), Santorini (Greece) and those in the Central Andes (Cas & Wright, 1987). Wall-rock lithics can be useful to constrain magma chamber depth or conduit locations, indicate the former presence of a hydrothermal system, or reconstruct events of vent erosion or caldera subsidence (Freundt *et al.*, 2000). In the Bishop tuff (California, USA), progressive vent opening during caldera collapse is recorded by variations in lithic types in the ignimbrite (Wilson & Hildreth, 1997). A decrease in the juvenile fraction together with a progressive increase of crystal and lithic fractions upwards through pumice fall deposits of the 79 AD Vesuvius eruption (Italy), suggests progressive erosion of the conduit (Lirer *et al.*, 1993).

Several types of source vents for ignimbrites have been proposed (Cas & Wright 1987; Druitt, 1998; Freundt *et al.* 2000 and references therein):

- Some voluminous ignimbrites are associated with linear fissures several tens of kilometres long apparently controlled by regional extensional faults. Activity probably focuses on several vents along the fissure in simultaneous or sequential activity rather than along its whole length (e.g., Mamaku and Okataina eruptions, Japan).
- Eruption from ring faults could occur during caldera subsidence and could explain extracaldera outflow sheets than are thinner than co-genetic intracaldera ignimbrites (up to more than 2 km thick).

Later updoming of the intracaldera pile may form a resurgent dome (e.g. Valles (USA) and Cerro Galan (Argentina)).

- During central vent eruptions (e.g. Rio Caliente ignimbrite (Mexico), Taupo AD 186 (New Zealand)) caldera collapse may occur very late or after the eruption (Minoan tuff (Greece), Krakatau caldera (Indonesia)) or being unrelated to any pre-existing volcano (Paricutin 1943 and Acatlán ignimbrite in Mexico).
- Two-stage caldera collapse models have been proposed for Santorini in Greece (Druitt & Sparks, 1984; Druitt, 1985) and Crater Lake in USA (Bacon, 1983; Druitt & Bacon, 1986), in which a first single-vent plinian phase was followed by caldera collapse. At Long Valley (USA), an earlier single vent eruption was followed by eruption from multiple vents along the ring fault of the caldera.

1.4.9 Secondary or reworked deposits

Erosion rates and sediment yields in active volcanic areas are amongst the highest known (Smith & Lowe, 1991). Enormous volumes of sediment are transported as mass flows of volcaniclastic debris and water from a volcano, described by the Indonesian word **lahar** (Smith & Lowe, 1991). Conditions for lahar formation include abundant loose sediment, steep slopes, sudden influxes of water and sparseness of vegetation (Arguden & Rodolfo, 1990). Lahars are not always directly related to eruptions and they encompass a continuum between debris flows (sediment concentration >80%) and hyperconcentrated flows (sediment concentration between 40 and 80%, Smith & Lowe, 1991).

According to their genesis, there are five main types of lahars (Neall, 1976 in Arguden & Rodolfo, 1990):

- The most destructive lahars occur when large volumes of water are suddenly released by an eruption through a crater lake or by a non-eruptive collapse of crater walls (e.g. 1919 Mount Kelut, Indonesia).
- Hot ejecta melt and erode snow or ice on a volcano (e.g. Nevado del Ruiz (Colombia) 1985, Mt St Helens (USA) 1980).
- Pyroclastic currents enter streams (e.g. Mount St Helens 1980).
- The largest are created by liquefaction of debris avalanches or remobilization of their deposits (e.g. Mount St Helens 1980 and other volcanoes in the Cascades, USA).
- Rainfall during or after the eruption in humid regions. **Hot "rain" lahars**, when the storms coincide with eruptions or when moist surface air is uplifted by eruption updrafts (e.g. Santa Maria (Guatemala) 1929 during which the lahar temperature was at or close to the boiling point of water; Mayon (Philippines) 1968, 1984). **Cold "rain" lahars**, months or years after eruptions in the tropics,

when loose sediments on steep slopes are mobilised by rain of sufficient intensity and duration. Hot rain lahars may travel further than cold lahars because hot water and vapour decrease internal friction.

Lahar deposits, and especially deposits from hot lahars, are often difficult to distinguish from pyroclastic flow deposits. Some criteria for differentiation include:

- Hot lahar deposits may have indurated buff-coloured crusts several centimetres thick that bond pebbles and cobbles into a surface looking like concrete (Arguden & Rodolfo, 1990)
- Vesicular matrices (voids 1-2 mm) caused by water vapour (Arguden & Rodolfo, 1990; Freundt *et al.*, 2000).
- Hot lahars may show soft-sediment deformation structures (Arguden & Rodolfo, 1990).
- Fragments that come to rest at temperatures greater than the Curie point (about 400°C) or higher (blocking temperature of ferromagnetic minerals) may have similar, well-grouped directions of thermoremanent magnetism. Random directions suggest that clasts were rotated by transport after they cooled below the Curie point (Fisher & Schmincke, 1984).
- Reddish tops signifying high temperature of emplacement (Fisher & Schmincke, 1984).
- Segregation pipes emanating from carbonised vegetation are good evidence for primary flows (Freundt *et al*., 2000).

Secondary pyroclastic flows commonly accompanied by secondary explosions and ash columns, occurred at Pinatubo (Philippines) more than 4 years after the climactic eruption and were contemporaneous with lahar formation (Torres *et al.*, 1996). Compared to the primary ignimbrite, the deposit has a relatively undissected surface, lighter tone, slight fines depletion and random TRM polarity of coarse clasts (Torres *et al.*, 1996). Similar segregation (pseudoflow) units have been recognised in the VTTS (Alaska, USA; Fierstein & Hildreth, 1992) and secondary mass flow and flow structures have been recognised in high-temperature rheomorphic ignimbrites and welded tuffs (Branney & Kokelaar, 1992).

1.4.10 Effects and hazards of pyroclastic density currents

Various measures of 'size' are applied to the products of explosive eruptions: **Magnitude** refers to the total volume emitted, **intensity** to the mean discharge rate, **dispersive power** to the extent of dispersal, **violence** to the importance of momentum and **destructive potential** to the extent of destruction of life or property (Walker, 1980).

Pyroclastic currents are lethal and highly destructive to human life, biota and environment. Type examples include the eruption of Vesuvius (Italy) in 79 A.D. which buried the towns of Pompeii and Ercolano, Krakatau (Indonesia) in 1883 where tsunamis killed more than 30,000 people, Tambora

(Indonesia) in 1815 which caused more than 90,000 deaths directly or by tsunamis and famine, and the 1902 *nuée ardente* of Montagne Pelée (Martinique, Lesser Antilles, France) which killed 29,000 people (Cas & Wright, 1987).

Records for the period 1900-1999 reveal a total of 491 volcanic events, ~53% of which resulted in a total death toll of 91,724 (Witham, 2005). Pyroclastic density currents were the main cause of death, being directly responsible for ~36,000 deaths in the period 1900-1986, followed by primary lahars (Blong, 1996; Witham, 2005). The high death and impact totals of volcanic phenomena since 1600 are controlled by a few large eruptions, rather than by the many other smaller ones (Blong, 1996; Witham, 2005). The two dominant eruptions were Montagne Pelée in 1902 followed by Nevado del Ruiz (Colombia) in 1985 (23,080 deaths) which together account for more than 50% of the total (Witham, 2005). They are followed by Asama (Japan, 1783), Lakigigar (Iceland, 1783), Unzen (Japan, 1792), Tambora (Indonesia, 1815) and Krakatau (Indonesia, 1883) events (Blong, 1996).

The predominant impact of explosive volcanism on the atmosphere relates to the effects of volcanic aerosols on the radiation budget of the Earth, whereas the ash effects are short-lived and minor (Devine *et al.*, 1984; Sigurdsson *et al.*, 1989), due to: (1) the formation of silicate ash aggregates by ash cohesion forces which fall-out close to source (Carey and Sigurdsson, 1982), and (2) reaction between volcanic gases (such as SO_2) with water in the eruption column and atmosphere, leading to their conversion into aerosol (Pollack *et al*., 1976), which may have stratospheric residence times of several years. For example, sulphuric acid particles from Agung 1963 (Indonesia) and El Chichón 1982 (Mexico) eruptions (Sigurdsson *et al.*, 1989) and 53-58 Tg of SO_2 release within about 24 hours from Tambora (Indonesia) on 1815, which was sufficient to generate 93-118 Tg of stratospheric sulphate aerosols (Self *et al.*, 2004). Release of sulphur from basaltic eruptions is generally an order of magnitude higher than that from silicic eruptions, whereas silicic magmas inject more fine ash and total volatiles (H_2O, CO_2) into the upper atmosphere (Devine *et al*., 1984).

Differences between sulphur and chlorine contents of glassy melt inclusions (trapped by tephra phenocrysts) and matrix glasses, respectively, provide estimates of minimum sulphur and chlorine yield to the atmosphere (Devine *et al.*, 1984). For example, the Minoan eruption (Greece) emitted 5.5×10^9 kg of sulphur into the atmosphere (corresponding to a 1.7×10^{10} kg sulphuric acid aerosols), somewhat higher than that from the Katmai 1912 (Alaska, USA) and Krakatau 1883 (Indonesia) eruptions (Sigurdsson *et al.*, 1989).

Interaction of volcanic aerosols with the Earth's radiation budget leads to absorption and back-scattering of solar radiation in the stratospheric aerosol layer, which can lead to significant surface cooling and temporary climate change (e.g., Laki 1783 (Iceland), Mount St Helens 1980 (USA), Agung 1963, Tambora 1815 and Krakatau 1883 (Indonesia)). A northern hemisphere temperature decrease of 0.5°C

followed the Minoaon eruption (Greece; Sigurdsson *et al.*, 1989). The magnitude of surface cooling correlates positively with the total mass of sulphur released (Devine *et al.*, 1984; Palais and Sigurdsson, 1989).

Lahars often cause the greatest damage during eruptions and may occur long after an eruption (Arguden & Rodolfo, 1990). In fact, many lahar-related fatalities occur from rain-fed secondary lahars when the volcano is no longer in eruption (Blong, 1996). Secondary, surge-derived pyroclastic flows formed by rapid sedimentation from the dilute upper cloud (Druitt *et al*., 2002) and secondary pyroclastic flows with associated ash plumes (Torres *et al.*, 1996), are recently discovered hazards and their prediction is even more difficult since no renewal of magmatic activity is involved.

An obvious classification of the human impacts of historical volcanic eruptions is by number of fatalities, but other impacts are also important, including injuries sustained, medical intervention (Witham, 2005), building and infrastructure damage, economic impact and secondary hazards or collateral damage (fires, noxious gases, floods by failure of landslide dams, leakage of hazardous materials from damaged industrial plants, etc.; Blong, 1996). Evacuation is also an important factor, since it is often a traumatic process that can lead to mortality by famine and epidemic disease, for example 49,000 deaths following the Tambora eruption (Indonesia) on 1815 (Witham, 2005).

Large ignimbrite-forming eruptions pose serious problems in hazard mitigation due to the suddenness with which many plinian eruptions develop following a lengthy period of quiescence (Walker, 1981). The longer the repose period, the more explosive the ensuing eruption is likely to be and because many volcanoes erupt infrequently, only those with significant historical eruptions receive much attention (Blong, 1996). However, it is still a matter of much debate if the remote possibility of a large ignimbrite-forming eruption should be considered in worst-case scenarios (Blong, 1996). Volcanic hazard risk assessment should include the development of a series of scenarios considering eruption magnitudes, hazard possibilities, and vulnerabilities of personnel and infrastructure, with the aim of identifying those areas/groups/links where the smallest expenditure will achieve the greatest risk reduction (Blong, 1996). A key issue for hazard mitigation is the better understanding of the physics of pyroclastic flows in order to develop appropriate models that aim to predict flow path, velocity and run-out (Roche *et al*., 2005).

CHAPTER 2 Reconstruction and eruptive evolution of the basaltic andesitic 3.6 ka BP Pucón eruption, Villarrica Volcano, Southern Andes, Chile

NOTE: This chapter has been modified and submitted to Bulletin of Volcanology (2008) by Silva, C., Druitt, T.H., Robin C., Moreno H. & Naranjo J.A.,, under the title: "The 3.6 ka BP Pucón eruption of Villarrica Volcano, Chile. Deposit architecture and eruption chronology".

ABSTRACT

The Pucón Ignimbrite (1.8 km^3 DRE) was emitted by the largest Holocene eruption of the Villarrica Volcano (Chile), one of the most active volcanoes of Southern Andes. After a long period of volcanic calm (~400 years) and with subglacial dacitic lava flows and/or domes near or at the ice-capped summit, the Pucón eruption started with a violent strombolian to subplinian scoria fallout (0.1 km^3 DRE, VEI = 3-4) which evolved into an ignimbrite-forming eruptive mechanism. The first phase (P1) started with a small base surge to the north of the volcano, followed by a series of vulcanian explosions producing multiple pyroclastic flows (20% of the total volume) over the western and northern flanks, leaving thicker and valley-confined deposits (subunits P1a, P1b and P1c). After a pause long enough for the P1 deposits to have cooled below the temperature necessary for charcoalization of wood (~200 °C) (several weeks to months?), a new eruptive phase started (P2), which lasted no more than a few days emitting 80% of the total volume and representing an increase in the eruptive intensity. The boundary marks also the abrupt appearance of very abundant and more diverse lithic-types including vent-derived granitoids, erupted as individual clasts and also mixed thoroughly into the magma. This shows that magma fragmentation during the violent phase P2 took place at deeper levels than during phase P1. These first pyroclastic flows of P2 are inferred to have had high velocities, with a turbulent, blast-like leading edge, that reached a large distance all around the volcano, forming thick valley ponds, a complete record on valley margins and a highly sheared and erosive lower contact with its substrate (P2a). Then, juvenile-rich high-concentration valley-confined pyroclastic flows were deposited from south to east of the volcano (P2b) and a major pyroclastic surge-forming phase (P2c) was emitted all around the volcano with important deposition on slope environments (P2c). The Pucón eruption culminated with low-energy valley-confined pyroclastic flows emitted to a short extent accross the northern flank (P2d). Immediately after the eruption, the ignimbrite surface was inundated by several lahar waves. A new cycle of explosive activity commenced no more than a few storm seasons later. Radiocarbon dates constrain the age of the Pucón eruption to be 3.6 $\pm$ 0.1 ka ^{14}C age BP, with a calendar age of 3640-3960 yr calBP.

2.1 INTRODUCTION

Explosive fragmentation of gas-rich magma and its ejection into the atmosphere is one of the most violent manifestations of terrestrial volcanism. Such events commonly involve the formation of pyroclastic currents, ground-hugging mixtures of hot pyroclasts and gas, with or without free water, which flow at high speed across the landscape, driven by their density contrast with the atmosphere. Most large-volume pyroclastic currents are generated by fallback or continuous fountaining of vertical eruption columns, although they also form by lateral blast or by gravitational collapse of lava domes (Druitt 1998; Branney & Kokelaar 2002). Pyroclastic currents have velocities of up to about 100 m/s or more, with travel distances of up to 100 km, and they can climb obstacles up to 1000 m high. The emplacement temperatures can be up to 700°C and their deposits may remain hot for months or years (Druitt, 1998).

Pyroclastic currents are highly destructive to human life and the environment (e.g., Montagne Pelée in Martinique 1902, Vesuvius in Italy AD79, Santorini in Greece 3600 BP). Prominent examples of the last two centuries include the eruption of Tambora (Indonesia) in 1815, Krakatau (west of Java) in 1883, Katmai (Alaska) in 1912, Mt St Helens (USA) in 1980, El Chichón (Mexico) in 1982 and Mt Pinatubo (Philippines) in 1991. Analysis of prehistoric eruptions suggests that pyroclastic current deposits with volumes of up to thousands of km^3 can be generated in a matter of days (Wilson & Hildreth, 1997). Large explosive events (about $>10^3$ km^3 of products) have occurred with a minimum frequency of ~1.4 per Ma in two pulses over the past 36 Ma (Mason *et al.* 2004). Huge buoyant ash clouds associated with pyroclastic currents can inject ash and aerosols high into the stratosphere, causing significant global climatic perturbation (e.g. Self *et al.* 1981). Pyroclastic currents were directly responsible for ~36,000 deaths in the period 1900-1986, corresponding to 47% of deaths by volcanic hazards (Blong, 1996).

Villarrica Volcano (39°25'S, Chile) in the central volcanic province of the Southern Andes (Figure 2.1) is one of the most historically active volcanoes in South America. It has shown recurrent explosive activity in postglacial times, in addition to its more typical effusive behaviour (Moreno, 1993, 2000; Moreno *et al*., 1994a; Lara & Clavero, 2004). Its explosive basaltic to andesitic eruptions have produced several large pyroclastic density currents, and have caused the formation of at least two calderas (Moreno, 1993, 2000; Moreno *et al*., 1994a; Lara & Clavero, 2004; Moreno & Clavero, 2006). The 3635 yr BP Pucón eruption, which is the subject of the present paper, generated a complicated sequence of pyroclastic current deposits that extends up to 16 km from the volcano, with a volume of about 3 km^3 (1.8 km^3 DRE - dense rock equivalent). The deposit from the eruption has been called the "Pucón Ignimbrite" (Moreno, 1993; Clavero & Moreno, 1994; Moreno *et al.*, 1994a; Clavero, 1996). Although scoriaceous, and hence not strictly an ignimbrite in conventional terms (e.g. Cas & Wright 1987), we retain this name in this paper.

It is estimated that approximately 80,000 people live within a 40-km radius of the volcano and if a Pucón-sized eruption occurred today, approximately 15,000 - 20,000 people would be directly threatened

by pyroclastic currents and even more by associated lahars and ash falls. If the eruption took place in summer, the number of threatened people increases to more than 40,000 just in the tourist town of Pucón, situated 15 km north of the volcano summit (Censo 2002 INE in Polanco & Clavero 2003) (Figure 2.2).

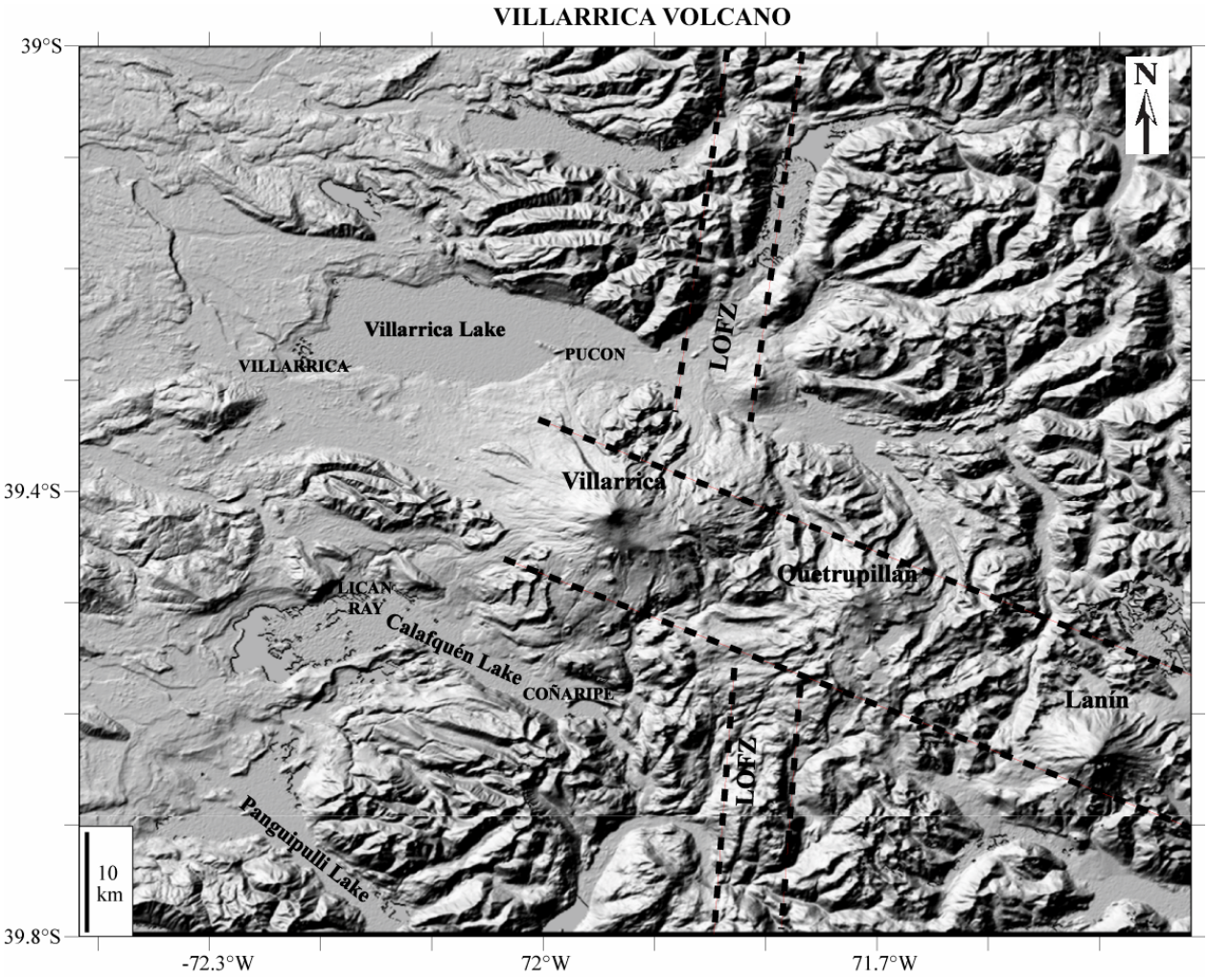

Figure 2.2: Shaded relief (digital elevation model) of Villarrica Volcano and surroundings, showing the main lakes and the main geological structures: The NS-trending Liquiñe-Ofqui Fault Zone (LOFZ) and the NW-trending Villarrica-Lanín volcanic chain are shown (after Moreno, 1993 and Clavero & Moreno, 2004).

Even if large pyroclastic currents have low probability, they are the hazard with the greatest potential destructive impact posed by Villarrica (Moreno, 2000; Lara, 2004a). These reasons, combined with the past tendency of Villarrica for large-scale explosive activity, make it important to reconstruct and better understand the dynamics of explosive eruptions at Villarrica and their associated hazards. A detailed study of the well preserved Pucón Ignimbrite is probably one way to approach this objective.

In terms of the volume of ejecta, the eruption can be assigned a volcanic explosivity index (VEI, Newhall & Self, 1982; Fisher & Schminke, 1984) of 5, larger than the eruption of Mt St Helens in 1980. Considering eruption frequencies over the last 200 years, a VEI 5 eruption can be expected once a decade or so somewhere in the world (Simkin, 1993; Blong, 1996).

In this context we have carried out research to reconstruct the Pucón eruption. Our work is founded on previous studies of the general geology of the volcano (Moreno, 1993, 2000; Moreno *et al*., 1994; Lara & Clavero, 2004; Moreno & Clavero, 2006) and of the deposits of the Pucón eruption (Clavero & Moreno, 1994; Moreno *et al.*, 1994a; Clavero, 1996). Our approach has involved logging of some 70 outcrops around the volcano, allowing us to reconstruct in 3D the internal architecture of the deposit. Correlation of the internal lithofacies within a chrono-stratigraphic framework has then allowed us to place constraints on the eruption dynamics, as well as on the transport and emplacement mechanisms of the pyroclastic currents.

2.2 GEOLOGICAL SETTING

Villarrica is a Late Pleistocene to Recent composite stratovolcano belonging to the volcanic front of the Southern Volcanic Zone (SVZ) of the Andes, associated with the east-dipping subduction of the Nazca plate beneath the South American plate (Figure 2.1). Located at 39°25'S, it is aligned with the Quetrupillán and Lanín volcanoes along a regional northwest-trending lineament (Moreno, 1974; Dalla Salda *et al.*, 1991; Cembrano & Moreno, 1994; Moreno *et al*., 1994b; Lara & Moreno, 1994; Lavenu & Cembrano, 1999; Bohm *et al*., 2002; Lara, 2004b) (Figure 2.2). The main regional structure is the Liquiñe-Ofqui Fault Zone (LOFZ) extending more than 1000 km N-S from about 38° to 47°S (Hervé *et al.*, 1974, 1979; Moreno & Parada, 1974; Hervé, 1976; Moreno, 1976; Hervé, 1994; López-Escobar *et al.*, 1995; Cembrano *et al.*, 1996, 2000, and references therein) (Figure 2.2). The products of Villarrica cover a surface of more than 700 km^2; the edifice covers an area of 400 km^2, and has a volume of ~250 km^3 (Moreno, 1993, 2000). The summit lies 2847 m above sea level (asl) and the base at about 400 m asl (Moreno, 1993, 2000; Clavero, 1996; Clavero & Moreno, 2004a). About 30 adventive cones lie on its flanks, grouped in two main sectors: “Los Nevados” to the northeast and “Chaillupén” to the southwest (Moreno, 1993) (Figure 2.3). Nine major drainages cut the flank of the volcano, separated by ridges up to 1700 m asl. There are referred to in what follows as drainages D1 to D9. Two lakes of glacial origin, Villarrica Lake and Calafquén Lake, lie toward the northwest and southwest, respectively (Figure 2.3).

The basement of Villarrica Volcano is composed mainly of Oligocene to Pleistocene volcanic rocks, Late Palaeozoic to Triassic metamorphic and sedimentary rocks and Late Palaeozoic and Upper Miocene plutonic rocks ranging from diorites to granitoids (Aguirre & Levi, 1964; Munizaga *et al*., 1988; Moreno, 1993; SERNAGEOMIN, 2002; Lara & Moreno, 2004) (Figure 2.4). The depth of the basement below the

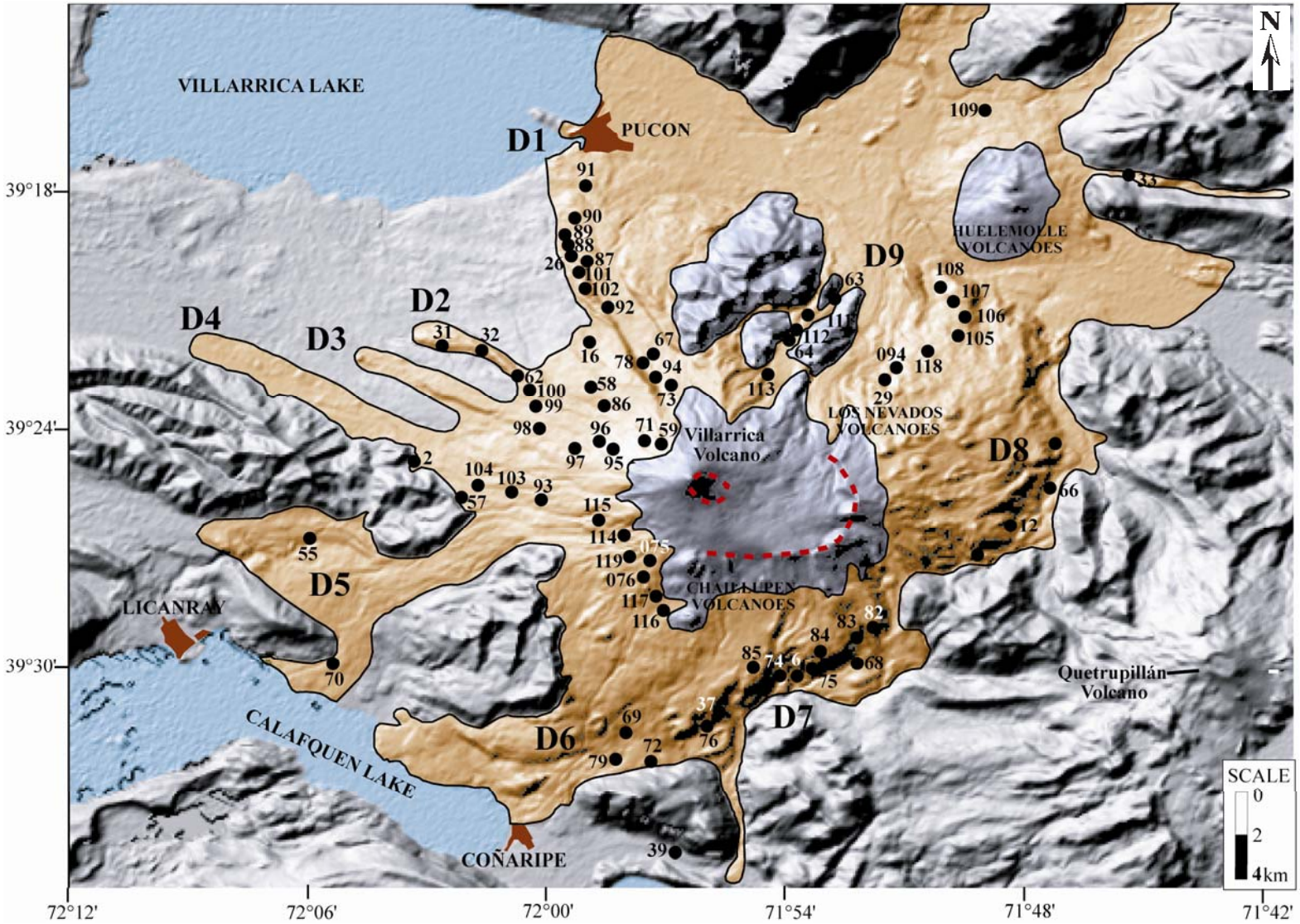

Figure 2.3: Shaded relief map of Villarrica Volcano and surroundings, including lakes, main residential areas and the nine main drainages (D1-D9) recognised in the text. Red dotted lines show the outlines of the two calderas of the volcano. Pale brown field shows the distribution of the Pucón Ignimbrite (modified from Clavero, 1996). Black dots are stratigraphic sections of the Pucón Ignimbrite logged for this study. Their coordenates UTM (in km) are in Table 2.1.

volcano summit is unknown, but Miocene granitoid hills on the eastern and southern flanks as close as 9 km from the crater reach up to 1600 m asl, and those on the northern flank reach up to 1300 m asl as close as 4.5 km from the crater. Palaeozoic granitoids crop out as 600-m asl hills on the southwestern flank of the volcano as close as 12 km from the summit (Figure 2.4).

The general geology of the volcano and of the deposits of the Pucón eruption is already well described (Moreno, 1993; Clavero & Moreno, 1994, 2004; Moreno *et al*., 1994a; Clavero, 1996; Clavero *et al*., 2004; Silva *et al*., 2004, 2005, 2008; Lara & Clavero, 2004; Moreno & Clavero, 2006). Villarrica Volcano has been studied using a broader array of petrologic and geochemical tools than any other Andean SVZ volcano, with the purpose of understanding its magmatic evolution and its relationship with nearby volcanoes (Hickey-Vargas *et al*., 1989, 2004; López-Escobar & Moreno, 1994; López-Escobar *et al*., 1995; Clavero, 1996; Sun, 2001; Lohmar *et al*. 2006, 2007; Lohmar, 2008; McCurry *et al*., 2001, 2004; Witter *et al.*, 2004), or of studying subduction zone processes (Sigmarsson *et al*., 1990, 2002; Morris *et al*., 1990; Hickey-Vargas *et al*., 2002; Chmeleff, 2005).

The history of Villarrica Volcano can be divided into 3 stages (Moreno, 1993; Figure 2.4), as now described.

2.2.1 Villarrica 1

The preglacial geology of the volcano comprises Middle (?) to Late Pleistocene basaltic to andesitic lavas, volcaniclastics, agglomerates and some ignimbrites (Figure 2.4). These formed a composite stratovolcano centred 3 km SE of the present one, which developed prior to, and during, the Last Glaciation (Moreno, 1993; Moreno *et al*., 1994; Clavero & Moreno, 2004; Gaytán *et al*., 2005, 2006; Gaytán, 2006). About 100 ky ago, a large elliptical (6.5 x 4.2 km) caldera elongated NW-SE was formed (Moreno, 1993, 2000; Clavero & Moreno, 1994, 2004; Moreno *et al*., 1994; Moreno & Clavero, 2006). About 95 ky ago, dacitic domes and dykes were emplaced and then explosive activity continued up to 14 ka, forming a new cone (Clavero & Moreno, 2004 and references therein). Intraglacial explosive activity, continuous since at least ~40 ka, emitted abundant dacitic pumices together with andesitic-basaltic scoria, probably generated during subplinian eruptions (Gaytán *et al*., 2005, 2006; Gaytán, 2006).

2.2.2 Villarrica 2

The first major postglacial explosive eruption occurred 13.9 ka, forming the ~10 km^3 (non-DRE) Licán Ignimbrite, of which remnants today occur up to 35 km from the volcano (Moreno, 1993, 2000; Clavero & Moreno, 1994, 2004; Moreno *et al*., 1994; Clavero, 1996, Figure 2.4). Associated caldera collapse probably reactivated the preglacial caldera (Moreno, 1993; Clavero & Moreno, 1994, 2004; Moreno *et al*., 1994; Clavero, 1996). After the Licán eruption, the modern cone started to grow on the northwestern edge

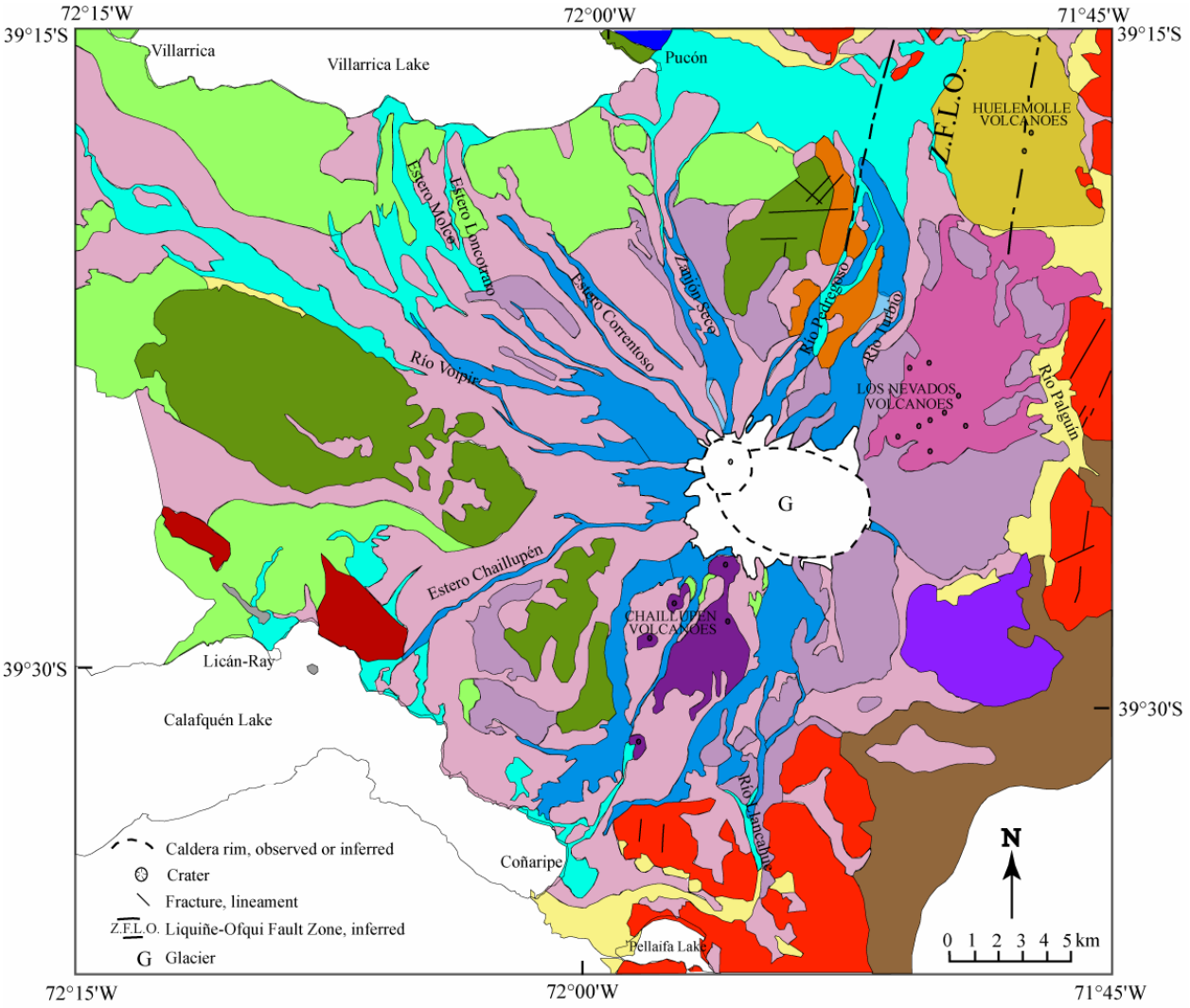

LEGEND

Villarrica Volcano

- Villarrica 3 Unit (Holocene): Basaltic andesite lavas, tephra fallout, pyroclastic flow and surge deposits, and lahar deposits
- Villarrica 2 Unit (Upper Pleistocene-Holocene): Mainly basaltic andesite pyroclastic flow, surge and tephra fallout deposits, and lavas. It includes the Licán and Pucón ignimbrites
- Villarrica 1 Unit (Middle?-Upper Pleistocene): Pre-to-intra-Last-Glaciation basaltic andesite lavas, pyroclastic breccias, and dacitic domes, and dikes

Los Nevados parasite centres (Holocene)

- Pyroclastic cones and basaltic andesite lavas

Chaillupén parasite centres (Holocene)

- Pyroclastic cones and basaltic andesite lavas

Independent eruptive centres

Quetrupillán Volcano (Upper Pleistocene-Holocene)

- Andesitic to dacitic lavas, pyroclastic flow and breccia deposits

Huelemolle Volcanoes (Holocene)

- Pyroclastic cones and basaltic andesitic lavas

Cordillera El Mocho Volcano (Pleistocene)

- Andesitic to basaltic lavas

Sedimentary deposits (Pleistocene-Holocene)

- Alluvial and gravitational deposits, including some fluvial and laharic terraces (Holocene)
- Lahar deposits (Holocene including historical)
- Glacial, fluvioglacial and lacustrine deposits associated to the Last and penultimate Glaciation and Villarrica Volcano glacier (Pleistocene-Holocene)

Basement

- Stratified volcanic rocks (Pliocene-Pleistocene, Upper Miocene? and Neogene? units)
- Late Paleozoic-Triassic: Metasedimentary rocks
- Upper Miocene: Tonalites and granodiorites, including some andesitic hypabyssal bodies
- Miocene: Mainly granodiorites and minor andesitic hypabyssal intrusions
- Late Paleozoic: Granites, granodiorites and tonalites

Figure 2.4: Simplified geological map of the Villarrica volcano (modified after Clavero & Moreno, 2004, and references therein).

of the caldera. Following nine minor pyroclastic eruptions and some lavas (each $\leq$ 0.9 km^3 non-DRE, Moreno 1993), there then occurred the "Pucón Ignimbrite" (3 km^3 non-DRE; Silva *et al.*, 2005, 2008). This represents the second largest eruption of the volcano and is characterised, like the Licán Ignimbrite, by a basaltic-andesitic composition (Moreno, 1993, 2000; Clavero & Moreno, 1994; Moreno *et al.*, 1994; Clavero, 1996). The Pucón eruption may have caused collapse of a 2.2-km-diameter summit caldera (Moreno, 1993, 2000; Clavero & Moreno, 1994; Clavero, 1996).

2.2.3 Villarrica 3

The present-day, 450-m-high cone is built within the youngest caldera and is composed of lava flows, pyroclastic falls and flows, and lahar deposits (Moreno, 1993, 2000; Moreno *et al.*, 1994; Clavero & Moreno, 2004, Figure 2.4). The prehistoric eruptions of Villarrica Volcano have varied from Hawaiian (VEI=0) to Plinian (VEI=6?) (Moreno, 1993; Lara, 2004a).

Construction of this new cone started with strong strombolian eruptions, which generated the "Chaimilla scoria fallout deposits" intercalated with thin fine ash and accretionary lapilli layers, mainly distributed on the eastern and northern flanks of the volcano (Moreno, 1993; Clavero & Moreno, 2004). A highly explosive event generated the 2600-yr "Pedregoso pyroclastic surge" (Clavero & Moreno, 2004; ex-"Oleada FP Refugio" of Moreno, 1993), the deposit of which is distributed radially around the volcano up to 4 m thick and has an estimated non-DRE volume of 0.6 km^3 (Moreno, 1993).

Documented eruptions at Villarrica are available from 1558 onwards, when the first Spanish conquerors arrived in southern Chile (Petit-Breuilh & Lobato, 1994), even if close to 10,000 years of inhabitation is recorded in the Villarrica area (Pino *et al.*, 2004). Since 1558, there have been at least 49 eruptions (one eruption each ~10 years) and, although not well documented, it is probable that this number could be closer to 90 (Petit-Breuilh, 1994; Lara, 2004a). The historical eruptions range from hawaiian to possible subplinian (VEI=0-3), but the most destructive and recurrent type of activity is the formation of lahars, causing more than 100 fatalities during the 20th century (Casertano, 1963a, 1963b; Moreno, 2000; Naranjo & Moreno, 2004; Castruccio, 2005; Castruccio *et al.*, 2005, 2006). The summit of the main cone and the old caldera are covered by a glacier which extends over 30.3 km^2 (value for 2005; Rivera *et al.*, 2006) with a volume of ~8 km^3 (Moreno, 1993, 2000; Casassa *et al.*, 2004 and references therein; Naranjo & Moreno, 2004). Lava erupts through upper flank fissures at high eruption rates, and the consequent rapid melting of snow and ice frequently triggers lahar formation. Fissure orientations on the crater rim define the most probable lahar flow directions (Naranjo & Moreno, 2004). Lateral or flank fissures have occurred in all eruptions of the 20th century: to the north (1908), WNW and ESE (1948-1949), WSW (1963), south (1964), NNE and SSW (1971) (Naranjo & Moreno, 2004).

Although a small eruption took place in 2000, the last significant eruption was in 1984-1985. The 200-m-diameter open crater that remains today, contains an active lava lake with a permanent fumarole and

persistent weak strombolian activity that varies in depth from 100 to 150 m (Moreno, 1993, 2000; Witter *et al.*, 2004; Witter & Delmelle, 2004; Calder *et al.*, 2004; Witter & Calder, 2004; Clavero & Moreno, 2004). Recent geochemical studies of samples from the lava lake indicate that ~1.2 km^3 of magma degassed between 1985 and 2002 (Witter *et al.*, 2004). This means an average degassing rate of 2.2 m^3/s below Villarrica's summit. It is suggested that convection in the conduit produces the observed emissions and prevents the lava lake from solidifying (Witter *et al.*, 2004). These volatile flux measurements are interpreted as representing the current baseline level of gas emission at Villarrica, which can be used to assess changes in the level of activity (Witter & Calder, 2004).

Assuming a random Poisson eruptive pattern, there exists a 99% probability of an eruption with VEI (Volcanic Explosivity Index)>=2 during the next 50 years (Polanco & Clavero, 2003).

2.2.4 Previous studies of the Pucón Ignimbrite

Defined by Moreno (1993), the Pucón Ignimbrite has been dated at 3700 years (Moreno, 1993; Clavero & Moreno, 1994) and its (non-DRE) volume has been estimated as between 4 and 5 km^3 (Moreno, 1993). Clavero (1996) mapped the distribution of the Pucón Ignimbrite and calculated a volume of 5 km^3 (non-DRE). With a total thickness of up to more than 100 m, he recognised a basal pyroclastic surge layer, three pyroclastic flow units (juvenile, lithic and massive; mostly as lenses in channel facies) and an upper surge layer.

Clavero (1996) recognised that the Pucón Ignimbrite started with an initial strombolian fallout phase. From geochemical and petrograhic evidence magma mixing was suggested as the trigger mechanism of the eruption, during which a basaltic pulse was injected into a slightly more differentiated magma chamber (Moreno *et al.*, 1994; Clavero, 1996). These authors invoked that the chamber became unstable, provoking the violent ejection of large quantities of magma, which melted the glacier cap and a low eruptive column was formed, like a "boiling over" (Clavero & Moreno, 1994; Moreno *et al.*, 1994; Clavero, 1996). They proposed that this produced highly fluidized and valley-confined pyroclastic flows; instability and collapse of the edifice walls then generating a 2-km-diameter Krakatoa-type caldera.

The high degree of fluidization of the pyroclastic flows was attributed to (Clavero, 1996): (1) water vapour incorporated into the flows by glacier fusion, (2) emplacement onto an irregular topography producing air incorporation at the flow fronts, and (3) incorporation of CO_2 from vegetation ignition. The transport mechanism of the Pucón Ignimbrite was envisaged as intermediate between a classic pyroclastic flow and a hot dense lahar. Thus, it evolved distally into a hyperconcentrated alluvial flow when it mixed with superficial water, and it exhibited similar channel and inundation facies with lahars. While aspects of this model have been confirmed by the present study, there are significant differences in the interpretations of the eruptive mechanisms.

In a stratigraphic and grain-size study of the northwestern exposures of the Pucón Ignimbrite, Palma (2001) recognised an initial lithic-rich eruptive phase responsible for major erosion of the summit, which then favoured emplacement of juvenile-rich flows of a subsequent scoriaceous phase. During a third phase, the emplacement of a lithic massive pyroclastic flow unit generated an upper surge layer.

Oxygen isotope ($\delta^{18}O$) data in the matrix of basaltic andesite pyroclasts (McCurry *et al*., 2001, 2004), indicates limited meteoric water (a maximum of 4%) interaction with the pre Pucón magma. Higher δ18O values found in the yellowish rind of some basaltic andesite pyroclasts can be interpreted as a result of palagonitisation (Cuadros *et al.*, 1999). Even if the homogenization in phenocryst melt inclusions was not systematically achieved, McCurry *et al.* (2004) suggested that the most homogeneous melt inclusions show "bulk-rock-like" analyses, high sulphur (1400 to 5000 ppm) and low electron microprobe (EMP) totals (96-98%).

2.3 DEPOSIT DESCRIPTIONS

The stratigraphy of the Pucón deposits is now described. Reconstruction of the architecture of the deposit was based on about 70 detailed logs distributed all around the volcano (Figure 2.3; Table 2.1). After a description of the underlying pre-Pucón deposits present in the different sectors studied, this section focusses on the main stratigraphic units of the Pucón Ignimbrite: the subordinate basal scoria fall deposit (A), overlain by two main pyroclastic current units, P1 and P2. The upper unit, P2, is characterised by the presence of basement granitoids, both as free fragments and as inclusions in scoria, whereas these are absent in the lower unit, P1. The two units show contrasting sectorial distributions: whereas P1 occurs only on the western and northern flanks, P2 was deposited all around the volcano.

We first define some terminology used. A *bed* is a distinct sedimentation unit with well defined upper and lower boundaries that are laterally continuous across individual outcrops. *Stratification* occurs within beds, and is defined by vertical or subvertical variations in grain size or composition on a vertical scale of a cm or more. It can be well defined or diffuse, and can include planar, wavy or cross varieties. *Lamination* is a fine-scale stratification, individual laminae being of the order of a few mm thick.

By *lithic-rich*, we refer to deposits having less than ~50% (number %) scoria in all grain sizes. By *juvenile-rich*, we mean those deposits having about 70 to 100% scoria in sizes 4 mm or coarser, and about 50 to 80% scoria in sizes 2 mm or finer. The numerous beds having scoria abundances between these two end-members are referred to as *intermediate*.

In this work, the term *pyroclastic flow* is used for a current in which it is inferred that the particle concentration was either high (tens of percent) throughout (excluding a dilute cloud), or which had a

Table 2.1: Coordenates UTM (in km) of the main outcrops logged in this study, shown in Figure 2.3

outcrop	drainage	x UTM	y UTM
VR101	1	243,4	5643,9
VR102	1	243,5	5643,3
VR26	1	243,3	5644,2
VR67	1	245,6	5638,3
VR73	1	246,1	5637,7
VR78	1	245,5	5638,3
VR87	1	243,4	5644,0
VR88	1	243,3	5644,5
VR89	1	243,3	5644,6
VR90	1	243,3	5645,2
VR91	1	243,1	5646,2
VR92	1	244,1	5641,6
VR94	1	245,7	5637,8
VR100	2	758,0	5639,1
VR31	2	752,5	5642,3
VR32	2	255,9	5641,9
VR58	2	244,3	5637,5
VR59	2	245,9	5635,8
VR62	2	757,7	5640,3
VR71	2	245,6	5635,8
VR86	2	244,4	5636,9
VR95	2	244,8	5635,8
VR96	2	244,6	5635,8
VR97	2	243,5	5636
VR98	2	242,0	5637,1
VR99	2	758,4	5637,8
VR16	1-2	243,6	5640,3
VR103	4	755,7	5632,3
VR104	4	755,1	5632,8
VR2	4	753,7	5633,6
VR57	4	754,8	5632,7
VR93	4	756,8	5632,2
075	5	244,4	5628,3
VR114	5	243,1	5629,9
VR115	5	242,5	5630,8
VR119	5	243,5	5628,6
VR55	5	751,3	5630,7
VR70	5	750,6	5624,6
076	6	245,0	5627,6
VR116	6	246,3	5626,7
VR117	6	245,8	5627,3
VR69	6	245,8	5620,9
VR72	6	246,3	5619,2
VR79	6	245	5619,1
VR37	7	248,9	5621,5
VR39	7	247,3	5615,1
VR6	7	252,1	5622,8
VR68	7	254,8	5623,3
VR74	7	251,4	5623,0
VR75	7	252,9	5622,6
VR76	7	248,6	5621,3
VR80	7	252,9	5624
VR82	7	255,5	5624,1
VR83	7	255,1	5623,9
VR84	7	253,5	5623,0
VR85	7	251,2	5623,3
046	8	260,5	5632,5
VR12	8	258,4	5629,4
VR66	8	260,0	5631,2
VR111	9	251,2	5640,7
VR112	9	250,6	5639,8
VR113	9	249,7	5638,0
VR63	9	252,1	5641,3
VR64	9	250,5	5639,6
094	8 - 9	254,5	5638,1
VR105	8 - 9	256,6	5640,0
VR106	8 - 9	256,6	5640,6
VR107	8 - 9	256,3	5641,1
VR108	8 - 9	255,9	5641,4
VR109	8 - 9	257,9	5649,9
VR118	8 - 9	255,2	5639,0
VR29	8 - 9	254,2	5638

continuous gradient from a high concentration base to a low concentration (few percent or less) top. It lay down deposits that thicken markedly into valleys and topographic depressions.

Pyroclastic surges are inferred to have had uniformly low (few percent or less) to intermediate particle concentrations, apart from a basal traction load. Sedimentation rates in pyroclastic surges are inferred to have been low enough to permit widespread and persistent traction along the depositional interface.

The rock classification used in this work is taken from Le Maitre *et al.* (1989) for subalcaline rocks: *basalt* 45-52 wt% SiO_2, *basaltic andesite* 53-57 wt%, *andesite* 57-63 wt% SiO_2, *dacite* >63 wt% SiO_2 and *rhyolite* >69 wt% SiO_2.

2.3.1 Pre-Pucón deposits

In the southern sector (drainages 6 and 7, Figure 2.3), the Pucón Ignimbrite overlies the 4100-yr "Afulnahue pyroclastic flow" deposit (Clavero & Moreno 2004, "FP-NN" of Moreno, 1993).

On the western flank of the volcano (drainage 5), two basaltic andesitic units of unknown age underlie the Pucón Ignimbrite. One is a lava flow exhibiting convoluted flow textures, with vesicular and dense bands, that underlies P1. The other deposit directly underlies P2 (P1 is not exposed) and is a > 5-m-thick monolithologic agglomerate, rich in dense bombs including the following types: (1) flat "slabby" bombs, (2) spherical bombs with prismatic jointing and/or concentric fracturing, (3) breadcrust bombs, and (4) spherical fragments without internal structure and with smooth surfaces (accretionary lava balls?). The agglomerate contains a matrix of angular dense lapilli fragments and grades downstream, over a few tens of metres, into a breccia poor in bombs and rich in angular lapilli. Possible origins of this deposit include: (1) a subglacial lava flow (probably remobilized), (2) a fines-poor block and ash flow, or (3) a pyroclastic flow formed by collapse and drainage of a lava lake similar to that from the 1993 eruption of Arenal Volcano (Alvarado & Soto, 2002). We favoured the first possibility and similar bombs and blocks to those of this deposit were observed in P1a.

On ridges located east of drainage 9 (Figure 2.3), the underlying deposits consist of orangish, reddish and blackish scoria falls and lava flows emitted by the nearby Los Nevados parasite centres (Figures 2.3 and 2.4) during its period of activity from 5500 to 4200 years (Moreno, 1993).

In the northern sector (drainages 4, 3, 2, 1, 9, 8, Figure 2.3), the Pucón Ignimbrite is underlain conformably by airfalls, pyroclastic flow deposits, and lavas. Because of that, the exact base of deposits from the Pucón eruption is rather difficult to define. A complete sequence logged at location VR113 is shown in Figure 2.5. Directly underlying the basal scoria fall of the Pucón Ignimbrite (Figure 2.5), there occurs a unit consisting of an airfall overlain by a pyroclastic surge deposit. The airfall is an orange to reddish well-sorted scoria lapilli fall deposit, a few tens of cm thick and increasingly rich in lithic fragments upwards. It is overlain in gradual contact by a brown, parallel and cross stratified tuff, rich in ash and lapilli, interpreted as a pyroclastic surge deposit. The vesicular lapilli (up to 2 cm) of the surge deposit can be subdivided into four main types: (1) pale yellowish brown (some fibrous), (2) gray, (3) banded gray - pale brown, and (4) a few black fragments. There is an inverse grading of the lighter-coloured fragments in the deposit. The most abundant pale yellowish brown juvenile fragments are dacitic in composition (63% SiO_2). No whole-rock analyses were done on the black fragments because of their very low abundance and size. The presence of non- or slightly-carbonized wood (up to 10 cm) and accretionary lapilli (1-4 mm) suggests wet emplacement of the pyroclastic surge. The basal Pucón scoria fall overlies this deposit conformably, without development of a palaeosol.

Underlying the Pucón Ignimbrite, the 4100-yr Afulnahue pyroclastic flow reaches a maximum thickness of 1.3 m and contains pumice and accretionary lapilli (Moreno, 1993; Clavero & Moreno, 2004).

A 4200-yr deposit of reddish air falls and flows, up to 0.5 m thick, underlies the Afulnahue pyroclastic flow on the NE flank (Clavero & Moreno, 2004). It is possible that these deposits correspond to those underlying the Pucón Ignimbrite at locality VR113 (Figure 2.5).

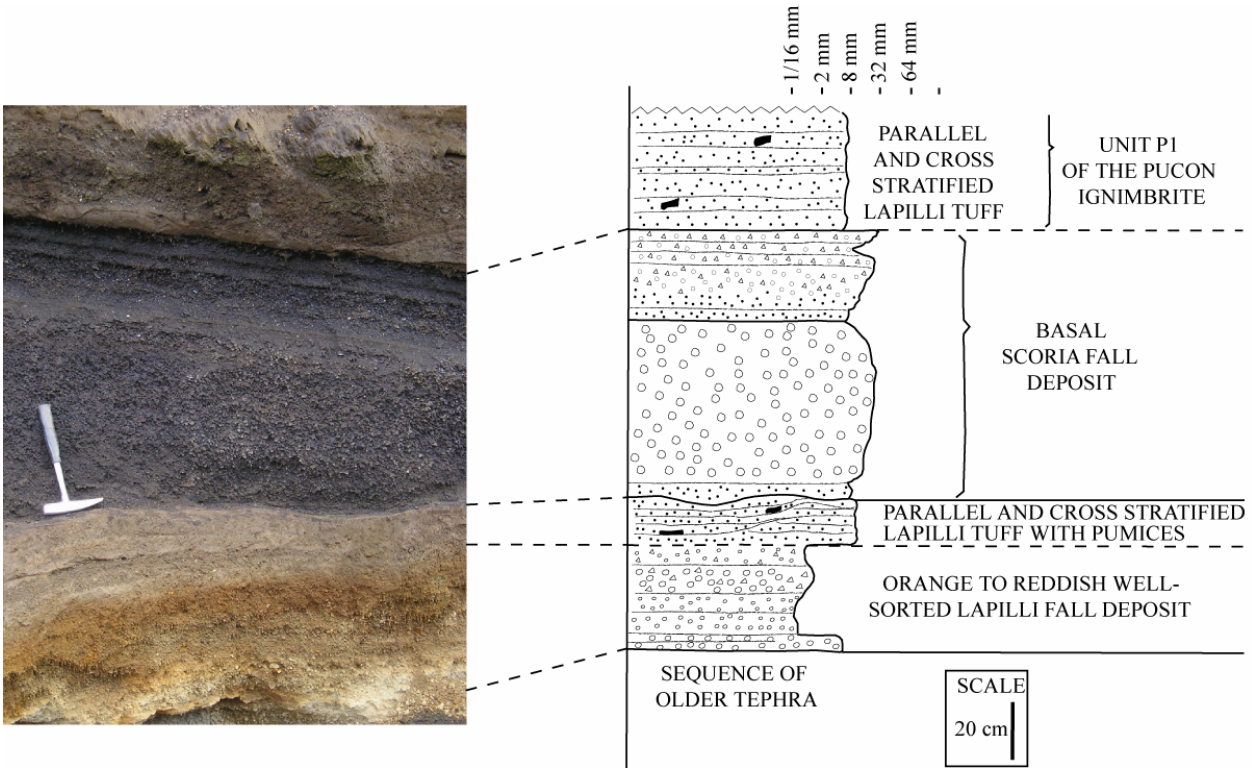

Figure 2.5: Generalised column of deposits at the base of the Pucón Ignimbrite on the northern flank of the volcano (VR113, Figure 2.3).

2.3.2 Basal scoria fall deposit

Fallout layers interpreted as the basal scoria fall deposit of the Pucón eruption were observed at nine locations on the northern, western and southern flanks of the volcano (Table 2.2, Figure 2.6). A probably similar deposit has also been observed on the eastern flank (Clavero, 1996), but not by the present author. The thickness of the deposit (Figure 2.6) varies from 90 cm at 6 km from source (VR113) to 6 cm at 14.5 km (VR72). The maximum scoria diameter (Table 2.2) varies from 3 cm at 6 km (VR113) up to 0.7 cm at 13.5 km (VR109).

Where the scoria fall is overlain by ignimbrite unit P1 (northern and western sectors), the contact is conformable and mostly planar, without an intervening paleosol, unconformities or reworking. This suggests that they were separated by an interval too short (hours to months?) for even minor erosion of the fall deposit by wind or rain. Where the scoria fall is directly overlain by unit P2 (distal northern and

southern sectors), it is partially eroded, folded, thrusted and sheared. This generates slices of the fall deposit completely immersed in the underlying pre-Pucón deposit.

In the thickest and most complete exposure on the northern flank (VR113, Figure 2.5), the fall deposit consists of two layers: a lower massive layer composed almost completely of juvenile scoria, and an upper, stratified layer richer in accidental lithics (Table 2.2). The scoria is basaltic andesitic in composition (56% SiO_2) and the glass composition is variable (58-61% SiO_2).

The occurrences are all interpreted as the same deposit related to the Pucón eruption because: (1) they all conformably underlie the Pucón Ignimbrite without development of paleosoils or reworked horizons indicative of a time lapse, (2) thickness and/or grain size variations consistent with distance from source, (3) when analysed (VR73 and VR113), the scoria compositions overlap compositionally with those of the overlying ignimbrite (see Chapter 3), and (4) the lithic populations contain distinctive dense prismatically jointed lava fragments, which also occur in the overlying ignimbrite especially to the base.

Although the fall layers at all 9 locations are interpreted as the same, there are some uncertainties listed below:

- The scoria content is very variable between the different fall layers, including scoria- and lithic-rich varieties ranging from ~50 to ~100% scoria in 2 mm fraction (Table 2.2). The lithic-rich fall at VR72 has additional particular features, including: (1) a thin overlying indurated pale-brown fine vesicular ash tuff of unknown origin also sheared by P2, (2) juvenile scoriae are well rounded (abraded?) and texturally variable, and (3) even if it contains about a 10% of golden brown scoriae with a similar glass composition to the fall scoriae at other localities (59-61% SiO_2), it has also about a 40% of greenish gray to dark scoria with dacitic glass composition (65-67% SiO_2), similar to those in the underlying dacitic tuffs of VR113 (Figure 2.5, see Chapter 2).
- There is a possibility that the two northernmost outcrops (VR108 and 109, Figure 2.3) could have been emitted by the Huelemolle eruptive centre (Figures 2.3 and 2.4). In fact, this volcano, with its main activity between the Licán and Pucón eruptions (Moreno, 1993), is located less than 5 km south of outcrop VR109. Even if the Huelemolle lavas have a different composition (51-52% SiO_2) than the Pucón basal scoria fall and the scoria glass composition of the fall layer at VR109 (58-59% SiO_2) is similar to the other Pucón basal scoria fall layers, no data on fallout deposits of the Huelemolle volcanoes are available, and a correlation with deposits of this volcano cannot be discarded.
- In exposure VR98, the fall layer and overlying pyroclastic flow deposits are only tentatively correlated with the Pucón Ignimbrite.

These few exposures describe two approximate isopachs (Figure 2.6). The shapes of the isopachs are not consistent with the predominant wind sense from the northwest during the last 14,000 years (deduced

from isopachs and isopleths maps of the main fallout deposits from this period by Moreno, 1993). So, either another wind direction prevailed during the Pucón eruption, or the shapes of the isopachs would be different if other outcrops are considered (especially on the eastern flank documented by Clavero, 1996). The volume of the scoria fall deposit is estimated at ~0.2 km^3 (see section *Volume*), which corresponds to a violent strombolian to subplinian eruption following the criteria for volcanic explosivity index (VEI) of Newhall & Self (1982).

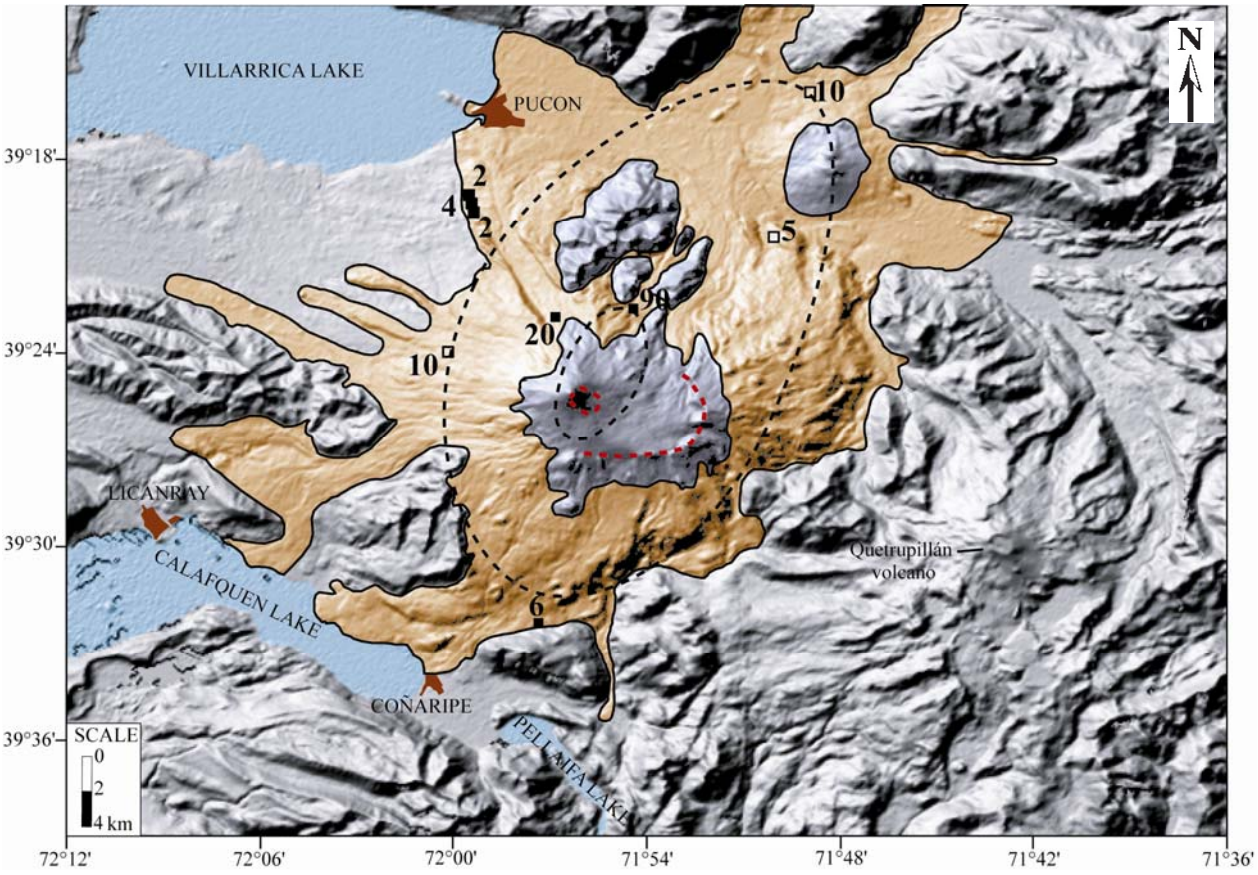

Figure 2.6: Tentative isopach map of the basal scoria fall deposit of the Pucón Ignimbrite (cm). The area enclosed by the 0.1 Tmax isopach is 440 km^2. Squares symbolise the fall outcrops; empty squares distinguish the scoria fall deposits with ambiguous temporal relationship to the Pucón Ignimbrite. Pale brown field shows the distribution of the Pucón Ignimbrite (modified from Clavero, 1996).

Table 2.2: Summary of the main features of the basal scoria fall of the Pucón Ignimbrite. The location of the outcrops is in Figure 2.3

OUTCROP	MAX THICKNESS (cm)	MAX DIST FROM SOURCE (km)	MS (cm)[1]	COMMENTS [2,3]
Scoria fall outcrops related to Pucón Ignimbrite:				
VR73	20	5	2	Juvenile-rich, scoria mostly black and a few golden-crusted scoria
VR113	90	6	3	*Lower layer:* Juvenile-rich, massive, well sorted, scoria is black fresh and angular *Upper layer:* Laminated, juvenile-rich containing black and brownish iridescent scoria but also accidental lithics. Lithics are mostly fresh including dense prismatically-jointed (DPJ) fragments
VR87	2	12.5		Lithic-rich, fines-poor overlain by a 1 cm-thick ash tuff
VR88	4	13		Fines-poor, discontinuous
VR89	2	13		Fines-poor, discontinuous and thrusted
Scoria fall outcrops for which the temporal relationship to Pucón Ignimbrite is ambiguous:				
VR108	5	13	1.5	Discontinuous, truncated and strongly deformed, eroded, thrusted and sheared by P2. Slices of the air fall completely mixed into the underlying pre-Pucón deposit. Rich in black fresh highly-vesicular scoria.
VR109	10	13.5	0.7	Discontinuous, truncated and strongly deformed, eroded, thrusted and sheared by P2. Juvenile-rich. Lithics are fresh, including dense prismatically-jointed (DPJ) fragments
VR98	10	7		
VR72	6	14.5		Pipe-like zones of fines elutriation at the base. Overlain by a 5-cm-thick indurated pale-brown fine ash tuff with elongated vesicles (1 to 5 mm long). Both layers thrusted, folded and truncated by the overlying P2. Lithic-rich; most of them are fresh including dense prismatically-jointed (DPJ) fragments. Scoria is diverse including golden, intermediate and black varieties.

NOTES:

[1] MS means maximum scoria. It was measured as the longest axis of the largest scoria found in the deposit

[2] Dense prismatically-jointed lava fragments correspond to the "DPJ fragments" of the Chapter 3.

[3] The term *lithic-rich* refers to deposits having less than ~50% scoria in all the sizes and *juvenile-rich*, to those having ~70 to 100% scoria in sizes 4 mm or coarser, and ~50 to 80% scoria in sizes 2 mm or finer. Beds with scoria abundances between these two end-members are referred to as *intermediate*.

2.3.3 Pucón Ignimbrite

The Pucón Ignimbrite is a complicated sequence of pyroclastic current deposits, including massive and stratified facies, which extends up to 21 km from the vent, but which is now intermittent due to strong erosion. It was originally formed as an essentially continuous sheet, but with strong topographic control. Where the topography is strongly incised (southeastern flank), it accumulated in deep valleys forming thick ponds (>70 m thick) with thinner veneers on interfluves (few m) which were correlated in detail. Where the topography was smooth, it formed extensive aprons at least several metres thick (NW and SW sectors).

The Pucón Ignimbrite is divided into two units, P1 and P2. The upper unit, P2, is characterised by the presence of basement granitoids, both as free fragments and as inclusions in scoria, whereas these are absent in the lower unit, P1. The boundary between P1 and P2 is very sharp. The two units show contrasting sectorial distributions; whereas P1 occurs only on the western and northern flanks, P2 was deposited all around the volcano (Figure 2.7). Each unit is composed of pyroclastic current deposits with significant vertical textural and compositional variations and can be subdivided into several laterally extensive subunits, each consisting of one or more beds.

A *unit* is the first-order stratigraphic term in the subdivision of the Pucón Ignimbrite. It is a sequence of beds, with a particular combination of components, stratification and fabrics, deposited during a specific eruptive phase and widespread around the volcano (e.g., P1 and P2). *Subunit* is the second-order term composed of one to several beds, distinct by some combination of composition, stratification and fabrics, and widespread around the volcano (e.g., P1a, P2c, etc., see below).

Proximal environments refer to locations 3 to 6 km from the present-day summit, *medial* to those 6 to 12 km and *distal* to those more than 12 km.

Two main lithofacies of pyroclastic flow deposits in the Pucón Ignimbrite are distinguished: *massive* and *diffusely stratified*. Deposits of the *massive pyroclastic flow facies* are poorly to very poorly sorted and comprise lapilli (with minor bombs and blocks) supported in a matrix of ash. Particle fabrics and grading are commonly absent. The facies occurs in beds ranging widely in thickness, from less than a metre to several tens of metres. The beds commonly show strong valley confinement. Valley accumulations usually exhibit flat tops, either horizontal or gently dipping downstream. Local preservation of steep flow fronts occurs, even if the massive deposits can also drape the landscape. There is commonly a gradation between this facies and the diffusely stratified facies described below.

Beds of massive pyroclastic flow facies several tens of metres thick probably imply quasi-steady depositional conditions (Branney & Kokelaar, 2002). Sedimentation rates must have been high enough to suppress traction along the depositional interface in order to produce this massive facies (Druitt, 1998). Valley accumulations with flat tops imply that the material was strongly fluidised with near-zero friction when it ceased motion.

Excluding perhaps some beds particularly rich in accidental components, this lithofacies would be called *scoria-flow deposit* in the terminology of Cas and Wright (1987). Local accumulations of large juvenile bombs have generated *scoria agglomerates*. Examples of the massive pyroclastic flow lithofacies are found in unit P1 and subunits P2b and P2d (see below).

The *diffusely stratified pyroclastic flow facies* occurs in beds up to several tens of metres thick. It comprises lapilli tuff beds with a subtle dm-to-m-thick stratification laterally impersistent over a few metres or tens of metres. Inclined grain fabrics are present, particularly in beds that are richer in accidental clasts. Cross stratification and dune-like bedforms on a horizontal scale of several tens of metres are observed at some locations. This facies is inferred to form by unsteady deposition from high-energy, turbulent (but high or intermediate concentration) pyroclastic flows. The presence of cross stratification and dunes shows that traction of particles along the depositional interface was an important process. Sedimentation rates from the currents can not have been high enough to totally supress tractive sorting and bedform development. The deposits of this lithofacies could also be termed *diffusely stratified scoria flow deposits*. Subunit P2a is composed largely of this facies.

Beds in the Pucón deposits laid down by pyroclastic surges are characterised by well developed cm-to-mm scale stratification and dune bedforms. The stratification includes planar, wavy and cross varieties; cross stratification, where present is typically low angle (<15°). Magnificent downstream-migrating dunes have wavelengths of several metres and heights up to few dm. Grain size constrasts between layers in pyroclastic surge deposits are greater than in diffusely-stratified pyroclastic flow deposits.

The juvenile component of the Pucón Ignimbrite is scoria of basaltic andesite composition (54 - 56 wt% SiO_2). The proportions of scoria and accidental components vary greatly in the deposits, ranging from lithic-rich deposits with pale brown matrix to juvenile-rich deposits, mostly with dark grey to black matrices.

2.3.3.1 Lower ignimbrite unit (P1)

Unit P1 occurs only on the western and northern flanks of the volcano, covering an area of ~180 km^2 and extending radially up to 15 km from the present-day summit (Figure 2.7A). The maximum thickness (20 m or more) is attained where confined to valleys, and the unit is drastically thinned (up to 2 m) on ridges, even proximally. Correlation of P1 from valleys to ridges was aided by (1) the near absence within P1 of accidental granitoids, either as individual clasts or as inclusions in scoria, and (2) the marked vertical variations of scoria abundance and colour within the unit.

P1 is composed of up to ten stacked beds, mostly of pyroclastic flow deposits (Figure 2.8; Table 2.3) but with local syn-eruptive reworked horizons. It can be divided into three main subunits (Table 2.3, Figure 2.8): a lower pale-brown, lithic- to juvenile-rich subunit (*P1a*), overlain by a black juvenile-rich subunit (*P1b*) and an upper intermediate subunit (*P1c*). P1a has the greatest extent of these subunits.

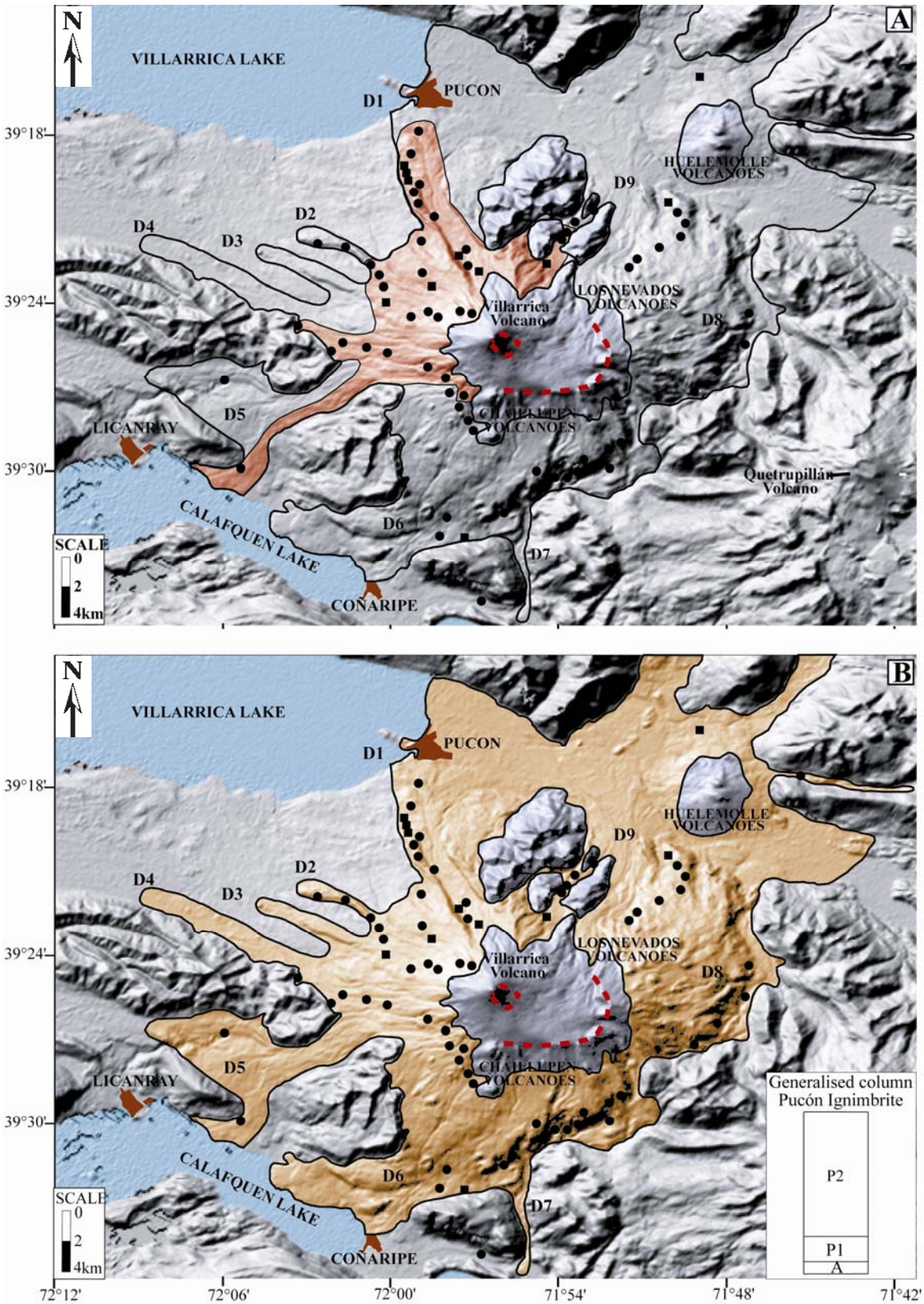

Figure 2.7: Distribution and generalised column of the main units of the Pucón Ignimbrite. Black dots are stratigraphic sections of the Pucón Ignimbrite logged for this study. Black squares are those sections including the scoria fall (A). Their coordenates UTM (in km) are in Table 2.1. Upper map (A) shows the distribution of the lower unit P1 and the lower map (B) shows the distribution of the upper unit P2. Note that P2 is distributed all around the volcano, whereas P1 is confined to the northern and western flanks.

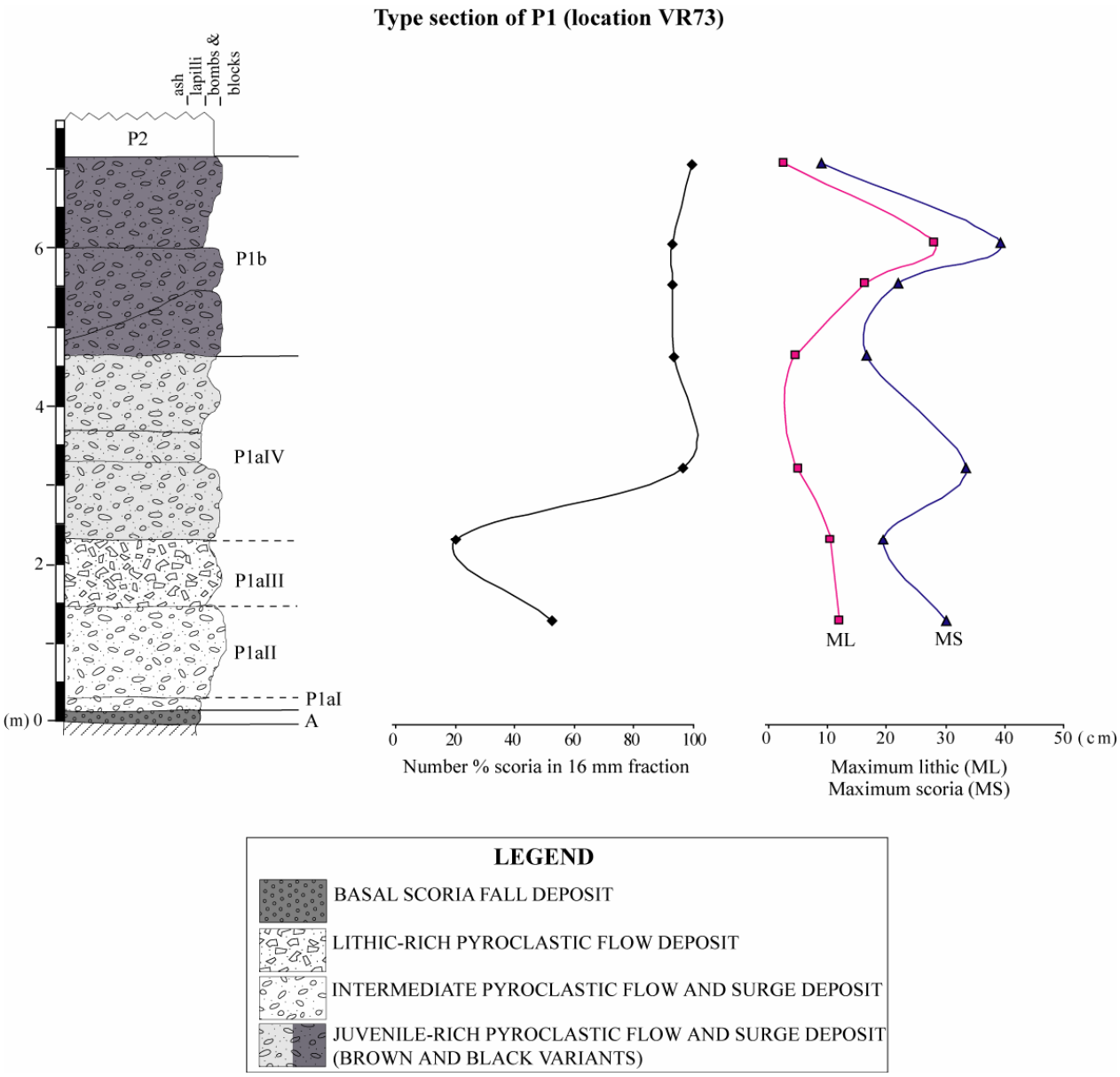

Figure 2.8: Generalised and simplified column of unit P1, including 16 mm number % scoria and maximum lithic (ML) and maximum scoria (MS) data. *Lithic rich* deposits have less than 50% scoria in all the sizes and their matrices are normally brown. *Juvenile rich* deposits have about 70 to 100% scoria in sizes 4 mm or coarser, and about 50 to 80% scoria in sizes 2 mm or finer. Their matrices are dark grey to black, but some brown-coloured variants also occur. *Intermediate* deposits have scoria abundances between these two end-members.

Table 2.3: Summary of the main features of unit P1 of the Pucón Ignimbrite

SUBUNIT		MAX THICKNESS (cm)	MAX RUN OUT (km)	N° BEDS	DRAINAGES	MAIN LITHOLOGIES	DEPOSIT DESCRIPTION	MAIN LITHOFACIES
P1a	**I**	40	6	1 to 2	2,1,9 (north)	Parallel and cross laminated intermediate ash tuff	Uniform thickness, drapes topography, locally plastered against charcoal obstacle. Fine-grained ash with juvenile scoria.	Pyroclastic surge possibly from phreatomagmatic explosions
	II	340	6	1 to 3	5,1,9 (west to north)	Massive intermediate lapilli tuff	Semi-indurated, poorly-sorted with inverse grading of light bombs. Rich in brittle goldish-brown-crusted bombs, goldish brown scoria lapilli and ash, dense prismatically-jointed (DPJ) and fumarolic-altered fragments.	Massive pyroclastic flow
	III	800	16	1 to 3	5,4,2,1,9 (west to north)	Massive lithic-rich lapilli tuff, massive lithic breccia, parallel and cross stratified lithic-rich lapilli tuff	Indurated, very-poorly sorted, non-graded. Very rich in fresh accidental lithics and variable-density juvenile pyroclasts, in a pale brown matrix. Underlain locally by a basal parallel and cross stratified fine-grained tuff. Grades proximally into a fines-poor lithic breccia.	Massive pyroclastic flow, pyroclastic surge
	IV	200	5.2	2	1,2 (north)	Massive juvenile-rich lapilli tuff, parallel and cross stratified juvenile-rich lapilli tuff	Black and low-density scoria, in a brown matrix. *Lower bed*: Lenticular, indurated and massive, with imbrication of lithics and inverse grading of lithics and bombs. *Upper bed*: Not consolidated, parallel and cross stratified lapilli tuff with massive inverse-graded centre.	Massive pyroclastic flow, pyroclastic surge
P1b		>1500	15	5	5,4,2,1,9 (west to north)	Massive juvenile-rich lapilli tuff to agglomerate, diffusely stratified juvenile-rich lapilli tuff	Black, massive, very rich in light scoria, inverse grading of bombs and normal grading of lithics, rich in charcoal and degassing pipes. Beds are lobed, lenticular and valley-confined. Local accumulations of bombs form agglomerates. Central layer richer in lithics. Diffuse and parallel-stratified variants proximally.	Massive pyroclastic flow
P1c		1000	12.5	1 to 3	9,1,4,5 (west and north)	Massive intermediate lapilli tuff (locally diffusely stratified)	Scoriaceous and brittle dense bombs, dense "slabby" bread-crusted blocks and dense prismatically-jointed lava fragments in a brown matrix. Higher lithic content than P1b. Inverse grading of bombs and blocks (proximally) and normal grading of bombs (distally). Large carbonised trunks with degassing pipes dipping downstream.	Massive pyroclastic flow

Lithic rich deposits have less than 50% scoria in all size fractions and their matrix is normally brown. *Juvenile rich* deposits have about 70 to 100% scoria in sizes 4 mm or coarser, and about 50 to 80% scoria in sizes 2 mm or finer. Their matrix is dark grey to black, but some brown-coloured variants also occur. *Intermediates* deposits have scoria abundances between these two end-members.

Subunit P1a

Subunit P1a is preserved in a sector from west to north of the present-day summit and up to 15 km radially. It exhibits an important deposition on valleys, where it consists mostly of a bedded sequence of brown lithic-rich to juvenile-rich pyroclastic flow deposits. Four main subdivisions in P1a are denoted P1aI to P1aIV (Table 2.3, Figure 2.8). Their different distributions are shown in Figure 2.9. The sectorial variations of P1a, from the western to northern flank are shown in Figure 2.10. The selected outcrops are well exposed valley-bottom sequences located at equivalent distances from source in medial environments (5 to 6 km from present-day crater).

The base of P1a is marked by a thin (15-40 cm) parallel- and cross-stratified pyroclastic surge layer (P1aI), preserved in drainages north of the volcano (drainages 2, 1 and 9) 4 to 6 km from the present-day crater (Figures 2.9 and 2.10). It is laterally continuous, but coarsens and thickens into depressions. It is locally thrusted by the overlying P1aII deposit, but it can also interfinger with P1aII at the contact (Figure 2.11A). The deposit is very fine-grained (about 90 wt% of the deposit is finer than 1 mm). It contains charcoal, but appears locally plastered against obstacles (Figure 2.11B), suggesting it was emplaced in a hot, possibly damp state. P1aI is interpreted as a pyroclastic surge from weak phreatomagmatic explosions.

P1aII to P1aIV are jointly up to more than 15 m thick. They are massive, brown pyroclastic flow beds, normally confined to valleys, with a restricted sectorial distribution, without lateral continuity and exhibiting interdigitation between them (Figure 2.10). This makes layer-by-layer correlation between isolated exposures difficult. Nevertheless, proximal-to-medial valley-fill sequences allow us to recognize three main subdivisions (P1aII to P1aIV), based on differences in distribution, scoria content and structures and fabric of the deposits (Table 2.3).

P1aI, P1aII and P1aIV are restricted to the upper flanks of the volcano, whereas P1aIII also occurs in drainage 4, and travelled further from source (Figure 2.9). P1a III is also coarsest and thickest (0.8 to 8 m thick, Figure 2.10). The underlying and overlying groups (P1aII and P1aIV) have comparable thicknesses (up to 4 m). P1aIII is also rich in blocks and is normally non-graded, whereas P1aII and P1aIV show inverse grading of scoria bombs and normal or inverse grading of the less abundant blocks (Figures 2.10, 2.11C-E-F and 2.12). The presence of multiple, well defined beds suggests emplacement by a succession of discrete, highly concentrated pyroclastic flows.

Although P1aII, P1aIII and P1aIV are mostly massive, there are also thin parallel and cross stratified layers associated with the main massive pyroclastic flow deposits. (1) As a thin (<1 m), impersistent layer at the base of P1aIII in proximal environments (Figures 2.10, 2.11C and 2.11F); this is interpreted as a pyroclastic surge preceding the pyroclastic flow. (2) As layers at the base and top of the upper bed of P1aIV (Figures 2.10, 2.11D and 2.11F); the basal layer is usually thicker than the upper layer and exhibits a locally wavy erosive base and planar gradual top (Figure 2.11D); they are interpreted as pyroclastic

surges associated with the main massive flow. (3) As fine-grained deposits on ridge-top environments, interpreted as the dilute equivalents of the valley-confined massive main flows.

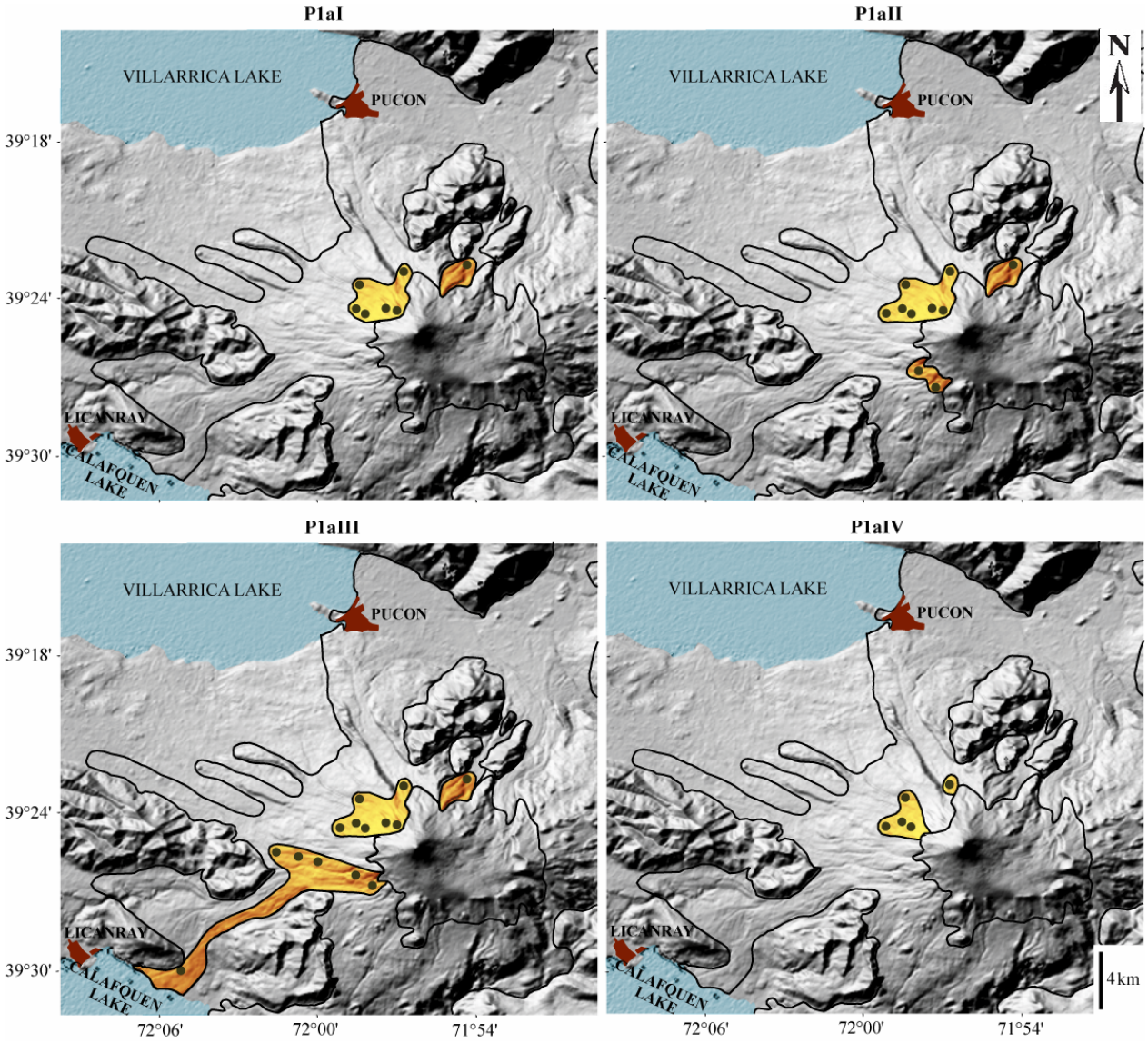

Figure 2.9: Distribution maps of the different groups of subunit P1a around the volcano. Black dots correspond to the main outcrops where these groups are preserved.

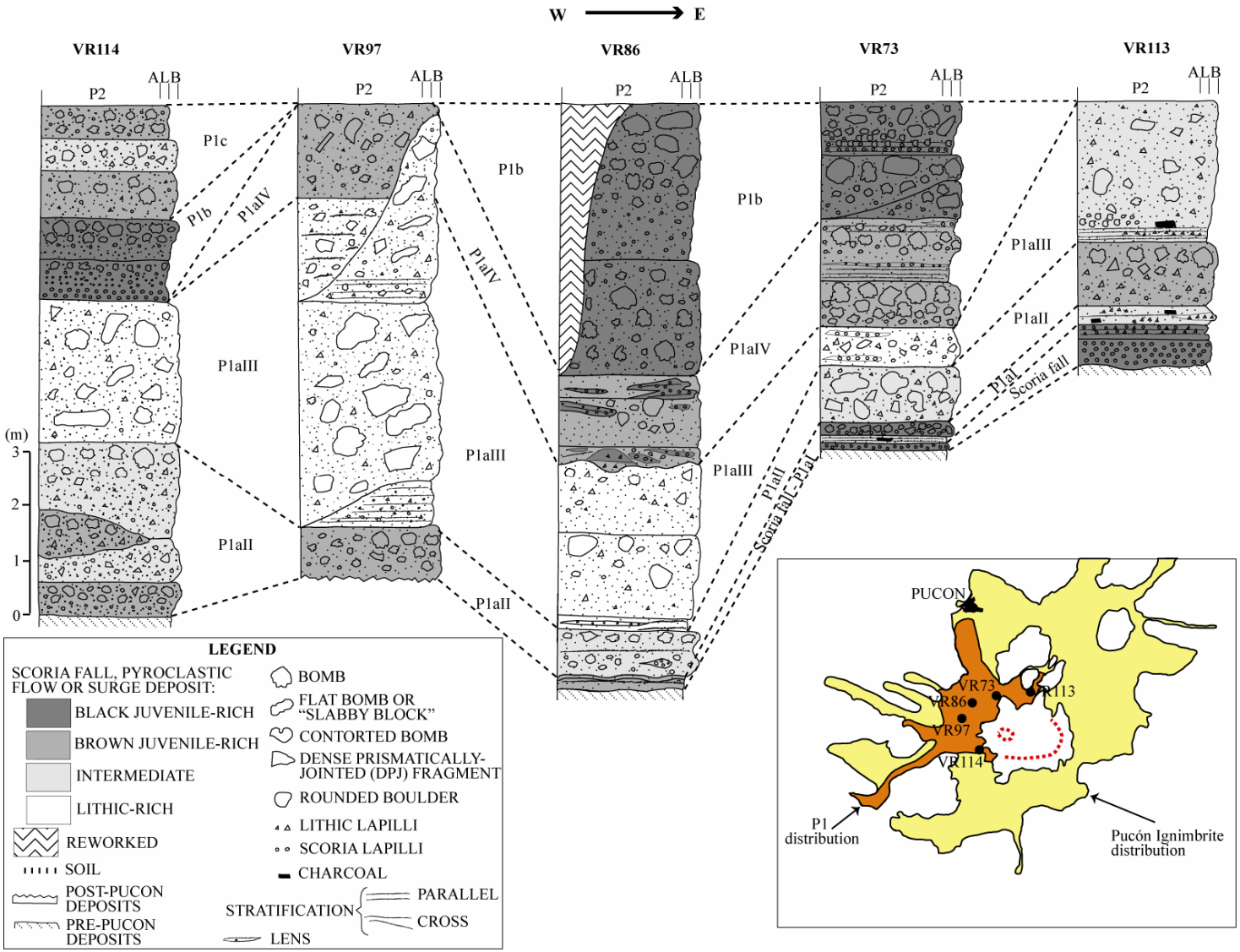

Figure 2.10: Correlation logs of unit P1 showing the sectorial variations on the western and northern flanks. Sections logged are shown in the insert map. *Lithic rich* deposits have less than 50% scoria in all the sizes and their matrix is normally brown. *Juvenile rich* deposits have about 70 to 100% scoria in sizes 4 mm or coarser, and about 50 to 80% scoria in sizes 2 mm or finer. Their matrix is dark grey to black, but some brown-coloured variants also occur. *Intermediates* deposits have scoria abundances between these two end-members. A = ash, L = lapilli, B = bombs & blocks.

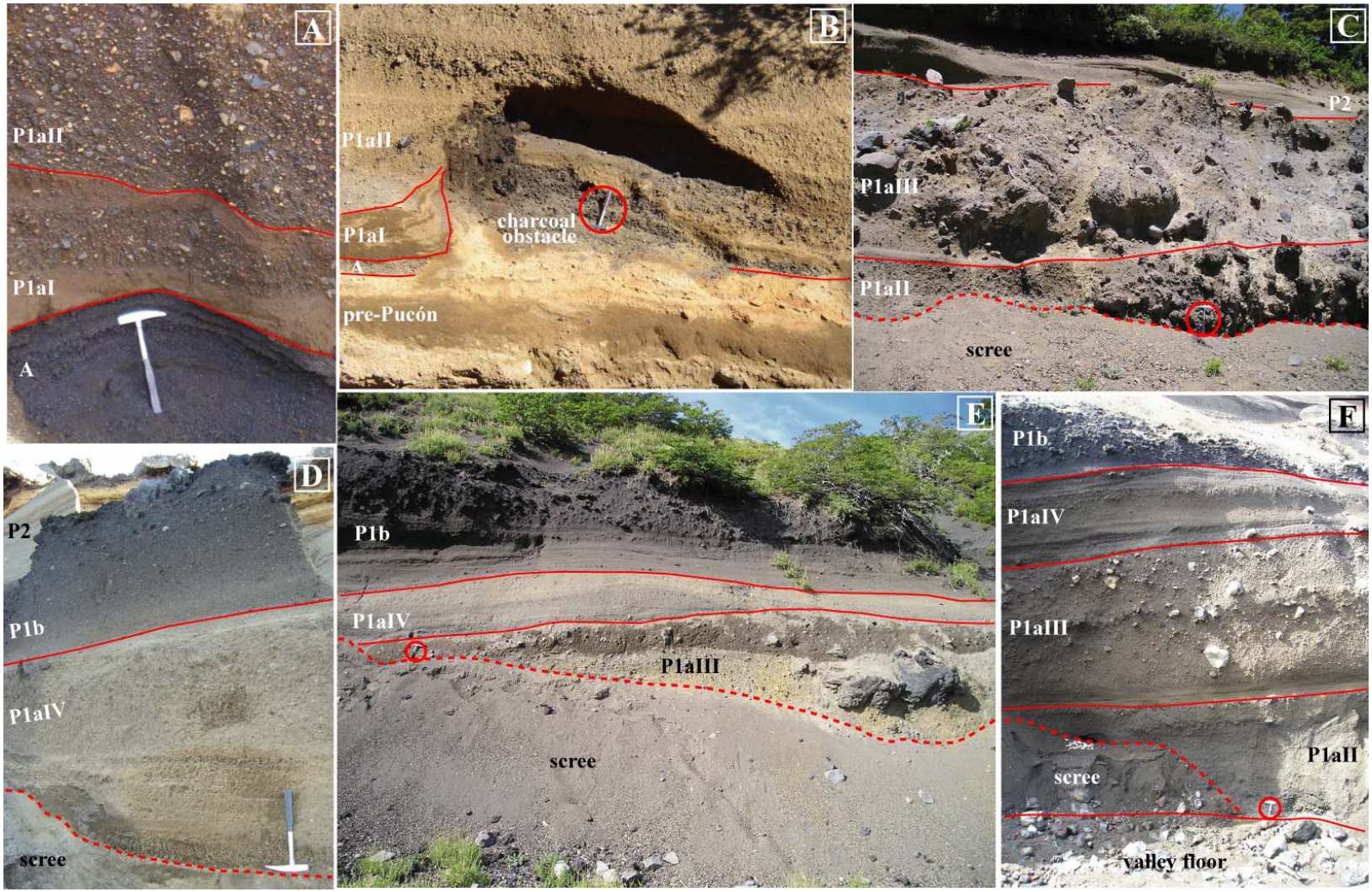

Figure 2.11: Plate showing valley fill exposures of unit P1 of the Pucón Ignimbrite. (A) The basal scoria fall (A), overlain by fine-grained deposits of P1aI interfingering with massive P1aII (VR113, proximal, drainage 9). Note the abundant orangish fumarolised fragments. (B) The P1aI surge is plastered against an obstacle of carbonised trunks indicating possible wet conditions of transport and emplacement (VR73, proximal, drainage 1). (C) Typical massive chaotic lithic-rich P1aIII deposits (VR97, drainage 2), overlying a juvenile-rich P1aII deposit. (D) A deposit of P1aIV grading up into the black juvenile-rich subunit P1b (VR73, proximal, drainage 1). (E) & (F) The massive to stratified deposits of subunit P1a, overlain by the juvenile-rich subunit P1b (VR96 and VR86 respectively, drainage 2). Locations in Figure 2.3.

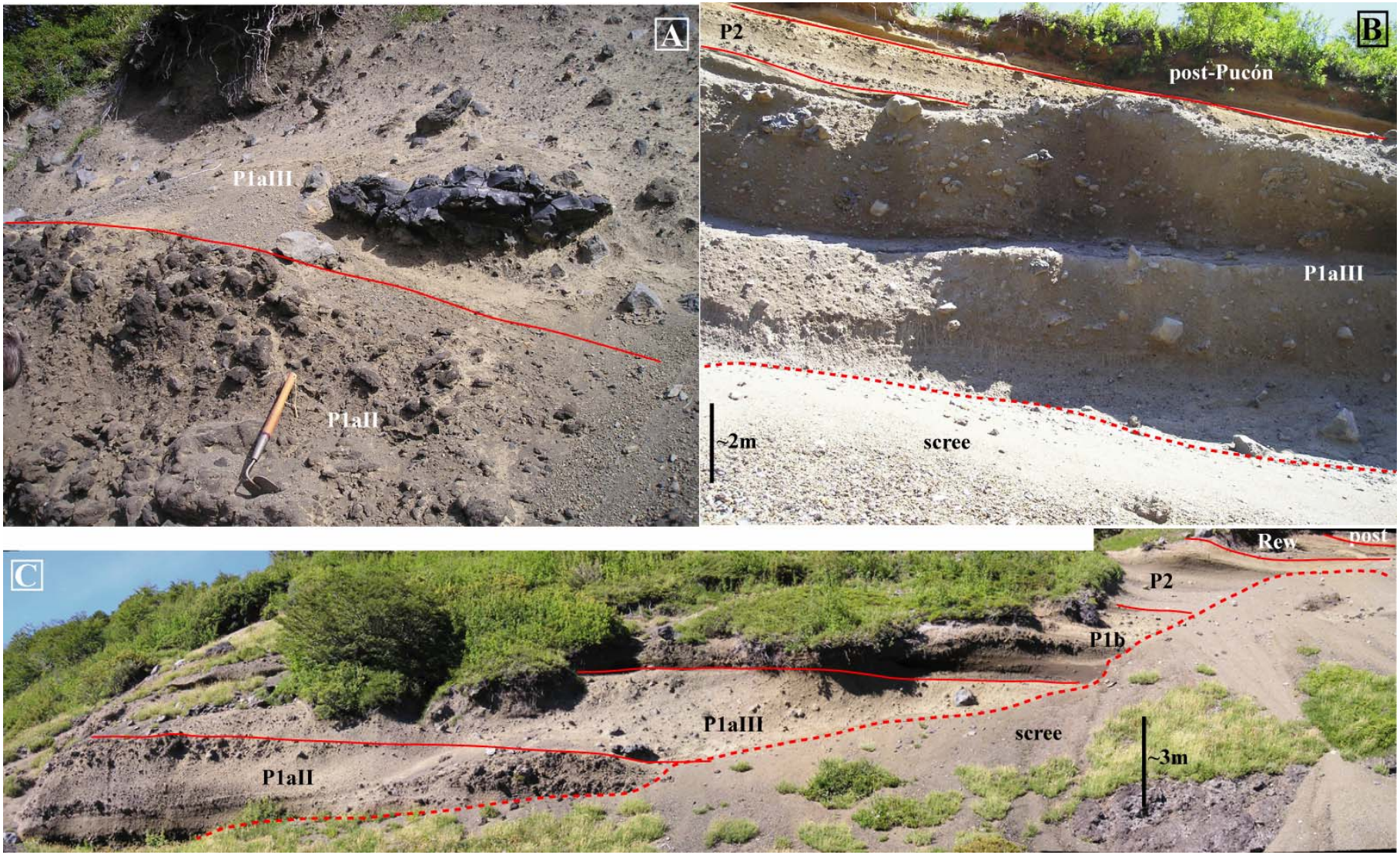

Figure 2.12: Plate showing valley fill exposures of unit P1 of the Pucón Ignimbrite. (A) Contrasting components of P1aII and P1aIII. Note a typical "slabby block" of P1aIII (VR114, proximal, drainage 5). (B) Two lithic-rich beds of P1aIII (VR97, drainage 2). (C) Complete sequence of the Pucón Ignimbrite on the western flank, more than 15 m thick (VR114, proximal, drainage 5). Locations in Figure 2.3.

A very different lithofacies of P1a is seen proximally in drainage 2 (Figure 2.13D). It is a yellowish-brown, poorly-sorted, massive breccia, at least 8 metres thick, very rich in accidental lithics with abundant fumarolically-stained rounded boulders and diverse types of bombs and fresh blocks. It has also splintered or spalled glassy rounded boulders. The deposit is very poor in ash particles and it exhibits towards the base pipe-like and disorganised extremely fines-depleted zones generating locally a clast-supported lithic breccia (Figure 2.13D). This breccia is correlated with the main bed of P1aIII, due to the presence of similar types of bombs and blocks. We tentatively interpret this facies as a lag breccia composed of lithic clasts too coarse or too dense to have been transported by the pyroclastic flows (Wright & Walker, 1977; Druitt & Sparks, 1982; Druitt & Bacon, 1986; Mellors & Sparks, 1991; Rosi *et al*., 1996; Druitt, 1998).

Some lenses of reworked material, mostly interpreted as debris flow deposits, occur intercalated in the drainage accumulations of P1a. Also, some beds such as P1a III are locally indurated, with vesicular matrices which could also suggest reworking. The presence of such beds shows that water was available for mobilisation and transport of pyroclastic debris during the eruption of P1a.

Subunit P1b

Overlying the brown P1a sequence, P1 is composed of black juvenile-rich pyroclastic flow deposits preserved in a sector from west to north of the volcano, mostly in valleys and depressions, with a maximum extent of 15 km from the present-day summit (Figure 2.14). The most important deposition of this subunit is in drainages 4, 2 and 1, and it is less important in drainages 5 and 9 (Figures 2.10 and 2.14). The black colour is very conspicuous, making P1b a useful marker horizon for the Pucón deposits in this sector of the volcano (Figure 2.15). The high-content of black juvenile scoria accounts for the dark grey to black colour of P1b, in contrast with the brownish colour of P1a which is not only less juvenile-rich but also provided with ash, scoria lapilli and vesicular rims of scoria bombs, commonly with yellowish tinges, possibly due to incipient palagonitization (Chapter 3).

P1b can reach up to more than 10 m in valleys. The number of beds is difficult to establish, being variable across nearby outcrops. This could be due to the occurrence of locally-derived flow units (lobate front, flow separation around obstacles, etc.). However, one to three main beds have been recognised (Figures 2.8, 2.10 and 2.14).

Inverse grading of bombs (up to 60 cm diameter) and normal grading of accidental lithics (rarely up to 2 m) is common (Figure 2.10). Although mostly massive, diffuse and parallel-stratified variants are deposited proximally, especially at the base of the deposits (Figure 2.15A-C). A parallel and cross stratified ash-cloud surge deposit is present locally at the top of a bed.

The presence of abundant charcoal in P1b indicates a high emplacement temperature, probably in part due to the high abundance of juvenile components. In drainages 1 and 4, charcoal is more abundant in

distal than in proximal exposures. This may suggest that dense forest was mostly present in medial and distal parts of the valleys, as is the case around Villarrica today.

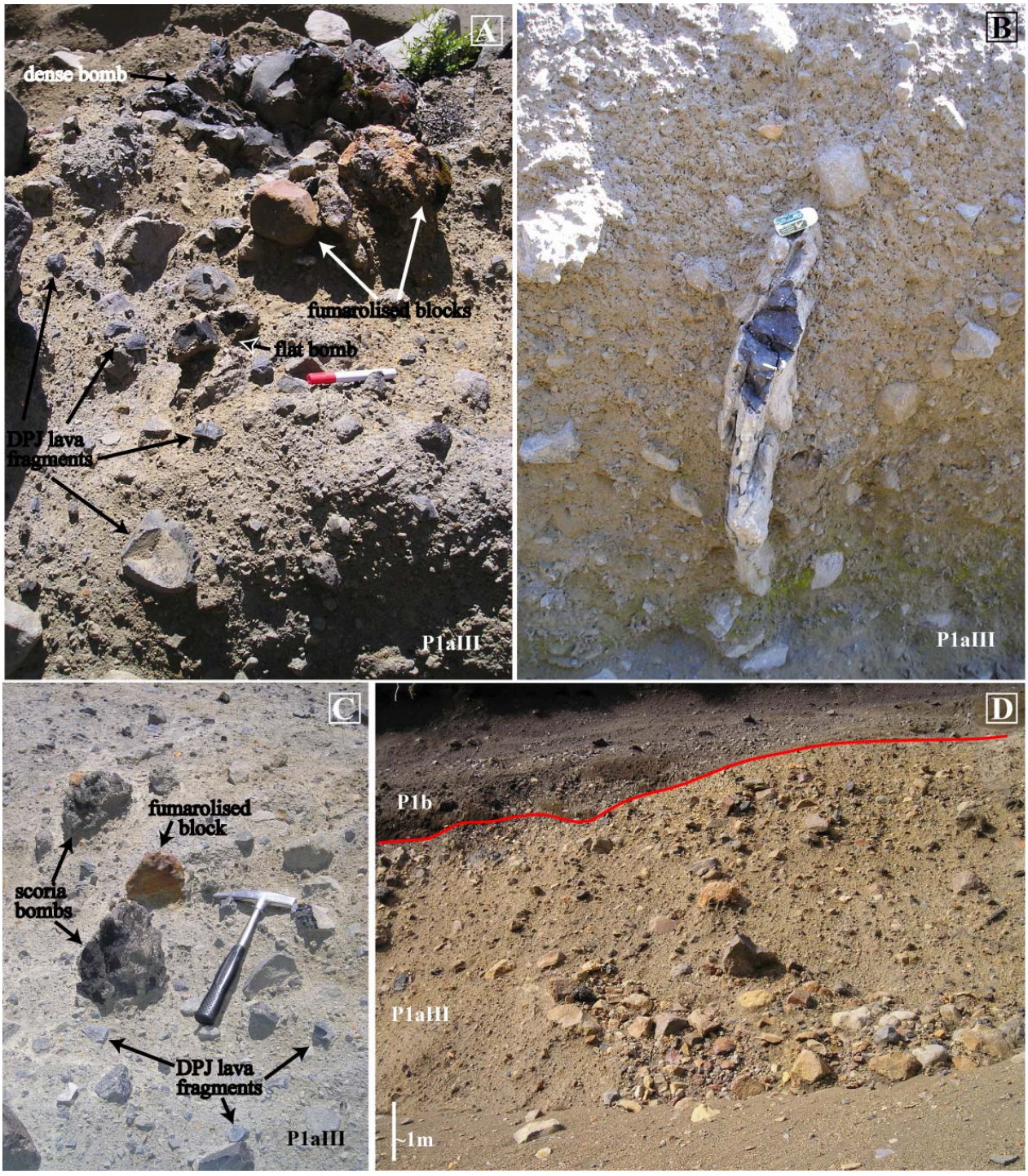

Figure 2.13: Plate showing some P1a deposits and components. (A) Lithic-rich massive deposit containing dense bombs, flat bombs, fumarolised blocks and dense prismatically-jointed (DPJ) lava fragments (VR97, drainage 2). (B) A bomb with strong flattening in the lithic-rich P1aIII (VR97, drainage 2). (C) Scoriaceous bombs of the lithic-rich P1aIII (VR97, drainage 2). (D) Proximal lithic breccia with pods of clast-supported breccia (VR95, proximal, drainage 2). Locations in Figure 2.3.

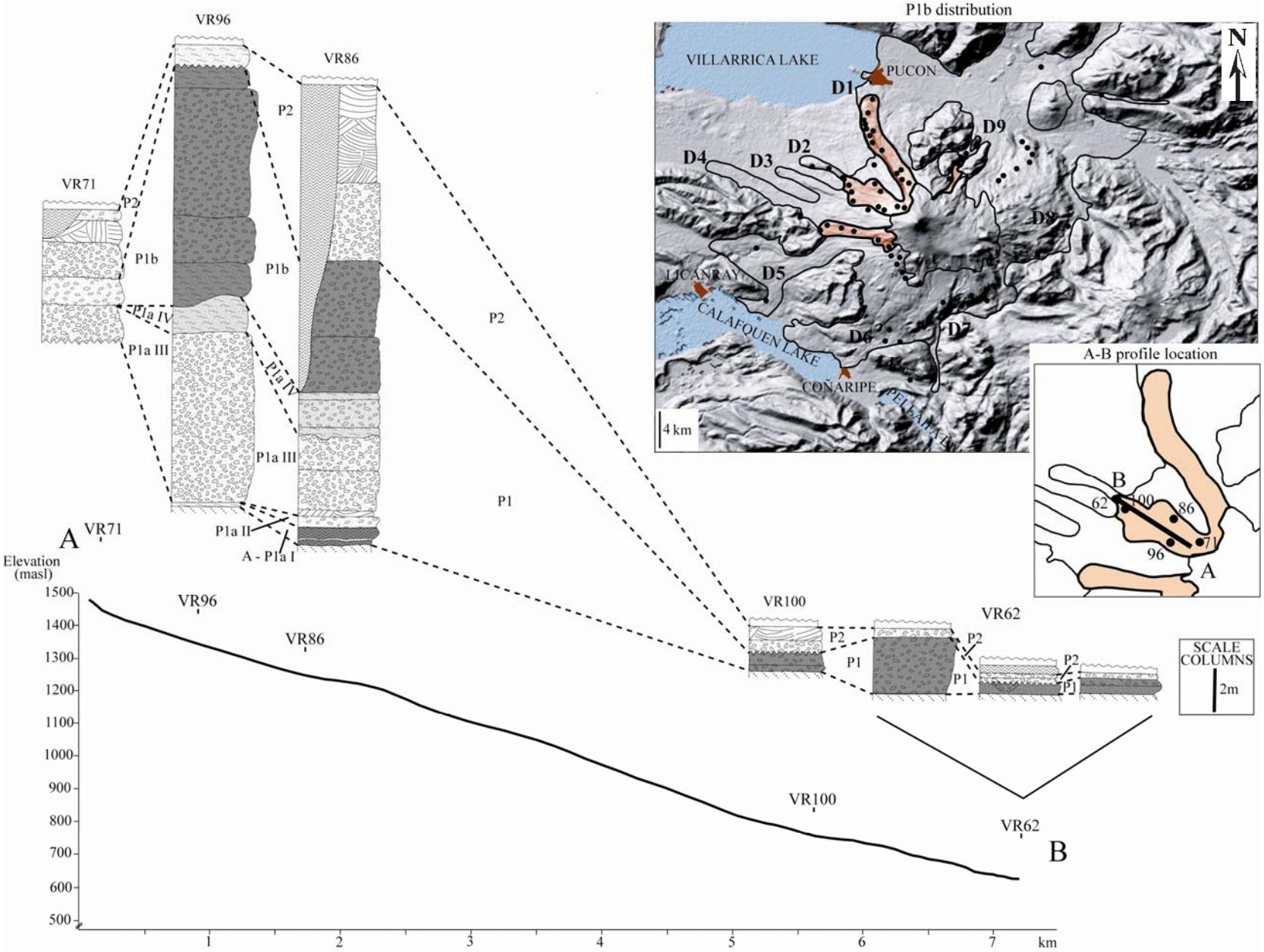
VR96
VR86
VR71
P2
P1b
P1a IV
P1a III
P1a II
A - P1a I
A
B
Elevation (masl)
1500
1400
1300
1200
1100
1000
900
800
700
600
500
1
2
3
4
5
6
7
km
VR100
VR62
P1
P1b distribution
VILLARRICA LAKE
PUCON
D1
D2
D3
D4
D5
D6
D7
D8
D9
LICANRAY
CALAFQUEN LAKE
COÑARIPE
PELLAIFA
4 km
N
A-B profile location
62
100
86
71
96
SCALE COLUMNS
2m

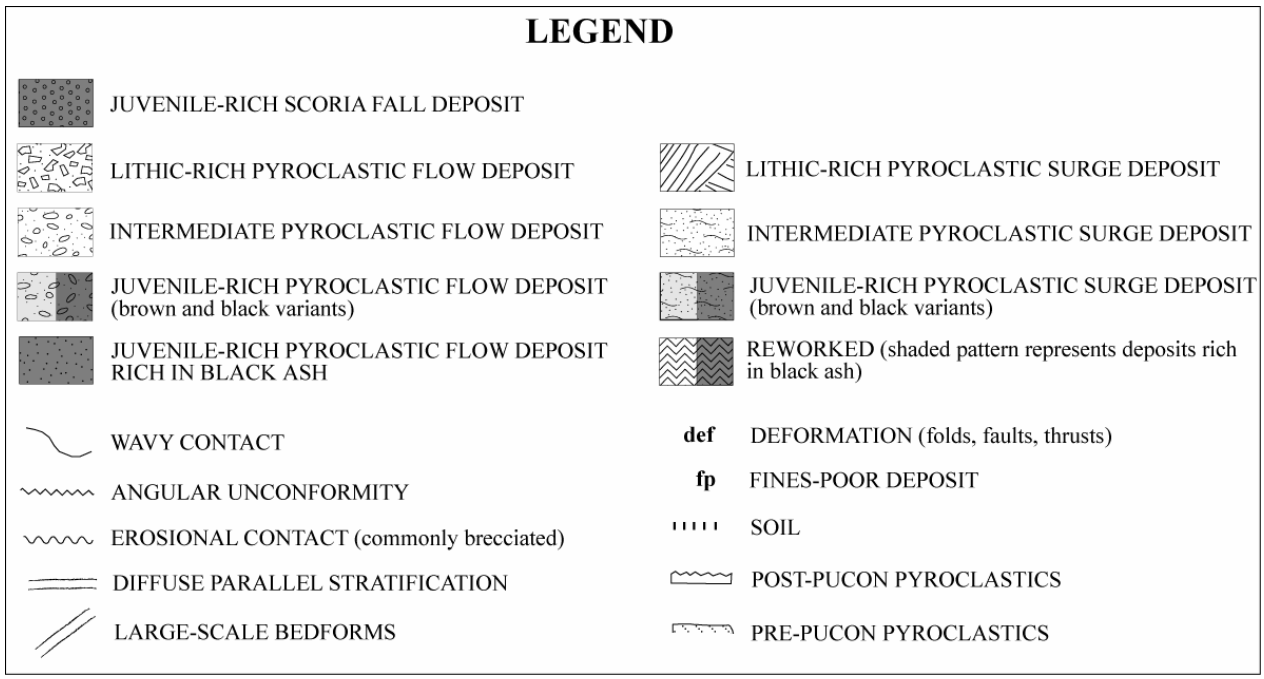

Figure 2.14: Stratigraphic logs of the Pucón Ignimbrite along a profile in drainage 2 (A-B). The distribution map of subunit P1b is also shown (field in red).

Locally in the distal portion of drainage 2 (9.5 km from the present-day summit), there was observed a steep exposure 2.5 m high of massive, inverse-graded P1b rich in scoria bombs (VR62, Figure 2.14). A few hundred of meters downstream, the bed thins and becomes richer in ash and much poorer in bombs (Figures 2.14 and 2.15D) and downstream of this locality, P1b doesn't crop out any more along this valley. This is consistent with the presence of a steep flow front showing that the P1b pyroclastic flows were highly concentrated by the time they reached this distance. However, the possibility that the flow with a lobate shape, can continue downstream but not be cut by the valley walls, cannot be discarded ("cut effect").

Local clast-supported accumulations of bombs occur, forming scoria agglomerate facies, probably due to: (1) elutriation of fines due to water or gases derived from carbonised wood, (2) local concentration of bombs into channels (Figure 2.15D), (3) local concentrations at steep flow fronts (Figure 2.14), and (4) the basal parts of thick valley ponds (more than 15 metres thick) in the narrower portions of valleys, where dense agglomerates can have flat bombs lying even in vertical position.

The P1b deposits are interpreted as a result of the emplacement of one to three hot, high-concentration pyroclastic flows rich in juvenile material.

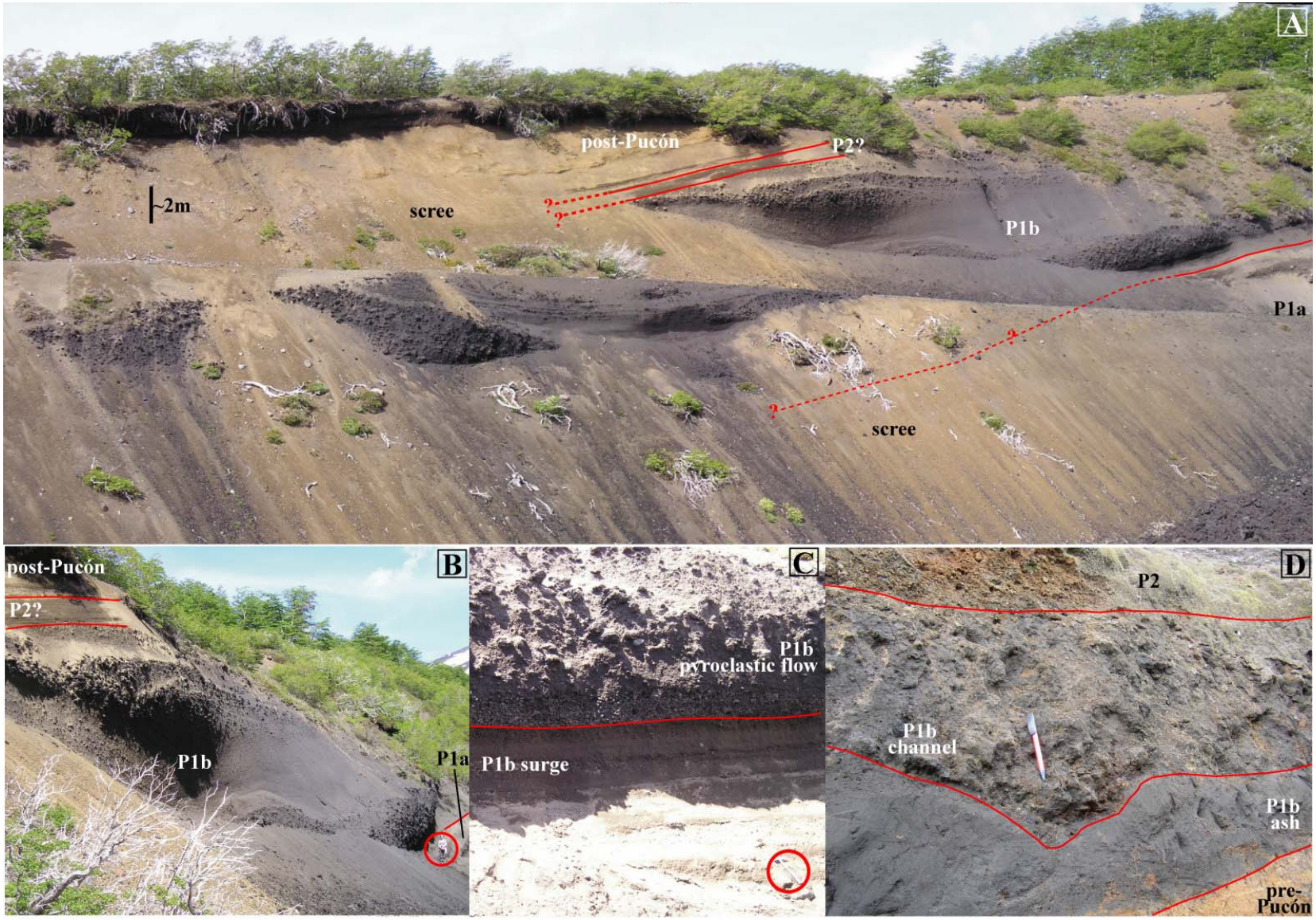

Figure 2.15: Plate showing valley fill exposures of subunit P1b along drainage 2. (A), (B) and (C) Proximal thick exposures showing massive and stratified beds, underlain and overlain by brown stratified beds of P1a and P2, respectively (VR96). (D) Ash rich distal bed cut by a channel rich in scoria lapilli (VR62). Locations in Figure 2.3.

Subunit P1c

P1 terminates with one to three, mostly massive, pyroclastic flow beds, 0.5 to 10 m thick. Diffusely stratified beds are locally seen. This subunit is distributed in some valleys on the western and northwestern flanks of the volcano (drainages 1, 4, 5), up to 12.5 km from the present-day summit. It contains abundant scoriaceous and jointed dense bombs (Figure 2.16A). It has brown matrix and a higher proportion of lithic fragments than P1b, including abundant dense prismatically-jointed lava (DPJ) fragments and dense "slabby" bread-crusted blocks.

P1c can exhibit strong inverse grading of bombs and blocks and magnificent degassing pipes dipping downstream (up to 5 m-long) growing from large carbonised trunks (>2 m long, Figure 2.16B). Distally, this subunit contains less abundant and smaller carbonised wood and degassing pipes, and it can incorporate locally-derived epiclastic boulders. The inverse grading more common at the proximal environments grades distally into a normal grading of bombs.

The basal contact of P1c is generally conformable and is cut by degassing pipes rooted on charcoal in P1b. This shows that the charcoal in P1b was still hot enough to release gases when the pyroclastic flows of P1c were emplaced, suggesting rapid emplacement of successive flows of the upper part of P1.

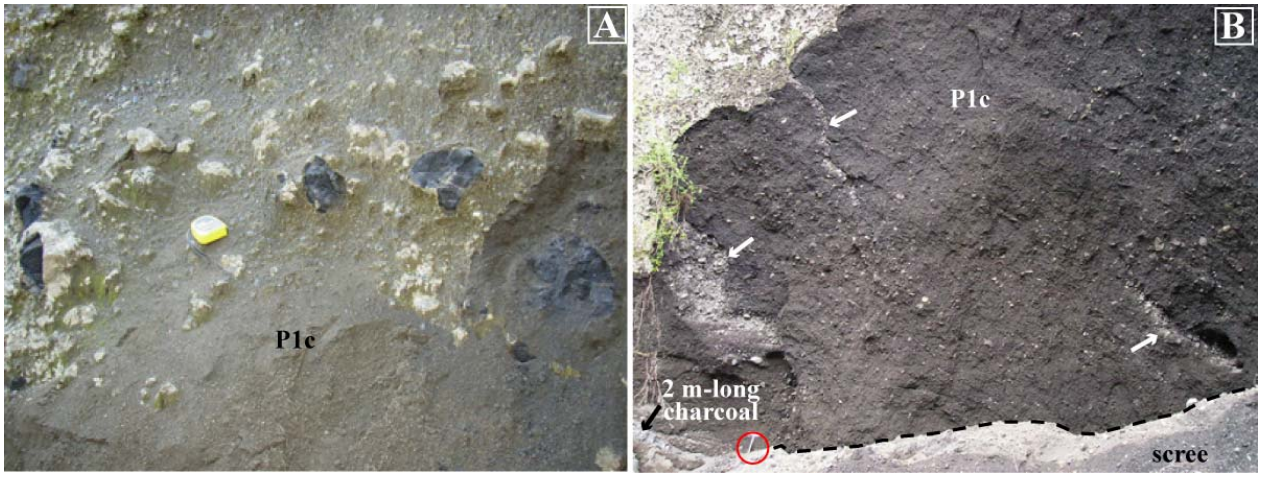

Figure 2.16: Plate showing subunit P1c. (A) Massive pyroclastic flow deposit with inverse grading (VR57, drainage 4). (B) Massive pyroclastic flow deposit containing magnificent degassing pipes dipping downstream (showed with arrows) growing from large carbonised trunks (VR102, drainage 1). Locations in Figure 2.3.

Interfluve and distal sequences of P1

Deposits corresponding to P1 are found on interfluves up to 200 m above adjacent valley floors (VR58 and VR16, Figure 2.3). Four to five beds (each 5 to 30 cm thick totalling about 1 m) of parallel-stratified ash and lapilli surges of subunit P1a were deposited on ridges up to 8.5 km from source (VR58 and VR16, Figures 2.3, 2.17 and 2.18), which appear to have been deposited from ash clouds associated with the P1a pyroclastic flows or from the upper, more dilute levels of those flows. They are overlain by a coarse-grained metre-thick veneer of P1b, the pyroclastic flows of which apparently overspilled the ridge up to 6 km from the vent (VR58, Figures 2.3 and 2.17B). The P1 sequence is strongly eroded, folded and thrusted, deformation which could be attributed to the subsequent violent P2a pyroclastic currents (Figure 2.18). Where the sequence is deposited onto an irregular paleotopography of lavas (e.g., location VR58), it is commonly completely eroded in the upper portion of the upstream side of obstacles (Figure 2.17B). An interesting feature at location VR58 is the presence of anastomosing networks of ash-filled tubes penetrating some of the ash layers in P1a, probably produced by bioturbation (Figure 2.18B). Centimetric pieces of charcoal with fines-depleted rims dispersed in some of these (Figure 2.18C) may be the sheared remains of vegetation buried by the accumulating P1a ashes layers, or of root networks established in the ashes prior to the emplacement of unit P2, and subsequently charcoalized by the overlying P1b and P2a pyroclastic flow deposits.

Deformed P1 sequences are also seen on medial to distal valley exposures of drainage 2 (VR100 and VR62, Figure 2.3). One of the most distal exposures of unit P1a is located 16 km from source on the western flank of the volcano (VR70, Figure 2.3). The deposit, about 85 cm thick, is composed of two beds, the upper one being thicker, coarser-grained and richer in lithics. They are interpreted as P1aII and P1aIII.

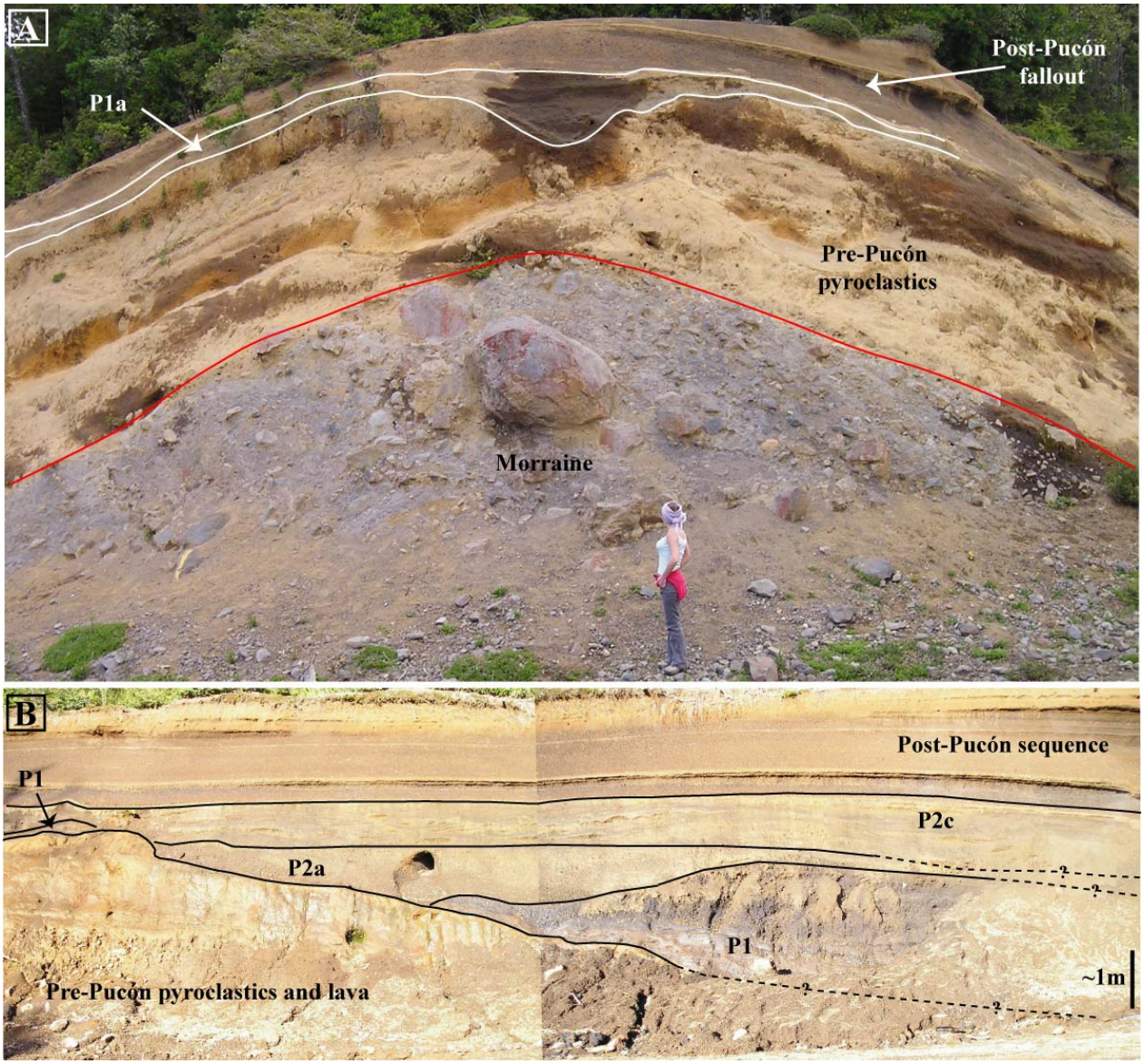

Figure 2.17: Plate showing P1 sequences on ridge environments between drainages 1 and 2. Flow direction from right to left. (A) Variable thickness of P1a. Note that P1b and P2 are locally absent (VR16). (B) P1 deposited onto a wavy topography (VR58). Details in the next figure. Locations in Figure 2.3.

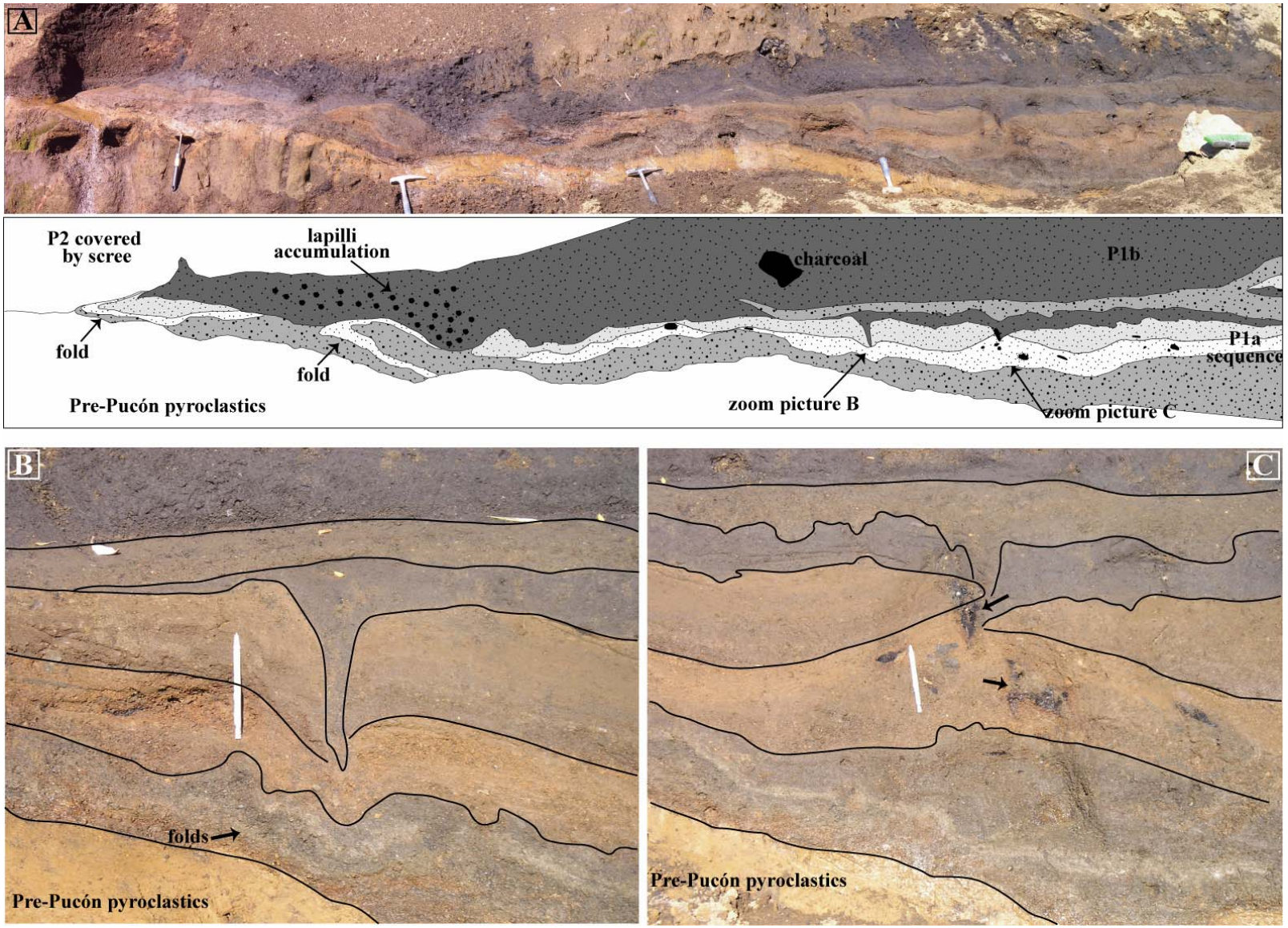

Figure 2.18: Plate showing P1 deposition on ridges (between drainages 1 and 2, VR58, Figure 2.3). P1 deformed probably due to violent emplacement of the subsequent P2 currents. P1a exhibits ash-filled tubes (bioturbation?) with charcoal remains (root networks?) (indicated by arrows in picture C).

2.3.3.2 Upper ignimbrite unit (P2)

In contrast to the restricted distribution of unit P1, P2 was deposited all around the volcano, covering an area of ~530 km^2 and extending radially up to 21 km from the present-day summit (Figure 2.7). It forms thick sequences in valleys (up to 70 m thick) with an important deposition on interfluves (up to 5 m thick). The generalised column of unit P2 consists of four main subunits (P2a, P2b, P2c and P2d), the main features of which are summarised in Table 2.4. The characteristic presence of granitoids in P2, both as free clasts and as inclusions in scoria, allows us to distinguish it unambiguously from P1 all around the volcano. However, certain lithologic and stratigraphic differences between the sequences of P2 deposits on the northern and southern flanks of the volcano, makes correlation *within P2* between these sectors difficult. The limit between the northern and southern sectors, and the contrasting type sections of P2 are shown in Figure 2.19. The main difference is that thick black pyroclastic flow deposits rich in juvenile components are present in the southern sector (P2b), but not in the northern sector. In fact, unit P2 in the northern sector comprises brown lithic-rich to intermediate deposits from subunits P2a, P2c and P2d (Figure 2.20A-C), whereas P2 sequence in the southern sector can be summarised as a main central black juvenile-rich layer (P2b) sandwiched between brown lithic-rich layers (P2a and P2c, Figure 2.20D).

The topography onto which the P2 pyroclastic currents were emplaced was deeply incised on the southeastern flank of the volcano, where P2 accumulates to great depth in deep valleys (P2 reaches ~70 m on the southern sector compared to ~15 m thick on the northern sector). Thus, the exposures preserve both valley-floor and valley-margin depositional facies, which can be correlated in detail. A particularly deeply incised drainage southeast of the volcano (drainage 7) was filled to a depth of up to 70 m with a flat-topped terrace of deposits, with well preserved, much thinner valley-margin facies (Figure 2.22). An important feature of the interfluve sequences (for example, VR68, VR84 and VR75 in Figure 2.22; VR58 and VR118-108 in Figure 2.23) is that they preserve an essentially complete record of all the pyroclastic currents that passed over a given location. This is not necessarily the case with the valley-fill facies, which commonly contain subtle internal amalgamation surfaces, thus preserving an incomplete record of sedimentation. To the southwest, the ignimbrite forms an extensive, gently downstream-inclined apron at least several metres thick (Figure 2.22). No important valley-floor and interfluves variations were observed in this sector of the volcano.

In the southern sector, the correlation between valley-floor and interfluves, and also radially along the valleys, was helped by the strong variations in the juvenile content of P2. The central black juvenile-rich layer (P2b) was particularly useful for correlation in this sector (Figure 2.22). To the north, the correlation was mostly helped by the internal structures of the deposits; the central stratified layer (P2c) was a particularly useful horizon for correlation in this sector (Figures 2.23 and 2.24).

Whereas in the north, unit P2 lies on unit P1, in the south, it lies directly on pre-Pucón volcanic strata, separated only by extensive mudflow deposits, commonly highly indurated. Interestingly, even these

mudflow deposits contain abundant granitoid clasts, as well as scoria containing granitoid inclusions. Therefore if the mudflows were related at all to the Pucón eruption, they were derived by remobilisation of P2, not P1. No evidence has been observed for P1 deposits underlying P2 in the south. Another difference between the P2 successions north and south of Villarrica is that P2 in the north and west is significantly poorer in carbonised wood than the underlying P1, probably because the vegetation was already largely buried and burned by the P1 pyroclastic flows. This is not the case in the south, where the P2 pyroclastic flows were emplaced onto terrain not yet impacted by the ongoing eruption, apart from the thin fallout layer.

Sectorial variations of P2 all around the volcano and their correlation are shown in Figure 2.21. Cross-valley variations illustrating correlations between valley-fill and interfluve facies in the northern sector are shown in Figure 2.23. Figure 2.24 shows a radial profile on the northern flank to illustrate the longitudinal variations of the subunits. Drainage 1 was chosen due to its abundant exposures, even if similar radial variations were observed in drainages 2, 4 or 9. Radial variations of the deposit in the southern sector are shown using the example of drainage 7 (Figure 2.22).

In what follows, we describe the four main subunits of P2, based on a tentative correlation between these sectors. A discussion of some uncertainities and alternative explanations is then presented.

It consists mainly of pyroclastic flow deposits with minor syn-eruptive reworked horizons only towards the top of the sequence.

Table 2.4: Summary of the main features of unit P2 of the Pucón Ignimbrite

SUBUNIT	MAX THICKNESS (m)	MAX RUN OUT	N° BEDS	MAIN LITHOFACIES	DRAINAGES	DEPOSIT DESCRIPTION	INTERPRETATION
P2a	20-25 m	21 km	1 to 5	Massive to diffusely-stratified fines-poor lapilli tuff to breccia grading up into massive to parallel and cross diffusely-stratified lapilli tuff	1, 2, 3, 4, 5, 6, 7, 8 and 9 (all around the volcano)	Widely dispersed as valley fills with an important deposition on ridges. Pale-brown lithic-rich beds with complicated internal structures and contact relationships. Highly erosive. Contact between facies gradual or sharp erosive. Thickened downstream. Possible large scale bedforms. Rich in goldish scorias, granitoids, lavas with granitoid inclusions and DPJ fragments. Abundant hydrotermally altered lithics to the base. Gradually rich in ash upwards. Gradual contact with P2b.	High-energy pyroclastic flows with a blast-like leading edge
P2b	30 m	12.5 km	1	Mostly massive lapilli tuff to agglomerate	7 and 8 (southeast)	Conspicuous black juvenile rich massive with subtle lens and grading. Strongly thinned on ridges. Carbonised wood with degassing pipes that traverse the contacts.	High-concentration pyroclastic flows
P2c	4 m (ridges) 9 m (valleys)	9.5 km (valleys), 13 km (ridges)	1 to 4	Planar and cross-stratified lapilli to ash tuff	1, 2, 3, 4, 5, 6, 7, 8 and 9 (all around the volcano)	Important deposition on valley slopes. Brown-coloured lithic rich. Variable thickness, locally thickened, locally eroded by P2d. Low angle cross stratification and eroded bed forms at the top. Highly erosive. Reworked distally. To the south, irregular base with evidences of bioturbation and oxidation levels.	Pyroclastic surge
P2d	7.5 m	9.5 km	1 to 3	Mostly massive lapilli-tuff	4, 3, 2, 1 and 9 (northwest)	Restricted distribution and extent. Mostly as valley fills with steep flow fronts. Well-bedded intermediate lithic to juvenile rich. Flat gently dipping downstream top. Thickened downstream. Contact with P2c gradual or erosive.	High-concentration pyroclastic flows

Lithic rich deposits have less than 50% scoria in all size fractions and their matrix is normally brown. *Juvenile rich* deposits have about 70 to 100% scoria in sizes 4 mm or coarser, and about 50 to 80% scoria in sizes 2 mm or finer. Their matrix is dark grey to black, but some brown-coloured variants also occur. *Intermediates* deposits have scoria abundances between these two end-members.

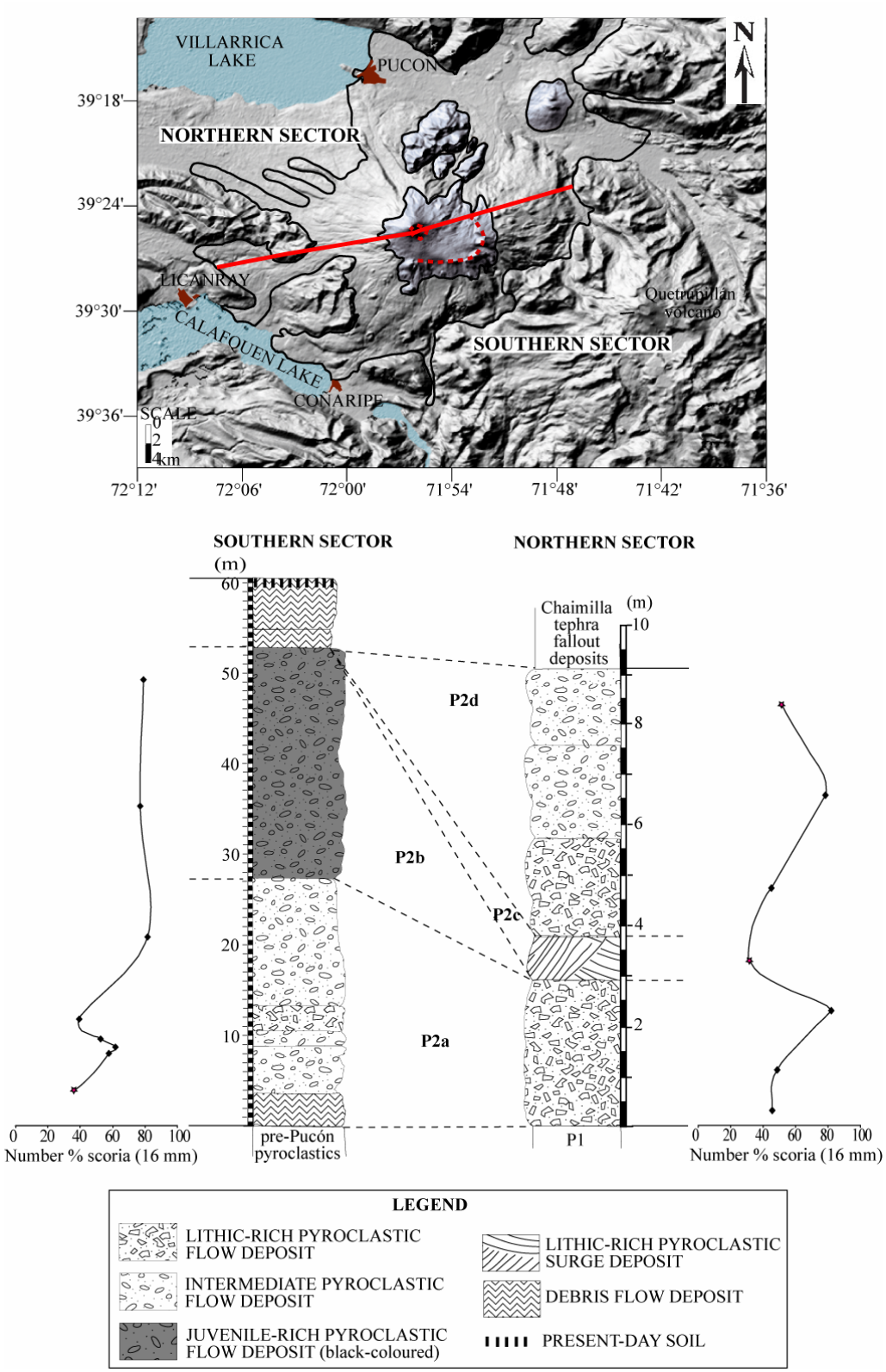

Figure 2.19: Contrasting type sections of unit P2 in the northern and southern sectors of the volcano and the correlation proposed. Type section of the southern sector is a valley sequence of P2 in drainage 7 (VR85) and that of the northern sector is a valley sequence of the Pucón Ignimbrite in drainage 1 (VR78). The graphs represent the number % scoria in 16 mm fraction (8 mm data is presented for two fine-grained levels and 4 mm data for a very fine-grained level. These values are distinguished by stars). Locations in Figure 2.3.

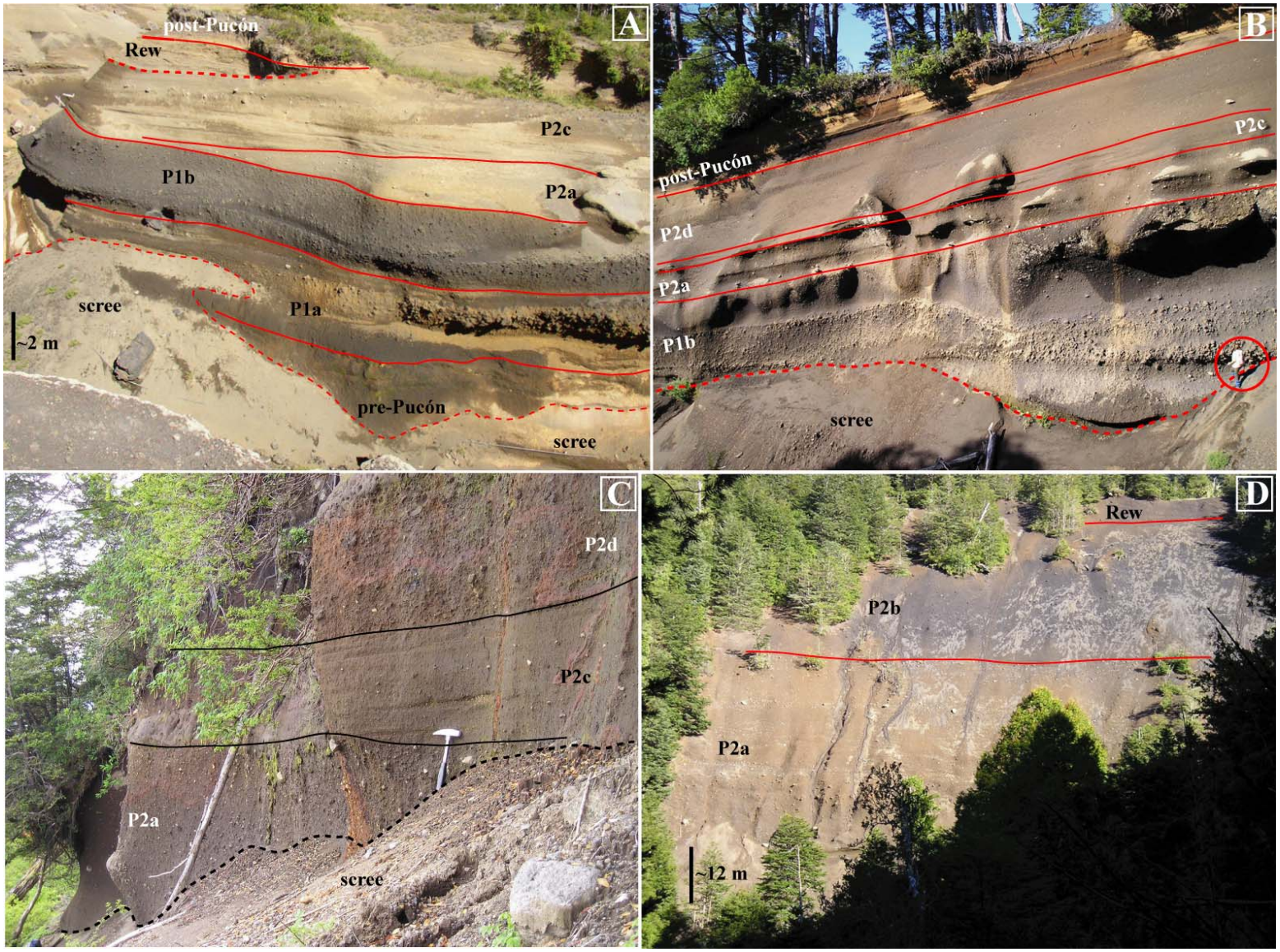

Figure 2.20: Plate showing valley fill exposures of unit P2 of the Pucón Ignimbrite. (A) The sharp P1/P2 boundary to the northern sector (VR73, drainage 1). (B) Typical stratigraphy of unit P2 to the northern sector (VR78, drainage 1). (C) Unit P2 to the western flank (VR93, drainage 4). (D) Complete stratigraphy of the deposit to the southeast (VR85, drainage 7). Note that the black layer P2b is only present to the southern sector.

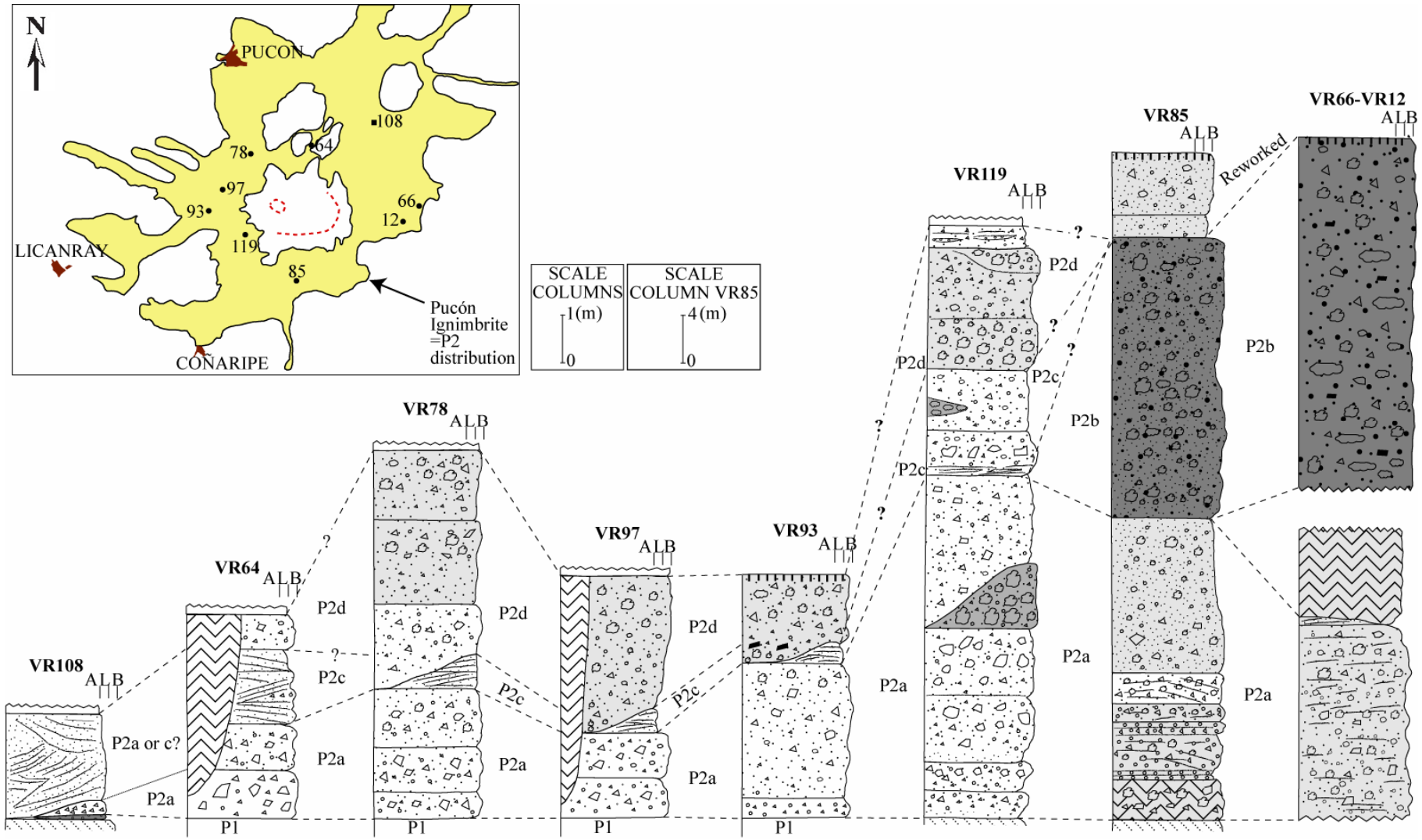

Figure 2.21: Correlation logs of unit P2 showing sectorial variations all around the volcano. Sections logged are shown in the insert map. Symbols as in Figure 2.10.

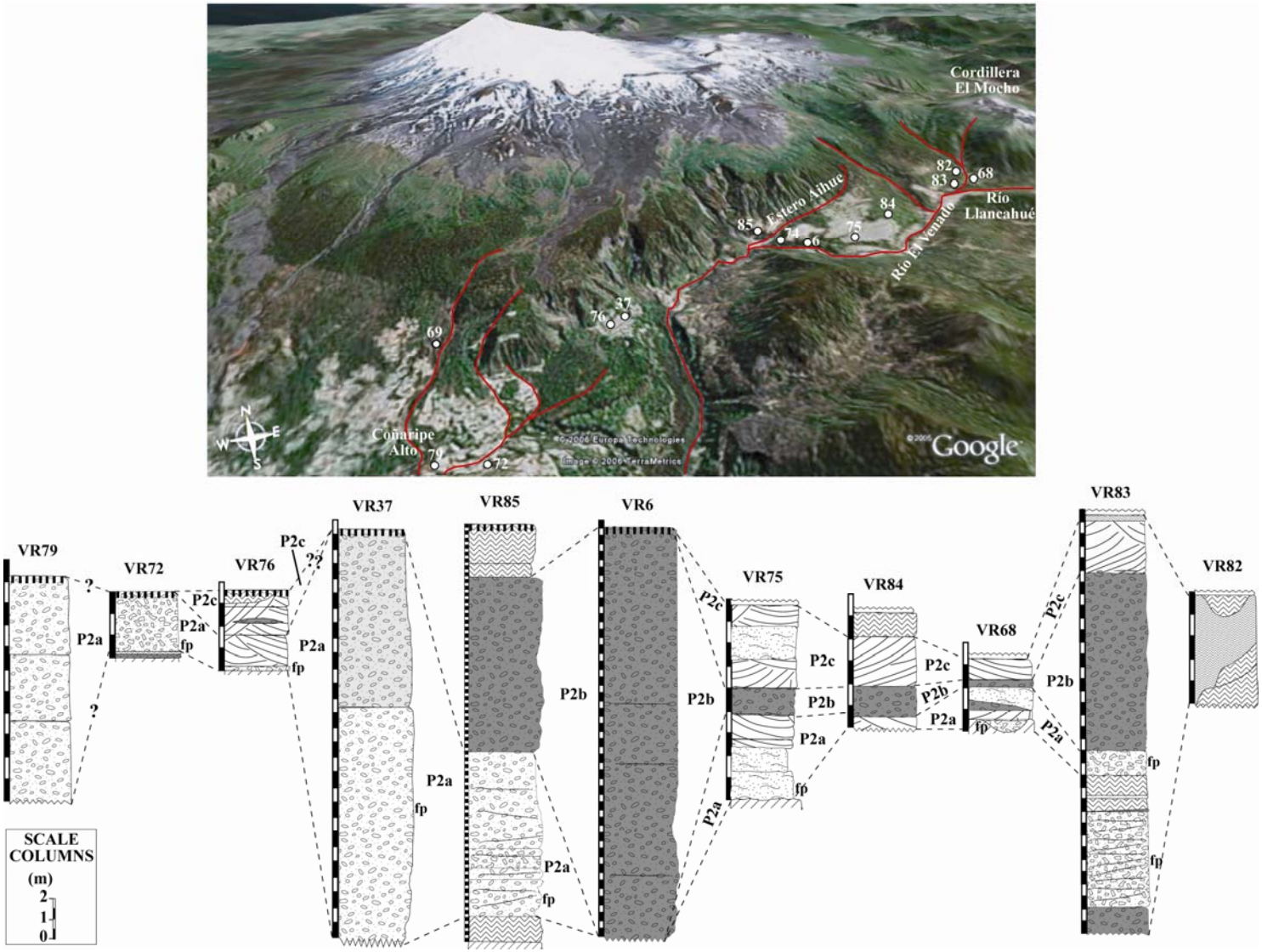

Figure 2.22: Longitudinal and cross-valley variations of the main subunits of the Pucón Ignimbrite in the southern sector (drainage 7). The location of the main outcrops is shown in the satellite image. Schematic stratigraphic columns of every outcrop with the correlation between them are also shown. Note the equivalent stratigraphy between valley slope (68-84-75) and valley-bottom sequences (83-6-85) and the short extent of P2b. The minimum distance between outcrops VR82 and VR79 is about 11.5 km. Symbols in Figure 2.14.

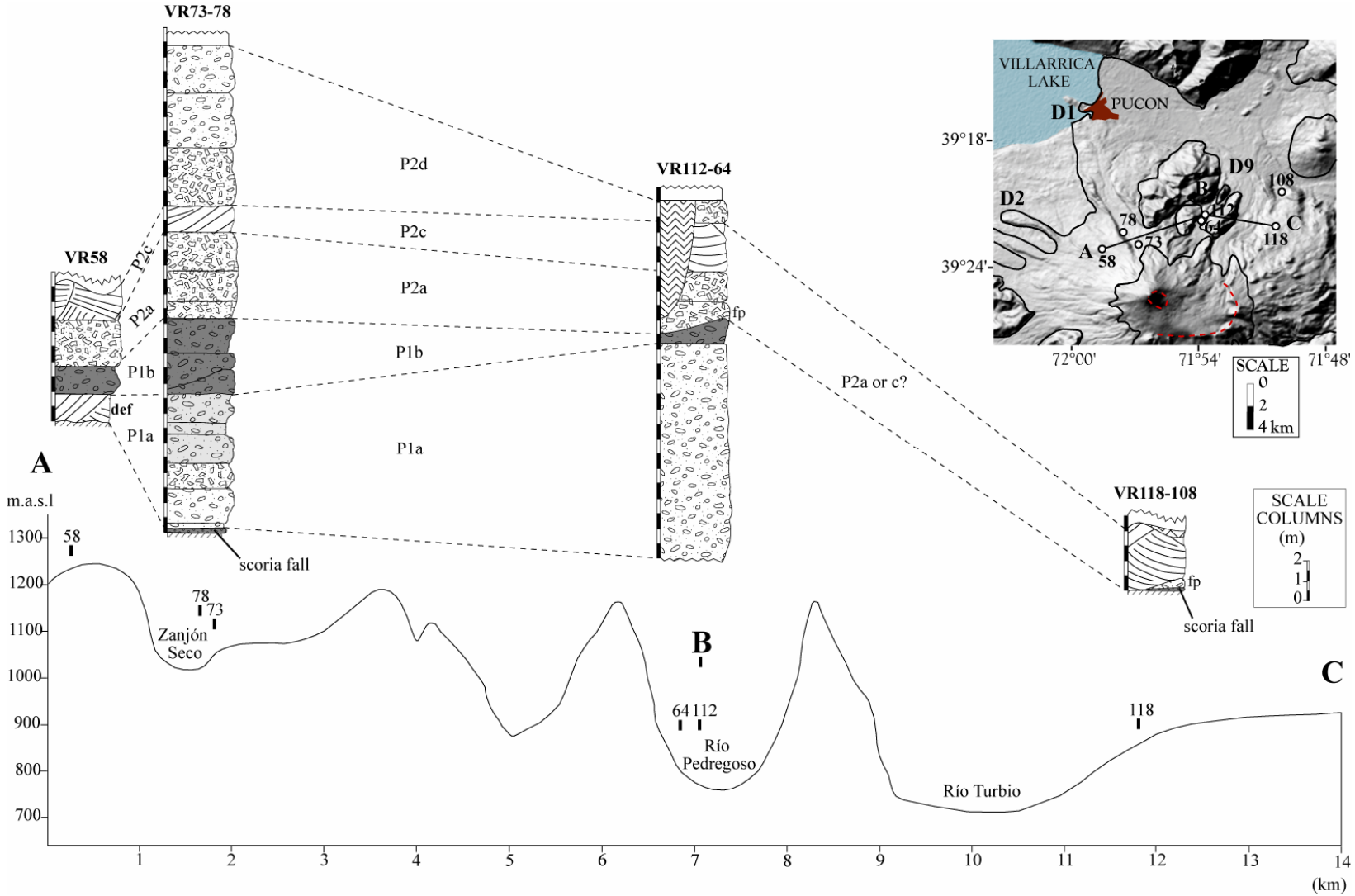

Figure 2.23: Profile along the northern sector showing the cross-valley variations of the main subunits of the Pucón Ignimbrite. The location of the profile (A-B-C) is shown in the insert map. It is about 14 km long and the maximum difference of elevation is about 500 m. The location of the main outcrops is also shown. Some columns are composite: in Zanjón Seco (drainage 1), P1 from VR73 and P2 from VR78 (far 800 m); in Pedregoso (drainage 9), P1 from VR112 and P2 from VR64 (far 200 m); the exposure VR118 has no base exposed, thus the underlying units were taken from the outcrop VR108, 2.5 km downstream. Symbols in Figure 2.14.

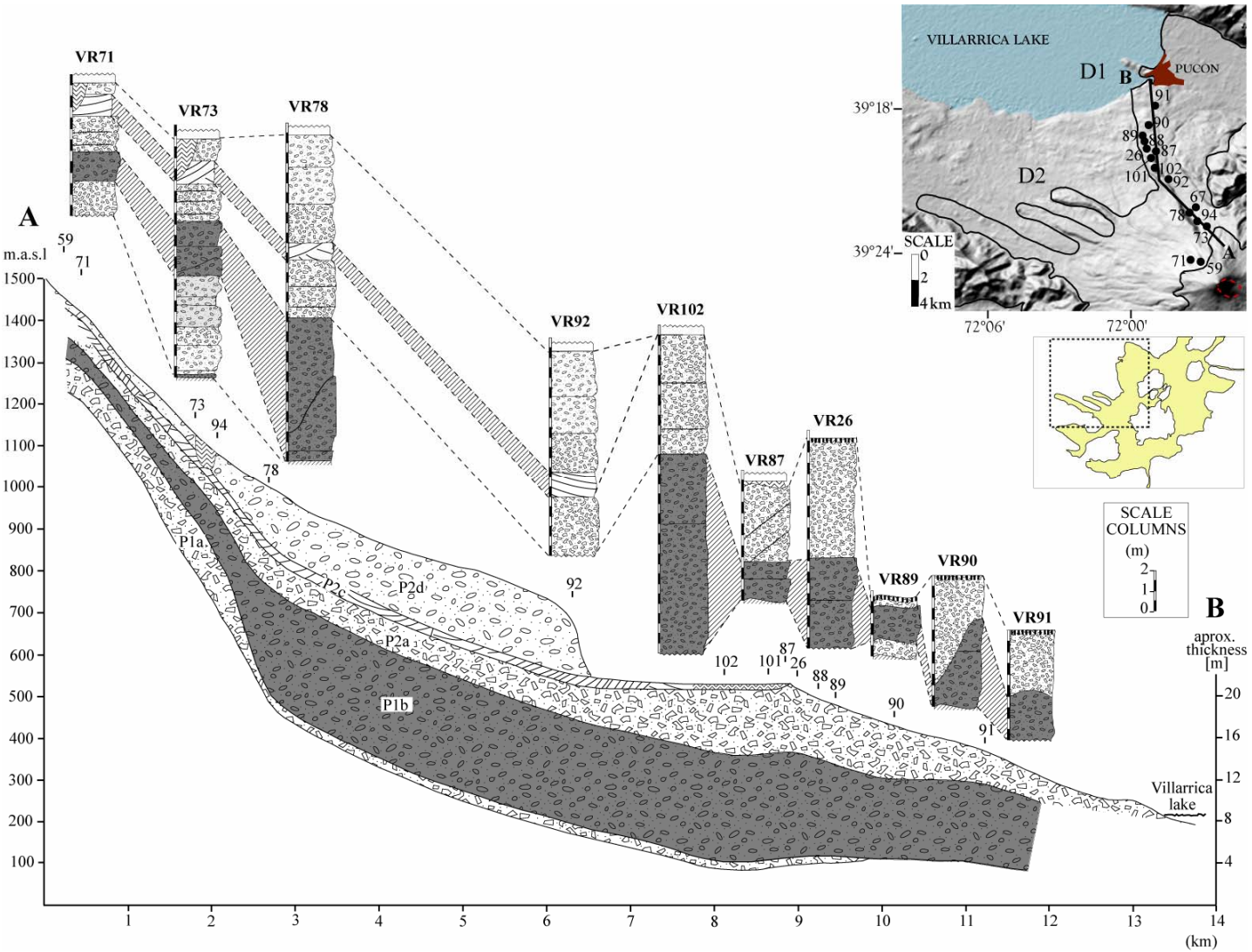

Figure 2.24: Longitudinal variations of the main units of the Pucón Ignimbrite in the northern sector. The profile A-B along drainage 1 is shown in the insert map. It is 14 km long and the elevation difference between A and B is 1200 m. The location of the main outcrops is also shown. The thickness of the units along the profile are exaggerated (right scale). The outcrops downstream from km 9 of the profile (VR87) are located about a hundred metres laterally from the valley bottom. Therefore, the units logged are thinned; in the profile they were exaggerated by extrapolating the probable thickness in the valley bottom. Symbols in Figure 2.14.

Subunit P2a

Valley environments

The most voluminous and widespread lithofacies of P2 is brown massive to diffusely stratified pyroclastic flow deposits (Figures 2.20 and 2.21), reaching their maximum thickness in the southern sector (up to more than 20 m thick, Table 2.4 and Figure 2.22) and their greatest runout to the northeast (~21 km, Table 2.4).

Both diffusely stratified and massive variants are interdigitated and grade into one another in complex ways. The diffusely stratified facies of P2a occurs mostly in proximal to medial environments (VR83 to VR85 in the southern sector, and VR59 to VR94 in the northern sector, Figures 2.22 and 2.24). In the northern sector, the diffuse stratification is defined by subtle grain-size fluctuations, producing layers with gradual contacts and laterally impersistent over a few metres or tens of metres (for example, Figure 2.20A), or it can grade into a stacked succession of one to three massive beds (totalling 1-2 m thick, for example Figure 2.20B-C), commonly exhibiting symmetrical (inverse to normal) grading. In the southern sector, the diffuse stratification in P2a is faint and best discerned from distance, and it exhibits large-scale parallel and cross variants (up to tens of m), with big bombs (up to 60 cm) occurring in the coarsest horizons (Figures 2.20D and 2.26A).

In medial to distal environments (VR85 to VR79 in the southern sector, and VR92 to VR91 in the northern sector, Figures 2.22 and 2.24), P2a is commonly massive. In the northern sector, P2a thickens progressively downstream (up to 10 m thick) and exhibits one to three beds commonly exhibiting inverse grading at the base (2a layer of Sparks *et al.*, 1973). To the south, P2a becomes richer in bombs downstream and inverse grading of bombs can be locally present. At locality VR85, there can be seen the more distal, mostly massive, facies with lenses that interfinger laterally with the more proximal diffusely stratified facies (Figure 2.26A).

On the southwestern flank of the volcano (outcrops VR115 to VR116 in the insert map of Figure 2.27 and Figure 2.28A), P2a exhibits both massive and diffusely stratified variants (Figures 2.27 and 2.28B-D).

At about 12.5 km from the present-day summit, the presence of large-scale inclined (both downstream and upstream) stratification, particularly near obstacles, hints at the possible existence of bed forms up to several tens of metres long, in which the deposit accreted progressively upstream as the pyroclastic flows swept by (Figure 2.30A), as has been recently described for the Poris Ignimbrite on the Canary Islands (Brown & Branney, 2004).

The base of subunit P2a is commonly poor in fines and grades vertically upwards into the main and volumetrically dominant fines-richer part of P2a, or it is sharply cut by it (Figures 2.26C and 2.31A). In what follows, both fines-poor and fines-rich parts of subunit P2a will be named as P2aFP and P2aFR, respectively. It is composed of massive to diffusely stratified fines-poor lapilli tuff to breccia, ~15 cm to 1 m thick in medial to distal localities of the northern flank, and up to 5 m thick on the southern flank. The

fines-depleted basal facies of P2a occurs in all sectors around the volcano and has the greatest radial extent of any layer in the Pucón Ignimbrite. It occurs up to 15 km south of the present-day summit (Figure 2.31C) and up to 21 km on the north flank. At distal northern location VR109, the Pucón Ignimbrite is represented by a single bed 70 cm thick of fines-depleted P2a tuff directly overlying the basal scoria fall (Figure 2.31B). It can exhibit local imbrication of blocks and parallel and cross stratification, which is diffuse and best discerned from far due to the coarse grain size. Compared to the main fines-rich part of P2a in which ~35% of the deposit is finer than 500 μm, the fines-poor base has less than ~10% of particles finer than 500 μm.

P2a is locally highly erosive onto the underlying deposits, forming angular unconformities and meter-scale channels with steeply inclined walls (Figures 2.29A and 2.29C). Unit P1, the basal scoria fall and pre-Pucón pyroclastics are all strongly deformed, folded, sheared and thrusted by the passage of P2a (VR72, Figure 2.31C; VR100, Figure 2.32A-C), resulting in pre-Pucón fragments completely immersed in P2a (VR109, Figure 2.31B) or P1b fragments mixed into the pre-Pucón deposits (Figure 2.32C). These relationships are similar to those found at the base of the Mount St Helens lateral blast deposit (layer A0 of Fisher, 1991; Druitt 1992). Carbonised branches in P2a are oriented parallel to flow and dipping upstream (VR62, Figure 2.32D); the surfaces of big carbonised trunks have been scraped smooth by erosion on top of P1b (Figure 2.30B). At one location down drainage 1 (VR88, Figure 2.3), erosional remnants of P1c form undulating outcrops with no overlying P2 or overlying remnant Chaimilla scoria fallout. Even though the P2a pyroclastic flow passed over this area (the deposits being preserved both upstream and downstream), no observable remains occur on this undulating outcrop. We tentatively interpret these features either as depositional bedforms formed by the P1c pyroclastic flows and bypassed by the P2a flows, or as erosional bedforms carved by the P2a flows into P1c. At several locations, degassing pipes rooted in P1c or P1b are sharply cut by P2a (localities VR90, VR102, VR87, VR26, Figures 2.29A-B and 2.30), indicating a pause between the emplacement of units P1 and P2.

Interfluve environments

The stratigraphic equivalent of P2a is found on slope environments up to ~50 m above the adjacent valley floors at several locations southeast of the summit (VR75, VR84 and VR68, Figure 2.22) and up to ~200 m above the valley floor in the northern sector (VR58 and ridges east of drainage 9, Figure 2.23). In the SE sector, these valley-margin sequences are formed of up to five beds of massive to parallel and cross-stratified lapilli and ash tuffs, each 20-80 cm thick and totalling about 2 m (VR75 and VR68, Figures 2.22 and 2.33A-B). In the northern interfluve environments, diffusely stratified to massive pyroclastic flow veneers of P2a (1-3 m thick) occur underlying P2c (Figures 2.23 and 2.25C). The fines-poor base of P2a appears as discontinuous lens up to ~30 cm thick. Some of the coarser-grained interfluve facies may be veneers left where the entire pyroclastic flow swept over the landscape; finer-grained beds probably record deposition from the upper, less concentrated levels of density-stratified flows.

On ridges, there is also evidence of the violence of the P2a flows (Figure 2.18). The fines-poor P2a shows evidence of having eroded, folded and sheared the underlying scoria fall and pre-Pucón pyroclastics, even leaving fragments of the scoria fall immersed in the pre-Pucón pyroclastics (ridges east of drainage 9, VR108, Figure 2.31A). Also, the fines-rich main part of P2a sheared off the fines-poor base (Figure 2.31A), which was locally only preserved where it filled depressions carved into the pre Pucón deposits (VR68, Figure 2.33B). Locally, moulds of large tree trunks are observed lying parallel to flow direction at the contact between P1 and P2a; these are interpreted as having been buried, but not felled, by the P1 currents, then knocked over by the P2a flows (Figure 2.34).

The parent pyroclastic currents of layer P2a are interpreted to have been high-energy pyroclastic flows, as suggested by: (1) significant deposition in both valley and ridge environments (Figures 2.22 and 2.24), (2) wide distribution and large radial extent up to distal localities (Figures 2.21, 2.22 and 2.24), (3) the presence of large-scale bed forms (Figure 2.30A), and (4) erosive and sheared basal contacts (Figures 2.29 to 2.33A-B). The interfluve sequences of P2a are interpreted as deposits from the dilute, upper parts or margins of the high-energy pyroclastic flows.

The fines-poor base of P2a is interpreted as a blast-like leading edge of the P2a pyroclastic flows. The low fines content is attributed to elutriation by turbulence (Figure 2.33C). It seems that this blast-like front travelled further than the fines-richer parts of the flows (VR109 in the northern sector, VR72 in the southern sector, Figures 2.31B-C), and that it was the most energetic component of the P2a pyroclastic flows.

Subunit P2b

Unit P2a is overlain gradationally by black, juvenile-rich pyroclastic flow deposits (P2b), preserved in a restricted sector from south to east of the volcano (drainages 7 and 8, Figure 2.21). In deep valleys, P2b can reach up to 30 m thick at ~11 km from the present-day summit (Figure 2.20B). Concentration of juvenile bombs (up to 60 cm diameter) can produce local diffuse stratification (Figure 2.26D) and local clast-supported accumulations of bombs occur. P2b usually forms the flat top of the Pucón Ignimbrite in drainages 7 and 8, except where it is locally overlain by P2c or reworked deposits. Further to the west, P2b is not present; however, P2a is locally overlain by one or two beds (<2 m thick) of brown massive pyroclastic flow units rich in coarse scoria that may be P2b (VR114 and VR117, Figures 2.27 and 2.28).

P2b is found on interfluves of drainage 7, being also massive but strongly thinned relative to the valley fills (<70 cm thick, Figure 2.22, 2.26B and 2.33A-B). The contact with P2c is commonly gradual (Figure 2.26E) and vertical degassing pipes rooted on charcoal traverse the P2b/P2c boundary, suggesting rapid emplacement of the successive flows (VR84, Figure 2.29D).

P2b is interpreted as the product of low-energy, highly-concentrated scoria flows, based on the largely massive texture of the deposit and its strong valley confinement.

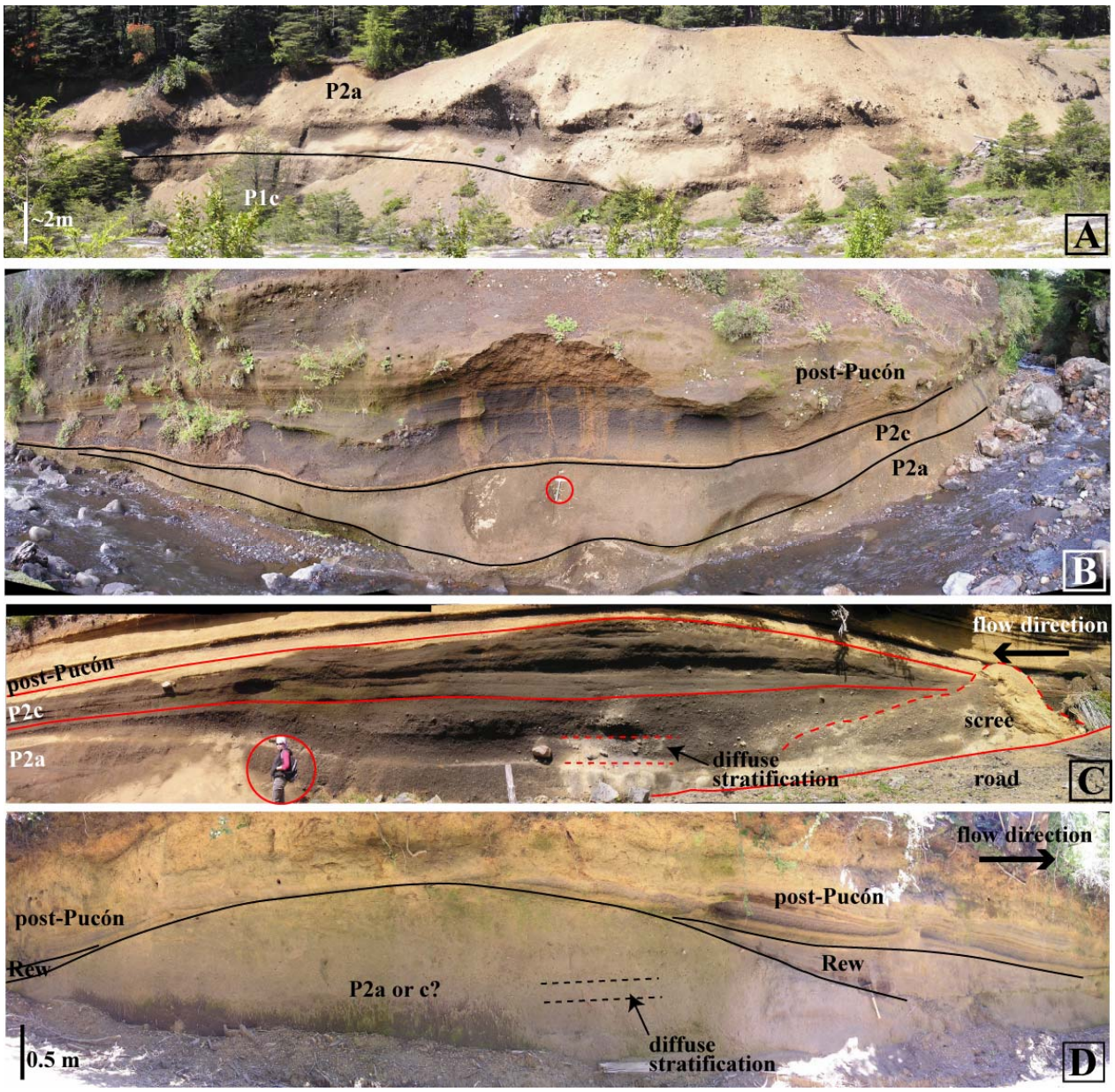

Figure 2.25: Some features of unit P2 in the northern sector of the volcano. (A) Flat-topped valley pond of P2a (VR57, drainage 4). (B) P2c becomes massive where thickened (VR92, drainage 2). Hammer for scale. (C) Ridges to the northwest (VR58). The top of P2c preserves bedforms (Strike of the section N190E). Person for scale. (D) Ridge east drainage 9. Diffusely stratified P2 with eroded dunes at the top (reworked zones thicker at the lee-sides than the stoss sides) (Strike of the section N50E, VR118). Locations in Figure 2.3.

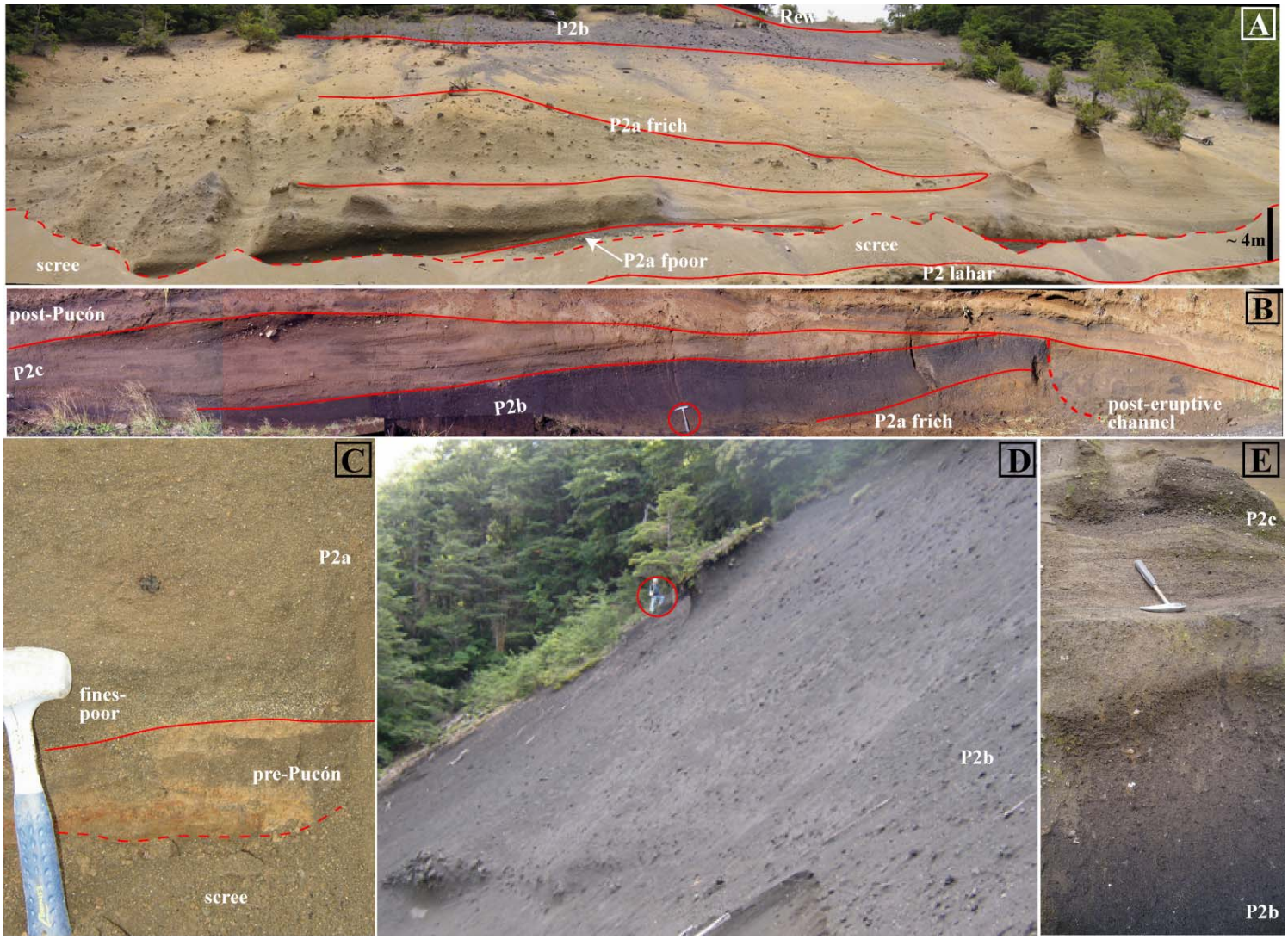

Figure 2.26: Unit P2 to the southeastern sector (drainage 7). (A) Coarse-grained, massive P2a facies grades laterally into a finer-grained facies with large scale parallel and cross diffuse stratification. A massive lens wedges laterally (Valley exposure VR85). (B) Interfluve equivalent of P2. The sequence is truncated due to a post-eruptive channel. The central black P2b was useful for correlation. Hammer for scale (VR84). (C) Fines-poor P2a base gradually richer in fines upwards. Piece of charcoal at the centre (VR76). (D) Typical massive valley-fill exposure of P2b. Person for scale (VR6, P2b thickness >30 m). (E) Gradual contact between P2b and P2c. P2c composed of a massive bed overlain by a stratified bed (VR75). Locations in Figure 2.3.

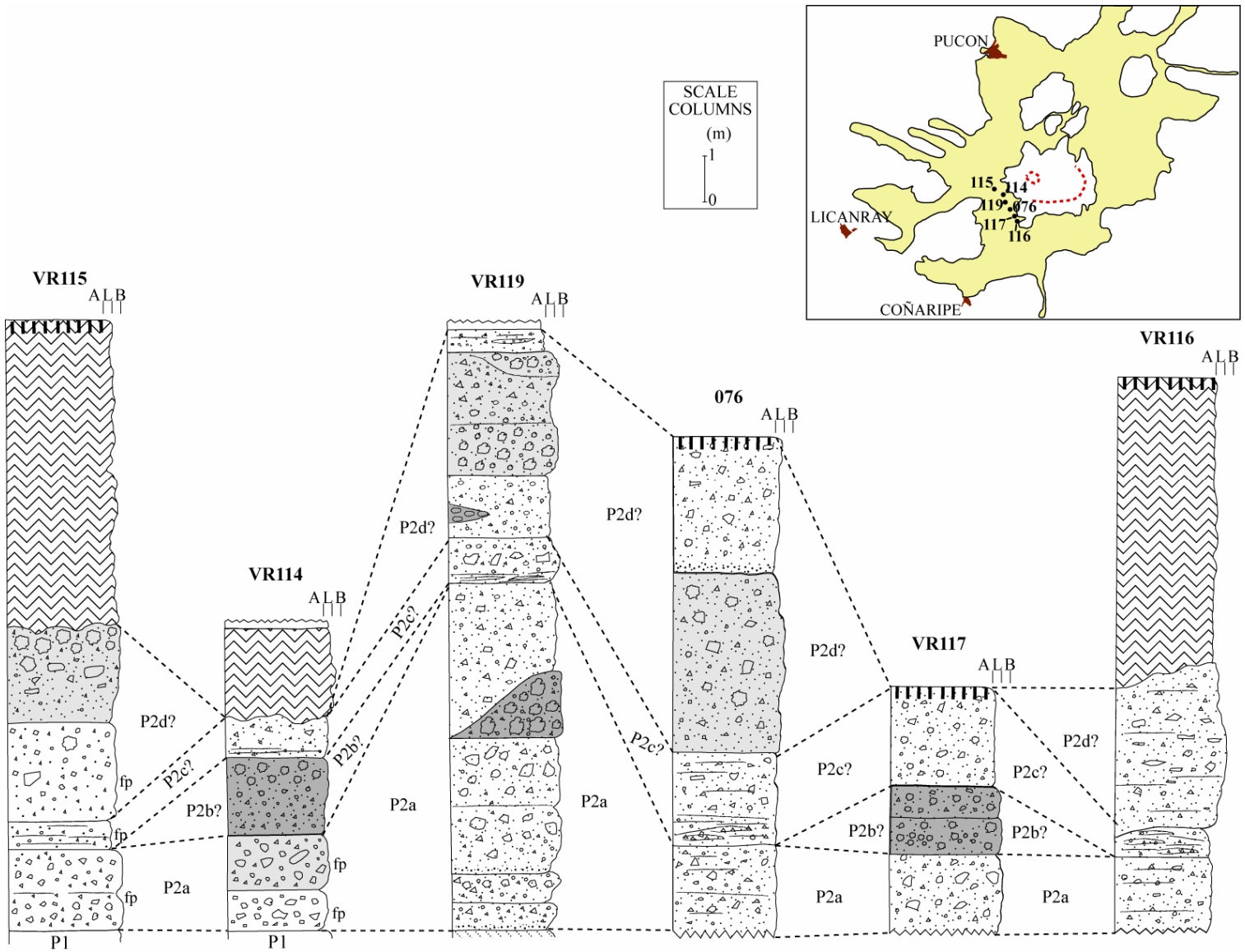

Figure 2.27: Correlation logs of the P2 sequences on the southwestern flank of the volcano. In the insert map, there are shown the main outcrops studied in this part of the volcano. They form a NW-SE oriented profile in the southwestern sector of the volcano where the contrasting northern and southern sequences, crossed. Symbols as in Figure 2.10.

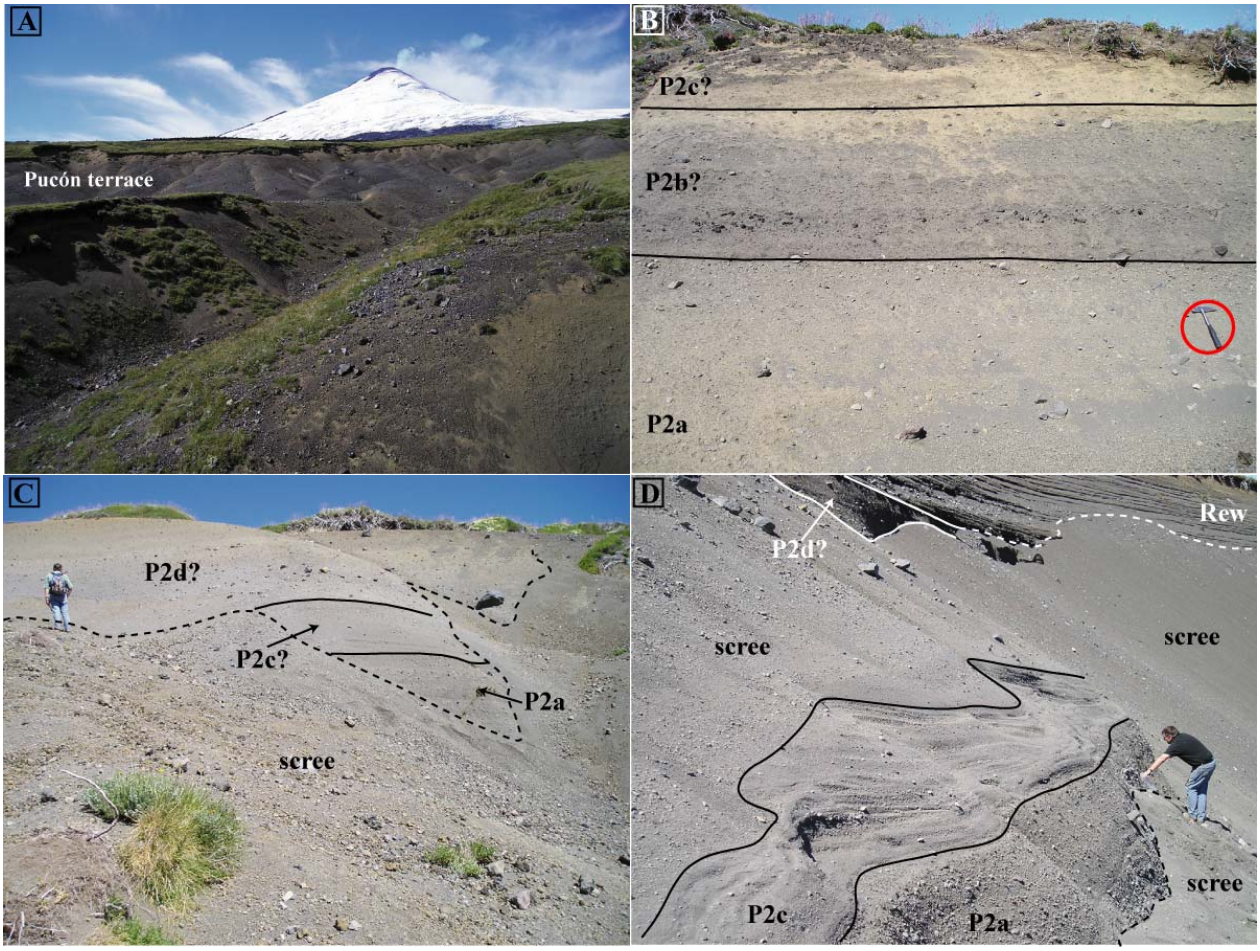

Figure 2.28: Plate showing exposures of the Pucón Ignimbrite on the southwestern flank. (A) Flat-topped downstream-dipping terrace formed by the Pucón deposit in this part of the volcano (between VR117 and 116). (B) White lithic-rich P2a is overlain by a gray juvenile-rich deposit (P2b?). Subordinate lithic-rich deposit at the top (P2c?) (VR117, drainage 6). (C) Lithic-rich to intermediate P2 sequence. Diffusely-stratified P2a is overlain by a parallel and cross stratified surge (P2c). The sequence is capped by 2 or 3 beds of massive pyroclastic flow deposits (P2d?) (076, drainage 6). (D) Same sequence partially eroded below a thick reworking zone (VR116, drainage 6). Locations in Figure 2.27.

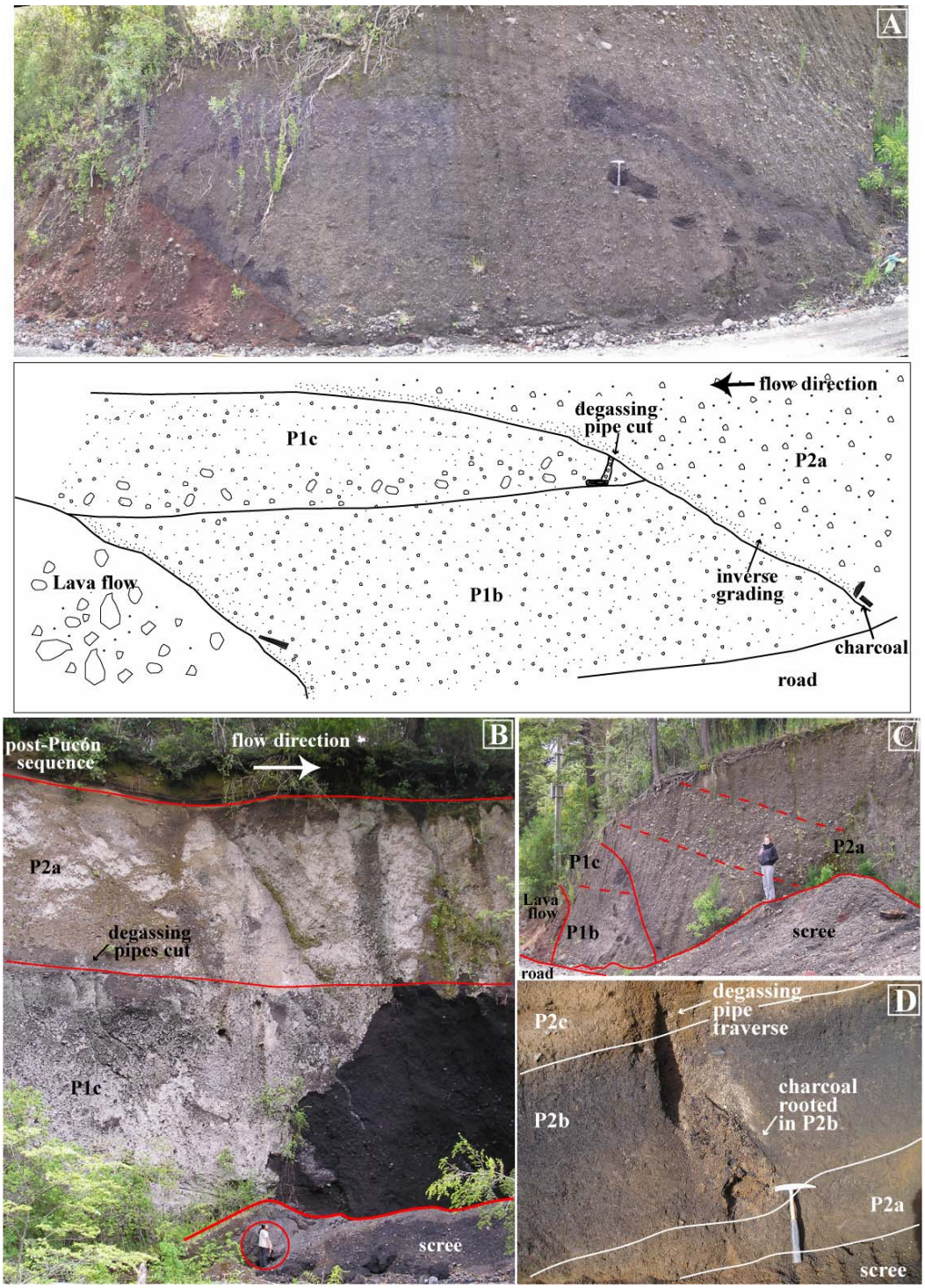

Figure 2.29: Plate showing some evidence of intensity and timing of the Pucón eruption. (A) P1 deposited upstream from and against a lava obstacle. Pipes rooted in P1c are sharply cut by a channel carved by P2a, suggesting an eruptive pause after P1. The unconformity shows the erosive nature of the P2 currents (VR90, drainage 1). (B) Spectacular m-sized downstream-dipping degassing pipes rooted on carbonised wood in P1c, cut by P2a, suggesting a pause between emplacement of P1 and P2 (VR102, drainage). Person for scale. (C) At the same locality of picture (A), the angular unconformity and the contrasting stratification of P1 and P2a (VR90, drainage 1). (D) Degassing pipes rooted in P2b traversing into P2c suggesting rapid emplacement of both subunits (VR84, drainage 7). Hammer for scale. Locations are in Figure 2.3.

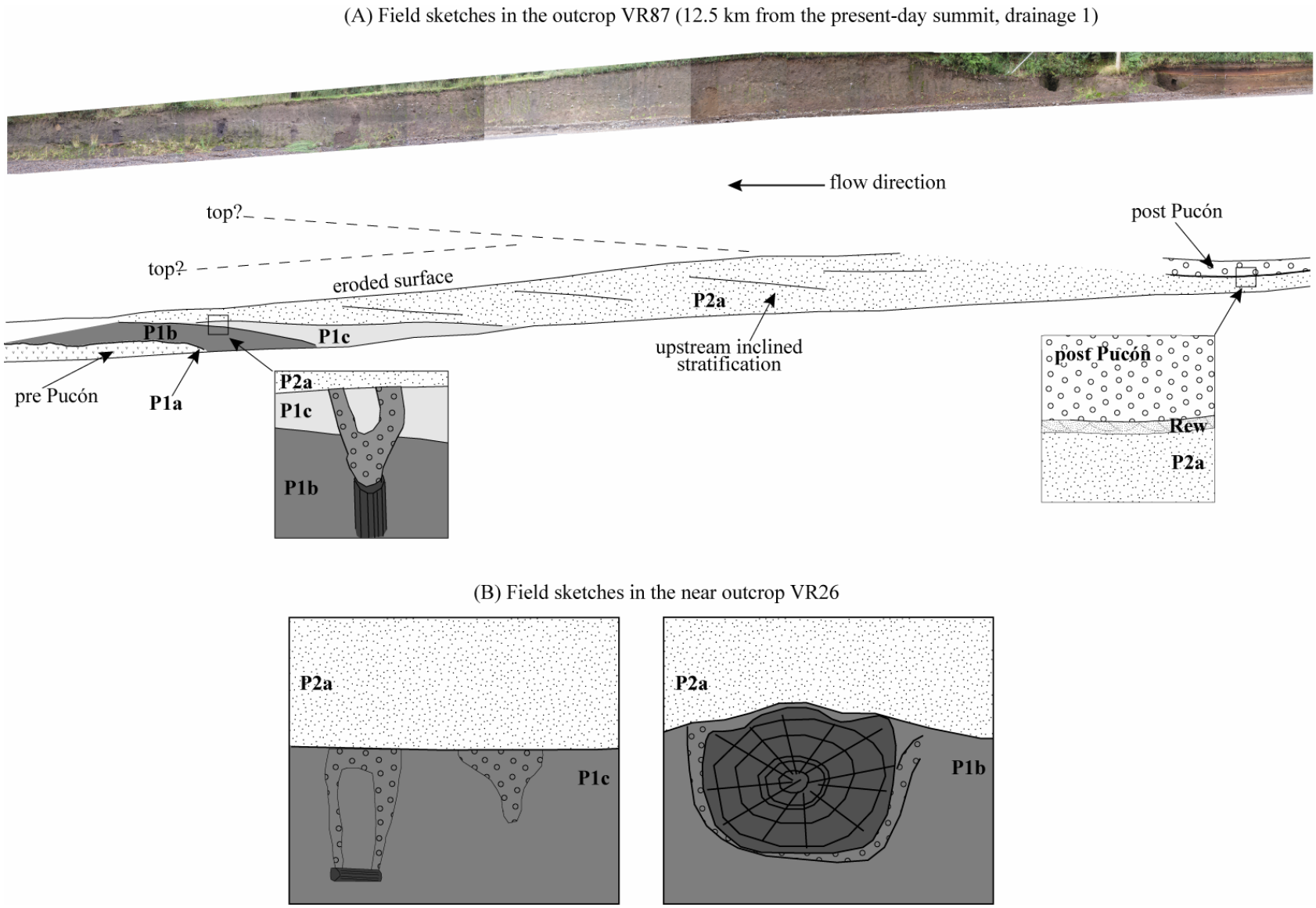

Figure 2.30: (A) Field sketches showing large scale bed forms of subunit P2a in distal environments. (A) & (B) Degassing pipes commonly rooted on P1b and traversing P1c (where present) are sharply cut by P2a, indication of a pause between emplacement of P1 and P2 (A from VR87, B from VR26, drainage 1, Figure 2.3).

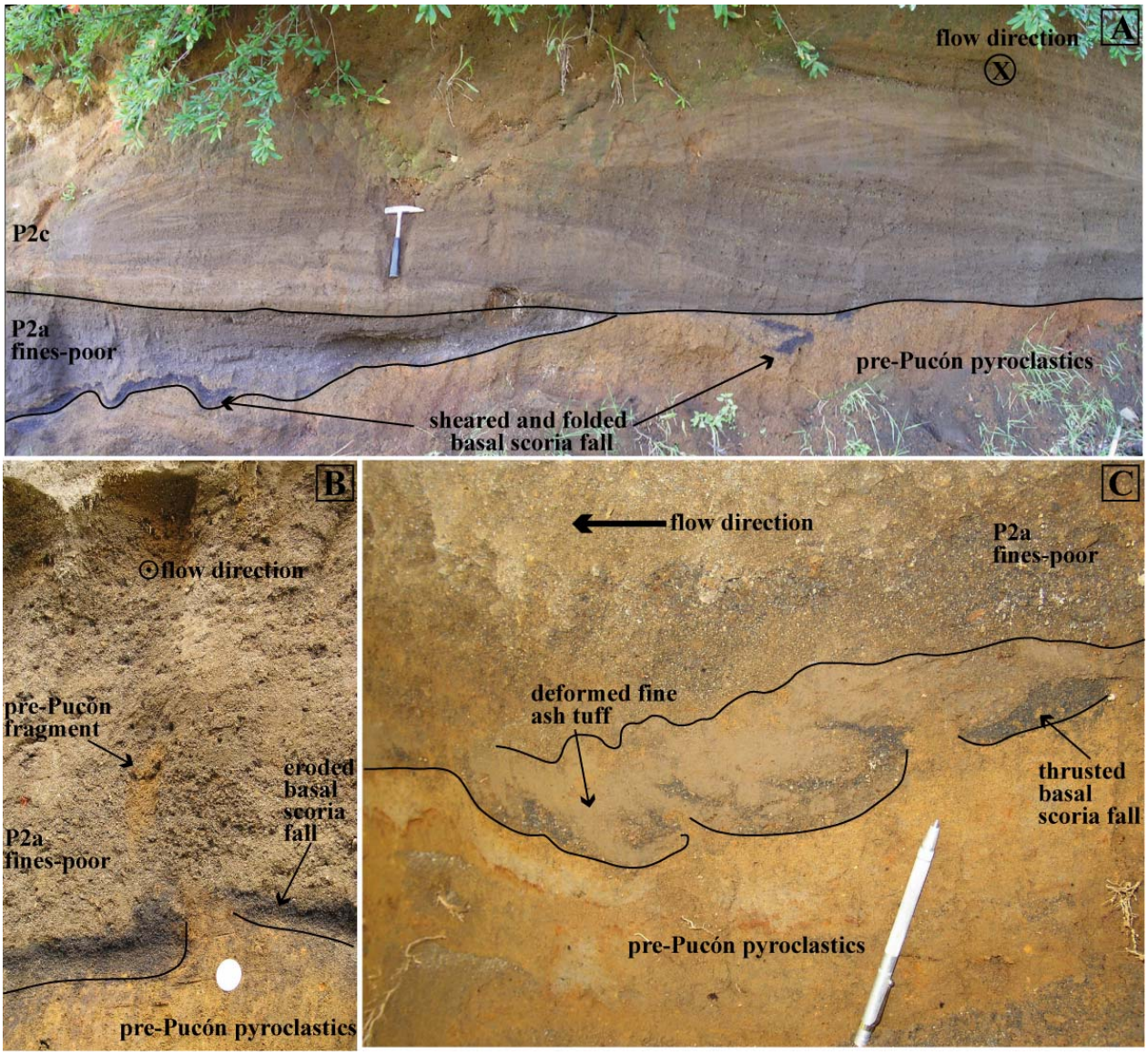

Figure 2.31: Plate showing some evidence of the erosion and shearing of the basal scoria fall deposit by the P2 currents (where P1 was not deposited). (A) The basal air fall is eroded, folded and truncated by the fines-poor P2a. The P2c (or P2a?) surge eroded the previous deposits producing a sharp contact. Strike of the section is near perpendicular to the flow (N65W), explaining the complex arrangement of bedsets and high-angle cross stratification (VR108, ridges east drainage 9). (B) Basal scoria fall and pre-Pucón pyroclastics sheared and folded by the erosive fines-poor P2a facies (VR109). (C) The fines-poor P2a base generated thrusts in the basal scoria fall (VR72, drainage 6). Locations are in Figure 2.3.

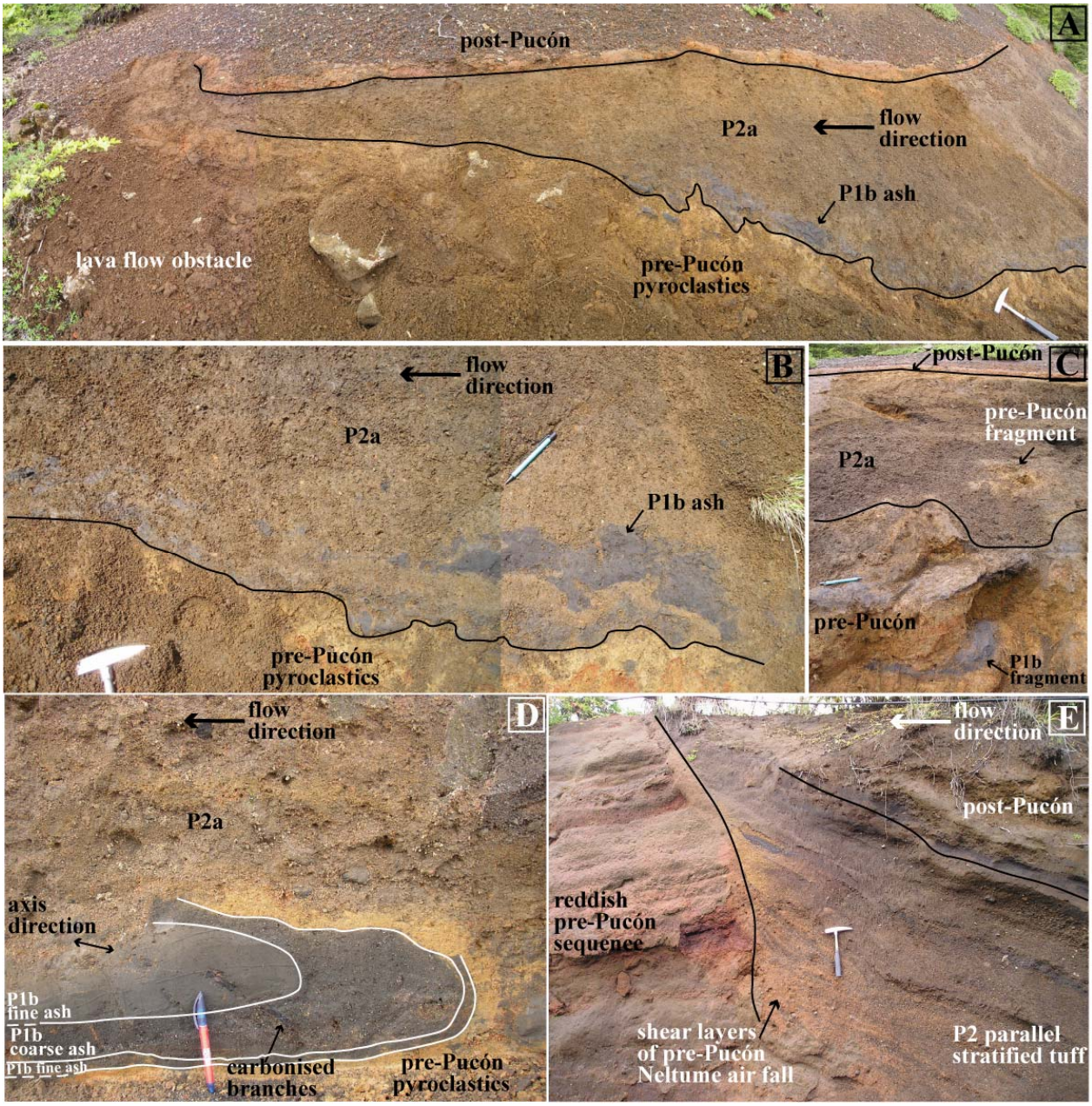

Figure 2.32: Plate showing some evidence of the highly erosive and violent P2a currents. (A) The P2a currents (fines-poor to the base and gradually fines-rich to the top) truncated P1b and pre-Pucón deposits in the crest of the lava obstacle (VR100, drainage 2). (B) P1b deformed fragments by P2a (VR100, drainage 2). (C) Pre-Pucón fragments completely immersed in P2a and P1b fragments lying in the pre-Pucón deposit (VR100, drainage 2). (D) Fold produced by the fines-poor P2a in the underlying P1b and pre-Pucón deposits (axis shown, VR62, drainage 2). (E) From southern ridges (VR68, drainage 7), shear layers produced by P2 in the underlying soft Neltume pumice fall from Choshuenco volcano (*ca.* 9000 yr BP, Clavero & Moreno, 2004). Locations are in Figure 2.3.

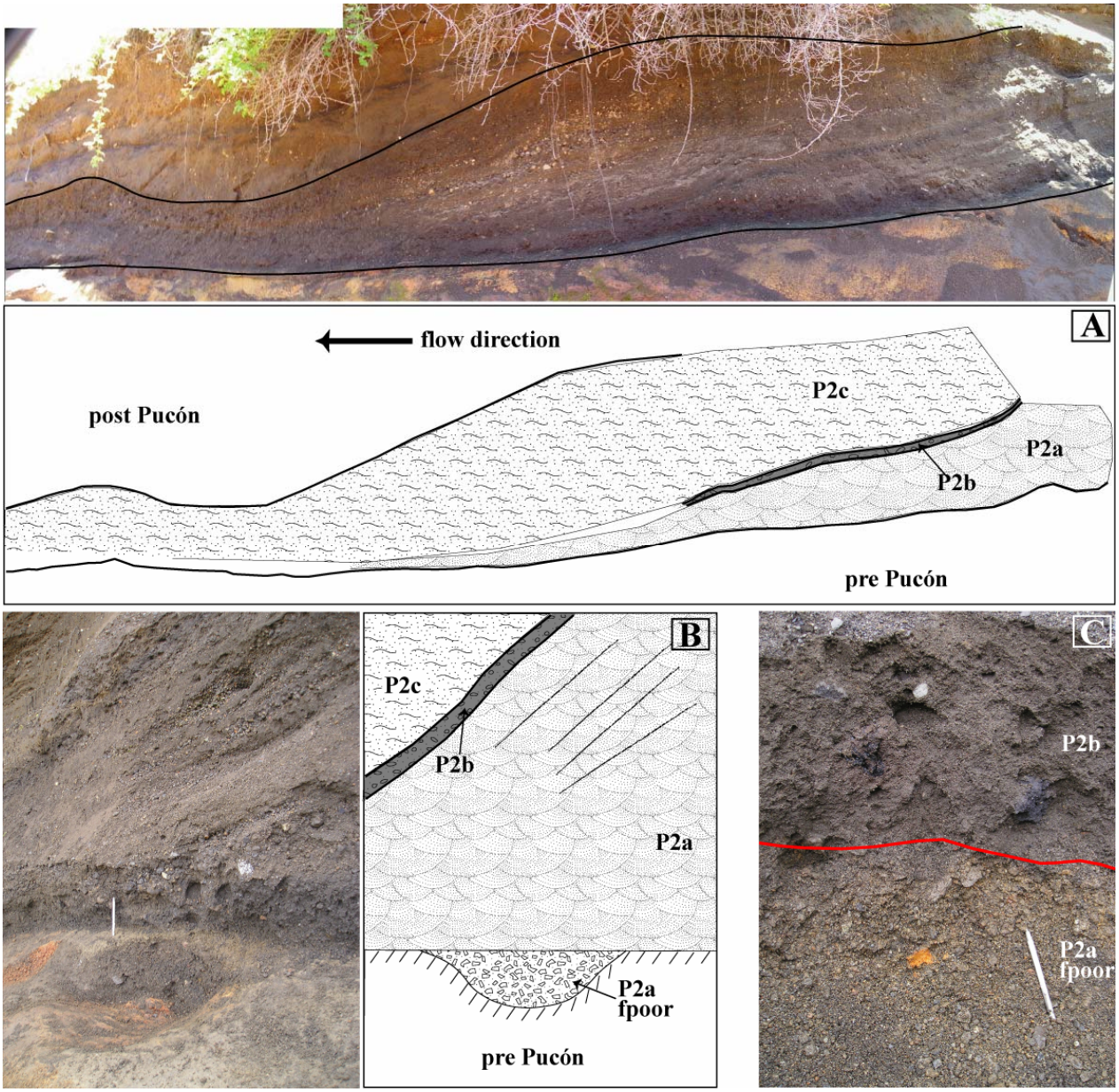

Figure 2.33: (A) P2 surge on interfluve environments (VR68, drainage 7). (B) The P2 surge sheared off the fines-poor tuff, which was only preserved where filled depressions caved into the pre Pucón deposits (VR68). (C) The fines-poor P2a overlain by the juvenile-rich P2b layer (VR83, drainage 7). Locations are in Figure 2.3.

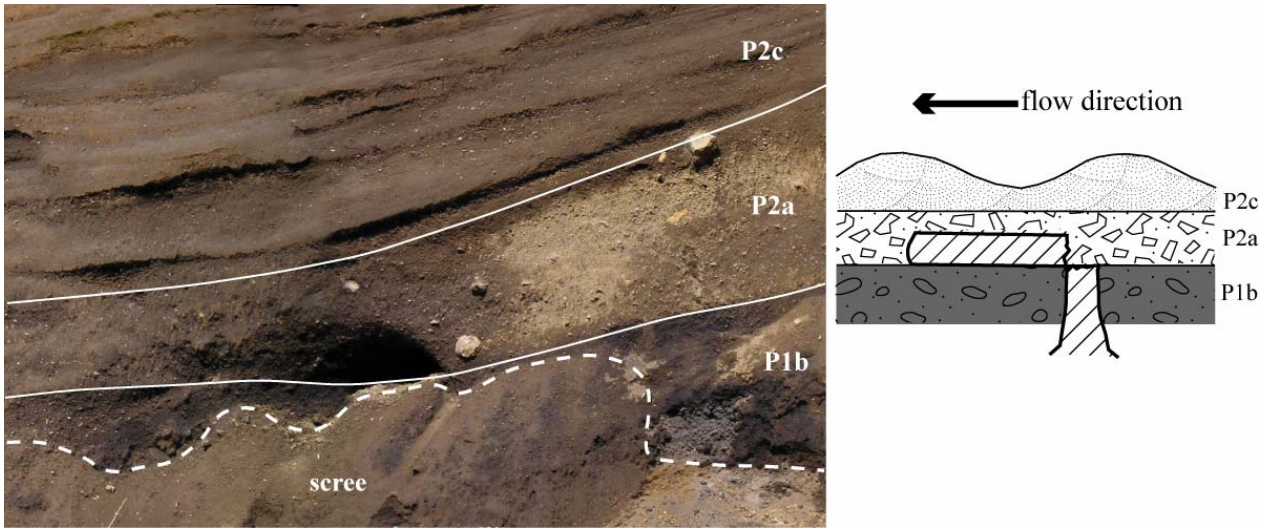

Figure 2.34: Elongated hole oriented near parallel to the flow direction (N110-160E) just on the P1/P2 boundary (several of these at this site). A possible explanation is that large trees stayed vertical during the passage of the more gentle P1 currents being knocked down then by the violent P2 currents (VR58, Figure 2.3).

Subunit P2c

This subunit consists of a pyroclastic surge bed on average ~0.5 – 1 m thick, widely distributed all around the volcano (Figure 2.21), up to ~12.5 km from the present-day summit, with important deposition on interfluves (Figures 2.22 and 2.23). The deposit is brown, lithic-rich to intermediate, and is the "upper surge layer" described on the northern, eastern and southern flanks by Clavero (1996). The correlation of this layer between the northern and southern sectors is only tentative, as discussed below. The surge is therefore described separately in the two main sectors (north and south, Figure 2.35).

P2c in the northern sector

In the northern sector, the top of P2a grades up into a parallel and cross stratified pyroclastic surge bed (P2c), present from about 3 to 11 km from the present-day summit (Figures 2.20A-C-D and 2.21). Along drainage 1, P2c is well-exposed up to 10 km; 2 km further downstream it shows thin mud drapes which could suggest reworking (Figures 2.24 and 2.30A). It has thicknesses varying from ~3 m locally in valleys (VR86) up to a few tens of cm in its more distal outcrops. Although typically well stratified, it can locally be diffusely stratified or even massive (VR92, Figure 2.25B). P2c is locally eroded by the overlying P2d pyroclastic flows. The contact with the underlying P2a can be locally sharp (planar or wavy) and the contact with the overlying P2d can be also gradual.

Good exposures of P2c occur in interfluves in the northern sector of the volcano, especially on the ridges between drainages 1 and 2, and east of drainage 9 (Figure 2.23). On ridges between drainages 1 and 2, the massive to diffusely stratified pyroclastic flow deposits of P2a are overlain in gradual contact by

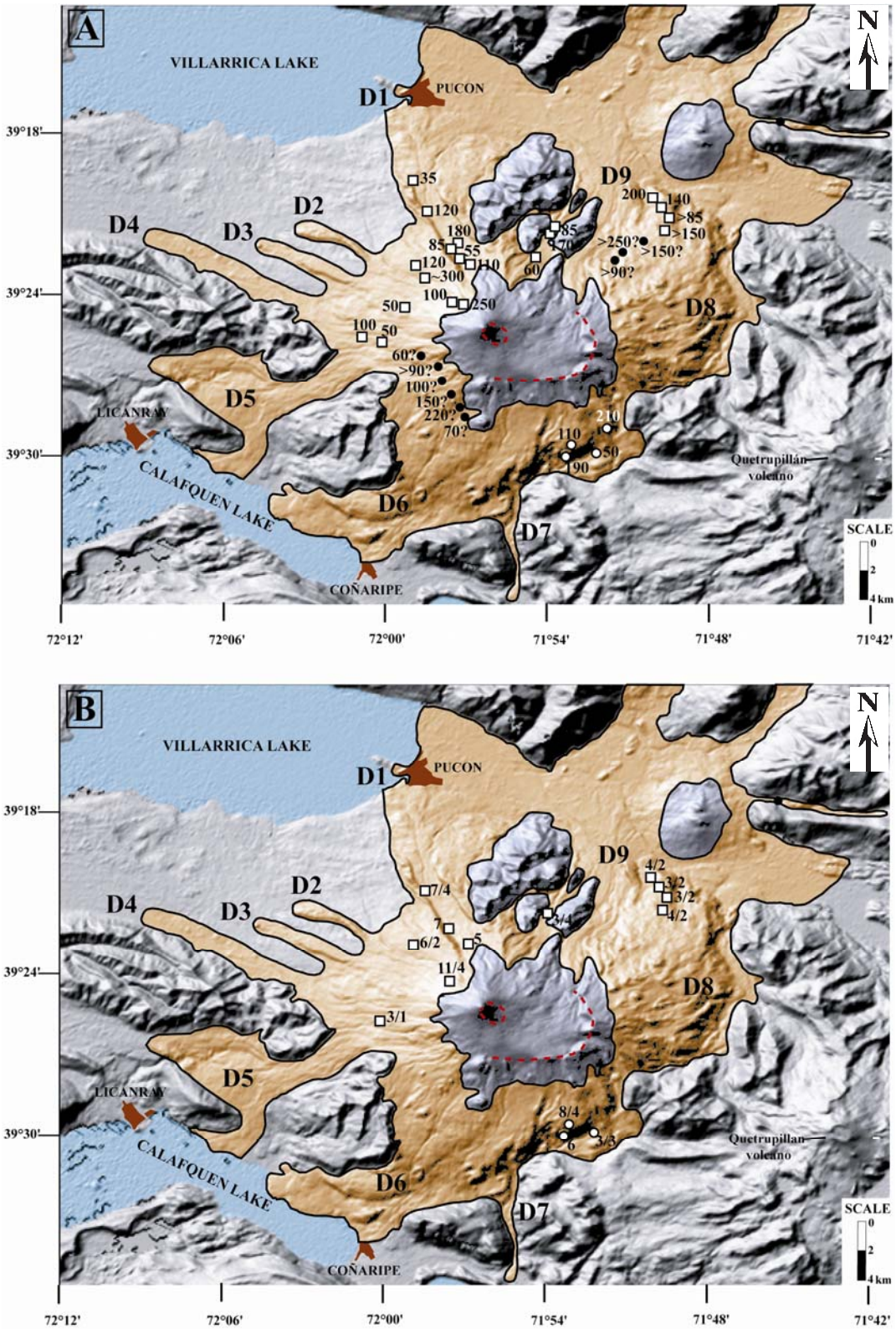

Figure 2.35: (A) Variation of the maximum thickness of P2c (in cm). White squares are the locations of the surge in the northern sector. White circles are the locations of the surge in the southern sector. Black circles represent the locations of the Pucón Ignimbrite where a P2 pyroclastic surge deposit is tentatively assigned to this subunit (thicknesses presented with question marks). (B) Maximum size of lithics and scoria (in cm) of P2c (lithic/scoria). Symbols as in (A). Maximum sizes were calculated as the mean of the longest axis of the three largest fragments.

P2c which has well-developed parallel stratification or low-angle cross stratification (Figure 2.34). This surge deposit has a variable thickness and it can be locally thickened up to 2 m thick, probably due to the irregular paleotopography of underlying lavas (*Antumalal* and *Zanjón Seco lavas*, Clavero & Moreno 2004). It exhibits spectacular downstream-migrating dune forms at the top, with wavelengths up to about 10 m long and amplitudes up to about 50 cm (Figure 2.25C), modified by deposition onto irregular topography.

On the ridges east of drainage 9, P2c is composed of multiple bedsets of parallel and cross stratified lapilli tuffs. Sections oriented perpendicular to the flow, exhibit high-angle cross stratification (Figure 2.31A). These pyroclastic surge deposits exhibit several m-long dunes at the top which are partially eroded (Figure 2.25D).

P2c in the southern sector

P2c was not recognised in valleys southeast of the volcano, and valley accumulations of P2b are overlain locally here by highly indurated mudflows and debris flow deposits up to 9 m thick (VR85, Figures 2.21 and 2.22). In contrast to valley environments, P2c is well exposed on slope environments of the southeastern flank of the volcano, up to 12.5 km from the present-day summit (VR68, 84, 75, Figure 2.22). In several locations, it comprises a single bed of brown lapilli tuff with cross and planar stratification on a vertical scale of mm to few cm (Figures 2.32E and 2.33A-B). This bed is locally underlain by a brown massive more indurated bed (Figure 2.26E). Beds range from 0.5 to 1 m thick, totalling about 2 m. A brown parallel and cross to diffusely stratified surge deposit up to 2 m thick on the southwestern flank of the volcano is tentatively correlated with P2c (Figures 2.27 and 2.28B-D).

P2c is interpreted to have been laid down by rapidly emplaced pyroclastic surges. Some of the diffusely stratified deposits on ridges east of drainage 9 may have been deposited from the dilute upper parts or margins of the P2a pyroclastic flows.

Subunit P2d

Valley sequences of P2 in the northern sector of the volcano (drainages 4, 3, 2, 1 and 9) are capped by one to three pyroclastic flow units (subunit P2d). They are mostly valley-confined and massive, and they thicken downstream (Figures 2.19 to 2.21, Table 2.4). Locally at about 10 km north from the present-day summit (VR92), P2d consists of one thick bed (more than 6 m) that drastically thins over about a hundred metres, possibly due to the former presence of a steep flow front (Figure 2.24). The P2 sequence to the southwest is also capped by one to three brown massive to diffusely stratified pyroclastic flow deposits, each 0.5 to 4 m thick and totalling 7 m thick, tentatively correlated with P2d (Figures 2.27 and 2.28C-D).

The lower bed of P2d can locally shear the underlying P2c surge deposit (VR93, 97, 78, Figure 2.21). Where preserved, the original surface of P2d is flat or gently undulating, and inclined downstream at a few

degrees (7° to 14°, 5.5 to 6 km from the crater; Figure 2.20B). P2d generated no significant deposition in interfluve environments. There is no evidence of deposition on ridges between drainages 1 and 2 (VR58), where the P2c surge with preserved bed forms caps the P2 sequence (Figure 2.25B-C).

The steep flow fronts, strong valley confinement, and more restricted distribution and lesser extent than P2a, shows that these P2d flows were highly concentrated and of lower energy than those of P2a.

Locally in drainages 1 and 2, P2d (or P2c downstream of the flow front of P2d) is capped by a black layer, a few cm thick, which is laterally discontinuous over a few metres or centimetres. The layer consists of black ash and fine lapilli scoria and lithics, together with desegregated carbonised or partially carbonised organic matter. It has centimetric irregular fines-poor pipe-like pods. It is tentatively interpreted as the deposit of fires accompanying and following the emplacement of the P2 pyroclastic currents.

2.3.4 Reworked deposits

The reworked deposits of the Pucón Ignimbrite include both syn- and post-eruptive facies. There are two main occurrences of syn-eruptive deposits locally in valley exposures. First, syn-eruptive reworking occurs within drainage accumulations of P1a on the northern flank. Thin (0.3-0.5 m) fines-depleted debris flow deposits with mud-coated scoria lapilli probably remobilised from the underlying basal scoria fall and P1a I surge deposits, occur proximally to the north and west of the volcano. The presence of such beds shows that water was available for mobilisation and transport of pyroclastic debris early during this eruptive phase. Second, cohesive debris flow deposits up to ~4 m thick underlie P2a on the southern flank of the volcano (Figure 2.26A). They are indurated or non consolidated massive poorly sorted polimyct deposits with muddy or fines-poor matrices. In one place (VR72) they overlie the basal scoria fall, proving that they are part of the Pucón sequence. They contain Pucón scoria with granitic inclusions and must have originated by the reworking of minor P2 material deposited higher on the cone prior to the onset of the main eruptive phase of P2a. In fact, in a proximal locality of drainage 7, a juvenile-rich pyroclastic flow deposit with abundant bombs containing granitoids underlie Pucón debris flow deposits and P2a and could correspond to minor initial P2 activity at this part of the volcano (VR83, Figure 2.22).

The post-eruptive reworked deposits are more voluminous than the syn-eruptive facies and occur at the top of P2, in channels, impersistent beds and pockets, from a few centimetres up to few meters long and a few centimetres to 3.5 m thick (Figure 2.36), with erosional surfaces that cut down into P2 and locally up to P1a-P1b boundary. Facies include bouldery, massive debris flow deposits, diffusely wavy to cross-stratified hyperconcentrated flood deposits, and stream-flow deposits. Features typical of reworked facies include induration, grading, cm to m-scale planar and cross stratification, rounding of scoria, grain fabrics (aligned clasts and imbrication), fines-depleted accumulations of mud-coated clasts, and thin mud drapes ~1-3 mm thick recovering erosional bases. Channel fills commonly contain one or more normally graded

cycles, from facies 1 to 2 to 3, each cycle recording the passage of a single lahar wave. Particularly thick and well exposed outcrops of post-eruptive lahar deposits occur at VR97, VR82 and VR66. Towards the ridges east of drainage 9, local erosion of the flanks of preserved dunes at the top of P2, generated non-consolidated diffusely stratified hyperconcentrated flow deposits, post-dated by the overlying Los Nevados air fall deposits (Figure 2.25D). An accumulation of debris flow and hyperconcentrated lahar deposits several metres thick (and underlain by primary or shortly remobilised pyroclastic flow deposit) occurs at VR39, where drainage 7 empties into the Calafquén basin.

2.3.5 Post-Pucón sequence

Overlying the Pucón Ignimbrite and below the "Pedregoso pyroclastic surge" (2600 yr BP, Moreno 1993; Clavero & Moreno 2004), there is a sequence of two main scoria fall deposits with intercalated ash layers, extending across the northern and eastern flanks of the volcano, the thickness of which decreases from ~3 m, 5 km from the summit to ~60 cm at 12 km ("Chaimilla scoria fallout deposits"; Clavero & Moreno 2004, Figure 2.37). Individual beds can reach up to 1 m thick, are non- to slightly graded, and represent vigorous strombolian to subplinian eruptions (Moreno, 1993).

The scoria fall beds are separated from the top of P2 by a thin bed (<10 cm thick) composed of abundant cohesive orange-coloured accretionary or armoured lapilli fragments in a brown ash matrix. The accretionary lapilli bed is itself commonly overlain by a thin (<10 cm thick) buff-coloured ash layer. These thin beds, also present intercalated upwards in the sequence, were probably produced during weak phreatic or phreatomagmatic events following the Pucón eruption.

The contact between the Pucón Ignimbrite and the accretionary lapilli ash is mostly conformable over large areas where reworked deposits are absent. In particular, the gently inclined top of P2d and the dune forms of P2c of the northern flank (e.g. location VR58) are perfectly preserved below the ash layer (Figure 2.37C). Where post-eruptive lahar deposits occur at the top of P2, the basal ashes lie on top of them, showing that eruption of the ashes post-dated the lahars. The implications of this contact for eruption timing are discussed below.

The post-Pucón sequence is rather different on the southern and southwestern flanks of the volcano. Overlying the Pucón Ignimbrite and below the "Pedregoso pyroclastic surge" (2600 yr BP, Moreno 1993, Clavero & Moreno 2004), there is a black lapilli to ash fall layer (< 10cm thick) locally separated with the ignimbrite by a fine-grained mudflow deposit. Nowhere in the Pucón products have we observed co-ignimbrite ash layers associated with the Pucón pyroclastic flows, either directly on top of, or intercalated between, flow units.

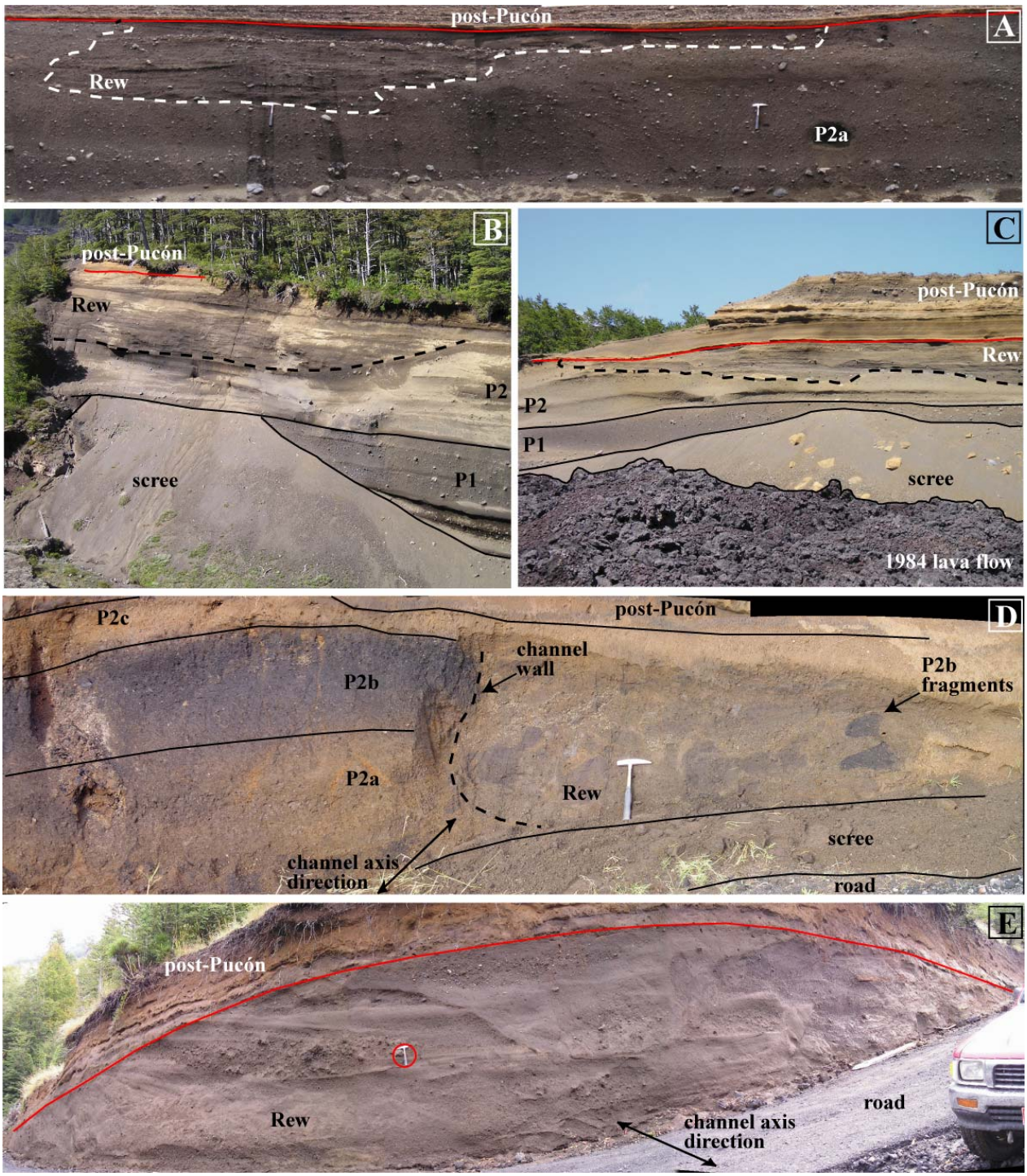

Figure 2.36: Some features of the post-eruptive reworked deposits of the Pucón Ignimbrite, overlain by post-Pucón deposits. (A), (B) & (C) To the northern flank of the volcano, the reworked deposits form discontinuous lens and channels with flat or gently wavy tops (A from VR71, B from VR94, C from VR97). (D) & (E) Post-eruptive channels filled with reworked deposits (southern flank). (D) The channel has a near vertical wall; its filling contains P2b fragments. Note the charcoal rooted in P2b with a degassing pipe traversing into P2c (VR84). (E) Proximal exposure with a set of channels (VR82). Locations are in Figure 2.3.

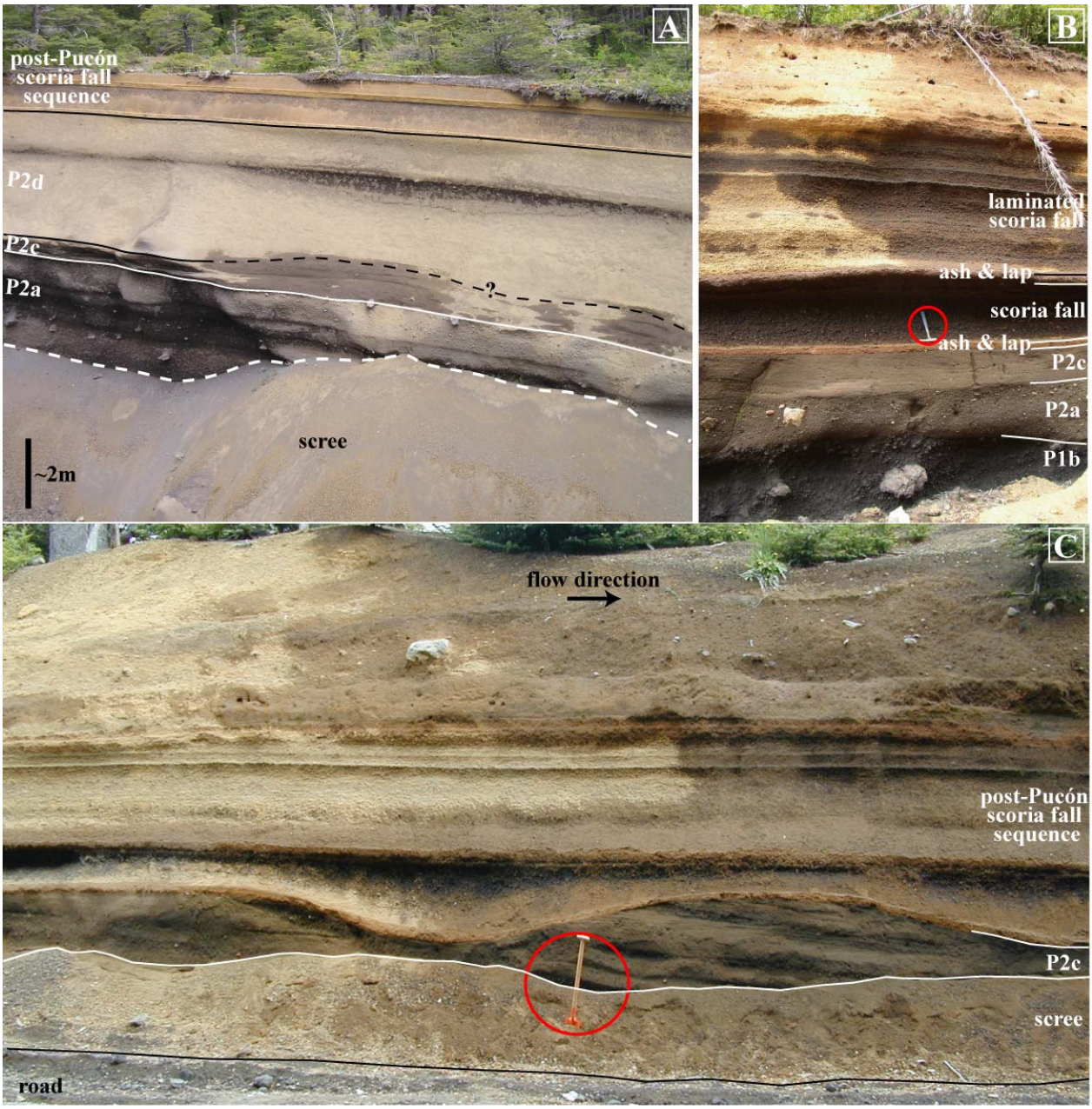

Figure 2.37: Some features of the post-Pucón deposits. (A), (B) & (C) Post-Pucón fallout sequence from the northern flank of the volcano ("Chaimilla scoria fallout deposits, Clavero & Moreno, 2004). (A) Flat contact between the ignimbrite and the post-Pucón sequence (VR94, drainage 1). (B) Complete exposure of the sequence (VR58, ridges between drainages 1 and 2). (C) Wavy contact between the ignimbrite and the post-Pucón sequence, due to the preservation of dunes at the top of P2c. The scale is about 1 m long (VR58, ridges between drainages 1 and 2). Photograph Alain Gourgaud.

2.3.6 Correlation of P2 between the northern and southern sectors

The reconstruction of the architecture of the Pucón Ignimbrite is aided by:

(1) the presence of granitoid clasts, either as individual clasts or as inclusions in scoria, that allows us to unambiguously distinguish P2 from P1;

(2) variations in lithic content; in particular, black juvenile-rich layers were very useful horizons for correlation, for P1 in the northern sector (P1b) and P2 in the southern sector (P2b);

(3) internal structures of the deposits; particularly the stratified layer P2c was a useful horizon for correlation all around the volcano.

These factors allowed to follow and correlate the two main units P1 and P2, as well as their different subunits, all around the volcano. However, the absence of the black juvenile-rich P2b in the northern sector made correlation of P2 between the northern and southern sectors very difficult.

First, similarities between the pyroclastic flow deposits from the base of P2, in the northern and southern sectors, favour a mutual correlation (called subunit P2a):

(1) Both sequences are interpreted as deposits from high-energy scoria flows, dominated by diffusely stratified pyroclastic flow lithofacies and exhibiting large-scale cross stratification and dune forms.

(2) Both have a fines-poor lapilli tuff to breccia at the base with a characteristic assemblage of fragments, including hydrotermally altered fragments, dense lavas with granites and goldish-brown scoria.

(3) They are both in the same stratigraphic position, at the base of unit P2.

Second, there are two correlation possibilities for the rest of the P2 sequence overlying P2a:

(1) The central stratified layer of the northern sector correlates with the upper stratified layer of the southern sector, forming the subunit P2c (the favoured interpretation given above)

(2) The northern P2 sequence correlates entirely with P2a of the southern sector.

Solution of this problem was helped by maps of thicknesses and maximum sizes of particles for surge P2c in the northern and southern sectors (Figure 2.35). If (as postulated) these correspond to the same surge, the radial variations of thicknesses and maximum sizes in the northern and southern sectors should be similar.

The arguments that favour correlation include:

(1) No main differences of the thicknesses of the surge can be seen between the northern and southern sectors (Figure 2.35A). In fact, even if no good isopachs can be drawn, overall the surge has a variable thickness between 0.5 and 3 m. There is no important difference of the maximum sizes of particles between the northern and southern sectors, and (as expected) the maximum lithic size is greater than the maximum scoria in both sectors (Figure 2.35B).

(2) If P2c in the north is the lateral equivalent of P2a, then it should underlie P2b in the south. In fact, the only deposit with surge-like characteristics in both valleys and ridges in the southern sector overlies P2b. So the main pyroclastic surge layer present in the south cannot correlate with P2a.

For this reason, the interpretation in which the central stratified layer of the northern sector correlates with the upper stratified layer of the southern sector, is strongly favoured. This subunit was called P2c in the general stratigraphy of P2 described in previous sections (Figure 2.19).

2.4 GRAIN SIZE DATA

Grain size analyses were done on twenty-two samples (sub-16 mm fractions) from the northern (composite VR73-78) and southern (VR85) type sections and in four samples from other sections (Appendix 2.1). The procedure in the laboratory included oven-drying (one night at 100°C), sieving and weighing of the different grain-size classes (8 mm to 63 µm, ø = -3 to 4, 1-ø intervals) with a high precision balance (precision = 0.01 g).

The cumulative curves of the grain size distribution were constructed on arithmetic probability paper (Figure 2.38). The intersection of the 16th, 50th and 84th percentiles with the grain size distributions curves gave the grain diameters used to derive the Inman (1952) parameters median diameter ($Md_{ø}$) and graphical standard deviation ($\sigma_{ø}$) which is a measure of sorting, as follows:

$$\mathbf{Md_{Ø} = Ø_{50}}$$

$$\mathbf{\sigma_{Ø} = (Ø_{84} - Ø_{16}) / 2}$$

Three plots using the grain size data are presented. The $Md_{Ø}$ / $\sigma_{Ø}$ plot (Figure 2.39A) is used to show the grain size characteristics of the different types of pyroclastic deposits (Walker, 1971). A plot of the fine ash fraction F2 (wt% finer than 63 µm) versus the ash fraction F1 (wt% finer than 1 mm) (Walker, 1983) is used to study the degree of fines-depletion of pyroclastic flow deposits (Figure 2.39B). A ternary diagram is also used to illustrate the grain size characteristics of the deposits (Figure 2.40).

From these diagrams, three main groups of deposits can be recognised. Compared to the juvenile-rich pyroclastic flow deposits (P1aIV, P1b and P2b), the lithic-rich to intermediate pyroclastic flow deposits (P1aII, P1aIII, P2a and P2d) are better sorted (Figure 2.39A), coarser grained and fines depleted (richer in fractions > 1 mm and poorer in fractions < 1 mm, Figures 2.39B and 2.40).

The base of P2a is the best sorted (Figure 2.39A), coarsest grained and most fines-depleted of all the Pucón deposits (Figures 2.39 and 2.40). P2a becomes gradually poorer sorted (Figure 2.39A), finer grained and fines-rich upwards (poorer in fractions > 1 mm and higher ratio <63µm/<1mm, Figures 2.39B and 2.40).

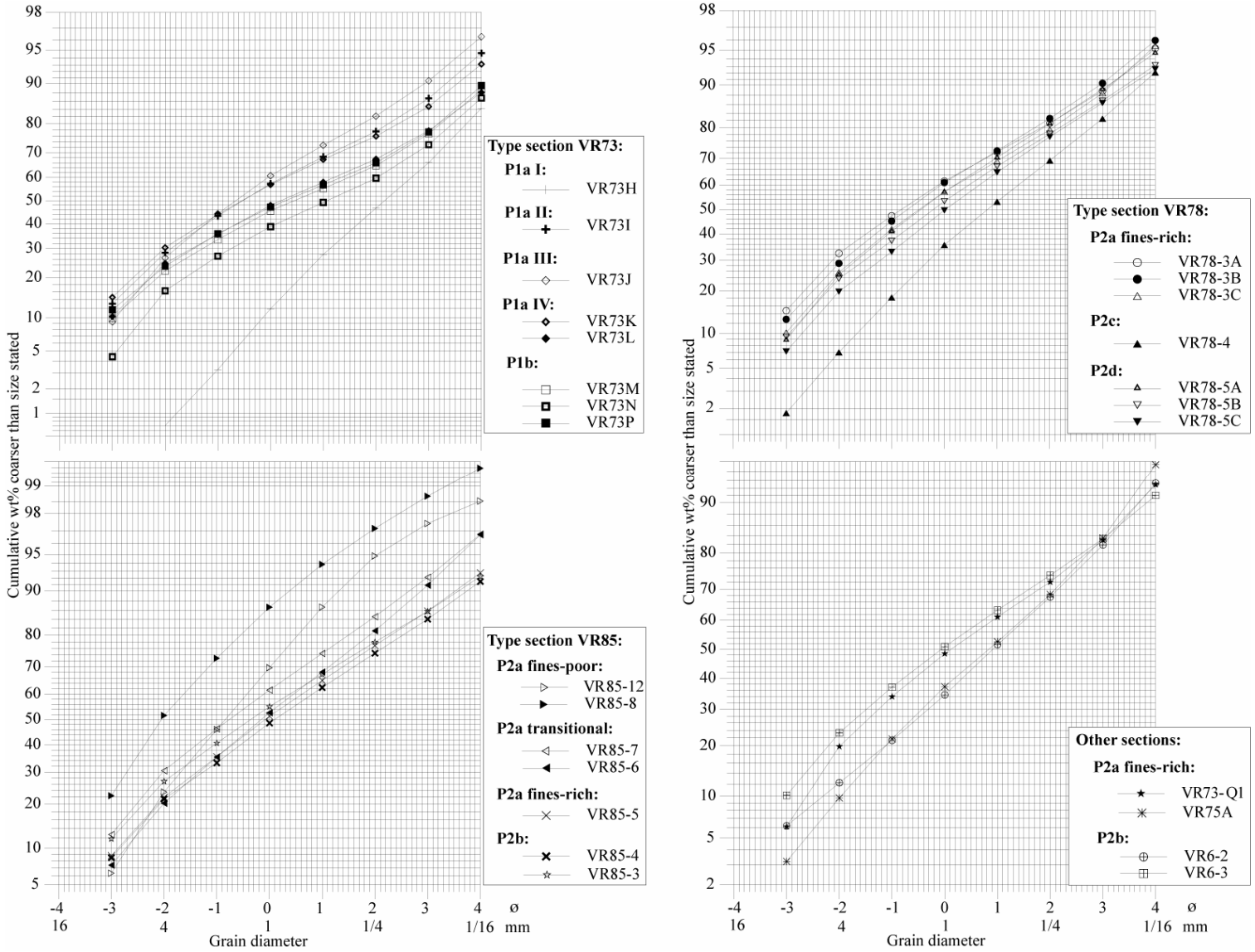

Figure 2.38: Cumulative plot on probability ordinate. The intersection of the 16th, 50th and 84th percentiles with the grain size distributions curves gives the grain diameters used to derive the Inman (1952) parameters. In this case, only the fractions below 16 mm were considered. Samples are from type sections (composite VR73-78 and VR85) and from other sections (VR75, VR6).

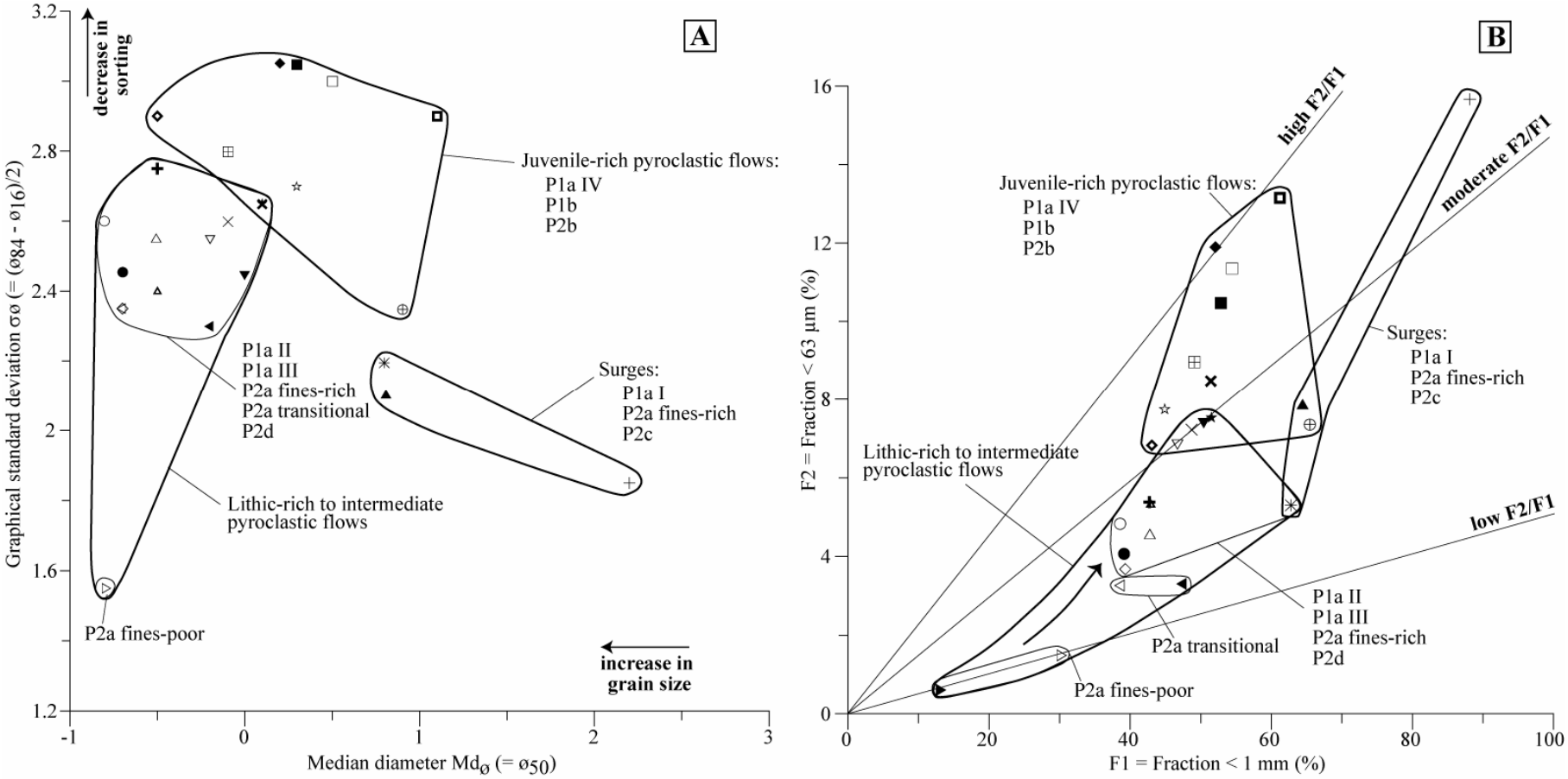

Figure 2.39: A) Graphical standard deviation ($\sigma_{ø}$) which is a measure of sorting versus the Median diameter ($Md_{ø}$), two parameters of Inman (1952) derived from Figure 2.38 (after Walker, 1971). **B)** F2 (wt % finer than 63 µm) versus F1 (wt% finer than 1 mm) diagram.
Lithic rich deposits have less than 50% scoria in all the sizes and their matrices are normally brown. *Juvenile rich* deposits have about 70 to 100% scoria in sizes 4 mm or coarser, and about 50 to 80% scoria in sizes 2 mm or finer. Their matrix is dark grey to black, but some brown-coloured variants also occur. *Intermediates* deposits have scoria abundances between these two end-members. Samples and symbols as in Figure 2.38.

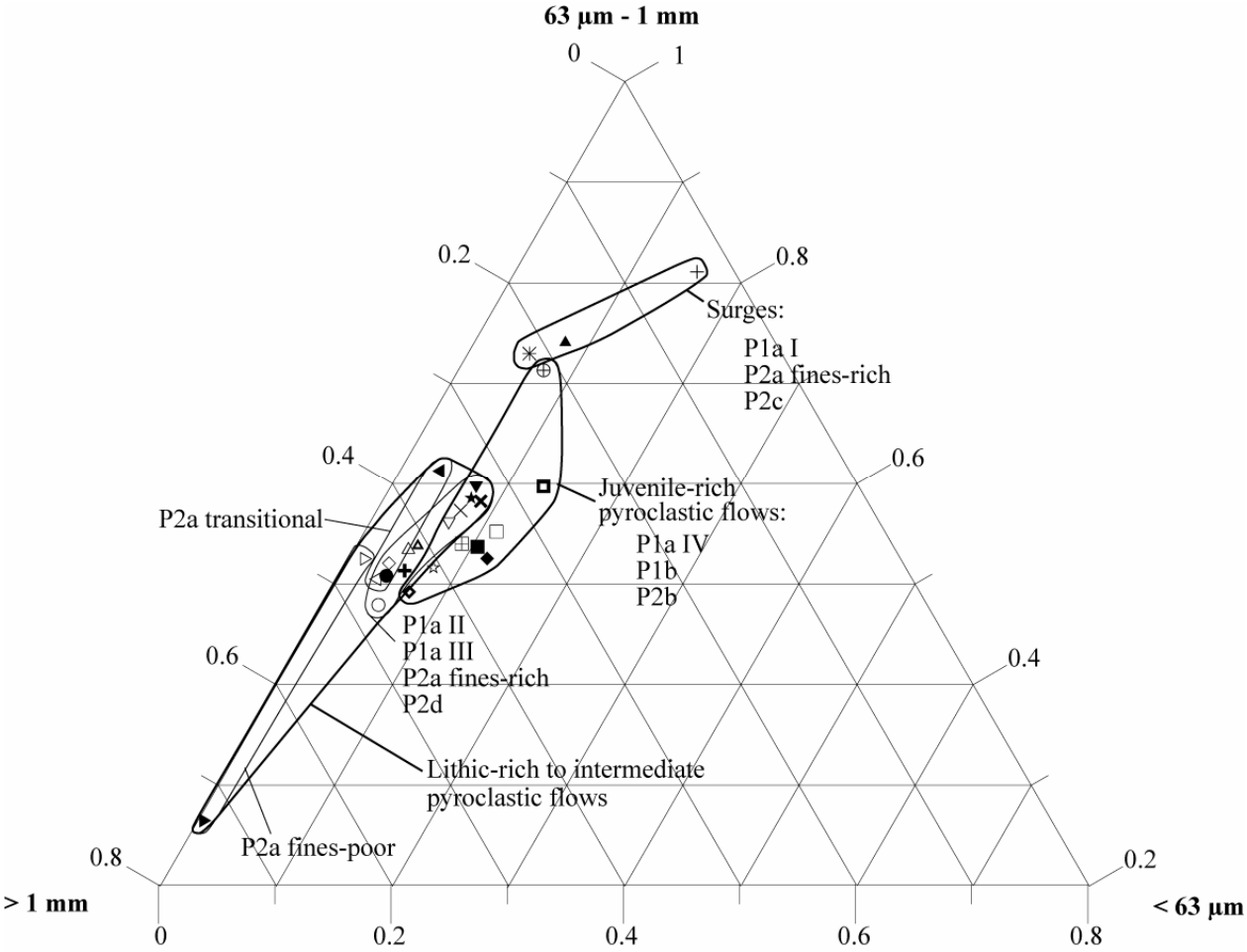

Figure 2.40: Ternary diagram of wt%: > 1 mm / 1 mm - 63 µm / < 63 µm. Definitions of lithic-rich, juvenile-rich and intermediate deposits, samples and symbols as in Figures 2.38 and 2.39.

Compared to the pyroclastic flows, the pyroclastic surge deposits (P1aI, P2c and the interfluve equivalents of P2a) are finer-grained (poorer in fractions > 1 mm, Figures 2.39 and 2.40) and richer in the ash fraction 63 µm - 1 mm (Figure 2.40). The surge deposits have similar sorting to the fines-poor to transitional P2a pyroclastic flow deposits but are generally better sorted than the pyroclastic flow deposits (Figure 2.39A).

2.5 VOLUME AND AGE OF THE DEPOSIT

2.5.1 Volume

The previously estimated volume for the Pucón Ignimbrite was 5 km^3 non-DRE (Clavero, 1996). We here present a new estimate of this volume (V). We subdivided the deposit into the basal scoria fall deposit (A), units P1 and P2, and reworked beds (R), so that V=A+P1+P2+R.

With the aim of obtaining a minimum estimate of the volume of the scoria fall deposit, a diagram of logarithm of thickness versus the square root of area (Pyle, 1989) was plotted (Figure 2.41) using the data of the two approximated isopachs, the areas of which are 26 km^2 (90 cm isopach) and 440 km^2 (10 cm isopach) (Figure 2.6). The approximate volume was calculated using the equation proposed by Fierstein & Nathenson (1992):

$$\mathbf{V = 2To/k^2}$$

where **k** is the slope of the line and **To** is the intersection of the line with the y axis (Figure 2.41). The resulting volume is **V ~ 0.2 km^3**.

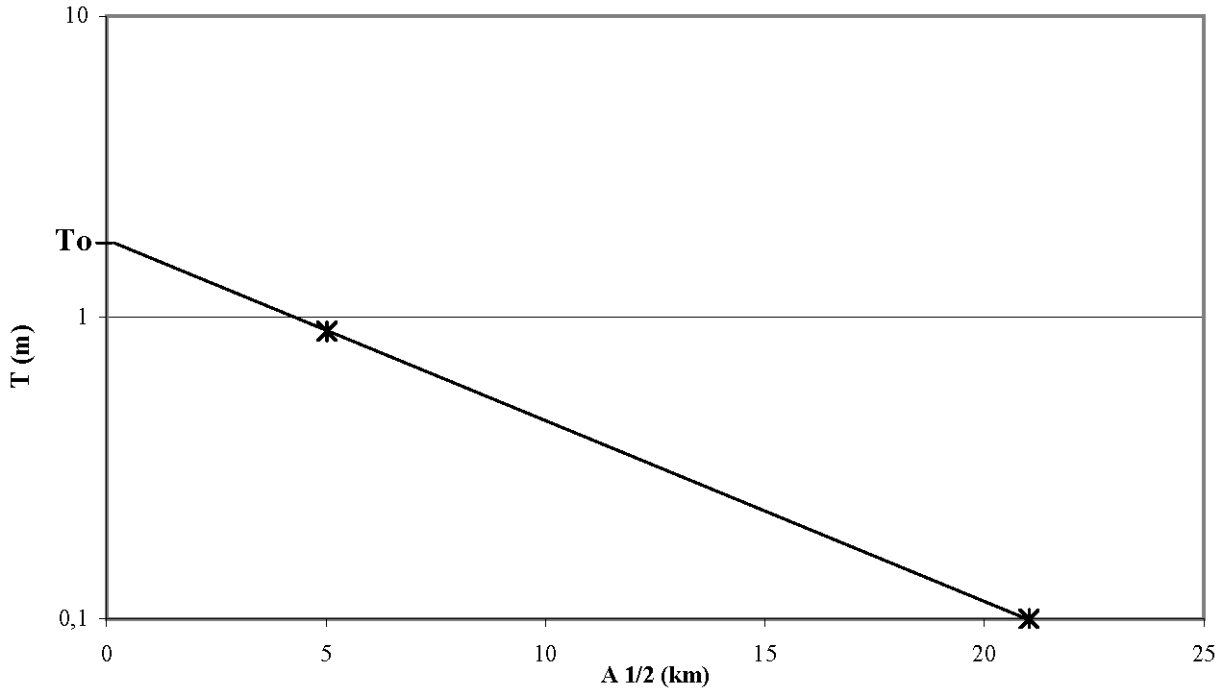

Figure 2.41: Logarithm of thickness versus the square root of area (Pyle, 1989) for the basal scoria fall of the Pucón Ignimbrite.

Surface areas of ~180 km^2 for P1, ~530 km^2 for P2 and ~40 km^2 for reworked layers, were estimated (total surface area after Clavero, 1996; Figures 2.3 and 2.7). The P1 area was subdivided into 9 subareas, each with an average thickness assigned. For unit P2, we considered 19 subareas, and for the reworked

layers, 6 subareas. We estimated a total non-compacted volume of the deposit of ~3.3 km^3 (Table 2.5), with ~0.2 km^3 represented by the scoria fall (<5% of the total volume), ~0.6 km^3 by unit P1 (~18% of the total volume), ~2.5 km^3 by P2 (~76%) and ~0.04 km^3 by reworked layers (~1%). The total volume is smaller than that estimated by Clavero (1996); however, given the large uncertainties involved (in particular due to erosion of the ignimbrite sheet), the two values are probably compatible.

The DRE (dense rock equivalent) volume was calculated as follows:

$$\mathbf{V\ (DRE)} = \rho_{deposit} \times \mathbf{V} / \rho_{magma}$$

where ρ is density. The DRE (dense rock equivalent) volume of magma was then calculated by:

$$\mathbf{V\ magma} = \mathbf{V\ (DRE)} - \mathbf{V}_{lithics}\ \mathbf{(DRE)}$$

The density of magma (ρ_{magma} assumed = ρ_{solid}) is calculated vesicle-free. The method is explained in the Appendix 2.2, resulting:

$$\rho_{solid} \sim 2.5 \times 10^3\ kg/m^3$$

The DRE volume of lithics ($\mathbf{V_{lithics}}$) corresponds to the total volume of lithics of the deposit. It was calculated from the grain size and counting data of the two type Pucón sequences (VR73+VR78 from the northern sector and VR85 of the southern sector, totalling 8 layers of unit P1 and 14 of P2, Chapter 3). For every layer, the lithic contents (%) of the different size fractions were averaged by considering the weight of every size in the layer (from the grain size analysis). Since not all the lithic contents of each size are available, the same lithic content for 16 and 32 mm sizes was assumed in the cases where the 32 mm counting was not available, the same lithic content for 2 mm, 1 mm and 500 µm were assumed (counting of 1 mm and 500 µm sizes was not available) and the same lithic content for the size 250 µm and lower were assumed (counting of sizes lower than 250 µm was not available). The total lithic content of every unit was calculated by averaging the lithic contents of every layer and by subdividing the DRE volume of every unit according to the relative mean thicknesses of the constituent subunits. The resulting $\mathbf{V_{lithics}}$ (DRE) is **0.7 km^3** (Table 2.5).

To estimate the bulk density of the deposit, six samples were chosen (< 4 mm fraction), covering both main stratigraphic units (P1 and P2), at the two type localities of the deposit (northern and southern sectors). They were put in a beaker of known volume and weighted. Taking the average of the six measurements:

$$\rho_{deposit} = 1.4 \times 10^3\ kg/m^3$$

The best estimate of the total DRE volume is **1.8 km^3,** composed of **1.1 km^3** of magma and **0.7 km^3** of accidental or cognate lithics (Table 2.5). It could be stressed that these are probably minimum values due to the difficulties in estimating the volume of deposit lost by erosion. Moreover, no account is taken of the volume lost as fine ash into the atmosphere, since no distal ash fall deposit from the eruption has been recognised.

Table 2.5: Volume calculation for the Pucón Ignimbrite

Unit	Surface area (km^2)	N° subareas	Volume (km^3)	DRE volume (km^3)	DRE volume of lithics (km^3)	DRE magma volume (km^3)
Basal scoria fall	440 (0.1 Tmax isopach)		0.2	0.11	0.02	0.08
Lower unit (P1)	180	9	0.6	0.34	0.1	0.24
Upper unit (P2)	530	19	2.5	1.40	0.6	0.80
Reworked layers	40	6	< 0.04			
Total			**3.3**	**1.8**	**0.7**	**1.1**

2.5.2 Age

Radiocarbon dating is a powerful tool for determining the age of recent (~< 40 000 years, Bowman, 1990) volcanic deposits from warm climates, using as datable material well-carbonised wood present in the deposit. Since one fundamental assumption of the method is that the radiocarbon geochronological clock starts with the death of the plant (Bowman, 1990), the deposit must be primary and the wood burned by it, if one is to obtain a depositional age. This is not always the case because volcanic successions contain normally an important component of reworked layers, which are often difficult to distinguish from the primary volcanic deposits. The presence of reworked horizons intercalated in the Pucón sequence shows that remobilisation and erosion of the primary Pucón deposits occurred shortly after their deposition.

In radiocarbon dating of carbonised wood, the “old wood problem” must also be considered. This means that the innermost heartwood will give radiocarbon results older than the sapwood in the case of long-lived trees (Bowman, 1990). This is the case at these latitudes, where the wet weather conditions have allowed the development of a very dense forest with abundant long-lived trees such as *Nothofagus* or *Araucaria* whose individual specimens may live hundreds or even thousands of years.

Radiocarbon results are given in uncalibrated years BP ("before present"), where 0 BP is defined as AD 1950. A complication is that the rate of production of radiocarbon varies through time, but fortunately the history of past levels of radiocarbon in the atmosphere can be determined from the study of tree rings, since each annual ring incorporates and so records that year’s average atmospheric radiocarbon content. The resulting measurement of the radiocarbon age may therefore be calibrated to convert it to a real

calendar age, currently expressed as calBC. To get a calibrated age (BP), it should be added to 1950. There is a widespread accepted current standard calibration called Intcal98 (Stuiver *et al.*, 1998) that goes back to 24,000 calendar years BP on the basis of dendrochronologically dated annual tree rings, U-Th-dated corals, and varved (annually layered) marine sediments.

Four new radiocarbon datations of carbonised wood from different units of the Pucón Ignimbrite from different parts of the volcano, are presented (Table 2.6). The radiocarbon analyses (conventional) were performed at the Centre for Isotope Research, Radiocarbon Laboratory, University of Groningen, The Netherlands.

Table 2.6: ^{14}C ages of the Pucón Ignimbrite

SAMPLE	COORD E	COORD N	UNIT	^{14}C AGE (BP)	ERROR	cal BP (*)	REFERENCE
VR-2	753.7	5633.6	P2	**3710**	**50**	**4225 – 4203**	this study (**)
						4179 – 4171	
						4155 – 3903	
VR-12	258.3	5629.3	P2	**3670**	**60**	**4151 – 4103**	this study (**)
						4101 – 3835	
VR-15D	244.3	5637.5	P1	**3650**	**30**	**4085 – 4029**	this study (**)
						4013 – 4003	
						3999 – 3889	
						3877 – 3873	
VR-15F	244.3	5637.5	P1	**3510**	**60**	**3959 – 3951**	this study (**)
						3927 – 3915	
						3911 – 3637	
271191-1	243.6	5643.2	P1 ?	3580	70		Moreno, 1993
240492-2	238	5629.5	P2	3740	70		Clavero &Moreno, 1994
021191-1	254.3	5623	P2	3770	80		Clavero &Moreno, 1994
021191-2	255.6	5623.7	P2	3950	70		Clavero &Moreno, 1994
Mean this study				**3635**	**87 (1 σ)**		
Mean all samples ***				**3661**	**91 (1 σ)**		

(*) Range of calibrated ages (BP) at 95.4% (2 sigma) confidence level

(**) Analysis made at the Centrum voor IsotopenOnderzoek, Rijks*universiteit* Groningen, The Netherlands

(***) Except sample 021191-2 (Clavero & Moreno, 1994) discarded by the “old-wood problem"

The average of these new radiocarbon ages is **3635±87** ^{14}C age BP (1 sigma error). Previous ^{14}C ages of carbonised wood (Moreno, 1993; Clavero & Moreno 1994, Table 2.6) allowed these authors to estimate the age of the Pucón Ignimbrite as *ca.* 3700 years, assuming that the age closest to the emplacement age corresponds to the youngest one, and the older one (last row in Table 2.6) is result of the "old wood problem" (Moreno *et al*., 1994a; Clavero 1996). If we also include these previous ages (except the oldest one), the average is 3661±91 ^{14}C BP, very similar to that of this study.

A puzzling result is that, although P1 is stratigraphically older than P2, the ages yielded by the P1 charcoal are younger than those yielded by P2 by about 150 years (Table 2.6). This might be explained if the less energetic pyroclastic flows of P1 unit were not able to knock down and burn big trees but only young branches and twigs. The subsequent energetic P2 flows would have knocked down and burned the old big trees. This idea is consistent with field observations described above where trees left standing in the P1 deposits were felled by the more violent P2a flows. If valid, this argument implies that the most accurate age estimate for the eruption is given by the youngest sample (VR15F), at 3510 BP. Given these uncertainties, the best age estimate for the eruption presented here is **3.6 ± 0.1 ka ^{14}C age BP.**

Table 2.6 also shows the ranges of calibrated ages (95.4% (2 sigma) confidence level), using Intcal98. By inspection, the maximum overlap between the four radiocarbon ages gives calendar ages that range from **3889 to 3959** years calBP (Figure 2.42A). This difference between the calibrated and non-calibrated radiocarbon ages can be observed directly from the calibration curve of Stuiver *et al.* (1998), which shows a ~300 yr difference for materials of age 3600-3700 years BP (Figure 2.42B).

However, with the same argument of the "old wood problem" used to discard old ages, the complete range of calibrated ages for the youngest ^{14}C age (BP) cannot be discarded (3510±60 yr) because the youngest age obtained could correspond to the real age of the deposit. Moreover, Moreno (1993) presented also a similar youngest ^{14}C age (BP) of 3580±70 yr. So, the calibrated age of the Pucón Ignimbrite can be estimated as **3637-3959 yr calBP (**Figure 2.42A**)**.

Another complication is that volcanoes emit CO_2 that has no ^{14}C activity and therefore dilutes the atmospheric concentration close to vents, yielding high apparent ages of plants growing in the vicinity of the volcanic source (Bowman, 1990). In practice, these observed effects are strictly limited to plants growing very close to the volcanic source and are virtually non-existent at >100 m, unless the local environment traps air and does not permit rapid atmospheric mixing (Manning, 1999, and references therein). In the case of the Pucón Ignimbrite, the charcoal in the deposits is present mostly in medial to distal portions of the valleys and hence far from the eruptive vent. Thus this effect could be ignored.

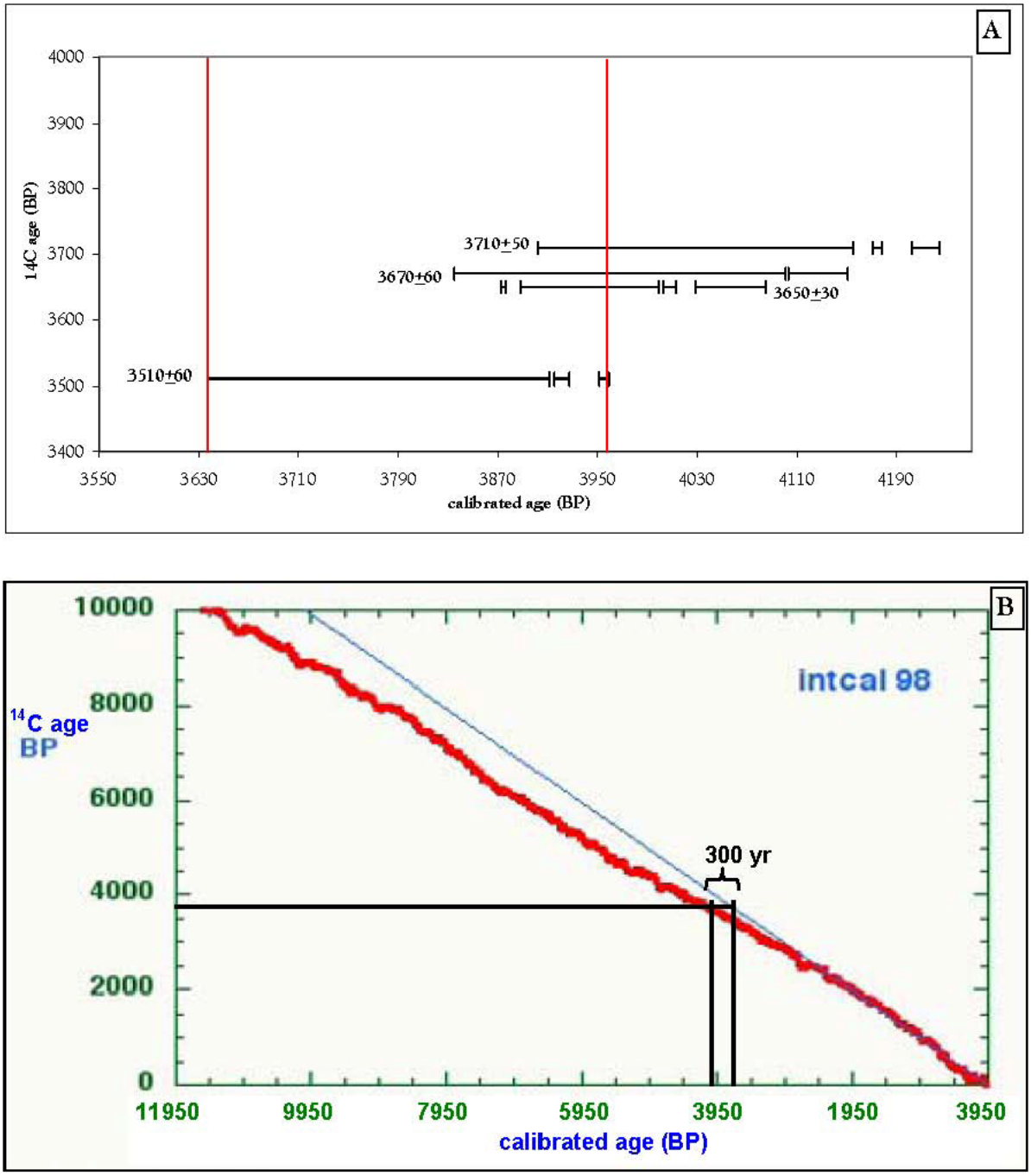

Figure 2.42: Diagram showing the four new radiocarbon dates for the Pucón Ignimbrite (mean: 3635±87 yr BP) with their ranges of calibrated ages at a 95.4% (2 sigma) confidence level using Intcal98 (Table 2.6). By inspection, the maximum overlap between the four radiocarbon ages including all calibrated ranges of the youngest age yield an age range for the Pucón Ignimbrite of 3637-3959 yr calBP (A). This difference between calibrated and non-calibrated radiocarbon ages can be observed directly from the calibration curve of Stuiver *et al.* (1998) that shows a ~300 yr difference for materials of 3600 to 3700 years BP (B).

2.6 DISCUSSION

Reconstruction of the 3.6 ka BP Pucón Ignimbrite (Villarrica volcano, Chile) involved correlation of internal lithofacies of the deposit within a chrono-stratigraphic framework. By logging multiple outcrops around the volcano, and building on previous studies of the geology of the volcano and the Pucón Ignimbrite (Moreno, 1993, 2000; Moreno *et al.*, 1994; Clavero & Moreno, 1994; Clavero, 1996; Lara & Clavero, 2004; Moreno & Clavero, 2006), our approach allowed us: (1) to reconstruct the Pucón eruption, (2) to constrain some parameters of the eruption dynamics (such as the number of eruptive phases, intensities, eruptive durations and timing, etc.), (3) to infer some physical characteristics of the pyroclastic currents (distribution and extent, particle concentration, ability to surmount obstacles, energy and ability to erode the substrate, etc.), and (4) to better understand the hazards posed by Villarrica to the surrounding area and inhabitation, associated with large explosive eruptions of the volcano.

2.6.1 Eruption timing

The only firm constraint on the duration of the repose period preceding the Pucón eruption is provided by the underlying 4100-yr Afulnahue pyroclastic flow (Clavero & Moreno 2004, ex-"FP-NN" of Moreno, 1993), suggesting a maximum repose period of ~400 years.

The basal scoria fall deposit underlies in conformable contact the Pucón Ignimbrite, without any intervening paleosol, though sheared (Figures 2.43 and 2.5). Any pause between the basal scoria fall and the onset of phase P1 cannot have been very long, because the fallout is widely preserved, even in some drainages and even where thin.

The duration of the Pucón eruption is very difficult to constrain. However, the eruption of P1 could have lasted perhaps a few days to months, suggested by: (1) P1a is composed of multiple stacked, well-defined beds with conformable contacts but some syn-eruptive reworking (Figures 2.11 and 2.12), (2) degassing pipes traverse the contact between P1b and P1c (Figures 2.43 and 2.30A).

The key field evidence for a pause between P1 and P2 is the systematic truncation, at the base of P2, of degassing pipes originating in P1 (Figures 2.43, 2.29A-B and 2.30). Charcoalization of wood takes place by chemical transformation and volatile loss in the absence of oxygen. Pipe truncation cannot be explained by rapid burial of burning wood because air is not necessary for charcoal formation. Even if the air supply was cut off by rapid burial by P2 deposits, pipes from wood being charcoalised at the time of P2 would be expected to generate pipes traversing the contact. Sharp truncation of even large degassing pipes rooted in the hot deposits of P1b shows conclusively that the temperature of the P1 deposits had dropped below that necessary for charcoalization (~200 °C; e.g., Scott and Glasspool, 2005). Pyroclastic flow deposits can remain at high temperatures for long times owing to the low thermal conductivity of ash (Ryan *et al.*, 1981). Temperatures up to 640 °C were measured in block-and-ash deposits on Montserrat

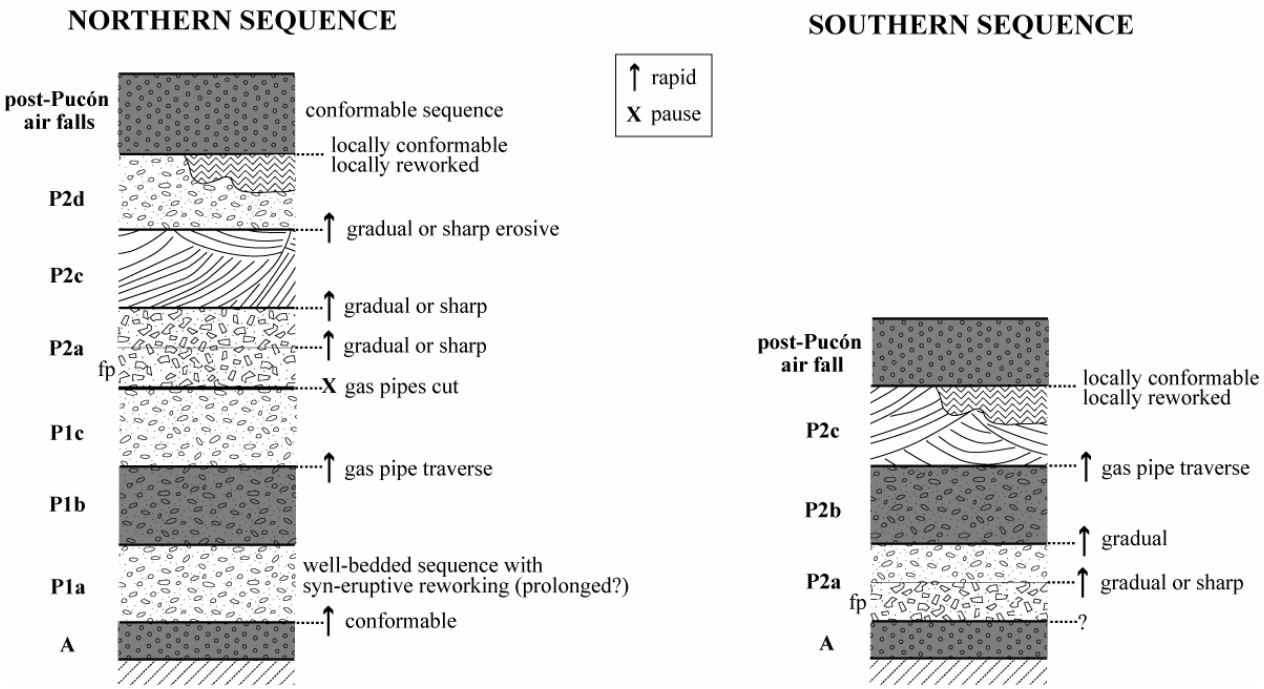

Figure 2.43: Summary of the constraints of timing. The lithology of the units is simplified for this figure (symbols after figure 2.14). Thicknesses not in scale.

20 days after emplacement (Cole *et al.*, 2002), the ignimbrite at Mount Pinatubo was still at 390 °C 1 m below the surface after 1.5 years (Torres *et al.*, 1996) and temperatures of up to 645°C were measured in fumaroles of the ash flow deposits in the Valley of Ten Thousands Smokes, 7 years after emplacement (Allen & Zies, 1923 in Fisher & Schminke, 1984). However, premature cooling of surface layers can occur if subjected to strong rain (Hoblitt *et al*. 1985). We conclude that a pause of at least several weeks to months is implied by the field observations.

There is also geochemical evidence for slight trace element differences between the juvenile components in P1 and P2. Enough time is therefore required between phases P1 and P2 for explain these differences (see Chapter 3).

The following evidence suggests that, following the P1/P2 pause, the second eruptive phase (P2) emitted voluminous pyroclastic currents on a timescale comparable to, or shorter than, P1: (1) the commonly gradational contacts between the different beds and subunits instead of well stacked and discrete beds, (2) the absence of intercalated lahar deposits, and (3) degassing pipes that traverse the contacts between P2b and P2c (Figure 2.29D). By analogy with other ignimbrite-forming eruptions of similar volume, such as the 60-h-long Novarupta 1912 eruption (e.g. Houghton *et al.*, 2004), the 20-h-long Vesuvius 79 eruption (e.g. Sigurdsson *et al.*, 1982) or the 9-h-long Pinatubo 1991 climactic eruption (Newhall and Punongbayan, 1996), phase P2 could have lasted hours to a few days.

The boundary between the top of the Pucón Ignimbrite and the overlying ash tuff with accretionary lapilli is mostly conformable over large areas. Even if some reworking is present locally at the top of the ignimbrite, the upper surface of P2 is well preserved (dune forms in P2c or flat downstream-inclined top of P2d). Thus, the accretionary lapilli ash at the base of the Chaimilla sequence probably occurred few storm seasons after the end of the Pucón eruption.

2.6.2 Eruption intensity

The Pucón eruption started with a scoria fall of ~0.2 km^3 (see below), which corresponds to a violent strombolian or subplinian fallout phase (Figures 2.5 and 2.6), following the terminology of Newhall & Self (1982).

Several lines of evidence suggest that the P1 pyroclastic currents were less energetic than those of unit P2 (Table 2.7): (1) they laid down mostly valley-confined deposits and only thin ash layers by associated weak surge clouds on interfluves; (2) the contacts with the underlying scoria fall deposit or pre-Pucón deposits and between the successive flow units were generally conformable (Figure 2.11A); (3) at least one pyroclastic flow (P1b) terminated in a steep bouldery flow front, as typical of highly concentrated flows; and (4) P1 deposits have a restricted distribution to the northern sector (Figure 2.7) and limited distal deposition (see example drainage 2, Figure 2.14). This may have had a topographic origin (e.g., a notch in the crater wall) or may have been due to asymmetric collapses of the eruption columns.

The P1/P2 boundary probably represents an increase of eruptive intensity, marked by the arrival of the violent and erosive P2a flows (Table 2.7). This is suggested by: (1) the sharp basal contact of P2 characterised by diverse erosive structures (channels, angular unconformities, folding, thrusting and shearing) in a manner similar to that beneath other high-velocity pyroclastic currents like the Mount St. Helens lateral blast (Fisher, 1991; Druitt, 1992) (Figures 2.30 to 2.32), (2) the presence of large toppled trees oriented towards the vent just at the P1-P2 boundary (Figure 2.34), (3) the diffuse stratification of P2a deposits, suggestive of sedimentation under highly unsteady conditions (Branney and Kokelaar, 2002), (4) the presence of large scale cross-bedding and dune structures (Figure 2.30A), (5) a basal, fines-depleted facies suggestive of a highly turbulent front, (6) the important interfluve deposition and great extent of P2a (Figures 2.23, 2.24, 2.25C, 2.26B, 2.31A, 2.32E, 2.33A-B), and (7) the sudden shift from intermediate (P1c) to lithic-rich facies (P2a), with the abrupt appearance of more diverse lithic-types including vent-derived granitoids.

The subsequent pyroclastic flows of P2b may have had a lower eruptive intensity, similar to P1b (Table 2.5), suggested by: (1) a restricted distribution (southern and eastern flanks of the volcano), and (2) confinement in valleys in the medial to distal environments (Figure 2.22).

The following subunit (P2c) represents a major surge-forming phase (Table 2.7), suggested by: (1) its widespread distribution (Figure 2.35), (2) the presence of dunes several metres in wavelength (Figure 2.37C), and (3) important deposition all around the volcano in both valleys and on ridges (Figures 2.25C-D, 2.26B, 2.33A). The Pucón eruption finished with a waning phase with the emission of low-intensity pyroclastic flows (P2d, Table 2.7), suggested by: (1) high-concentration valley-confined deposits with little or no deposition on interfluves environments (Figure 2.23), (2) restricted distribution to the northwestern flank (drainages 4 to 9, Figure 2.21), and (3) short extent (Figure 2.24).

Table 2.7: Summary of the constraints on eruptive intensity

Unit	Relative eruptive intensity	Evidence
P2d		Restricted distribution to the northwestern flank (drainages 4 to 9). High-concentration valley-confined massive pyroclastic flows, locally erosive. Scarce or null deposition on interfluves environments.
P2c		Widespread all around the volcano. Parallel and cross stratified pyroclastic surge deposit. Dunes several metres in wavelength at the top. Important ridge deposition.
P2b		Restricted distribution from the southern to east of the volcano. High-concentration valley-confined massive pyroclastic flows.
P2a		Widespread all around the volcano. Massive to diffusely stratified pyroclastic flow deposits with large scale cross-bedding and dune structures. Important ridge deposition and distal facies. Sharp base with diverse erosive structures (channels, angular unconformities, folding, truncations, thrusting, shearing and shear layers produced in the substrate). Downed large trees. Sudden appearance of abundant lithic-types including vent-derived granitoids. Fines-depleted base suggestive of initial blast-like flow.
PAUSE		Sharp contact P1/P2. Degassing pipes at the top of P1c cut by P2a. Geochemical results (Chapter 3) suggest that enough time is required for the differentiation of the P2 magmatic suite.
P1c		Restricted distribution (some valleys to the west and north). High-concentration valley-confined massive pyroclastic flows.
P1b		Restricted distribution from the west to north of the volcano. High-concentration valley-confined massive pyroclastic flows.
P1a		Restricted distribution to the west and north of the volcano. Valley-confined pyroclastic flows and minor surges. Limited (fine-grained) ridge deposition.
A		Violent strombolian or subplinian fallout phase (~0.2 km^3).

2.6.3 Eruptive narrative

We now reconstruct the series of events leading up to, during, and immediately following the Pucón eruption.

Villarrica volcano is located in an area that was glaciated 14,600 to 10,200 years ago (tardiglacial period in the region; Denton *et al.*, 1999) and today remains as an ice-capped volcano, which means that very likely the volcano was covered by a more extensive ice cap when the Pucón eruption took place.

Prior to the Pucón eruption, basaltic-andesite to rhyolite lava domes and/or flows of unknown age that probably extruded beneath the ice cap, were probably present near or at the volcano summit. These were fragmented during the Pucón eruption which started after a maximum repose period of ~400 years (Pucón components are fully described in Chapter 3).

Before the Pucón eruption, there was probably fumarolic activity around the crater when violent strombolian or subplinian fallout started (0.2 km^3 of deposits, 0.1 km^3 of magma, VEI = 3 to 4), marking the onset of the Pucón eruption. The magma was very hot and fluidal, probably ejecting abundant spatter fragments proximally. The eruptive dynamics of the volcano then changed rapidly towards an ignimbrite-forming mechanism.

During phase P1 multiple pyroclastic flows were produced and covered a minimum area of ~180 km^2 in a sector on the western to northern flanks of the volcano, extending radially up to 16 km from the present-day summit. About 0.6 km^3 of deposits (0.24 km^3 of magma) were emitted during phase P1, which represents about the 20% of the total volume produced during the eruption.

Phase P1 started with small phreatomagmatic explosions that generated a small pyroclastic surge in the upper reaches of the northern drainages of the volcano (P1aI). The eruptive intensity then increased during a series of vulcanian explosions that resulted in the emission of at least two lithic-rich to intermediate pyroclastic flow units that spread more widely, covering a sector from the western to northern flanks of the volcano, up to 15 km radially (P1aII-III). The pyroclastic flows were highly concentrated, being deposited in valleys and depressions. Lithic clasts too coarse or too dense to be transported by the pyroclastic flows were left proximally, generating lag breccias. Subordinate pyroclastic surges were deposited mostly in proximal slope environments, probably by the upper, more dilute levels of the pyroclastic flows. Spatter fragments, emitted either during the initial fallout phase or during eruption of P1a, were transported by the pyroclastic flows. Some vegetation was burned by the passage of the pyroclastic flows. The eruption intensity then declined with the emission of at least two brown juvenile-rich pyroclastic flows with a restricted distribution (P1aIV).

The P1a phase left a deposit of multiple stacked, well-defined flow units. Available water from the melting of the ice cap mobilised and transported some pyroclastic debris. This was followed by the emission of at least three black, juvenile-rich pyroclastic flows that were emitted across the western to northern flanks of the volcano (P1b). These highly concentrated scoria flows overspilled the topography,

depositing strongly thinned veneers on proximal valley margins. The flows were very hot, causing strong charcoalization of wood and forming abundant degassing pipes.

While wood in P1b was still being charcoalised, at least three less juvenile-rich pyroclastic flows were discharged into valleys on the western and northwestern flanks of the volcano (P1c).

A repose period of several weeks to months followed phase P1, allowing the deposits to cool sufficiently for charcoalization of wood to cease, at least near the surface of the P1 deposits.

Following this pause, a new eruptive phase started (P2) with the arrival of higher-intensity, erosive pyroclastic flows that spread all around the volcano, covering a minimum area of ~530 km^2 and up to 21 km radially, probably up to the present town of Pucón (P2a). The turbulent, blast-like leading edge of these flows arrived first, eroding, shearing and deforming the substrate during its path, and representing the most energetic and violent pulse of all the pyroclastic currents of P2. It travelled further than the rest of P2, leaving a fines-depleted deposit up to 5 m thick along the valleys with important interfluve deposition. Three or more high-energy P2a pyroclastic flows followed in rapid succession, forming thick and commonly amalgamated valley ponds that locally thicken downstream. Some of the coarser-grained interfluve facies of P2a are veneers left where the entire pyroclastic flow swept over the landscape; finer-grained beds probably record deposition from the dilute upper part or margins of density-stratified flows, which formed an almost completely record of the deposits on interfluves. The P2a flows were highly erosive, forming angular unconformities, shearing and thrusting the underlying strata. The flows were unsteady and of high- to intermediate-concentration, deduced from their dominantly diffusely stratified aspect and from the presence of huge bed forms. Old big trees partly buried, but not felled by the less energetic P1 flows were now knocked over by the arrival of the more violent flows of P2a. However, in some sectors of the northern and western flanks, little vegetation was probably available by this time, because it had already been buried by the P1 flows. In places, the initial fines-depleted facies was eroded or sheared off, leaving isolated pockets preserved in channels and depressions. Channels were carved into P1 deposits of the northern flank.

The P2 phase then continued with the emission of juvenile-rich pyroclastic flows (P2b), extending up to ~11 km from the summit in a restricted sector from the south to east of the volcano. These high-concentration pyroclastic flows formed thick deposits in the valleys and thinner ones on interfluves; they burned much of the available wood due to their high temperature.

At least two rapidly emplaced pyroclastic surges (P2c) then covered the previous hot deposits with charcoal still burning (degassing pipes traverse the contact). This represents a major surge-forming phase, the product of which is distributed all around the volcano. The Pucón eruption terminated with a low-intensity waning phase, during which three high-concentration pyroclastic flows were emitted on the northern flank up to 10 km from the present-day crater (P2d).

In all, about 2.5 km^3 of deposits (0.8 km^3 of magma) were emitted during the P2 phase. This volume represents about the 80% of the total volume produced during the eruption and was probably emitted in no more than a few days or even hours.

Shortly following the eruption, lahars swept across all sectors of the Pucón pyroclastic deposits, causing strong erosion. After no more than a few storm seasons, the Pucón eruption was followed by vigorous strombolian to subplinian eruptions and phreatic/phreatomagmatic explosions, heralding construction of the new cone.

A notable feature of the eruption is the almost complete lack of co-ignimbrite ash fall from pyroclastic flow emplacement, either between flow units or at the top of P2. Three possibilities can be envisaged: (1) fragmentation of the basaltic andesite magma generated too little fine ash to form a large phoenix cloud; (2) the cloud was dispersed by strong winds, leaving little on the Pucón Ignimbrite itself, or (3) the Pucón eruption could occurred by instantaneous collapse of low and very dense columns or by the exit and instantaneous precipitation of a dense pyroclastic mass without generating a high column (boiling over), as it has been postulated before (Clavero & Moreno, 1994).

2.6.4 Implications for volcanic hazards at Villarrica

Villarrica volcano is one of the most historically active volcanoes in South America, with a past tendency for large-scale explosive activity and the generation of pyroclastic currents highly destructive to life and the environment. Even infrequent on a human timescale, if a Pucón-sized eruption (VEI = 5) occurred today, approximately 15,000 - 40,000 people would be directly threatened by pyroclastic currents and even more by associated lahars and ash falls.

The Pucón eruption started with a fallout phase that quickly evolved towards an ignimbrite-forming eruptive mechanism. The absence of paleosoils or reworking between the scoria fall and the base of the ignimbrite suggests that this interval was too short for even minor erosion of the fall deposit by wind or rain (hours to months?). This may have implications for hazards at Villarrica, because the possible occurrence of a violent strombolian or subplinian eruption may quickly evolve towards the generation of voluminous pyroclastic flows of much higher volcanic hazard.

The evolution of the Pucón eruption shows that a real ignimbrite-type episode (such as P2), of short duration but large magnitude (0.8 km^3 of magma, ~ 80% of the total volume), catastrophic on a regional scale affecting all the flanks with the generation of very violent pyroclastic currents, can occur after a pause of several weeks to months following a period of already important pyroclastic activity (P1). This pause at the end of P1 marked a prolonged adjustment phase of the plumbing system, rather than the end of the eruption, as could be assumed during monitoring of a similar event today.

2.7 CONCLUSIONS

1. The Pucón Ignimbrite (~1.8 km^3 DRE, ~40% of lithics) consists of a basal scoria fall deposit (A) overlain by two main pyroclastic current units, P1 and P2. The upper unit, P2, is characterised by the presence of basement granitoids, both as free fragments and as inclusions in scoria, whereas these are absent in the lower unit, P1. The two units show contrasting sectorial distributions: whereas P1 occurs only on the western and northern flanks, P2 was deposited all around the volcano.
2. The eruption started with a violent strombolian or subplinian phase of scoria fallout (0.1 km^3 DRE, VEI = 3-4).
3. Ignimbrite phase P1 started with a small (probably wet) surge north of the volcano, followed by a series of vulcanian explosions generating multiple pyroclastic flows that spread more widely over the western and northern flanks, leaving thick valley-confined deposits that cover ~180 km^2 up to 15 km from the present-day summit. Unit P1 (0.3 km^3 DRE) is mostly lithic-rich to the base (P1a) and gradually more juvenile-rich upwards (P1b and P1c).
4. After the P1 phase, there was an eruptive pause of several weeks or months.
5. Unit P2 has a larger volume (1.4 km^3 DRE) forming thick valley ponds with a complete record on interfluves. It was emitted in a short time (no more than a few hours to days) and represents an increase in the eruptive intensity, possibly associated with summit collapse. During this climactic phase, the fragmentation level reached basement granitoids, which were mixed thoroughly into the magma during the eruption.
6. The first pyroclastic flows of phase P2 (P2a) were preceeded by a violent, blast-like leading edge; they were emitted all around the volcano covering ~530 km^2 and extending up to 21 km from the present-day summit. The flows were highly erosive on the underlying ground surface. Then, lower-intensity more juvenile-rich pyroclastic flows were discharged towards the south and east of the volcano (P2b), rapidly followed by a major pyroclastic surge (P2c). The eruption terminated with low-energy pyroclastic flows emitted onto the northern flank (P2d).
7. After the inundation of several lahar waves during no more than a few storm seasons, the eruption was followed by violent strombolian to subplinian eruptions that laid down a sequence of scoria fall deposits on the eastern and northern flanks (Chaimilla fallout deposits).
8. The age of the eruption is estimated as **3.6 ± 0.1 ^{14}C age BP**, corresponding to a calendar age of **3640-3960 yr calBP.**
9. Based on this study of the Pucón eruption, it can be postulated that a strombolian or subplinian eruption at Villarrica could potentially evolve rapidly into the generation of pyroclastic flows. After important explosive activity, adjustment of the plumbing system during a pause of several weeks to months, could culminate in a second, more violent and voluminous outburst.

Appendix 2.1: Grain size analyses of <16 mm fractions of samples from different stratigraphic layers of the Pucón Ignimbrite.

sample	unit	mm/µm	8	4	2	1	500	250	125	63	<63	dry total	Md ø (*)	ø 84	ø 16	σ ø (*)	> 1 mm	1mm-63µm	< 1 mm
		ø	-3	-2	-1	0	1	2	3	4									
VR73H	P1a	wt%	0	0,7	2,5	8,6	15,9	18,9	19,4	18,3	15,7	100	2,2	4,0	0,3	1,9	3,2	81,1	88,1
VR73I	P1a	wt%	13,0	15,5	14,8	14,0	11,1	9,1	9,3	7,8	5,4	100	-0,5	2,7	-2,8	2,8	43,3	51,3	42,7
VR73J	P1a	wt%	9,3	17,3	17,7	16,4	12,0	9,5	8,3	5,9	3,7	100	-0,7	2,2	-2,5	2,4	44,3	52,1	39,3
VR73K	P1a	wt%	14,5	15,8	13,6	13,0	10,4	8,6	8,8	8,4	6,8	100	-0,5	2,9	-2,9	2,9	44,0	49,2	43,1
VR73L	P1a	wt%	10,3	14,4	10,9	12,4	10,0	9,5	10,2	10,4	11,9	100	0,2	3,6	-2,5	3,1	35,6	52,5	52,1
VR73M	P1b	wt%	10,0	12,1	11,4	12,1	9,7	9,6	11,8	11,9	11,4	100	0,5	3,6	-2,4	3,0	33,5	55,2	54,4
VR73N	P1b	wt%	4,4	11,8	11,0	11,6	10,4	10,5	13,2	13,9	13,2	100	1,1	3,8	-2,0	2,9	27,2	59,7	61,2
VR73P	P1b	wt%	11,6	12,0	12,2	11,3	9,7	9,2	11,3	12,2	10,5	100	0,3	3,5	-2,6	3,1	35,8	53,7	52,8
VR78-3A	P2a	wt%	14,8	17,6	14,8	14,2	10,9	9,0	7,6	6,2	4,8	100	-0,8	2,3	-2,9	2,6	47,3	47,9	38,6
VR78-3B	P2a	wt%	12,8	16,0	16,3	15,7	11,8	9,9	7,8	5,6	4,1	100	-0,7	2,2	-2,7	2,5	45,1	50,8	39,1
VR78-3C	P2a	wt%	10,1	15,6	16,1	15,4	11,8	10,4	9,0	6,9	4,6	100	-0,5	2,5	-2,6	2,6	41,8	53,6	42,8
VR85-12	P2a	wt%	6,3	17,2	22,5	23,7	17,1	8,0	2,6	1,1	1,5	100	-0,8	0,8	-2,3	1,6	46,0	52,5	30,3
VR85-8	P2a	wt%	22,4	29,2	21,3	13,9	7,1	3,3	1,6	0,7	0,6	100	-2,1	-0,2		-0,1	72,9	26,5	13,2
VR85-7	P2a	wt%	12,6	17,9	15,8	15,3	12,9	10,3	7,4	4,6	3,3	100	-0,7	1,9	-2,8	2,4	46,3	50,5	38,5
VR85-6	P2a	wt%	7,4	12,8	15,2	17,3	15,4	13,0	9,8	5,8	3,3	100	-0,2	2,3	-2,3	2,3	35,4	61,3	47,3
VR85-5	P2a	wt%	8,8	13,2	13,6	15,8	13,8	11,8	9,1	6,8	7,2	100	-0,1	2,8	-2,4	2,6	35,5	57,3	48,7
VR73-Q1	P2a	wt%	6,1	13,7	14,1	14,5	12,6	11,0	10,8	9,5	7,5	100	0,1	3,1	-2,2	2,7	34,0	58,5	51,5
VR75A	P2a	wt%	3,2	6,5	12,0	15,5	15,4	15,8	15,0	11,3	5,3	100	0,8	3,0	-1,4	2,2	21,7	73,0	62,8
VR85-4	P2b	wt%	8,4	13,0	11,9	15,3	13,9	12,1	9,6	7,4	8,5	100	0,1	3,0	-2,3	2,7	33,3	58,2	51,4
VR85-3	P2b	wt%	11,7	15,1	13,8	14,4	12,2	10,6	8,0	6,4	7,7	100	0,3	2,8	-2,6	2,7	40,7	51,6	44,9
VR6-3	P2b	wt%	10,1	13,2	13,7	13,9	12,5	10,7	9,2	7,8	9,0	100	-0,1	3,1	-2,5	2,8	37,0	54,0	49,1
VR6-2	P2b	wt%	6,2	6,0	9,1	13,2	17,1	16,0	14,2	10,8	7,4	100	0,9	3,2	-1,5	2,4	21,3	71,3	65,5
VR78-4	P2c	wt%	1,8	5,2	11,2	17,4	17,6	16,1	13,2	9,6	7,9	100	0,8	3,1	-1,1	2,1	18,1	74,0	64,4
VR78-5A	P2d	wt%	8,9	16,0	16,0	16,2	13,3	10,8	8,1	5,4	5,3	100	-0,5	2,3	-2,5	2,4	40,9	53,7	42,9
VR78-5B	P2d	wt%	9,4	14,2	13,6	16,1	13,8	11,0	8,7	6,3	6,8	100	-0,2	2,6	-2,5	2,6	37,2	56,0	46,7
VR78-5C	P2d	wt%	7,1	12,7	13,2	16,6	15,3	12,4	9,1	6,2	7,4	100	0,0	2,7	-2,2	2,5	33,0	59,6	50,4

(*) $Md_{ø}$ (median diameter) and $\sigma_{ø}$ (graphical standard deviation) Inman parameters (1952) derived from the intersection of the 16th, 50th and 84th percentiles with the grain size distributions curves (Figure 2.39):

$$\mathbf{Md_{Ø} = Ø_{50}}$$

$$\mathbf{\sigma_{Ø} = (Ø_{84} - Ø_{16}) / 2}$$

Appendix 2.2: Calculation of the density of solid

The density of solid was determined according to the following procedure:

1. Two dense black scoria samples were finely crushed with the tungsten mill. 25 ml of sample were placed in a graduated test tube and weighed ($wt_{sample+tube}$).
2. Water was mixed with a small quantity of soap to diminish the surface tension. The density was measured with a test tube and it resulted ρ_{water}= 0.98 g/ml (1 σ error of 5 measurements = 0.003).
3. The sample is mixed with the water and it is left decanting. The excess of water was taken out with a pipette and the new volume corresponds to the volume of the solid plus the pores (V). The tube is weighed again ($wt_{sample+water+tube}$).
4. The density of solid (ρ solid) is calculated as follows:

$$\rho\ solid = wt_{sample} / (V - (wt_{sample+water+tube} - wt_{sample+tube})/ \rho_{water})$$

And it was obtained ρ solid = 2.5 g/ml (1 σ error of 4 measurements = 0.05).

CHAPTER 3 Dynamics of the basaltic andesitic Pucón eruption (3.6 ka BP, Villarrica Volcano, Chile)

3.1 INTRODUCTION

The Pucón Ignimbrite (3.3 km^3, equivalent to 1.8 km^3 DRE - dense rock equivalent) is a well preserved and complicated sequence of airfall and pyroclastic current deposits emitted by the largest Holocene eruption of Villarrica Volcano, one of the most active volcanoes of the Southern Andes (Moreno, 1993, 2000; Clavero & Moreno, 1994, 2004; Moreno *et al.*, 1994; Clavero, 1996; Moreno & Clavero, 2006). Several eruptive phases, involving the emission of pyroclastic currents with contrasting intensities, timings and responses to topography, generated a deposit with highly variable scoria/lithic ratios, distributions and facies variations. Facies include pyroclastic flow deposits (massive valley-pond and diffusely-stratified with large-scale bedforms) and well-stratified pyroclastic surge deposits with magnificent bedforms. These features makes the Pucón eruption an excellent target for the study of the dynamics of an explosive eruption, particularly considering the basaltic andesitic juvenile composition (54 - 56 wt% SiO_2) of the deposit, rarer and less studied than more typical silicic ignimbrites.

The evolution of the eruption was described in Chapter 2. The aim in the present chapter is now to constrain the eruptive dynamics through detailed study of pyroclastic textures, chemical composition and componentry. Textural characterization and densities (vesicularities) of juvenile pyroclasts has proved to be important in studying physical processes such as the conditions and relative timing of magma vesiculation and fragmentation, conduit ascent and the role of magmatic volatiles versus external water in driving explosive eruptions (Houghton & Wilson, 1989; Klug & Cashman, 1994, 1996; Gardner *et al.*, 1996, 1998; Hammer *et al.*, 1999; Polacci *et al.*, 2001, 2003; Klug *et al.*, 2002). In this study, when combined with compositional variations, textural observations and density/vesicularity help to constrain the conduit processes operating prior to, and during, the eruption and also to speculate on the possible role of phreatomagmatism. This last aspect is then treated in more detail in Chapter 4. Three different methods were used to calculate densities of juvenile pyroclasts, which were then converted into vesicularities. Microscopic observations focused on the vesicularity and crystallinity of pyroclasts using optical and electron (SEM) microscopes.

Accidental components are useful for constraining magma chamber depth or conduit locations, for indicating the former presence of a hydrothermal system, or for reconstructing events of vent erosion or caldera subsidence (Freundt *et al.*, 2000). For example, in the Bishop tuff, characteristic vent-derived lithic types show that the eruption evolved from a single vent to multiple vents along a ring fracture that defines the structural outline of Long Valley caldera (Wilson & Hildreth, 1997; Freundt *et al.*, 2000). A progressive increase of lithic fractions with time may reveal progressive erosion and enlargement of the conduit (Heiken & McCoy, 1984; Lirer *et al.*, 1993) which has been associated with a steady increase in

average vesicularity with time (Kaminski & Jaupart, 1997). A detailed study of the components of the Pucón Ignimbrite was therefore carried out.

Most voluminous ignimbrites are compositionally zoned, thus recording geochemical heterogeneities in the underlying magma chamber. In this study, geochemical data (whole-rock major and trace element composition) of juvenile and accidental components were used with the aim of (1) identifying the juvenile component of the Pucón Ignimbrite and comparing it with the pre and post-Pucón products, (2) establishing possible vertical variations up through the deposit that could reflect zoning of the parent magma chamber, (3) constraining correlations and relationships between different magma batches during episodes of magma differentiation, reservoir replenishment or magma mixing, and (4) determining the origin of the dense prismatically-jointed (DPJ) fragments (see below).

3.2 THE PUCÓN ERUPTION

The Pucón eruption started with a violent strombolian to subplinian fallout phase (0.2 km^3, VEI = 3-4), which evolved into an ignimbrite-forming eruption rapidly enough to prevent significant erosion of the fall deposit or development of a paleosol. The ignimbrite is divided into two main units, which correspond to two main eruptive phases (P1 and P2). During the first phase (P1), pyroclastic flows (0.6 km^3, 20% of the total volume) covered ~180 km^2 of the western and northern flanks of the volcano up to 15 km from the present-day summit. This phase started with a small base surge directed north of the volcano, which was followed by a series of vulcanian explosions. The explosions generated pyroclastic flows that spread widely over the western and northern flanks, leaving mostly valley-confined deposits (<15 m thick; subunits P1a, P1b and P1c).

After this first eruptive phase (P1), there occurred a pause long enough for charcoalization of wood in P1 to cease, before a second, more intense, eruptive phase (P2) began. The P1-P2 boundary also marks the abrupt appearance in the lithic assemblage of vent-derived granitoids, erupted as individual clasts and also mixed thoroughly into scoria. The occurrence of distinct accidental lithic assemblages in P1 and P2 has implications for the eruptive dynamics, as discussed in the present chapter. A larger volume was emitted during phase P2 (2.5 km^3, 80% of the total volume), mainly of pyroclastic flows deposited all around the volcano, covering ~530 km^2 up to 21 km from the present-day summit. These P2 flows left thick sequences in valleys (<70 m thick) with an important deposition on interfluves (<5 m thick). Phase (P2) started with a violent and erosive blast-like surge that was immediately followed by voluminous and energetic pyroclastic flows that impacted all flanks of the volcano (subunit P2a). This was followed by

lower-intensity and valley-confined pyroclastic flows rich in black scoria, deposited southeast of the volcano (subunit P2b), then by a pyroclastic-surge-forming phase (subunit P2c). The eruption terminated with low-energy, valley-confined pyroclastic flows emplaced across the northern flank (subunit P2d).

After one to a few storm seasons, the Pucón eruption was followed by vigorous strombolian to subplinian and phreatic eruptions that laid down pyroclastic air fall deposits on the eastern and northern flanks ("Chaimilla scoria fallout deposits", Moreno, 1993; Clavero & Moreno 2004).

3.3 REVIEW ON VESICULATION AND FRAGMENTATION PROCESSES AND ERUPTIVE DYNAMICS

To constrain the eruptive dynamics of the Pucón Ignimbrite, it should be understood the main processes involved in the development of explosive eruptions. This review includes what are considered as "dry" magmatic explosive eruptions and a review about phreatomagmatism is presented in Chapter 4.

Vesicles are inferred to nucleate readily in magmas and to grow at rates primarily dependent on the concentration and diffusion coefficient of the volatile species (generally H_2O) until bubble interference inhibits further growth at vesicularities (or volume % vesicles) of the order 75%-83% (Sparks, 1978). If magma rises and is discharged sufficiently quickly to preclude significant non-explosive degassing, it will be fragmented at the peak of vesiculation. The result should be a more-or-less uniform assemblage of pumices with that critical fragmentation vesicularity, which is assumed in most models (Houghton & Wilson, 1989).

Pumice has commonly been taken to represent the state of magma at the point of fragmentation but this assumption relies on an unspecified process which quenches instantaneously the pieces of vesicular magma as they form (Gardner *et al.*, 1996). However, pumice preserves a wider range of vesicularity (~60 to 93%) because clasts of vesiculated magma are not quenched instantaneously when fragmentation occurs and cool only when the eruption column enters the atmosphere (Witham & Sparks, 1986; Houghton & Wilson, 1989; Thomas *et al.*, 1994). In fact, physical modelling (Thomas *et al.*, 1994) and textural evidence (Klug & Cashman, 1994) suggest that between fragmentation and quenching, several effects can deform pumices and modify significantly their vesicularities (Klug & Cahsman, 2004). Viscosity is the main control on pumice vesicularity since high magma viscosity retards gas bubble expansion rate and bubble wall thinning and thus limits bubble coalescence and clast expansion after fragmentation producing lower vesicularities (Kaminski & Jaupart, 1997; Thomas *et al.*, 1994; Klug & Cashman, 1996; Gardner *et al.*, 1996; Papale, 1999).

Fragmentation is the transition from a continuous melt with a dispersed gas phase to disconnected parcels of bubbly melt within a continuous gas, pumice and ash being the quenched products (Klug & Cahsman, 1996). Fragmentation is considered to occur when gas bubble overpressure exceeds the magma tensile strength (Sparks, 1978). However, several other factors can determine the degree to which magma is fragmented and produce vesicularity and textural variations in crystal and vesicle sizes, shapes and distributions and crystal contents of the juvenile clasts:

Strain-induced fragmentation: Fragmentation results from the action of shear rather than that of bubble overpressure (Gardner *et al.*, 1996). Numerical models demonstrate the feasibility of strain-induced brittle fragmentation of magma above a conduit region of remarkably high magma acceleration (Papale, 1999; Thomas *et al.*, 1994). The amount of shear that erupting magma experiences is proportional to its velocity of rise and once bubbles become packed closely and mixture is sheared strongly, magma fragments when it reaches a vesicularity of ~64 vol% (Gardner *et al.*, 1996).

Bubble coalescence and magma permeability: Bubble coalescence, mostly occurring prior to magma fragmentation, creates permeability that allows exsolved and expanded gas to escape, thus preserving a sufficiently interconnected region of vesicular magma as a pumice clast, rather than fully fragmenting it to ash (Klug & Cashman, 1996). Slow rise rates promote bubble coalescence and permeability (Klug & Cashman, 1996) which is consistent with the observation that degree of fragmentation (i.e. amount of ash) increases with increasing eruption rate or intensity (mass flux; e.g. Walker 1973 in Klug *et al.*, 2002) and that waning eruption rates lead to effusive extrusion of melt that has degassed through a permeable network of bubbles on ascent (Eichelberger *et al.*, 1986). Bubble coalescence has also been identified as a major factor affecting the ascent dynamics of silicic magma by numerical models (Papale, 2001), which relates the degree of gas bubble coalescence which is a measurable pumice texture parameter with the efficiency of pumice degassing.

Propagation of a decompressive wave as a control of bubble coalescence and fragmentation: Conditions leading to fragmentation of rhyolitic melt and preservation of pumice during this process are similar in eruptions of varying magnitude and intensity (VEI~5-7) and bubble nucleation is mostly controlled by downward propagation of a decompression wave followed by rapid bubble growth and coalescence prior to magma disruption; fragmentation results from subsequent expansion and acceleration of bubbly melt (Klug & Cashman, 1994, 1996; Klug *et al.*, 2002).

Different crystallinities and microlite contents: Klug & Cashman (1994) determined that low vesicularity microlite-bearing pumices underwent a small amount of degassing prior to the explosive eruption increasing viscosity and hindering bubble expansion and coalescence, thus affecting magma

fragmentation. Thus, deposits with microlite-bearing and microlite-free pumice of otherwise similar compositions have been observed to have diverse clast densities within a single deposit (Carey & Sigurdsson, 1987). The driving force behind crystallization, i.e. cooling- or degassing-induced (decompression) crystallization has also been studied. In fact, witnessed repose interval durations between events together with detailed textural characterization of clasts were used to determine rates of crystal nucleation and growth. Syn-eruptive groundmass crystallization may be possible primarily in response to rapid decompression and volatile loss rather than cooling of magma in the conduit during short interval durations between events on the order of months or less (Cashman, 1992; Hammer *et al.*, 1999; Blundy & Cashman, 2005; D'Oriano *et al*., 2005; Piochi *et al*., 2005).

Heterogeneous flow conditions and processes in the conduit: By means of a textural (vesicularities and microlite contents by SEM image analysis) and compositional study of two main types of pumices, Polacci *et al.* (2001) and Rosi *et al.* (2004) interpreted that the less viscous magma may be originated by heating of the original magma in a strongly sheared region close to the conduit walls by viscous dissipation and crystal grinding and resorption. These heterogeneities affect the whole eruption dynamics because the absence of less viscous pumice in the pre-climactic deposits suggests that viscous dissipation was the key factor for the onset and preservation of a high mass flow rate of the climactic phase and establishment of a sustained Plinian column, otherwise difficult to explain for highly viscous crystal-rich magmas (Polacci *et al.*, 2001; Rosi *et al.*, 2004). Progressive coalescence promoted by efficient shear stresses at conduit walls was most likely the driving process in pumice degassing, strongly influencing the development of magma permeability (Polacci *et al.*, 2003).

Vesicularity and textural variations can also be explained by post-fragmentation processes which are controlled by viscosity, including (Gardner *et al.*, 1996): (1) expansion of pumice as a result of decompression if gas bubbles remain isolated from the exterior, for example bomb breadcrust is fractured by continued expansion of gas within the still-plastic core (Fisher & Schmincke, 1984) under conditions of low magma viscosity (Kaminski & Jaupart, 1997), (2) development of bubble connectivity to form permeable networks and gas release, and (3) collapse of the melt surrounding the interconnected bubbles as a result of surface tension forces, if magma has sufficient low viscosity. For example, the preservation of highly elongated and coalesced vesicles and the lack of post-fragmentation expansion features in pumice suggest that its vesicularity is close to that at fragmentation (Polacci *et al.*, 2001).

Conditions of shallow ascent more than pre-eruption volatile concentrations control eruptive behaviour (Eichelberger *et al.*, 1986). Recent numerical models (Sahagian, 2005 and references therein) developed to account realistically for eruptive processes to promote reliable, real-time prediction and mitigation, indicate that eruption dynamics is highly sensitive to magma bulk rheology which is the most important

parameter. Correlation of systematic variations in textures to changes in eruption dynamics such as effusive-explosive and plinian fall-pyroclastic flow transitions have been studied (Gardner *et al.*, 1996; Eichelberger *et al.*, 1986; Gonnermann & Manga, 2003; Tadeucci & Wohletz, 2001; Pollacci *et al.*, 2001; Klug *et al.*, 2002; Mastrolorenzo & Pappalardo, 2006; Szramek *et al.*, 2006).

3.4 PHYSICAL CHARACTERISTICS OF THE PRODUCTS

3.4.1 Pucón Ignimbrite

3.4.1.1 Juvenile components

Textures

Methods

Pyroclastic textures were studied macroscopically in hand samples, under the petrographic microscope and using the scanning-electron microscope (SEM). The microscopic observations focused on vesicularities and crystallinities of the different types of juvenile lapilli and bombs. Shapes and distributions of vesicles were observed on SEM images of 20 pyroclast samples from the basal scoria fall and subunits P1a, P1b, P2a and P2b. Phenocryst contents and sizes were determined from 10 thin sections of juvenile lapilli samples (8 mm fraction) from P1a, P1b and P2a. The data of microlite contents and vesicularities are presented fully in Chapter 4.

Macroscopic textures

Scoriae of the basal fall deposit are black to goldish-brown, light and highly vesicular, exhibiting irregular, angular shapes including folded varieties (Figure 3.1A).

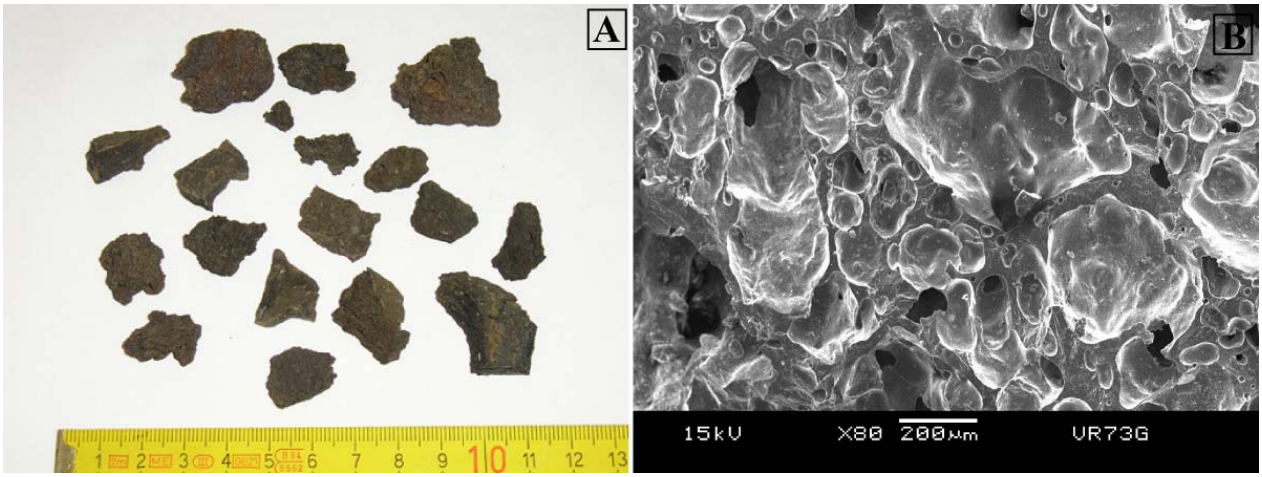

Figure 3.1: Plate showing basal fall scoria lapilli. (A) Highly-vesicular scoria lapilli with irregular angular shapes including folded varieties. (B) Secondary electron image (SEI) under SEM showing the glassy texture, small rounded and big elongated irregular vesicles with evidence of bubble coalescence.

Pyroclasts of the overlying ignimbrite are black to goldish-brown including vesicular and dense varieties. Bombs reach up to about 60 cm in diameter (Figure 3.2A) and several types have been recognised with variable shapes and textures, being especially diverse in subunit P1a (specifically P1a III, Chapter 2). The main types include:

- Vesicular rounded bombs, mostly spherical, homogeneous or prismatically jointed (Figure 3.2A). They are the most typical bomb type of the Pucón Ignimbrite, especially abundant in the more juvenile-rich layers.
- Folded, contorted and ropy bombs, some with goldish-brown crusts, which are very abundant in P1aII. Also, dense flat bombs with aspect ratios reaching normally up to 1:2 but locally up to 1:5.5 that exhibit scoriaceous bands and thin goldish-brown scoriaceous crusts, particularly abundant in P1aIII (Figures 3.3A and B). The morphologies suggest that these bombs could be spatter fragments emitted during the initial fallout phase, then picked by the P1a pyroclastic flows. Alternatively, they could have been discharged during phase P1a itself.
- Dense bombs with prismatic and/or concentric jointing, some with breadcrusting, present in P1 and especially in P1aIII (Figures 3.2B, C and D).

The bombs of unit P2 belonging to any of the types described before, may contain granitoid inclusions, either rigid (Figure 3.3C) or partially melted. In the latter case, the granitoid enclaves could be very abundant exhibiting rounded vesicles or being deformed (Figure 3.3D). Some dense P2 bombs have internal fabrics cut by the surface of the bomb, showing that the fabric predates magma fragmentation (Figure 3.3C).

Some goldish-brown iridiscence is locally seen in highly vesiculated scoria lapilli and in bomb crusts, especially to the bottom of both main units (P1 and P2) of the ignimbrite. It has been observed that in general the larger or denser the fragment, the lower the ratio between the thicknesses of goldish crust and black centre (Figures 3.3B and C).

A dense flat-shaped bomb from P2b shows a macroscopic vesicle fabric consisting in a planar elongation of vesicles parallel to the bomb flattening. This fabric is parallel and not concentric and is cut by the irregular surface of the bomb. This indicates that the planar fabric was developed before the formation of the bomb (pre-fragmentation deformation).

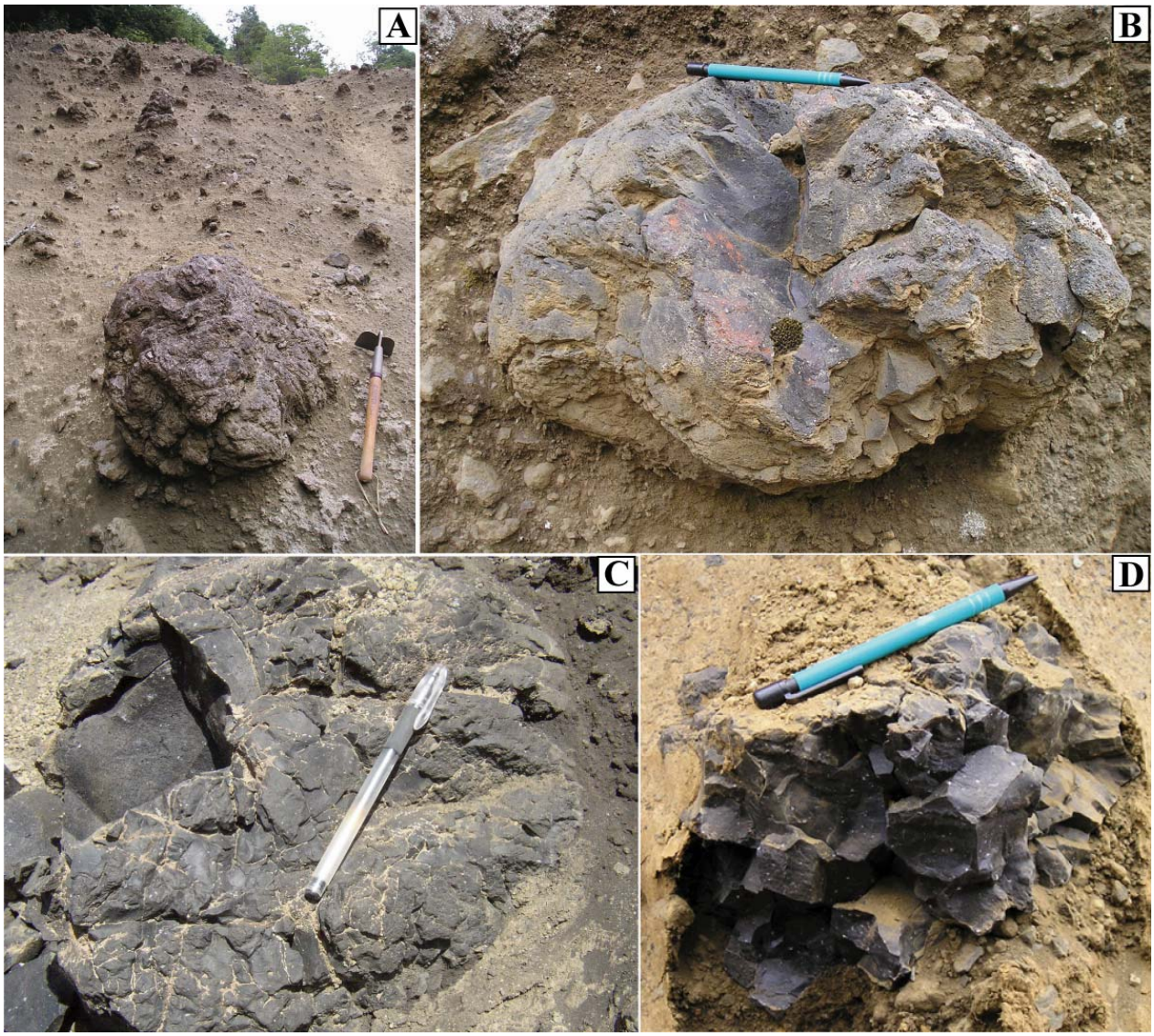

Figure 3.2: Plate showing some types of bombs of the Pucón Ignimbrite. (A) Big scoriaceous bomb (60 x 45 x 50 cm) from P2a (VR85). (B) Big prismatically-jointed bomb (40 x 26 x >20 cm) from P1a III (VR112). (C) Breadcrusted and prismatically-jointed dense bomb from P1b (VR73). (B) Brittle bomb with prismatic and concentric fracturing from subunit P1a III (VR112). A similar bomb from this outcrop has 55.8% SiO_2.

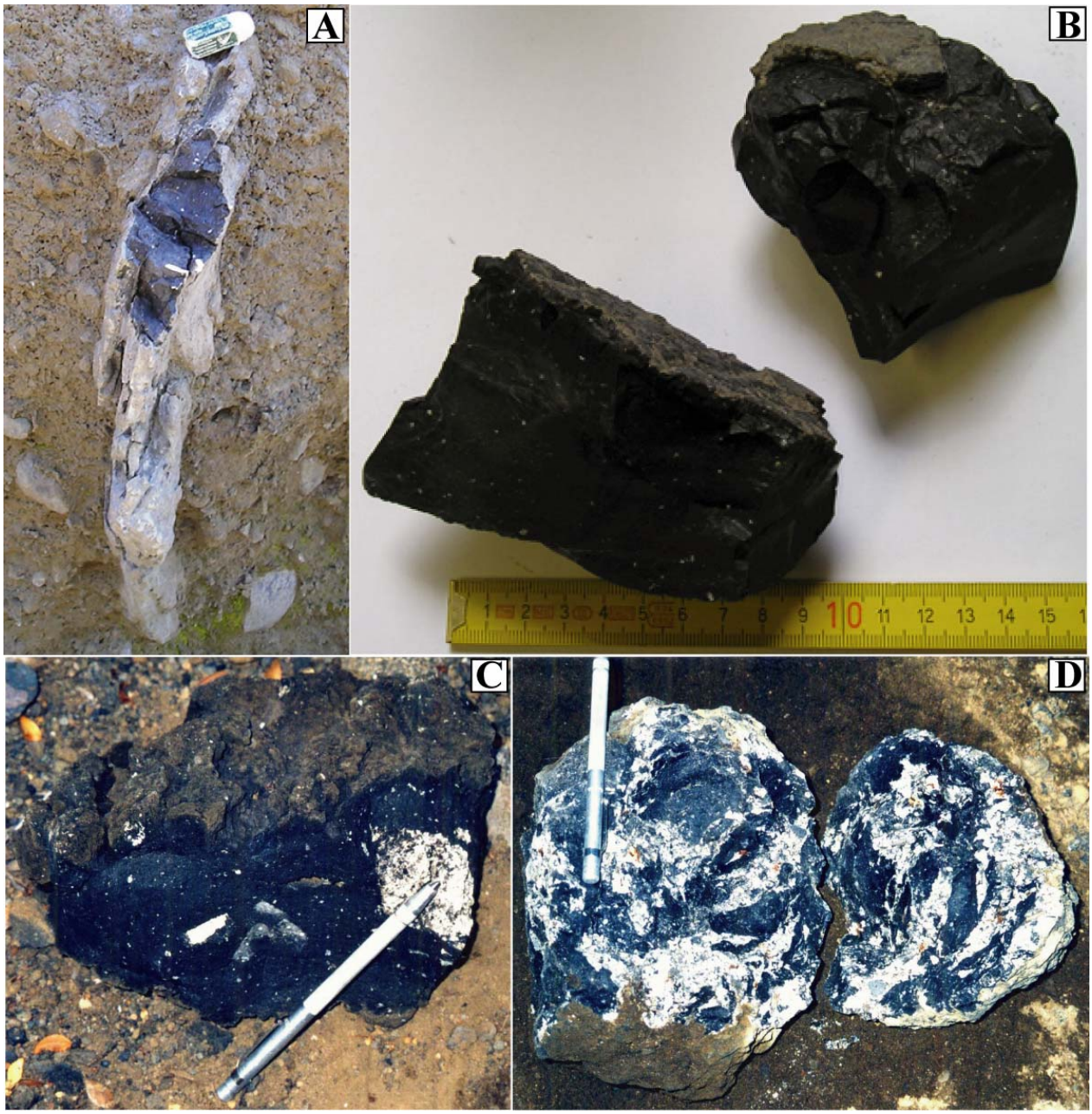

Figure 3.3: Pucón dense bombs. (A) and (B) Bomb with strong flattening (30 x 30 x 15 cm) in the lithic-rich P1aIII (VR97, drainage 2). (C) Dense bomb with wavy crust and rigid granitoid inclusions from P2b (VR12). (D) Bomb with abundant partially-melted granitoid inclusions from P2a (VR57).

Microscopic textures

The scoriae of the basal scoria fall are very glassy and have two populations of bubbles: small rounded isolated vesicles of uniform size (100 μm on average) and large elongated, more irregular vesicles (~300 μm to 2 mm) with evidence of coalescence (Figure 3.1B).

The ignimbrite pyroclasts are overall phenocryst-poor (1-10 vol%, vesicle-free), with slightly higher mean abundances in P2 (~10%) than in P1 (~2%), probably due to (1) to xenocrysts derived from the granitoid inclusions and wrongly considered as phenocrysts, and/or (2) to tapping of the lower portions of the chamber richer in accumulated phenocrysts. The phenocrysts are (in decreasing order of abundance) plagioclase, clinopyroxene and olivine. Typical sizes range from less than 0.1 mm up to 2 mm, with plagioclase being normally around 0.2 mm and clinopyroxene and olivine even smaller (0.1-0.2 mm).

Groundmass microlite contents are highly variable (~5 to 65%**,** vesicle-free). Microlite sizes range from less than 1 μm up to ~50 μm, being commonly <30 μm. Vesicularities of the juvenile lapilli are also highly variable and typically less than 75%. More detailed data and description of the methods used to estimate microlite contents and vesicularities are described in Chapter 4.

The microlite-poor scoria lapilli and bombs are vesicular (typically >50%), exhibiting rounded bubbles of two main families: abundant, small isolated spherical vesicles and larger connected vesicles with evidence of bubble coalescence (Figures 3.4A, 3.4C, 3.4E and 3.5A). The most vesicular scoriae exhibit very narrow walls between bubbles (Figure 3.4E). The scarce microlites (~5-25%) grow normally in clusters, some with spherulite-like forms and exhibiting textures of rapid cooling (Figure 3.6).

The microlite-rich dense juvenile lapilli and bombs with vesicularities of <60% have bubbles of more uniform sizes, irregular shapes (normally interconnected and slightly elongated) and wider walls between them (Figures 3.4B, 3.4D, 3.4F and 3.5B). Small isolated vesicles not impregnated with resin are less common than in light scoria (compare Figures 3.5A and 3.5B). The groundmass is normally formed by a dense network of microlites ranging from ~45 to 65% (Figure 3.7).

Both microlite-poor and microlite-rich textures described above can coexist in the same fragment. A dense zoned juvenile lapilli of P2a has a vesicle-poor band with small isolated spherical vesicles and scarce microlites (left part of the scoria in Figure 3.8A), which grow normally in clusters and from phenocrysts (Figure 3.8B). This vesicle-poor zone is interlayered with a vesicle-rich band with large irregular vesicles (right part of the scoria in Figure 3.8A) and a groundmass formed by a dense network of microlites, with some glass (Figure 3.8C).

Zoning of microlite content can also be concentric. A scoria lapilli of P2b has a central zone with big vesicles (Figure 3.8D) and scarce microlites, which grow from phenocrysts or in clusters that can form spherulite-like arrangements (Figure 3.8E). The rim of the scoria has small vesicles (Figure 3.8D) and a dense network of microlites in the groundmass (Figure 3.8F).

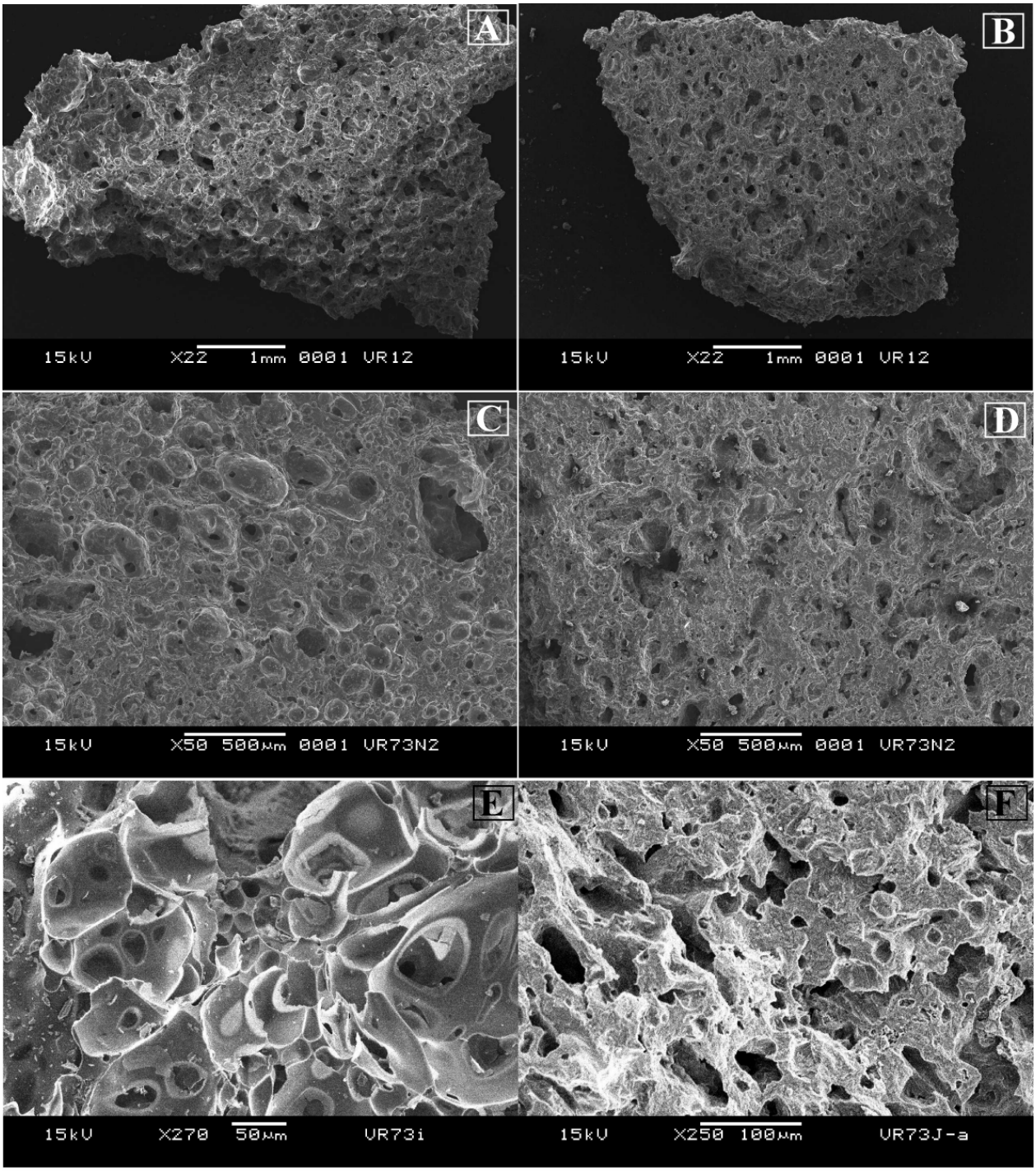

Figure 3.4: Plate of secondary electron images under SEM showing the contrasting vesicularities, bubble distributions and shapes between the scoria (left hand) and dense juvenile lapilli and bombs (right hand). (A) Light highly-vesicular scoria bomb (density=0.986 g/ml, 128 mm fraction, P2b). (B) Dense bomb with big elongated vesicles (density=1.514 g/ml, 128 mm fraction, P2b). (C) Scoria bomb with small spherical and bigger elongated vesicles, and evidence of bubble coalescence (density=1.167 g/ml, 128 mm fraction, P1b). (D) Dense folded bomb with big elongated vesicles (density=1.511 g/ml, 128 mm fraction, P1b). (E) Goldish-brown glassy scoria lapilli exhibiting narrow walls between vesicles, cellular texture and evidence of bubble coalescence (8 mm fraction, P1a II). (F) Microlite-rich dense juvenile lapilli with wide walls between big elongated and irregular vesicles (8 mm fraction, P1a III).

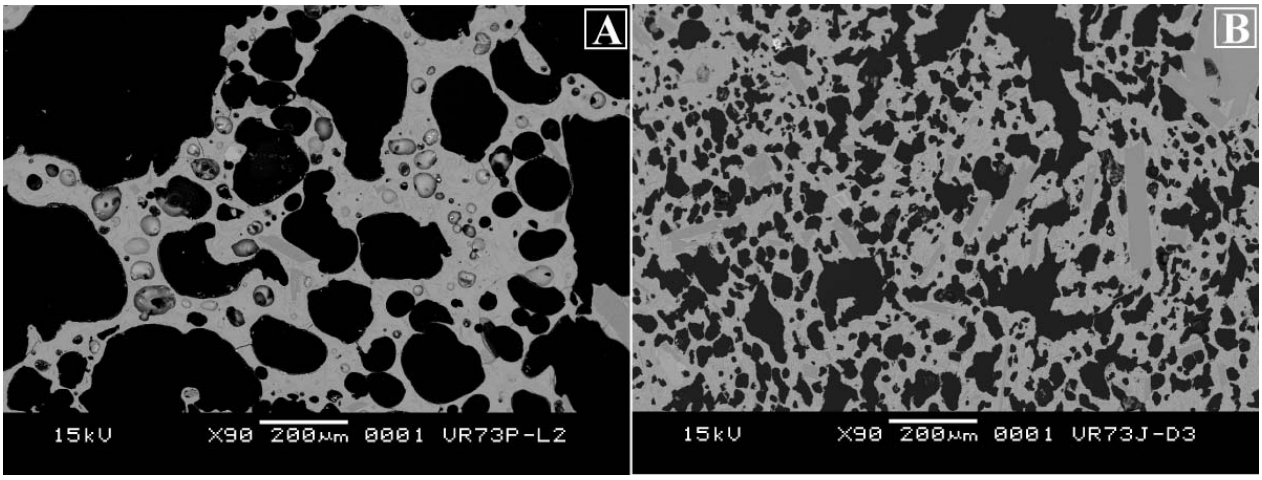

Figure 3.5: Plate of backscattered-electron composition images under SEM, showing the two main juvenile types of the Pucón Ignimbrite. (A) Microlite-poor scoria lapilli with small spherical non-connected and non-impregnated vesicles and bigger connected vesicles with evidence of bubble coalescence (16-mm-diameter scoria, P1b). (B) Microlite-rich and finely-vesiculated dense juvenile lapilli with irregular connected vesicles (16-mm-diameter fragment, P1a III).

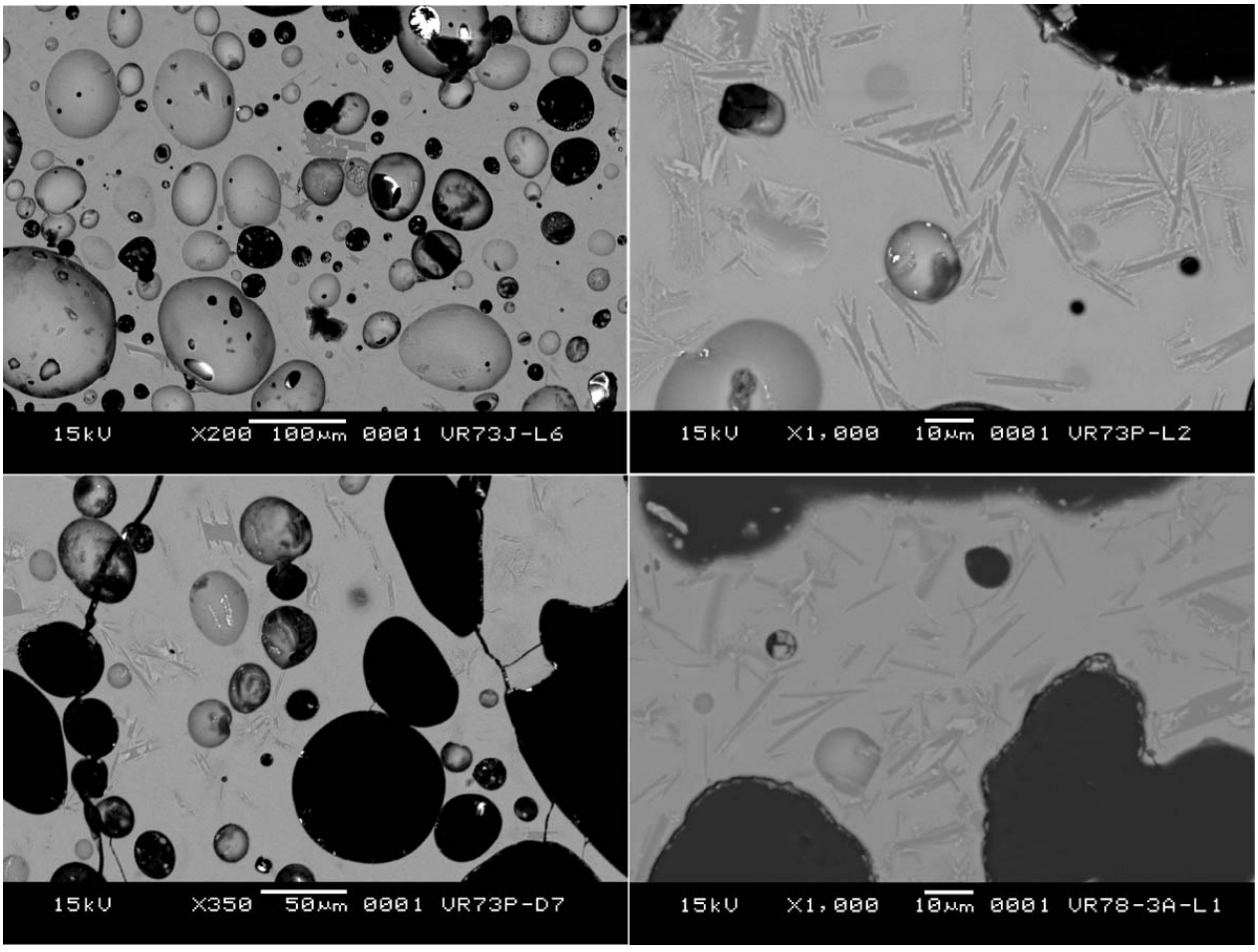

Figure 3.6: Plate showing four microlite-poor juvenile scoria lapilli from different stratigraphic levels (P1a, P1b and P2a). Microlite contents and vesicularities of every sample are in Table 3.1. Note the spherulite-like clusters and textures of rapid growth of some microlites.

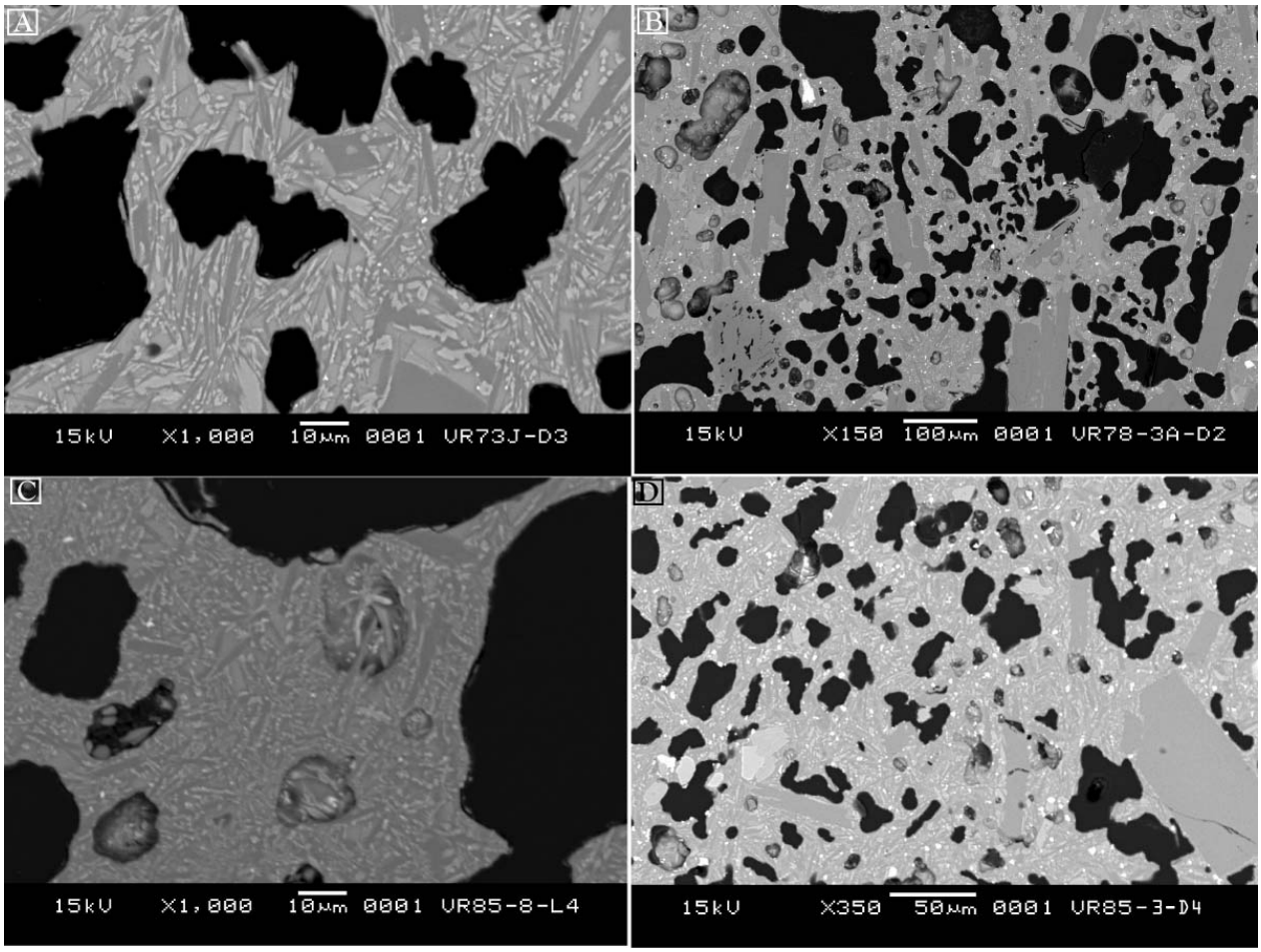

Figure 3.7: Plate showing four microlite-rich juvenile lapilli. The groundmass is formed by a dense network of microlites. (A) Dense lapilli with 81% of microlites and 44% of vesicularity (P1a III). (B) Dense lapilli with 55% of microlites and 47% of vesicularity (P2a). (C) Scoria lapilli with 96% of microlites and 60% of vesicularity (P2a). (D) Dense lapilli with 91% of microlites and 33% of vesicularity (P2b).

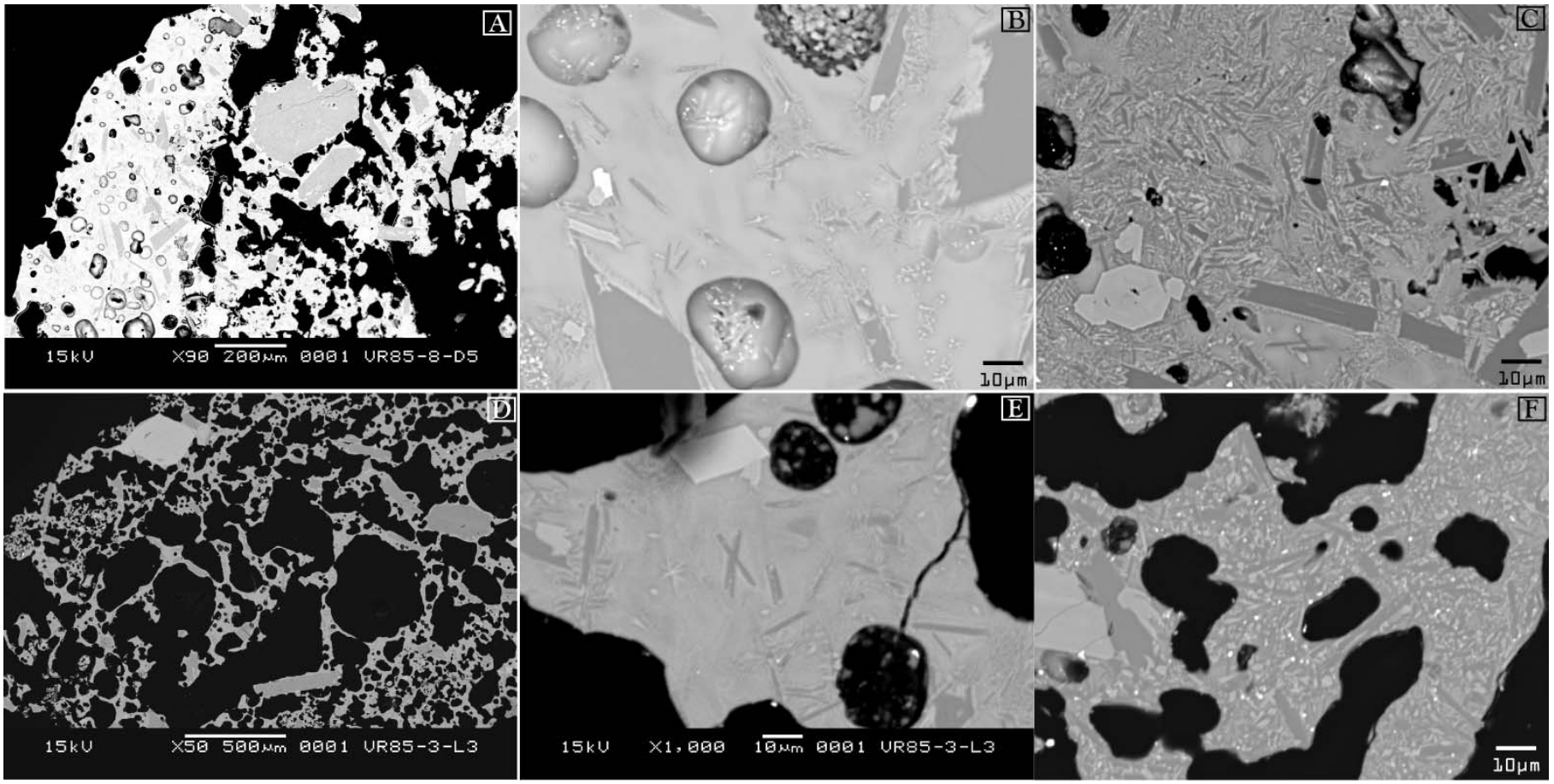

Figure 3.8: Plate showing two heterogeneous juvenile lapilli: a dense lapilli of P2a (images A to C) and a scoria lapilli of P2b (images D to F). (A) A microlite-poor band (left hand) is interlayered with a microlite-rich band (right hand). (B) Detail of the microlite-poor band. (C) Detail of the microlite-rich band. (D) Concentric zoning with a microlite-poor centre and a microlite-rich rim. (E) Detail of the microlite-poor centre. (F) Detail of the microlite-rich rim.

Scoria contents

Methods

Component analysis of the coarse fractions 32 and 16 mm was done in the field in number %, using about 150 clasts for the 16 mm fraction and ~20-30 clasts for the 32 mm fraction. A representative <16 mm sample was then taken back to the laboratory and sieved. The 8 mm, 4 mm, 2 mm and 250 µm fractions were then cleaned (samples rich in fine ash were cleaned with the ultrasonic machine) and the component analysis of these fractions was done under binocular microscope, also in number % (Appendix 3.1, Table 3.1).

As it was stated before in section 2.3.3.1 (Chapter 2), the brownish units are not only less juvenile-rich than the dark grey to black units, but they also contain ash, scoria lapilli and vesicular rims of scoria bombs, commonly with yellowish tinges, possibly due to incipient palagonitization.

Vertical variation of scoria abundances with stratigraphic height

The vertical variation of the scoria content from 32 mm to 250 µm fractions in the type sections of the Pucón Ignimbrite are shown in Figures 3.9 and 3.10. Some deductions are summarised as follows:

- The juvenile content of the Pucón Ignimbrite ranges from 5-100% in the 32 mm fraction, 30-90% in 4 mm fraction and 20-80% in the 250 µm fraction. Hence, the vertical variation of scoria content is in general smaller in finer fractions than in coarser ones.
- A gradual and sustained upward increase in the scoria content characterises unit P1 in all fractions, with the highest values in P1b.
- The upper part of unit P1 (P1aIV and P1b) exhibits generally higher juvenile contents than unit P2 in all fractions (40-90% versus 30-70% in 4 mm fraction, 40-80% versus 20-55% in 250 µm fraction). Moreover, the gradient in scoria content is stronger in P1 than P2.
- Of the two black, juvenile-rich subunits (P1b and P2b), P1b has the higher juvenile content (85-90% versus 70% in 4 mm fraction and 75-80% versus 50-55% in 250 µm fraction) and P2b is only slightly rich in scoria than the lithic-rich upper part of P2a.
- Southern section VR85 exhibits a similar vertical variations in scoria content in 4 mm fraction than the corresponding interfluve section (VR75), confirming the correlation between them (see Chapter 2) (P2a: 35-60% scoria in the valley and 35-65% on the interfluve; P2b: 70% in the valley and 65% on the interfluve).
- The scoria content of P2a is similar between the southern and northern sectors in 250 µm fraction (40-45%). For coarser fractions, P2a in the south extends to higher contents (35-65% versus 30-50% in 8 mm, 35-60% versus 30-40% in 4 mm, 30-60% versus 35-50% in 2 mm) than P2a in the north.

Table 3.1: Scoria and lithic abundances (in number %) of selected samples from different stratigraphic layers of the Pucón Ignimbrite, including fractions 32, 16, 8, 4 and 2 mm and components of the 4 mm and 250 µm fractions (in number %). Abundances of lithics in number % of total lithics. The complete set of component data in Appendix 3.1 and 3.2.

		32 mm				16 mm				8 mm			
Sample	**unit**	**sc**	**lit**	**n**	**sc**	**sc**	**lit**	**n**	**sc**	**sc**	**lit**	**n**	**sc**
					N° %				**N° %**				**N° %**
VR73H	**P1a I**	0	0	0	0	0	0	0	0	0	0	0	0
VR73I	**P1a II**	8	9	17	47	21	19	40	53	134	94	228	59
VR73J	**P1a III**	1	30	31	3	31	122	153	20	52	84	136	38
VR73L	**P1a IV**	29	1	30	97	527	38	565	93	236	38	274	86
VR73P	**P1b**	63	0	63	100	520	2	522	100	187	8	195	96
VR78-3A	**P2a**	6	18	24	25	92	110	202	46	116	261	377	31
VR85-6	**P2a**	2	1	3	0	60	92	152	39	111	206	317	35
VR85-4	**P2b**	16	3	19	84	120	36	156	77	218	88	306	71
VR78-4	**P2c**	0	0	0	0	0	3	3		3	27	30	10
VR78-5B	**P2d**	6	9	15	40	69	19	88	78	209	142	351	60

		4 mm													
Sample	**unit**	**sc**	**lit**	**n**	**sc**	**G**	**DPJ**	**alt**	**fresh**	**F**	**G**	**DPJ**	**alt**	**fresh**	**F**
					N° %						**N° %**	**N° %**	**N° %**	**N° %**	**N° %**
VR73H	**P1a I**	14	7	21	67										
VR73I	**P1a II**	1483	681	2164	69	0	211	332	108	30	0	31	49	16	4
VR73J	**P1a III**	820	1112	1932	42	1	395	427	250	39	0	36	38	22	4
VR73L	**P1a IV**	1959	435	2394	82	0	88	299	48	0	0	20	69	11	0
VR73P	**P1b**	1204	128	1332	90	0	6	115	7	0	0	5	90	5	0
VR78-3A	**P2a**	233	361	594	39	2	28	147	184	0	1	8	41	51	0
VR85-6	**P2a**	187	319	506	37	9	14	114	182	0	3	4	36	57	0
VR85-4	**P2b**	400	176	576	69	5	9	90	72	0	3	5	51	41	0
VR78-4	**P2c**	161	347	508	32										
VR78-5B	**P2d**	259	264	523	50	0	11	66	187	0	0	4	25	71	0

		2 mm				250 µm								
Sample	**unit**	**sc**	**lit**	**n**	**sc**	**sc**	**gl**	**cxx**	**lit**	**n**	**sc**	**gl**	**cxx**	**lit**
					N° %						**N° %**	**N° %**	**N° %**	**N° %**
VR73H	**P1a I**	52	47	99	53	323	193	32	62	610	53	32	5	10
VR73I	**P1a II**	138	104	242	57	319	142	102	117	680	47	21	15	17
VR73J	**P1a III**	97	125	222	44	117	117	21	26	281	42	42	7	9
VR73L	**P1a IV**	139	58	197	71	320	114	60	81	575	56	20	10	14
VR73P	**P1b**	213	52	265	80	394	26	34	35	489	81	5	7	7
VR78-3A	**P2a**	81	88	169	48	105	64	40	42	251	42	25	16	17
VR85-6	**P2a**	86	188	274	31	136	85	65	73	359	38	24	18	20
VR85-4	**P2b**	176	104	280	63	166	57	67	19	309	54	18	22	6
VR78-4	**P2c**	118	129	247	48	87	126	45	24	282	31	45	16	9
VR78-5B	**P2d**	123	86	209	59	143	96	52	40	331	43	29	16	12

sc = scoria
lit = lithics
n = total of counted clasts
gl = dense glass shards
cxx = crystals
G = granitoids
DPJ = dense prismatically-jointed lithics
alt = altered lithics
fresh = fresh lithics
F = fumarolized lithics

Abundances in number %.
Abundances of lithics in number % of total lithics.

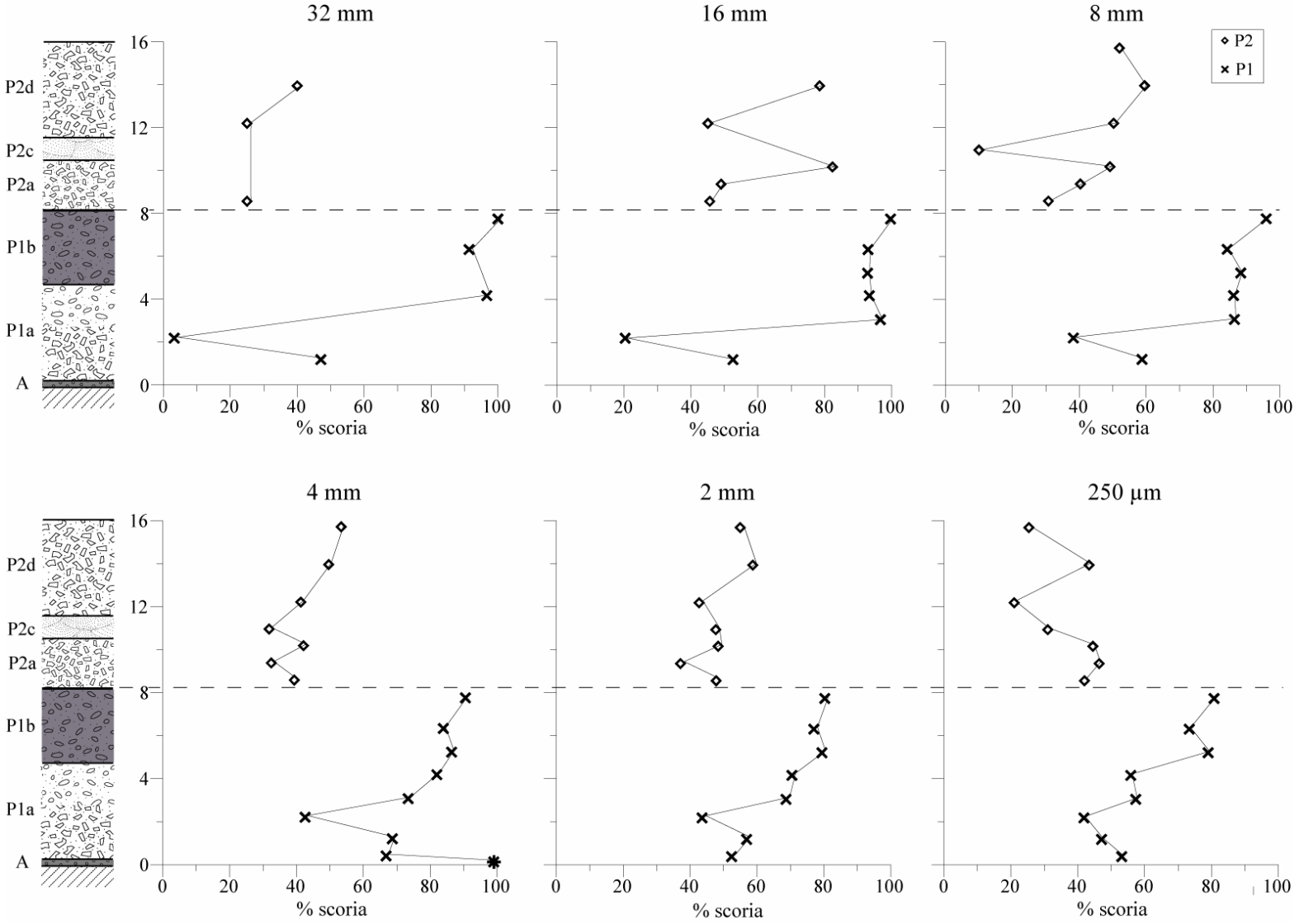
32 mm
16 mm
8 mm
4 mm
2 mm
250 µm
P2d
P2c
P2a
P1b
P1a
A
P2
P1
% scoria
0
4
8
12
16
0
20
40
60
80
100

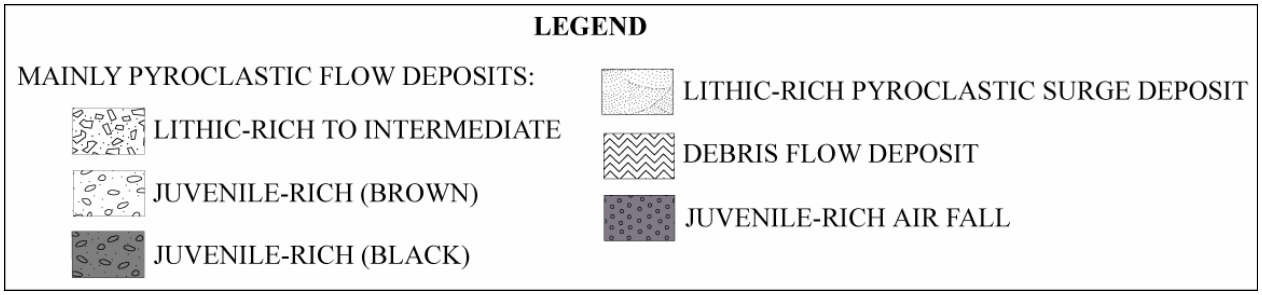

Figure 3.9: Vertical variation of the scoria content of the Pucón Ignimbrite in the type section of the northern sector (composite section, P1 from VR73 and P2 from VR78), showing fractions from 32 mm to 250 µm. A schematic stratigraphic column of the section is included. A single data point of the scoria % in 4 mm fraction for the basal scoria fall in locality VR113 is shown with a different symbol.

3.4.1.2 Accidental components

Types of accidental components and their textures

Accidental clasts in the deposits may be classified into three main groups: fresh volcanic lavas or intrusives, altered lavas or intrusives and basement granitoids (Table 3.2).

The fresh volcanics include:

- Dense blueish-black prismatically-jointed (DPJ) fragments, which are almost vesicle-free (0-1%) with smooth to slightly rough surfaces commonly formed by prismatic jointing (Figure 3.11A-B). They occur throughout the sequence (including the basal airfall), being particularly abundant at the base of P1 (especially P1aIII) and at the base of P2 (P2a). Sizes range from ash grade up to 60 cm. They are compositionally diverse, ranging from basaltic andesite to rhyolite but most are basaltic andesitic, andesitic and dacitic. Phenocryst phases of mafic varieties are similar to those in the Pucón juvenile clasts: plagioclase, clinopyroxene and olivine (in decreasing order of abundance). However, the phenocryst contents are higher and more variable (1 to 15% with a mean of ~6%, vesicle-free) in the DPJ fragments. Plagioclase phenocrysts range from about 0.1 to 2 mm (around 0.3 mm on average) and mafic phenocrysts are smaller (< 1 mm). Although glassy in appearance, the dark groundmasses of the DPJ fragments are rich in strongly aligned plagioclase microlites (Figure 3.11C-D). The DPJ clasts are interpreted as fragments of lava domes or flows emitted before the Pucón eruption (unknown age). Components resembling the DPJ occur in some volcanic breccias underlying the Pucón Ignimbrite on the western flank of Villarrica.

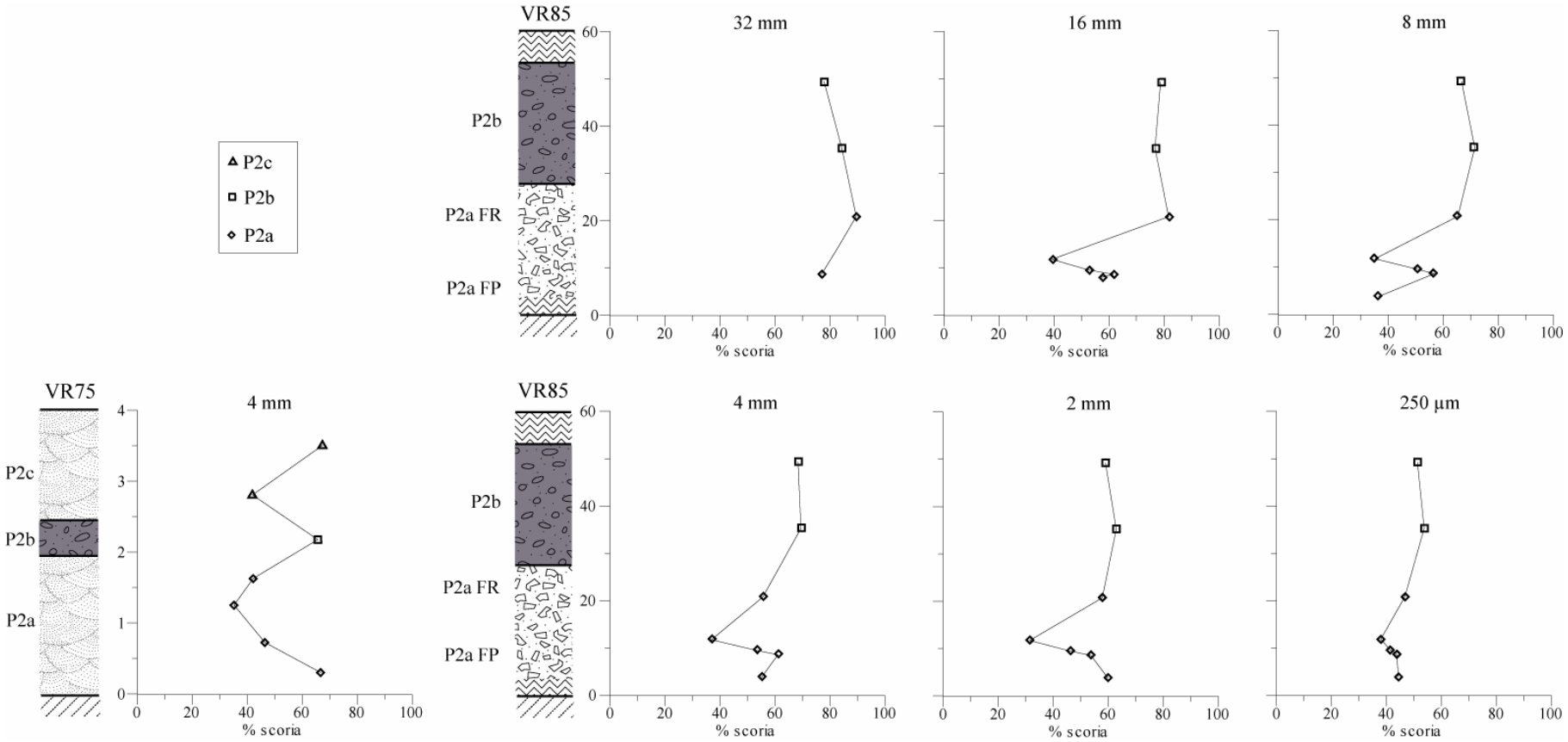

Figure 3. 10: Vertical variation of the scoria content of the Pucón Ignimbrite in the type section of the southern sector (VR85), showing fractions from 32 mm to 250 µm. The 4 mm data of an equivalent section on ridges is also shown (VR75). Schematic stratigraphic columns of the sections are included (Symbols in Figure 3.9).

- A second distinct type of fresh component is restricted to the ash fractions of subunits P1a and P1b (with decreasing abundance upwards). This component is composed of dacitic dense blocky shards with curviplanar surfaces and low or null vesicularity. The shards are variably pale yellowish and microlite-poor, to black and microlite-rich. Some have black centres and yellowish rims.

- Texturally diverse fresh lithologies interpreted as older lavas of the Villarrica edifice (Table 3.2). Some such accidental clasts are texturally and chemically similar to a lava flows and lava breccias underlying P1 on the western flank (Figures 3.12). Some rounded glassy lava boulders present in P1aIII may have experienced thermal spalling when incorporated into the hot pyroclastic flows.

Chemically altered components are lithologically diverse (lavas, breccias and plutonic rocks), with variable types of alteration. They are present all through the Pucón Ignimbrite, especially in the upper part of P1 and in P2a, and are interpreted mostly as accidental vent-derived lithics derived from deep in the edifice. Soft orange-stained volcanic and intrusive rocks and breccias, which are abundant at the base of P1 especially in the proximal exposures, are interpreted as altered by superficial fumarolic activity.

The granitoid clasts are mineralogically and texturally variable. Some have been partially melted and contain vesicles, making them friable. They appear abruptly in P2 and even if some locally-derived free clasts are probably present, they could be mostly derived from the basement of Villarrica volcano, as suggested by: (1) their ubiquitous presence all around the volcano and restricted stratigraphically (only in P2), (2) their presence as free clasts and as inclusions in scoria, either rigid or partially melted (Table 3.2, Figure 3.3C-D). McCurry *et al.* (2001) have analysed medium grained, equigranular granodioritic xenoliths of Pucón bombs (73% SiO_2) overlapping compositionally with the most evolved parts of the northern Patagonian Batholith.

Accidental rock debris constitutes on average 45% of the Pucón deposits. In contrast to many larger ignimbrite eruptions, lithics therefore comprise a large proportion of the eruption volume. However, given their strong textural similarities, some dense juvenile fragments could have been wrongly counted as fresh lithics, especially in the finer fractions where the recognition becomes even more difficult. Overall lithic proportions in the Pucón deposits are approximately 8% DPJ, 42% other fresh lavas, 48% altered lavas, and 2% basement granitoids. The granitoid proportion is underestimated owing to their dissagregation during sieving and the large amount of granitoids in scoria fragments. In the absence of information on the thicknesses of different formations within the volcano, little can be said on the depths of origin of these lithologies.

A qualitative analysis of the lithic inclusions in Pucón bombs shows that their lithologies are similar to those of the free clasts (variable fresh and altered volcanic fragments, and granitoids). A particular

abundant and ubiquous type of lithic inclusion is a pale gray to green aphanitic and slightly altered volcanic rock. P2 bombs are not only characterised by the sudden appearance of granitoid inclusions but also of more diverse lithic types, which seems also to be the case of the free clasts.

Table 3.2: Main chemical and textural features of the accidental fragments of the Pucón Ignimbrite

TYPE	ACRONYM	COLOR	DESCRIPTION	INTERPRETATION
Fresh volcanic lithics	DPJ [1]	Shiny blueish black	Prismatic jointing producing smooth to slightly rough surfaces, dense, almost vesicle-free (0-1%), very fresh, 5-15% phenocrysts (0.1 – 1.5 mm), dark groundmass very rich in strongly aligned plagioclase microlites. Basaltic andesitic to rhyolitic in composition	Fragments of subglacial pre-Pucón lava domes or flows located near or at the summit
		Dull black or gray	Fresh to slightly altered, with rough irregular surfaces, dense, vesicular and non-vesicular variants, highly-crystallized groundmass	Diverse old lava and volcanic fragments
Altered lithics		Orange, yellow or red stained	Soft hydrothermally altered volcanic and intrusive rocks and breccias	Altered by superficial fumarolic activity before the eruption
		Variable green, white, yellow	Diverse protoliths (breccias, volcanic or intrusives rocks) and types of alteration	Deep accidental vent-derived lithics
Granitoids		Light-coloured (white, rose)	Slightly altered granitoids mineralogically and texturally variable, some partially melted and vesicular	Deep accidental vent-derived lithics

1 The data for the DPJ (dense prismatically-jointed) fragments are from petrographic observations of three thin sections of 8 to 4 mm-sized DPJ fragments from unit P1.

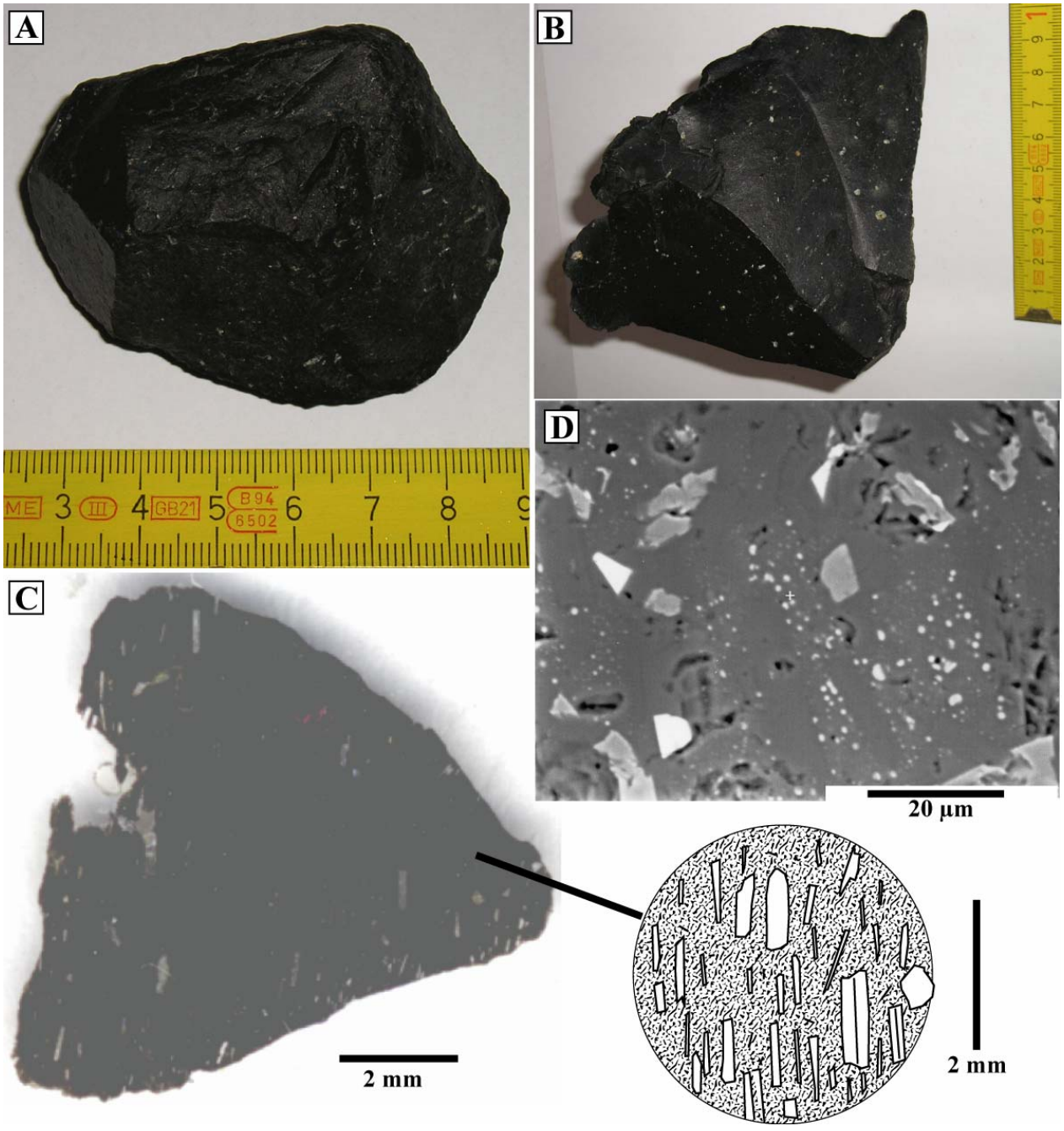

Figure 3.11: Dense prismatically-jointed (DPJ) dacitic fragments from subunit P1a III. Note how difficult is to distinguish a DPJ block from a fragment of a dense bomb (Figure 3.3). (A) DPJ fragment with 64.3% SiO_2 (VR73JP). (B) DPJ fragment with 63.2% SiO_2 (VR115-9D). (C) Thin section of a microlite-rich DPJ lapilli with strong plagioclase alignment and rhyolitic to dacitic glass composition (VR73J). (D) BSE image of 4-mm-fraction microlite-rich DPJ lapilli with rhyolitic glass composition (VR73J).

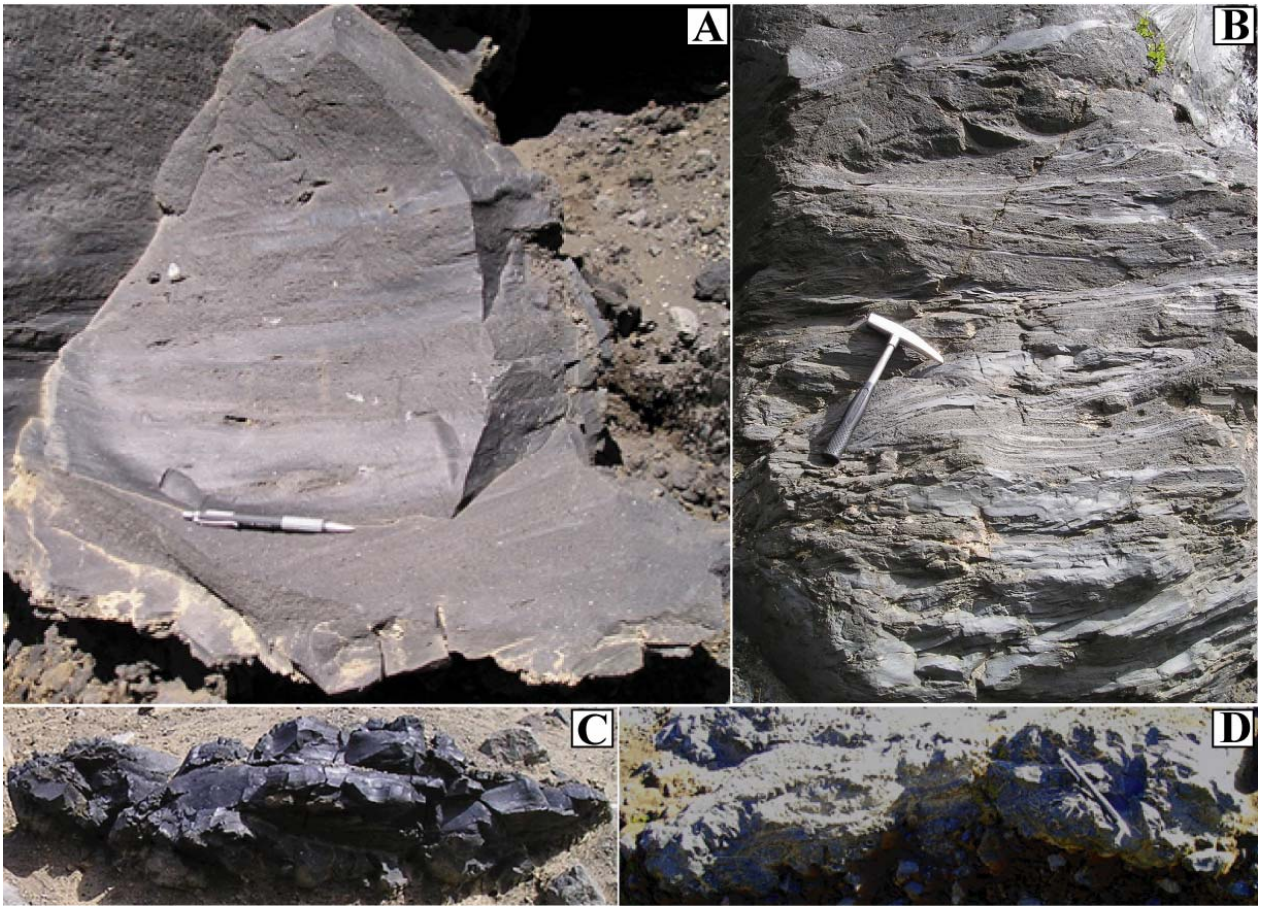

Figure 3.12: Dense blocks of the Pucón Ignimbrite compared to pre-Pucón lavas. (A) Flow banding in huge breadcrusted block (2 m diameter) from P1b (VR73). (B) Flow banding in lava flow underlying P1 (VR114). (C) Flat "slabby" block from P1a III (VR114). (D) Flat "slabby" block from pre-Pucón brecciated lava flow directly underlying P2 on the western flank (VR119).

Variations of the accidental components with stratigraphic height

Dense prismatically-jointed (DPJ) fragments make up to 10% of total lithics of the upper layer of the Pucón basal scoria fall (see section 2.3.2). Locally, the Pucón basal scoria fall presents abundant very crystal-rich black scoria (~30% of 2 mm fraction, VR72A SB) and pumices (~10% of 2 mm fraction, VR72A SI) of probable accidental origin (see Chapter 4).

The vertical variations of the accidental component abundances normalized to 100% total lithics for the 4 mm fraction are shown in Figures 3.13 and 3.14 (northern and southern sectors, respectively) and are given in Appendix 3.2. From these diagrams, it can be deduced that:

- The DPJ clasts account from a few % up to 35% of this size fraction. They are very abundant at the base of P1a, especially in P1a III (30-35%), then progressively decrease upwards through P1 (Figure 3.13). They then remain rather constant in P2 (<10%), being more abundant towards the base of P2a. The DPJ contents are low in juvenile-rich subunits P1b and P2b compared to the other, more lithic-rich levels (Figures 3.13 and 3.14).
- The vertical variation of other types of fresh lavas is similar to that of the DPJ fragments. This is shown by plotting the contents of fresh volcanic fragments with and without DPJ clasts (Figures 3.13 and 3.14). This similar vertical variation of the abundance of the fresh volcanic fragments with and without the DPJ clasts is used as an argument below in favour of a non-juvenile origin of the DPJ fragments.
- Chemically altered fragments constitute between 20 and 90% of the 4 mm fraction. Up through P1, the progressive decrease in the abundance of the accidental fresh volcanics is accompanied by a corresponding increase in the abundance of the altered lithologies (Figure 3.13). The P1/P2 boundary is characterised by a sudden reversal of this trend. The highest abundance of altered fragments in P2 occurs at the base (Figure 3.14). Thereafter, both fresh and altered fragments remain rather constant upwards through P2, with a slight increase in altered fragments in P2b (Figures 3.13 and 3.14). The abundance of altered fragments in P2a is slightly higher in the southern than the northern sector.
- Fumarolically stained fragments occur at the base of the ignimbrite (up to 5% of total lithics in 4 mm fraction) and decrease up through P1 to complete disappearance (Figure 3.13).
- Since the partially-melted granitoids are friable, the abundances presented in this study are probably underestimated (dissagregation of some of them occured during sieving). Moreover, a significant proportion of granitoids occurs in the scoria of P2. There is a sudden appearance of granitoids at the base of P2, reaching up to 6% of total lithics in 4 mm fraction (Figures 3.13 and 3.14). Granitoids are slightly more abundant in the southern than the northern sector.

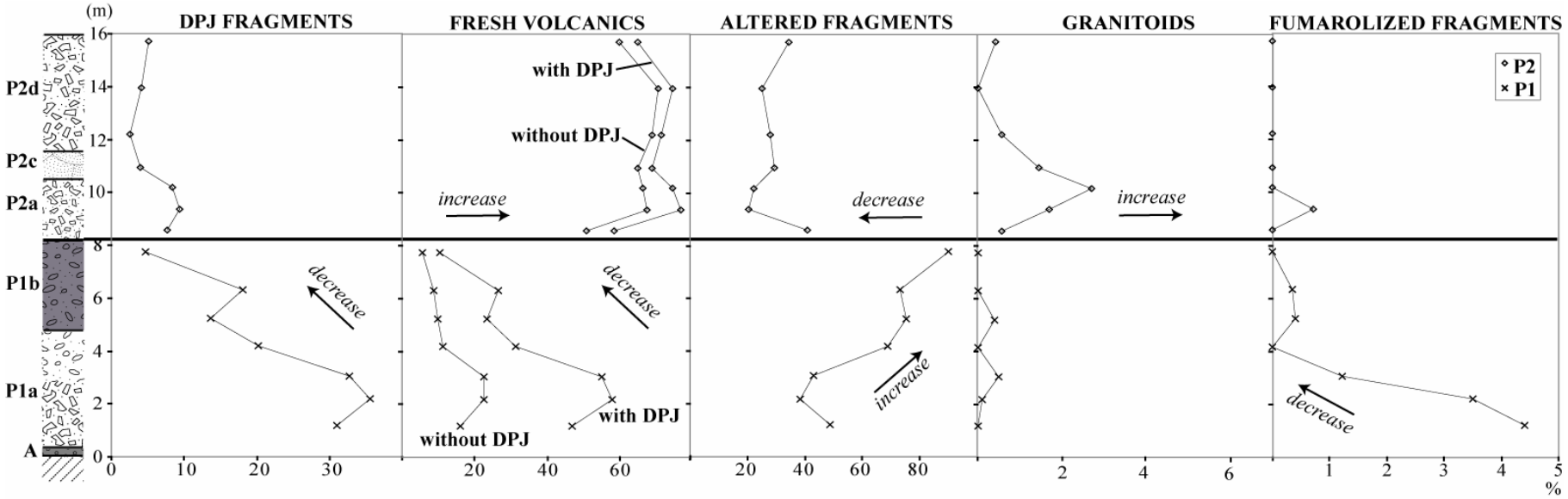

Figure 3.13: Abundance of accidental fragments (dense prismatically-jointed (DPJ) fragments, fresh volcanics, altered fragments, granitoids and fumarolized fragments) in % of total lithics in 4 mm fraction of the northern composite section of the Pucón Ignimbrite (P1 from VR73 and P2 from VR78). A schematic stratigraphic column is shown (Symbols in Figure 3.9).

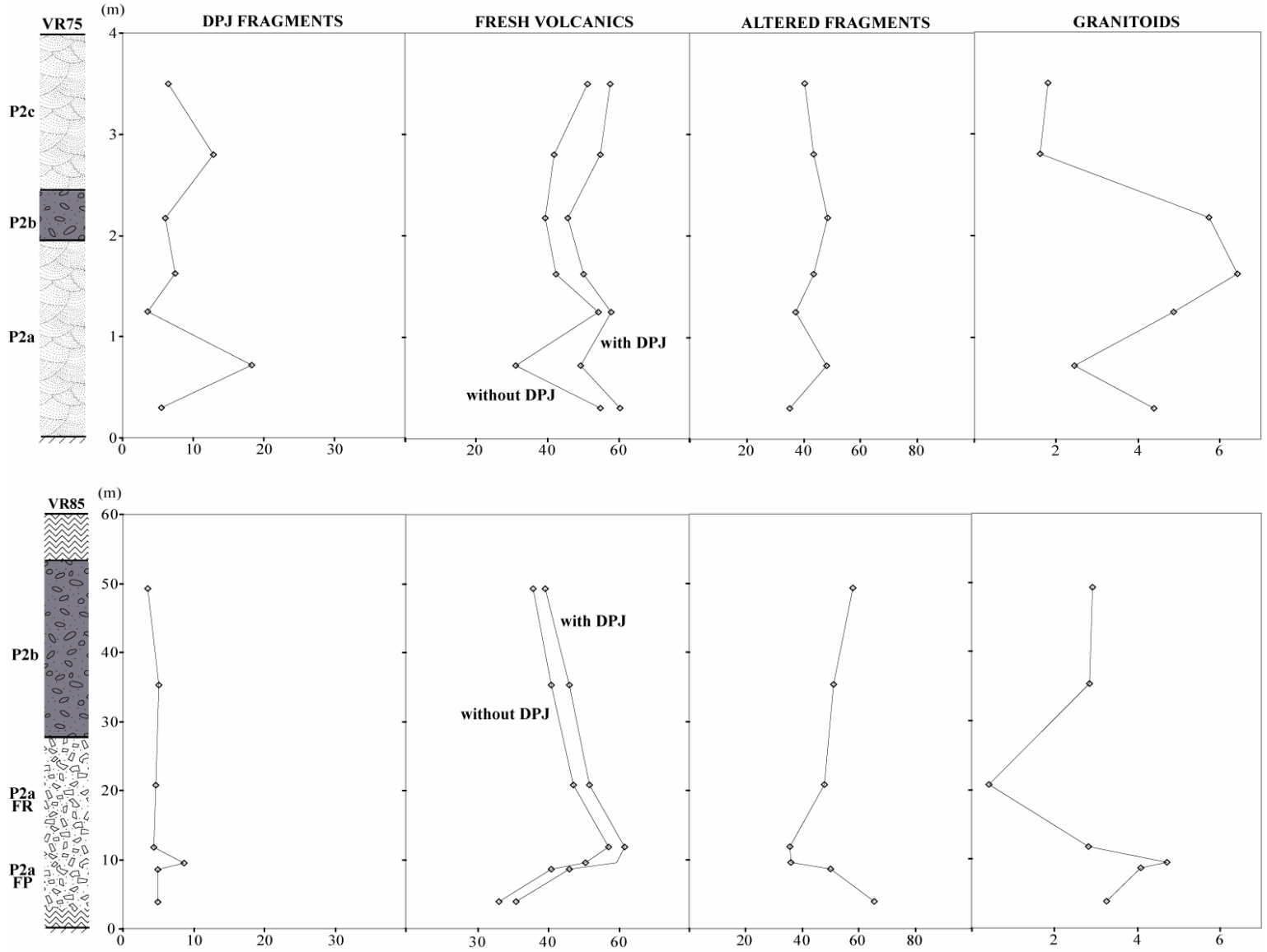

Figure 3.14: Abundance of accidental fragments (dense prismatically-jointed (DPJ) fragments, fresh volcanics, altered and granitoid fragments) in % of total lithics in 4 mm fraction of the southern valley section of the Pucón Ignimbrite (VR85) and its interfluve equivalent section (VR75). Schematic stratigraphic columns are shown (Symbols in Figure 3.9).

The components of the 250 μm fraction and their vertical variations are shown in Figure 3.15. From this figure it can be deduced that:

- P2 is richer in crystals than P1, probably due to the presence of xenocrysts derived from disrupted granitoid inclusions in P2 (Figure 3.15) and/or a slightly higher phenocryst content of P2 scoria.
- From P1a to P1b, there is enrichment in juvenile ash at similar crystal/lithic ratio (Figure 3.15A). The highest juvenile ash contents are exhibited by P1b (Figure 3.15A).
- P1b and P2b are the poorest in accidental lithics (Figure 3.15A). However, unit P2b is only barely enriched in juvenile ash than P2a.
- The matrix composition in 250 μm fraction of P2a is similar between the northern and southern sectors, except for a slightly higher crystal content of the southern section (Figure 3.15B). This is in agreement with the granitoid abundances which are also higher in the southern sections (Figures 3.13 and 3.14).
- Dense glass ash from the Pucón basal surge (P1a I) occurs very scarcely in 1 mm fraction (<4 wt%) but it is abundant in 250 μm fraction (32 wt%). The abundance of dense dacitic shards increases slightly first and then declines progressively along P1 (Figure 3.15B). This trend mimics that of the DPJ fragments (Figure 3.13) which, as shown below, have similar whole-rock composition to the shards, suggesting a similar origin.
- The matrix of the Pucón deposits (250 μm) has a more restricted juvenile content than the coarser fractions, vertically along the deposit. This could suggest that the coarse fragments were more controlled to local topographic conditions than the finer fractions.

Brief description of the volume calculations

As it was described in section 2.5.1, we used an average thickness for different subareas for estimating a total volume of the deposit of ~3.3 km^3 (~0.2 km^3 represented by the scoria fall, ~0.6 km^3 by unit P1, ~2.5 km^3 by P2 and ~0.04 km^3 by reworked layers, Table 2.6). We converted these non-compacted volumes into dense rock equivalent (DRE) volumes (total DRE volume = 1.8 km^3, composed of 1.1 km^3 of magma and 0.7 km^3 of accidental lithics, Table 2.6), using the bulk density of the deposit and the density of magma. The bulk density of the deposit ($\rho_{deposit}$ = 1.4 x 10^3 kg/m^3) was calculated weighting Pucón samples in a known-volume recipient. The density of magma (ρ_{magma} ~ 2.5 x 10^3 kg/m^3) was calculated weighting crushed Pucón sample with and without water in a graduate test tube (Appendix 2.2). The DRE volume of lithics ($V_{lithics}$ = 0.7 km^3, Table 2.6) was calculated by averaging the weighted mean of the lithic contents in the different size fractions of every layer of the Pucón type sequences and by subdividing the DRE volume of every unit according to the relative mean thicknesses of the constituent subunits. The DRE volume of magma was then calculated by substraction between the last two DRE volume estimations.

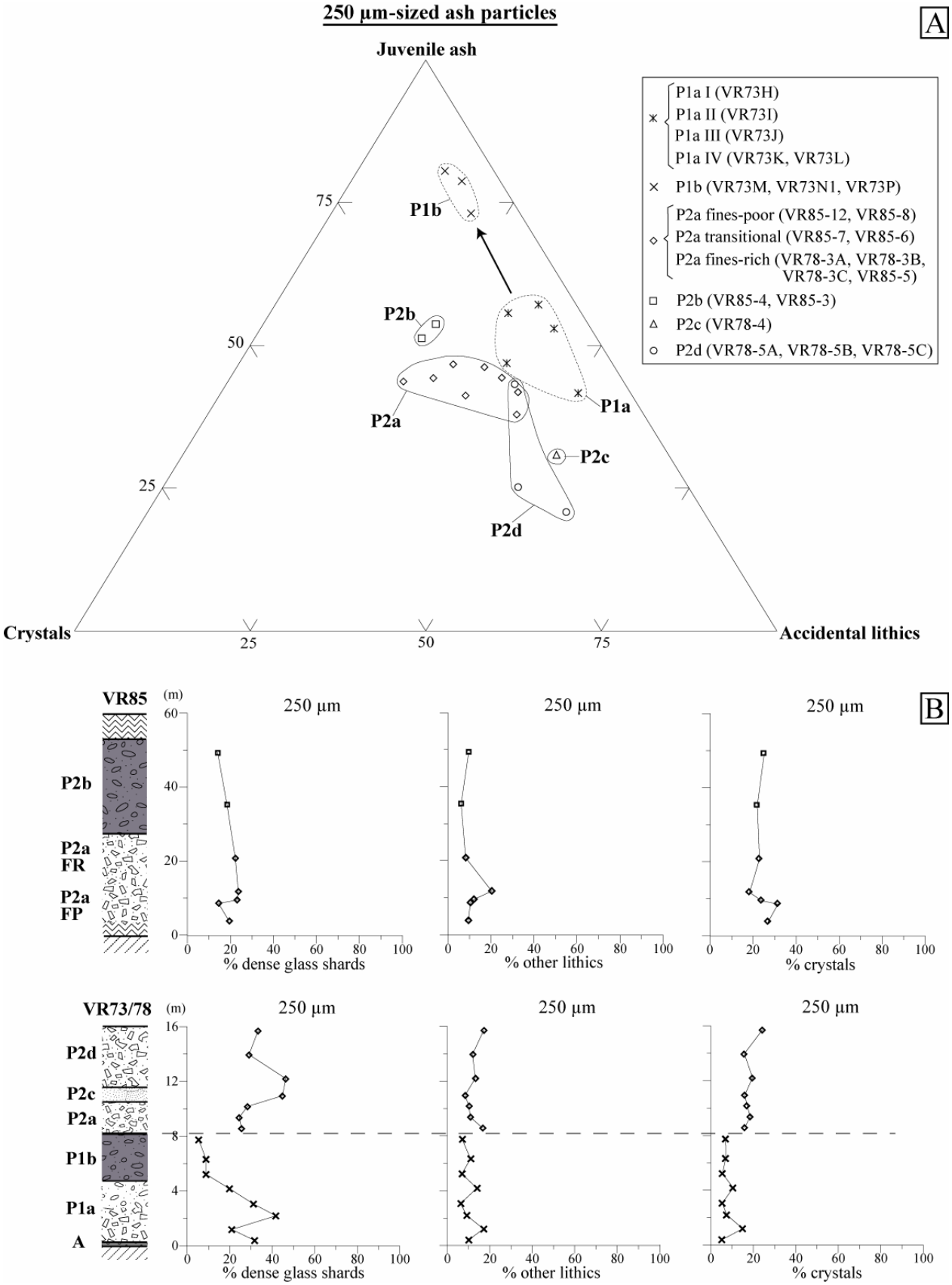

Figure 3.15: (A) Ternary diagram of the components of the matrix of the main subunits of the Pucón Ignimbrite. (B) Vertical abundances of the different components of the matrix in the type sections of the southern (VR85) and northern sectors (composite section VR73-78). Column symbols in Figure 3.10.

3.5 CHEMICAL COMPOSITION

Methods

A total of 84 samples taken all around the volcano and covering all the stratigraphic levels of the Pucón Ignimbrite were chosen for whole-rock chemical analysis of major and trace elements using a Jobin-Yvon JY70PLUS Inductive Coupled Plasma-Atomic Emission Spectrometer (ICP-AES). The analytical methods are explained in Appendix 3.3. Some selected major and trace element analyses and some ratios between them are presented in Tables 3.3 to 3.5 (for symbols see legend at the end of Table 3.3). The complete set of whole-rock chemical data is presented in Appendixes 3.4 to 3.6.

The samples were divided into three main types (Table 3.3, Appendix 3.4): (1) scoriaceous juvenile bombs and lapilli (44 samples), (2) dense juvenile bombs, block and lapilli fragments (13 samples), and (3) dense prismatically-jointed (DPJ) fragments (26 samples). Most analyses of lapilli were done on multiple fragments. No main chemical differences between single and multiple lapilli analyses, or between lapilli and bombs (within a given type), were observed.

Additionally, some pre and post-Pucón samples were analysed, including (1) a lava flow underlying P1 and a monolithologic agglomerate that directly underlies P2 on the western flank (see Chapter 2), (2) dacitic pumice lapilli from a pre-Pucón pyroclastic surge deposit underlain in gradual contact by scoria fall deposits and conformably overlain by the basal Pucón scoria fall in the northern sector (Figure 2.5, Chapter 2), and (3) 5 samples of post-Pucón fallout deposits (*Chaimilla tephra fallout deposits* of Clavero & Moreno 2004).

The whole-rock data are presented on a total-alkali-silica diagram (Figure 3.16). The vertical variation of the silica content through the main stratigraphic units is shown in Figure 3.17 and some selected Harker diagrams are shown in Figures 3.18 to 3.20.

3.5.1 Pucón Ignimbrite

3.5.1.1 Juvenile components

The complete range of silica of 44 analysed scoria clasts of Pucón deposit is very restricted, ranging from 54 to 56% SiO_2 (normalised to 100% volatile free, Figures 3.16 and 3.17, Table 3.3, Appendix 3.4). The 12 samples of dense fragments (lapilli, bomb or block) have a range of 55-56% SiO_2.

The Pucón basal scoria fall has a major and trace element composition similar to the P1 juvenile fragments, except for a slightly lower Th content (Figures 3.16 to 3.20).

Apart from silica, the scoria of the Pucón Ignimbrite *ss.* has a very restricted major and trace element composition. However, some slight chemical differences can be observed between units P1 and P2. Compared to P1, the P2 scoria has compositions that extend towards compositions lower in SiO_2, Fe_2O_3, Na_2O, MnO, Nd, Sm, Eu, Dy and Er, and richer in CaO, K_2O, Al_2O_3, P_2O_5, Rb, Sr, Y, Nb and Th (Figures

3.17 to 3.19). This shows that the second phase of the Pucón eruption (P2) emitted a slightly more basic magma than phase P1. P2 scoria also extends slightly to higher ratios of La/Sm, La/Yb, Zr/Y, Th/Rb and Th/La, and lower ratios of Na_2O/K_2O, Na_2O/Al_2O_3, Ba/Th, Sr/Rb, Sr/Ni and Nb/Th.

3.5.1.2 Dense prismatically-jointed (DPJ) fragments

The DPJ fragments range overall from basaltic andesite to rare rhyolite, but most are basaltic andesite or andesite (Figure 3.16). Those of unit P1 range compositionally from basaltic andesite to dacite. Most are chemically distinct from the Pucón juvenile fragments (Figure 3.16) and some are chemically similar to pre-Pucón deposits (see below). The P2 DPJ fragments exhibit even more variable compositions than P1, extending from basaltic andesite to rhyolite (Figure 3.16).

On some Harker diagrams, the P1 juvenile and DPJ fragments follow a trend which is distinct from that followed by the P2 juvenile and DPJ fragments. The P2 trend exhibits higher contents of Nb, Th, Zr, La, Ce, Rb, K, Ba, and higher ratios of La/Sm, La/Dy, La/Yb, Zr/Y and Ba/Sr, and lower ratios of Na_2O/K_2O than P1, some of which are shown in Figures 3.9 and 3.20.

3.5.2 Pre- and post-Pucón deposits

The pre-Pucón pyroclastic surge deposit that immediately underly the Pucón airfall at location VR113 (Figure 2.5, Chapter 2) is mostly composed of pale yellowish-brown pumices that are dacitic in composition (63% SiO_2, Figure 3.17) and are chemically similar to some of the most silicic P1 DPJ fragments (Figure 3.16). The pumices have lower MgO, CaO, Fe_2O_3, Al_2O_3, TiO_2, Sr, Sc and V contents, and higher contents of SiO_2, Na_2O, K_2O, P_2O_5, low field strength (LFS) elements (Rb, Ba) and high field strength (HFS) elements, including REE, Th, Zr and Nb, compared to Pucón scoria (Figures 3.16 to 3.20, Tables 3.3 and 3.4, Appendixes 3.4 and 3.5).

A lava flow underlying P1 and a monolithologic agglomerate directly underlying P2 on the western flank (see Chapter 2) have similar major and trace element compositions to the juvenile Pucón scoria, especially to the P1 dense juvenile bombs and blocks (Figure 3.16).

The Chaimilla fallout exhibits less silicic compositions than the previous Pucón eruption. It also exhibits higher CaO, MgO, Al_2O_3 and Sr contents, and lower content of Fe_2O_3, Na_2O, TiO_2, K_2O, MnO, P_2O_5, low field strength (LFS) elements (Rb, Ba) and high field strength (HFS) elements, including REE, Th, Zr and Nb, compared to the Pucón scoria (Figures 3.16 to 3.20, Tables 3.3 and 3.4, Appendixes 3.4 and 3.5). The scoria of the post-Pucón fallout is richer in plagioclase phenocrysts than Pucón scoria, perhaps explaining their higher Sr contents.

Table 3.3: Major element whole-rock composition of some selected samples of the Pucón Ignimbrite, and pre and post-Pucón deposits. The complete set of data is in Appendix 3.4. Trace elements in Table 3.4.

Sample	unit	type	size	SiO_2	TiO_2	Al_2O_3	Fe_2O_3	MnO	MgO	CaO	Na_2O	K_2O	P_2O_5	LOI 1050°C	Total
pre-Pucón															
VR113-6P		**PJ**	**M**	62,0	1,1	15,5	6,9	0,2	1,5	4,1	4,8	1,6	0,4	1,3	99,1
VR114		**DL**		56,4	1,2	16,3	10,0	0,2	3,6	7,8	3,8	0,9	0,2	-0,3	100,1
Pucón															
VR 73G	**A**	**SJ**	**M**	55,5	1,2	16,5	10,1	0,2	3,7	8,0	3,7	0,8	0,2	-0,1	99,6
VR 73J	**P1a**	**DJ**	**B**	55,2	1,2	16,3	10,0	0,2	3,6	7,9	3,8	0,8	0,2	0,4	99,6
VR97-3BD	**P1a**	**DJ**	**B**	56,2	1,2	16,4	10,0	0,2	3,7	7,8	3,9	0,9	0,2	-0,4	99,9
VR115-9P	**P1a**	**DPJ**	**B**	56,3	1,2	16,4	10,0	0,2	3,7	7,8	3,9	0,9	0,2	-0,4	100,1
VR97-3AP	**P1a**	**DPJ**	**B**	61,2	1,2	15,3	8,5	0,2	2,1	5,2	4,7	1,4	0,3	-0,4	99,8
VR73JP	**P1a**	**DPJ**	**L**	64,2	1,1	14,9	6,9	0,2	1,5	4,3	4,8	1,6	0,4	0,0	99,9
VR73LB	**P1a**	**SJ**	**B**	56,0	1,2	16,3	10,2	0,2	3,6	7,9	3,8	0,8	0,2	-0,4	99,8
VR112cS	**P1a**	**SJ**	**B**	55,2	1,2	16,7	10,2	0,2	3,8	8,1	3,7	0,8	0,2	-0,3	99,6
VR64AC	**P1b**	**DJ**	**B**	56,0	1,2	16,5	10,1	0,2	3,6	7,9	3,9	0,8	0,2	-0,4	100,0
VR73N1R	**P1b**	**DPJ**	**M**	57,4	1,2	16,3	9,6	0,2	3,3	7,3	4,0	0,9	0,3	-0,4	99,9
VR-73Mb	**P1b**	**SJ**	**B**	55,8	1,2	16,7	10,0	0,2	3,8	8,2	3,7	0,8	0,2	-0,4	100,2
VR58-0	**P1b**	**SJ**	**B**	55,3	1,2	16,8	10,2	0,2	3,8	8,2	3,7	0,8	0,2	-0,2	100,1
VR57-2C	**P1c**	**DJ**	**B**	55,7	1,2	16,5	10,1	0,2	3,7	7,8	3,9	0,8	0,2	-0,4	99,7
VR57-2D	**P1c**	**DPJ**	**B**	56,0	1,2	16,4	10,1	0,2	3,6	7,8	3,9	0,8	0,2	-0,5	99,7
VR57-1	**P1c**	**DPJ**	**B**	61,2	1,2	15,4	8,6	0,2	2,1	5,3	4,7	1,3	0,3	-0,4	99,8
VR57-1B	**P1c**	**SJ**	**B**	55,0	1,2	16,6	10,0	0,2	4,2	8,0	3,7	0,8	0,2	-0,3	100,4
VR57-2A	**P1c**	**SJ**	**B**	55,2	1,2	16,5	10,2	0,2	3,8	7,8	3,8	0,8	0,2	-0,3	99,4
VR58-1B	**P2a**	**DJ**	**B**	55,5	1,2	16,4	10,2	0,2	3,7	7,9	3,8	0,8	0,2	-0,4	99,5
VR113-11P	**P2a**	**DPJ**	**B**	64,7	0,8	15,2	6,5	0,2	1,4	3,9	4,9	2,1	0,2	-0,2	99,7
VR85-7P	**P2a**	**DPJ**	**L**	54,2	1,2	16,6	9,9	0,2	4,6	9,1	3,5	0,7	0,2	-0,2	100,0
VR85-5P	**P2a**	**DPJ**	**B**	69,3	0,5	14,2	4,8	0,1	0,6	2,4	5,1	2,6	0,1	0,0	99,6
VR78-3AS	**P2a**	**SJ**	**B**	55,6	1,2	16,7	10,0	0,2	3,9	8,3	3,7	0,8	0,2	-0,5	99,9
VR-79-1b	**P2a**	**SJ**	**B**	54,2	1,2	18,1	9,5	0,2	3,4	8,8	3,6	0,9	0,2	-0,2	99,9
VR85-3D	**P2b**	**DJ**	**L**	55,0	1,2	17,1	9,9	0,2	3,6	8,3	3,6	0,9	0,2	-0,3	99,7
VR12P	**P2b**	**DPJ**	**B**	56,0	1,6	15,7	10,2	0,2	3,5	7,3	3,9	1,0	0,5	0,1	100,0
VR85-4P	**P2b**	**DPJ**	**L**	54,7	1,3	16,2	10,3	0,2	4,2	8,3	3,6	0,9	0,3	-0,1	99,8
VR6-3	**P2b**	**SJ**	**B**	55,2	1,2	17,2	9,8	0,2	3,7	8,4	3,6	0,8	0,2	-0,4	100,1
VR85-3S	**P2b**	**SJ**	**L**	55,0	1,2	16,9	9,9	0,2	3,5	8,2	3,7	0,9	0,2	-0,2	99,5
VR75HR	**P2c**	**DPJ**	**M**	56,8	1,4	15,8	10,0	0,2	3,4	7,2	4,0	1,1	0,3	-0,3	99,8
VR75H	**P2c**	**SJ**	**M**	54,3	1,2	17,2	10,0	0,2	3,6	8,0	3,4	0,8	0,2	1,2	100,0
VR67C	**P2d**	**DJ**	**B**	55,3	1,2	17,1	9,8	0,2	3,8	8,3	3,7	0,8	0,2	-0,2	100,1
VR78-5AS	**P2d**	**SJ**	**B**	55,2	1,2	17,1	9,9	0,2	3,7	8,3	3,7	0,9	0,2	-0,3	100,1
VR78-5BS	**P2d**	**SJ**	**M**	54,8	1,2	17,1	9,9	0,2	3,7	8,3	3,6	0,8	0,2	-0,1	99,7
post-Pucón fallout deposits															
VR73S		**SJ**	**M**	53,4	1,0	19,1	8,7	0,2	3,9	9,9	3,2	0,6	0,2	0,2	100,2

LEGEND

TYPES OF FRAGMENTS:
SJ = scoriaceous juvenile
PJ = pumiceous juvenile
DJ = dense juvenile
DPJ = dense prismatically-jointed fragment
DL = dense lava fragment

SIZES:
M = multiple lapilli fragments
L = single lapilli fragment
B = bomb or block

Table 3.4: Trace element whole-rock composition of some selected samples of the Pucón Ignimbrite, and pre and post-Pucón deposits. See Table 3.3 for footnotes. The complete set of data is in Appendix 3.5. Major elements given in Table 3.3 for same samples.

sample	unit	type	size	Sc	V	Cr	Co	Ni	Rb	Sr	Y	Zr	Nb	Ba	La	Ce	Nd	Sm	Eu	Gd	Dy	Er	Yb	Th
pre-Pucón																								
VR113-6P		PJ	M	19.0	58.0	3.0	8.0	2.0	41.0	330.0	42.5	196.0	4.7	440.0	17.5	42.0	27.0	6.4	1.6	6.9	6.9	4.3	4.3	4.4
VR114		DL		31.0	289.0	26.0	24.0	12.0	20.5	415.0	27.0	106.0	2.5	253.0	9.5	23.0	15.7	4.0	1.2	4.3	4.5	2.7	2.7	1.9
Pucón																								
VR 73G	A	SJ	M	30.0	290.0	14.0	23.0	11.0	19.4	422.0	27.0	100.0	2.6	239.0	9.1	21.5	14.5	4.1	1.2	4.3	4.4	2.7	2.6	1.5
VR 73J	P1a	DJ	B	30.5	295.0	15.0	24.0	10.0	20.5	416.0	27.5	103.0	2.3	245.0	9.0	22.0	14.5	4.1	1.3	4.5	4.5	2.8	2.7	1.9
VR97-3BD	P1a	DJ	B	31.0	287.0	20.0	23.0	12.0	21.0	420.0	27.8	104.0	2.3	250.0	9.3	23.3	15.5	3.8	1.2	4.4	4.5	2.8	2.8	1.8
VR115-9P	P1a	DPJ	B	31.0	290.0	18.0	24.0	12.0	20.2	418.0	28.5	105.0	2.6	254.0	9.6	23.0	15.4	4.3	1.2	4.3	4.5	2.9	2.9	1.8
VR97-3AP	P1a	DPJ	B	23.0	139.0	11.0	15.0	2.0	34.5	371.0	39.5	167.0	3.5	385.0	15.2	35.5	24.0	5.7	1.6	6.2	6.2	4.0	3.9	3.3
VR73JP	P1a	DPJ	L	20.0	60.0	6.0	8.5	0.0	41.5	330.0	43.0	200.0	4.4	482.0	16.5	40.0	26.0	6.2	1.6	6.9	6.7	4.2	4.1	4.0
VR73LB	P1a	SJ	B	32.0	320.0	17.0	34.0	15.0	19.9	416.0	27.5	105.0	2.6	270.0	9.4	23.5	14.5	4.1	1.3	4.4	4.5	2.8	2.7	2.0
VR112cS	P1a	SJ	B	31.0	306.0	20.0	26.0	13.0	19.5	423.0	26.0	101.0	2.6	240.0	9.0	21.5	15.0	3.7	1.2	4.0	4.3	2.7	2.6	1.8
VR64AC	P1b	DJ	B	31.0	300.0	18.0	24.0	11.5	19.9	422.0	27.5	103.0	2.5	255.0	9.7	23.0	15.5	4.2	1.3	4.7	4.6	2.8	2.8	1.8
VR73N1R	P1b	DPJ	M	28.5	250.0	11.0	21.0	9.0	22.8	406.0	30.0	116.0	2.6	275.0	10.5	25.0	17.0	4.7	1.3	5.0	5.1	3.1	3.0	2.2
VR-73Mb	P1b	SJ	B	31.0	300.0	22.0	34.0	14.0	19.3	416.0	26.5	101.0	2.9	240.0	8.9	22.0	14.5	3.9	1.2	4.4	4.4	2.6	2.6	2.0
VR58-0	P1b	SJ	B	32.0	315.0	28.0	26.0	15.0	18.7	420.0	27.0	103.0	2.6	245.0	9.0	21.5	14.5	4.1	1.1	4.3	4.4	2.7	2.6	1.9
VR57-2C	P1c	DJ	B	31.0	295.0	16.0	25.0	13.0	18.6	424.0	26.8	103.0	2.6	245.0	9.4	23.0	15.0	4.1	1.3	4.4	4.5	2.7	2.8	1.8
VR57-2D	P1c	DPJ	B	30.0	293.0	17.5	23.5	11.0	19.9	419.0	27.2	103.0	2.3	251.0	9.5	23.5	15.0	4.1	1.3	4.5	4.5	2.8	2.8	1.9
VR57-1	P1c	DPJ	B	23.0	143.0	4.0	15.0	2.0	33.3	370.0	38.0	162.0	3.6	372.0	14.8	36.0	23.0	5.8	1.6	6.3	6.3	3.8	3.9	3.1
VR57-1B	P1c	SJ	B	31.0	293.0	44.0	30.0	22.0	18.2	437.0	25.2	96.0	2.3	236.0	9.3	23.0	14.5	4.0	1.2	4.1	4.2	2.6	2.6	1.9
VR57-2A	P1c	SJ	B	31.0	300.0	19.0	26.0	14.5	18.8	424.0	26.7	101.0	2.4	240.0	9.4	22.5	15.0	4.0	1.3	4.3	4.4	2.7	2.7	1.8
VR58-1B	P2a	DJ	B	32.0	320.0	16.0	25.0	12.0	20.0	420.0	28.0	107.0	2.7	265.0	9.4	22.5	15.0	4.1	1.2	4.6	4.6	2.8	2.7	1.9
VR113-11P	P2a	DPJ	B	17.0	57.0	13.0	8.0	5.0	54.0	287.0	46.0	248.0	5.4	560.0	21.5	49.5	30.0	6.9	1.6	7.2	7.3	4.7	4.8	5.7
VR85-7P	P2a	DPJ	L	34.0	305.0	67.0	29.0	26.0	19.0	419.0	27.0	101.0	2.7	232.0	9.2	22.0	15.0	3.8	1.2	4.2	4.4	2.7	2.7	1.7
VR85-5P	P2a	DPJ	B	12.5	13.0	5.0	3.0	2.0	70.0	197.0	52.0	297.0	6.4	675.0	24.5	56.0	33.0	7.4	1.5	8.1	8.0	5.3	5.4	7.4
VR78-3AS	P2a	SJ	B	31.0	302.0	27.0	25.5	19.0	19.5	421.0	26.0	99.0	2.5	237.0	8.9	21.0	14.2	3.6	1.2	4.1	4.2	2.6	2.6	1.8
VR-79-1b	P2a	SJ	B	27.5	300.0	18.0	54.0	15.0	20.5	445.0	26.5	105.0	2.6	263.0	9.8	24.0	15.4	4.0	1.2	4.4	4.5	2.6	2.7	2.1
VR85-3D	P2b	DJ	L	30.0	302.0	24.0	24.0	15.0	21.0	428.0	27.0	107.0	2.8	255.0	9.7	23.4	15.6	4.0	1.2	4.2	4.3	2.7	2.7	1.9
VR12P	P2b	DPJ	B	32.0	290.0	14.0	24.0	10.0	23.5	424.0	31.0	127.0	3.6	320.0	12.5	29.0	20.0	4.9	1.5	5.5	5.2	3.0	3.0	2.3
VR85-4P	P2b	DPJ	L	33.0	330.0	43.0	28.0	19.0	21.0	406.0	29.5	112.0	3.1	260.0	10.1	24.0	16.3	4.3	1.3	4.5	4.7	2.9	2.9	1.9
VR6-3	P2b	SJ	B	30.0	305.0	25.0	28.0	18.0	20.6	430.0	27.0	107.0	2.7	246.0	9.2	22.5	15.0	4.1	1.2	4.5	4.5	2.7	2.6	2.0
VR85-3S	P2b	SJ	L	30.0	310.0	18.0	25.0	14.0	21.0	425.0	27.3	106.0	2.7	253.0	9.9	23.4	15.4	3.9	1.2	4.4	4.4	2.7	2.7	1.9
VR75HR	P2c	DPJ	M	31.0	295.0	17.0	22.0	11.0	26.8	387.0	34.5	141.0	3.8	320.0	13.5	31.0	21.0	5.2	1.5	5.6	5.7	3.4	3.4	2.5
VR75H	P2c	SJ	M	31.0	297.0	22.0	25.0	13.0	19.3	420.0	28.5	107.0	2.7	250.0	10.0	23.0	15.0	4.3	1.2	4.5	4.6	2.8	2.8	2.1
VR67C	P2d	DJ	B	29.0	301.0	29.0	26.0	1.0	20.2	426.0	27.0	105.0	2.4	246.0	9.6	22.5	15.0	3.8	1.2	4.4	4.5	2.6	2.6	2.0
VR78-5AS	P2d	SJ	B	29.0	292.0	20.0	25.0	17.0	21.0	427.0	27.0	103.0	2.8	256.0	9.6	23.5	15.2	3.9	1.2	4.5	4.4	2.7	2.7	1.9
VR78-5BS	P2d	SJ	M	30.0	300.0	22.0	24.0	16.0	20.0	427.0	27.0	105.0	2.6	245.0	9.6	23.0	15.5	4.0	1.2	4.2	4.4	2.7	2.7	2.0
post-Pucón fallout deposits																								
VR73S		SJ	M	30.0	253.0	49.0	26.0	24.0	14.3	458.0	22.0	81.0	1.8	190.0	7.1	17.5	10.8	3.1	1.0	3.4	3.5	2.2	2.2	1.5

Table 3. 5: Some selected ratios of whole-rock major and trace elements of samples of the Pucón Ignimbrite, and pre and post-Pucón deposits. See Table 3.3 for footnotes. The complete set of data is in Appendix 3.6. Major elements given in Table 3.3 and trace elements in Table 3.4 for same samples.

sample	unit	type	size	Na2O/Al2O3	Na2O/K2O	Sr/Rb	Ba/Sr	Rb/La	Sr/La	La/Yb	La/Sm	La/Dy	Sr/Nb	La/Nb	Sr/Ce	Sr/Nd	Sr/Y	Ti/Zr	Ti/Nb	Sc/Y	Zr/Y
pre-Pucón																					
VR113-6P		PJ	M	0.31	2.96	8.05	1.33	2.34	18.86	4.06	2.73	2.54	70.21	3.72	7.86	12.22	7.76	33.15	1382.62	0.45	4.61
VR114		DL		0.24	4.41	20.24	0.61	2.16	43.68	3.52	2.38	2.13	166.00	3.80	18.04	26.43	15.37	65.88	2793.36	1.15	3.93
Pucón																					
VR 73G	A	SJ	M	0.22	4.49	21.75	0.57	2.13	46.37	3.50	2.22	2.07	162.31	3.50	19.63	29.10	15.63	70.97	2729.54	1.11	3.70
VR 73J	P1a	DJ	B	0.24	4.63	20.29	0.59	2.28	46.22	3.30	2.20	2.00	180.87	3.91	18.91	28.69	15.13	68.66	3074.84	1.11	3.75
VR97-3BD	P1a	DJ	B	0.24	4.59	20.00	0.60	2.26	45.16	3.38	2.45	2.07	182.61	4.04	18.03	27.10	15.11	67.80	3065.57	1.12	3.74
VR115-9P	P1a	DPJ	B	0.24	4.53	20.69	0.61	2.10	43.54	3.36	2.26	2.16	160.77	3.69	18.17	27.14	14.67	67.03	2707.00	1.09	3.68
VR97-3AP	P1a	DPJ	B	0.31	3.40	10.75	1.04	2.27	24.41	3.88	2.67	2.45	106.00	4.34	10.45	15.46	9.39	43.73	2086.76	0.58	4.23
VR73JP	P1a	DPJ	L	0.32	3.01	7.95	1.46	2.52	20.00	4.00	2.66	2.46	75.00	3.75	8.25	12.69	7.67	31.53	1433.06	0.47	4.65
VR73LB	P1a	SJ	B	0.23	4.57	20.90	0.65	2.12	44.26	3.48	2.32	2.09	160.00	3.62	17.70	28.69	15.13	68.37	2761.12	1.16	3.82
VR112cS	P1a	SJ	B	0.22	4.73	21.69	0.57	2.17	47.00	3.46	2.43	2.12	162.69	3.46	19.67	28.20	16.27	70.66	2744.96	1.19	3.88
VR64AC	P1b	DJ	B	0.24	4.77	21.21	0.60	2.05	43.51	3.51	2.31	2.11	168.80	3.88	18.35	27.23	15.35	68.98	2841.96	1.13	3.75
VR73N1R	P1b	DPJ	M	0.24	4.36	17.81	0.68	2.17	38.67	3.50	2.23	2.08	156.15	4.04	16.24	23.88	13.53	60.82	2713.48	0.95	3.87
VR-73Mb	P1b	SJ	B	0.22	4.54	21.55	0.58	2.17	46.74	3.42	2.31	2.02	143.45	3.07	18.91	28.69	15.70	70.22	2445.58	1.17	3.81
VR58-0	P1b	SJ	B	0.22	4.72	22.46	0.58	2.08	46.67	3.52	2.20	2.07	161.54	3.46	19.53	28.97	15.56	68.50	2713.75	1.19	3.81
VR57-2C	P1c	DJ	B	0.23	4.71	22.80	0.58	1.98	45.11	3.42	2.32	2.09	166.27	3.69	18.43	28.27	15.82	69.22	2795.98	1.16	3.84
VR57-2D	P1c	DPJ	B	0.24	4.70	21.06	0.60	2.09	44.11	3.45	2.32	2.11	182.17	4.13	17.83	27.93	15.40	68.57	3070.78	1.10	3.79
VR57-1	P1c	DPJ	B	0.30	3.50	11.11	1.01	2.25	25.00	3.84	2.57	2.37	102.78	4.11	10.28	16.09	9.74	45.05	2027.18	0.61	4.26
VR57-1B	P1c	SJ	B	0.23	4.73	24.01	0.54	1.96	46.99	3.62	2.33	2.21	190.00	4.04	19.00	30.14	17.34	72.56	3028.41	1.23	3.81
VR57-2A	P1c	SJ	B	0.23	4.69	22.55	0.57	2.00	45.11	3.53	2.35	2.14	180.43	4.00	18.84	28.27	15.88	71.48	3072.02	1.16	3.78
VR58-1B	P2a	DJ	B	0.23	4.52	21.00	0.63	2.13	44.68	3.44	2.29	2.04	158.49	3.55	18.67	28.00	15.00	67.85	2739.80	1.14	3.82
VR113-11P	P2a	DPJ	B	0.32	2.33	5.31	1.95	2.51	13.35	4.53	3.12	2.97	53.15	3.98	5.80	9.57	6.24	18.89	867.59	0.37	5.39
VR85-7P	P2a	DPJ	L	0.21	4.73	22.05	0.55	2.07	45.54	3.45	2.42	2.11	155.19	3.41	19.05	27.93	15.52	69.36	2594.72	1.26	3.74
VR85-5P	P2a	DPJ	B	0.36	1.94	2.81	3.43	2.86	8.04	4.54	3.31	3.06	30.78	3.83	3.52	5.97	3.79	9.72	451.20	0.24	5.71
VR78-3AS	P2a	SJ	B	0.22	4.48	21.59	0.56	2.19	47.30	3.42	2.51	2.12	168.40	3.56	20.05	29.65	16.19	69.97	2770.87	1.19	3.81
VR-79-1b	P2a	SJ	B	0.20	4.15	21.71	0.59	2.09	45.41	3.70	2.45	2.18	171.15	3.77	18.54	28.90	16.79	70.20	2834.96	1.04	3.96
VR85-3D	P2b	DJ	L	0.21	4.21	20.38	0.60	2.16	44.12	3.65	2.43	2.26	152.86	3.46	18.29	27.44	15.85	68.35	2612.10	1.11	3.96
VR12P	P2b	DPJ	B	0.25	3.86	18.04	0.75	1.88	33.92	4.24	2.55	2.43	117.78	3.47	14.62	21.20	13.68	76.08	2683.78	1.03	4.10
VR85-4P	P2b	DPJ	L	0.22	4.07	19.33	0.64	2.08	40.20	3.53	2.35	2.17	130.97	3.26	16.92	24.91	13.76	68.09	2459.95	1.12	3.80
VR6-3	P2b	SJ	B	0.21	4.33	20.87	0.57	2.24	46.74	3.51	2.24	2.04	162.26	3.47	19.11	28.67	15.93	66.97	2703.90	1.11	3.96
VR85-3S	P2b	SJ	L	0.22	4.24	20.24	0.60	2.12	42.93	3.69	2.54	2.25	160.38	3.74	18.16	27.60	15.57	69.21	2768.26	1.10	3.88
VR75HR	P2c	DPJ	M	0.25	3.60	14.44	0.83	1.99	28.67	3.97	2.60	2.39	103.20	3.60	12.48	18.43	11.22	58.60	2203.51	0.90	4.09
VR75H	P2c	SJ	M	0.20	4.27	21.76	0.60	1.93	42.00	3.58	2.35	2.17	155.56	3.70	18.26	28.00	14.74	68.08	2697.89	1.09	3.75
VR67C	P2d	DJ	B	0.21	4.35	21.09	0.58	2.10	44.38	3.69	2.53	2.13	177.50	4.00	18.93	28.40	15.78	68.85	3012.23	1.07	3.89
VR78-5AS	P2d	SJ	B	0.21	4.29	20.33	0.60	2.19	44.48	3.57	2.49	2.21	152.50	3.43	18.17	28.09	15.81	70.79	2604.03	1.07	3.81
VR78-5BS	P2d	SJ	M	0.21	4.29	21.35	0.57	2.08	44.48	3.60	2.40	2.21	164.23	3.69	18.57	27.55	15.81	69.78	2818.11	1.11	3.89
post-Pucón fallout deposits																					
VR73S		SJ	M	0.17	5.18	32.03	0.41	2.01	64.51	3.30	2.29	2.03	254.44	3.94	26.17	42.41	20.82	74.01	3330.55	1.36	3.68

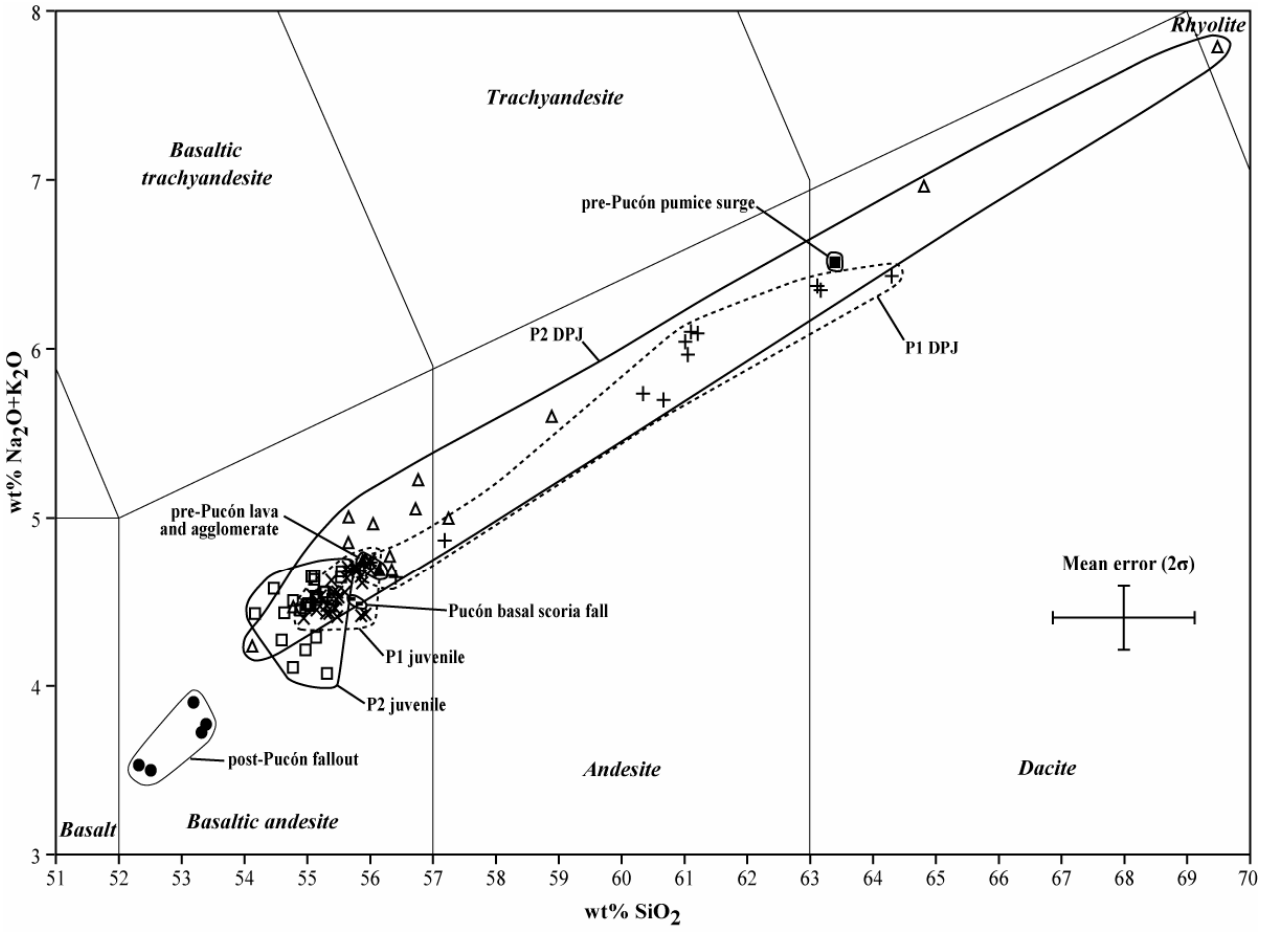

Figure 3.16: Total alkalis versus silica (TAS) diagram (after Le Maitre *et al.*, 1989) showing the juvenile and dense prismatically-jointed (DPJ) fragments of the Pucón Ignimbrite and the pre and post-Pucón deposits. A mean error of the samples (2σ) is also shown. The relative standard deviation is *ca.* 1% for SiO_2 and 2% for Na_2O and K_2O (Appendixes 3.3 and 3.4).

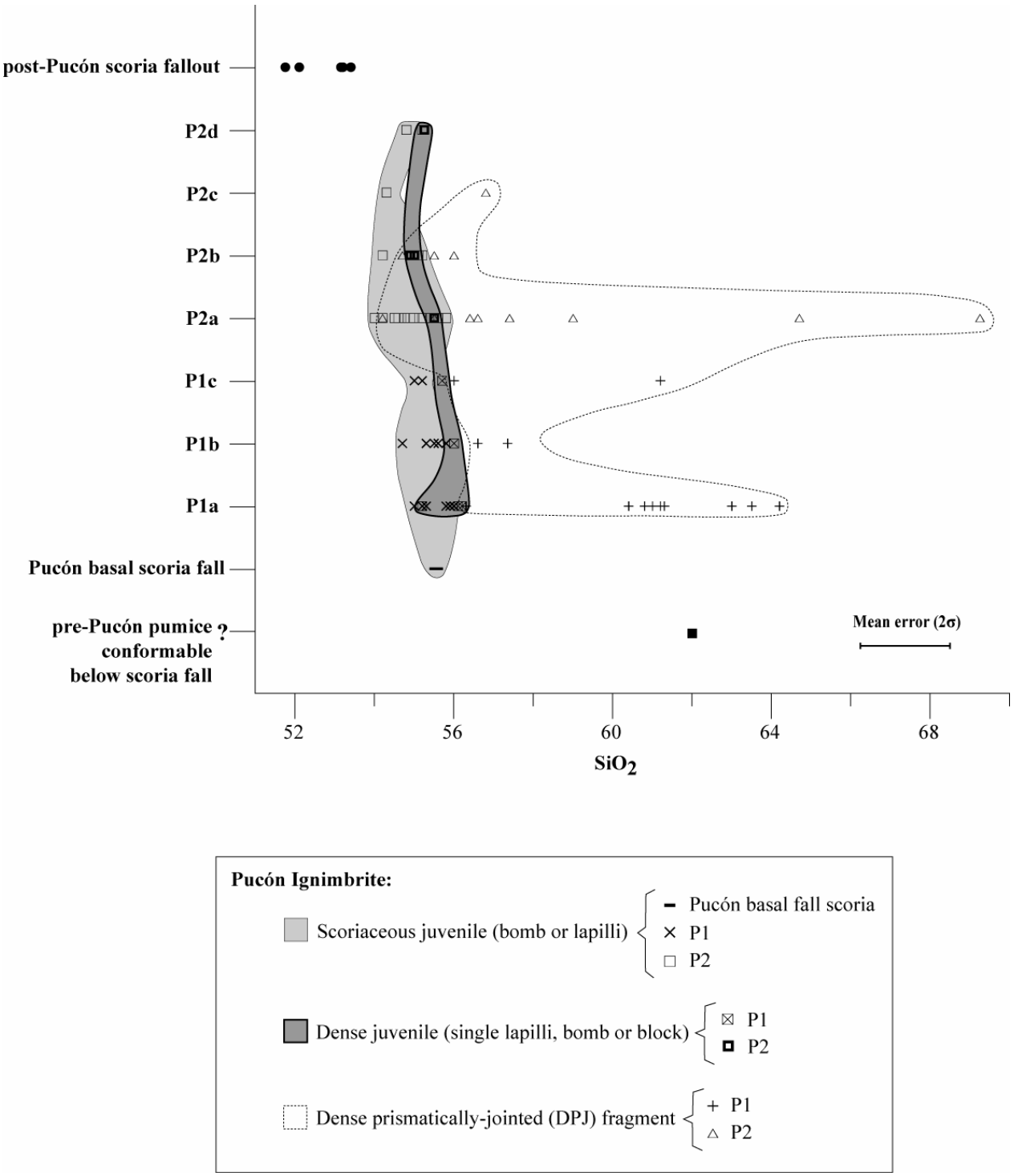

Figure 3. 17: Vertical variation of the silica content of the juvenile fragments (scoriaceous and dense) and dense prismatically-jointed (DPJ) fragments of the Pucón Ignimbrite and the pre and post-Pucón deposits all around the volcano. The pre-Pucón lavas and pre-Pucón surge are presented with a question mark in the diagram because the stratigraphic position between them is unknown. A mean error of the samples (2σ) is also shown. The relative standard deviation for SiO_2 is *ca.* 1% (Appendix 3.3).

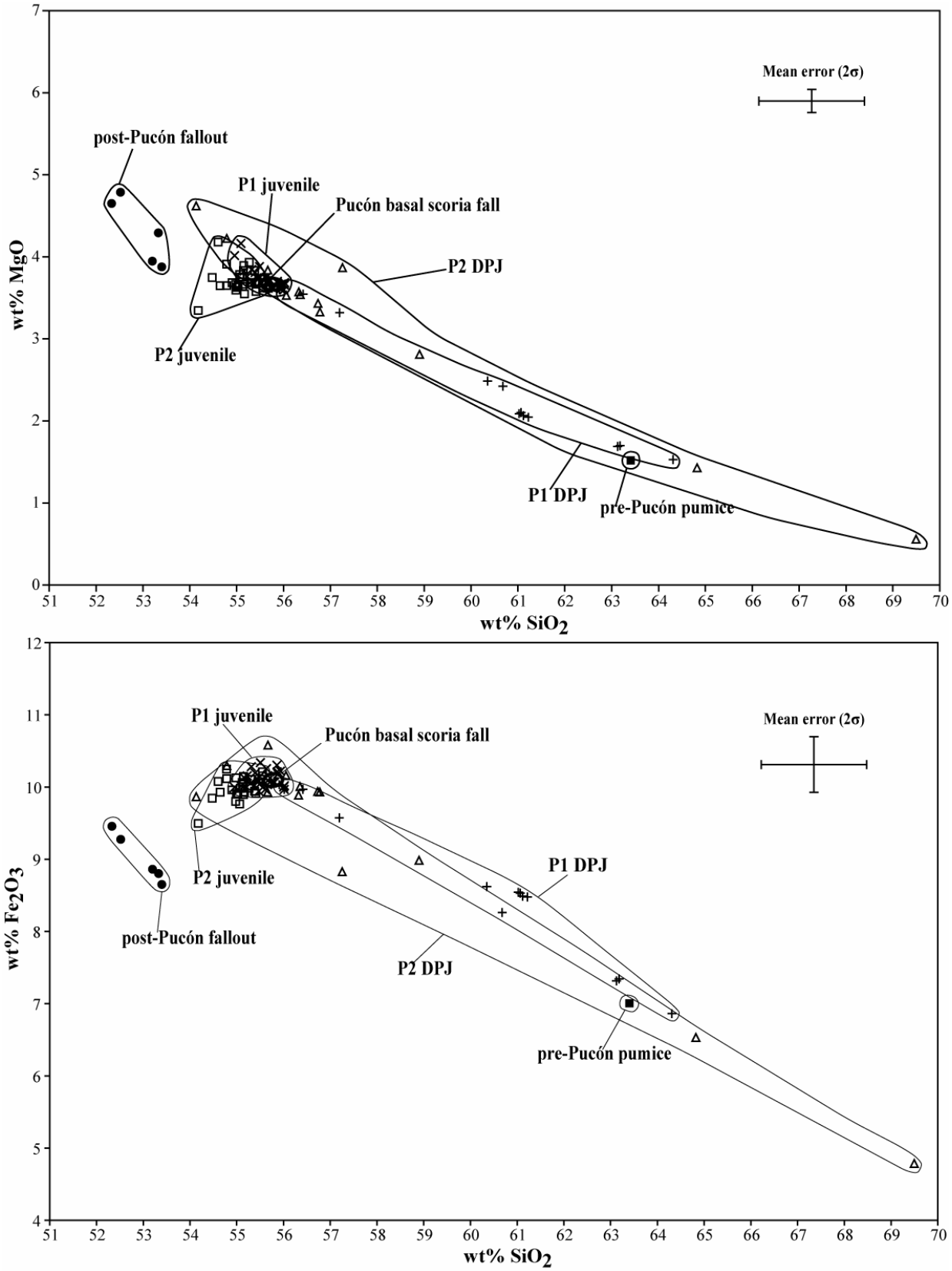

Figure 3.18: Harker diagrams of MgO and Fe_2O_3 of juvenile and dense prismatically-jointed (DPJ) fragments of Pucón Ignimbrite and pre and post-Pucón deposits. A mean error of the samples (2σ) is also shown. The relative standard deviation is *ca.* 1% for SiO_2 and 2% for MgO and Fe_2O_3 (Appendix 3.3). Symbols as in Figure 3.16.

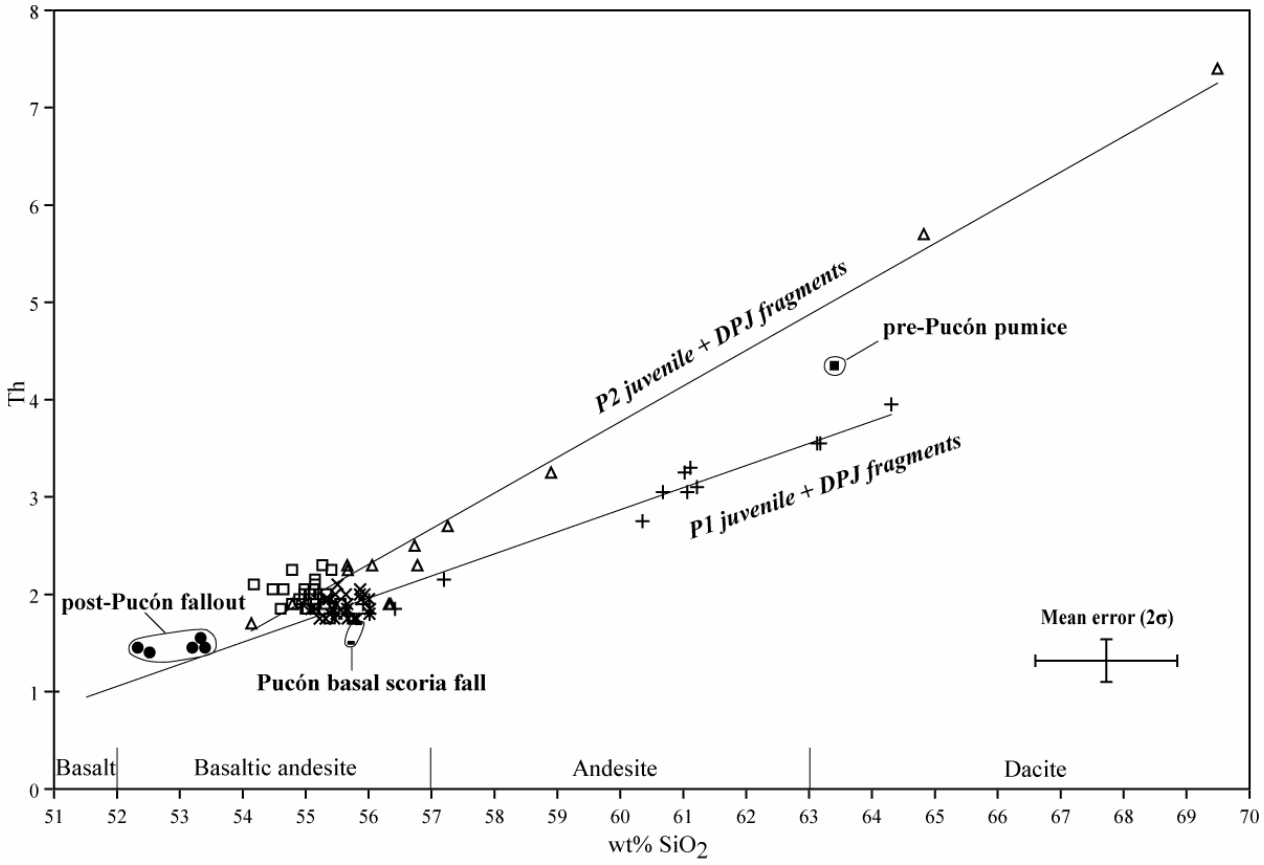

Figure 3.19: Harker diagram of Th (ppm) of the juvenile and dense prismatically-jointed (DPJ) fragments of the Pucón Ignimbrite and the pre and post-Pucón deposits. A mean error of the samples (2σ) is also shown. The relative standard deviation is *ca.* 1% for SiO_2 and *ca.* 5% for Th (Appendix 3.3). Symbols as in Figure 3.16.

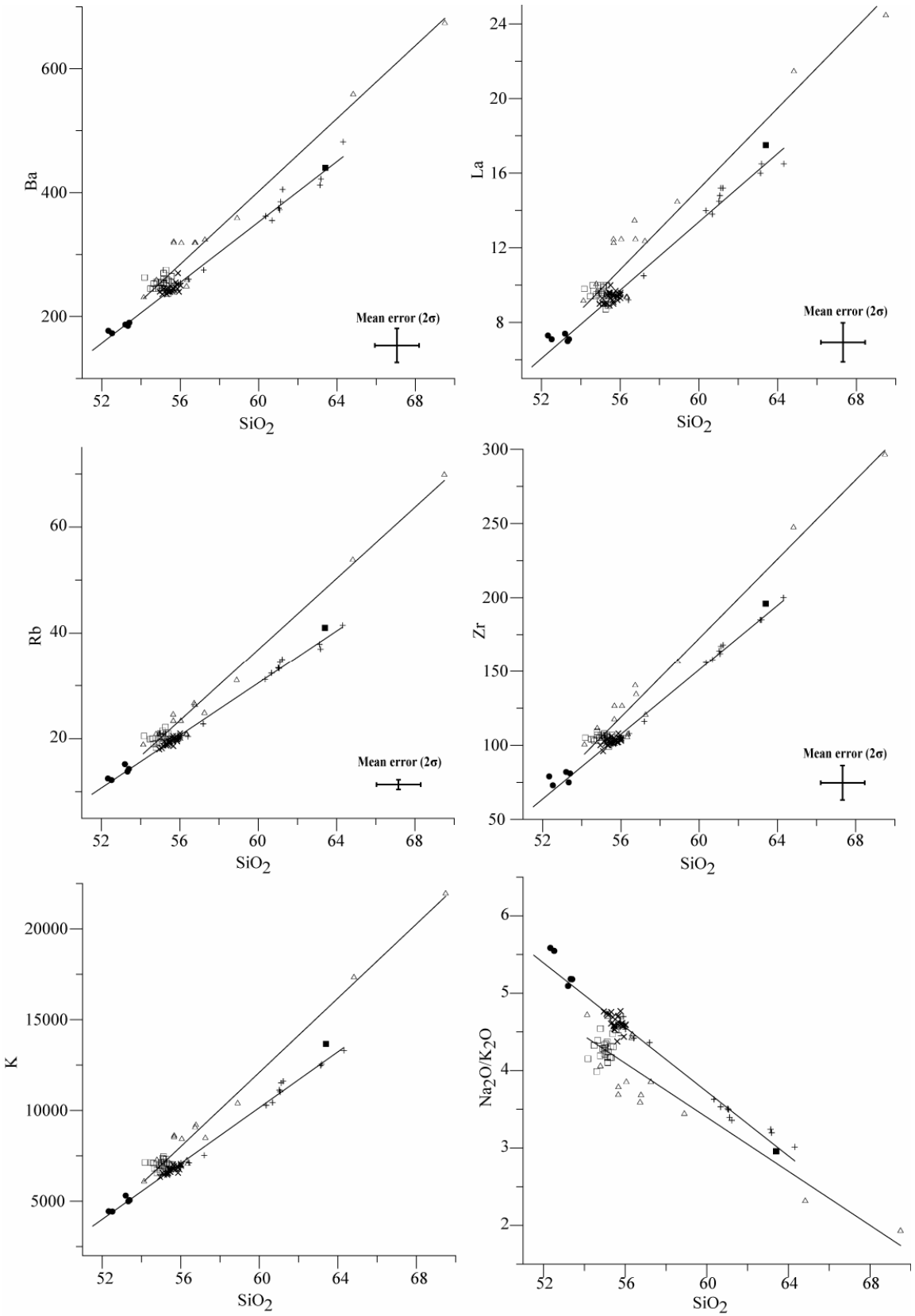

Figure 3.20: Harker diagrams of some trace elements (in ppm) and Na_2O/K_2O ratio of the juvenile and dense prismatically-jointed (DPJ) fragments of the Pucón Ignimbrite and the pre and post-Pucón deposits. A mean error of the samples (2σ) is also shown. The relative standard deviation is *ca.* 1% for SiO_2 and *ca.* 5% for the trace elements except for Rb (*ca.* 2%) (Appendix 3.3). Symbols as in Figure 3.16.

3.6 DISCUSSION

The different data are now brought together to reconstruct the dynamics of the Pucón eruption.

3.6.1 Nature of the juvenile components

Vesicular scoria clasts ranging from 54 to 56% SiO_2 and dense scoria fragments with a range of 55-56% SiO_2 are juvenile in origin, suggested by: (1) most of the samples of both groups have textural evidence of having been fragmented in a fluidal state (i.e. juvenile origin) such as: breadcrusting, prismatic jointing, folded, contorted and ropy shapes, etc., (2) both groups are compositionally similar, and (3) both groups become slightly more basic upwards through the Pucón Ignimbrite, from the basal scoria fall up to the top of P2 (Figure 3.18).

The black colour of P1b and P2b could not only be explained by a higher juvenile content compared to the brown subunits, but also due to the abundance of black juvenile material instead of goldish-brown juvenile fragments which are more abundant in the lower lithic-rich P1a and P2a units. This produces the black subunit P2b to be only barely enriched in juvenile ash than the brown P2a. The goldish-brown colour of some vesicular scoria lapilli and bomb crusts especially to the bottom of both main units (P1 and P2) could correspond to palagonitization of the basaltic andesitic glass. This theme is taken up again in Chapter 4.

3.6.2 Magmatic processes and chemical evolution of the magma body

In previous sections about the abundance variation of components, it was stated that the Pucón Ignimbrite exhibits highly variable scoria contents (30-90% of the 4 mm fraction) and that on average the accidental debris constitute about 45% of the Pucón deposits. The remaining lithic fraction is divided into dense prismatically-jointed (DPJ) clasts (~8% on average), other fresh lavas (~42%), chemically altered fragments (~48%) and basement granitoids only in unit P2 (~2%). In what follows, some magma and lithic volumes are used. For details of the calculations and values on which the numbers are based, refer to section “Brief description of the volume calculations”.

The presence of basaltic-andesitic to dacitic effusive fragments in P1 (DPJ fragments and glass ash shards), especially abundant towards the base, suggests that prior to the Pucón eruption, basaltic-andesitic to dacitic lava domes and flows of moderate-volume (about 0.02 km^3) and of unknown age were probably present at or near the volcano summit. The presence of old dacitic domes and dykes around the old caldera today (95 ka BP; Clavero & Moreno, 2004) proves the existence of such products at Villarrica Volcano.

The basal scoria fall accumulated during violent strombolian or subplinian eruption of ~0.1 km^3 of basaltic andesite magma (Chapter 2) under normal, open-conduit magmatic conditions.

The total volume of magma involved in the P1 vulcanian explosions was about 0.14 km^3, or roughly 0.014 km^3 per explosion. This is greater than any reasonable conduit volume. For example even a cylindrical conduit 50 m in diameter and 5 km long only has a volume of 0.01 km^3. The figures therefore seem to require that each explosion during P1 emptied the conduit and tapped into the main reservoir at depth. Following each discharge event, magma would have partially refilled the conduit prior to the next explosion.

Pucón scoriae become slightly more basic upwards through the deposit, from the basal scoria fall up to the top of P2 (compositions progressively poorer in Si_2O and Na_2O and richer in CaO). Also, P1 and P2 scoria and DPJ fragments exhibit respectively distinct trends in several Harker diagrams, with the P2 suite been characterised by higher contents in incompatible elements (Figures 3.20 and 3.21). A possibility could be that P1 and P2 have been separated by a time interval long enough for reservoir replenishment by a new magma batch enriched in incompatible elements, followed by differentiation to generate the evolved magmas (up to rhyolite) represented by the P2 DPJ components. Rapid differentiation of magma batches has been recently postulated elsewhere (e.g. Reagan *et al.*, 2005) and field evidence suggests a pause of at least several weeks and probably months between P1 and P2 (Chapter 2). However, the chemical differences between both suites are slight, in some cases within the analytical error, and more analyses of representative P2 DPJ fragments are required to conclusively prove this hypothesis. On the other hand, considering the contrasting distribution of P1 and P2 units, the new chemical assemblage of P2 DPJ fragments could be the result of vent erosion and widening in different sectors than those from P1 phase. During the eruptive pause, changes in the plumbing system of the volcano probably took place to produce a new juvenile assemblage (P2).

In fact, the subsequent generation of a new magma (represented by P2 scoria) which is slightly poorer in silica, enriched in incompatible elements and more crystal-rich than the P1 magma, could be explained by: (1) more basic P2 magma came from deeper levels in the same (zoned) magma reservoir as P1, and during repose this magma was slightly contaminated by basement granitoids, or (2) P1 magma remaining in the reservoir was replenished by a more primitive, incompatible-enriched magma batch from depth, with which it mixed to form P2 magma. The P2a eruptive phase that terminated the repose period was both voluminous and of high intensity, requiring the development of high overpressures in the reservoir, and replenishment is an efficient way of generating large overpressures. Subsequent low energy, small volume and restricted pyroclastic flows (P2c-d) are consistent with greatly decreased reservoir pressure.

The first post-Pucón explosive activity started no more than a few rain seasons after the discharge of the final pyroclastic flow (Chapter 2). The magma of the Chaimilla scoria fall deposits was more crystal rich and less evolved than Pucón magmas, and its composition lies close to regression lines through the P1 and P2 magma batches, with affinities to both (Figures 3.17 to 3.21). This could suggest: (1) that the magmatic chamber was not completely emptied during the Pucón eruption; the Chaimilla scoriae

representing cumulates from residual P1 and P2 magmas containing geochemical signals of both P1 and P2 components, and/or (2) a mafic replenishement of the magma chamber after the Pucón eruption.

3.6.3 Origin of the DPJ components

A non-juvenile origin for the dense prismatically-jointed (DPJ) clasts is suggested by: (1) the similarity of their vertical variation of abundance with that of other types of fresh, accidental volcanic fragments (Figure 3.13), and (2) they are compositionally and texturally distinct (crystal-rich) from Pucón juvenile scoria.

The origin of the DPJ clasts could be the fragmentation of summit pre-Pucón lavas and domes possibly interacted with ice, occurring mostly at the onset of each P1 and P2 phase and then incorporated into the subsequent pyroclastic currents. This is suggested by:

(1) Their mm- to cm-scale prismatic jointing.
(2) Basaltic-andesitic DPJ fragments together with flat "slabby" blocks and parallel-banded breadcrusted blocks present in P1 are texturally and chemically similar to lava flow and breccias that crop out stratigraphically immediately below the Pucón Ignimbrite.
(3) The higher abundance of DPJ fragments towards the base of P1 and P2 and then progressively declining upwards (Figures 3.13 and 3.14). In the case of P1, this trend is also exhibited by dacitic ash shards (Figure 3.15).

3.6.4 Vent erosion and fragmentation level during the eruption

Early vent erosion and widening during the eruption could be suggested by: (1) DPJ fragments appear abruptly in the upper layer of the scoria fall deposit and reach a maximum in subunit P1 (Figure 3.13), and (2) The low volume of the basal scoria fall deposit (it accounts for only 7% (magma DRE) of the total eruption volume) which could be explained by an early widening of the vent radius making unstable the eruptive column. During the subsequent series of at least ten powerful vulcanian explosions (P1a, Chapter 2), explosive expansion of water probably caused pulverization on wall rock, progressively eroding and widening the conduit, generating quantities of lithic debris that was mixed into the magma (maximum DPJ abundances in P1a).

Both P1 and P2 units have lithic-rich deposits to the base containing abundant fresh volcanics particularly DPJ fragments, goldish-brown (probably palagonite) and high-density (see Chapter 4) scoria, that gradually evolve into juvenile-rich deposits with more vesicular and black scoria, and more abundant altered lithics relative to fresh ones (subunits P1b and P2b, respectively). This suggests a similar evolution during two main eruptive cycles. Two possible explanations (not mutually exclusive) for the evolution of each cycle could be proposed:

(1) Initial vent erosion supplied of abundant lithics the generated pyroclastic flows (P1a and P2a) and progressive widening of the vent radius gives place to open-conduit conditions when more juvenile-rich flows are produced (P1b and P2b).

(2) The role of external water decreases upwards through each cycle, as shown by the decrease in accidental debris (Figures 3.13 and 3.14) and palagonitized material (this possibility is studied fully in Chapter 4).

Changes in lithic populations throughout the Pucón sequence probably record changes in magma fragmentation conditions during the eruption. Assuming that, on average, altered lithologies were derived from deeper in the cone than fresh ones, the progressive decrease in the abundance of the fresh volcanics accompanied by a parallel increase in the abundance of altered clasts upwards through P1, could be interpreted as a progressive deepening of the fragmentation level during the eruption of P1 (Figure 3.13). A similar but more subtle trend of fresh versus altered fragments along the upper part of P2 (P2aFR and P2b) could also suggest a slight progressive deepening along the upper part of P2 (Figure 3.14).

Fragmentation during phase P1 must have been confined to within the volcanic edifice and above the level of the granitoid basement, because granitoids are essentially absent in the P1 products, either as free clasts or as inclusions within scoria. The abrupt appearance of a significant proportion of free clasts of basement granitoids in P2 suggests that immediately before or very rapidly after the start of this phase the magma level sudden dropped to within the granitoid basement, at a level lower than that during phase P1. Dispersal of granitoid fragments in P2 scoria must record either vigorous inmixing of shattered wall rock into the magma near the fragmentation surface, or stoping of roof material into a magma reservoir residing within granitoid basement. The granitoid fragments in P2 scoria include many angular, non-melted and unreacted inclusions, but also vesicle-bearing, actively disaggregating, partially melted examples, showing that inmixing of granitoids must have occurred in part during eruption when they were actively mixed into the magma. Strong vent erosion and widening probably accompanying this climactic phase involved the incorporation of abundant lithic debris into the pyroclastic currents (P2a).

Component data suggest that granitoids as free clasts and inclusions in scoria, as well as matrix free crystals (due in part to granitoid disaggregation), are more abundant in the southern exposures of P2 than in the north. Even if the depth of the basement below the volcano summit is unknown, this could suggest that this depth is lower towards the southern sector allowing earlier contact of granitoids with magma, producing more abundant granitoid fragments and inclusions, and probably xenocrysts derived from them.

3.6.5 Possible caldera collapse during the eruption

Two caldera structures are visible in the field and on air photos of Villarrica volcano. An arcuate escarpment present east and south of the summit appears to define part of an ancient caldera, the northern and western sectors of which have been buried beneath younger products. Given the absence of evidence

for sector collapse at Villarrica (e.g., large debris avalanches deposits), this structure is tentatively interpreted as the partial remnant of a collapse caldera approximately 4 x 6 km in size (Moreno, 1993), elongated in the northwest-southeast direction, with an average elevation of 1900 metres above sea level. It has been described as two nested calderas, formed 90,000 and 14,000 years ago (Moreno, 1993). The first one has been related to a voluminous (~10 km^3 non-DRE; Moreno, 1993) preglacial ignimbrite, the remnants of which have been found to the west of the area of study and the second one related to the Licán Ignimbrite (Moreno, 1993; Moreno & Clavero, 2006).

The rim of a second, much smaller caldera is visible on the northern flank, as a subtle, but distinct change in slope of the modern cone about 450 m below the summit. This caldera is about 2.2 km in diameter and is approximately circular. It has been linked with the Pucón Ignimbrite eruption (Moreno, 1993, 2000; Clavero & Moreno, 1994, 2004; Clavero, 1996). The magma level drop to within the granitoid basement during phase P2 (see previous section) is probably explained by the high magma discharge rate, causing the fragmentation level of the magma to fall rapidly, probably accompanied by the climactic phase of caldera collapse. If the 2-km-diameter caldera was associated with the Pucón eruption at all, the evidence of a few time elapse between the Pucón and Chaimilla eruptions (Chapter 2), suggest that the construction of the modern cone started very short after the caldera collapse associated with the Pucón eruption.

Given the DRE volume of the Pucón (1.8 km^3), the diameter of the Villarrica caldera is large, but not unreasonable. Assuming a cylindrical shape, the caldera would need to have been 470 m deep to account for the erupted volumes of magma and lithics. For comparison, the caldera formed during the 3.7-5.3 km^3 1991 Mount Pinatubo eruption has a diameter of 2.5 km (Newhall & Punongbayan, 1996).

3.7 CONCLUDING REMARKS

The combined physical and chemical analysis of the Pucón products presented here together with the architecture reconstruction of the deposit (Chapter 2), allowed us to advance our understanding of the eruptive dynamics of the Pucón Ignimbrite (3.6 ka BP, 3 km^3).

Some concluding remarks can be summarised as follows:

1. Prior to the Pucón eruption, the volcano summit was covered by a probably extensive ice cap and subglacial basaltic-andesitic to dacitic lava domes and/or flows were possibly present near or at the Villarrica summit, supplying the P1 pyroclastic density currents of abundant lithics (0.02 km^3), mostly dense prismatically-jointed (DPJ) fragments.
2. The Pucón eruption started under normal, open-conduit magmatic conditions when 7% of the total Pucón basaltic-andesitic magma volume was emitted during a violent strombolian to subplinian eruption. Vent erosion and conduit widening started.
3. During subsequent vulcanian eruptions (P1a), progressive erosion and widening of the wall rock generated quantities of lithic debris that were mixed into magma. Each explosion (0.014 km^3 DRE) tapped the reservoir at depth. Magma would have partially refilled the conduit prior to the next explosion.
4. The magma level in the conduit dropped with time during phase P1 and the conduit progressively widens giving place to the juvenile-rich phase (P1b).
5. During a pause of weeks to months, replenishment by a more primitive, incompatible-rich magma batch from depth and/or slight contamination by basement granitoids occurred in the plumbing system. Vent erosion and widening all around the volcano or at least in different and more extensive areas than during P1 phase, provided the P2 pyroclastic density currents of a new assemblage of basaltic-andesitic to rhyolitic lava fragments.
6. More basic, crystal-rich and voluminous magma was subsequently erupted at high intensity during the climactic phase of the eruption (P2a).
7. A high magma discharge rate during phase P2a caused the fragmentation level of the magma to fall rapidly to within the granitoid basement, probably accompanied by strong vent erosion and widening, and caldera collapse at least 470 m depth. The magma was actively mixed with granitoids which could produce quenching of scoriae, limiting degassing and reducing vesicularity.
8. Juvenile-rich flows were produced (P2b-c) until the reservoir overpressure dropped below that necessary for explosive eruption after the low-energy final pyroclastic flow (P2d).
9. The construction of the modern cone started a few rain seasons after the Pucón eruption and caldera collapse, with the emission of the residual cumulates from Pucón magma (Chaimilla scoria falls).

Appendix 3.1: Scoria and lithic abundances (in number %) of samples from different stratigraphic layers of the Pucón Ignimbrite, including fractions 32, 16, 8, 4 and 2 mm and components of the 250 µm fraction.

		32 mm				16 mm				8 mm				4 mm				2 mm				250 µm								
sample	**unit**	**sc**	**lit**	**n**	**sc**	**sc**	**lit**	**n**	**sc**	**sc**	**lit**	**n**	**sc**	**sc**	**lit**	**n**	**sc**	**sc**	**lit**	**n**	**sc**	**sc**	**gl**	**cxx**	**lit**	**n**	**sc**	**gl**	**cxx**	**lit**
					N° %				**N° %**				**N° %**				**N° %**				**N° %**						**N° %**	**N° %**	**N° %**	**N° %**
VR73H	**P1a I**	0	0	0	0	0	0	0	0	0	0	0	0	14	7	21	67	52	47	99	53	323	193	32	62	610	53	32	5	10
VR73I	**P1a II**	8	9	17	47	21	19	40	53	134	94	228	59	1483	681	2164	69	138	104	242	57	319	142	102	117	680	47	21	15	17
VR73J	**P1a III**	1	30	31	3	31	122	153	20	52	84	136	38	820	1112	1932	42	97	125	222	44	117	117	21	26	281	42	42	7	9
VR73K	**P1a IV**					141	5	146	97	184	29	213	86	1124	410	1534	73	172	78	250	69	160	87	15	18	280	57	31	5	6
VR73L	**P1a IV**	29	1	30	97	527	38	565	93	236	38	274	86	1959	435	2394	82	139	58	197	71	320	114	60	81	575	56	20	10	14
VR73M	**P1b**	7	0	7		166	13	179	93	196	26	222	88	1555	248	1803	86	175	45	220	80	405	45	28	36	514	79	9	5	7
VR73N1	**P1b**	85	8	93	91	365	28	393	93	96	18	114	84	1520	294	1814	84	155	46	201	77	493	59	47	75	674	73	9	7	11
VR73P	**P1b**	63	0	63	100	520	2	522	100	187	8	195	96	1204	128	1332	90	213	52	265	80	394	26	34	35	489	81	5	7	7
VR78-3A	**P2a**	6	18	24	25	92	110	202	46	116	261	377	31	233	361	594	39	81	88	169	48	105	64	40	42	251	42	25	16	17
VR78-3B	**P2a**	3	6	9		23	24	47	49	209	309	518	40	199	416	615	32	89	150	239	37	207	109	83	49	448	46	24	19	11
VR78-3C	**P2a**					37	8	45	82	177	183	360	49	214	296	510	42	128	136	264	48	94	60	36	22	212	44	28	17	10
VR85-12	**P2a**	0	0	0	0	0	0	0	0	32	56	88	36	301	245	546	55	149	100	249	60	182	80	110	39	411	44	19	27	9
VR85-9	**P2a**	0	0	0	0	102	75	177	58																					
VR85-8	**P2a**	20	6	26	77	95	59	154	62	309	238	547	56	346	220	566	61	111	96	207	54	138	46	99	33	316	44	15	31	10
VR85-7	**P2a**	0	5	5	0	86	77	163	53	194	188	382	51	292	255	547	53	85	99	184	46	134	75	77	39	325	41	23	24	12
VR85-6	**P2a**	2	1	3	0	60	92	152	39	111	206	317	35	187	319	506	37	86	188	274	31	136	85	65	73	359	38	24	18	20
VR85-5	**P2a**	17	2	19	89	126	28	154	82	217	116	333	65	298	238	536	56	108	79	187	58	113	54	55	20	242	47	22	23	8
VR73Q1	**P2a**					46	75	121	38	77	42	119	65	1137	447	1584	72													
VR73Q2	**P2a**					34	72	106	32	52	70	122	43	880	652	1532	57													
VR75A	**P2a**													182	91	273	67													
VR75B	**P2a**													142	164	306	46													
VR75D	**P2a**													133	245	378	35													
VR75E	**P2a**													261	358	619	42													
VR85-4	**P2b**	16	3	19	84	120	36	156	77	218	88	306	71	400	176	576	69	176	104	280	63	166	57	67	19	309	54	18	22	6
VR85-3	**P2b**	14	4	18	78	165	44	209	79	258	130	388	66	370	171	541	68	115	80	195	59	185	51	90	35	361	51	14	25	10
VR75F	**P2b**													1306	682	1988	66													
VR78-4	**P2c**	0	0	0	0	0	3	3		3	27	30	10	161	347	508	32	118	129	247	48	87	126	45	24	282	31	45	16	9
VR78-5A	**P2d**	4	12	16	25	27	33	60	45	174	172	346	50	252	360	612	41	110	147	257	43	67	149	63	43	322	21	46	20	13
VR78-5B	**P2d**	6	9	15	40	69	19	88	78	209	142	351	60	259	264	523	50	123	86	209	59	143	96	52	40	331	43	29	16	12
VR78-5C	**P2d**	0	0	0	0	2	11	13		155	143	298	52	269	236	505	53	130	106	236	55	109	144	105	75	433	25	33	24	17
VR75G	**P2d**													406	563	969	42													
VR75H	**P2d**													1622	786	2408	67													

sc = scoria
lit = lithics
n = total of counted clasts
gl = dense glass shards
cxx = crystals

Abundance of scoria in number %

Appendix 3.2: Components of the 4 mm fraction (in number %) of samples from different stratigraphic layers of the Pucón Ignimbrite. Abundances of lithics in number % of total lithics.

	SAMPLE	UNIT	sc	G	DPJ	alt	fresh	F	total	lithics	sc	G	DPJ	alt	fresh	F
											N° %	N° %	N° %	N° %	N° %	N° %
1	**VR73H**	**P1a I**	14						21	7	67					
2	**VR73I**	**P1a II**	1483	0	211	332	108	30	2164	681	69	0	31	49	16	4
3	**VR73J**	**P1a III**	820	1	395	427	250	39	1932	1112	42	0	36	38	22	4
4	**VR73K**	**P1a IV**	1124	2	134	177	92	5	1534	410	73	0	33	43	22	1
5	**VR73L**	**P1a IV**	1959	0	88	299	48	0	2394	435	82	0	20	69	11	0
6	**VR57-1**	**P1a**	1500	0	272	635	233	39	2679	1179	56	0	23	54	20	3
7	**VR73M**	**P1b**	1555	1	34	188	24	1	1803	248	86	0	14	76	10	0
8	**VR73N1**	**P1b**	1520	0	53	215	25	1	1814	294	84	0	18	73	9	0
9	**VR73P**	**P1b**	1204	0	6	115	7	0	1332	128	90	0	5	90	5	0
10	**VR73Q1**	**P2a**	1137	30	62	243	112	0	1584	447	72	7	14	54	25	0
11	**VR73Q2**	**P2a**	880	15	115	302	199	21	1532	652	57	2	18	46	31	3
12	**VR78-3A**	**P2a**	233	2	28	147	184	0	594	361	39	1	8	41	51	0
13	**VR78-3B**	**P2a**	199	7	39	85	282	3	615	416	32	2	9	20	68	1
14	**VR78-3C**	**P2a**	214	8	25	66	197	0	510	296	42	3	8	22	67	0
15	**VR85-12**	**P2a**	301	8	12	161	64	0	546	245	55	3	5	66	26	0
16	**VR85-8**	**P2a**	346	9	11	110	90	0	566	220	61	4	5	50	41	0
17	**VR85-7**	**P2a**	292	12	22	92	129	0	547	255	53	5	9	36	51	0
18	**VR85-6**	**P2a**	187	9	14	114	182	0	506	319	37	3	4	36	57	0
19	**VR85-5**	**P2a**	298	1	11	114	112	0	536	238	56	0	5	48	47	0
20	**VR75A**	**P2a**	182	4	5	32	50	0	273	91	67	4	5	35	55	0
21	**VR75B**	**P2a**	142	4	30	79	51	0	306	164	46	2	18	48	31	0
22	**VR75D**	**P2a**	133	12	9	92	134	0	380	247	35	5	4	37	54	0
23	**VR75E**	**P2a**	261	23	27	156	152	0	619	358	42	6	8	44	42	0
24	**VR85-4**	**P2b**	400	5	9	90	72	0	576	176	69	3	5	51	41	0
25	**VR85-3**	**P2b**	370	5	6	99	61	0	541	171	68	3	4	58	36	0
26	**VR6A**	**P2b**	624	33	23	514	293	0	1487	863	42	4	3	60	34	0
27	**VR75F**	**P2b**	1306	39	42	332	269	0	1988	682	66	6	6	49	39	0
28	**VR78-4**	**P2c**	161	5	14	102	226	0	508	347	32	1	4	29	65	0
29	**VR78-5A**	**P2d**	252	2	9	100	249	0	612	360	41	1	3	28	69	0
30	**VR78-5B**	**P2d**	259	0	11	66	187	0	523	264	50	0	4	25	71	0
31	**VR78-5C**	**P2d**	269	1	12	81	142	0	505	236	53	0	5	34	60	0
32	**VR75G**	**P2d**	406	9	73	246	235	0	969	563	42	2	13	44	42	0
33	**VR75H**	**P2d**	1622	15	54	340	427	0	2458	836	66	2	6	41	51	0

sc = scoria
G = granitoids
DPJ = dense prismatically-jointed lithics
alt = altered lithics
fresh = fresh lithics
F = fumarolized lithics

Abundances of the 4 mm fraction (in number %).
Abundances of lithics in number % of total lithics.

Appendix 3.3: Analytical methods of the whole-rock analyses

The whole-rock major and trace element data were obtained on agate-ground powders at UMR 6538 Domaines océaniques (Laboratoire de Petrologie, Université du Brest Occidental, France; responsible: Jo Cotten), using a Jobin-Yvon JY70PLUS Inductive Coupled Plasma-Atomic Emission Spectrometer (ICP-AES). The relative standard deviation is *ca.* 1% for SiO_2 and 2% for the other major elements except for low values (<=0.50%) for which the absolute standard deviation is $\pm$0.01%. The relative standard deviation is *ca.* 5% for all the trace elements except for Rb and Sr (*ca.* 2%) (Legendre *et al.*, 2005). 300 mg of powder were digested with 4 ml of concentrated acid mixture (1:7 HNO_3-HF) in a 30-ml hermetically sealed Teflon (PFA) vessel. Next, 96 ml of H_3BO_3 aqueous solution (25 g l^{-1} H_3BO_3 and 0.5 g l^{-1} CsCl) were added to neutralize the excess HF and dissolve the precipitated fluoride, CsCl acting as a buffer of the ionization phenomena in the flame and the argon plasma. 100 ml of the final clear solution were obtained after achievement of a 2-day complexation process of fluoride as fluoboric acid HBF_4. All reagents used are analytical grade. All the elements were determined from the final solution without selective extraction, boron being used as an internal standard for ICP-AES analyses. Calibrations were made using international standards JB2, BEN, ACE, Mica-Fe as well as specific reference samples (Cotten *et al*., 1995).

Appendix 3.4: Major element whole-rock composition of samples of the Pucón Ignimbrite, and pre and post-Pucón deposits

	sample	unit	type	size	SiO2	TiO2	Al2O3	Fe2O3	MnO	MgO	CaO	Na2O	K2O	P2O5	LOI	Total	Total	Ti ppm	K ppm	P ppm
															1050°C		vol-free			
	pre-Pucón																			
1	VR113-6P		PJ	M	62.0	1.1	15.5	6.9	0.2	1.5	4.1	4.8	1.6	0.4	1.3	99.1	97.8	6498.3	13667.4	1607.4
2	VR119		DL	B	56.3	1.2	16.5	10.2	0.2	3.7	7.8	3.9	0.9	0.2	-0.4	100.3	100.7	7022.8	7087.5	996.9
3	VR114		DL		56.4	1.2	16.3	10.0	0.2	3.6	7.8	3.8	0.9	0.2	-0.3	100.1	100.4	6983.4	7190.7	999.8
	Pucón																			
1	VR 73G	A	SJ	M	55.5	1.2	16.5	10.1	0.2	3.7	8.0	3.7	0.8	0.2	-0.1	99.6	99.7	7096.8	6829.1	1007.4
2	VR113-7a	A	SJ	M	55.6	1.2	16.6	10.1	0.2	3.7	7.7	3.7	0.8	0.2	-0.1	99.6	99.7	7219.3	6831.1	1007.8
3	VR 73J	P1a	DJ	B	55.2	1.2	16.3	10.0	0.2	3.6	7.9	3.8	0.8	0.2	0.4	99.6	99.2	7072.1	6947.2	1012.5
4	VR 73Kc	P1a	DJ	B	56.2	1.2	16.3	10.1	0.2	3.7	7.8	3.9	0.8	0.2	-0.4	99.9	100.3	6991.8	6951.0	1001.0
5	VR97-3BD	P1a	DJ	B	56.2	1.2	16.4	10.0	0.2	3.7	7.8	3.9	0.9	0.2	-0.4	99.9	100.3	7050.8	7033.1	957.4
6	VR112aD	P1a	DJ	B	56.1	1.2	16.3	10.1	0.2	3.7	8.0	3.9	0.8	0.2	-0.4	100.1	100.5	7037.5	6937.2	999.0
7	VR 73JN	P1a	DJ	M	55.0	1.2	16.6	*10.0*	0.2	3.9	7.8	3.6	0.8	0.2	0.3	99.5	99.1	7136.2	6615.7	969.0
8	VR115-9P	P1a	DPJ	B	56.3	1.2	16.4	10.0	0.2	3.7	7.8	3.9	0.9	0.2	-0.4	100.1	100.5	7038.2	7103.1	999.1
9	VR97-3AP	P1a	DPJ	B	61.2	1.2	15.3	8.5	0.2	2.1	5.2	4.7	1.4	0.3	-0.4	99.8	100.1	7303.7	11522.9	1482.4
10	VR113-9P	P1a	DPJ	L	61.3	1.2	15.3	8.5	0.2	2.1	5.2	4.7	1.4	0.4	-0.1	100.1	100.1	7304.4	11607.0	1526.2
11	VR73JP	P1a	DPJ	L	64.2	1.1	14.9	6.9	0.2	1.5	4.3	4.8	1.6	0.4	0.0	99.9	99.8	6305.5	13305.0	1705.7
12	VR 73Ic	P1a	DPJ	M	63.0	1.1	15.3	7.3	0.2	1.7	4.5	4.9	1.5	0.4	-0.2	99.6	99.8	6727.8	12477.2	1575.0
13	VR 73JR	P1a	DPJ	M	60.4	1.2	15.6	8.6	0.2	2.5	5.6	4.5	1.2	0.3	-0.3	99.8	100.1	7128.3	10285.6	1352.4
14	VR 73JV	P1a	DPJ	M	60.8	1.1	15.7	8.3	0.2	2.4	5.7	4.5	1.3	0.3	-0.3	100.0	100.2	6701.0	10439.0	1307.2
15	VR115-9D	P1a	DPJ	B	63.5	1.1	15.2	7.4	0.2	1.7	4.7	4.9	1.5	0.4	-0.4	100.1	100.5	6620.7	12554.2	1650.7
16	VR 73Ie	P1a	DPJ*	M	61.0	1.2	15.4	8.5	0.2	2.1	5.2	4.7	1.3	0.4	-0.3	99.7	100.0	7256.8	11128.4	1528.8
17	VR115-9	P1a	DL	B	51.7	0.9	17.4	9.5	0.2	6.8	10.4	2.9	0.5	0.2	-0.1	100.2	100.4	5555.9	3970.8	652.6
18	VR-73Ib	P1a	SJ	B	55.9	1.2	16.4	10.2	0.2	3.7	7.9	3.9	0.8	0.2	-0.4	100.0	100.4	7222.9	6943.4	999.9
19	VR73IB	P1a	SJ	B	56.0	1.2	16.4	10.3	0.2	3.8	7.9	3.9	0.8	0.2	-0.5	100.2	100.7	7266.7	6763.3	997.7
20	VR 73Kb	P1a	SJ	B	56.0	1.2	16.2	10.3	0.2	3.7	7.8	3.8	0.8	0.2	-0.5	99.8	100.3	7235.8	6873.1	1001.7
21	VR73LB	P1a	SJ	B	56.0	1.2	16.3	10.2	0.2	3.6	7.9	3.8	0.8	0.2	-0.4	99.8	100.2	7178.9	6875.8	1002.1
22	VR112cS	P1a	SJ	B	55.2	1.2	16.7	10.2	0.2	3.8	8.1	3.7	0.8	0.2	-0.3	99.6	100.0	7136.9	6560.8	917.3
23	VR 73Il	P1a	SJ	M	55.0	1.2	16.4	10.1	0.2	3.6	7.4	3.6	0.8	0.2	1.1	99.4	98.3	7316.2	6754.0	976.9
24	VR 73Kl	P1a	SJ	M	55.8	1.2	16.4	10.2	0.2	3.7	7.8	3.6	0.8	0.2	0.2	100.0	99.9	7322.7	6566.1	1005.4
25	VR 73Ll	P1a	SJ	M	55.3	1.2	16.5	10.3	0.2	3.7	7.8	3.7	0.8	0.2	0.2	99.8	99.6	7401.2	6749.2	1051.8
26	VR64AC	P1b	DJ	B	56.0	1.2	16.5	10.1	0.2	3.6	7.9	3.9	0.8	0.2	-0.4	100.0	100.4	7104.9	6779.4	1043.6
27	VR73K=CR1	P1b	DJ	B	56.0	1.2	16.3	10.0	0.2	3.6	7.8	3.9	0.9	0.2	-0.5	99.5	100.0	7134.8	7057.0	1004.3
28	VR73N1R	P1b	DPJ	M	57.4	1.2	16.3	9.6	0.2	3.3	7.3	4.0	0.9	0.3	-0.4	99.9	100.3	7055.0	7534.0	1132.2
29	VR73NP	P1b	DPJ*	B	56.6	1.2	16.1	10.0	0.2	3.6	7.8	3.8	0.9	0.3	-0.5	99.9	100.3	7051.5	7116.5	1088.1
30	VR-73Mb	P1b	SJ	B	55.8	1.2	16.7	10.0	0.2	3.8	8.2	3.7	0.8	0.2	-0.4	100.2	100.6	7092.2	6767.3	998.3
31	VR73N2b	P1b	SJ	B	55.8	1.2	16.5	10.2	0.2	3.8	8.2	3.8	0.8	0.2	-0.5	100.1	100.6	7153.9	6769.3	998.6
32	VR73N3	P1b	SJ	B	55.6	1.2	16.7	10.2	0.2	3.8	8.0	3.8	0.8	0.2	-0.5	99.8	100.3	7052.2	6786.2	1001.1
33	VR73P	P1b	SJ	B	55.6	1.2	16.7	10.1	0.2	3.8	8.1	3.7	0.8	0.2	-0.3	99.9	100.3	7115.5	6624.0	958.1
34	VR-78-2b	P1b	SJ	B	55.8	1.2	16.5	10.0	0.2	3.8	8.1	3.7	0.9	0.2	-0.4	100.0	100.3	7109.9	7032.4	1000.8
35	VR58-0	P1b	SJ	B	55.3	1.2	16.8	10.2	0.2	3.8	8.2	3.7	0.8	0.2	-0.2	100.1	100.3	7055.7	6458.4	1001.6

	sample	unit	type	size	SiO2	TiO2	Al2O3	Fe2O3	MnO	MgO	CaO	Na2O	K2O	P2O5	LOI	Total	Total	Ti ppm	K ppm	P ppm
															1050°C		vol-free			
36	VR58-1A	P1b	SJ	B	54.7	1.2	16.9	10.0	0.2	4.0	8.1	3.6	0.8	0.2	0.2	99.7	99.5	6926.1	6338.3	1008.9
37	VR64AB	P1b	SJ	B	55.5	1.2	16.8	10.1	0.2	3.9	8.1	3.7	0.8	0.2	-0.5	99.9	100.3	6991.1	6453.9	957.4
38	VR73M	P1b	SJ	M	55.5	1.2	16.9	10.0	0.2	3.7	8.1	3.7	0.8	0.2	-0.2	100.0	100.3	6996.6	6541.8	1001.7
39	VR73N1	P1b	SJ	M	55.3	1.2	16.7	10.3	0.2	3.7	8.0	3.6	0.8	0.2	0.1	100.1	100.0	7315.4	6559.5	1004.4
40	VR57-2C	P1c	DJ	B	55.7	1.2	16.5	10.1	0.2	3.7	7.8	3.9	0.8	0.2	-0.4	99.7	100.1	7129.8	6803.1	1003.6
41	VR57-2B	P1c	DJ	B	51.8	1.0	18.3	9.1	0.2	6.0	9.4	3.3	0.7	0.2	-0.2	99.8	99.9	5939.2	5565.9	1004.9
42	VR57-2D	P1c	DPJ	B	56.0	1.2	16.4	10.1	0.2	3.6	7.8	3.9	0.8	0.2	-0.5	99.7	100.2	7062.8	6879.2	1002.6
43	VR57-1	P1c	DPJ	B	61.2	1.2	15.4	8.6	0.2	2.1	5.3	4.7	1.3	0.3	-0.4	99.8	100.2	7297.8	11016.7	1481.2
44	VR57-1B	P1c	SJ	B	55.0	1.2	16.6	10.0	0.2	4.2	8.0	3.7	0.8	0.2	-0.3	100.4	99.8	6965.3	6568.7	962.1
45	VR57-2A	P1c	SJ	B	55.2	1.2	16.5	10.2	0.2	3.8	7.8	3.8	0.8	0.2	-0.3	99.4	99.7	7219.3	6747.8	1007.8
46	VR58-1B	P2a	DJ	B	55.5	1.2	16.4	10.2	0.2	3.7	7.9	3.8	0.8	0.2	-0.4	99.5	99.9	7260.5	6979.5	1048.8
47	VR78-3AP	P2a	DPJ	L	56.4	1.2	16.3	9.9	0.2	3.6	7.7	3.9	0.9	0.2	-0.4	99.8	100.1	7064.2	7295.1	1002.8
48	VR73Q2	P2a	DPJ	M	59.0	1.3	15.8	9.0	0.2	2.8	6.2	4.4	1.3	0.3	-0.3	99.9	100.2	7660.6	10442.1	1438.4
49	VR113-11P	P2a	DPJ	B	64.7	0.8	15.2	6.5	0.2	1.4	3.9	4.9	2.1	0.2	-0.2	99.7	99.8	4685.0	17383.1	1006.1
50	VR85-7P	P2a	DPJ	L	54.2	1.2	16.6	9.9	0.2	4.6	9.1	3.5	0.7	0.2	-0.2	100.0	100.1	7005.7	6135.7	1003.0
51	VR75EV	P2a	DPJ	M	56.6	1.4	15.9	9.9	0.2	3.3	7.0	4.1	1.1	0.3	-0.2	99.5	99.7	8118.4	9243.3	1270.1
52	VR75ER	P2a	DPJ	M	55.5	1.4	16.2	9.9	0.2	3.8	7.7	3.8	1.0	0.3	0.1	99.8	99.7	8176.9	8575.4	1357.5
53	VR85-5P	P2a	DPJ	B	69.3	0.5	14.2	4.8	0.1	0.6	2.4	5.1	2.6	0.1	0.0	99.6	99.7	2887.7	21992.9	525.8
54	VR75EP	P2a	DPJ	M	57.4	1.3	16.3	8.9	0.2	3.9	7.0	4.0	1.0	0.4	-0.2	100.1	100.3	7654.5	8529.2	1611.5
55	VR78-3AD	P2a	DPJ*	L	56.6	1.2	16.1	10.1	0.2	3.6	7.8	3.9	0.9	0.2	-0.4	100.0	100.4	7043.1	7108.0	999.8
56	VR57-4A	P2a	SJ	B	55.2	1.2	16.7	10.0	0.2	3.9	8.0	3.7	0.9	0.2	-0.1	99.8	99.9	7022.6	7314.1	1049.1
57	VR57-4B	P2a	SJ	B	54.9	1.2	16.6	10.1	0.2	3.8	8.1	3.7	0.8	0.2	0.3	99.9	99.6	7105.4	6587.2	1008.7
58	VR57-4C	P2a	SJ	B	54.6	1.2	16.8	10.1	0.2	3.9	8.2	3.7	0.8	0.2	-0.2	99.5	99.7	6977.9	6747.1	1007.7
59	VR63A	P2a	SJ	B	55.8	1.2	16.5	10.2	0.2	3.6	8.0	3.9	0.9	0.2	-0.4	100.1	100.4	7222.2	7025.4	956.4
60	VR78-3AS	P2a	SJ	B	55.6	1.2	16.7	10.0	0.2	3.9	8.3	3.7	0.8	0.2	-0.5	99.9	100.4	6927.2	6780.8	956.8
61	VR73Q2l	P2a	SJ	M	54.0	1.2	17.3	10.1	0.2	3.6	7.9	3.3	0.8	0.2	1.5	100.1	98.6	7420.0	6569.1	1063.1
62	VR-79-1b	P2a	SJ	B	54.2	1.2	18.1	9.5	0.2	3.4	8.8	3.6	0.9	0.2	-0.2	99.9	100.0	7370.9	7136.4	1047.5
63	VR-79-3b	P2a	SJ	B	54.5	1.2	17.3	9.9	0.2	3.6	8.4	3.6	0.8	0.2	0.2	99.9	99.7	7333.7	6825.6	1050.7
64	VR69	P2a	SJ	B	54.5	1.2	17.4	9.9	0.2	3.8	8.4	3.7	0.9	0.2	-0.3	99.7	100.0	7191.1	7136.4	1003.8
65	VR85-5S	P2a	SJ	B	55.0	1.2	16.8	10.0	0.2	3.8	8.0	3.8	0.9	0.2	-0.3	99.5	99.8	7269.9	7155.0	962.7
66	VR85-8S	P2a	SJ	L	55.5	1.2	16.8	10.1	0.2	3.7	8.2	3.7	0.9	0.2	-0.2	100.2	100.4	7227.9	7113.7	1000.6
67	VR75A	P2a	SJ	M	54.8	1.2	17.1	10.0	0.2	3.7	7.8	3.3	0.8	0.2	0.9	99.9	99.0	7511.9	6543.2	1014.8
68	VR75E	P2a	SJ	M	55.2	1.2	16.9	10.2	0.2	3.9	8.0	3.5	0.8	0.3	0.2	100.3	100.1	7367.2	6967.0	1090.6
69	VR85-9S	P2a	SJ	M	55.4	1.2	16.9	9.9	0.2	3.6	8.1	3.7	0.9	0.2	0.0	100.0	100.0	7195.4	7057.7	960.8
70	VR85-4D	P2b	DJ	L	54.9	1.2	16.9	9.9	0.2	3.7	8.2	3.6	0.9	0.2	0.1	99.6	99.6	7286.7	7338.3	1008.8
71	VR85-3D	P2b	DJ	L	55.0	1.2	17.1	9.9	0.2	3.6	8.3	3.6	0.9	0.2	-0.3	99.7	100.0	7313.9	7139.3	1004.2
72	VR12P	P2b	DPJ	B	56.0	1.6	15.7	10.2	0.2	3.5	7.3	3.9	1.0	0.5	0.1	100.0	99.9	9661.6	8476.0	2054.2
73	VR85-4P	P2b	DPJ	L	54.7	1.3	16.2	10.3	0.2	4.2	8.3	3.6	0.9	0.3	-0.1	99.8	99.8	7625.8	7317.0	1093.3
74	VR85-3P	P2b	DPJ	L	55.5	1.5	15.9	10.6	0.2	3.6	7.2	4.0	1.0	0.3	0.0	99.7	99.7	9139.8	8659.5	1401.4

	sample	unit	type	size	SiO2	TiO2	Al2O3	Fe2O3	MnO	MgO	CaO	Na2O	K2O	P2O5	LOI	Total	Total	Ti ppm	K ppm	P ppm
															1050°C		vol-free			
75	VR-6.2	P2b	SJ	B	55.1	1.2	17.0	10.0	0.2	3.6	8.0	3.8	0.9	0.2	-0.3	99.7	100.0	7317.5	7475.1	1004.7
76	VR6-3	P2b	SJ	B	55.2	1.2	17.2	9.8	0.2	3.7	8.4	3.6	0.8	0.2	-0.4	100.1	100.4	7165.3	6945.5	1043.7
77	VR-12	P2b	SJ	B	55.2	1.2	17.0	10.0	0.2	3.8	8.1	3.8	0.9	0.2	-0.4	99.9	100.2	7238.0	7372.1	1002.0
78	VR85-3S	P2b	SJ	L	55.0	1.2	16.9	9.9	0.2	3.5	8.2	3.7	0.9	0.2	-0.2	99.5	99.7	7335.9	7160.8	1051.0
79	VR75F	P2b	SJ	M	54.2	1.2	17.1	10.0	0.2	4.2	8.0	3.4	0.9	0.2	0.4	99.7	99.3	7126.8	7108.9	1011.7
80	VR75HR	P2c	DPJ	M	56.8	1.4	15.8	10.0	0.2	3.4	7.2	4.0	1.1	0.3	-0.3	99.8	100.1	8263.2	9120.7	1395.5
81	VR75H	P2c	SJ	M	54.3	1.2	17.2	10.0	0.2	3.6	8.0	3.4	0.8	0.2	1.2	100.0	98.8	7284.3	6640.5	1061.0
82	VR67C	P2d	DJ	B	55.3	1.2	17.1	9.8	0.2	3.8	8.3	3.7	0.8	0.2	-0.2	100.1	100.3	7229.4	6949.6	1000.8
83	VR78-5AS	P2d	SJ	B	55.2	1.2	17.1	9.9	0.2	3.7	8.3	3.7	0.9	0.2	-0.3	100.1	100.3	7291.3	7034.5	1001.1
84	VR78-5BS	P2d	SJ	M	54.8	1.2	17.1	9.9	0.2	3.7	8.3	3.6	0.8	0.2	-0.1	99.7	99.8	7327.1	6985.8	1006.0
	post-Pucón fallout deposits																			
1	VR73S		SJ	M	53.4	1.0	19.1	8.7	0.2	3.9	9.9	3.2	0.6	0.2	0.2	100.2	100.0	5995.0	5063.9	829.6
2	VR-15H**				53.2	1.0	19.0	8.9	0.2	4.0	9.8	3.3	0.6	0.2	-0.2	99.8	100.0	5995.0	5313.0	785.9
3	VR 15H**				53.2	1.0	18.8	8.8	0.2	4.3	9.7	3.1	0.6	0.2	0.2	99.9	99.7	5774.8	4998.2	744.4
4	VR 15I**				52.1	1.0	18.4	9.2	0.2	4.8	10.0	2.9	0.5	0.2	0.8	100.0	99.2	5741.2	4435.5	747.9
5	VR 15J**				51.8	1.0	18.8	9.4	0.2	4.6	9.6	3.0	0.5	0.2	0.9	99.8	98.9	5880.4	4449.4	794.3

LEGEND

TYPES OF FRAGMENTS:
SJ = scoriaceous juvenile
PJ = pumiceous juvenile
DJ = dense juvenile
DPJ = dense prismatically-jointed fragment
DPJ* = dense or vesicular lava fragment chemically similar to DPJ
DL = dense lava fragment

SIZES:
M = multiple lapilli fragments
L = single lapilli fragment
B = bomb or block

** = not sampled by the author

Appendix 3.5: Trace element whole-rock composition of samples of the Pucón Ignimbrite, and pre and post-Pucón deposits

	sample	unit	type	size	Sc	V	Cr	Co	Ni	Rb	Sr	Y	Zr	Nb	Ba	La	Ce	Nd	Sm	Eu	Gd	Dy	Er	Yb	Th
	pre-Pucón																								
1	VR113-6P		PJ	M	19.0	58.0	3.0	8.0	2.0	41.0	330.0	42.5	196.0	4.7	440.0	17.5	42.0	27.0	6.4	1.6	6.9	6.9	4.3	4.3	4.4
2	VR119		DL	B	30.0	286.0	24.0	24.0	13.0	20.5	422.0	28.5	106.0	2.5	245.0	9.5	22.5	15.6	4.1	1.2	4.3	4.5	2.9	2.9	1.9
3	VR114		DL		31.0	289.0	26.0	24.0	12.0	20.5	415.0	27.0	106.0	2.5	253.0	9.5	23.0	15.7	4.0	1.2	4.3	4.5	2.7	2.7	1.9
	Pucón																								
1	VR 73G	A	SJ	M	30.0	290.0	14.0	23.0	11.0	19.4	422.0	27.0	100.0	2.6	239.0	9.1	21.5	14.5	4.1	1.2	4.3	4.4	2.7	2.6	1.5
2	VR113-7a	A	SJ	M	31.0	292.0	14.5	24.0	11.0	19.4	422.0	27.0	104.0	2.4	250.0	9.4	22.5	15.5	3.9	1.2	4.4	4.4	2.7	2.7	1.7
3	VR 73J	P1a	DJ	B	30.5	295.0	15.0	24.0	10.0	20.5	416.0	27.5	103.0	2.3	245.0	9.0	22.0	14.5	4.1	1.3	4.5	4.5	2.8	2.7	1.9
4	VR 73Kc	P1a	DJ	B	31.0	300.0	21.0	23.0	13.0	20.2	414.0	28.0	105.0	2.4	250.0	9.6	23.0	15.0	4.0	1.3	4.5	4.5	2.8	2.7	1.9
5	VR97-3BD	P1a	DJ	B	31.0	287.0	20.0	23.0	12.0	21.0	420.0	27.8	104.0	2.3	250.0	9.3	23.3	15.5	3.8	1.2	4.4	4.5	2.8	2.8	1.8
6	VR112aD	P1a	DJ	B	31.0	298.0	23.0	25.0	12.0	20.5	417.0	27.0	102.0	2.6	252.0	9.4	22.4	15.5	3.7	1.2	4.3	4.3	2.7	2.7	1.8
7	VR 73JN	P1a	DJ	M	31.5	285.0	41.0	27.0	20.0	20.0	416.0	27.5	104.0	2.6	240.0	9.6	23.0	15.5	4.3	1.2	4.7	4.7	2.8	2.8	1.9
8	VR115-9P	P1a	DPJ	B	31.0	290.0	18.0	24.0	12.0	20.2	418.0	28.5	105.0	2.6	254.0	9.6	23.0	15.4	4.3	1.2	4.3	4.5	2.9	2.9	1.8
9	VR97-3AP	P1a	DPJ	B	23.0	139.0	11.0	15.0	2.0	34.5	371.0	39.5	167.0	3.5	385.0	15.2	35.5	24.0	5.7	1.6	6.2	6.2	4.0	3.9	3.3
10	VR113-9P	P1a	DPJ	L	23.0	138.0	5.0	14.0	2.0	35.0	366.0	39.0	168.0	3.8	405.0	15.2	36.0	24.0	6.0	1.6	6.3	6.3	3.9	3.9	3.1
11	VR73JP	P1a	DPJ	L	20.0	60.0	6.0	8.5	0.0	41.5	330.0	43.0	200.0	4.4	482.0	16.5	40.0	26.0	6.2	1.6	6.9	6.7	4.2	4.1	4.0
12	VR 73Ic	P1a	DPJ	M	20.0	65.0	4.0	9.0	1.5	37.9	346.0	42.0	185.0	4.6	412.0	16.0	38.5	25.5	6.3	1.7	6.7	6.7	41.5	4.1	3.6
13	VR 73JR	P1a	DPJ	M	24.0	164.0	8.0	17.0	9.0	31.2	375.0	36.5	156.0	3.6	362.0	14.0	33.0	22.0	5.7	1.5	6.1	6.0	3.7	3.6	2.8
14	VR 73JV	P1a	DPJ	M	24.5	157.0	9.0	16.0	7.0	32.4	374.0	37.0	158.0	3.8	355.0	13.8	32.5	21.0	5.6	1.5	6.1	6.0	3.7	3.7	3.1
15	VR115-9D	P1a	DPJ	B	20.0	66.0	5.0	10.0	3.0	37.0	347.0	42.0	185.0	4.2	422.0	16.5	38.5	26.0	6.2	1.7	6.8	6.7	4.2	4.2	3.6
16	VR 73Ie	P1a	DPJ*	M	23.0	148.0	2.5	14.0	2.0	33.4	366.0	38.0	164.0	3.9	375.0	14.5	34.0	23.0	5.9	1.5	6.2	6.3	3.7	3.5	3.3
17	VR115-9	P1a	DL	B	34.0	260.0	215.0	34.0	78.0	10.7	400.0	19.6	67.0	1.4	148.0	6.0	14.0	10.0	2.8	0.9	3.1	3.3	2.0	2.0	1.0
18	VR-73Ib	P1a	SJ	B	31.5	310.0	14.0	31.0	11.0	20.5	419.0	27.0	105.0	2.8	244.0	9.1	22.5	15.1	3.8	1.2	4.5	4.5	2.7	2.7	1.9
19	VR73IB	P1a	SJ	B	31.5	315.0	15.0	36.0	15.0	20.0	416.0	27.5	102.0	2.4	245.0	9.5	23.0	15.0	4.2	1.3	4.5	4.5	2.8	2.8	2.0
20	VR 73Kb	P1a	SJ	B	31.0	315.0	15.0	28.0	11.5	19.9	416.0	27.5	102.0	2.4	245.0	9.2	23.0	14.5	4.0	1.3	4.5	4.5	2.8	2.6	2.0
21	VR73LB	P1a	SJ	B	32.0	320.0	17.0	34.0	15.0	19.9	416.0	27.5	105.0	2.6	270.0	9.4	23.5	14.5	4.1	1.3	4.4	4.5	2.8	2.7	2.0
22	VR112cS	P1a	SJ	B	31.0	306.0	20.0	26.0	13.0	19.5	423.0	26.0	101.0	2.6	240.0	9.0	21.5	15.0	3.7	1.2	4.0	4.3	2.7	2.6	1.8
23	VR 73Il	P1a	SJ	M	31.0	289.0	19.0	24.0	14.0	20.1	415.0	28.0	105.0	2.6	240.0	9.5	23.0	16.0	4.4	1.3	4.6	4.7	2.9	2.8	2.0
24	VR 73Kl	P1a	SJ	M	32.0	306.0	17.0	26.0	13.0	19.5	415.0	28.0	108.0	2.5	245.0	9.2	22.0	15.0	4.0	1.2	4.5	4.6	2.8	2.8	2.1
25	VR 73Ll	P1a	SJ	M	31.0	300.0	16.0	25.0	13.0	19.5	418.0	28.5	106.0	2.5	250.0	10.0	23.5	15.5	4.4	1.3	4.6	4.7	2.9	2.9	2.1
26	VR64AC	P1b	DJ	B	31.0	300.0	18.0	24.0	11.5	19.9	422.0	27.5	103.0	2.5	255.0	9.7	23.0	15.5	4.2	1.3	4.7	4.6	2.8	2.8	1.8
27	VR73K=CR1	P1b	DJ	B	30.0	295.0	14.0	23.0	11.0	20.6	415.0	28.0	103.0	2.4	250.0	9.5	23.0	15.0	4.0	1.3	4.5	4.5	2.8	2.8	2.0
28	VR73N1R	P1b	DPJ	M	28.5	250.0	11.0	21.0	9.0	22.8	406.0	30.0	116.0	2.6	275.0	10.5	25.0	17.0	4.7	1.3	5.0	5.1	3.1	3.0	2.2
29	VR73NP	P1b	DPJ*	B	31.0	290.0	24.0	25.0	12.0	20.4	407.0	27.7	108.0	2.5	260.0	9.2	22.5	14.8	3.9	1.2	4.4	4.5	2.8	2.7	1.9
30	VR-73Mb	P1b	SJ	B	31.0	300.0	22.0	34.0	14.0	19.3	416.0	26.5	101.0	2.9	240.0	8.9	22.0	14.5	3.9	1.2	4.4	4.4	2.6	2.6	2.0
31	VR73N2b	P1b	SJ	B	31.0	312.0	20.0	28.0	14.0	19.3	419.0	27.0	102.0	2.5	240.0	9.5	23.0	14.5	4.1	1.2	4.4	4.3	2.7	2.6	1.8
32	VR73N3	P1b	SJ	B	31.5	310.0	23.0	26.0	15.0	19.4	419.0	27.0	102.0	2.4	245.0	9.6	23.0	14.5	4.0	1.3	4.5	4.5	2.8	2.7	1.9
33	VR73P	P1b	SJ	B	31.5	302.0	26.0	25.0	15.0	19.1	422.0	27.5	102.0	2.4	240.0	9.5	23.5	14.5	3.9	1.3	4.5	4.5	2.8	2.7	1.8
34	VR-78-2b	P1b	SJ	B	30.0	296.0	22.0	25.0	16.0	19.7	416.0	26.5	101.0	2.8	240.0	9.2	21.5	14.7	3.8	1.2	4.2	4.3	2.6	2.6	1.8
35	VR58-0	P1b	SJ	B	32.0	315.0	28.0	26.0	15.0	18.7	420.0	27.0	103.0	2.6	245.0	9.0	21.5	14.5	4.1	1.1	4.3	4.4	2.7	2.6	1.9
36	VR58-1A	P1b	SJ	B	32.0	304.0	39.0	35.0	24.0	18.0	424.0	26.0	100.0	2.4	240.0	9.0	21.5	14.5	3.9	1.2	4.2	4.3	2.6	2.5	1.9
37	VR64AB	P1b	SJ	B	31.0	307.0	25.0	29.0	18.0	18.7	420.0	26.2	100.0	2.4	236.0	9.0	22.0	14.5	4.0	1.3	4.3	4.4	2.7	2.6	1.8
38	VR73M	P1b	SJ	M	31.0	300.0	22.0	25.0	14.0	19.0	422.0	27.0	100.0	2.4	240.0	9.5	22.5	14.5	3.9	1.2	4.4	4.5	2.8	2.8	2.0
39	VR73N1	P1b	SJ	M	32.0	302.0	19.0	25.0	12.0	19.1	418.0	27.5	104.0	2.5	245.0	9.0	22.0	14.8	4.1	1.2	4.5	4.6	2.8	2.7	2.0
40	VR57-2C	P1c	DJ	B	31.0	295.0	16.0	25.0	13.0	18.6	424.0	26.8	103.0	2.6	245.0	9.4	23.0	15.0	4.1	1.3	4.4	4.5	2.7	2.8	1.8
41	VR57-2B	P1c	DJ	B	29.0	247.0	123.0	30.5	63.0	11.0	620.0	19.0	72.0	2.0	214.0	9.8	22.5	13.6	3.1	1.2	3.3	3.2	1.9	1.9	2.3
42	VR57-2D	P1c	DPJ	B	30.0	293.0	17.5	23.5	11.0	19.9	419.0	27.2	103.0	2.3	251.0	9.5	23.5	15.0	4.1	1.3	4.5	4.5	2.8	2.8	1.9
43	VR57-1	P1c	DPJ	B	23.0	143.0	4.0	15.0	2.0	33.3	370.0	38.0	162.0	3.6	372.0	14.8	36.0	23.0	5.8	1.6	6.3	6.3	3.8	3.9	3.1
44	VR57-1B	P1c	SJ	B	31.0	293.0	44.0	30.0	22.0	18.2	437.0	25.2	96.0	2.3	236.0	9.3	23.0	14.5	4.0	1.2	4.1	4.2	2.6	2.6	1.9
45	VR57-2A	P1c	SJ	B	31.0	300.0	19.0	26.0	14.5	18.8	424.0	26.7	101.0	2.4	240.0	9.4	22.5	15.0	4.0	1.3	4.3	4.4	2.7	2.7	1.8
46	VR58-1B	P2a	DJ	B	32.0	320.0	16.0	25.0	12.0	20.0	420.0	28.0	107.0	2.7	265.0	9.4	22.5	15.0	4.1	1.2	4.6	4.6	2.8	2.7	1.9
47	VR78-3AP	P2a	DPJ	L	30.0	280.0	27.0	24.0	11.0	21.0	414.0	27.0	106.0	2.4	250.0	9.4	22.5	15.2	3.9	1.2	4.6	4.5	2.7	2.7	1.9
48	VR73Q2	P2a	DPJ	M	26.0	196.0	12.0	18.0	7.5	31.2	385.0	37.0	157.0	3.7	360.0	14.5	34.5	22.5	5.9	1.5	6.2	6.1	3.7	3.6	3.3
49	VR113-11P	P2a	DPJ	B	17.0	57.0	13.0	8.0	5.0	54.0	287.0	46.0	248.0	5.4	560.0	21.5	49.5	30.0	6.9	1.6	7.2	7.3	4.7	4.8	5.7
50	VR85-7P	P2a	DPJ	L	34.0	305.0	67.0	29.0	26.0	19.0	419.0	27.0	101.0	2.7	232.0	9.2	22.0	15.0	3.8	1.2	4.2	4.4	2.7	2.7	1.7
51	VR75EV	P2a	DPJ	M	29.0	290.0	12.0	23.0	10.0	26.5	394.0	33.0	135.0	3.2	320.0	12.5	31.0	19.0	5.0	1.4	5.4	5.3	3.3	3.3	2.3
52	VR75ER	P2a	DPJ	M	31.0	295.0	30.0	25.0	15.0	24.7	425.0	30.5	118.0	3.4	322.0	12.5	30.0	18.0	4.7	1.4	5.0	5.0	3.0	3.0	2.3
53	VR85-5P	P2a	DPJ	B	12.5	13.0	5.0	3.0	2.0	70.0	197.0	52.0	297.0	6.4	675.0	24.5	56.0	33.0	7.4	1.5	8.1	8.0	5.3	5.4	7.4
54	VR75EP	P2a	DPJ	M	27.0	208.0	70.0	23.0	31.0	25.0	410.0	30.5	121.0	3.1	325.0	12.4	28.5	18.0	4.9	1.4	4.9	4.9	2.9	2.9	2.7
55	VR78-3AD	P2a	DPJ*	L	31.0	290.0	19.0	25.0	11.0	21.0	408.0	27.7	108.0	2.6	260.0	9.4	22.5	15.3	3.9	1.2	4.4	4.5	2.8	2.8	1.9
56	VR57-4A	P2a	SJ	B	31.0	310.0	29.0	28.0	24.0	22.2	422.0	26.0	107.0	2.7	275.0	8.7	22.0	13.7	3.6	1.1	4.0	4.1	2.5	2.4	2.3
57	VR57-4B	P2a	SJ	B	33.0	320.0	21.0	31.0	18.0	19.0	428.0	27.5	106.0	2.8	260.0	9.0	22.5	15.0	3.9	1.2	4.6	4.7	2.8	2.7	1.9
58	VR57-4C	P2a	SJ	B	34.0	320.0	34.0	36.0	21.0	19.1	424.0	28.0	107.0	2.8	256.0	9.5	24.0	14.7	4.3	1.2	4.5	4.7	2.8	2.7	2.3
59	VR63A	P2a	SJ	B	30.5	308.0	13.5	27.0	12.0	19.7	421.0	27.0	103.0	2.5	245.0	9.4	22.5	15.0	4.1	1.2	4.6	4.7	2.8	2.8	1.9
60	VR78-3AS	P2a	SJ	B	31.0	302.0	27.0	25.5	19.0	19.5	421.0	26.0	99.0	2.5	237.0	8.9	21.0	14.2	3.6	1.2	4.1	4.2	2.6	2.6	1.8
61	VR73Q2l	P2a	SJ	M	30.0	295.0	25.0	24.0	16.0	18.3	414.0	27.5	109.0	2.7	245.0	9.4	22.0	14.5	4.2	1.2	4.5	4.4	2.7	2.6	1.9
62	VR-79-1b	P2a	SJ	B	27.5	300.0	18.0	54.0	15.0	20.5	445.0	26.5	105.0	2.6	263.0	9.8	24.0	15.4	4.0	1.2	4.4	4.5	2.6	2.7	2.1
63	VR-79-3b	P2a	SJ	B	29.0	305.0	24.0	34.0	17.0	19.0	424.0	26.8	103.0	2.7	253.0	9.7	22.5	15.4	4.0	1.2	4.5	4.5	2.6	2.6	2.1
64	VR69	P2a	SJ	B	30.0	300.0	26.0	28.0	17.0	19.9	443.0	27.0	104.0	2.9	245.0	9.4	23.0	15.0	4.1	1.2	4.4	4.5	2.8	2.7	2.1
65	VR85-5S	P2a	SJ	B	31.0	303.0	32.0	24.0	16.0	21.0	425.0	27.3	105.0	2.8	245.0	9.5	22.0	16.0	3.9	1.2	4.5	4.5	2.7	2.7	2.0

	sample	unit	type	size	Sc	V	Cr	Co	Ni	Rb	Sr	Y	Zr	Nb	Ba	La	Ce	Nd	Sm	Eu	Gd	Dy	Er	Yb	Th
66	VR85-8S	P2a	SJ	L	31.0	310.0	20.0	26.0	16.0	21.0	424.0	27.5	105.0	2.7	254.0	9.4	22.5	15.6	3.8	1.2	4.4	4.5	2.8	2.7	1.9
67	VR75A	P2a	SJ	M	32.0	288.0	24.0	24.0	18.0	19.7	428.0	28.5	106.0	2.6	260.0	10.0	23.0	14.5	4.2	1.3	4.8	4.5	2.8	2.8	2.0
68	VR75E	P2a	SJ	M	32.0	300.0	28.0	26.0	24.0	20.3	420.0	27.8	107.0	2.5	255.0	10.0	23.0	15.0	3.9	1.3	4.5	4.4	2.8	2.7	2.2
69	VR85-9S	P2a	SJ	M	30.5	302.0	20.0	25.0	15.0	21.0	435.0	27.0	105.0	2.7	258.0	9.4	22.5	15.4	3.8	1.2	4.4	4.4	2.7	2.7	2.3
70	VR85-4D	P2b	DJ	L	30.5	306.0	22.0	25.0	16.0	21.0	425.0	27.2	108.0	2.7	270.0	9.9	23.8	15.6	4.0	1.2	4.5	4.4	2.7	2.7	2.1
71	VR85-3D	P2b	DJ	L	30.0	302.0	24.0	24.0	15.0	21.0	428.0	27.0	107.0	2.8	255.0	9.7	23.4	15.6	4.0	1.2	4.2	4.3	2.7	2.7	1.9
72	VR12P	P2b	DPJ	B	32.0	290.0	14.0	24.0	10.0	23.5	424.0	31.0	127.0	3.6	320.0	12.5	29.0	20.0	4.9	1.5	5.5	5.2	3.0	3.0	2.3
73	VR85-4P	P2b	DPJ	L	33.0	330.0	43.0	28.0	19.0	21.0	406.0	29.5	112.0	3.1	260.0	10.1	24.0	16.3	4.3	1.3	4.5	4.7	2.9	2.9	1.9
74	VR85-3P	P2b	DPJ	L	31.0	325.0	31.0	25.5	16.0	23.5	415.0	31.2	127.0	3.4	320.0	12.3	30.0	19.2	4.6	1.4	5.1	5.1	3.1	3.0	2.3
75	VR-6.2	P2b	SJ	B	29.0	300.0	21.0	28.0	13.0	21.5	425.0	27.0	107.0	2.9	242.0	9.7	23.5	15.4	4.0	1.2	4.5	4.4	2.7	2.7	2.1
76	VR6-3	P2b	SJ	B	30.0	305.0	25.0	28.0	18.0	20.6	430.0	27.0	107.0	2.7	246.0	9.2	22.5	15.0	4.1	1.2	4.5	4.5	2.7	2.6	2.0
77	VR-12	P2b	SJ	B	29.5	300.0	3.5	22.0	3.0	21.0	425.0	27.0	107.0	2.6	242.0	9.5	23.0	15.5	3.9	1.2	4.5	4.5	2.7	2.7	2.0
78	VR85-3S	P2b	SJ	L	30.0	310.0	18.0	25.0	14.0	21.0	425.0	27.3	106.0	2.7	253.0	9.9	23.4	15.4	3.9	1.2	4.4	4.4	2.7	2.7	1.9
79	VR75F	P2b	SJ	M	30.0	290.0	30.0	26.0	24.0	20.0	418.0	27.0	104.0	2.6	245.0	10.0	23.0	15.0	3.9	1.3	4.5	4.4	2.7	2.7	1.9
80	VR75HR	P2c	DPJ	M	31.0	295.0	17.0	22.0	11.0	26.8	387.0	34.5	141.0	3.8	320.0	13.5	31.0	21.0	5.2	1.5	5.6	5.7	3.4	3.4	2.5
81	VR75H	P2c	SJ	M	31.0	297.0	22.0	25.0	13.0	19.3	420.0	28.5	107.0	2.7	250.0	10.0	23.0	15.0	4.3	1.2	4.5	4.6	2.8	2.8	2.1
82	VR67C	P2d	DJ	B	29.0	301.0	29.0	26.0	1.0	20.2	426.0	27.0	105.0	2.4	246.0	9.6	22.5	15.0	3.8	1.2	4.4	4.5	2.6	2.6	2.0
83	VR78-5AS	P2d	SJ	B	29.0	292.0	20.0	25.0	17.0	21.0	427.0	27.0	103.0	2.8	256.0	9.6	23.5	15.2	3.9	1.2	4.5	4.4	2.7	2.7	1.9
84	VR78-5BS	P2d	SJ	M	30.0	300.0	22.0	24.0	16.0	20.0	427.0	27.0	105.0	2.6	245.0	9.6	23.0	15.5	4.0	1.2	4.2	4.4	2.7	2.7	2.0
	post-Pucón fallout deposits																								
1	VR73S		SJ	M	30.0	253.0	49.0	26.0	24.0	14.3	458.0	22.0	81.0	1.8	190.0	7.1	17.5	10.8	3.1	1.0	3.4	3.5	2.2	2.2	1.5
2	VR-15H**				29.0	260.0	50.0	23.0	22.0	15.2	455.0	21.4	82.0	2.0	187.0	7.4	17.2	11.8	3.1	1.0	3.7	3.6	2.2	2.1	1.5
3	VR 15H**				29.0	255.0	85.0	26.0	35.0	13.8	465.0	20.6	75.0	1.9	185.0	7.0	17.2	11.3	3.0	1.0	3.4	3.4	2.1	2.0	1.6
4	VR 15I**				32.0	250.0	84.0	29.0	37.0	12.2	446.0	20.3	73.0	2.2	173.0	7.1	18.0	12.0	3.1	1.0	3.4	3.4	2.1	2.0	1.4
5	VR 15J**				32.0	253.0	84.0	27.0	35.0	12.5	444.0	21.0	79.0	2.1	177.0	7.3	18.2	12.2	3.2	1.0	3.6	3.6	2.1	2.1	1.5

LEGEND

TYPES OF FRAGMENTS:
SJ = scoriaceous juvenile
PJ = pumiceous juvenile
DJ = dense juvenile
DPJ = dense prismatically-jointed fragment
DPJ* = dense or vesicular lava fragment chemically similar to DPJ
DL = dense lava fragment

SIZES:
M = multiple lapilli fragments
L = single lapilli fragment
B = bomb or block

** = not sampled by the author

Appendix 3.6: Some selected ratios of whole-rock major and trace elements of samples of the Pucón Ignimbrite, and pre and post-Pucón deposits. (See Appendix 3.4 for footnote explanations).

	sample	unit	type	K/La	Sr/La	P/La	Zr/La	La/Yb	La/Sm	La/Dy	Dy/Yb	Ba/Nb	K/Nb	Sr/Nb	La/Nb	Zr/Nb	Sr/Ce	Sr/Nd	Sr/Y	Ti/Zr	Ti/Nb	Sc/Y	V/Ti	Zr/Y	Nb/Y	1000Eu/Ti
	pre-Pucón																									
1	VR113-6P		PJ	781.0	18.9	91.8	11.2	4.1	2.7	2.5	1.6	93.6	2908.0	70.2	3.7	41.7	7.9	12.2	7.8	33.2	1382.6	0.4	0.0	4.6	0.1	0.3
2	VR119		DL	746.1	44.4	104.9	11.2	3.3	2.3	2.1	1.6	98.0	2835.0	168.8	3.8	42.4	18.8	27.1	14.8	66.3	2809.1	1.1	0.0	3.7	0.1	0.2
3	VR114		DL	756.9	43.7	105.2	11.2	3.5	2.4	2.1	1.6	101.2	2876.3	166.0	3.8	42.4	18.0	26.4	15.4	65.9	2793.4	1.1	0.0	3.9	0.1	0.2
	Pucón																									
1	VR 73G	A	SJ	750.4	46.4	110.7	11.0	3.5	2.2	2.1	1.7	91.9	2626.6	162.3	3.5	38.5	19.6	29.1	15.6	71.0	2729.5	1.1	0.0	3.7	0.1	0.2
2	VR113-7a	A	SJ	726.7	44.9	107.2	11.1	3.4	2.4	2.1	1.6	104.2	2846.3	175.8	3.9	43.3	18.8	27.2	15.6	69.4	3008.0	1.1	0.0	3.9	0.1	0.2
3	VR 73J	P1a	DJ	771.9	46.2	112.5	11.4	3.3	2.2	2.0	1.6	106.5	3020.5	180.9	3.9	44.8	18.9	28.7	15.1	68.7	3074.8	1.1	0.0	3.7	0.1	0.2
4	VR 73Kc	P1a	DJ	724.1	43.1	104.3	10.9	3.6	2.4	2.1	1.7	104.2	2896.3	172.5	4.0	43.8	18.0	27.6	14.8	66.6	2913.2	1.1	0.0	3.8	0.1	0.2
5	VR97-3BD	P1a	DJ	756.2	45.2	102.9	11.2	3.4	2.4	2.1	1.6	108.7	3057.8	182.6	4.0	45.2	18.0	27.1	15.1	67.8	3065.6	1.1	0.0	3.7	0.1	0.2
6	VR112aD	P1a	DJ	738.0	44.4	106.3	10.9	3.5	2.5	2.2	1.6	96.9	2668.1	160.4	3.6	39.2	18.6	26.9	15.4	69.0	2706.7	1.1	0.0	3.8	0.1	0.2
7	VR 73JN	P1a	DJ	689.1	43.3	100.9	10.8	3.5	2.2	2.1	1.7	92.3	2544.5	160.0	3.7	40.0	18.1	26.8	15.1	68.6	2744.7	1.1	0.0	3.8	0.1	0.2
8	VR115-9P	P1a	DPJ	739.9	43.5	104.1	10.9	3.4	2.3	2.2	1.6	97.7	2731.9	160.8	3.7	40.4	18.2	27.1	14.7	67.0	2707.0	1.1	0.0	3.7	0.1	0.2
9	VR97-3AP	P1a	DPJ	758.1	24.4	97.5	11.0	3.9	2.7	2.5	1.6	110.0	3292.3	106.0	4.3	47.7	10.5	15.5	9.4	43.7	2086.8	0.6	0.0	4.2	0.1	0.2
10	VR113-9P	P1a	DPJ	763.6	24.1	100.4	11.1	3.9	2.5	2.4	1.6	106.6	3054.5	96.3	4.0	44.2	10.2	15.3	9.4	43.5	1922.2	0.6	0.0	4.3	0.1	0.2
11	VR73JP	P1a	DPJ	806.4	20.0	103.4	12.1	4.0	2.7	2.5	1.6	109.5	3023.9	75.0	3.8	45.5	8.3	12.7	7.7	31.5	1433.1	0.5	0.0	4.7	0.1	0.3
12	VR 73Ic	P1a	DPJ	779.8	21.6	98.4	11.6	4.0	2.5	2.4	1.7	89.6	2712.4	75.2	3.5	40.2	9.0	13.6	8.2	36.4	1462.6	0.5	0.0	4.4	0.1	0.2
13	VR 73JR	P1a	DPJ	734.7	26.8	96.6	11.1	3.9	2.5	2.4	1.7	100.6	2857.1	104.2	3.9	43.3	11.4	17.0	10.3	45.7	1980.1	0.7	0.0	4.3	0.1	0.2
14	VR 73JV	P1a	DPJ	756.4	27.1	94.7	11.4	3.7	2.5	2.3	1.6	93.4	2747.1	98.4	3.6	41.6	11.5	17.8	10.1	42.4	1763.4	0.7	0.0	4.3	0.1	0.2
15	VR115-9D	P1a	DPJ	760.9	21.0	100.0	11.2	4.0	2.7	2.5	1.6	100.5	2989.1	82.6	3.9	44.0	9.0	13.3	8.3	35.8	1576.4	0.5	0.0	4.4	0.1	0.3
16	VR 73Ie	P1a	DPJ*	767.5	25.2	105.4	11.3	4.1	2.5	2.3	1.8	97.4	2890.5	95.1	3.8	42.6	10.8	15.9	9.6	44.2	1884.9	0.6	0.0	4.3	0.1	0.2
17	VR115-9	P1a	DL	661.8	66.7	108.8	11.2	3.1	2.1	1.8	1.7	105.7	2836.3	285.7	4.3	47.9	28.6	40.0	20.4	82.9	3968.5	1.7	0.0	3.4	0.1	0.2
18	VR-73Ib	P1a	SJ	763.0	46.0	109.9	11.5	3.4	2.4	2.0	1.7	87.1	2479.8	149.6	3.3	37.5	18.6	27.7	15.5	68.8	2579.6	1.2	0.0	3.9	0.1	0.2
19	VR73IB	P1a	SJ	711.9	43.8	105.0	10.7	3.5	2.3	2.1	1.6	102.1	2818.0	173.3	4.0	42.5	18.1	27.7	15.1	71.2	3027.8	1.1	0.0	3.7	0.1	0.2
20	VR 73Kb	P1a	SJ	747.1	45.2	108.9	11.1	3.5	2.3	2.1	1.7	102.1	2863.8	173.3	3.8	42.5	18.1	28.7	15.1	70.9	3014.9	1.1	0.0	3.7	0.1	0.2
21	VR73LB	P1a	SJ	731.5	44.3	106.6	11.2	3.5	2.3	2.1	1.7	103.8	2644.5	160.0	3.6	40.4	17.7	28.7	15.1	68.4	2761.1	1.2	0.0	3.8	0.1	0.2
22	VR112cS	P1a	SJ	729.0	47.0	101.9	11.2	3.5	2.4	2.1	1.6	92.3	2523.4	162.7	3.5	38.8	19.7	28.2	16.3	70.7	2745.0	1.2	0.0	3.9	0.1	0.2
23	VR 73Il	P1a	SJ	710.9	43.7	102.8	11.1	3.4	2.2	2.0	1.7	92.3	2597.7	159.6	3.7	40.4	18.0	25.9	14.8	69.7	2813.9	1.1	0.0	3.8	0.1	0.2
24	VR 73Kl	P1a	SJ	713.7	45.1	109.3	11.7	3.3	2.3	2.0	1.7	98.0	2626.4	166.0	3.7	43.2	18.9	27.7	14.8	67.8	2929.1	1.1	0.0	3.9	0.1	0.2
25	VR 73Ll	P1a	SJ	674.9	41.8	105.2	10.6	3.5	2.3	2.1	1.6	100.0	2699.7	167.2	4.0	42.4	17.8	27.0	14.7	69.8	2960.5	1.1	0.0	3.7	0.1	0.2
26	VR64AC	P1b	DJ	698.9	43.5	107.6	10.6	3.5	2.3	2.1	1.7	102.0	2711.8	168.8	3.9	41.2	18.3	27.2	15.3	69.0	2842.0	1.1	0.0	3.7	0.1	0.2
27	VR73K=CR1	P1b	DJ	742.8	43.7	105.7	10.8	3.4	2.4	2.1	1.6	104.2	2940.4	172.9	4.0	42.9	18.0	27.7	14.8	69.3	2972.8	1.1	0.0	3.7	0.1	0.2
28	VR73N1R	P1b	DPJ	717.5	38.7	107.8	11.0	3.5	2.2	2.1	1.7	105.8	2897.7	156.2	4.0	44.6	16.2	23.9	13.5	60.8	2713.5	1.0	0.0	3.9	0.1	0.2
29	VR73NP	P1b	DPJ*	773.5	44.2	118.3	11.7	3.4	2.4	2.1	1.6	104.0	2846.6	162.8	3.7	43.2	18.1	27.5	14.7	65.3	2820.6	1.1	0.0	3.9	0.1	0.2
30	VR-73Mb	P1b	SJ	760.4	46.7	112.2	11.3	3.4	2.3	2.0	1.7	82.8	2333.5	143.4	3.1	34.8	18.9	28.7	15.7	70.2	2445.6	1.2	0.0	3.8	0.1	0.2
31	VR73N2b	P1b	SJ	712.6	44.1	105.1	10.7	3.7	2.3	2.2	1.7	96.0	2707.7	167.6	3.8	40.8	18.2	28.9	15.5	70.1	2861.6	1.1	0.0	3.8	0.1	0.2
32	VR73N3	P1b	SJ	706.9	43.6	104.3	10.6	3.6	2.4	2.1	1.7	102.1	2827.6	174.6	4.0	42.5	18.2	28.9	15.5	69.1	2938.4	1.2	0.0	3.8	0.1	0.2
33	VR73P	P1b	SJ	697.3	44.4	100.8	10.7	3.6	2.4	2.1	1.7	100.0	2760.0	175.8	4.0	42.5	18.0	29.1	15.3	69.8	2964.8	1.1	0.0	3.7	0.1	0.2
34	VR-78-2b	P1b	SJ	764.4	45.2	108.8	11.0	3.5	2.4	2.1	1.6	85.7	2511.6	148.6	3.3	36.1	19.3	28.3	15.7	70.4	2539.2	1.1	0.0	3.8	0.1	0.2
35	VR58-0	P1b	SJ	717.6	46.7	111.3	11.4	3.5	2.2	2.1	1.7	94.2	2484.0	161.5	3.5	39.6	19.5	29.0	15.6	68.5	2713.7	1.2	0.0	3.8	0.1	0.2
36	VR58-1A	P1b	SJ	704.3	47.1	112.1	11.1	3.6	2.3	2.1	1.7	102.1	2697.1	180.4	3.8	42.6	19.7	29.2	16.3	69.3	2947.3	1.2	0.0	3.8	0.1	0.2
37	VR64AB	P1b	SJ	717.1	46.7	106.4	11.1	3.4	2.3	2.1	1.7	98.3	2689.1	175.0	3.8	41.7	19.1	29.0	16.0	69.9	2912.9	1.2	0.0	3.8	0.1	0.2
38	VR73M	P1b	SJ	688.6	44.4	105.4	10.5	3.5	2.5	2.1	1.6	100.0	2725.8	175.8	4.0	41.7	18.8	29.1	15.6	70.0	2915.3	1.1	0.0	3.7	0.1	0.2
39	VR73N1	P1b	SJ	728.8	46.4	111.6	11.6	3.3	2.2	2.0	1.7	100.0	2677.3	170.6	3.7	42.4	19.0	28.2	15.2	70.3	2985.9	1.2	0.0	3.8	0.1	0.2
40	VR57-2C	P1c	DJ	723.7	45.1	106.8	11.0	3.4	2.3	2.1	1.6	96.1	2667.9	166.3	3.7	40.4	18.4	28.3	15.8	69.2	2796.0	1.2	0.0	3.8	0.1	0.2
41	VR57-2B	P1c	DJ	567.9	63.3	102.5	7.3	5.2	3.2	3.1	1.7	107.0	2782.9	310.0	4.9	36.0	27.6	45.6	32.6	82.5	2969.6	1.5	0.0	3.8	0.1	0.2
42	VR57-2D	P1c	DPJ	724.1	44.1	105.5	10.8	3.5	2.3	2.1	1.6	109.1	2991.0	182.2	4.1	44.8	17.8	27.9	15.4	68.6	3070.8	1.1	0.0	3.8	0.1	0.2
43	VR57-1	P1c	DPJ	744.4	25.0	100.1	10.9	3.8	2.6	2.4	1.6	103.3	3060.2	102.8	4.1	45.0	10.3	16.1	9.7	45.0	2027.2	0.6	0.0	4.3	0.1	0.2

	sample	unit	type	K/La	Sr/La	P/La	Zr/La	La/Yb	La/Sm	La/Dy	Dy/Yb	Ba/Nb	K/Nb	Sr/Nb	La/Nb	Zr/Nb	Sr/Ce	Sr/Nd	Sr/Y	Ti/Zr	Ti/Nb	Sc/Y	V/Ti	Zr/Y	Nb/Y	1000Eu/Ti
44	VR57-1B	P1c	SJ	706.3	47.0	103.5	10.3	3.6	2.3	2.2	1.6	102.6	2855.9	190.0	4.0	41.7	19.0	30.1	17.3	72.6	3028.4	1.2	0.0	3.8	0.1	0.2
45	VR57-2A	P1c	SJ	717.9	45.1	107.2	10.7	3.5	2.4	2.1	1.7	102.1	2871.4	180.4	4.0	43.0	18.8	28.3	15.9	71.5	3072.0	1.2	0.0	3.8	0.1	0.2
46	VR58-1B	P2a	DJ	742.5	44.7	111.6	11.4	3.4	2.3	2.0	1.7	100.0	2633.8	158.5	3.5	40.4	18.7	28.0	15.0	67.9	2739.8	1.1	0.0	3.8	0.1	0.2
47	VR78-3AP	P2a	DPJ	776.1	44.0	106.7	11.3	3.5	2.4	2.1	1.6	104.2	3039.6	172.5	3.9	44.2	18.4	27.2	15.3	66.6	2943.4	1.1	0.0	3.9	0.1	0.2
48	VR73Q2	P2a	DPJ	720.1	26.6	99.2	10.8	4.0	2.5	2.4	1.7	97.3	2822.2	104.1	3.9	42.4	11.2	17.1	10.4	48.8	2070.4	0.7	0.0	4.2	0.1	0.2
49	VR113-11P	P2a	DPJ	808.5	13.3	46.8	11.5	4.5	3.1	3.0	1.5	103.7	3219.1	53.1	4.0	45.9	5.8	9.6	6.2	18.9	867.6	0.4	0.0	5.4	0.1	0.3
50	VR85-7P	P2a	DPJ	666.9	45.5	109.0	11.0	3.4	2.4	2.1	1.6	85.9	2272.5	155.2	3.4	37.4	19.0	27.9	15.5	69.4	2594.7	1.3	0.0	3.7	0.1	0.2
51	VR75EV	P2a	DPJ	739.5	31.5	101.6	10.8	3.8	2.5	2.4	1.6	100.0	2888.5	123.1	3.9	42.2	12.7	20.7	11.9	60.1	2537.0	0.9	0.0	4.1	0.1	0.2
52	VR75ER	P2a	DPJ	686.0	34.0	108.6	9.4	4.2	2.7	2.5	1.7	94.7	2522.2	125.0	3.7	34.7	14.2	23.6	13.9	69.3	2405.0	1.0	0.0	3.9	0.1	0.2
53	VR85-5P	P2a	DPJ	897.7	8.0	21.5	12.1	4.5	3.3	3.1	1.5	105.5	3436.4	30.8	3.8	46.4	3.5	6.0	3.8	9.7	451.2	0.2	0.0	5.7	0.1	0.5
54	VR75EP	P2a	DPJ	687.8	33.1	130.0	9.8	4.3	2.5	2.5	1.7	104.8	2751.4	132.3	4.0	39.0	14.4	22.8	13.4	63.3	2469.2	0.9	0.0	4.0	0.1	0.2
55	VR78-3AD	P2a	DPJ*	756.2	43.4	106.4	11.5	3.4	2.4	2.1	1.6	100.0	2733.8	156.9	3.6	41.5	18.1	26.7	14.7	65.2	2708.9	1.1	0.0	3.9	0.1	0.2
56	VR57-4A	P2a	SJ	840.7	48.5	120.6	12.3	3.6	2.4	2.1	1.7	101.9	2708.9	156.3	3.2	39.6	19.2	30.8	16.2	65.6	2601.0	1.2	0.0	4.1	0.1	0.2
57	VR57-4B	P2a	SJ	731.9	47.6	112.1	11.8	3.3	2.3	1.9	1.7	94.5	2395.3	155.6	3.3	38.5	19.0	28.5	15.6	67.0	2583.8	1.2	0.0	3.9	0.1	0.2
58	VR57-4C	P2a	SJ	710.2	44.6	106.1	11.3	3.5	2.2	2.0	1.7	93.1	2453.5	154.2	3.5	38.9	17.7	28.8	15.1	65.2	2537.4	1.2	0.0	3.8	0.1	0.2
59	VR63A	P2a	SJ	747.4	44.8	101.7	11.0	3.4	2.3	2.0	1.7	98.0	2810.1	168.4	3.8	41.2	18.7	28.1	15.6	70.1	2888.9	1.1	0.0	3.8	0.1	0.2
60	VR78-3AS	P2a	SJ	761.9	47.3	107.5	11.1	3.4	2.5	2.1	1.6	94.8	2712.3	168.4	3.6	39.6	20.0	29.6	16.2	70.0	2770.9	1.2	0.0	3.8	0.1	0.2
61	VR73Q2l	P2a	SJ	698.8	44.0	113.1	11.6	3.6	2.3	2.1	1.7	90.7	2433.0	153.3	3.5	40.4	18.8	28.6	15.1	68.1	2748.1	1.1	0.0	4.0	0.1	0.2
62	VR-79-1b	P2a	SJ	728.2	45.4	106.9	10.7	3.7	2.5	2.2	1.7	101.2	2744.8	171.2	3.8	40.4	18.5	28.9	16.8	70.2	2835.0	1.0	0.0	4.0	0.1	0.2
63	VR-79-3b	P2a	SJ	703.7	43.7	108.3	10.6	3.7	2.4	2.2	1.7	93.7	2528.0	157.0	3.6	38.1	18.8	27.5	15.8	71.2	2716.2	1.1	0.0	3.8	0.1	0.2
64	VR69	P2a	SJ	759.2	47.1	106.8	11.1	3.5	2.3	2.1	1.7	84.5	2460.8	152.8	3.2	35.9	19.3	29.5	16.4	69.1	2479.7	1.1	0.0	3.9	0.1	0.2
65	VR85-5S	P2a	SJ	753.2	44.7	101.3	11.1	3.6	2.4	2.1	1.7	89.1	2601.8	154.5	3.5	38.2	19.3	26.6	15.6	69.2	2643.6	1.1	0.0	3.8	0.1	0.2
66	VR85-8S	P2a	SJ	756.8	45.1	106.4	11.2	3.4	2.5	2.1	1.6	94.1	2634.7	157.0	3.5	38.9	18.8	27.2	15.4	68.8	2677.0	1.1	0.0	3.8	0.1	0.2
67	VR75A	P2a	SJ	654.3	42.8	101.5	10.6	3.6	2.4	2.2	1.6	100.0	2516.6	164.6	3.8	40.8	18.6	29.5	15.0	70.9	2889.2	1.1	0.0	3.7	0.1	0.2
68	VR75E	P2a	SJ	696.7	42.0	109.1	10.7	3.7	2.6	2.3	1.6	102.0	2786.8	168.0	4.0	42.8	18.3	28.0	15.1	68.9	2946.9	1.2	0.0	3.8	0.1	0.2
69	VR85-9S	P2a	SJ	750.8	46.3	102.2	11.2	3.5	2.5	2.2	1.6	97.4	2663.3	164.2	3.5	39.6	19.3	28.2	16.1	68.5	2715.3	1.1	0.0	3.9	0.1	0.2
70	VR85-4D	P2b	DJ	741.2	42.9	101.9	10.9	3.7	2.5	2.3	1.6	101.9	2769.2	160.4	3.7	40.8	17.9	27.2	15.6	67.5	2749.7	1.1	0.0	4.0	0.1	0.2
71	VR85-3D	P2b	DJ	736.0	44.1	103.5	11.0	3.6	2.4	2.3	1.6	91.1	2549.7	152.9	3.5	38.2	18.3	27.4	15.9	68.4	2612.1	1.1	0.0	4.0	0.1	0.2
72	VR12P	P2b	DPJ	678.1	33.9	164.3	10.2	4.2	2.6	2.4	1.7	88.9	2354.4	117.8	3.5	35.3	14.6	21.2	13.7	76.1	2683.8	1.0	0.0	4.1	0.1	0.2
73	VR85-4P	P2b	DPJ	724.5	40.2	108.2	11.1	3.5	2.3	2.2	1.6	83.9	2360.3	131.0	3.3	36.1	16.9	24.9	13.8	68.1	2459.9	1.1	0.0	3.8	0.1	0.2
74	VR85-3P	P2b	DPJ	704.0	33.7	113.9	10.3	4.1	2.7	2.4	1.7	94.1	2546.9	122.1	3.6	37.4	13.8	21.6	13.3	72.0	2688.2	1.0	0.0	4.1	0.1	0.2
75	VR-6.2	P2b	SJ	770.6	43.8	103.6	11.0	3.6	2.4	2.2	1.7	83.4	2577.6	146.6	3.3	36.9	18.1	27.6	15.7	68.4	2523.3	1.1	0.0	4.0	0.1	0.2
76	VR6-3	P2b	SJ	754.9	46.7	113.4	11.6	3.5	2.2	2.0	1.7	92.8	2620.9	162.3	3.5	40.4	19.1	28.7	15.9	67.0	2703.9	1.1	0.0	4.0	0.1	0.2
77	VR-12	P2b	SJ	776.0	44.7	105.5	11.3	3.6	2.4	2.1	1.7	93.1	2835.4	163.5	3.7	41.2	18.5	27.4	15.7	67.6	2783.9	1.1	0.0	4.0	0.1	0.2
78	VR85-3S	P2b	SJ	723.3	42.9	106.2	10.7	3.7	2.5	2.3	1.6	95.5	2702.2	160.4	3.7	40.0	18.2	27.6	15.6	69.2	2768.3	1.1	0.0	3.9	0.1	0.2
79	VR75F	P2b	SJ	710.9	41.8	101.2	10.4	3.8	2.6	2.3	1.6	94.2	2734.2	160.8	3.8	40.0	18.2	27.9	15.5	68.5	2741.1	1.1	0.0	3.9	0.1	0.2
80	VR75HR	P2c	DPJ	675.6	28.7	103.4	10.4	4.0	2.6	2.4	1.7	85.3	2432.2	103.2	3.6	37.6	12.5	18.4	11.2	58.6	2203.5	0.9	0.0	4.1	0.1	0.2
81	VR75H	P2c	SJ	664.1	42.0	106.1	10.7	3.6	2.4	2.2	1.6	92.6	2459.5	155.6	3.7	39.6	18.3	28.0	14.7	68.1	2697.9	1.1	0.0	3.8	0.1	0.2
82	VR67C	P2d	DJ	723.9	44.4	104.3	10.9	3.7	2.5	2.1	1.7	102.5	2895.7	177.5	4.0	43.8	18.9	28.4	15.8	68.9	3012.2	1.1	0.0	3.9	0.1	0.2
83	VR78-5AS	P2d	SJ	732.8	44.5	104.3	10.7	3.6	2.5	2.2	1.6	91.4	2512.3	152.5	3.4	36.8	18.2	28.1	15.8	70.8	2604.0	1.1	0.0	3.8	0.1	0.2
84	VR78-5BS	P2d	SJ	727.7	44.5	104.8	10.9	3.6	2.4	2.2	1.6	94.2	2686.9	164.2	3.7	40.4	18.6	27.5	15.8	69.8	2818.1	1.1	0.0	3.9	0.1	0.2
	post-Pucón fallout deposits																									
1	VR73S		SJ	713.2	64.5	116.8	11.4	3.3	2.3	2.0	1.6	105.6	2813.3	254.4	3.9	45.0	26.2	42.4	20.8	74.0	3330.6	1.4	0.0	3.7	0.1	0.2
2	VR-15H**			718.0	61.5	106.2	11.1	3.5	2.4	2.1	1.7	93.5	2656.5	227.5	3.7	41.0	26.5	38.6	21.3	73.1	2997.5	1.4	0.0	3.8	0.1	0.2
3	VR 15H**			714.0	66.4	106.3	10.7	3.5	2.3	2.1	1.7	97.4	2630.6	244.7	3.7	39.5	27.0	41.2	22.6	77.0	3039.4	1.4	0.0	3.6	0.1	0.2
4	VR 15I**			624.7	62.8	105.3	10.3	3.6	2.3	2.1	1.7	78.6	2016.2	202.7	3.2	33.2	24.8	37.2	22.0	78.6	2609.6	1.6	0.0	3.6	0.1	0.2
5	VR 15J**			609.5	60.8	108.8	10.8	3.6	2.3	2.0	1.8	84.3	2118.8	211.4	3.5	37.6	24.4	36.4	21.1	74.4	2800.2	1.5	0.0	3.8	0.1	0.2

CHAPTER 4 The role of fluids in the basaltic andesitic Pucón eruption (3.6 ka BP, Villarrica Volcano, Chile)

4.1 INTRODUCTION

The Pucón eruption is the largest Holocene eruption of Villarrica Volcano, one of the most active volcanoes of the Southern Andes (Lara, 2004a). The deposit architecture and eruption chronology of the Pucón Ignimbrite is already well constrained (Chapter 2) and establish the occurrence of several eruptive phases, involving the emission of pyroclastic currents with contrasting intensities, timings and responses to topography, that generated a deposit with highly variable scoria/lithic ratios, distributions and facies variations. A detailed study of the deposits including componentry, textural and chemical determinations, allowed then to constrain the dynamics of the eruption involving episodes of vent erosion, changes in fragmentation level, caldera collapse and chemical evolution of the magma body (Chapter 3).

However, the remaining unclear role of phreatomagmatism in the eruption merits a separated section for a detailed analysis involving specific petrological tools to assess this objective.

Opposed views about the role of fluids in the Pucón eruption has been proposed by different authors. López-Escobar & Moreno (1994) suggested that the most differentiated and volatile-rich levels of a chemically stratified and not-completely-emptied magma chamber were emitted during the Licán and Pucón eruptions, representing a repeated cycle of chemically-evolved and explosive eruptions followed by the eruption of the lower and less differentiated levels (higher Al_2O_3/CaO and major element/MgO ratios than lavas of similar age).

In contrast, Clavero (1996) suggested that after a precursor strombolian fallout, the injection of basaltic magma in the chamber caused the violent ejection of abundant juvenile material which suddenly melted the ice cover and magma-water interaction took place. Marked vulcanian and phreatomagmatic characteristics of the Pucón Ignimbrite are suggested by a high lithic content, local imbrication, gradation, vesicles (Clavero & Moreno, 1994) and by the presence cauliflower bombs (Moreno *et al.*, 1994).

Oxygen isotope ($\delta^{18}O$) data in the matrix of basaltic andesite pyroclasts (McCurry *et al*., 2001, 2004), indicates limited meteoric water (a maximum of 4%) interaction with the pre Pucón magma. Higher δ18O values found in the yellowish rind of some basaltic andesite pyroclasts can be interpreted as a result of palagonitisation (Cuadros *et al.*, 1999). Even if the homogenization in phenocryst melt inclusions was not systematically achieved, McCurry *et al.* (2004) suggested that the most homogeneous melt inclusions show “bulk-rock-like” analyses, high sulphur (1400 to 5000 ppm) and low electron microprobe (EMP) totals (96-98%).

This study attempts to constrain the role of external fluids in the explosivity of the magma and trigger of the eruption by means of a new and different approach combining density/vesicularity measurements of scorias together with direct volatile measurements (S, Cl, F) of the matrix glasses by probe. Using the most vesicular expanded and the densest juvenile scoriae of each of five different stratigraphic levels comprising the whole sequence, this method allowed to test whether the dense clasts have higher volatile

contents than the more vesiculated ones, suggesting quenching at depth by ground water (e.g. Houghton & Wilson, 1989). This is because, in the case of phreatomagmatism, the dense clasts have retained and quenched the high abundances of volatiles, whereas the vesiculated ones have lost them. On the contrary, in the case of a magmatic pure eruption, all clasts (vesiculated and dense, if present) should have the same volatile content (e.g. Thordarson *et al.*, 1996). Alternative explanations can explain the presence of dense clasts in this case, as for example the bubble coalescence.

Additional density/vesicularity determinations as a function of the stratigraphy and as a function of size together with microlite measurements and major glass composition helped to reach the objectives.

4.2 THE EVOLUTION AND DYNAMICS OF THE PUCÓN ERUPTION

The data presented in two previous chapters allowed placing many constraints on the eruptive evolution and mechanisms of the Pucón eruption, which are summarised below.

The Pucón Ignimbrite (3.6 ka BP, 3 km^3) was emitted by the largest Holocene eruption of the Villarrica volcano, one of the most active volcanoes of Southern Andes. Prior to the Pucón eruption, subglacial basaltic-andesitic to dacitic lava domes and/or flows were possibly present near or at the ice-capped volcano summit. The fragmentation of these lavas and domes at the onset of the Pucón eruption generated abundant dense prismatically-jointed (DPJ) clasts and dense ash shards that were incorporated by the Pucón products (~0.02 km^3).

After a long period of volcanic calm (~400 years) and with the summit exhibiting fumarolic activity, the Pucón eruption started with a violent strombolian or subplinian basaltic andesite scoria fallout phase (0.1 km^3 of magma, VEI = 3-4) under normal, open-conduit magmatic conditions. Vent erosion and conduit widening started during this phase, as suggested by the sudden appearance of DPJ fragments in the upper part of the basal scoria fall deposit.

The fallout phase was followed by a small base surge to the northern flank and then by a series of about ten powerful vulcanian explosions (0.14 km^3 of magma, 20% of the total volume). Each explosion (0.014 km^3) emptied the conduit and tapped into the main reservoir at depth. Following each discharge event, magma would have partially refilled the conduit prior to the next explosion. Explosive expansion of water caused erosion and pulverization on wall rock generating quantities of lithic debris that were incorporated into the pyroclastic flows (P1a) and progressive widening of the conduit gave place to the magmatic pyroclastic currents of P1b. The generated pyroclastic flows left thick (<15 m thick) and valley-confined deposits covering ~180 km^2 from western to northern flanks of the volcano up to 15 km from the present-day summit. A progressive deepening of the fragmentation level during P1 could increase the supply of altered fragments and decrease of fresh volcanics upwards through P1.

During a pause in explosive activity following phase P1, which was probably several weeks to months long, the P1 deposits cooled below the temperature necessary for charcoalization of wood (~200°C) and changes took place in the plumbing system of the volcano, including the replenishment by a more primitive, incompatible-rich magma batch from depth and/or slight contamination by basement granitoids. Vent erosion and widening all around the volcano, or at least in different and more extensive areas than during P1 phase, provided the P2 pyroclastic density currents of a new assemblage of basaltic-andesitic to rhyolitic lava fragments (at least 0.03 km^3).

During the second eruptive phase (P2) which probably lasted no more than a few days, voluminous pyroclastic flows and minor surges (0.2 km^3 of magma, 80% of the total volume) were deposited all around the volcano, covering ~530 km^2 and extending up to 21 km from the present-day summit, leaving thick sequences on valleys (<70 m thick) with an important deposition on interfluves (<5 m thick). The climactic phase represented an increase in the eruptive intensity and was characterised by the abrupt appeareance of a significant proportion of free clasts of basement granitoids, suggesting that very rapidly after the start of this phase the magma level dropped to within the granitoid basement, at a level lower than that during phase P1. This is probably explained by the high magma discharge rate, causing the fragmentation level of the magma to fall rapidly, probably accompanied by the climactic phase of caldera collapse. Granitoid fragments in P2 scoria include vesicle-bearing, actively disaggregating, partially melted examples, but also many angular, non-melted ones, showing that the granitoid was being actively mixed into the magma during eruption. The depth of granitoid basement could have been shallower towards the southern sector, thus allowing earlier contact of granitoids with magma, producing more abundant granitoids and xenocrysts. The pyroclastic flows of P2a are inferred to have had high velocities, with a turbulent, blast-like leading edge, that reached a broad extent all around the volcano and a highly sheared and erosive lower contact with its substrate.

Then, juvenile-rich high-concentration valley-confined pyroclastic flows were deposited from south to east of the volcano (P2b) and a major surge-forming phase (P2c) was emitted all around the volcano with an important deposition on slope environments (P2c). Eruption continued until the reservoir overpressure dropped below that necessary for explosive eruption. The Pucón eruption culminates with low-energy valley-confined pyroclastic flows emitted to a short extent to the northern flank (P2d) consistent with greatly decreased reservoir pressure. Immediately after the eruption, the ignimbrite surface was inundated by several lahar waves.

A new cycle of explosive activity started no more than a few rain seasons after the discharge of the final pyroclastic flow. The porphyric magma of the Chaimilla scoria fall deposit is interpreted as residual cumulates from Pucón magma, containing geochemical signals of both P1 and P2 components, indication that the magmatic chamber was not completely emptied during the Pucón eruption.

If the 2-km-diameter caldera was associated with the Pucón eruption at all, the evidence of a few time elapse between the Pucón and Chaimilla eruptions, suggest that the construction of the modern cone started very short after the caldera collapse associated with the Pucón eruption.

4.3 PARTICLE DENSITIES

Method

Three different methods were used to calculate the densities of the juvenile pyroclasts: (1) silicone sealing of scoriae, (2) water saturation of bombs, and (3) immersion of scoriae in glass beads (Appendix 4.1). The laboratory work of the two first methods was done by M. Mercier (undergraduate student 2004/2005) under the author's supervision. Silicone sealing was used to study the vertical variation of scoria density and the variation of density with size in the range 16-32 mm. This method avoided the problem of water infiltration into vesicles, but the samples ended up unusable for further purposes (Method 1, Appendix 4.1). The method of water saturation was used for 128 mm-sized bombs to explore the variation of density with size. This method allowed to avoid the problem of silicone contamination of the sample, but the disadvantage was that only the connected vesicles were filled with water, and large pores on the surface of the sample leaked immediately. This could have induced large errors and thus the method was only used for large bombs (Method 2, Appendix 4.1). The method of immersion in glass beads was used for scoriae of ~16 mm in diameter. It avoided the problem of water infiltration and left samples clean for further analysis. This method was extremely sensitive to the assumed bulk densities of the glass beads, which were therefore measured very carefully to obtain precise results (Method 3, Appendix 4.1). Clast density values were converted into vesicularity using measured values for the solids (i.e., vesicle-free) density (Appendix 4.2).

About 60 density measurements (on average) per stratigraphic level were done by silicone sealing in scoriae from the northern and southern type sections of the ignimbrite (7 levels in the composite section VR73+VR78 in the northern sector and 5 levels in VR85 in the southern sector, Table 4.2, Appendix 4.4). Ten samples from each of five stratigraphic layers (P1a, P1b, P2a FP, P2a FR and P2b) were chosen for density measurements by immersion in glass beads, trying to choose the five densest and the five lightest samples (perceived by hand). A 2σ precision was calculated from the 5 measurements performed per sample; propagation of errors was discarded since it seems to overestimate the real error (Table 4.1, Appendix 4.3). Figure 4.1 shows the results of the density measurements using the glass beads compared with those done by silicone sealing. Even if the mean densities using the method of the glass beads are in general slightly lower than those of the silicone sealing, both set of data overlap very well giving confidence in the methods.

Table 4.1: Mean density, vesicularity and microlite content of scoria lapilli (~16 mm diameter), from different stratigraphic levels of the Pucón Ignimbrite. Density measured by immersion of scorias in glass beads (Method 3 of Appendix 4.1). The complete set of density data measured by this method is shown in Appendix 4.3.

	sample	unit	Microlite content	Mean density	2 σ error*	2 σ error**	Vesicularity
			% vesic-free	g/ml	g/ml	g/ml	%
1	VR73J-L6	P1a	2	0.82	0.05	0.11	67
2	VR73J-D3	P1a	81	1.38	0.03	0.11	44
3	VR73P-L2	P1b	32	0.59	0.07	0.12	76
4	VR73P-D7	P1b	9	1.08	0.06	0.14	57
5	VR78-3A-L1	P2a	28	0.92	0.06	0.10	63
6	VR78-3A-D2	P2a	55	1.31	0.06	0.12	47
7	VR85-8-L4	P2a	98	0.99	0.02	0.08	60
8	VR85-8-D5	P2a	32/90	1.47	0.08	0.14	41
9	VR85-3-L3	P2b	31/97	0.97	0.04	0.13	61
10	VR85-3-D4	P2b	91	1.65	0.14	0.24	33
	mean			**1.12**	**0.08**	**0.13**	**55**

Microlite content measured by image analysis. Samples VR85-8-D5 and VR85-3-L3 are heterogeneous and the microlite contents correspond to their microlite-poor and microlite-rich zones, respectively.

Mean density of 5 measurements following the method of immersion of scorias in glass beads (Method 3 of Appendix 4.1).

* Standard deviation (2 σ) of the 5 density measurements.

** Density error (2 σ) calculated by propagation of errors.

Vesicularity was calculated from density measurements (Appendix 4.2).

Table 4.2: Mean density measured by silicone-sealing (Method 1 of Appendix 4.1) of scoria lapilli (16 mm fraction) covering different stratigraphic levels of the Pucón Ignimbrite. Mean densities measured by water saturation (Method 2 of Appendix 4.1) of scoria bombs (128 mm fraction) are also included. The complete set of density data measured by these methods is shown in Appendix 4.4.

	unit	sample	size	Density [1]	Error vol [2]	1σ st dev [3]
				g/ml	%	g/ml
1	P1a	VR 73 I	16 mm	1,1	22	0,2
2	P1a	VR 73 L	16 mm	0,9	17	0,3
3	P1b	VR73N2	128 mm	1,3		1,3
4	P1b	VR 73 P	16 mm	1,0	11	0,2
5	P2a	VR 78 3A	16 mm	1,1	19	0,2
6	P2a	VR 78 3B-C	16 mm	1,0	23	0,2
7	P2a	VR 85 8	16 mm	1,3	13	0,3
8	P2a	VR 85 6	16 mm	1,2	23	0,3
9	P2a	VR 85 5	16 mm	1,2	15	0,2
10	P2b	VR 85 4	16 mm	1,3	13	0,2
11	P2b	VR 85 3	16 mm	1,4	16	0,3
12	P2b	VR12	16 mm	1,1	13	0,2
13	P2b	VR12	128 mm	1,3		0,3
14	P2d	VR 78 5A	16 mm	1,2	17	0,2
15	P2d	VR 78 5B	16 mm	1,3	20	0,3

[1] Density of the scoria lapilli (16 mm fraction) was measured following the method of silicone-sealing of the scorias (Method 1 of Appendix 4.1). Density of the scoria bombs (128 mm fraction) was measured following the method of water saturation of bombs (Method 2 of Appendix 4.1).

[2] The error associated to the balance is negligible and the error of the volume varies according to the sample volume (vol, in ml) as:

error (%) = 1 (ml) / vol (ml) * 100 (precision of the test tube = 1 ml)

[3] The standard deviation (1σ) of the density measurements of scorias from every stratigraphic layer (about 60 scorias measured per layer).

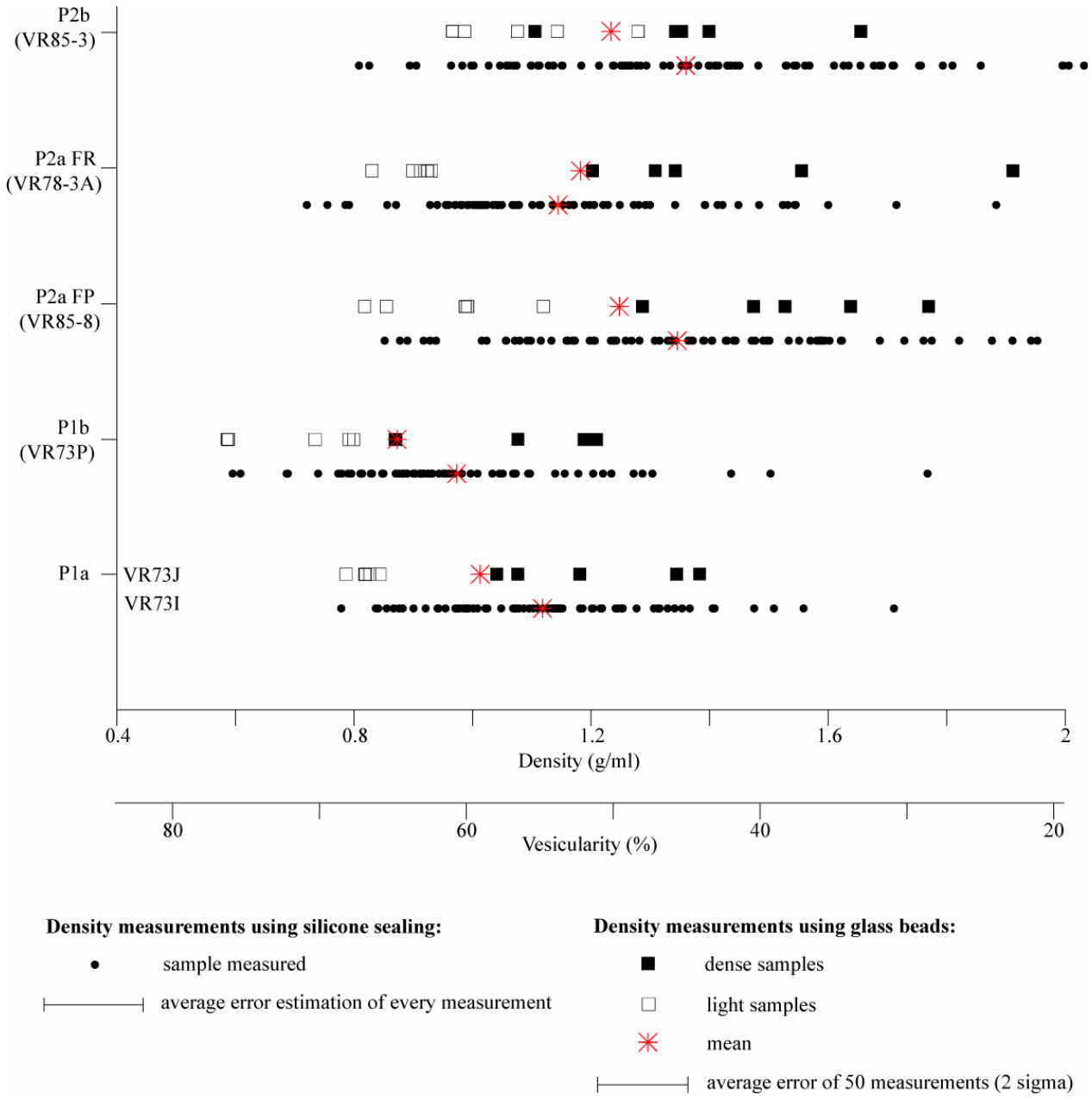

Figure 4.1: Scoria densities using glass beads (Method 3, Appendix 4.1) compared to the density measurements using silicone sealing (Method 1, Appendix 4.1). Vesicularities are also shown (converted from densities, Appendix 4.2).

4.3.1 Variation of density with size

The two juvenile-rich subunits, P1b and P2b, were chosen to evaluate the variation of clast density with size. Two size fractions were chosen for the comparison, 16 mm (lapilli) and 128 mm (bombs). Even if the number of bombs measured is low, their densities are slightly higher than those of the lapilli (Figure 4.2). Vesicularity therefore seems to increase with decreasing particle size.

By inspection, P2 scoriae containing partially-melted granitoids seem to be denser than those without them.

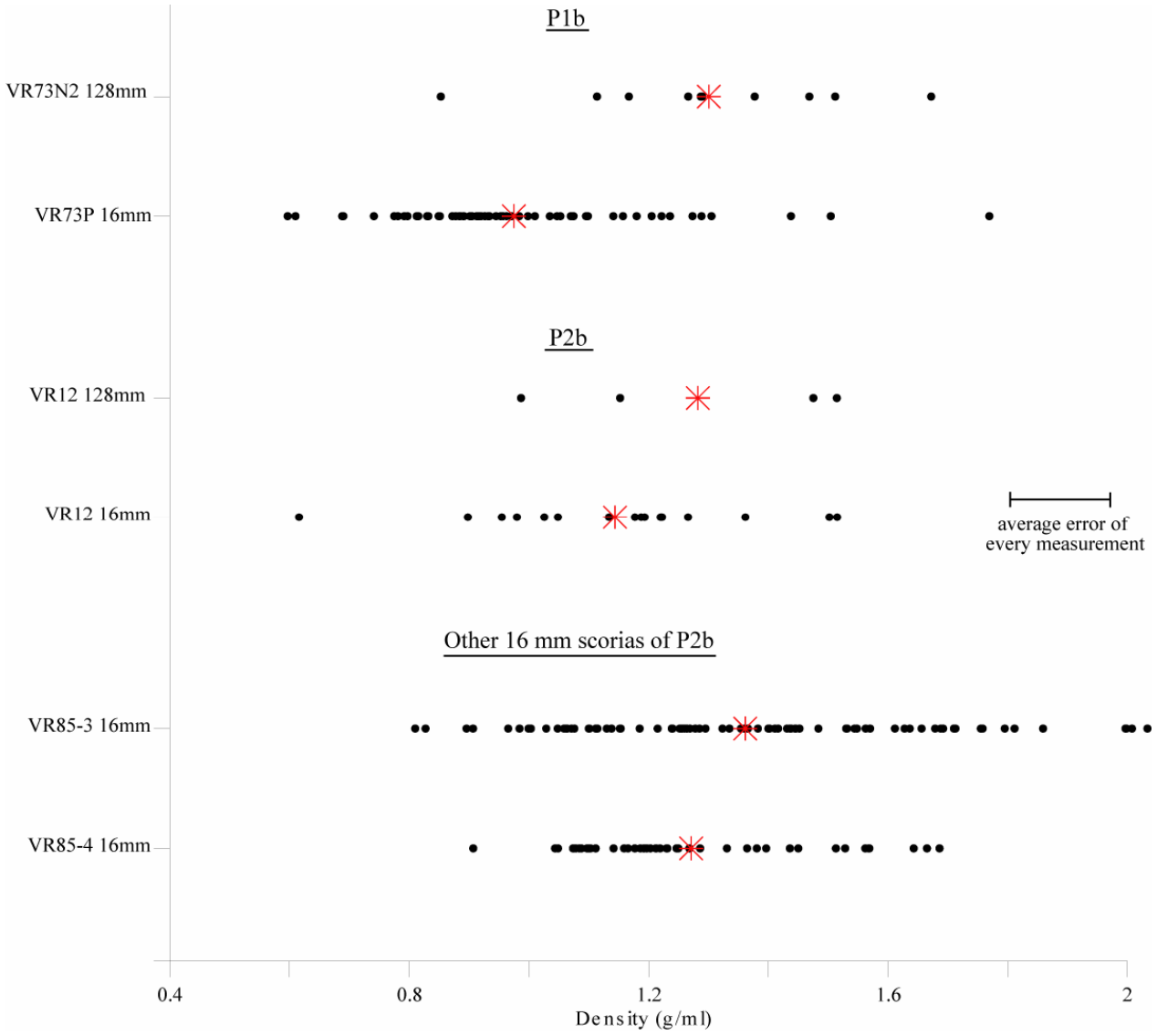

Figure 4.2: Scoria density variation with size in the two main black juvenile-rich levels P1b and P2b. Measurements carried out using the silicone-sealing method for the lapilli scorias and water-displacement method for the bombs.

4.3.2 Variation of density with stratigraphic height

The range of scoria densities measured by silicone sealing is 0.6 to 2.1 g/ml with an average around 1.2 g/ml (Figures 4.3 and 4.4, Table 4.2, Appendix 4.4). The glass-bead method gave 0.6 to 1.9 g/ml with an average of 1.1 g/ml (Figure 4.1, Table 4.1, Appendix 4.3). The two methods therefore gave very similar results. Since we consider the glass-bead method to be more accurate, this provides confidence in the more numerous measurements carried out by water immersion. Figures 4.3 and 4.4 show the variation of clast densities with height in two sections. The principal conclusions to be drawn from these plots are as follows.

- On average, P2 scoriae are denser than P1 scoriae (Figures 4.1, 4.3 and 4.4), although the difference is relatively minor (mean of 0.9 – 1.0 g/ml for P1 and 1.2 g/ml for P2).
- In P1, the density averages decrease from the more lithic-rich lower part of P1a up into the more juvenile-rich P1b (Figures 4.1, 4.3 and 4.4).
- The juvenile-rich subunits (P1b and P2b) exhibit a wide range of density values, even wider than some lithic rich levels (Figure 4.3). P1b and the top of P1a have the lowest mean density of the whole sequence. However, P2b does not have a low mean density.
- On average, P2a scoria densities from the southern and northern sectors are similar (Figure 4.1).

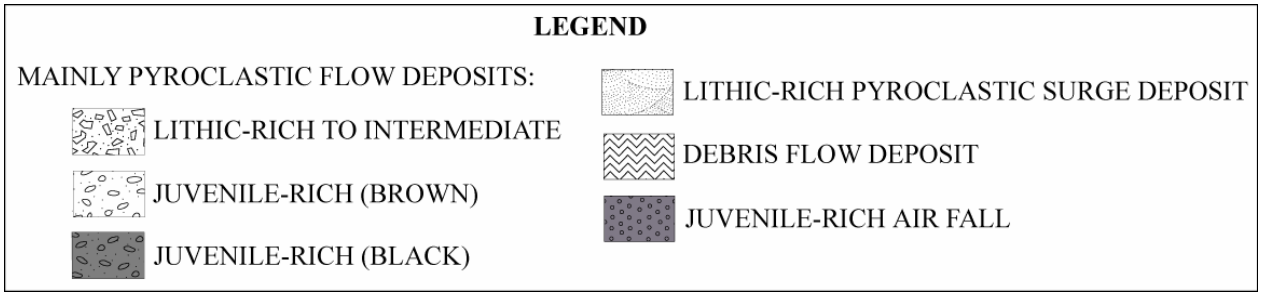

Figure 4.3 (next page): Scoria density variation with stratigraphic height of the Pucón Ignimbrite. The type section VR85 was used in the southern section and the composite section VR73+VR78 was chosen from the northern sector. To the left, individual measurements with the average error and to the right, the mean densities with the standard deviations (1σ).

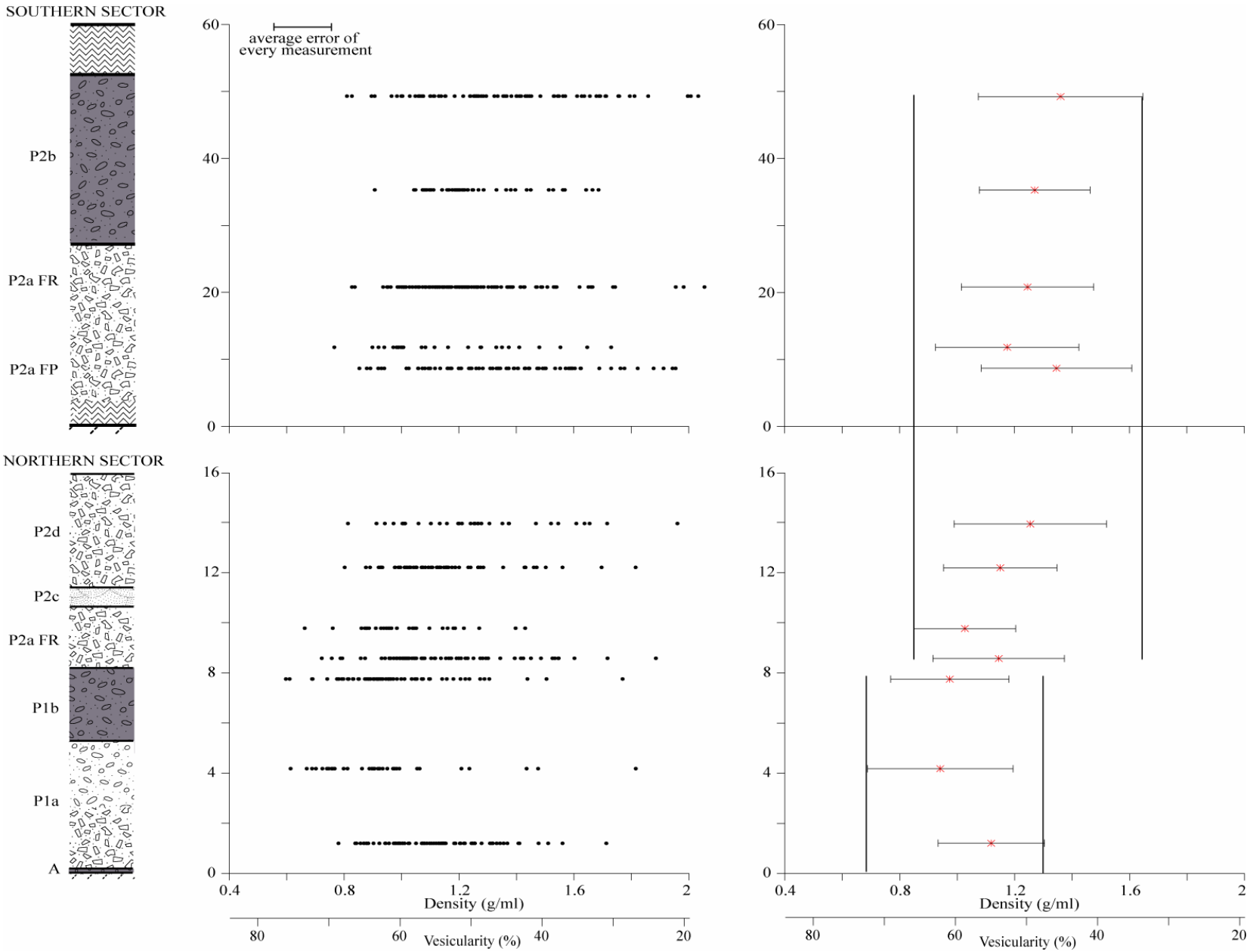
SOUTHERN SECTOR
P2b
P2a FR
P2a FP
NORTHERN SECTOR
P2d
P2c
P2a FR
P1b
P1a
A
average error of every measurement
Density (g/ml)
Vesicularity (%)

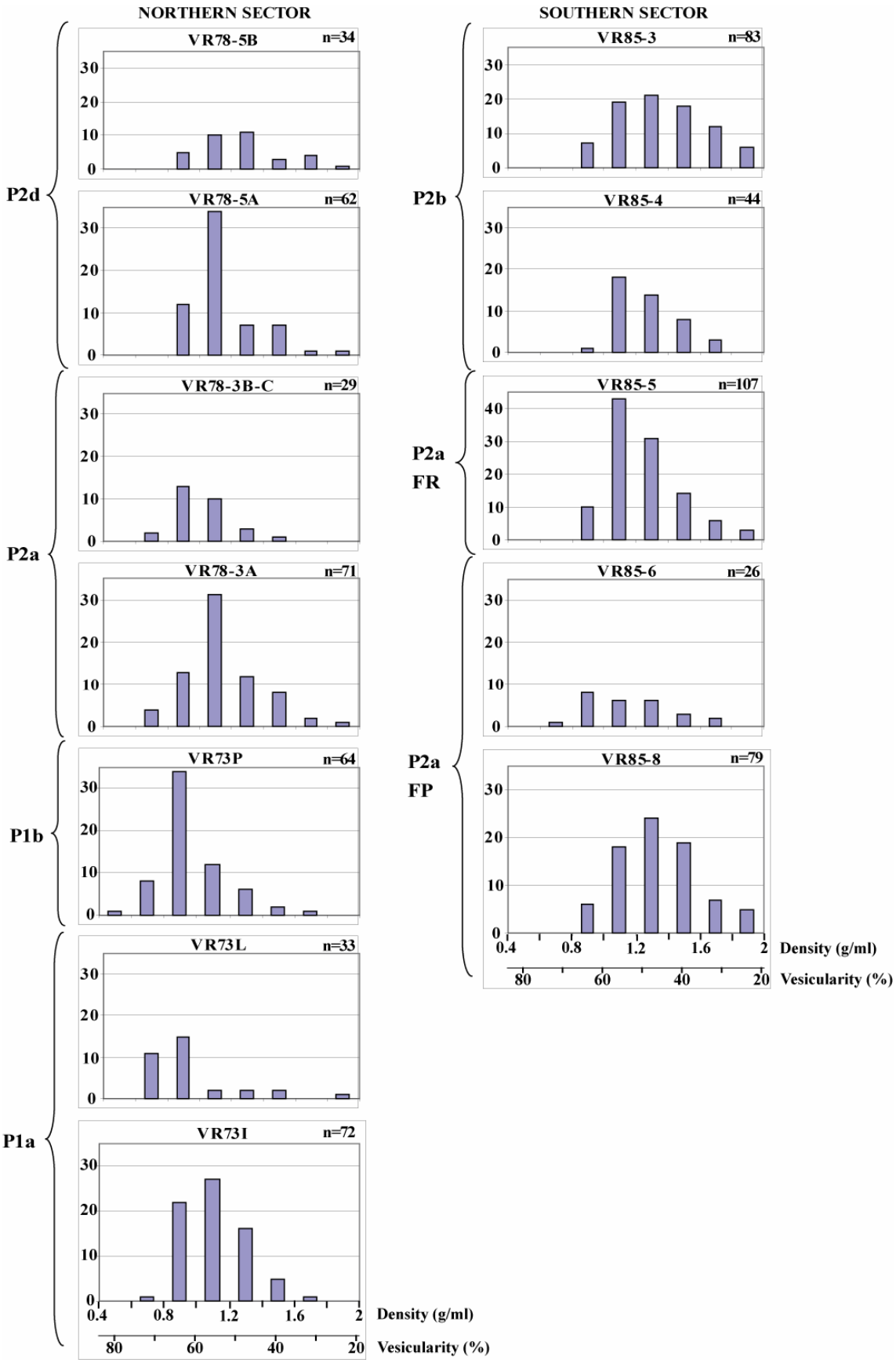

Figure 4.4: Density histograms of the different stratigraphic levels of the Pucón Ignimbrite, for the northern (composite section VR73+VR78) and southern sectors (VR85).

4.4 GLASS MAJOR ELEMENT COMPOSITION

Method

Major element glass composition of 31 Pucón and pre-Pucón fragments were analysed by electron microprobe in metalised polished thin sections and resins (preparation method in Appendix 4.5) following the analytical methods detailed in Appendix 4.6. The analysis conditions for the samples and standards used in the microprobe are described in Table 4.6. Mean errors of glass analyses were calculated after Appendix 4.6. These errors are very similar between the samples, thus mean errors were shown in the diagrams (Figures 4.5 and 4.6).

Samples include ten scoria lapilli and a dense prismatically-jointed (DPJ) lapilli (2 and 4 mm fractions) from five different outcrops of the basal scoria fall, thirteen scoria lapilli (~16 mm diameter) from six different stratigraphic levels of the Pucón Ignimbrite, five 250 µm-sized dense ash shards of the basal Pucón surge P1aI and two pre-Pucón pumice lapilli (4 and 8 mm fractions). Samples have variable crystal contents, thus different beam sizes were used during probe analyses (10 µm, 5 µm, 2 µm or focussed beam). The effects of the beam-size variation are discussed in Appendix 4.8 and show that the variations with beam size of these elements are lower than the precision of the measurements and can be considered negligible. Different beam sizes were also used for dacitic glasses (5 µm, 2 µm or focussed beam) but the beam size effect in dacitic glasses was not studied. However, a dacitic glass show similar composition when analysed under beam size 5 µm or under focussed beam (VR73H PD, Appendix 4.7), thus the effect of the beam size is probably negligible between 5 µm and a focussed beam.

Samples without microlite content measurements were classified approximately into very crystal-poor (glass surfaces of ~5 to 20 µm), crystal-poor (glass surfaces of ~2 to 5 µm), crystal-rich (glass surfaces of ~1 to 2 µm) and very crystal-rich glasses (glass surfaces of less than ~1 µm).

Some selected major element data are presented in Table 4.3 and the complete set of data is presented in Appendix 4.7.

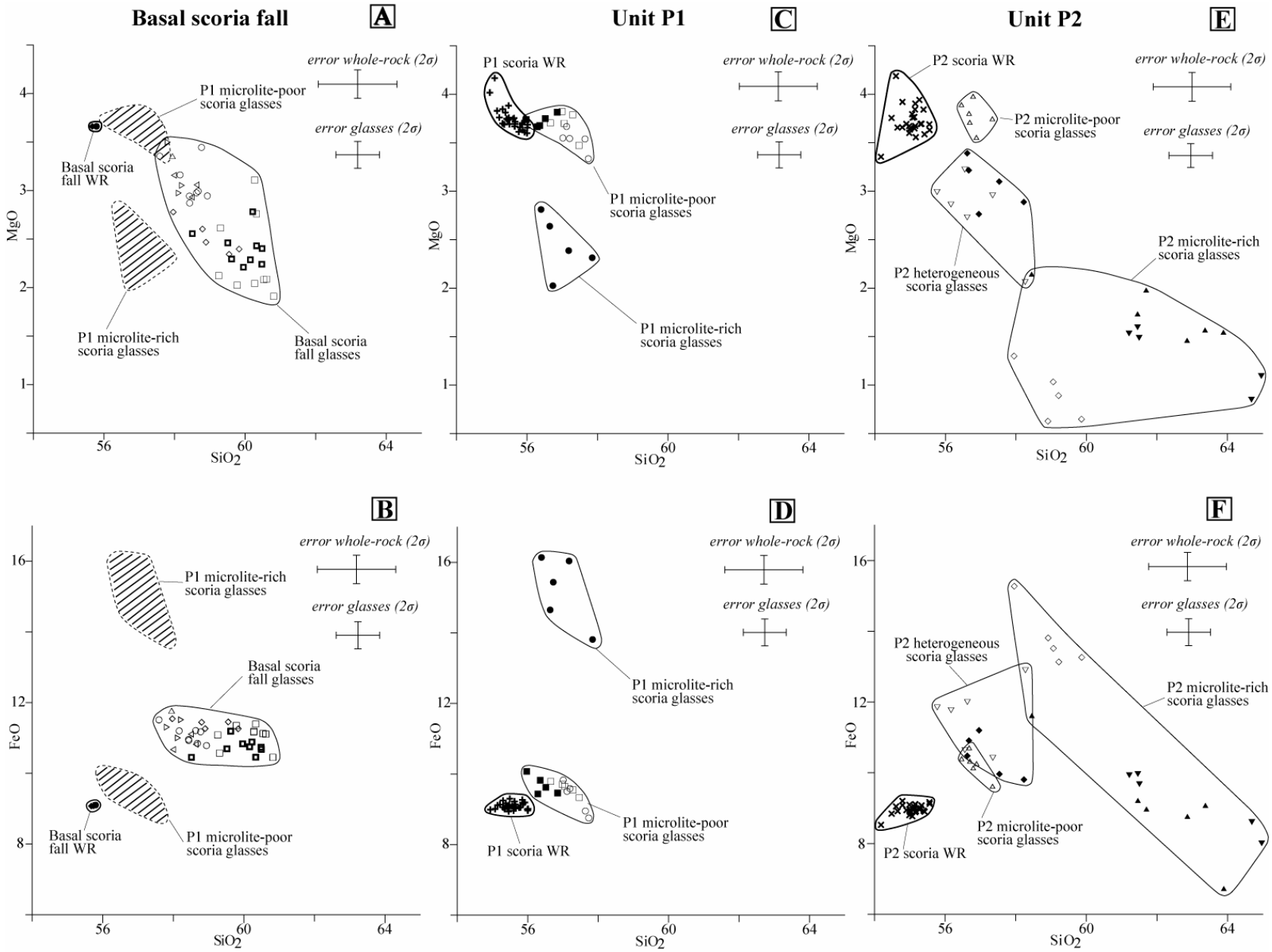
Basal scoria fall
A
Unit P1
C
Unit P2
E
error whole-rock (2σ)
error glasses (2σ)
P1 microlite-poor scoria glasses
Basal scoria fall WR
P1 microlite-rich scoria glasses
Basal scoria fall glasses
P1 scoria WR
P2 scoria WR
P2 microlite-poor scoria glasses
P2 heterogeneous scoria glasses
P2 microlite-rich scoria glasses
MgO
SiO2
B
D
F
FeO

Figure 4.5: Harker variation diagrams of MgO and FeO of scoria glasses from the basal scoria fall, unit P1 and unit P2 of the Pucón Ignimbrite. **A) and B)** Glass analyses of the basal scoria fall (*open symbols*) from four main outcrops (*diamonds* from VR73G, *circles* and *thick squares* from the basal VR113-7a and upper layer VR113-7b, *thin squares* from VR72A and *triangles* from VR109) analysed with beam size 2 µm, except VR109 with analyses under 5 µm and focussed beam. Whole-rock analyses of the basal scoria fall (*filled symbols*) and P1 glasses (*shaded fields*) are shown for comparison. **C) to F)** Glass analyses of the Pucón Ignimbrite *ss*. of light scorias (5 samples, *open symbols*) and dense scorias (5 samples, *filled symbols*) performed with 10 µm (VR73J-L6 and VR73P-D7), 5 µm (VR73P-L2, VR78-3A-L1 and VR85-8D5) and the rest with focussed beam. Whole-rock analyses shown for comparison (*crosses* and *X*). Mean errors of glass analyses were calculated after Appendix 4.6.

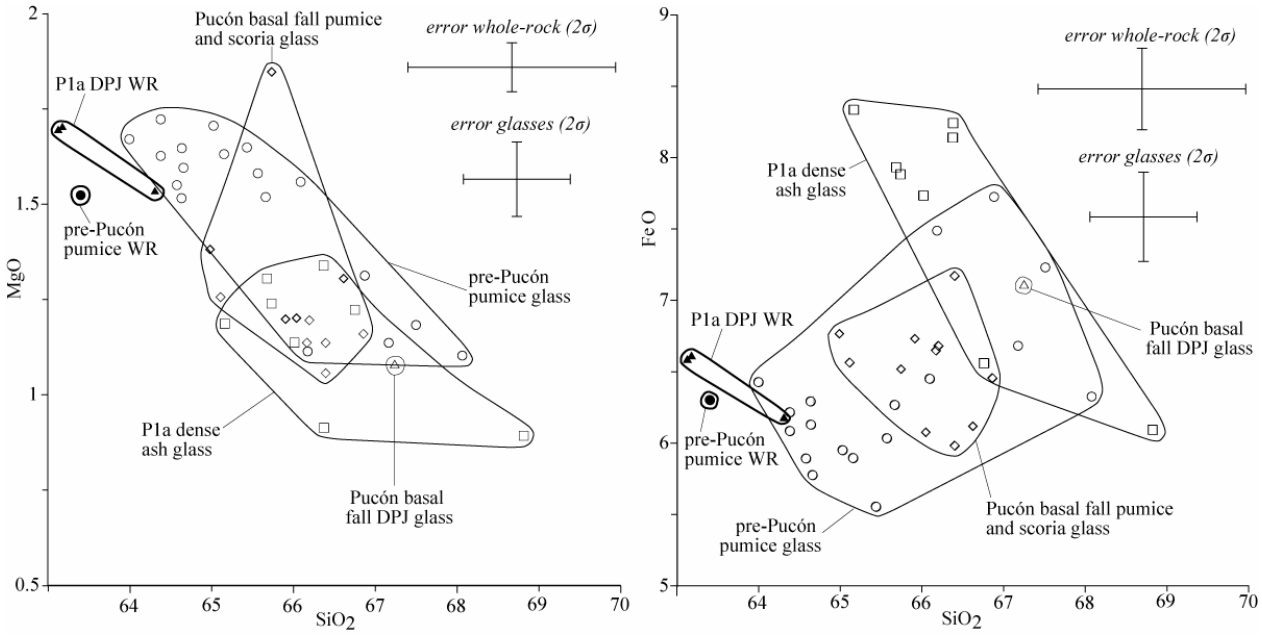

Figure 4.6: Harker variation diagrams of MgO and FeO of dacitic pre-Pucón and Pucón glasses (*open symbols*). *Circles* represent pre-Pucón crystal-poor pumices including banded (VR113-6B, 5 µm) and dark richer in crystals (VR113-6S, 2 µm). From the Pucón basal scoria fall, *triangles* represent a crystal-rich dense prismatically-jointed (DPJ) fragment (VR113-7b, focussed beam) and *diamonds* moderate to crystal-rich pumice and scoria (VR72A SI, 2 µm and VR72A SB, focussed beam, respectively). *Squares* represent crystal-poor dense ash shards from the P1a basal surge (VR73H, 5 µm). *Filled symbols* indicate whole-rock (WR) compositions shown for comparison, including pre-Pucón pumices (VR113-6P, *circles*) and P1a DPJ fragments (VR73JP, VR73Ic and VR115-9D, *triangles*). Mean errors of glass analyses were calculated after Appendix 4.6.

Table 4.3: Major element glass compositions of pre-Pucón pumice and Pucón scoria

BS	N°an	sample	unit	type	cxx	Na_2O	MgO	K_2O	CaO	TiO_2	P_2O_5	FeO	MnO	SiO_2	Al_2O_3	Total
µm					%	wt%	wt%	wt%	wt%	wt%	wt%	wt%	wt%	wt%	wt%	wt%
5	#2	VR109-1	A	SJ	P	3,3	3,4	1,2	6,2	1,8	0,4	11,1	0,2	56,8	13,9	98,3
5	#4	VR109-1	A	SJ	P	2,9	2,9	1,2	6,5	1,5	0,3	10,8	0,2	57,0	14,6	98,0
10	#1	VR73J-L6	P1a	SJ	2	4,0	3,6	1,0	7,3	1,4	0,0	9,6	0,2	57,4	15,8	100,4
10	#3	VR73J-L6	P1a	SJ	2	3,6	3,7	0,9	7,5	1,4	0,3	9,6	0,2	57,4	16,0	100,5
5	#9	VR73H	P1a	PD	VP	3,3	1,3	2,1	3,5	1,5	0,5	8,0	0,1	65,6	12,8	98,8
5	#10	VR73H	P1a	PD	VP	3,5	1,3	2,1	3,8	1,5	0,5	7,8	0,2	64,8	13,0	98,6
5	#16	VR73H	P1a	SJ	VP	4,1	3,5	1,1	7,3	1,4	0,3	9,0	0,2	57,1	15,9	99,8
5	#19	VR73H	P1a	SJ	VP	3,8	3,5	1,0	6,9	1,5	0,4	9,5	0,2	57,2	15,7	99,7
10	#39	VR73P-D7	P1b	DJ	9	3,9	3,7	0,9	7,7	1,4	0,3	10,0	0,2	55,8	15,8	99,6
10	#40	VR73P-D7	P1b	DJ	9	3,9	3,7	0,9	7,6	1,3	0,2	9,8	0,2	56,4	16,2	100,1
5	#32	VR78-3A-L1	P2a	SJ	28	3,5	3,7	1,1	7,1	1,3	0,3	9,5	0,2	56,7	15,5	98,9
5	#33	VR78-3A-L1	P2a	SJ	28	3,4	3,8	1,1	6,9	1,5	0,2	10,7	0,2	56,5	15,5	99,7
5	#23	VR85-8-D5	P2a	DJ	32	4,0	3,1	1,2	6,5	1,5	0,2	9,9	0,2	57,1	15,7	99,3
5	#19	VR85-8-D5	P2a	DJ	90	3,6	2,9	1,5	6,5	1,4	0,2	9,7	0,2	57,8	15,4	99,2
5	#44	VR113-6B	pre	BA	VP	3,9	1,6	1,7	4,1	1,1	0,4	6,1	0,2	64,4	16,1	99,6
5	#50	VR113-6B	pre	BA	VP	4,3	1,5	1,8	4,4	1,0	0,4	6,3	0,2	64,6	15,5	100,0

Error % (2 σ)*

BS	N°an	sample	unit	type	cxx	Na_2O	MgO	K_2O	CaO	TiO_2	P_2O_5	FeO	MnO	SiO_2	Al_2O_3
µm					%										
5	#2	VR109-1	A	SJ	P	6,1	4,5	10,4	4,4	9,8	51,4	3,5	31,7	1,1	1,6
5	#4	VR109-1	A	SJ	P	6,5	4,9	10,2	4,3	10,8	58,4	3,6	30,5	1,1	1,5
10	#1	VR73J-L6	P1a	SJ	2	5,4	4,4	11,2	4,1	11,1	418,3	3,7	27,5	1,1	2,0
10	#3	VR73J-L6	P1a	SJ	2	5,8	4,3	11,8	4,0	11,1	61,6	3,7	28,0	1,1	2,0
5	#9	VR73H	P1a	PD	VP	6,1	7,5	7,6	6,0	10,6	42,4	4,1	40,4	1,0	1,6
5	#10	VR73H	P1a	PD	VP	5,8	7,5	7,6	5,6	11,1	40,0	4,2	23,5	1,0	1,6
5	#16	VR73H	P1a	SJ	VP	5,4	4,5	10,7	4,1	11,2	59,1	3,9	28,1	1,1	1,5
5	#19	VR73H	P1a	SJ	VP	5,7	4,5	11,8	4,2	10,3	41,3	3,8	26,6	1,1	1,5
10	#39	VR73P-D7	P1b	DJ	9	5,6	4,3	12,4	4,0	11,5	66,1	3,7	27,1	1,1	1,5
10	#40	VR73P-D7	P1b	DJ	9	5,6	4,3	12,5	4,0	12,2	105,9	3,7	34,1	1,1	1,5
5	#32	VR78-3A-L1	P2a	SJ	28	5,8	4,3	11,1	4,1	12,0	61,0	3,8	32,6	1,1	1,5
5	#33	VR78-3A-L1	P2a	SJ	28	6,0	4,3	10,8	4,2	11,0	75,5	3,6	29,1	1,1	1,5
5	#23	VR85-8-D5	P2a	DJ	32	5,5	4,8	10,4	4,4	10,9	70,1	3,7	26,8	1,1	1,5
5	#19	VR85-8-D5	P2a	DJ	90	5,8	5,0	9,2	4,3	11,2	94,2	3,7	26,0	1,1	1,5
5	#44	VR113-6B	pre	BA	VP	5,5	6,6	8,7	5,5	13,9	40,0	4,8	30,3	1,0	1,5
5	#50	VR113-6B	pre	BA	VP	5,2	6,9	8,3	5,3	14,4	48,5	4,7	31,7	1,0	1,5

BS = beam size used during the analysis (in µm)
pre = pre-Pucón pumice
SJ = scoriaceous juvenile lapilli
PD = pale dense ash
DJ = dense juvenile lapilli
BA = banded vesicular lapilli
cxx = microlite content of the samples (in % vesicle-free)
For samples with microlite content not available:
VP = very crystal-poor (glass surfaces of ~5 to 20 µm)
P = crystal-poor (glass surfaces of ~2 to 5 µm)

* The error (%) was estimated statistically using the counting times and the number of counts par second obtained for the peak and background of the sample and for the peak and background of the standard (Ancey *et al*., 1978; PhD these of M.Laubier, S.Moune and S.Jannot, 2005/2006).

Analytical conditions in Appendix 4.6.

4.4.1 Pucón Ignimbrite

4.4.1.1 Juvenile components

Basal scoria fall

Harker variation diagrams of MgO and FeO of Pucón basal fall scorias from four main outcrops are shown in Figures 4.5A-B. Glasses of P1 scoria are also shown for comparison. The scoria glasses of the Pucón basal fall have similar compositions (Figures 4.5A-B, Table 4.3, Appendix 4.7), supporting the field correlation between their different isolated exposures (see section 2.3.2). They have lower MgO, CaO, Al_2O_3 and higher SiO_2, TiO_2 and FeO contents than their whole-rock composition and the P1 microlite-poor scoria glasses. They have FeO and Al_2O_3 contents transitional towards the microlite-rich P1 scoria glasses and comparable MgO and CaO contents. The silica contents extend towards values higher than the P1 scoria glasses more comparable to those of the unit P2.

P1 and P2 ignimbrite units

The glass composition of ten scoria samples (five lights and five dense) covering five stratigraphic layers of the Pucón Ignimbrite is presented in Harker diagrams for units P1 and P2 (Figures 4.5C-F, Table 4.3, Appendix 4.7), together with their whole-rock scoria compositions for comparison.

In contrast to the basaltic andesitic whole-rock composition of the Pucón scorias, the glasses extend towards andesitic and dacitic compositions (Figures 4.5C-F, Table 4.3).

The scorias of unit P1 that are microlite-poor (<30%, vesicle-free) exhibit a similar glass composition to the whole-rock composition of P1 scorias (VR73J-L6, VR73P-L2 and VR73P-D7, Figures 4.5C-D). One microlite-rich scoria exhibits higher FeO, TiO_2 and K_2O and lower MgO, CaO and Al_2O_3 contents (VR73J-D3).

The scorias of unit P2 exhibit variable microlite crystallization, including a microlite-poor scoria (microlite content ~30%, vesicle-free) with similar glass composition than the whole-rock P2 scoria composition (VR78-3A-L1, Figure 4.5E-F), and also microlite-rich glasses with a variable composition probably due also to variable contamination by melted granitoids. Heterogeneous samples exhibit glass compositions intermediate between the microlite-poor and microlite-rich scorias.

4.4.1.2 Accidental components

Glass compositions were analysed in a dense prismatically-jointed (DPJ) fragment and scoria glasses from the basal scoria fall, and dense ash glass from the P1a basal surge (refer to sections 2.3.2 and 3.4.1.2,

Figure 4.6). No whole-rock analyses, nor microlite measurements, are available for these samples, so these data should be interpreted carefully. They are shown together with whole-rock analyses of P1a DPJ fragments and also glass and whole-rock compositions of pre-Pucón pumices, for comparison.

Dense prismatically-jointed (DPJ) fragments of the Pucón basal scoria fall and are very rich in microlites with glass areas smaller than ~1 μm^2. Given their low abundance and fine grain size, no whole-rock analyses are available but compared to the P1a DPJ fragment whole-rock composition, their glass is dacitic richer in silica and FeO, and poorer in MgO, Na_2O, Al_2O_3 and CaO (Figure 4.6).

The Pucón basal scoria fall presents locally abundant very crystal-rich black scoria and pumices (see section 3.4.1.2) with dacitic glass of similar composition. Based on qualitative observations, it can be said that these pumices have comparable or even lower microlite contents than the typical basaltic andesitic to andesitic glasses of the Pucón basal scoria fall. They have also a similar glass composition to the DPJ fragments being only slightly poorer in silica and richer in Al_2O_3 (Figure 4.6).

Glass analyses were performed in dense glass ash shards from the Pucón basal surge (see section 3.4.1.2). They are very crystal-poor translucent yellow, crystal-poor black or zoned (black centre, translucent rim), all of them exhibiting similar glass composition (VR73H PD-BD-ZD, Appendix 4.7). They have similar dacitic glass composition to the other accidental components, especially with the DPJ fragments (Figure 4.6).

Glass compositions were analysed in pumices from the pre-Pucón surge described towards the northern flank of the volcano (VR113, Figure 2.5) which contains abundant pale-brown pumices but also dark and banded pumices (with pale-brown and dark bands). The glass composition of both bands (VR113-6B) is similar (and only slightly richer in silica) than the whole-rock composition of the pale-brown pumices (VR113-6P), according to their very crystal-poor texture. The dark crystal-poor pumice glass (VR113-6S) extends towards lower MgO, CaO and Al_2O_3 contents and higher SiO_2 and FeO contents having a similar composition to the accidental fragments described above (Figure 4.6).

4.5 MICROLITE CONTENT AND VESICULARITY DATA

Method

The determination of microlite contents was done by analysis of SEM images for the lightest and densest juvenile lapilli samples (~16 mm in diameter) from different stratigraphic levels (P1a, P1b, P2aFP, P2aFR and P2b), using the method explained in Appendix 4.9. To determine how reliable the microlite measurements performed by image analyses are, the crystallinities were calculated by another approach, using the K_2O data from the whole-rock and crystals from microprobe (Appendix 4.9; Table 4.4).

Table 4.4: Crystallinities of the Pucón scoriae estimated by SEM image analyses and using the K2O% of the whole-rock and crystals by microprobe (see text for details).

BS	sample	unit	cxx%	Kwr	Kg	Kc	Xc	Kmic	Xmic*	Xph	Xmic
						(i)		(i)			
10	VR73J-L6	P1a	2	0.81	0.97	0.09	18	0.22	6.78	12.50	5.94
~1	VR73J-D3	P1a	81	0.81	1.58	0.09	52	0.22	48.75	6.24	45.71
5	VR73P-L2	P1b	32	0.81	1.06	0.09	26	0.22	17.04	11.05	15.16
10	VR73P-D7	P1b	9	0.81	0.99	0.09	20	0.22	9.35	12.14	8.21
5	VR78-3A-L1	P2a	28	0.84	1.14	0.10	29	0.17	23.04	7.18	21.38
~1	VR78-3A-D2	P2a	55	0.84	1.89	0.10	58	0.17	56.57	4.14	54.22
~1	VR85-8-L4	P2a	98	0.84	2.42	0.10	68	0.17	66.76	3.18	64.63
5	VR85-8-D5	P2a	32	0.84	1.30	0.10	38	0.17	33.60	6.24	31.50
5	VR85-8-D5	P2a	90	0.84	1.62	0.10	51	0.17	48.35	4.90	45.98
5	VR85-8-D5	P2a	61	0.84	1.42	0.10	44	0.17	40.41	5.63	38.13
~1	VR85-3-L3	P2b	31	0.84	0.92	0.10	9	0.17	0.00	9.16	0.00
~1	VR85-3-L3	P2b	97	0.84	1.40	0.10	43	0.17	39.32	5.73	37.07
~1	VR85-3-L3	P2b	64	0.84	1.16	0.10	30	0.17	24.47	7.05	22.75
~1	VR85-3-D4	P2b	91	0.84	1.91	0.10	59	0.17	57.03	4.10	54.69

BS = beam size in µm
cxx% = microlite content measured by image treatment
Kwr = potassium content (K20%) of the whole rock (normalised, Appendix 3.4). We took an average for P1 and P2 scoriae:

Kwr = 0.81 for P1

Kwr = 0.84 for P2

Kg = potassium content (K20%) of the glass fraction by microprobe (normalised)
Kc = potassium content (K20%) of the total crystal fraction by microprobe (mean of the K2O content of microlites and phenocrysts for P1 and P2)
Xc = total crystal fraction of the sample calculated as:

$Xc = (Kwr - Kg) / (Kc - Kg)$

Kmic = potassium content (K2O%) of the microlites by microprobe. We took an average for P1 and P2 scoriae.
Xmic* = total microlite fraction of the groundmass, calculated assuming the non-crystallised composition of K2O as Kg = 0.92 which is the lowest value obtained in the glasses:

$Xmic^* = (0.92 – Kg) / (Kmic – Kg)$

Xph = total phenocryst fraction of the sample calculated as:

$Xph = (Xc – Xmic^*) / (1 - Xmic^*)$

Xmic = total microlite fraction calculated as:

$Xmic = (Xmic^*) * (1 – Xph)$

(i) Values of Lohmar (2008, written communication)

A plot of the potassium content (K_2O%) of the glass fraction (Kg) versus the total crystal fraction of the sample (Xc) is presented, using the crystallinities estimated by SEM image treatment and the K_2O-derived crystal contents (left plot of Figure 4.7). A plot Kg versus the total microlite fraction in the groundmass (Xmic*) is also presented, using both methods to determine crystallinities (right plot of Figure 4.7).

In the Figure 4.7, it can be seen that both approaches are similar for the microlite-poor samples but not for the microlite-rich samples. So, the microlite contents estimated from the image analyses in microlite-rich samples seem to have been overestimated.

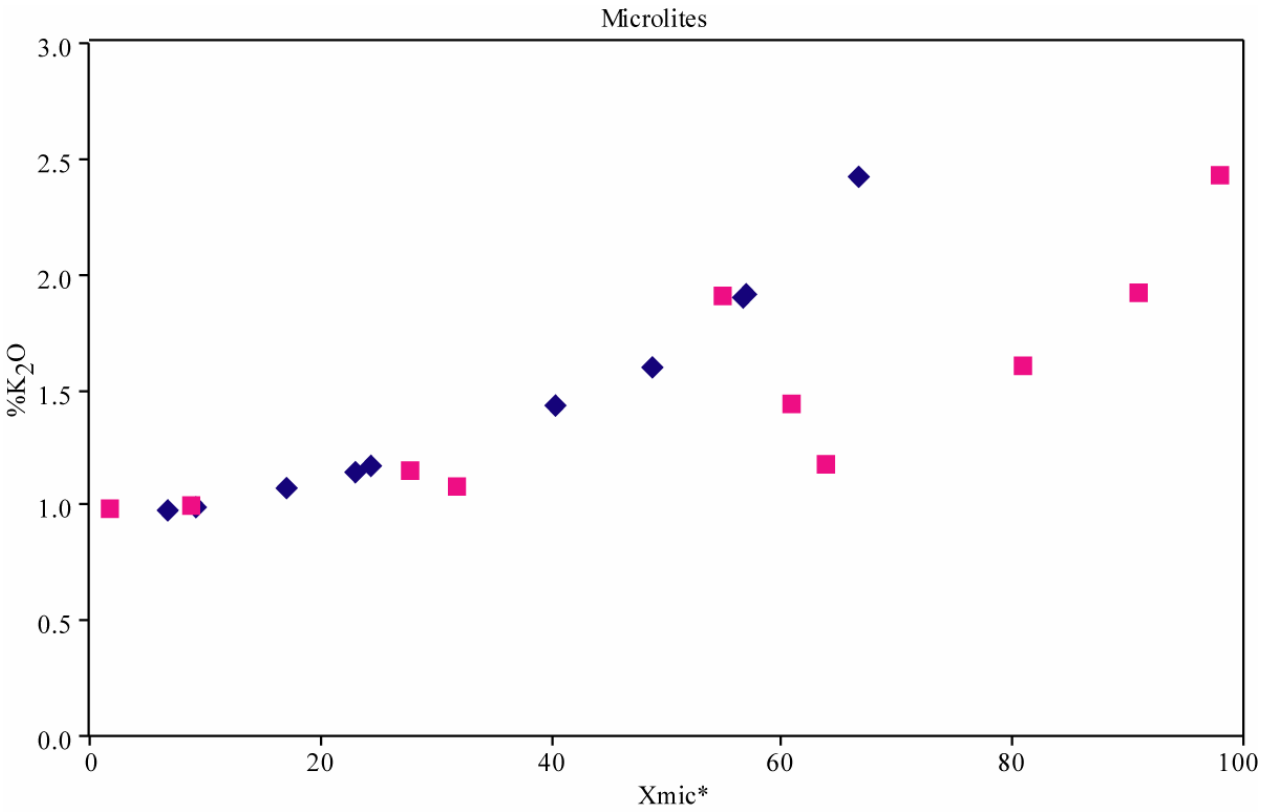

Figure 4.7: Potassium content (K_20) of the glass fraction (Kg) versus the total microlite content (Xmic*) of the Pucón scoriae. Squares represent the crystallinities estimated by SEM image treatment and diamonds those calculated using the K_2O contents of the whole-rock and crystals by microprobe (see text for details).

In Chapter 3, there have been described three main textural types of Pucón scoriae:

(1) Microlite-poor (~5-25%) vesicular scoria (vesicularity typically >50%) with abundant rounded isolated vesicles (Figure 3.4E) together with large connected vesicles with evidence of bubble coalescence (Figures 3.4A, 3.4C, 3.4E and 3.5A). Microlites grow normally in clusters, some with spherulite-like forms and exhibiting textures of rapid cooling (Figure 3.6).

(2) Microlite-rich (~45-65%) dense scoria (vesicularity <60%) with vesicles of uniform sizes, irregular shapes, normally interconnected, slightly elongated and wider walls between them (Figures 3.4B, 3.4D, 3.4F and 3.5B), and only a few small isolated vesicles in a groundmass formed by a dense network of microlites (Figure 3.7).

(3) Heterogeneous scoria with both textural types interlayered in bands or concentrically (Figure 3.8)

The K_2O, SiO_2 and MgO contents of the glass versus the microlite contents calculated by both methods, are presented (Figures 4.8, 4.9 and 4.10). With the K_2O-derived microlite contents (plots from the right side), the K_2O, SiO_2 enrichment and MgO decrease with crystallization are more systematic.

The variation of density/vesicularity versus microlite content calculated with both methods is also shown (Figure 4.11). There is a rough correlation between microlite content and vesicularity of the juvenile lapilli with a considerable amount of scatter. Denser samples have groundmasses normally richer in microlites than the more vesicular samples.

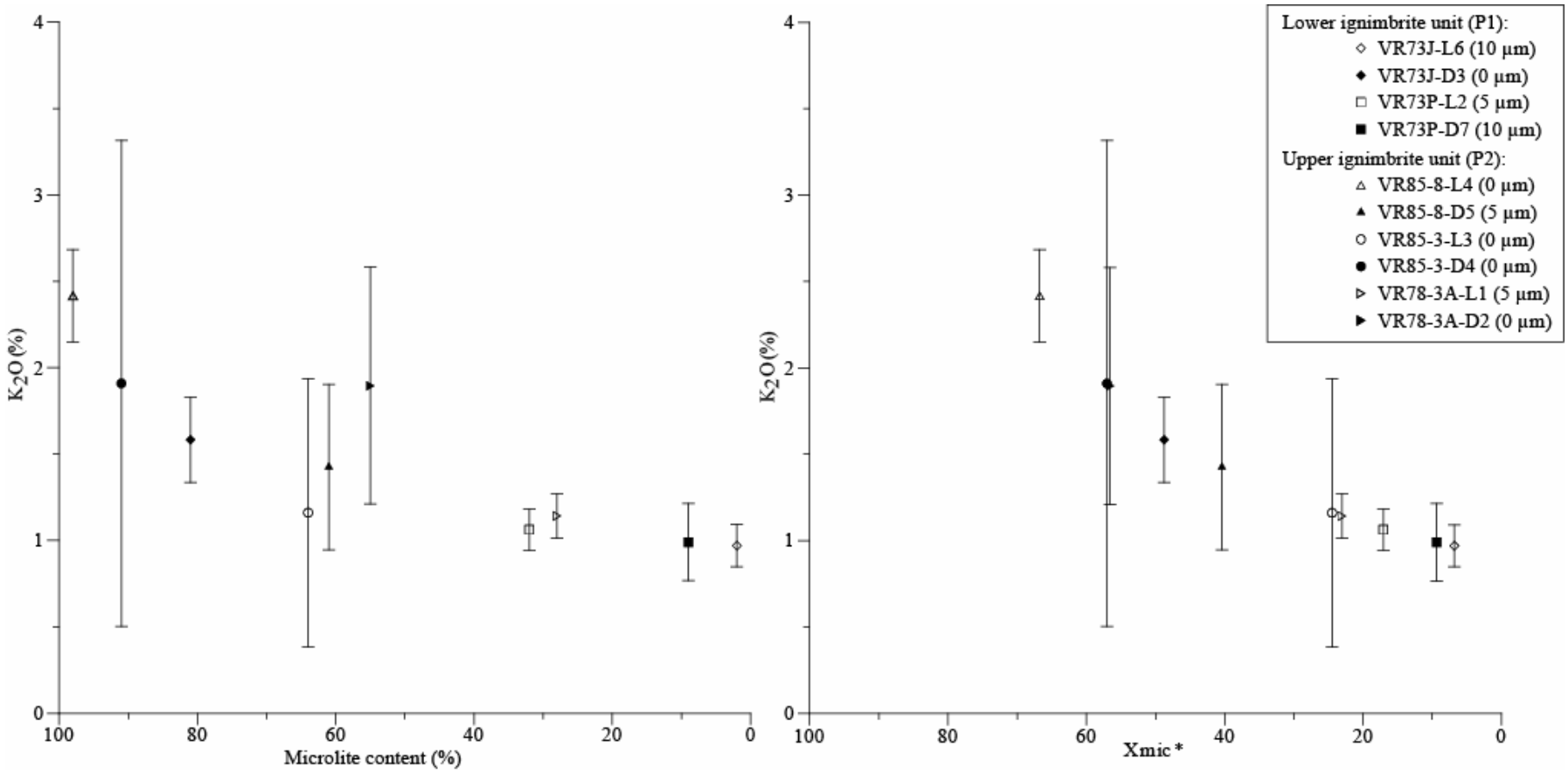

Figure 4.8: K_2O content of the glass versus the microlite content estimated by SEM image analyses (left) and by K_2O-derived calculations (right) of the Pucón scoriae (see text for details).

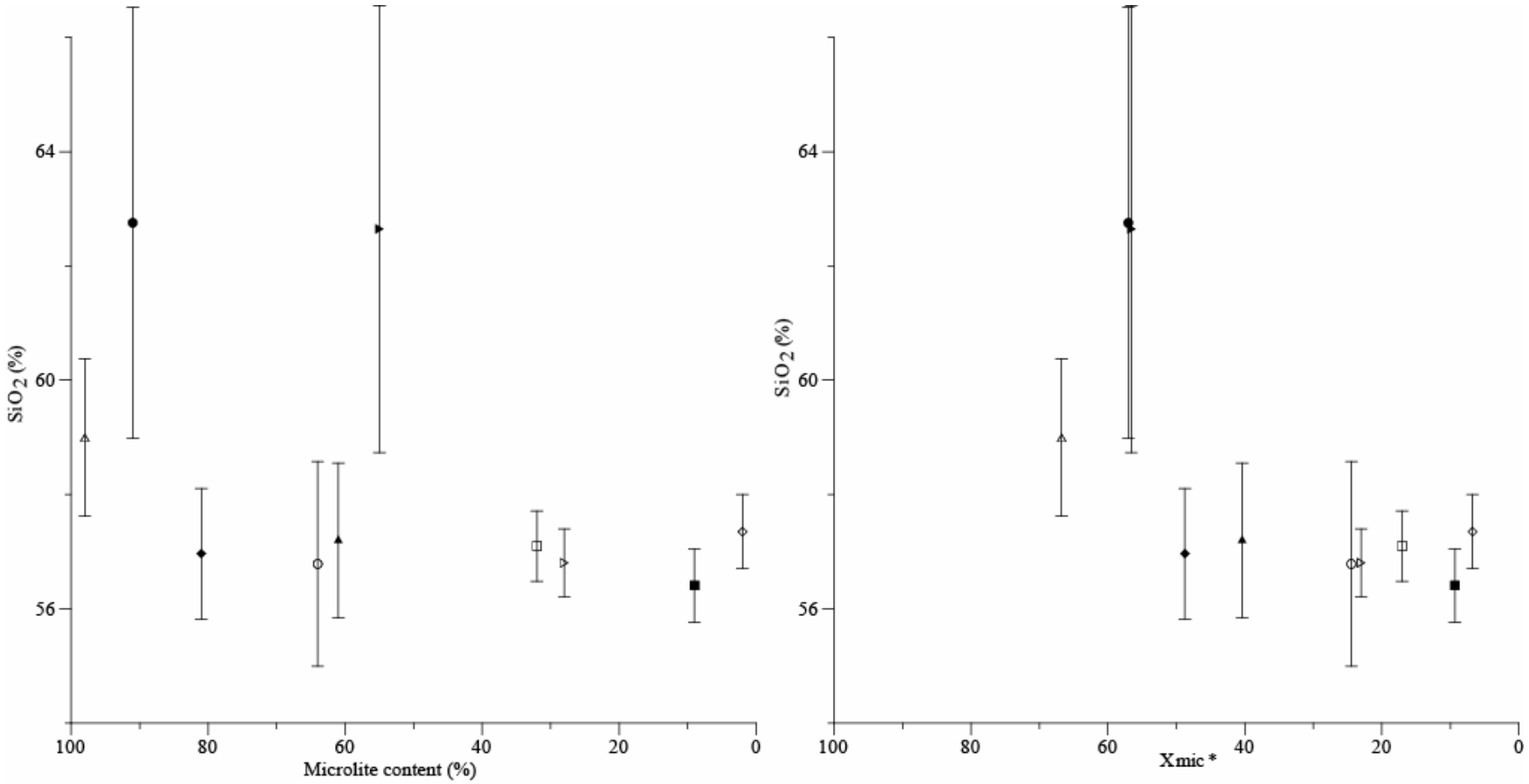

Figure 4.9: SiO_2 content of the glass versus the microlite content estimated by SEM image analyses (left) and by K_2O-derived calculations (right) of the Pucón scoriae (see text for details). Symbols as in Figure 4.8.

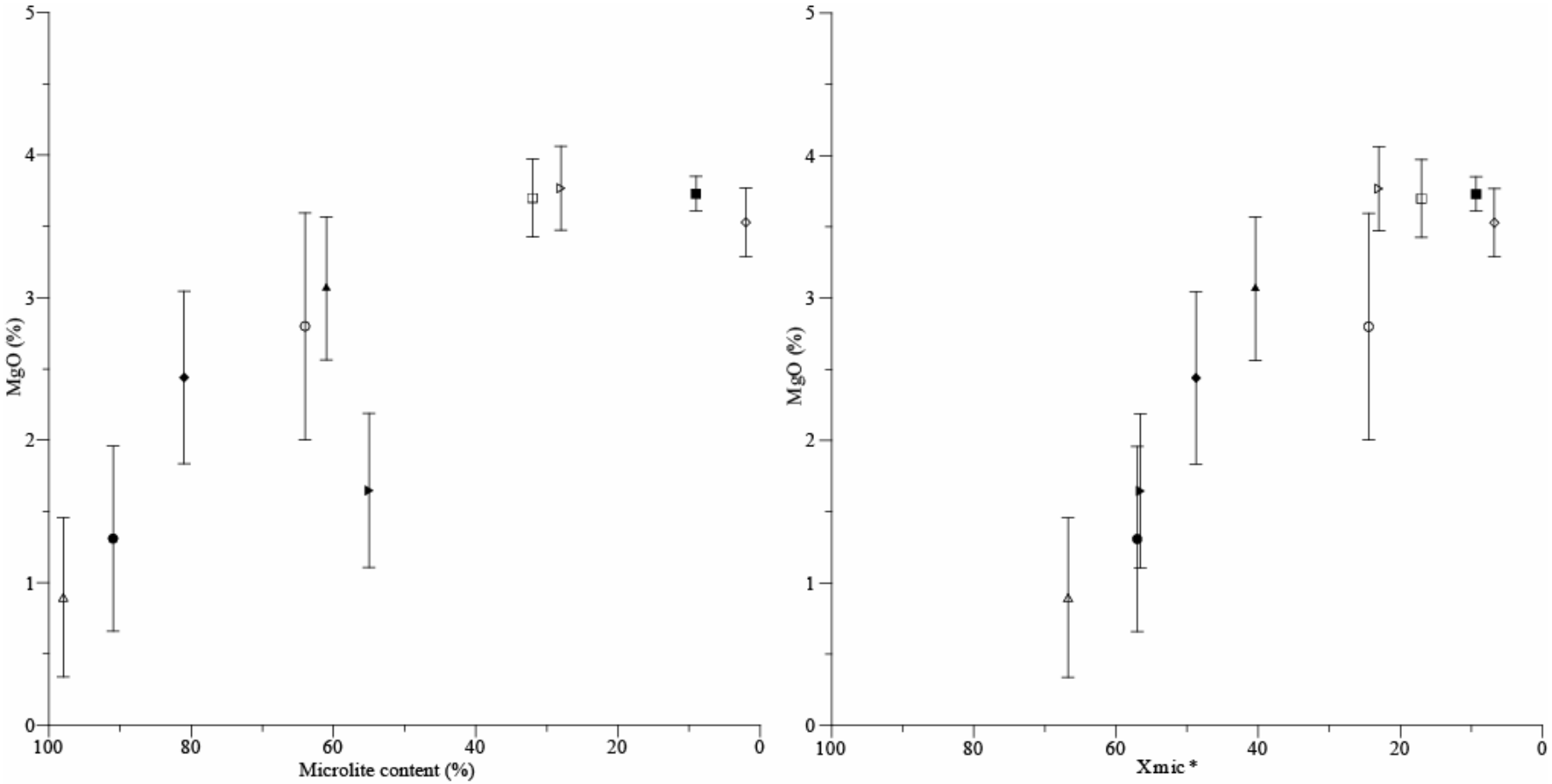

Figure 4.10: MgO content of the glass versus the microlite content estimated by SEM image analyses (left) and by K2O-derived calculations (right) of the Pucón scoriae (see text for details). Symbols as in Figure 4.8.

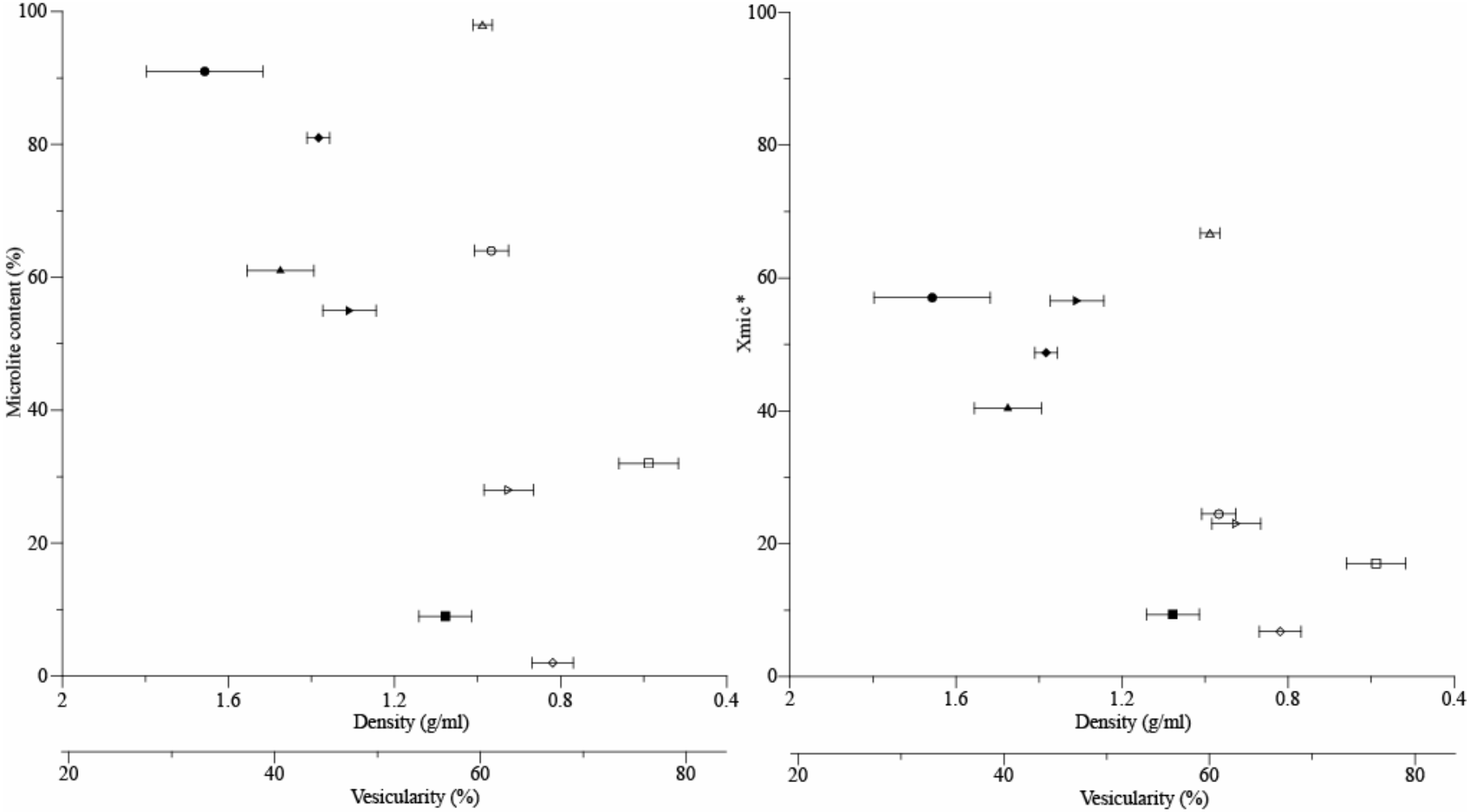

Figure 4.11: Microlite content (%) estimated by SEM image analyses (left) and by K2O-derived calculations (right) of the Pucón scoriae versus density/vesicularity (see text for details). Symbols as in Figure 4.8.

4.6 GLASS VOLATILE COMPOSITION

Method

From each of the five stratigraphic levels (P1a, P1b, P2aFP, P2aFR and P2b) with density measurements using glass beads (Figure 4.1), a dense and a light scoria were chosen for analyses of S, Cl and F contents in the matrix glasses. The preparation of the samples for the microprobe analyses is described in Appendix 4.5. The procedure and analytical conditions are described in Appendix 4.6.

Figures 4.12 to 4.14 show the variation of Cl, F and S versus microlite contents estimated by image analyses and calculated by using the K_2O contents of the whole-rock and crystals by microprobe. These diagrams show that the microlite-rich samples exhibit higher errors (2σ standard deviation of the average of 5 analyses per sample) than the microlite-poor ones due to the small size of the available glass surfaces to direct the beam.

Six crystal-poor to heterogeneous samples (VR73J-L6, VR73P-L2, VR73P-D7, VR78-3A-L1, VR85-8-D5 and VR85-3-L3) exhibit ~300 to ~1200 ppm of Cl , <100 to ~500 ppm of F and ~50 to ~300 ppm of S (Figures 4.12 to 4.14, Appendix 4.10). These ranges could be considered as representative of the composition of the normal crystal-poor Pucón glass which is independent of the stratigraphy (samples are from P1a, P1b, P2aFP, P2aFR and P2b).

Similar than K_2O and SiO_2 (Figures 4.8 and 4.9), Cl increases more clearly with the K_2O-derived microlite contents than those estimated by image analyses (Figure 4.12). This correlation explains why Cl and K_2O are correlated (Figure 4.15, left hand) and to a lesser degree SiO_2 and MgO (Figures 4.16 and 4.17, left hand). However, Cl exhibits no clear correlation with FeO (left hand of Figure 4.19). F exhibits a very weak correlation with microlite content (Figure 4.13) and no clear correlation with K_2O, SiO_2 and MgO (Figures 4.15 to 4.17, right hand). The S exhibits no correlation with microlite content (Figure 4.14), neither with SiO_2 and MgO (Figure 4.18) which is consistent with the compatible character of S with sulphides. Correlation of Cl and F with SiO_2 is not clear (Figure 4.16). Cl exhibits a weak correlation whereas F and S exhibit no clear correlation with density/vesicularity (Figures 4.19 and 4.20).

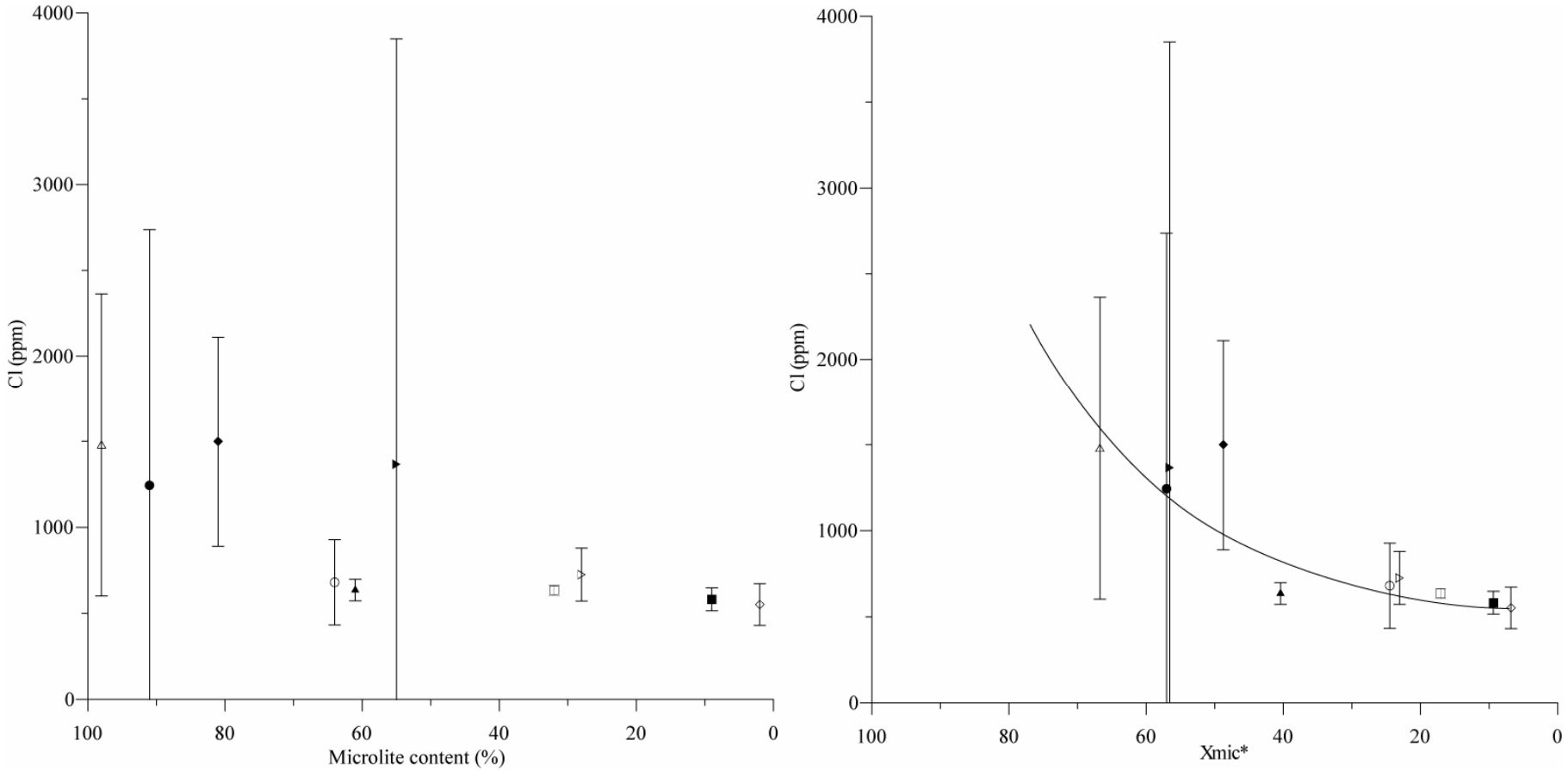

Figure 4.12: Cl content (ppm) versus the microlite content (%) estimated by SEM image analyses (left) and by K2O-derived calculations (right) of the Pucón scoriae. A curve of perfect incompatibility of Cl is also shown (see text for details). Symbols as in Figure 4.8.

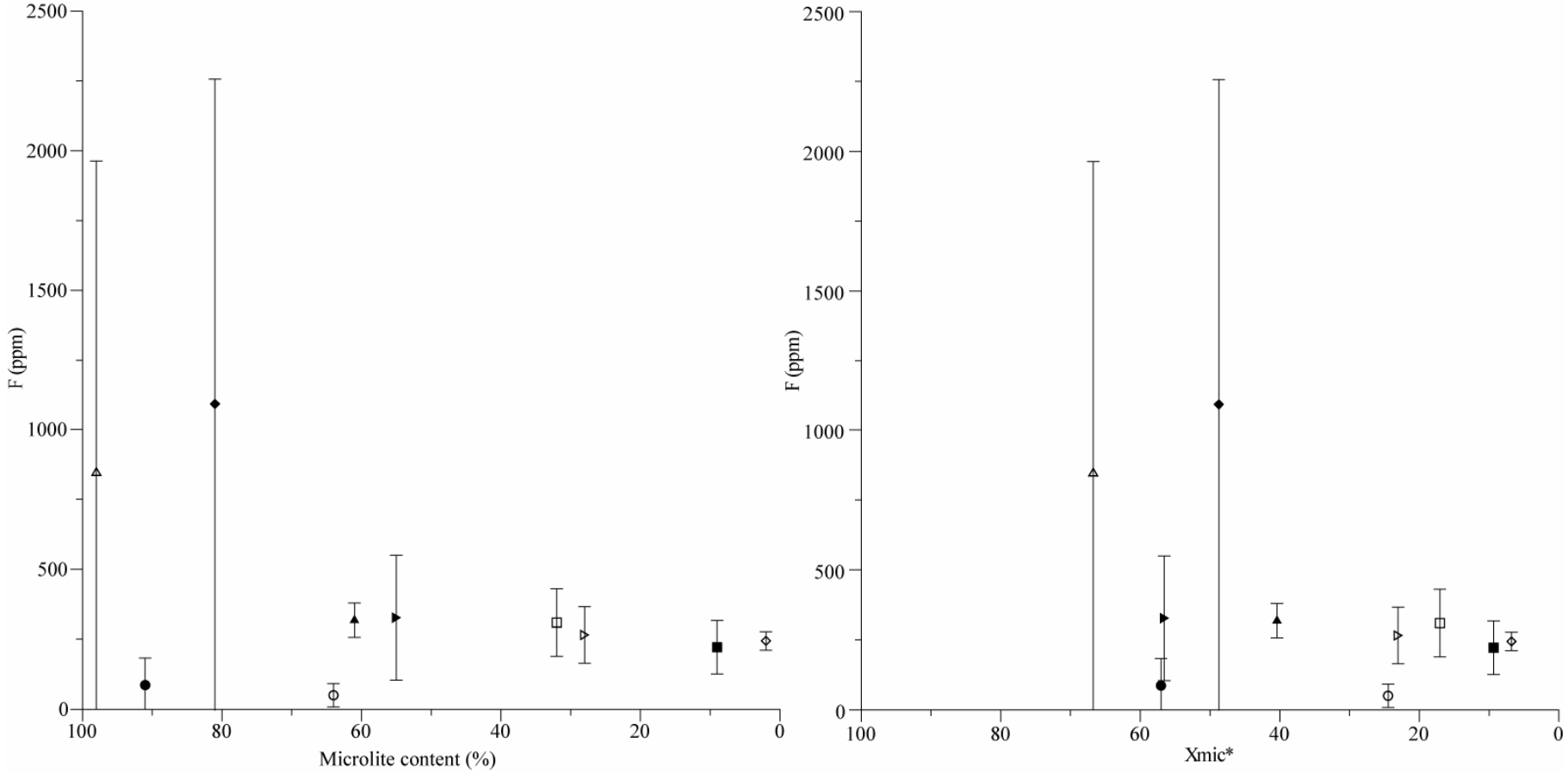

Figure 4.13: F content (ppm) versus the microlite content (%) estimated by SEM image analyses (left) and by K2O-derived calculations (right) of the Pucón scoriae (see text for details). Symbols as in Figure 4.8.

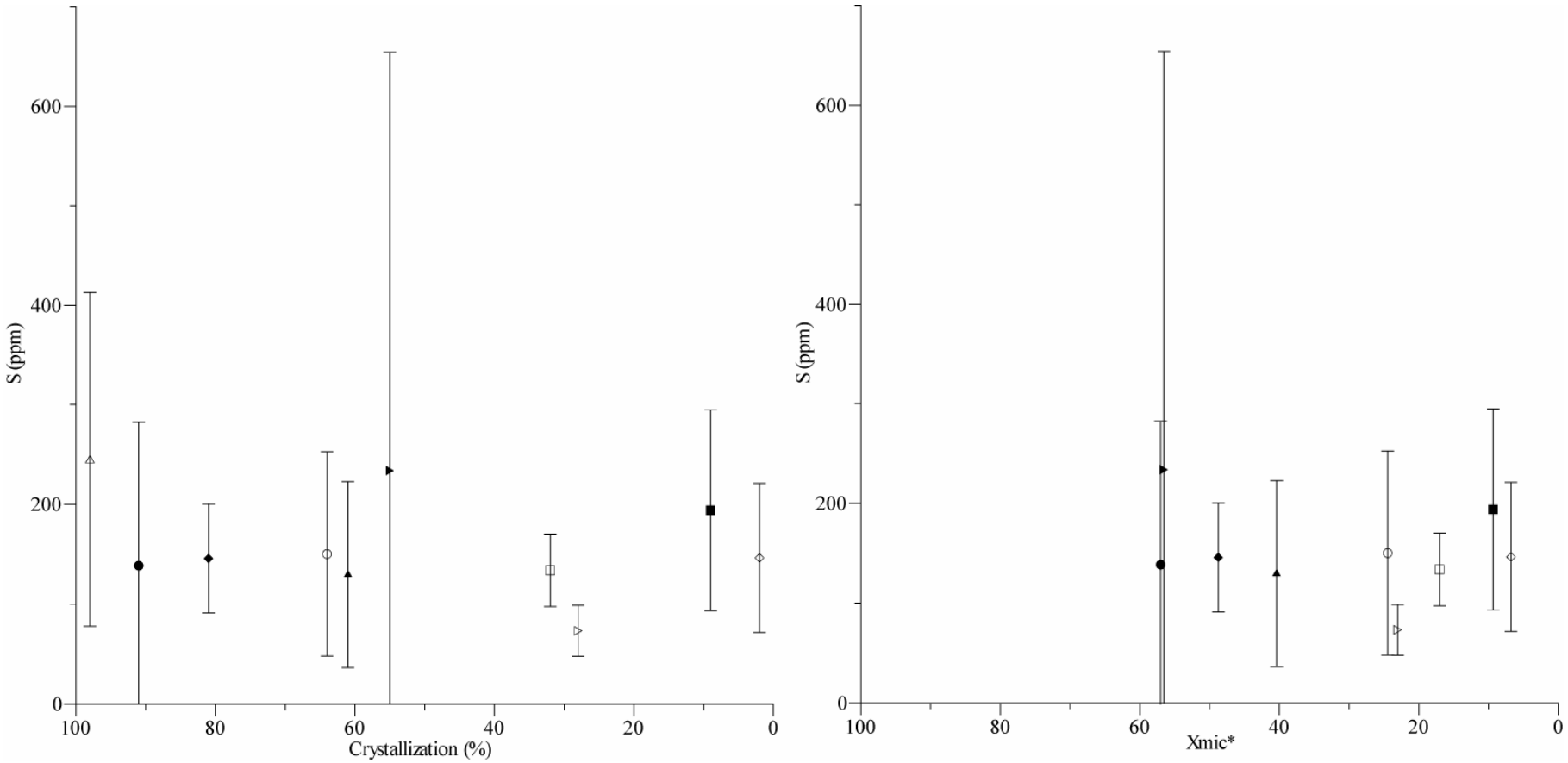

Figure 4. 14: S content (ppm) versus the microlite content (%) estimated by SEM image analyses (left) and by K2O-derived calculations (right) of the Pucón scoriae (see text for details). Symbols as in Figure 4.8.

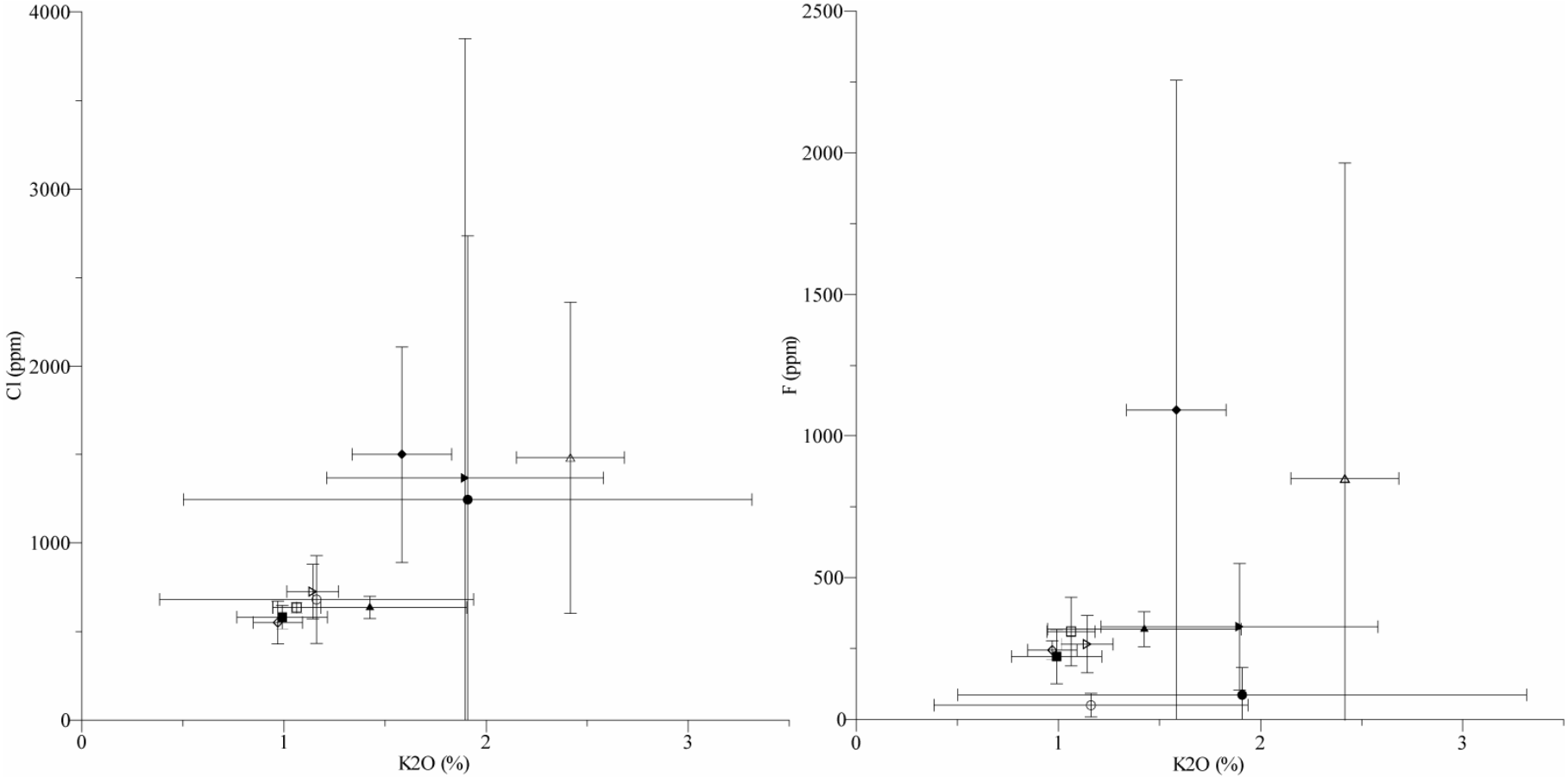

Figure 4.15: Cl and F content (ppm) versus the K_2O% of the Pucón scoriae (see text for details). Symbols as in Figure 4.8.

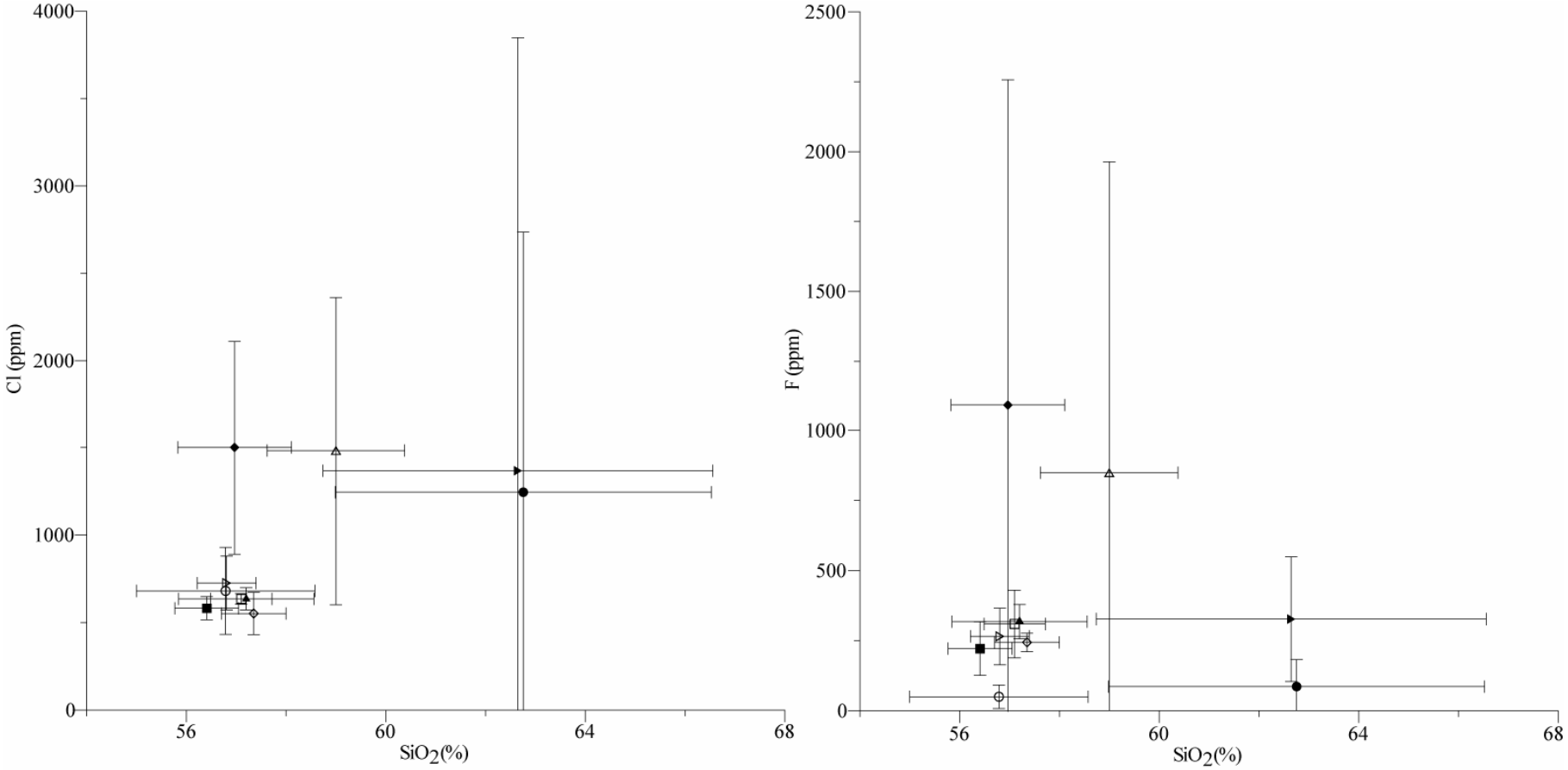

Figure 4.16: Cl and F content (ppm) versus the SiO_2% of the Pucón scoriae (see text for details). Symbols as in Figure 4.8.

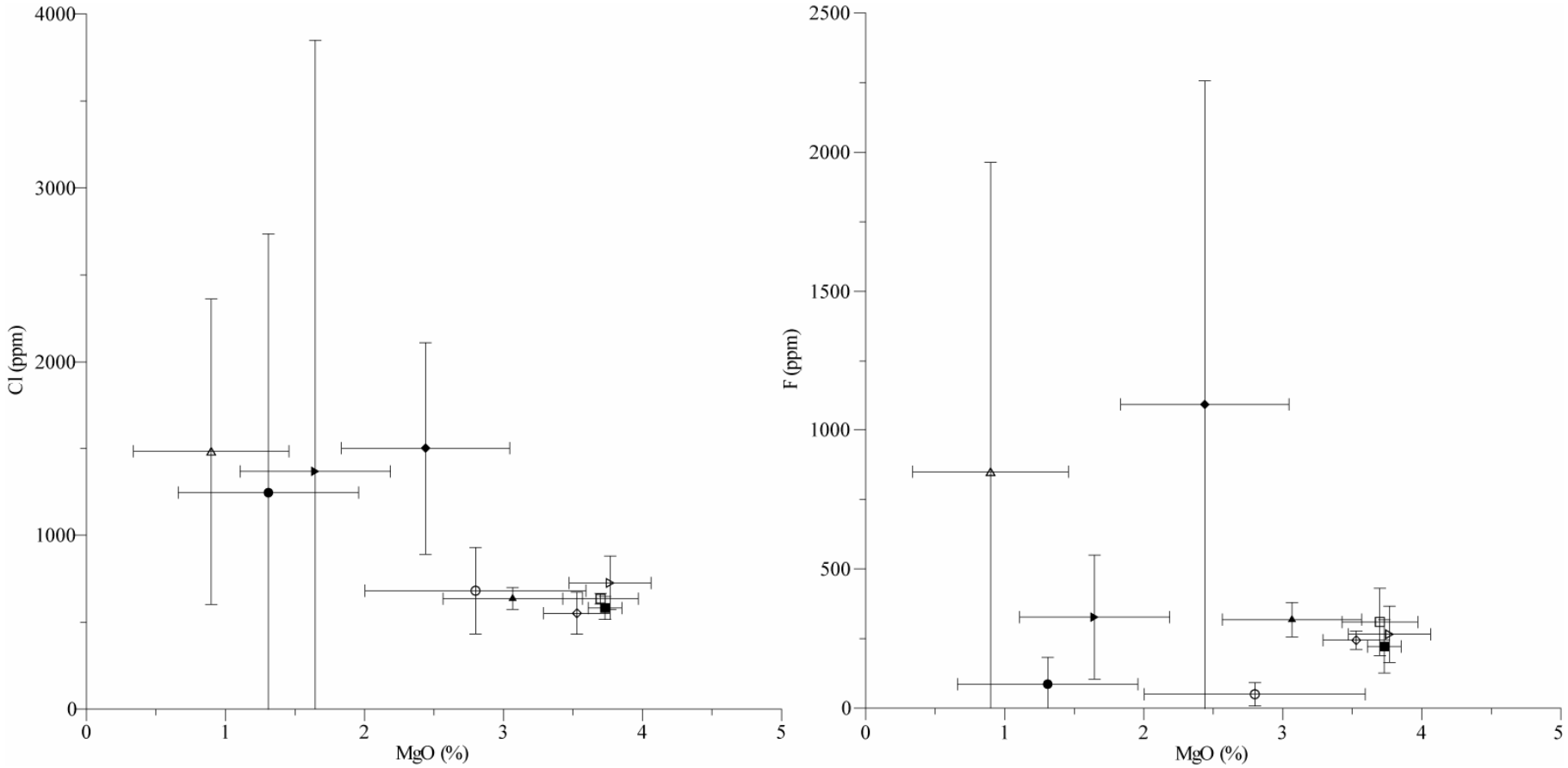

Figure 4.17: Cl and F content (ppm) versus the MgO% of the Pucón scoriae (see text for details). Symbols as in Figure 4.8.

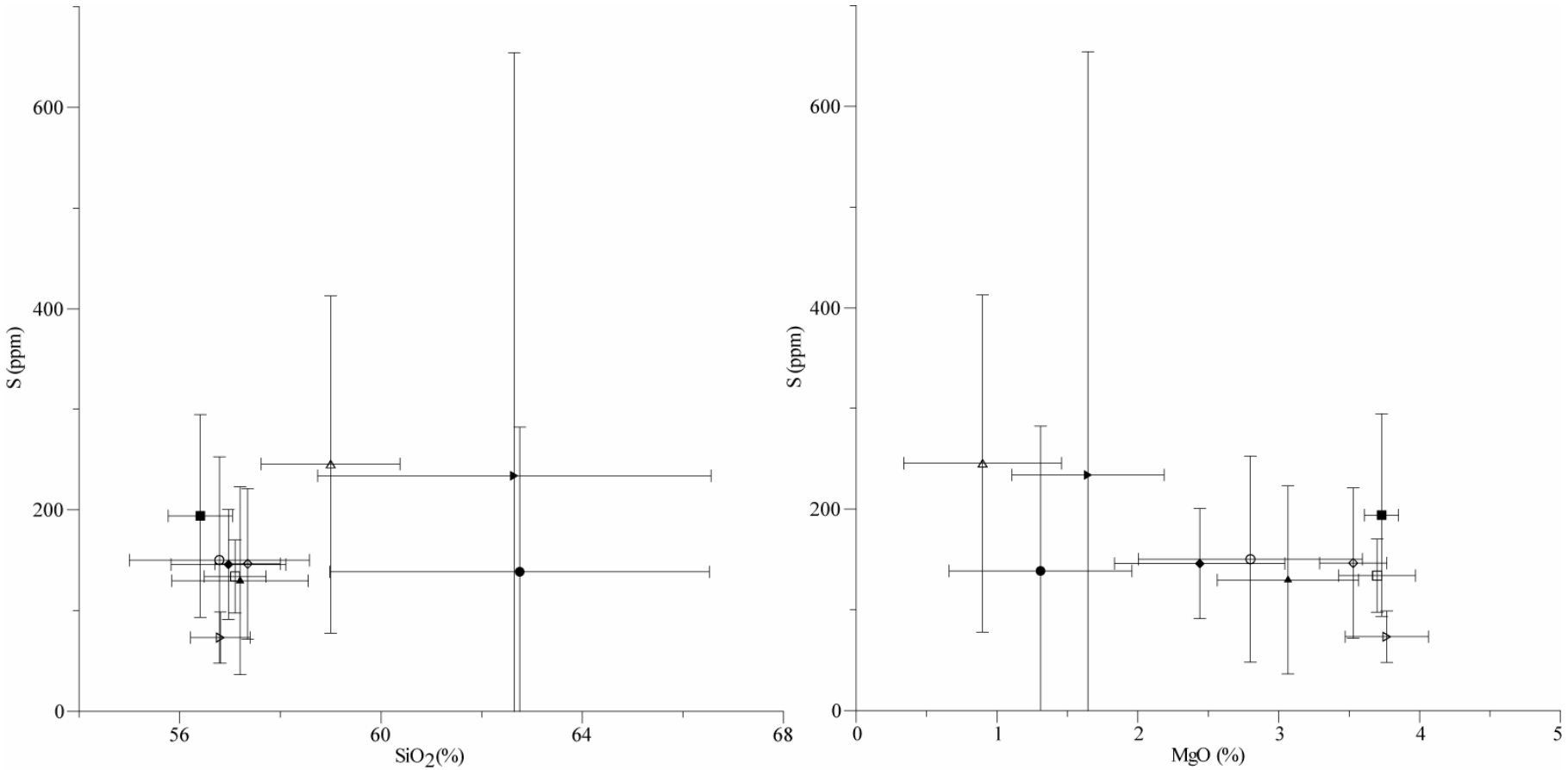

Figure 4.18: S content (ppm) versus SiO_2% and MgO% of the Pucón scoriae (see text for details). Symbols as in Figure 4.8.

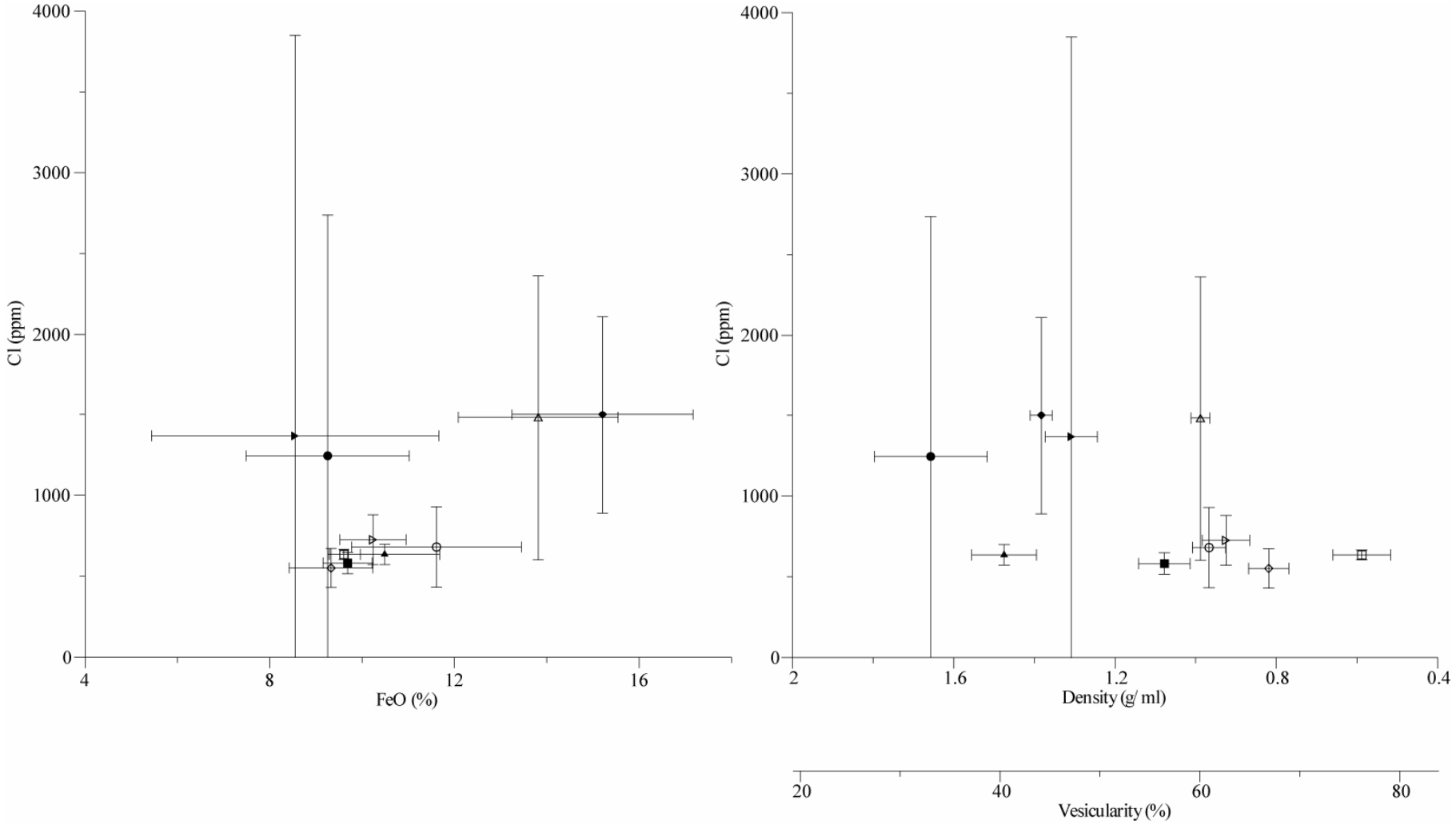

Figure 4.19: Cl content (ppm) versus FeO% (left) and versus density/vesicularity of the Pucón scoriae (right). Symbols as in Figure 4.8.

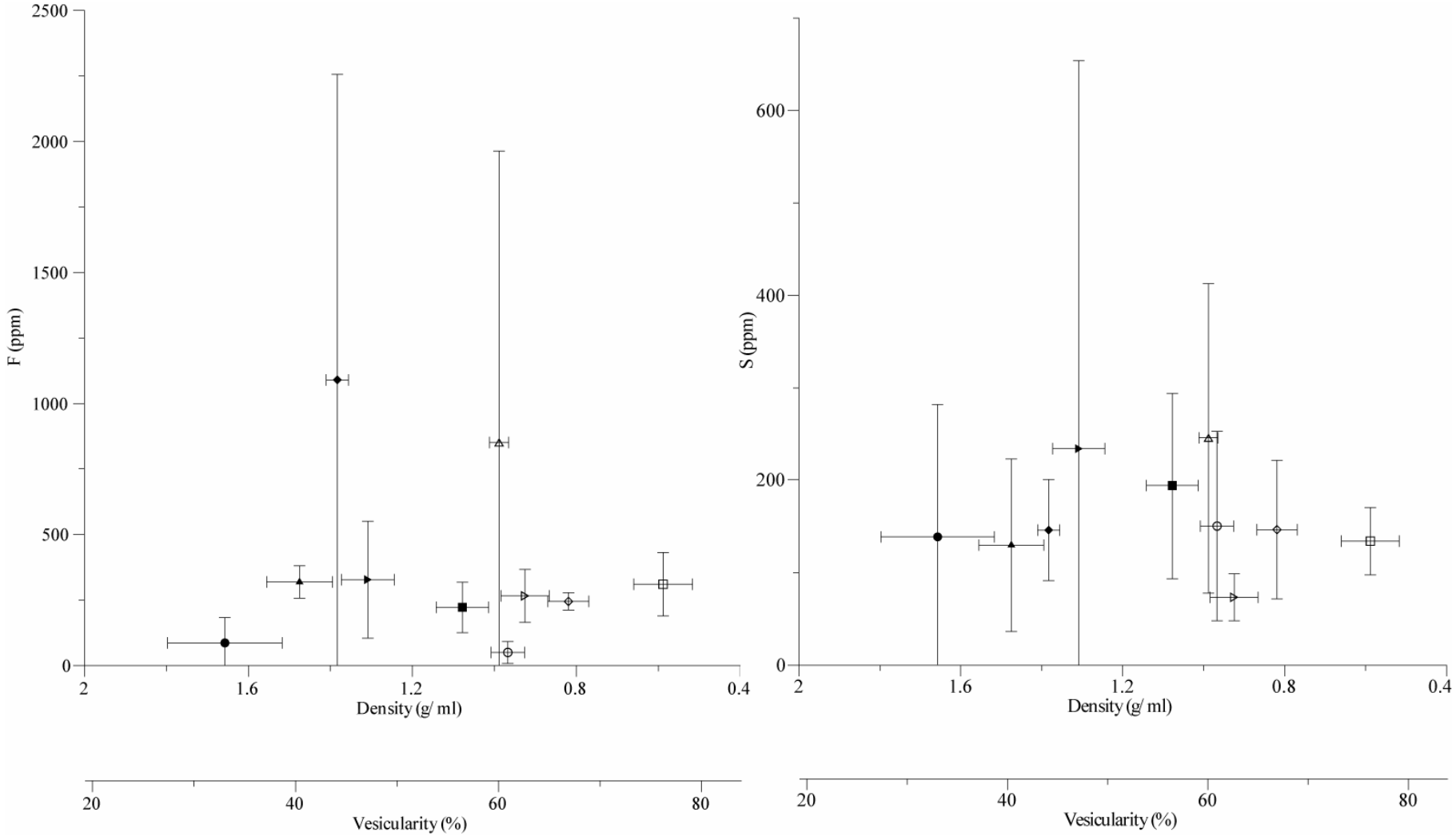

Figure 4.20: F and S contents versus density/vesicularity of the Pucón scoriae. Symbols as in Figure 4.8.

4.7 DISCUSSION

Some evidence could suggest water-magma interaction during P1 and P2 phases:

- Variable, but on average high, lithic contents, achieving up to about 80% in some fractions of some layers (Chapter 3).
- The broad range of vesicularities at all levels from 25 to 75%.
- The presence of dense prismatically-jointed bombs.
- The presence of goldish-brown colour of some vesicular scoria lapilli and bomb crusts especially at the lithic-rich layers to the bottom of both main units (P1a and P2a) which could correspond to palagonitization of the basaltic andesitic glass.

All these features are commonly observed in the products of phreatomagmatism (Fisher & Schmincke, 1984). Certain features of the Pucón Ignimbrite are, however, less consistent with water-magma interaction playing the dominant role in the explosivity of the eruption. From previous chapters, this evidence includes:

- None of the features described above are evident in the basal scoria fall, which appears to be the product of normal, open-conduit, magmatic activity.
- A great proportion of the juvenile particles in the deposits are moderately to highly vesicular (for example, 80% of P1 scoria with vesicularities >50%), showing that the magma was sufficiently rich in volatiles at depth to drive magmatic fragmentation.
- The high-temperature, juvenile-rich horizons P1b and P2b, which have the appearances of normal magmatic products, have vesicularity ranges comparable to those in the lithic-rich horizons, suggesting that the dense juvenile clasts are not related to the same process that causes high lithic contents in the deposits. Many dense clasts are more compatible with an origin by densification following magmatic outgassing at low pressure, either in the conduit or during the eruption.

In this chapter, it has been shown that Cl (and to a lesser extent F) contents correlate with microlite content better than clast density. The correlation of Cl with microlite contents, K_2O and to a lesser degree SiO_2 and MgO suggests that the melt was not saturated in Cl, and thus Cl did not exsolve into the gas phase, but simply concentrated progressively in melt with crystallization, like K.

There is therefore no evidence to support phreatomagmatic quenching of clasts in this dataset and it can be concluded that the Pucón eruption was driven essentially by gas exsolution from the magma. The data are more consistent with degassing and associated crystallization for the origin of the density clasts, rather than by premature quenching by water. An increasing number of studies interpreted textural heterogeneities in pumices as a record of the complexities of conduit processes during the ascent, such as vesiculation, fragmentation and rheological behaviours in different regions of the conduit below magma

fragmentation (e.g. Polacci *et al.*, 2001, 2003; Rosi *et al.*, 2004; D'Oriano *et al.*, 2005; Noguchi *et al.*, 2006). It has been shown that syn-eruptive crystallization of feldspar microlites could have occurred in response to rapid degassing over the time scale of the eruption of Mt Pinatubo in Philippines in 1991 (Hammer *et al.*, 1999). The general trend of higher microlite contents of denser clasts compared with more vesicular clasts can be explained by rapid crystallization accompanying degassing.

Heterogeneities shown by vesicle and crystal textures between differing pumice types but also within single pyroclasts, has been elsewhere described (Polacci *et al.*, 2001). Vesicular microlite-poor and denser microlite-rich textures, being parallel or concentrically interlayered in some Pucón scoriae could reflect different cooling or degassing histories of the scoria, towards the centre and near the conduit walls and could indicate that these textural types could interact in the conduit during magma ascent or fountaining where they mixed and accreted together.

There is also some evidence of pre-fragmentation deformation and reduction of vesicularity of a fluidal magma, such as bubble coalescence, flattening and planar elongation of vesicles cut by the surface of the bomb and higher densities of bombs than lapilli scoria (section 3.4.1.1).

External water may, on the other hand, have played an important role in pulverizing large quantities of rock from the conduit margins progressively eroding and widening the conduit. This could account for the lithic-rich nature of much of the P1 and P2 sequences. Fluctuations in the amount of water involved could account for the observed variations in lithic content (Chapter 3). It is possible that external water was present in larger quantities early on each phase (P1 and P2) and in smaller amount later on because most of the summit glacier and snow had by then melted. Even if this could explain the high lithic contents at the base of P1 and P2, the explanation of the whole lithic variations during the eruption should be more complicated than that, as suggested by the higher lithic contents up through each main unit (P1b to P1c and P2b to P2c). The vertical shift from dense to more vesiculated scoriae upwards through P1 could be explained by the progressive deepening of the fragmentation level during the first phase suggested by the increase the supply of altered fragments and decrease of fresh volcanics along P1 (Chapter 3).

Biotite can incorporate F in its structure, and amphiboles, F and Cl, which are common phases in granitoids. Lohmar *et al.* (2006) reported that these hydrous minerals are absent in granitoid xenoliths of Pucón bombs which display only anhydrous phases. These authors suggest that the assimilation of these materials could have played a role in the eruption of this ignimbrite.

The P2 microlite-rich sample VR85-8-L4 show high contents of F, Cl, SiO_2 and K_2O which could be due to fractional crystallization. However, some contribution of these elements by assimilation of granitoids cannot be discarded.

Additional analyses should be performed in the goldish-brown material to determine if it actually corresponds to palagonite and/or if it has different water content than the normal black scoria which could be important for interpretation.

4.7 CONCLUDING REMARKS

1. The great proportion of vesicular scoria and the high-temperature magmatic P1b and P2b horizons with vesicularities comparable to those in the lithic-rich horizons, suggest that magma was sufficiently rich in volatiles at depth to drive magmatic fragmentation. Thus, the microlite-rich dense clasts can be explained by rapid crystallization accompanying degassing at low pressure.

2. External water, probably from the melting of the summit ice cap, may have played an important role in pulverizing large quantities of rock from the conduit margins, accounting for the lithic-rich nature of much of the sequence, the broad range of vesicularities and the presence of dense prismatically-jointed bombs. Fluctuations in the amount of water involved could account for the observed variations in lithic content.

Appendix 4.1: Particle density measurements

Density is a measure of mass per unit of volume. In the case of individual vesicular particles as the scorias, the concept of bulk density is used, that is the mass divided by the volume including the pores.

$$\textbf{Bulk density} = wt_{\text{dry rock in air}} / V_{\text{displaced water}}$$

A number of methods to measure the bulk density of vesicular fragments (pumice or scorias) is described in the literature. Most of them are based in the Archimedes principle (water-displacement method). Measuring the bulk density of porous and permeable rocks is difficult due to water infiltration into the pores producing an underestimation of the sample volume.

In this study, three methods were used for density measurements, performed in the "Laboratoire Magmas et Volcans" (LMV), Université Blaise-Pascal-CNRS-IRD, Clermont-Ferrand, France.

Method 1: Silicone-sealing of the scorias

The problem of water infiltration in the sample can be overcome by sealing the sample (Houghton & Wilson, 1989; Gardner *et al*., 1991; Polacci *et al*., 2003; Rosi *et al*., 2004; Kueppers *et al.* 2005). In this study, scorias in the range 16-32 mm were impermeabilised with a silicone-based aerosol spray (after Houghton & Wilson, 1989). This laboratory work was done by M. Mercier (undergraduate student 2004/2005). It consists first in weighting the dried samples in a balance (precision = 0.01 g). Then, the samples were made waterproof with a thin film of silicone-based aerosol spray and immersed in a 200 ml graduated test tube (precision $\pm$ 1 ml). The density was calculated by the water-displacement method using the Archimedes principle. Clasts which floated were sunk with a steel spatula and their effective volume calculated by substraction of the spatula volume. The error associated with the balance is negligible and the error of the volume is variable according to the sample volume (vol, in ml) as:

$$\textbf{error (\%) = 1 (ml) / vol (ml) * 100} \qquad \text{(precision of the test tube = 1 ml)}$$

In this case, the error estimations vary from ~3 to 50% with an average of 16%.

The disadvantage of this method is that it implies necessarily the contamination of the sample leaving it unusable for further purposes as for example chemical measurements.

Method 2: Water saturation of bombs

To avoid the problem of sample contamination of method 1, there is commonly used the water saturation of the sample (Robertson & Peck, 1974; Cas & Wright, 1987; Gardner et al., 1996). In this case, we used 128 mm-sized bombs. The laboratory work was done by M. Mercier (undergraduate student 2004/2005, LMV). The sample is oven-dried, weighed in air ($wt_{\text{dry rock in air}}$) and immersed in water. The excess of water from the surface of the saturated sample is quickly removed. It is slowly immersed in a recipient filled completely with water and the volume of the overflowed water is measured with a test tube ($V_{\text{displaced water}}$).

The disadvantage of this method is that only the connected pores are filled with water and not the unconnected vesicles. Moreover, not all pores are completely water-filled, especially large pores on the surface of the sample will leak immediately. Therefore, this method was only used in big bombs.

Method 3: Immersion of scorias in glass beads

Alternative methods that attempt to avoid contamination of vesicular samples consist for example in machining or sealing the samples with plastic film or bags (Rust 1998; Kueppers et al., 2005; Poussineau, 2005; Paquereau 2006). These methods were discarded due to the reduced size of the scoria samples used in this study (about 16 mm sized).

A non-contaminating method was used in this study that consisted in using a granular material instead of water. There were used glass beads of 600-800 µm diameter.

The procedure for measuring the density of the scorias can be described as following:

1. Oven-dry the sample
2. Weigh the sample in air ($wt_{\text{dry rock in air}}$)
3. A recipient is filled with glass particles up to one third of the volume and tapped 20 times, the sample is slowly half-immersed, the recipient is then almost completely filled and tapped 30 times again. The recipient is finally completely filled and the surface is levelled flat with a ruler.
4. The glass particles used for the measure are weighed ($wt_{\text{particles}}$)
5. The density of the sample is calculated as follows:

$$\textbf{Bulk density} = wt_{\text{dry rock in air}} / (V_{\text{recipient}} - wt_{\text{particles}} / \rho_{\text{particles}})$$

Volume of the recipient **($V_{recipient}$):**

The volume of the chosen recipient is critical because the calculated volume of the sample by this method is extremely sensitive to the density of the glass particles. And this influence is more important the larger the recipient. Therefore, the size of the recipient should be as small as possible allowing the complete immersion of the sample.

The volume of the chosen recipient was calculated by three different methods: measuring the dimensions with a ruler, with callipers and weighing the quantity of water to fill it fully (every measure was repeated 3 times). Given the better error of the calliper method, the volume of the recipient is estimated in: 23.6 $\pm$ 0.04 ml.

Table 4. 5: Volume calculations of the recipient used for density measurements

METHOD	VOLUME (ml)	N° MESURES	2σ error
Ruler	21.2	1	
Calliper	23.6	3	0.04
Water volume	24.0	10	0.4

Density of particles **($\rho_{particles}$):**

Since the density of the glass particles is the most relevant parameter for the volume calculation of the sample, their determination was done very carefully.

First, three types of density of particles were tried varying the number of taps to the recipient. To obtain the "loose" density, the recipient was slowly filled with glass particles, the surface was levelled flat with a ruler and the glass particles were weighted. The resulting density was calculated dividing this weight by the volume of the recipient. A "medium" density was obtained in a similar way but tapping 5 times the recipient filled with particles. A "tight" or "packed" density was obtained tapping several tens of times the recipient filled with particles. Considering the lower spread of the data using the "tight" or "packed" density, this was the method finally chosen for the measurements.

Another consideration was to use a density of the glass particles measured the same day as the sample density measurements. This is because the physical properties such as density of granular materials change with the moisture content that they naturally acquire with time. In fact, a difference of 1.2% was observed in the density of particles measured over a 2 weeks span time. For this reason, the particles were oven-dry during a night at 70°C and their density was measured every day of measurement.

The mean density of the particles obtained with this method ($\rho_{particles}$) is 1.62 $\pm$ 0.01 [g/ml]. The associated error was obtained repeating the measurements 10 times and estimated in two ways: the standard deviation of the densities (2σ) and the standard deviation of the weights and then the error calculated by propagation of errors. The difference is negligible, since the error of the volume of the recipient and of the weight balance are both negligible.

Table 4.6: Density of the glass particles measured during the different days of work

Day	Density (g/ml)	N° mesures	Precision (2 σ)	Propagated error (2 σ)
1	1.61	10	0.02	0.02
2	1.62	10	0.01	0.01
3 (AM)	1.62	10	0.01	0.01
3 (PM)	1.62	10	0.01	0.01
4	1.63	10	0.01	0.01
5	1.62	10	0.01	0.01
mean	1.62		0.01	

Appendix 4.2: Calculation of the density of solid and conversion into vesicularity

The density of solid was determined according to the following procedure:

1. Two dense black scoria samples were finely crushed with the tungsten mill. 25 ml of sample were placed in a graduated test tube and weighed ($wt_{sample+tube}$).
2. Water was mixed with a small quantity of soap to diminish the surface tension. The density was measured with a test tube and it resulted ρ_{water}= 0.98 g/ml (1 σ error of 5 measurements = 0.003).
3. The sample was mixed with the water and is left decanting. The excess of water was taken out with a pipette and the new volume corresponds to the volume of the solid plus the pores (V). The tube was weighed again ($wt_{sample+water+tube}$).
4. The density of solid (ρ solid) was calculated as follows:

$$\rho\ solid = wt_{sample} / (V - (wt_{sample+water+tube} - wt_{sample+tube})/ \rho_{water})$$

And it was obtained ρ solid = 2.5 g/ml (1 σ error of 4 measurements = 0.05).

The bulk densities (bulk ρ) calculated with the method of immersion of scoria in glass beads (Method 3, Appendix 4.1) were transformed into vesicularity using the density of solid (ρ solid), as follows:

$$Vesicularity = 100 * (1 - bulk\ \rho/\rho\ solid)$$

Appendix 4.3: Mean density, vesicularity and microlite content, of scoria lapilli (~16 mm diameter) from different stratigraphic levels of the Pucón Ignimbrite. Density measured by immersion of scorias in glass beads (Method 3 of Appendix 4.1)

sample	unit	microlite content [1]	mean density [2]	2σ error [3]	2 σ error [4]	vesicularity [5]
		% vesic-free	g/ml	g/ml	g/ml	%
VR73J-L1	**P1a**		0,82	0,07	0,15	67
VR73J-L2	**P1a**		0,83	0,01	0,08	67
VR73J-L4	**P1a**		0,79	0,12	0,18	68
VR73J-L5	**P1a**		0,84	0,05	0,12	66
VR73J-L6	**P1a**	2	0,82	0,05	0,11	67
VR73J-D1	**P1a**		1,34	0,09	0,19	46
VR73J-D2	**P1a**		1,18	0,06	0,12	52
VR73J-D3	**P1a**	81	1,38	0,03	0,11	44
VR73J-D4	**P1a**		1,04	0,04	0,11	58
VR73J-D5	**P1a**		1,08	0,08	0,13	57
VR73P-L1	**P1b**		0,80	0,08	0,12	68
VR73P-L2	**P1b**	32	0,59	0,07	0,12	76
VR73P-L4	**P1b**		0,79	0,07	0,12	68
VR73P-L5	**P1b**		0,73	0,08	0,13	70
VR73P-L6	**P1b**		0,59	0,06	0,11	76
VR73P-D2	**P1b**		1,21	0,06	0,13	51
VR73P-D4	**P1b**		1,19	0,13	0,21	52
VR73P-D5	**P1b**		0,87	0,07	0,14	65
VR73P-D6	**P1b**		0,87	0,07	0,12	65
VR73P-D7	**P1b**	9	1,08	0,06	0,14	57
VR78-3A-L1	**P2a**	28	0,92	0,06	0,10	63
VR78-3A-L2	**P2a**		0,91	0,09	0,13	63
VR78-3A-L4	**P2a**		0,83	0,06	0,10	67
VR78-3A-L5	**P2a**		0,93	0,05	0,10	62
VR78-3A-L6	**P2a**		0,90	0,02	0,09	64
VR78-3A-D2	**P2a**	55	1,31	0,06	0,12	47
VR78-3A-D3	**P2a**		1,55	0,05	0,15	37
VR78-3A-D4	**P2a**		1,91	0,07	0,17	23
VR78-3A-D5	**P2a**		1,34	0,07	0,14	46
VR78-3A-D6	**P2a**		1,20	0,02	0,12	51
VR85-8-L2	**P2a**		1,12	0,08	0,14	55
VR85-8-L3	**P2a**		0,85	0,06	0,14	66
VR85-8-L4	**P2a**	98	0,99	0,02	0,08	60
VR85-8-L5	**P2a**		0,82	0,08	0,13	67
VR85-8-L6	**P2a**		0,99	0,07	0,13	60
VR85-8-D1	**P2a**		1,29	0,05	0,10	48
VR85-8-D2	**P2a**		1,77	0,04	0,13	29
VR85-8-D4	**P2a**		1,64	0,09	0,16	34
VR85-8-D5	**P2a**	32/90	1,47	0,08	0,14	41
VR85-8-D6	**P2a**		1,53	0,06	0,13	38
VR85-3-L2	**P2b**		1,28	0,13	0,18	48
VR85-3-L3	**P2b**	31/97	0,97	0,04	0,13	61
VR85-3-L4	**P2b**		1,14	0,12	0,20	54
VR85-3-L5	**P2b**		1,08	0,05	0,15	57
VR85-3-L6	**P2b**		0,99	0,06	0,14	60
VR85-3-D2	**P2b**		1,34	0,11	0,21	46
VR85-3-D3	**P2b**		1,40	0,26	0,37	44
VR85-3-D4	**P2b**	91	1,65	0,14	0,24	33
VR85-3-D5	**P2b**		1,35	0,23	0,31	45
VR85-3-D6	**P2b**		1,11	0,09	0,18	55
mean			1,11	0,08	0,15	55

[1] Microlite content measured from image analysis. Samples VR85-8-D5 and VR85-3-L3 are heterogeneous and the microlite contents correspond to their microlite-poor and microlite-rich zones, respectively.
[2] Mean density of 5 measurements following the method of immersion of scorias in glass beads (Method 3 of Appendix 4.1).
[3] Standard deviation (2σ) of the 5 density measurements.
[4] Density error (2σ) calculated by propagation of errors.
[5] Vesicularity calculated from density measurements (Appendix 4.2).

Appendix 4.4: Density measurements of scoria lapilli (16 mm fraction) and scoria bombs (128 mm fraction), measured by silicone-sealing (Method 1, Appendix 4.1) and by water saturation (Method 2, Appendix 4.1), respectively. Samples cover different stratigraphic levels of the Pucón Ignimbrite

	unit	sample	size	density	error vol
				g/ml	%
1	P1a	VR 73 I	16 mm	0,9	33
2	P1a	VR 73 I	16 mm	1,4	33
3	P1a	VR 73 I	16 mm	1,1	50
4	P1a	VR 73 I	16 mm	1,2	33
5	P1a	VR 73 I	16 mm	1,3	6
6	P1a	VR 73 I	16 mm	1,3	7
7	P1a	VR 73 I	16 mm	1,3	8
8	P1a	VR 73 I	16 mm	1,1	13
9	P1a	VR 73 I	16 mm	1,1	13
10	P1a	VR 73 I	16 mm	1,0	8
11	P1a	VR 73 I	16 mm	1,0	8
12	P1a	VR 73 I	16 mm	1,1	7
13	P1a	VR 73 I	16 mm	1,2	11
14	P1a	VR 73 I	16 mm	1,3	13
15	P1a	VR 73 I	16 mm	0,9	13
16	P1a	VR 73 I	16 mm	1,0	33
17	P1a	VR 73 I	16 mm	1,2	14
18	P1a	VR 73 I	16 mm	1,0	8
19	P1a	VR 73 I	16 mm	1,0	17
20	P1a	VR 73 I	16 mm	0,9	13
21	P1a	VR 73 I	16 mm	1,1	14
22	P1a	VR 73 I	16 mm	1,0	10
23	P1a	VR 73 I	16 mm	0,9	13
24	P1a	VR 73 I	16 mm	0,8	25
25	P1a	VR 73 I	16 mm	1,0	13
26	P1a	VR 73 I	16 mm	1,2	14
27	P1a	VR 73 I	16 mm	1,3	25
28	P1a	VR 73 I	16 mm	1,2	17
29	P1a	VR 73 I	16 mm	1,0	25
30	P1a	VR 73 I	16 mm	1,0	33
31	P1a	VR 73 I	16 mm	1,2	14
32	P1a	VR 73 I	16 mm	1,1	33
33	P1a	VR 73 I	16 mm	1,1	33
34	P1a	VR 73 I	16 mm	1,0	33
35	P1a	VR 73 I	16 mm	1,1	33
36	P1a	VR 73 I	16 mm	1,0	40
37	P1a	VR 73 I	16 mm	1,6	10
38	P1a	VR 73 I	16 mm	1,3	25
39	P1a	VR 73 I	16 mm	1,0	13
40	P1a	VR 73 I	16 mm	1,1	7
41	P1a	VR 73 I	16 mm	1,1	33
42	P1a	VR 73 I	16 mm	1,2	40
43	P1a	VR 73 I	16 mm	1,2	33
44	P1a	VR 73 I	16 mm	1,5	50
45	P1a	VR 73 I	16 mm	0,9	25
46	P1a	VR 73 I	16 mm	1,1	17
47	P1a	VR 73 I	16 mm	1,3	14
48	P1a	VR 73 I	16 mm	1,5	33
49	P1a	VR 73 I	16 mm	1,2	14
50	P1a	VR 73 I	16 mm	0,9	20
51	P1a	VR 73 I	16 mm	1,2	14
52	P1a	VR 73 I	16 mm	1,0	17
53	P1a	VR 73 I	16 mm	1,1	7
54	P1a	VR 73 I	16 mm	0,9	14
55	P1a	VR 73 I	16 mm	1,7	25
56	P1a	VR 73 I	16 mm	1,0	33
57	P1a	VR 73 I	16 mm	1,4	20
58	P1a	VR 73 I	16 mm	1,1	20
59	P1a	VR 73 I	16 mm	0,9	13
60	P1a	VR 73 I	16 mm	0,9	25
61	P1a	VR 73 I	16 mm	0,9	17
62	P1a	VR 73 I	16 mm	1,1	25
63	P1a	VR 73 I	16 mm	1,0	33
64	P1a	VR 73 I	16 mm	1,1	20
65	P1a	VR 73 I	16 mm	0,8	17
66	P1a	VR 73 I	16 mm	1,1	20
67	P1a	VR 73 I	16 mm	1,4	50
68	P1a	VR 73 I	16 mm	1,1	33
69	P1a	VR 73 I	16 mm	1,3	25
70	P1a	VR 73 I	16 mm	0,8	25
71	P1a	VR 73 I	16 mm	1,1	40
72	P1a	VR 73 I	16 mm	1,4	25
1	P1a	VR 73 L	16 mm	1,8	13
2	P1a	VR 73 L	16 mm	0,9	13
3	P1a	VR 73 L	16 mm	1,0	7
4	P1a	VR 73 L	16 mm	1,0	10
5	P1a	VR 73 L	16 mm	0,7	20
6	P1a	VR 73 L	16 mm	1,0	13
7	P1a	VR 73 L	16 mm	0,8	8
8	P1a	VR 73 L	16 mm	0,9	20
9	P1a	VR 73 L	16 mm	1,2	20
10	P1a	VR 73 L	16 mm	0,8	7
11	P1a	VR 73 L	16 mm	1,2	14
12	P1a	VR 73 L	16 mm	0,7	5
13	P1a	VR 73 L	16 mm	0,7	17
14	P1a	VR 73 L	16 mm	0,7	13
15	P1a	VR 73 L	16 mm	1,5	13
1	P1a	VR 73 L	16 mm	0,9	8
2	P1a	VR 73 L	16 mm	0,9	14
3	P1a	VR 73 L	16 mm	0,9	14
4	P1a	VR 73 L	16 mm	0,9	20
5	P1a	VR 73 L	16 mm	0,8	6
6	P1a	VR 73 L	16 mm	1,1	20
7	P1a	VR 73 L	16 mm	0,7	20
8	P1a	VR 73 L	16 mm	0,8	20
9	P1a	VR 73 L	16 mm	0,8	20
10	P1a	VR 73 L	16 mm	1,4	50
11	P1a	VR 73 L	16 mm	1,0	25
12	P1a	VR 73 L	16 mm	0,9	8
13	P1a	VR 73 L	16 mm	0,7	11
14	P1a	VR 73 L	16 mm	1,1	25
15	P1a	VR 73 L	16 mm	0,6	17
16	P1a	VR 73 L	16 mm	1,0	20
17	P1a	VR 73 L	16 mm	0,9	25
18	P1a	VR 73 L	16 mm	0,9	33
1	P1b	VR73N2	128 mm	1,3	
2	P1b	VR73N2	128 mm	1,3	
3	P1b	VR73N2	128 mm	1,4	
4	P1b	VR73N2	128 mm	1,1	
5	P1b	VR73N2	128 mm	1,3	
6	P1b	VR73N2	128 mm	1,2	
7	P1b	VR73N2	128 mm	0,9	
8	P1b	VR73N2	128 mm	1,5	
9	P1b	VR73N2	128 mm	1,5	
10	P1b	VR73N2	128 mm	1,7	
1	P1b	VR 73 P	16 mm	0,9	7
2	P1b	VR 73 P	16 mm	0,8	17
3	P1b	VR 73 P	16 mm	0,8	17
4	P1b	VR 73 P	16 mm	0,9	9
5	P1b	VR 73 P	16 mm	1,2	14
6	P1b	VR 73 P	16 mm	1,1	11
7	P1b	VR 73 P	16 mm	0,7	10
8	P1b	VR 73 P	16 mm	0,8	10
9	P1b	VR 73 P	16 mm	0,9	14
10	P1b	VR 73 P	16 mm	1,8	8
11	P1b	VR 73 P	16 mm	0,6	10
12	P1b	VR 73 P	16 mm	1,4	11
13	P1b	VR 73 P	16 mm	1,0	13
14	P1b	VR 73 P	16 mm	1,0	6
15	P1b	VR 73 P	16 mm	1,2	10
16	P1b	VR 73 P	16 mm	0,8	13
17	P1b	VR 73 P	16 mm	1,0	14
18	P1b	VR 73 P	16 mm	0,9	11
19	P1b	VR 73 P	16 mm	0,8	11
20	P1b	VR 73 P	16 mm	0,9	13
21	P1b	VR 73 P	16 mm	1,5	14
22	P1b	VR 73 P	16 mm	1,2	8
23	P1b	VR 73 P	16 mm	0,8	10
24	P1b	VR 73 P	16 mm	0,7	11
25	P1b	VR 73 P	16 mm	1,0	9
26	P1b	VR 73 P	16 mm	1,1	25
27	P1b	VR 73 P	16 mm	0,9	9
28	P1b	VR 73 P	16 mm	0,9	11
29	P1b	VR 73 P	16 mm	0,9	10
30	P1b	VR 73 P	16 mm	1,3	25
31	P1b	VR 73 P	16 mm	0,9	10
32	P1b	VR 73 P	16 mm	0,9	11
33	P1b	VR 73 P	16 mm	0,8	8
34	P1b	VR 73 P	16 mm	1,2	14
35	P1b	VR 73 P	16 mm	0,9	10
36	P1b	VR 73 P	16 mm	1,3	6
37	P1b	VR 73 P	16 mm	0,9	13
38	P1b	VR 73 P	16 mm	0,8	8
39	P1b	VR 73 P	16 mm	0,9	7
40	P1b	VR 73 P	16 mm	0,8	7
41	P1b	VR 73 P	16 mm	1,0	17
42	P1b	VR 73 P	16 mm	0,8	13
43	P1b	VR 73 P	16 mm	0,9	13
44	P1b	VR 73 P	16 mm	1,0	8
45	P1b	VR 73 P	16 mm	0,9	7
46	P1b	VR 73 P	16 mm	0,9	14
47	P1b	VR 73 P	16 mm	1,3	11
48	P1b	VR 73 P	16 mm	0,8	7
49	P1b	VR 73 P	16 mm	0,9	6
50	P1b	VR 73 P	16 mm	0,7	10
51	P1b	VR 73 P	16 mm	0,6	6
52	P1b	VR 73 P	16 mm	1,2	8
53	P1b	VR 73 P	16 mm	1,0	8
54	P1b	VR 73 P	16 mm	1,1	9
55	P1b	VR 73 P	16 mm	1,1	9
56	P1b	VR 73 P	16 mm	1,1	13

	unit	sample	size	density	error vol
				g/ml	%
57	P1b	VR 73 P	16 mm	0,9	10
58	P1b	VR 73 P	16 mm	1,0	8
59	P1b	VR 73 P	16 mm	1,1	10
60	P1b	VR 73 P	16 mm	1,1	14
61	P1b	VR 73 P	16 mm	1,0	13
62	P1b	VR 73 P	16 mm	0,9	10
63	P1b	VR 73 P	16 mm	0,9	8
64	P1b	VR 73 P	16 mm	0,9	10
1	P2a	VR 78 3A	16 mm	1,1	5
2	P2a	VR 78 3A	16 mm	1,1	6
3	P2a	VR 78 3A	16 mm	1,3	9
4	P2a	VR 78 3A	16 mm	1,2	9
5	P2a	VR 78 3A	16 mm	1,1	7
6	P2a	VR 78 3A	16 mm	1,5	25
7	P2a	VR 78 3A	16 mm	1,0	13
8	P2a	VR 78 3A	16 mm	1,0	10
9	P2a	VR 78 3A	16 mm	0,9	20
10	P2a	VR 78 3A	16 mm	0,7	20
11	P2a	VR 78 3A	16 mm	1,9	25
12	P2a	VR 78 3A	16 mm	1,1	33
13	P2a	VR 78 3A	16 mm	1,0	20
14	P2a	VR 78 3A	16 mm	1,4	33
15	P2a	VR 78 3A	16 mm	0,8	33
16	P2a	VR 78 3A	16 mm	1,4	22
17	P2a	VR 78 3A	16 mm	1,1	25
18	P2a	VR 78 3A	16 mm	0,9	13
19	P2a	VR 78 3A	16 mm	1,0	10
20	P2a	VR 78 3A	16 mm	1,2	25
21	P2a	VR 78 3A	16 mm	1,5	11
22	P2a	VR 78 3A	16 mm	0,9	14
23	P2a	VR 78 3A	16 mm	1,0	14
24	P2a	VR 78 3A	16 mm	1,2	25
25	P2a	VR 78 3A	16 mm	1,1	14
26	P2a	VR 78 3A	16 mm	1,1	33
27	P2a	VR 78 3A	16 mm	1,5	25
28	P2a	VR 78 3A	16 mm	1,1	20
29	P2a	VR 78 3A	16 mm	1,4	25
30	P2a	VR 78 3A	16 mm	1,0	25
31	P2a	VR 78 3A	16 mm	1,0	14
32	P2a	VR 78 3A	16 mm	1,1	17
33	P2a	VR 78 3A	16 mm	1,5	33
34	P2a	VR 78 3A	16 mm	1,6	8
35	P2a	VR 78 3A	16 mm	1,5	17
36	P2a	VR 78 3A	16 mm	1,0	14
37	P2a	VR 78 3A	16 mm	1,4	20
38	P2a	VR 78 3A	16 mm	1,7	33
39	P2a	VR 78 3A	16 mm	1,0	17
40	P2a	VR 78 3A	16 mm	1,3	33
41	P2a	VR 78 3A	16 mm	1,0	20
42	P2a	VR 78 3A	16 mm	1,0	14
43	P2a	VR 78 3A	16 mm	1,0	25
44	P2a	VR 78 3A	16 mm	0,9	25
45	P2a	VR 78 3A	16 mm	1,0	20
46	P2a	VR 78 3A	16 mm	1,0	20
47	P2a	VR 78 3A	16 mm	1,0	20
48	P2a	VR 78 3A	16 mm	1,0	25
49	P2a	VR 78 3A	16 mm	0,8	33

	unit	sample	size	density	error vol
				g/ml	%
50	P2a	VR 78 3A	16 mm	1,1	10
51	P2a	VR 78 3A	16 mm	1,5	25
52	P2a	VR 78 3A	16 mm	1,0	8
53	P2a	VR 78 3A	16 mm	1,2	17
54	P2a	VR 78 3A	16 mm	1,3	25
55	P2a	VR 78 3A	16 mm	1,0	33
56	P2a	VR 78 3A	16 mm	1,2	25
57	P2a	VR 78 3A	16 mm	1,2	29
58	P2a	VR 78 3A	16 mm	1,2	20
59	P2a	VR 78 3A	16 mm	1,3	10
60	P2a	VR 78 3A	16 mm	1,2	8
61	P2a	VR 78 3A	16 mm	1,2	8
62	P2a	VR 78 3A	16 mm	1,0	7
63	P2a	VR 78 3A	16 mm	1,0	8
64	P2a	VR 78 3A	16 mm	1,0	25
65	P2a	VR 78 3A	16 mm	1,3	33
66	P2a	VR 78 3A	16 mm	1,0	17
67	P2a	VR 78 3A	16 mm	1,2	20
68	P2a	VR 78 3A	16 mm	1,1	10
69	P2a	VR 78 3A	16 mm	0,9	20
70	P2a	VR 78 3A	16 mm	0,8	14
71	P2a	VR 78 3A	16 mm	1,3	20
1	P2a	VR 78 3B	16 mm	1,0	6
2	P2a	VR 78 3B	16 mm	1,1	7
3	P2a	VR 78 3B	16 mm	0,7	25
4	P2a	VR 78 3B	16 mm	1,0	20
5	P2a	VR 78 3B	16 mm	0,8	25
6	P2a	VR 78 3B	16 mm	1,2	20
7	P2a	VR 78 3B	16 mm	0,9	20
8	P2a	VR 78 3B	16 mm	1,2	33
1	P2a	VR 78 3C	16 mm	1,3	20
2	P2a	VR 78 3C	16 mm	1,0	20
3	P2a	VR 78 3C	16 mm	1,0	6
4	P2a	VR 78 3C	16 mm	1,1	13
5	P2a	VR 78 3C	16 mm	1,0	17
6	P2a	VR 78 3C	16 mm	1,2	33
7	P2a	VR 78 3C	16 mm	0,9	8
8	P2a	VR 78 3C	16 mm	1,2	50
9	P2a	VR 78 3C	16 mm	0,9	40
10	P2a	VR 78 3C	16 mm	1,0	17
11	P2a	VR 78 3C	16 mm	0,9	40
12	P2a	VR 78 3C	16 mm	0,9	33
13	P2a	VR 78 3C	16 mm	0,9	7
14	P2a	VR 78 3C	16 mm	1,4	20
15	P2a	VR 78 3C	16 mm	0,9	9
16	P2a	VR 78 3C	16 mm	0,9	40
17	P2a	VR 78 3C	16 mm	1,0	33
18	P2a	VR 78 3C	16 mm	1,2	11
19	P2a	VR 78 3C	16 mm	0,9	25
20	P2a	VR 78 3C	16 mm	1,1	33
21	P2a	VR 78 3C	16 mm	1,4	33
1	P2a	VR 85 8	16 mm	1,2	8
2	P2a	VR 85 8	16 mm	1,1	11
3	P2a	VR 85 8	16 mm	1,1	15
4	P2a	VR 85 8	16 mm	1,4	6
5	P2a	VR 85 8	16 mm	1,4	8
6	P2a	VR 85 8	16 mm	1,6	10

	unit	sample	size	density	error vol
				g/ml	%
7	P2a	VR 85 8	16 mm	1,9	7
8	P2a	VR 85 8	16 mm	1,2	11
9	P2a	VR 85 8	16 mm	0,9	17
10	P2a	VR 85 8	16 mm	0,9	11
11	P2a	VR 85 8	16 mm	1,3	6
12	P2a	VR 85 8	16 mm	1,2	13
13	P2a	VR 85 8	16 mm	1,6	25
14	P2a	VR 85 8	16 mm	1,3	17
15	P2a	VR 85 8	16 mm	1,1	14
16	P2a	VR 85 8	16 mm	1,4	7
17	P2a	VR 85 8	16 mm	1,2	25
18	P2a	VR 85 8	16 mm	1,6	20
19	P2a	VR 85 8	16 mm	1,4	5
20	P2a	VR 85 8	16 mm	1,8	25
21	P2a	VR 85 8	16 mm	1,1	12
22	P2a	VR 85 8	16 mm	1,2	14
23	P2a	VR 85 8	16 mm	1,1	4
24	P2a	VR 85 8	16 mm	0,9	5
25	P2a	VR 85 8	16 mm	0,9	9
26	P2a	VR 85 8	16 mm	1,6	11
27	P2a	VR 85 8	16 mm	0,9	8
28	P2a	VR 85 8	16 mm	1,1	17
29	P2a	VR 85 8	16 mm	1,4	13
30	P2a	VR 85 8	16 mm	1,3	13
31	P2a	VR 85 8	16 mm	1,7	20
32	P2a	VR 85 8	16 mm	1,2	17
33	P2a	VR 85 8	16 mm	1,0	8
34	P2a	VR 85 8	16 mm	1,2	7
35	P2a	VR 85 8	16 mm	1,3	10
36	P2a	VR 85 8	16 mm	1,1	13
37	P2a	VR 85 8	16 mm	1,6	13
38	P2a	VR 85 8	16 mm	1,3	14
39	P2a	VR 85 8	16 mm	1,5	10
40	P2a	VR 85 8	16 mm	1,4	22
41	P2a	VR 85 8	16 mm	1,3	8
42	P2a	VR 85 8	16 mm	1,1	11
43	P2a	VR 85 8	16 mm	1,4	7
44	P2a	VR 85 8	16 mm	1,1	11
45	P2a	VR 85 8	16 mm	1,2	8
46	P2a	VR 85 8	16 mm	1,3	11
47	P2a	VR 85 8	16 mm	1,4	20
48	P2a	VR 85 8	16 mm	1,4	13
49	P2a	VR 85 8	16 mm	1,5	20
50	P2a	VR 85 8	16 mm	1,8	25
51	P2a	VR 85 8	16 mm	1,5	25
52	P2a	VR 85 8	16 mm	1,2	14
53	P2a	VR 85 8	16 mm	1,2	8
54	P2a	VR 85 8	16 mm	1,6	25
55	P2a	VR 85 8	16 mm	1,6	13
56	P2a	VR 85 8	16 mm	1,5	20
57	P2a	VR 85 8	16 mm	1,0	7
58	P2a	VR 85 8	16 mm	1,3	13
59	P2a	VR 85 8	16 mm	1,3	11
60	P2a	VR 85 8	16 mm	1,5	17
61	P2a	VR 85 8	16 mm	1,3	17
62	P2a	VR 85 8	16 mm	0,9	20
63	P2a	VR 85 8	16 mm	1,2	20

	unit	sample	size	density	error vol
				g/ml	%
64	P2a	VR 85 8	16 mm	1,1	17
65	P2a	VR 85 8	16 mm	1,2	4
66	P2a	VR 85 8	16 mm	1,3	10
67	P2a	VR 85 8	16 mm	1,2	10
68	P2a	VR 85 8	16 mm	1,6	11
69	P2a	VR 85 8	16 mm	1,2	5
70	P2a	VR 85 8	16 mm	1,6	5
71	P2a	VR 85 8	16 mm	2,0	11
72	P2a	VR 85 8	16 mm	1,9	8
73	P2a	VR 85 8	16 mm	1,5	4
74	P2a	VR 85 8	16 mm	1,9	8
75	P2a	VR 85 8	16 mm	1,7	13
76	P2a	VR 85 8	16 mm	1,4	9
77	P2a	VR 85 8	16 mm	1,6	14
78	P2a	VR 85 8	16 mm	1,8	13
79	P2a	VR 85 8	16 mm	1,4	8
1	P2a	VR 85 6	16 mm	1,0	11
2	P2a	VR 85 6	16 mm	0,9	13
3	P2a	VR 85 6	16 mm	1,4	9
4	P2a	VR 85 6	16 mm	1,0	17
5	P2a	VR 85 6	16 mm	1,1	33
6	P2a	VR 85 6	16 mm	1,3	20
7	P2a	VR 85 6	16 mm	1,4	20
8	P2a	VR 85 6	16 mm	1,2	20
9	P2a	VR 85 6	16 mm	1,0	17
10	P2a	VR 85 6	16 mm	1,0	11
11	P2a	VR 85 6	16 mm	1,0	20
12	P2a	VR 85 6	16 mm	0,8	20
13	P2a	VR 85 6	16 mm	1,2	20
14	P2a	VR 85 6	16 mm	1,3	25
15	P2a	VR 85 6	16 mm	0,9	29
16	P2a	VR 85 6	16 mm	1,5	50
17	P2a	VR 85 6	16 mm	1,6	33
18	P2a	VR 85 6	16 mm	1,0	29
19	P2a	VR 85 6	16 mm	1,0	29
20	P2a	VR 85 6	16 mm	1,1	25
21	P2a	VR 85 6	16 mm	1,1	33
22	P2a	VR 85 6	16 mm	0,9	25
23	P2a	VR 85 6	16 mm	1,7	25
24	P2a	VR 85 6	16 mm	1,3	25
25	P2a	VR 85 6	16 mm	1,4	25
26	P2a	VR 85 6	16 mm	1,6	11
1	P2a	VR 85 5	16 mm	1,2	8
2	P2a	VR 85 5	16 mm	1,0	6
3	P2a	VR 85 5	16 mm	1,2	11
4	P2a	VR 85 5	16 mm	1,1	8
5	P2a	VR 85 5	16 mm	1,7	17
6	P2a	VR 85 5	16 mm	1,4	10
7	P2a	VR 85 5	16 mm	1,0	13
8	P2a	VR 85 5	16 mm	1,3	13
9	P2a	VR 85 5	16 mm	1,0	10
10	P2a	VR 85 5	16 mm	1,0	11
11	P2a	VR 85 5	16 mm	1,0	9
12	P2a	VR 85 5	16 mm	1,5	11
13	P2a	VR 85 5	16 mm	1,0	13
14	P2a	VR 85 5	16 mm	1,1	7
15	P2a	VR 85 5	16 mm	1,2	11

	unit	sample	size	density	error vol
				g/ml	%
16	P2a	VR 85 5	16 mm	1,4	17
17	P2a	VR 85 5	16 mm	1,0	17
18	P2a	VR 85 5	16 mm	1,7	25
19	P2a	VR 85 5	16 mm	1,0	17
20	P2a	VR 85 5	16 mm	1,2	20
21	P2a	VR 85 5	16 mm	1,2	13
22	P2a	VR 85 5	16 mm	1,4	13
23	P2a	VR 85 5	16 mm	1,0	14
24	P2a	VR 85 5	16 mm	1,2	6
25	P2a	VR 85 5	16 mm	1,1	8
26	P2a	VR 85 5	16 mm	1,0	20
27	P2a	VR 85 5	16 mm	1,1	17
28	P2a	VR 85 5	16 mm	1,4	20
29	P2a	VR 85 5	16 mm	1,1	17
30	P2a	VR 85 5	16 mm	1,2	17
31	P2a	VR 85 5	16 mm	1,2	14
32	P2a	VR 85 5	16 mm	1,2	18
33	P2a	VR 85 5	16 mm	1,2	33
34	P2a	VR 85 5	16 mm	1,2	14
35	P2a	VR 85 5	16 mm	1,0	20
36	P2a	VR 85 5	16 mm	1,1	25
37	P2a	VR 85 5	16 mm	1,2	25
38	P2a	VR 85 5	16 mm	1,3	20
39	P2a	VR 85 5	16 mm	1,3	33
40	P2a	VR 85 5	16 mm	1,1	10
41	P2a	VR 85 5	16 mm	1,4	8
42	P2a	VR 85 5	16 mm	1,5	7
43	P2a	VR 85 5	16 mm	1,1	14
44	P2a	VR 85 5	16 mm	1,1	17
45	P2a	VR 85 5	16 mm	1,1	10
46	P2a	VR 85 5	16 mm	1,2	13
47	P2a	VR 85 5	16 mm	1,0	9
48	P2a	VR 85 5	16 mm	0,9	20
49	P2a	VR 85 5	16 mm	1,1	7
50	P2a	VR 85 5	16 mm	1,2	20
51	P2a	VR 85 5	16 mm	0,8	13
52	P2a	VR 85 5	16 mm	1,2	14
53	P2a	VR 85 5	16 mm	1,1	20
54	P2a	VR 85 5	16 mm	1,2	9
55	P2a	VR 85 5	16 mm	1,0	25
56	P2a	VR 85 5	16 mm	1,2	13
57	P2a	VR 85 5	16 mm	1,1	14
58	P2a	VR 85 5	16 mm	1,1	14
59	P2a	VR 85 5	16 mm	1,2	20
60	P2a	VR 85 5	16 mm	1,0	25
61	P2a	VR 85 5	16 mm	1,1	20
62	P2a	VR 85 5	16 mm	1,1	17
63	P2a	VR 85 5	16 mm	1,1	33
64	P2a	VR 85 5	16 mm	1,1	20
65	P2a	VR 85 5	16 mm	1,1	20
66	P2a	VR 85 5	16 mm	1,0	25
67	P2a	VR 85 5	16 mm	0,8	25
68	P2a	VR 85 5	16 mm	1,1	25
69	P2a	VR 85 5	16 mm	1,2	33
70	P2a	VR 85 5	16 mm	1,4	7
71	P2a	VR 85 5	16 mm	1,1	13
72	P2a	VR 85 5	16 mm	1,4	9

	unit	sample	size	density	error vol
				g/ml	%
73	P2a	VR 85 5	16 mm	1,3	8
74	P2a	VR 85 5	16 mm	1,5	8
75	P2a	VR 85 5	16 mm	1,5	13
76	P2a	VR 85 5	16 mm	1,4	17
77	P2a	VR 85 5	16 mm	1,2	10
78	P2a	VR 85 5	16 mm	1,4	7
79	P2a	VR 85 5	16 mm	1,3	8
80	P2a	VR 85 5	16 mm	1,2	11
81	P2a	VR 85 5	16 mm	1,3	11
82	P2a	VR 85 5	16 mm	1,2	13
83	P2a	VR 85 5	16 mm	1,5	14
84	P2a	VR 85 5	16 mm	1,4	14
85	P2a	VR 85 5	16 mm	1,6	25
86	P2a	VR 85 5	16 mm	1,4	11
87	P2a	VR 85 5	16 mm	1,2	5
88	P2a	VR 85 5	16 mm	1,3	11
89	P2a	VR 85 5	16 mm	1,5	9
90	P2a	VR 85 5	16 mm	1,3	14
91	P2a	VR 85 5	16 mm	1,7	13
92	P2a	VR 85 5	16 mm	1,0	14
93	P2a	VR 85 5	16 mm	1,7	10
94	P2a	VR 85 5	16 mm	1,5	7
95	P2a	VR 85 5	16 mm	1,3	8
96	P2a	VR 85 5	16 mm	1,3	13
97	P2a	VR 85 5	16 mm	1,1	6
98	P2a	VR 85 5	16 mm	1,4	8
99	P2a	VR 85 5	16 mm	1,1	11
100	P2a	VR 85 5	16 mm	2,1	13
101	P2a	VR 85 5	16 mm	1,7	11
102	P2a	VR 85 5	16 mm	2,0	25
103	P2a	VR 85 5	16 mm	2,0	25
104	P2a	VR 85 5	16 mm	1,2	20
105	P2a	VR 85 5	16 mm	1,5	25
106	P2a	VR 85 5	16 mm	1,3	20
107	P2a	VR 85 5	16 mm	1,3	20
1	P2b	VR 85 4	16 mm	0,9	5
2	P2b	VR 85 4	16 mm	1,2	11
3	P2b	VR 85 4	16 mm	1,1	5
4	P2b	VR 85 4	16 mm	1,4	9
5	P2b	VR 85 4	16 mm	1,4	6
6	P2b	VR 85 4	16 mm	1,1	13
7	P2b	VR 85 4	16 mm	1,2	8
8	P2b	VR 85 4	16 mm	1,2	6
9	P2b	VR 85 4	16 mm	1,2	13
10	P2b	VR 85 4	16 mm	1,2	5
11	P2b	VR 85 4	16 mm	1,7	20
12	P2b	VR 85 4	16 mm	1,1	14
13	P2b	VR 85 4	16 mm	1,5	25
14	P2b	VR 85 4	16 mm	1,2	13
15	P2b	VR 85 4	16 mm	1,0	14
16	P2b	VR 85 4	16 mm	1,2	3
17	P2b	VR 85 4	16 mm	1,6	7
18	P2b	VR 85 4	16 mm	1,1	4
19	P2b	VR 85 4	16 mm	1,7	13
20	P2b	VR 85 4	16 mm	1,1	20
21	P2b	VR 85 4	16 mm	1,2	8
22	P2b	VR 85 4	16 mm	1,4	11

	unit	sample	size	density	error vol
				g/ml	%
23	P2b	VR 85 4	16 mm	1,2	15
24	P2b	VR 85 4	16 mm	1,1	8
25	P2b	VR 85 4	16 mm	1,1	13
26	P2b	VR 85 4	16 mm	1,2	10
27	P2b	VR 85 4	16 mm	1,1	17
28	P2b	VR 85 4	16 mm	1,1	14
29	P2b	VR 85 4	16 mm	1,2	17
30	P2b	VR 85 4	16 mm	1,0	13
31	P2b	VR 85 4	16 mm	1,4	20
32	P2b	VR 85 4	16 mm	1,1	13
33	P2b	VR 85 4	16 mm	1,3	20
34	P2b	VR 85 4	16 mm	1,3	15
35	P2b	VR 85 4	16 mm	1,2	20
36	P2b	VR 85 4	16 mm	1,3	20
37	P2b	VR 85 4	16 mm	1,6	25
38	P2b	VR 85 4	16 mm	1,2	25
39	P2b	VR 85 4	16 mm	1,2	20
40	P2b	VR 85 4	16 mm	1,6	6
41	P2b	VR 85 4	16 mm	1,5	17
42	P2b	VR 85 4	16 mm	1,5	14
43	P2b	VR 85 4	16 mm	1,6	10
44	P2b	VR 85 4	16 mm	1,5	13
1	P2b	VR 85 3	16 mm	1,2	13
2	P2b	VR 85 3	16 mm	1,2	25
3	P2b	VR 85 3	16 mm	1,3	17
4	P2b	VR 85 3	16 mm	1,3	20
5	P2b	VR 85 3	16 mm	1,3	17
6	P2b	VR 85 3	16 mm	1,7	20
7	P2b	VR 85 3	16 mm	1,1	10
8	P2b	VR 85 3	16 mm	1,5	20
9	P2b	VR 85 3	16 mm	1,2	17
10	P2b	VR 85 3	16 mm	1,2	17
11	P2b	VR 85 3	16 mm	1,8	25
12	P2b	VR 85 3	16 mm	1,1	22
13	P2b	VR 85 3	16 mm	1,1	9
14	P2b	VR 85 3	16 mm	0,9	11
15	P2b	VR 85 3	16 mm	1,1	8
16	P2b	VR 85 3	16 mm	1,0	6
17	P2b	VR 85 3	16 mm	1,3	20
18	P2b	VR 85 3	16 mm	1,6	25
19	P2b	VR 85 3	16 mm	2,0	33
20	P2b	VR 85 3	16 mm	1,1	13
21	P2b	VR 85 3	16 mm	1,1	8
22	P2b	VR 85 3	16 mm	1,0	8
23	P2b	VR 85 3	16 mm	1,1	8
24	P2b	VR 85 3	16 mm	1,1	9
25	P2b	VR 85 3	16 mm	1,7	25
26	P2b	VR 85 3	16 mm	1,3	20
27	P2b	VR 85 3	16 mm	1,3	13
28	P2b	VR 85 3	16 mm	1,0	33
29	P2b	VR 85 3	16 mm	1,5	20
30	P2b	VR 85 3	16 mm	1,1	11
31	P2b	VR 85 3	16 mm	1,2	8
32	P2b	VR 85 3	16 mm	1,1	5
33	P2b	VR 85 3	16 mm	0,9	14
34	P2b	VR 85 3	16 mm	0,8	14
35	P2b	VR 85 3	16 mm	1,3	20

	unit	sample	size	density	error vol
				g/ml	%
36	P2b	VR 85 3	16 mm	1,4	25
37	P2b	VR 85 3	16 mm	2,0	33
38	P2b	VR 85 3	16 mm	1,4	20
39	P2b	VR 85 3	16 mm	1,6	29
40	P2b	VR 85 3	16 mm	1,0	20
41	P2b	VR 85 3	16 mm	1,2	14
42	P2b	VR 85 3	16 mm	1,2	25
43	P2b	VR 85 3	16 mm	1,3	25
44	P2b	VR 85 3	16 mm	1,1	20
45	P2b	VR 85 3	16 mm	0,8	9
46	P2b	VR 85 3	16 mm	1,3	10
47	P2b	VR 85 3	16 mm	1,0	11
48	P2b	VR 85 3	16 mm	1,3	25
49	P2b	VR 85 3	16 mm	1,4	33
50	P2b	VR 85 3	16 mm	1,4	20
51	P2b	VR 85 3	16 mm	1,0	14
52	P2b	VR 85 3	16 mm	1,3	8
53	P2b	VR 85 3	16 mm	1,4	13
54	P2b	VR 85 3	16 mm	1,4	10
55	P2b	VR 85 3	16 mm	1,1	14
56	P2b	VR 85 3	16 mm	1,2	10
57	P2b	VR 85 3	16 mm	1,5	25
58	P2b	VR 85 3	16 mm	1,4	14
59	P2b	VR 85 3	16 mm	1,4	14
60	P2b	VR 85 3	16 mm	1,6	6
61	P2b	VR 85 3	16 mm	1,5	5
62	P2b	VR 85 3	16 mm	1,7	5
63	P2b	VR 85 3	16 mm	1,4	6
64	P2b	VR 85 3	16 mm	1,4	9
65	P2b	VR 85 3	16 mm	1,5	10
66	P2b	VR 85 3	16 mm	1,7	13
67	P2b	VR 85 3	16 mm	1,5	9
68	P2b	VR 85 3	16 mm	1,4	14
69	P2b	VR 85 3	16 mm	2,0	25
70	P2b	VR 85 3	16 mm	1,4	20
71	P2b	VR 85 3	16 mm	1,8	7
72	P2b	VR 85 3	16 mm	1,5	11
73	P2b	VR 85 3	16 mm	1,6	8
74	P2b	VR 85 3	16 mm	1,6	11
75	P2b	VR 85 3	16 mm	1,3	10
76	P2b	VR 85 3	16 mm	1,9	10
77	P2b	VR 85 3	16 mm	1,8	25
78	P2b	VR 85 3	16 mm	1,8	20
79	P2b	VR 85 3	16 mm	2,0	20
80	P2b	VR 85 3	16 mm	1,7	14
81	P2b	VR 85 3	16 mm	1,4	13
82	P2b	VR 85 3	16 mm	1,4	5
83	P2b	VR 85 3	16 mm	1,7	20
1	P2b	VR12	16 mm	0,9	7
2	P2b	VR12	16 mm	1,3	6
3	P2b	VR12	16 mm	1,4	17
4	P2b	VR12	16 mm	1,5	10
5	P2b	VR12	16 mm	1,0	11
6	P2b	VR12	16 mm	1,0	11
7	P2b	VR12	16 mm	1,5	17
8	P2b	VR12	16 mm	1,2	17
9	P2b	VR12	16 mm	1,1	13

	unit	sample	size	density	error vol
				g/ml	%
10	P2b	VR12	16 mm	1,2	5
11	P2b	VR12	16 mm	1,0	14
12	P2b	VR12	16 mm	1,0	8
13	P2b	VR12	16 mm	0,6	20
14	P2b	VR12	16 mm	1,2	25
15	P2b	VR12	16 mm	1,2	14
16	P2b	VR12	16 mm	1,2	14
1	P2b	VR12	128 mm	1,2	
2	P2b	VR12	128 mm	1,5	
3	P2b	VR12	128 mm	1,0	
4	P2b	VR12	128 mm	1,5	
1	P2d	VR 78 5A	16 mm	1,4	13
2	P2d	VR 78 5A	16 mm	1,1	10
3	P2d	VR 78 5A	16 mm	1,5	17
4	P2d	VR 78 5A	16 mm	1,0	8
5	P2d	VR 78 5A	16 mm	1,1	11
6	P2d	VR 78 5A	16 mm	1,0	17
7	P2d	VR 78 5A	16 mm	0,9	14
8	P2d	VR 78 5A	16 mm	1,1	7
9	P2d	VR 78 5A	16 mm	1,0	13
10	P2d	VR 78 5A	16 mm	1,5	25
11	P2d	VR 78 5A	16 mm	1,2	20
12	P2d	VR 78 5A	16 mm	1,2	33
13	P2d	VR 78 5A	16 mm	1,0	20
14	P2d	VR 78 5A	16 mm	1,0	17
15	P2d	VR 78 5A	16 mm	1,3	20
16	P2d	VR 78 5A	16 mm	0,9	17
17	P2d	VR 78 5A	16 mm	1,1	17
18	P2d	VR 78 5A	16 mm	1,1	11
19	P2d	VR 78 5A	16 mm	0,9	25
20	P2d	VR 78 5A	16 mm	1,1	33
21	P2d	VR 78 5A	16 mm	1,1	8
22	P2d	VR 78 5A	16 mm	1,1	6
23	P2d	VR 78 5A	16 mm	1,2	8
24	P2d	VR 78 5A	16 mm	1,1	9
25	P2d	VR 78 5A	16 mm	1,2	14
26	P2d	VR 78 5A	16 mm	1,1	10
27	P2d	VR 78 5A	16 mm	1,1	11
28	P2d	VR 78 5A	16 mm	0,9	10
29	P2d	VR 78 5A	16 mm	1,0	11
30	P2d	VR 78 5A	16 mm	1,1	10
31	P2d	VR 78 5A	16 mm	1,0	17
32	P2d	VR 78 5A	16 mm	1,0	14
33	P2d	VR 78 5A	16 mm	1,4	22
34	P2d	VR 78 5A	16 mm	1,0	7
35	P2d	VR 78 5A	16 mm	1,3	11
36	P2d	VR 78 5A	16 mm	1,2	33
37	P2d	VR 78 5A	16 mm	1,1	14
38	P2d	VR 78 5A	16 mm	1,0	14
39	P2d	VR 78 5A	16 mm	0,9	13
40	P2d	VR 78 5A	16 mm	1,2	20
41	P2d	VR 78 5A	16 mm	1,2	8
42	P2d	VR 78 5A	16 mm	0,9	11
43	P2d	VR 78 5A	16 mm	1,0	20
44	P2d	VR 78 5A	16 mm	1,2	17
45	P2d	VR 78 5A	16 mm	1,0	20
46	P2d	VR 78 5A	16 mm	1,1	20

	unit	sample	size	density	error vol
				g/ml	%
47	P2d	VR 78 5A	16 mm	1.5	17
48	P2d	VR 78 5A	16 mm	1.2	10
49	P2d	VR 78 5A	16 mm	1.2	50
50	P2d	VR 78 5A	16 mm	1.0	9
51	P2d	VR 78 5A	16 mm	1.8	9
52	P2d	VR 78 5A	16 mm	1.4	13
53	P2d	VR 78 5A	16 mm	1.6	25
54	P2d	VR 78 5A	16 mm	1.3	25
55	P2d	VR 78 5A	16 mm	1.0	22
56	P2d	VR 78 5A	16 mm	1.3	20
57	P2d	VR 78 5A	16 mm	1.2	33
58	P2d	VR 78 5A	16 mm	1.4	33
59	P2d	VR 78 5A	16 mm	0.8	17
60	P2d	VR 78 5A	16 mm	1.7	20
61	P2d	VR 78 5A	16 mm	1.2	20
62	P2d	VR 78 5A	16 mm	1.1	20
1	P2d	VR 78 5B	16 mm	1.4	8
2	P2d	VR 78 5B	16 mm	0.9	13
3	P2d	VR 78 5B	16 mm	1.3	6
4	P2d	VR 78 5B	16 mm	1.0	9
5	P2d	VR 78 5B	16 mm	0.9	8
6	P2d	VR 78 5B	16 mm	1.0	8
7	P2d	VR 78 5B	16 mm	1.5	29
8	P2d	VR 78 5B	16 mm	1.1	25
9	P2d	VR 78 5B	16 mm	1.5	25
10	P2d	VR 78 5B	16 mm	1.0	17
11	P2d	VR 78 5B	16 mm	1.0	17
12	P2d	VR 78 5B	16 mm	1.3	17
13	P2d	VR 78 5B	16 mm	1.1	17
14	P2d	VR 78 5B	16 mm	0.9	14
15	P2d	VR 78 5B	16 mm	0.8	10
16	P2d	VR 78 5B	16 mm	1.0	20
17	P2d	VR 78 5B	16 mm	1.2	33
18	P2d	VR 78 5B	16 mm	1.4	25
19	P2d	VR 78 5B	16 mm	1.1	14
20	P2d	VR 78 5B	16 mm	1.3	33
21	P2d	VR 78 5B	16 mm	1.3	25
22	P2d	VR 78 5B	16 mm	1.3	25
23	P2d	VR 78 5B	16 mm	1.5	25
24	P2d	VR 78 5B	16 mm	1.2	33
25	P2d	VR 78 5B	16 mm	1.2	40
26	P2d	VR 78 5B	16 mm	1.6	40
27	P2d	VR 78 5B	16 mm	1.6	17
28	P2d	VR 78 5B	16 mm	2.0	33
29	P2d	VR 78 5B	16 mm	1.3	9
30	P2d	VR 78 5B	16 mm	1.2	25
31	P2d	VR 78 5B	16 mm	1.2	25
32	P2d	VR 78 5B	16 mm	1.7	29
33	P2d	VR 78 5B	16 mm	1.4	6
34	P2d	VR 78 5B	16 mm	1.7	7

MEAN VALUES					
unit	**sample**	**size**	**density**	**error vol**	**1σ st dev**
			g/ml	**%**	**g/ml**
P1a	**VR 73 I**	**16 mm**	**1.1**	**22**	**0.2**
P1a	**VR 73 L**	**16 mm**	**0.9**	**17**	**0.3**
P1b	**VR73N2**	**128 mm**	**1.3**		**1.3**
P1b	**VR 73 P**	**16 mm**	**1.0**	**11**	**0.2**
P2a	**VR 78 3A**	**16 mm**	**1.1**	**19**	**0.2**
P2a	**VR 78 3B-C**	**16 mm**	**1.0**	**23**	**0.2**
P2a	**VR 85 8**	**16 mm**	**1.3**	**13**	**0.3**
P2a	**VR 85 6**	**16 mm**	**1.2**	**23**	**0.3**
P2a	**VR 85 5**	**16 mm**	**1.2**	**15**	**0.2**
P2b	**VR 85 4**	**16 mm**	**1.3**	**13**	**0.2**
P2b	**VR 85 3**	**16 mm**	**1.4**	**16**	**0.3**
P2b	**VR12**	**16 mm**	**1.1**	**13**	**0.2**
P2b	**VR12**	**128 mm**	**1.3**		**0.3**
P2d	**VR 78 5A**	**16 mm**	**1.2**	**17**	**0.2**
P2d	**VR 78 5B**	**16 mm**	**1.3**	**20**	**0.3**

Density of the scoria lapilli (16 mm fraction) was measured following the method of silicone-sealing of the scorias (Method 1 of Appendix 3.2).

Density of the scoria bombs (128 mm fraction) was measured following the method of water saturation of bombs (Method 2 of Appendix 3.2).

The error associated to the balance is negligible and the error of the volume varies according to the sample volume (vol, in ml) as:

error (%) = 1 (ml) / vol (ml) * 100 (precision of the test tube = 1 ml)

Appendix 4.5: Preparation of polished and metalised resins for SEM and microprobe analyses

A small part of the sample (about 5 mm in diameter) was impregnated in resin following this procedure:

1. The sample was placed in a little plastic bottle (fixed with sticky paper), filled with a mix of resin with indurator (7.5 : 1 ratio) and allowed to harden for at least 12 hours.
2. The resin cylinder was then polished until the fragment crops out (For the highly vesiculated samples, the sample was filled with resin and allowed to harden again).
3. The cylinder is polished with the polishing machine using diamond paste of 6, 4 and ½ µm. In between, the resin cylinder was carefully cleaned with the ultrasonic machine.
4. The sample was finally metallized with carbon to eliminate the electric charges at the surface.

Appendix 4.6: Analytical conditions of microanalysis by probe (after Maurice, 1978; Ruste, 1978 and Moune, 2005)

In this study, major and trace elements were analysed punctually in glasses by means of the electron microprobe CAMECA SX-100 of the "Laboratoire Magmas et Volcans" (LMV) at Clermont-Ferrand. In this technique of microanalysis, the sample, bombarded by an incoming beam of accelerated electrons, emits a spectrum of X-ray photons which is diffracted by a curved crystal monochromator and then its intensity detected by a gas-filled counter (technique of analysis of X spectrum called WDS, Wavelength Dispersive Spectrometry). The positions of the crystal and the counter are adjusted satisfying Bragg's law. The LMV microprobe has a system of four spectrometers and eight different crystals (in this case, we used the crystals TAP, PET and LLIF, Table 4.6). For the calibrations of the different elements, there are natural and artificial standards of well-known compositions (Table 4.6). An accelerating voltage of 15 kV was used in all the analyses.

In this study, the microprobe analyses were performed as follows. In the morning, only major elements are analysed (five points by sample) under the conditions detailed in Table 4.6. The coordinates of the points are saved, thus the same points are analysed at the afternoon for volatile measurements. For the volatile analyses (S, Cl, F), it is necessary to entry a mean of the major element analyses (cation numbers) of the sample. In the case of heterogeneous glasses, the mean of a group of points or individual points are entered. The analytical conditions for the volatile elements are detailed in Table 4.6.

A strong beam current (80 nA) and longer counting times than for major elements were used for S, Cl and F due to their very low contents (trace elements). A non-automated procedure has been developed in the LMV in which the counting time is fragmented in periods of analysis. Between these intervals of measurement, the electron beam is intercepted by the Faraday cage, allowing the regular cooling of the analysed surface. This method minimizes the heating of the sample, thus avoiding its damage and the lost due to volatilization of elements. As a result, the analyses are more precise and accurate. The samples were analysed during 20 periods of 10 s for Cl and S, and 20 periods of 20 s for F. For the standards, there were done 5 analyses of 20 s for S and F, and 5 analyses of 10 s for the Cl. The background was analysed during 5 periods of 40 s in the case of S and F, and 5 periods of 20 s, for the Cl.

During the sessions of volatile analyses, some glasses with well-known compositions are analysed to control the quality of the measurements along the session (Table 4.7).

Since the sulphur is present under reduced (S^{2-}) and oxidised (S^{6+}) forms, the peak of S can be progressively be displaced from the reduced pole (standard ZnS) towards the oxidised pole (standard $BaSO_4$). The sulphur is calibrated with a basaltic glass ALV 981R23 for which the speciation (S^{6+}/S_{tot} = 0.166) and the concentration (1125 ppm) are documented by Métrich & Clocchiatti (1989, 1996). If the speciation of the sulphur is different between the sample and the standard, a correction is applied between the position of the spectrometer used for ALV 981R23 and for the sample. In this case, the S contents of most of the samples is variable (60 to 619 ppm, Appendix 4.10) but normally very low, thus they

commonly don't exhibit a well-developed peak and the correction due to S speciation, was very small or unnecessary in many cases.

The detection limit for Cl and S is around 20-30 ppm.

The analysis of F was done using the crystal TAP, which produces an elevated detection limit (150-200 ppm) and induces important errors in samples with low concentrations of this element. Even with a better detection limit (around 40 ppm) and of lower error, the analysis of F using the crystal PC1 was discarded because the analyses are very much longer than using TAP.

The precision associated with every element (2σ) during an analysis was estimated statistically using the counting times and the number of counts par second obtained for the peak and background of the sample and for the peak and background of the standard (Ancey et al., 1978). In this study, we used a program developed in excel by M.Laubier, S.Moune and S.Jannot during their PhD these in the LMV (2005/2006). Sulphur measurements induced variable errors (~3 to 19%, Appendix 4.10). The precision (2σ) of the Cl measurements is very low (1 to 3%, Appendix 4.10) according to their high contents (about 487 to 3787 ppm). The error of the F is also very variable (6 to 469%) depending on the concentration in the sample (30 to 1880 ppm).

The accuracy was not determined in this study because the aim was to compare the concentrations between the different samples.

Table 4.7: Summary of the conditions for the samples, standards and background during the analyses of major and trace elements of glasses by electron microprobe (accelerating voltage = 15 kV).

	sample			**standard**						
						peack			**background**	
element	**beam current (nA)**	**counting time (s)**	**spectrometer crystal**	**standard**	**beam current (nA)**	**peack (c/s)**	**time (s)**	**N° analyses**	**peack (c/s)**	**time (s)**
Na	8	10	TAP	Albite	15	898,5	40	4	11,8	10
Mg	8	10	TAP	MgO	15	13036,9	40	4	50,9	10
K	8	10	PET	orthoclase	15	1040,9	40	4	5,9	10
Ca	8	10	PET	wollastonite	15	3079,4	30	3	13	10
Ti	8	10	PET	$MnTiO_3$	15	3344	50	5	21,3	10
P	8	10	PET	Apatite	15	709,7	50	5	3,2	10
Fe	8	10	LLIF	Fe_2O_3	15	5426,3	50	5	32,6	10
Mn	8	30	LLIF	$MnTiO_3$	15	2584,8	50	5	26,23	10
Si	8	10	TAP	ATHO	8	5437,9	40	4	24,3	10
Al	8	20	TAP	VG2	8	992,1	90	9	13,7	10
S	80	200	LPET	ALV 981R23	80	132,2	100	5	27,55	40
Cl	80	200	LPET	scapolite	80	6163,8	50	5	54,5	20
F	80	400	TAP	apatite Durango	80	84,2	100	5	2,43	40

Table 4.8: Chemical composition of some quality control glasses used to control the trace elements S, Cl and F (in ppm). The errors (in ppm) are in parenthesis.

	S	Cl	F	ERROR	METHOD	REFERENCE
ALV 981R23	1170 (90)			2 sigma	EPM	Métrich & Clocchiatti (1989)
	1050 (140)			2 sigma	EPM	Métrich *et al.* (1991)
	1110 (220)			2 sigma	EPM	Métrich & Clocchiatti (1996)
			130 (30)			Mosbah *et al.* (1991)
			190 (3)		SIMS	Straub & Layne (2003)
KE12		3270 (110)			EPM	Métrich & Rutherford (1991)
		3300	4200		whole rock	Métrich & Rutherford (1991)
			4338 (1096)	2 sigma	EMP	reported in Palais & Sigurdsson (1989)
			4400			accepted values reported in Palais & Sigurdsson (1989)
			4000 (240)	2 sigma	Ion Selective Electrode	Mosbah *et al.* (1991)
			4513 (88)	2 sigma	EMP	Witter & Kuehner (2004)
A99	170 (30)			1 sigma	EPM	Dixon *et al.* (1991)
	135 (50)	229 (40)			EPM, CAMECA trace routine	Thorardsson *et al.* (1996)
	220 (12)	227 (20)	765 (79)	1 sigma (F)	EPM, CSIRO trace routine	Thorardsson *et al.* (1996)
	96 (63)				EPM	Thornber *et al.* (2002)
			709 (47)		SIMS	Straub & Layne (2003)
			976 (8)	2 sigma	EMP	Witter & Kuehner (2004)
VG2	1340 (80)			1 sigma	EPM	Dixon *et al.* (1991)
	1348 (62)	291 (52)			EPM, CAMECA trace routine	Thorardsson *et al.* (1996)
	1365 (29)	316 (19)	300 (72)	1 sigma (F)	EPM, CSIRO trace routine	Thorardsson *et al.* (1996)
	1305 (135)				EPM	Thornber *et al.* (2002)
			334 (14)		SIMS	Straub & Layne (2003)
CFA		4850 (90)		1 sigma	EPM	Métrich & Clocchiatti (1989)
		4815 (100)		1 sigma	XRF	Métrich & Villemant
			2000 (120)	2 sigma	Ion Selective Electrode	Mosbah *et al.* (1991)
			2500 (1200)	2 sigma	EMP	Signorelli *et al.* (1999)
			2483 (32)	2 sigma	EMP	Witter & Kuehner (2004)
ATHO		530	770			Oskarsson et al.

NOTES:
ALV 981R23 Submarine basaltic glass
KE12 Pantellerite of Kenya, Africa
A99 Basaltic glass fragment of Kilauea
VG2 Basaltic glass
CFA
ATHO Rhyolitic glass

Appendix 4.7: Major element glass compositions and respective errors of pre-Pucón pumice and Pucón scoria

	BS*	N°an	sample	unit	type**	cxx***	Na2O	MgO	K2O	CaO	TiO2	P2O5	FeO	MnO	SiO2	Al2O3	Total	Na2O	MgO	K2O	CaO	TiO2	P2O5	FeO	MnO	SiO2	Al2O3	Na2O	MgO	K2O	CaO	TiO2	P2O5	FeO	MnO	SiO2	Al2O3
	µm					%	wt%											error % (2 sigma)										reproducibility % (1 sigma)									
1	10	#1	VR73J-L6	P1a	SJ	10	4.0	3.6	1.0	7.3	1.4	0.0	9.6	0.2	57.4	15.8	100.4	5.4	4.4	11.2	4.1	11.1	418.3	3.7	27.5	1.1	2.0	7.6	3.4	6.3	2.4	6.6	47.3	4.9	9.8	0.6	1.5
2	10	#2	VR73J-L6	P1a	SJ	10	4.1	3.4	1.0	7.2	1.2	0.2	8.8	0.2	58.1	16.4	100.7	5.3	4.5	11.2	4.1	12.4	84.0	3.9	25.5	1.1	1.9										
3	10	#3	VR73J-L6	P1a	SJ	10	3.6	3.7	0.9	7.5	1.4	0.3	9.6	0.2	57.4	16.0	100.5	5.8	4.3	11.8	4.0	11.1	61.6	3.7	28.0	1.1	2.0										
4	10	#4	VR73J-L6	P1a	SJ	10	4.1	3.6	0.9	7.2	1.4	0.2	10.0	0.2	57.8	16.0	101.4	5.4	4.4	12.3	4.1	11.1	77.3	3.6	24.3	1.1	2.0										
5	10	#5	VR73J-L6	P1a	SJ	10	3.5	3.6	1.0	7.4	1.4	0.3	9.0	0.2	57.9	16.2	100.4																				
6	5	#1	VR73J-L6	P1a	SJ	10	3.7	3.6	0.9	7.1	1.4	0.2	9.1	0.2	57.6	16.1	99.9	5.6	4.4	12.4	4.1	11.3	67.1	3.8	25.5	1.1	1.9	2.3	2.4	2.0	2.5	5.8	52.6	2.6	4.6	0.5	1.0
7	5	#2	VR73J-L6	P1a	SJ	10	3.6	3.7	0.9	7.6	1.5	0.3	9.3	0.2	57.4	15.9	100.3	5.7	4.3	12.4	4.0	10.7	58.3	3.8	26.0	1.1	2.0										
8	5	#3	VR73J-L6	P1a	SJ	10	3.7	3.7	0.9	7.6	1.3	0.0	9.6	0.2	58.1	16.1	101.2	5.6	4.3	12.3	4.0	11.8	536.8	3.7	25.4	1.1	1.9										
9	5	#4	VR73J-L6	P1a	SJ	10	3.6	3.8	0.9	7.6	1.4	0.3	9.8	0.2	57.2	15.8	100.7	5.8	4.2	12.3	4.0	11.5	53.2	3.7	26.0	1.1	2.0										
10	5	#8	VR73J-L6	P1a	SJ	10	3.8	3.7	0.9	7.3	1.4	0.3	9.6	0.2	57.6	15.9	100.8	5.6	4.3	12.0	4.1	11.1	54.2	3.7	28.1	1.1	2.0										
11	~1	#1	VR73J-L6	P1a	SJ	10	3.6	3.8	0.9	7.5	1.2	0.3	10.3	0.1	57.6	16.1	101.4	5.8	4.3	12.2	4.0	12.0	53.5	3.6	38.1	1.1	2.0	3.2	1.6	5.9	1.4	8.7	37.9	4.2	15.6	0.4	1.1
12	~1	#2	VR73J-L6	P1a	SJ	10	3.7	3.7	0.9	7.4	1.3	0.3	9.5	0.2	57.2	16.1	100.2	5.6	4.3	12.5	4.0	11.7	58.3	3.8	27.3	1.1	1.9										
13	~1	#3	VR73J-L6	P1a	SJ	10	3.5	3.7	0.8	7.6	1.3	0.2	9.5	0.1	56.7	15.8	99.2	5.8	4.3	12.7	4.0	12.1	81.6	3.8	34.9	1.1	2.0										
14	~1	#4	VR73J-L6	P1a	SJ	10	3.6	3.6	0.8	7.5	1.5	0.1	9.9	0.2	57.3	15.9	100.4	5.7	4.4	13.2	4.0	10.5	150.8	3.7	27.4	1.1	2.0										
15	~1	#5	VR73J-L6	P1a	SJ	10	3.4	3.6	0.9	7.3	1.3	0.2	9.0	0.2	56.8	16.0	98.8	6.0	4.3	12.4	4.1	11.4	77.3	3.9	33.0	1.1	2.0										
16	~1	#1	VR73J-D3	P1a	DJ	83	2.9	2.0	1.8	6.1	2.3	0.4	15.3	0.3	56.4	11.9	99.4	6.6	6.1	8.3	4.4	8.2	43.4	2.9	19.4	1.1	2.3	13.3	12.4	7.8	3.6	7.1	32.8	6.4	18.6	1.0	6.8
17	~1	#2	VR73J-D3	P1a	DJ	83	2.2	2.3	1.5	6.0	1.9	0.4	15.7	0.3	55.8	11.5	97.7	7.6	5.6	9.1	4.4	9.4	42.0	2.9	21.0	1.1	2.3										
18	~1	#3	VR73J-D3	P1a	DJ	83	2.1	2.8	1.5	6.6	2.1	0.5	15.9	0.3	55.7	11.3	98.7	7.9	5.1	9.5	4.3	8.9	35.4	2.9	18.0	1.1	2.3										
19	~1	#4	VR73J-D3	P1a	DJ	83	2.4	2.3	1.5	6.2	1.9	0.2	13.6	0.2	56.8	13.2	98.2	7.3	5.6	9.1	4.4	9.4	81.6	3.1	26.8	1.1	2.1										
20	~1	#5	VR73J-D3	P1a	DJ	83	2.5	2.6	1.5	6.1	2.0	0.5	14.5	0.2	56.0	12.8	98.8	7.1	5.3	9.0	4.4	8.8	35.2	3.0	25.1	1.1	2.2										
21	5	#1	VR73P-L2	P1b	SJ	32	3.2	3.9	1.2	7.8	1.3	0.3	9.8	0.2	57.6	15.9	101.0	6.1	4.2	10.4	3.9	12.0	61.6	3.7	33.2	1.1	2.0	4.4	3.7	5.6	2.1	3.9	13.2	1.8	14.6	0.5	0.9
22	5	#2	VR73P-L2	P1b	SJ	32	3.4	3.7	1.0	7.5	1.4	0.3	9.6	0.2	56.5	15.5	98.9	6.0	4.4	11.3	4.0	11.4	67.1	3.8	25.1	1.1	2.0										
23	5	#3	VR73P-L2	P1b	SJ	32	3.4	3.7	1.0	7.7	1.3	0.2	9.8	0.2	56.6	16.0	99.8	5.9	4.3	11.4	3.9	11.5	84.0	3.7	25.8	1.1	2.0										
24	5	#4	VR73P-L2	P1b	SJ	32	3.5	3.5	1.1	7.3	1.4	0.2	9.3	0.2	57.4	16.0	99.8	5.8	4.5	11.1	4.1	11.1	70.4	3.8	31.3	1.1	2.0										
25	5	#5	VR73P-L2	P1b	SJ	32	3.3	3.8	1.0	7.5	1.4	0.2	9.6	0.2	57.6	15.8	100.5	6.0	4.3	11.3	4.0	11.2	70.1	3.7	32.6	1.1	2.0										
26	10	#37	VR73P-D7	P1b	DJ	9	3.6	3.7	1.0	7.2	1.3	0.2	9.3	0.1	55.8	15.9	98.2	5.8	4.3	11.5	4.1	12.0	74.1	3.8	36.7	1.1	1.5	3.1	1.6	11.3	1.5	4.0	17.5	2.8	13.4	0.6	1.3
27	10	#38	VR73P-D7	P1b	DJ	9	3.8	3.7	1.0	7.4	1.4	0.2	9.5	0.2	55.8	15.7	98.7	5.6	4.3	11.8	4.0	11.9	75.5	3.8	29.6	1.1	1.5										
28	10	#39	VR73P-D7	P1b	DJ	9	3.9	3.7	0.9	7.7	1.4	0.3	10.0	0.2	55.8	15.8	99.6	5.6	4.3	12.4	4.0	11.5	66.1	3.7	27.1	1.1	1.5										
29	10	#40	VR73P-D7	P1b	DJ	9	3.9	3.7	0.9	7.6	1.3	0.2	9.8	0.2	56.4	16.2	100.1	5.6	4.3	12.5	4.0	12.2	105.9	3.7	34.1	1.1	1.5										
30	10	#41	VR73P-D7	P1b	DJ	9	3.7	3.6	1.2	7.5	1.4	0.2	9.4	0.1	55.9	16.2	99.3																				
31	5	#31	VR78-3A-L1	P2a	SJ	28	3.5	3.9	1.1	7.2	1.3	0.0	9.9	0.2	55.7	15.3	98.1	5.9	4.2	10.8	4.1	12.1	87.7	3.7	27.2	1.1	1.5	2.6	3.9	5.6	2.1	5.7	51.0	3.5	8.8	0.5	0.7
32	5	#32	VR78-3A-L1	P2a	SJ	28	3.5	3.7	1.1	7.1	1.3	0.3	9.5	0.2	56.7	15.5	98.9	5.8	4.3	11.1	4.1	12.0	61.0	3.8	32.6	1.1	1.5										
33	5	#33	VR78-3A-L1	P2a	SJ	28	3.4	3.8	1.1	6.9	1.5	0.2	10.7	0.2	56.5	15.5	99.7	6.0	4.3	10.8	4.2	11.0	75.5	3.6	29.1	1.1	1.5										
34	5	#34	VR78-3A-L1	P2a	SJ	28	3.4	3.6	1.1	7.1	1.5	0.2	10.2	0.2	56.0	15.4	98.7	6.0	4.4	11.3	4.1	11.0	84.0	3.6	26.0	1.1	1.5										
35	5	#35	VR78-3A-L1	P2a	SJ	28	3.3	3.8	1.2	7.1	1.3	0.3	10.1	0.2	54.9	15.1	97.2																				
36	5	#36	VR78-3A-L1	P2a	SJ	28	3.5	3.5	1.2	7.0	1.3	0.2	10.3	0.2	56.9	15.8	100.0																				
37	~1	#25	VR78-3A-D2	P2a	DJ	55	3.8	2.1	1.8	4.7	1.7	0.4	11.4	0.2	57.4	14.7	98.2	5.7	5.9	8.3	5.1	9.8	47.1	3.4	25.8	1.1	1.5	12.5	15.6	18.1	6.7	15.0	53.2	17.2	19.1	3.2	2.1
38	~1	#26	VR78-3A-D2	P2a	DJ	55	4.0	1.5	2.5	4.1	1.2	0.3	6.6	0.1	63.1	15.3	98.8	5.4	7.0	7.0	5.5	12.7	62.0	4.6	40.3	1.0	1.5										
39	~1	#27	VR78-3A-D2	P2a	DJ	55	3.1	1.9	1.7	4.9	1.7	0.5	8.8	0.2	60.6	14.9	98.2	6.3	6.1	8.5	5.0	10.0	39.7	3.9	31.9	1.0	1.5										
40	~1	#28	VR78-3A-D2	P2a	DJ	55	3.5	1.7	1.6	5.0	1.7	0.4	9.1	0.2	60.8	14.8	98.9	5.9	6.6	8.7	4.9	9.9	45.9	3.9	25.5	1.0	1.5										
41	~1	#29	VR78-3A-D2	P2a	DJ	55	3.0	1.5	1.6	4.6	1.5	0.0	8.8	0.2	61.1	14.2	96.5	6.5	7.0	8.9	5.2	10.9	342.6	3.9	27.2	1.0	1.5										
42	~1	#30	VR78-3A-D2	P2a	DJ	55	3.0	1.4	1.8	4.6	1.3	0.3	8.6	0.2	61.9	15.3	98.6	6.4	7.2	8.1	5.1	11.6	52.9	4.0	27.2	1.0	1.5										
43	~1	#4	VR85-8-L4	P2a	SJ	97	2.6	0.6	2.5	5.0	3.0	0.7	13.7	0.2	58.6	12.5	99.4	7.0	12.1	6.9	4.9	7.1	32.0	3.1	26.7	1.0	1.6	12.0	31.2	5.5	5.0	11.7	22.8	6.3	14.0	1.2	3.5
44	~1	#5	VR85-8-L4	P2a	SJ	97	2.6	1.0	2.5	4.9	2.4	0.4	13.2	0.2	57.5	12.7	97.4	7.0	9.0	7.0	5.0	8.2	45.4	3.2	23.5	1.1	1.6										
45	~1	#6	VR85-8-L4	P2a	SJ	97	2.0	1.3	2.2	5.3	2.5	0.4	15.0	0.3	56.9	12.2	98.1	8.0	7.8	7.4	4.8	8.0	43.3	3.0	20.1	1.1	1.6										
46	~1	#7	VR85-8-L4	P2a	SJ	97	2.7	0.9	2.3	4.7	2.9	0.5	12.9	0.2	58.2	13.0	98.3	6.8	9.7	7.2	5.1	7.2	39.9	3.2	24.1	1.1	1.6										
47	~1	#9	VR85-8-L4	P2a	SJ	97	2.9	0.6	2.3	4.8	3.2	0.5	13.1	0.2	59.0	12.0	98.6	6.5	12.0	7.4	5.1	7.0	41.9	3.2	22.8	1.0	1.6										
48	5	#18	VR85-8-D5	P2a	DJ	41	3.7	3.3	1.1	6.8	1.5	0.3	10.3	0.2	55.8	15.4	98.5	5.7	4.6	10.9	4.2	10.7	55.9	3.6	27.5	1.1	1.5	10.2	8.2	16.8	2.9	3.7	21.5	5.7	3.6	1.2	0.6
49	5	#22	VR85-8-D5	P2a	DJ	41	3.1	3.2	1.5	6.8	1.5	0.3	10.7	0.2	55.7	15.4	98.4	6.2	4.8	9.1	4.2	10.8	70.7	3.6	27.2	1.1	1.5										
50	5	#23	VR85-8-D5	P2a	DJ	41	4.0	3.1	1.2	6.5	1.5	0.2	9.9	0.2	57.1	15.7	99.3	5.5	4.8	10.4	4.4	10.9	70.1	3.7	26.8	1.1	1.5										
51	5	#19	VR85-8-D5	P2a	DJ	95	3.6	2.9	1.5	6.5	1.4	0.2	9.7	0.2	57.8	15.4	99.2	5.8	5.0	9.2	4.3	11.2	94.2	3.7	26.0	1.1	1.5										
52	5	#20	VR85-8-D5	P2a	DJ	95	3.1	2.7	1.7	6.6	1.5	0.2	11.0	0.2	55.9	15.2	98.2	6.3	5.1	8.7	4.3	10.9	71.4	3.5	25.1	1.1	1.5										
53	~1	#24	VR85-3-L3	P2b	SJ	45	3.8	3.0	1.0	6.7	1.6	0.3	11.8	0.2	55.6	15.6	99.7	5.6	4.9	11.8	4.2	10.6	58.2	3.4	25.5	1.1	1.5	7.5	14.2	33.5	9.0	15.3	18.4	7.9	9.6	1.6	5.6
54	~1	#25	VR85-3-L3	P2b	SJ	45	3.9	2.9	0.8	6.8	1.6	0.3	11.8	0.2	56.3	15.5	100.2	5.6	5.0	13.0	4.2	10.4	49.0	3.4	21.4	1.1	1.5										
55	~1	#30	VR85-3-L3	P2b	SJ	45	3.7	3.2	1.0	7.2	1.6	0.3	10.7	0.2	56.8	15.8	100.5	5.7	4.7	11.7	4.1	10.7	62.0	3.5	27.3	1.1	1.5										
56	~1	#26	VR85-3-L3	P2b	SJ	98	3.2	2.0	1.8	5.4	2.1	0.2	12.7	0.2	57.3	13.3	98.4	6.2	6.1	8.1	4.8	8.6	79.4	3.3	27.2	1.1	1.6										
57	~1	#27	VR85-3-L3	P2b	SJ	98	3.5	3.0	1.0	6.8	1.5	0.4	10.4	0.2	57.3	15.9	100.0	5.8	4.9	11.6	4.2	11.0	44.3	3.6	25.8	1.1	1.5										
58	~1	#28	VR85-3-L3	P2b	SJ	98	3.3	2.7	1.4	6.7	1.7	0.3	12.0	0.2	56.7	15.0	100.1	6.0	5.1	9.6	4.3	9.9	53.5	3.3	22.4	1.1	1.5										
59	~1	#19	VR85-3-D4	P2b	DJ	91	4.8	1.5	1.2	4.7	1.7	0.4	9.8	0.1	61.9	14.7	100.7	5.0	7.1	10.6	5.1	10.2	55.8	3.7	38.2	1.0	1.5	22.9	24.8	36.8	19.3	3.3	15.2	9.5	14.9	3.0	3.1
60	~1	#20	VR85-3-D4	P2b	DJ	91	3.3	1.1	2.7	3.3	1.7	0.5	7.9	0.1	63.8	13.9	98.2	6.1	8.5	6.8	6.2	10.0	42.1	4.2	33.2	1.0	1.5										
61	~1	#22	VR85-3-D4	P2b	DJ	91	3.1	0.8	2.5	3.6	1.6	0.6	8.4	0.2	63.3	13.8	97.8	6.2	10.0	7.0	5.9	10.2	38.6	4.0	29.2	1.0	1.6										
62	~1	#23	VR85-3-D4	P2b	DJ	91	4.7	1.6	1.3	4.9	1.7	0.5	10.0	0.2	61.7	13.8	100.4	5.1	6.8	9.9	4.9	9.8	40.0	3.7	31.9	1.0	1.6										

63	~1	#24	VR85-3-D4	P2b	DJ	91	3.0	1.5	1.9	5.4	1.6	0.5	10.0	0.2	61.4	14.9	100.3	6.5	6.9	8.1	4.8	10.5	44.9	3.7	26.7	1.0	1.5										
64	2	#1	VR113-7a	A	SB	R	3.2	3.3	1.2	6.4	1.7	0.6	11.3	0.2	56.6	13.7	98.2	6.2	4.6	10.3	4.4	10.0	31.7	3.5	25.6	1.1	1.6	5.9	6.8	6.5	3.2	5.6	26.1	2.2	10.4	0.7	1.2
65	2	#2	VR113-7a	A	SB	R	2.8	2.9	1.4	6.2	1.8	0.4	11.1	0.2	58.0	14.2	98.9	6.6	4.9	9.9	4.4	9.6	49.8	3.5	22.8	1.1	1.6										
66	2	#3	VR113-7a	A	SB	R	3.1	2.9	1.1	6.3	1.7	0.3	10.6	0.2	57.4	14.2	97.9																				
67	2	#4	VR113-7a	A	SB	R	3.0	3.1	1.3	6.4	1.8	0.3	11.0	0.2	57.0	13.9	98.0																				
68	2	#5	VR113-7a	A	SB	R	3.1	3.4	1.3	5.8	1.7	0.3	11.0	0.2	58.0	13.9	98.6																				
69	2	#5	VR113-7a	A	SB	R	3.3	2.9	1.3	6.4	1.8	0.4	10.9	0.2	58.0	14.1	99.2	6.1	4.9	9.8	4.3	9.9	46.5	3.5	24.2	1.1	1.6										
70	2	#6	VR113-7a	A	SB	R	3.4	2.8	1.3	6.2	1.6	0.5	10.8	0.2	57.9	14.3	99.0																				
71	2	#7	VR113-7a	A	SB	R	3.2	2.9	1.2	6.3	1.6	0.4	10.6	0.2	57.9	14.0	98.2																				
72	2	#6	VR113-7b	A	SG	R	3.3	2.5	1.3	6.2	1.6	0.5	10.3	0.2	57.5	14.9	98.2											11.8	7.5	3.0	2.4	6.0	20.2	2.1	10.4	1.1	2.4
73	2	#7	VR113-7b	A	SG	R	2.7	2.2	1.4	5.8	1.8	0.5	10.7	0.2	59.0	14.3	98.4	6.8	5.8	9.9	4.6	9.9	43.3	3.6	30.7	1.1	1.6										
74	2	#8	VR113-7b	A	SG	R	2.5	2.4	1.4	5.8	1.6	0.4	10.5	0.2	59.7	14.2	98.8																				
75	2	#9	VR113-7b	A	SG	R	2.6	2.3	1.4	6.0	1.9	0.4	11.0	0.2	58.4	13.8	98.0																				
76	2	#10	VR113-7b	A	SG	R	2.6	2.4	1.4	5.9	1.7	0.6	10.5	0.2	58.3	14.3	97.9																				
78	2	#1	VR113-7b	A	SG	R	2.5	2.2	1.4	5.9	1.7	0.4	10.6	0.2	59.5	14.1	98.3	7.1	5.7	9.6	4.6	10.0	42.2	3.6	27.1	1.0	1.6										
79	2	#2	VR113-7b	A	SG	R	2.6	2.3	1.3	5.9	1.8	0.3	10.6	0.2	59.4	14.4	98.7																				
80	2	#3	VR113-7b	A	SG	R	2.4	2.4	1.4	6.0	1.7	0.4	10.2	0.2	59.1	14.1	97.9																				
81	2	#4	VR113-7b	A	SG	R	2.2	2.7	1.4	5.9	1.8	0.4	10.7	0.2	59.2	13.7	98.4																				
77	~1	#11	VR113-7b	A	DPJ	R	3.8	1.1	1.7	3.6	1.3	0.6	7.1	0.2	66.8	13.4	99.3																				
82	2	#12	VR72A	A	SG 2	R	3.1	1.9	1.6	5.3	1.8	0.3	10.3	0.2	59.9	14.1	98.6	6.2	6.2	8.8	4.8	9.6	60.4	3.6	34.8	1.0	1.6	12.3	18.8	7.0	4.3	8.1	22.7	2.6	12.9	0.8	2.0
83	2	#13	VR72A	A	SG 2	R	2.7	2.1	1.4	6.1	1.8	0.5	10.9	0.2	58.3	14.3	98.4																				
84	2	#14	VR72A	A	SG 2	R	2.2	3.0	1.6	5.6	1.5	0.4	11.0	0.2	59.0	13.4	98.0																				
85	2	#15	VR72A	A	SG 2	R	2.5	2.0	1.5	5.6	2.0	0.3	10.8	0.2	58.3	13.6	96.7																				
86	2	#16	VR72A	A	SG 2	R	2.6	2.0	1.6	5.6	1.9	0.4	11.1	0.2	58.4	14.0	97.7																				
88	2	#11	VR72A	A	SG 2	R	2.2	2.1	1.6	5.5	1.9	0.4	10.9	0.2	59.7	14.0	98.4	7.5	5.9	8.9	4.7	9.2	46.5	3.6	25.5	1.0	1.6										
89	2	#12	VR72A	A	SG 2	R	2.3	2.7	1.3	5.7	1.7	0.2	11.3	0.2	59.8	13.7	99.1																				
90	2	#14	VR72A	A	SG 2	R	2.3	2.0	1.6	5.6	1.9	0.3	10.9	0.2	59.5	13.8	98.3																				
87	2	#17	VR72A	A	SG 1	R	2.7	2.6	1.4	6.0	1.5	0.3	10.3	0.2	57.9	14.8	97.6																				
91	2	#18	VR72A	A	SI 1	P	3.2	1.1	2.0	3.5	1.5	0.4	6.5	0.2	64.8	14.8	97.9	6.0	8.2	7.9	6.0	11.1	54.2	4.7	30.7	1.0	1.5	3.7	4.5	7.8	4.8	4.3	35.3	6.5	16.0	0.4	1.8
92	2	#19	VR72A	A	SI 1	P	3.2	1.1	2.1	3.4	1.4	0.3	7.1	0.2	65.6	14.5	98.8																				
93	2	#20	VR72A	A	SI 1	P	3.3	1.2	1.7	3.8	1.5	0.3	6.6	0.2	65.1	14.7	98.4																				
94	2	#21	VR72A	A	SI 1	P	3.1	1.1	1.8	3.5	1.3	0.4	6.3	0.2	65.4	14.6	97.8																				
95	2	#22	VR72A	A	SI 1	P	3.5	1.1	2.0	3.5	1.4	0.7	6.0	0.1	66.2	15.4	99.7																				
96	2	#23	VR72A	A	SI 2	P	4.5	1.3	1.9	3.8	1.1	0.5	6.6	0.2	65.1	15.1	100.1																				
97	~1	#24	VR72A	A	SB 2	VR	3.7	1.3	1.6	3.8	1.4	0.4	6.1	0.1	66.8	15.0	100.2	5.6	7.5	8.9	5.7	11.4	46.2	4.8	34.9	1.0	1.5	31.5	19.4	44.1	9.1	5.4	14.9	5.1	20.5	0.9	2.5
98	~1	#25	VR72A	A	SB 2	VR	3.7	1.8	2.2	3.2	1.4	0.6	6.4	0.2	64.7	14.2	98.5																				
99	~1	#26	VR72A	A	SB 2	VR	2.3	1.2	3.5	2.9	1.3	0.4	6.6	0.2	64.4	15.0	97.7																				
100	~1	#27	VR72A	A	SB 2	VR	2.3	1.4	4.0	3.3	1.2	0.4	6.7	0.2	64.4	15.2	99.2																				
101	~1	#28	VR72A	A	SB 2	VR	4.9	1.2	1.5	3.5	1.4	0.4	6.1	0.1	66.1	14.8	100.1																				
102	~1	#1	VR109-1	A	SG	P	3.4	3.2	1.2	5.8	1.7	0.5	11.4	0.2	56.1	13.2	96.8											7.3	7.7	1.9	4.3	6.5	42.2	2.9	9.1	0.3	3.7
103	5	#2	VR109-1	A	SG	P	3.3	3.4	1.2	6.2	1.8	0.4	11.1	0.2	56.8	13.9	98.3	6.1	4.5	10.4	4.4	9.8	51.4	3.5	31.7	1.1	1.6										
104	5	#3	VR109-1	A	SG	P	3.3	3.0	1.3	6.0	1.7	0.1	11.2	0.2	56.8	13.9	97.6																				
105	5	#4	VR109-1	A	SG	P	2.9	2.9	1.2	6.5	1.5	0.3	10.8	0.2	57.0	14.6	98.0	6.5	4.9	10.2	4.3	10.8	58.4	3.6	30.5	1.1	1.5										
106	~1	#5	VR109-1	A	SB	R	3.9	3.1	1.0	6.2	1.8	0.4	10.6	0.2	57.5	14.3	99.1	5.6	4.8	11.4	4.4	9.5	42.4	3.6	22.7	1.1	1.6	12.6	3.7	8.0	2.1	2.2	15.1	2.0	16.4	0.6	0.6
107	~1	#6	VR109-1	A	SB	R	3.1	3.0	1.2	6.2	1.8	0.4	10.8	0.2	58.3	14.4	99.4	6.3	4.8	10.6	4.4	9.8	50.0	3.5	21.4	1.1	1.6										
108	~1	#7	VR109-1	A	SB	R	3.2	2.9	1.2	5.9	1.8	0.3	10.9	0.2	57.2	14.2	97.7																				
109	2	#1	VR73G	A	SG	R	3.0	2.6	1.5	6.0	1.8	0.5	11.3	0.2	58.1	13.9	98.8	6.4	5.3	9.3	4.5	9.6	37.1	3.5	27.0	1.1	1.6	12.3	7.0	7.7	2.9	7.2	19.9	1.1	9.4	1.2	2.3
110	2	#2	VR73G	A	SG	R	3.5	2.4	1.6	5.8	1.8	0.4	11.1	0.2	58.3	13.7	99.0																				
111	2	#3	VR73G	A	SG	R	3.4	2.8	1.4	6.3	1.8	0.3	11.5	0.2	57.9	14.3	99.9																				
112	2	#4	VR73G	A	SG	R	2.7	2.4	1.6	5.9	2.0	0.3	11.2	0.2	59.4	13.8	99.4																				
113	2	#5	VR73G	A	SG	R	2.7	2.3	1.7	5.9	2.1	0.4	11.3	0.2	58.8	13.2	98.7																				
114	~1	#8	VR73H	P1a	PD 1	VP	3.7	1.3	2.0	3.7	1.6	0.5	8.1	0.2	64.5	13.0	98.6											5.3	3.6	4.3	4.0	5.6	30.7	1.9	31.1	0.6	0.8
115	5	#9	VR73H	P1a	PD 1	VP	3.3	1.3	2.1	3.5	1.5	0.5	8.0	0.1	65.6	12.8	98.8	6.1	7.5	7.6	6.0	10.6	42.4	4.1	40.4	1.0	1.6										
116	5	#10	VR73H	P1a	PD 1	VP	3.5	1.3	2.1	3.8	1.5	0.5	7.8	0.2	64.8	13.0	98.6	5.8	7.5	7.6	5.6	11.1	40.0	4.2	23.5	1.0	1.6										
117	5	#11	VR73H	P1a	PD 1	VP	3.4	1.2	1.9	3.6	1.7	0.8	7.7	0.3	64.3	12.9	97.8	6.0	7.9	8.2	5.9	10.1	27.9	4.2	20.5	1.0	1.6										
118	5	#12	VR73H	P1a	PD 2	VP	3.9	1.2	1.9	3.5	1.1	0.2	6.4	0.1	65.6	14.3	98.3																				
119	5	#13	VR73H	P1a	PD 3	VP	3.8	0.9	2.4	2.8	1.5	0.4	6.1	0.2	68.8	13.1	99.9																				
120	5	#14	VR73H	P1a	ZD 1		4.1	1.2	2.3	3.5	1.8	0.6	8.2	0.2	64.5	12.7	98.9	5.4	8.1	7.3	6.0	9.7	34.5	4.1	25.4	1.0	1.6	2.9	3.0	1.5	1.7	11.6	16.0	5.3	15.3	0.9	1.9
121	5	#15	VR73H	P1a	ZD 1		3.9	1.1	2.3	3.5	1.5	0.4	7.6	0.2	65.3	13.0	98.9																				
122	5	#17	VR73H	P1a	BD 5		3.0	0.9	2.5	3.5	1.9	0.6	8.1	0.2	65.3	12.6	98.4	6.4	9.5	7.1	6.0	9.4	33.5	4.1	32.3	1.0	1.6										
124	5	#31	VR73H	P1a	SG 1	VP	3.7	3.7	1.0	7.3	1.4	0.3	10.0	0.2	56.2	15.6	99.4	5.8	4.3	11.6	4.1	11.2	62.0	3.7	31.9	1.1	1.5	8.1	4.2	4.9	2.3	4.4	20.3	4.4	10.0	0.9	1.1
125	5	#32	VR73H	P1a	SG 1	VP	3.6	3.5	1.0	6.9	1.4	0.3	9.3	0.2	55.8	15.2	97.3																				
126	5	#33	VR73H	P1a	SG 1	VP	3.9	3.7	1.0	7.1	1.4	0.3	9.9	0.2	55.4	15.7	98.7																				

127	5	#34	VR73H	P1a	SG 1	VP	4.0	3.6	1.0	7.3	1.4	0.3	9.6	0.2	55.9	15.8	99.1																						
128	5	#35	VR73H	P1a	SG 1	VP	3.5	3.6	1.0	7.0	1.5	0.3	9.6	0.2	54.6	15.6	96.9																						
132	5	#15	VR73H	P1a	SG 1	VP	3.0	3.6	0.9	7.0	1.4	0.3	10.1	0.2	55.4	15.6	97.5																						
133	5	#16	VR73H	P1a	SG 1	VP	4.1	3.5	1.1	7.3	1.4	0.3	9.0	0.2	57.1	15.9	99.8	5.4	4.5	10.7	4.1	11.2	59.1	3.9	28.1	1.1	1.5											
134	5	#17	VR73H	P1a	SG 1	VP	3.7	3.7	1.0	7.3	1.5	0.2	10.1	0.2	56.2	15.4	99.3																						
135	5	#18	VR73H	P1a	SG 1	VP	4.0	3.3	1.0	6.9	1.4	0.3	9.1	0.2	57.2	15.7	99.2																						
136	5	#19	VR73H	P1a	SG 1	VP	3.8	3.5	1.0	6.9	1.5	0.4	9.5	0.2	57.2	15.7	99.7	5.7	4.5	11.8	4.2	10.3	41.3	3.8	26.6	1.1	1.5											
123	2	#30	VR73H	P1a	SG 2	VP	3.1	3.6	1.1	6.8	1.4	0.3	9.9	0.2	56.1	15.7	98.2																						
129	~1	#36	VR73H	P1a	SB	VR	3.3	0.4	2.6	4.2	2.7	0.7	9.4	0.2	63.2	12.9	99.6	6.0	14.9	6.8	5.4	7.8	33.2	3.8	27.0	1.0	1.6	1.0	9.5	27.9	23.4	9.3	3.8	6.1	17.2	4.7	9.8
130	~1	#37	VR73H	P1a	SB	VR	3.4	0.5	1.8	6.0	3.0	0.6	10.3	0.2	59.4	14.9	100.2																						
131	~1	#38	VR73H	P1a	SB	VR	2.6	0.5	2.7	4.2	3.0	1.0	10.2	0.2	61.9	11.7	98.1																						
137	5	#42	VR113-6B		BA	VP	3.8	1.5	1.8	4.2	1.1	0.5	5.8	0.2	63.7	16.1	98.7											27.8	10.5	7.2	6.0	8.3	17.9	3.8	19.4	1.9	2.2
138	5	#43	VR113-6B		BA	VP	4.1	1.7	1.7	4.3	1.2	0.5	6.2	0.2	64.5	15.9	100.2																						
139	5	#44	VR113-6B		BA	VP	3.9	1.6	1.7	4.1	1.1	0.4	6.1	0.2	64.4	16.1	99.6	5.5	6.6	8.7	5.5	13.9	40.0	4.8	30.3	1.0	1.5											
140	5	#45	VR113-6B		BA	VP	3.6	1.7	1.7	4.6	1.1	0.3	6.4	0.2	63.4	16.1	99.1																						
141	5	#46	VR113-6B		BA	VP	3.8	1.6	2.0	4.3	1.2	0.5	5.8	0.2	64.4	16.0	99.6																						
142	5	#47	VR113-6B		BA	VP	3.7	1.6	1.9	4.4	1.1	0.4	6.0	0.2	63.6	15.9	98.8																						
143	5	#49	VR113-6B		BA	VP	4.0	1.5	2.0	3.7	1.2	0.4	6.2	0.2	65.1	14.8	99.2																						
144	5	#50	VR113-6B		BA	VP	4.3	1.5	1.8	4.4	1.0	0.4	6.3	0.2	64.6	15.5	100.0	5.2	6.9	8.3	5.3	14.4	48.5	4.7	31.7	1.0	1.5											
145	5	#8	VR113-6B		BA	VP	3.5	1.6	1.9	3.9	1.2	0.4	6.0	0.2	65.3	15.6	99.6	5.8	6.8	8.0	5.6	12.7	49.5	4.8	26.9	1.0	1.5											
146	5	#9	VR113-6B		BA	VP	3.9	1.6	1.8	4.2	1.0	0.5	5.5	0.2	65.3	15.7	99.8																						
147	5	#10	VR113-6B		BA	VP	3.7	1.7	1.9	4.1	1.2	0.3	5.9	0.2	64.9	15.9	99.9																						
148	5	#20	VR113-6B		BA	VP	2.6	1.6	1.8	4.2	1.0	0.5	6.4	0.1	65.7	15.5	99.4																						
149	5	#21	VR113-6B		BA	VP	3.6	1.6	1.7	4.4	1.3	0.4	5.9	0.2	65.2	15.8	100.0																						
150	2	#6	VR113-6S		SB	P	2.8	1.1	2.2	3.4	1.3	0.5	6.6	0.2	66.0	14.2	98.2	6.5	8.3	7.5	6.0	11.6	42.5	4.6	32.1	1.0	1.5	10.5	7.3	4.6	8.2	7.1	32.5	8.1	12.7	1.1	3.1
151	2	#7	VR113-6S		SB	P	3.1	1.1	2.2	3.4	1.6	0.8	7.4	0.2	65.2	13.7	98.6																						
152	2	#8	VR113-6S		SB	P	2.7	1.1	2.3	2.9	1.6	0.4	6.2	0.2	66.7	14.1	98.0																						
153	2	#9	VR113-6S		SB	P	2.3	1.2	2.2	3.6	1.6	0.5	7.2	0.2	66.9	13.4	99.1																						
154	2	#10	VR113-6S		SB	P	2.5	1.3	2.0	3.5	1.6	0.4	7.7	0.2	66.2	13.6	99.0																						

* Beam size used during the analysis (in µm)

** Fragment types:
DJ = dense juvenile lapilli
SJ = scoriaceous juvenile lapilli
SG = goldish-brown scoria lapilli
SI = greenish-brown scoria lapilli
SB = black scoria lapilli
BA = banded vesicular lapilli
DPJ = dense prismatically-jointed lapilli
PD = pale dense ash
BD = black dense ash
ZD = zoned dense ash

*** Microlite content of the samples (in % vesicle-free).
Samples with microlite content not available were described as follows:
VP = very crystal-poor (glass surfaces of less than ~ 5 - 20 µm)
P = crystal poor (glass surfaces of less than ~ 2 - 5 µm)
R = crystal rich (glass surfaces of less than ~ 1 - 2 µm)
VR = very crystal rich (glass surfaces of less than ~ 1 µm)

Analytical conditions in Appendix 4.6.

The error (%) was estimated statistically using the counting times and the number of counts par second obtained for the peak and background of the sample and for the peak and background of the standard (Ancey et al., 1978; PhD these of M.Laubier, S.Moune and S.Jannot, 2005/2006). The reproducibility (%) was calculated from the average of the analyses done in every sample.

Appendix 4.8: Effects of electron beam-size variation on major element glass analyses

It is well known that natural and synthetic glasses are inherently unstable during electron bombardment, especially sodium and to a lesser extent, potassium. This results in lower sodium values and proportionally higher values for other elements (Hunt & Hill, 2001). In order to adopt the optimal analytical conditions to minimise sodium mobility, microprobe analyses have been done in rhyolitic glasses (Hunt & Hill, 2001), showing SiO_2 overrepresentation and Na_2O underrepresentation in the range of beam raster dimensions 3 to 10 µm and a reversed trend below 3 µm (less Na less Si), with 'accurate' analyses occurring in the range 10 to 15 µm (Hunt & Hill, 2001).

Even if these effects are more acute in the more silicic glasses richer in alkalis such as rhyolites and dacites (Hunt & Hill, 2001), a defocussed beam of 10 and 5 µm and a focussed beam (~ 1 µm) were employed during the analysis of basaltic andesitic glass of a crystal-poor scoria (VR73J-L6, subunit P1a) in order to study the sodium, potassium, silica and aluminium response to varying beam size (Figure 4.21). The precision (2σ) associated with every element during an analysis was estimated statistically (see Appendix 4.6). For every element, the errors calculated in the sample were very similar (Appendix 4.7), thus to simplify the figure, a mean error is shown (left diagrams of Figure 4.21). A mean of the 5 analyses done for every beam size with the reproducibility (2σ) is shown in the diagrams to the right (Figure 4.21).

There is a slight increase in the Na_2O, K_2O and SiO_2 values in the range of beam sizes from focussed (~1 µm) up to 10 µm (Figure 4.21). The accepted values are Na_2O = 3.8%, SiO_2 = 57.3% and K_2O = 1.0%. As it was expected for a basaltic andesitic glass, these variations are much less important than for silicic glasses. In fact, on average there is a Na loss of about 7% with a beam size variation from 10 µm to a focussed beam (~ 1 µm), accompanied of a slight decrease of less than 0.5% in the silica content. For comparison, a Na loss of about 60% accompanied by a decrease of about 1% of silica has been reported in rhyolitic glasses for similar beam sizes variations (e.g. Hunt & Hill, 2001). The precision of sodium of the Pucón glasses varies from about 5 to 7% (Appendix 4.7), thus the Na variations with beam sizes can be considered very small or negligible.

The Pucón glass exhibits a potassium decrease of about 10% from 10 µm to focussed beam (Figure 4.21), whereas Al_2O_3 decreases, then increases with a total variation of less than 0.7% (not shown). Considering that the precision is about 1% for silica, about 11% for potassium and about 2% for aluminium (Appendix 4.7), the variations with beam size of these elements can be considered negligible.

The best reproducibility for alkalis was obtained with a beam size 5 µm and for silica with a focussed beam (Figure 4.21). For Na_2O, K_2O and SiO_2, the higher errors (reproducibility) were produced for beam size 10 µm (Figure 4.21), which could be due to the presence of microlites not easily recognised in the image. In any case, the number of analysis was too low to calculate a standard deviation. Thus, the reproducibility should be interpreted carefully.

The samples of the Pucón Ignimbrite show large differences in crystallinity with microlite contents ranging from about 2 to 98% (vesicle-free) (Appendix 4.7). Thus, beam sizes were used ranging from 10 µm in the very crystal-poor samples up to a focussed beam (~1 µm) in the crystal-rich ones where the glass surfaces normally don't reach more than 1 µm in diameter. For uniforming the beam sizes, the analyses were corrected considering the Na variation but given that the variations with the beam size are negligible (see above), this correction was not used.

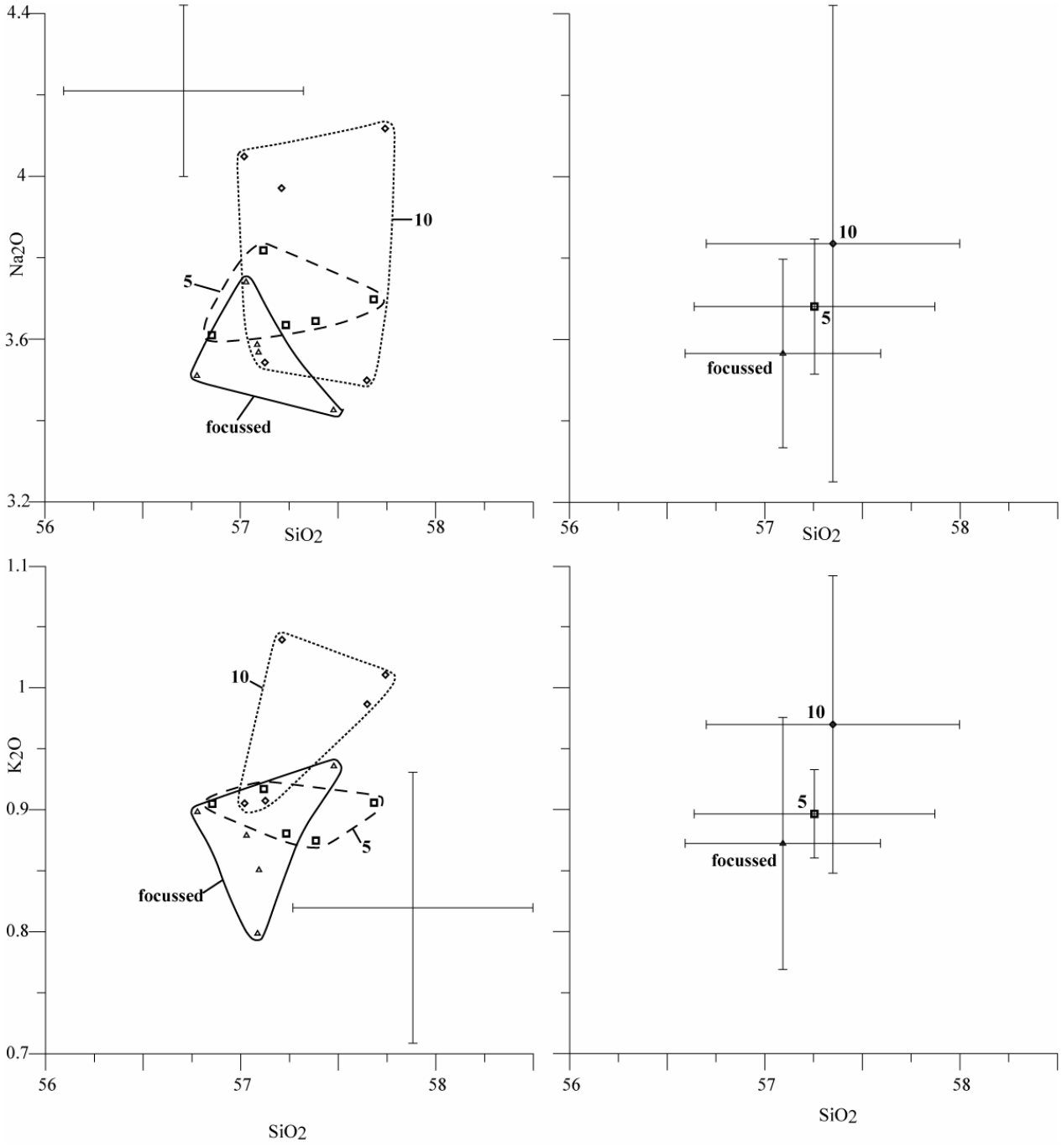

Figure 4.21: Pattern of sodium, potassium and silica response to varying beam size. A defocused beam of 10 and 5 µm and a focussed beam (~ 1 µm) were used during the glass analyses of a juvenile scoria of the Pucón Ignimbrite (VR73J-L6, subunit P1a). Analytical conditions given in Appendix 4.6. Number is size of beam in µm. The precision (2σ) of every analysis was calculated statistically (Appendix 4.6) and a mean of the errors is shown in the diagrams to the left. Diagrams to the right show the mean of the 5 analyses done for every beam size with the reproducibility (2σ). The accepted values are Na_2O = 3.8%, SiO_2 = 57.3% and K_2O = 1%.

Appendix 4.9: Estimation of the microlite content of the juvenile fragments

For estimating the microlite content, the samples were first analysed with the SEM (Scanning Electron Microscope Jeol JSM-5910 LV of the « Laboratoire Magmas et Volcans » (LMV), Université Blaise-Pascal-CNRS-IRD, Clermont-Ferrand, France). The general method of image treatment can be described as follows. Pictures at different scales were taken with the SEM. With the aim to have a representative number of microlites to estimate their content (more than ~50), there were used magnifications of 350X for the microlite-poor samples and 1000X for the microlite-rich and zoned samples. The different areas (picture, vesicles and crystals areas) were calculated combining the software Adobe Photoshop and ImageJ. The crystal content (vesicle-free) is calculated as:

$$\text{Crystal content (vesic-free)} = \frac{\text{Area cxx} * 100}{\text{Area picture - Area vesicles}}$$

In the microlite-rich samples, the glass content was calculated (by convenience):

$$\text{Glass content (vesic-free)} = \frac{\text{Area glass} * 100}{\text{Area picture - Area vesicles}}$$

and then, the crystal content was calculated as:

$$\text{Crystal content (vesic-free)} = 100 - \text{Glass content (vesic-free)}$$

To determine how reliable the microlite measurements performed by image analyses are, we calculate the crystallinities by another approach (Table 4.4). We define:

Xc = total crystal fraction of the sample

Xph = total phenocryst fraction of the sample

Xmic* = total microlite fraction in the groundmass

Xmic = total microlite fraction

Kc = potassium content (K_2O%) of the total crystal fraction (microlites + phenocrysts, from Lohmar 2008, written communication)

Kg = potassium content (K_2O%) of the glass fraction

Kwr = potassium content (K_2O%) of the whole rock

Kmic = potassium content (K_2O%) of the microlites (values of Lohmar 2008, written communication)

cxx% = microlite content measured by image treatment

So,

$$Xc = Xph + Xmic \quad (1)$$

And

$$Kwr = Xc * Kc + (1 - Xc) * Kg$$

From the whole-rock data (Appendix 3.4), we took an average of the K_2O content in scoriae for units P1 and P2:

Kwr = 0.81 for P1

Kwr = 0.84 for P2

Rearranging:

$$Xc = (Kwr - Kg) / (Kc - Kg)$$

Then, we assume the non-crystallised composition of K_2O as Kg = 0.92 which is the lowest value obtained in the glasses (Table 4.4) and we use this value as follows:

$$0.92 = (Xmic^*) * Kmic + (1 – Xmic^*) * Kg$$

Rearranging:

$$Xmic^* = (0.92 – Kg) / (Kmic – Kg)$$

Considering that $Xmic = (Xmic^*) * (1 – Xph)$, using equation (1) and rearranging, we calculate (Table 4.4):

$$Xph = (Xc – Xmic^*) / (1 - Xmic^*)$$

Appendix 4.10: Trace element (Cl, F and S) glass compositions and respective errors of Pucón scoria

							normalised			error % (2 sigma)			error ppm (2 sigma)			mean			st dev (2 sigma)		
BS	**sample**	**unit**	**F**	**Cl**	**S**	**total**	**F**	**Cl**	**S**	**F**	**Cl**	**S**	**F**	**Cl**	**S**	**F**	**Cl**	**S**	**F**	**Cl**	**S**
µm			ppm	ppm	ppm		ppm	ppm	ppm				ppm	ppm	ppm	ppm	ppm	ppm	ppm	ppm	ppm
10	VR73J-L6	P1a	230	630	180	101	228	625	179	39	3	8	89	16	15	244	551	146	33	121	75
10	VR73J-L6	P1a	228	491	161	101	226	487	160	35	3	9	81	15	14						
10	VR73J-L6	P1a	264	600	176	101	262	595	175	32	3	8	83	16	14						
10	VR73J-L6	P1a	248	557	130	101	246	553	129	34	3	10	85	16	14						
10	VR73J-L6	P1a	260	500	90	101	258	496	89				0	0	0						
0	VR73J-D3	P1a	390	1270	150	99	395	1287	152	21	2	9	83	21	14	1091	1500	146	1166	610	55
0	VR73J-D3	P1a	1440	1560	160	99	1457	1578	162	7	1	9	107	23	14						
0	VR73J-D3	P1a	1860	1980	170	99	1880	2001	172	6	1	8	118	26	14						
0	VR73J-D3	P1a	770	1270	140	99	780	1286	142	12	2	10	91	21	14						
0	VR73J-D3	P1a	930	1330	100	99	942	1347	101	10	2	13	97	21	13						
5	VR73P-L2	P1b	250	650	150	100	250	649	150	33	3	9	83	16	14	310	635	134	121	30	36
5	VR73P-L2	P1b	410	620	140	100	409	619	140	20	3	10	83	16	14						
5	VR73P-L2	P1b	300	640	110	100	300	639	110	28	3	12	84	16	13						
5	VR73P-L2	P1b	310	650	120	100	310	649	120	26	2	11	80	16	13						
5	VR73P-L2	P1b	280	620	150	100	280	619	150	32	3	9	89	16	14						
10	VR73P-D7	P1b	250	540	150	99	252	544	151	30	3	9	74	15	13	222	582	194	96	67	101
10	VR73P-D7	P1b	230	580	200	99	232	584	201	34	3	7	77	16	14						
10	VR73P-D7	P1b	150	620	260	99	151	624	262	52	3	6	78	16	15						
10	VR73P-D7	P1b	250	570	160	99	252	574	161	32	3	8	79	15	13						
10	VR73P-D7	P1b											0	0	0						
5	VR78-3A-L1	P2a	300	650	70	99	303	657	71	26	2	17	77	16	12	265	725	73	101	154	25
5	VR78-3A-L1	P2a	230	670	90	99	233	677	91	36	2	13	82	16	12						
5	VR78-3A-L1	P2a	210	820	70	99	212	829	71	39	2	16	82	17	12						
5	VR78-3A-L1	P2a	310	730	60	99	313	738	61	26	2	21	82	17	13						
5	VR78-3A-L1	P2a											0	0	0						
5	VR78-3A-L1	P2a											0	0	0						
0	VR78-3A-D2	P2a	290	1580	320	98	295	1606	325	26	1	5	75	23	16	327	1367	234	223	2483	420
0	VR78-3A-D2	P2a	440	580	70	99	445	587	71	17	3	17	77	16	12						
0	VR78-3A-D2	P2a	430	740	100	98	438	754	102	18	2	12	78	17	12						
0	VR78-3A-D2	P2a	300	680	100	98	306	693	102	26	2	13	78	16	13						
0	VR78-3A-D2	P2a	140	3730	610	98	*142*	*3787*	*619*	69	1	3	96	37	21						
0	VR78-3A-D2	P2a	330	760	180	98	336	774	183	23	2	8	77	17	14						
0	VR85-8-L4	P2a	470	960	200	99	477	974	203	16	2	7	77	18	15	849	1482	245	1114	880	168
0	VR85-8-L4	P2a	1770	1770	330	99	*1792*	*1792*	*334*	6	1	5	108	24	16						
0	VR85-8-L4	P2a	760	1490	200	99	771	1511	203	12	2	7	92	22	14						
0	VR85-8-L4	P2a	800	1990	330	99	811	2017	334	11	1	5	88	26	16						
0	VR85-8-L4	P2a	390	1100	150	99	396	1116	152	19	2	9	75	20	13						
5	VR85-8-D5	P2a	300	660	170	99	304	668	172	25	2	8	74	16	14	318	636	130	62	63	93
5	VR85-8-D5	P2a	290	580	140	99	293	587	142	26	3	10	74	16	14						
5	VR85-8-D5	P2a	290	630	70	99	293	638	71	26	3	19	76	16	13						
5	VR85-8-D5	P2a	330	620	170	99	334	627	172	22	3	8	72	16	13						
5	VR85-8-D5	P2a	360	650	90	99	364	658	91	21	3	14	76	16	13						
0	VR85-3-L3	P2b	40	840	170	100	40	838	170	247	2	8	99	18	14	50	681	150	42	248	102
0	VR85-3-L3	P2b	90	650	130	100	90	649	130	469	3	10	422	16	13						
0	VR85-3-L3	P2b	50	590	170	100	50	589	170	137	3	8	68	16	14						
0	VR85-3-L3	P2b	50	520	60	100	50	522	60	234	3	19	117	15	11						
0	VR85-3-L3	P2b	40	670	160	100	40	673	161	100	2	9	40	16	14						
0	VR85-3-L3	P2b	30	810	210	100	30	813	211	136	2	7	41	18	15						
0	VR85-3-D4	P2b	110	1060	260	100	110	1064	261	83	2	6	91	19	15	86	1244	138	97	1492	144
0	VR85-3-D4	P2b	160	2550	140	100	160	2556	140	47	1	9	75	30	12						
0	VR85-3-D4	P2b	60	790	80	100	60	793	80	449	2	16	270	17	13						
0	VR85-3-D4	P2b	50	760	100	100	50	763	100	407	2	13	204	17	13						
0	VR85-3-D4	P2b	50	1040	110	100	50	1044	110	350	2	11	175	19	12						

Appendix 4.11: Effects of electron beam-size variation on trace element (Cl, F and S) glass analyses

Given the large differences in crystallinity between the samples, different beam sizes were used in the different samples. The variation of the volatile contents measured with different beam sizes was explored with the same crystal poor sample of unit P1 used for study the variations in major elements with the beam size (VR73J-L6, Figure 4.21). The results for 10µm, 5µm and a focussed beam (~1µm), are presented in Figure 4.22. At the left hand, there are presented the single measurements (5 analyses for each of the three beam sizes) with their associated errors (2σ, Appendix 4.10). At the right hand, there are presented the mean with the precision or reproducibility (2σ) of the five measurements for each beam size. With an increasing beam size, the average values of S, Cl and F decrease first (focussed beam to 5 µm) and then increase (5 to 10 µm).

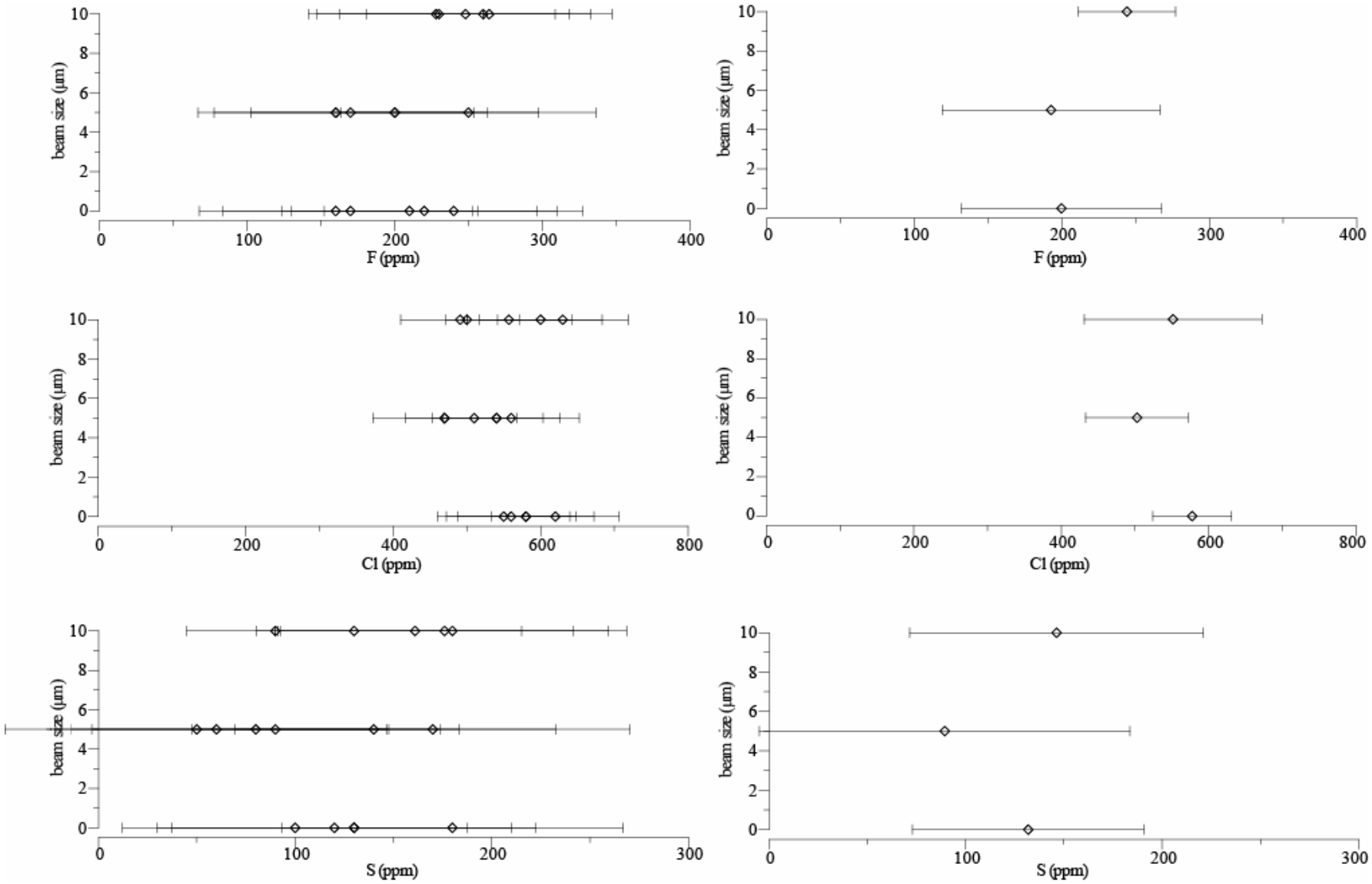

Figure 4.22: Variation of the S, Cl and F contents with the beam size (focussed beam, 5 and 10 µm). On the left hand, the five analyses done with each beam size and on the right hand, the mean of them. Individual errors (Appendix 4.10) and standard deviation (2σ) are also shown. The scoria sample used is the same chosen for study the Na loss (VR73J-L6, Figure 4.21).

CHAPTER 5 General conclusions

The Pucón Ignimbrite (3.6 ka BP, 3.3 km^3 equivalent to 1.8 km^3 DRE) is a well preserved and complicated sequence of airfall and pyroclastic current deposits with basaltic andesitic juvenile composition (54-56% SiO_2), emitted by the largest Holocene eruption of Villarrica Volcano (Southern Chile).

Prior to the Pucón eruption, the volcano summit was covered by a probably extensive ice cap and basaltic-andesitic to rhyolitic lava domes and/or flows of unknown age were possibly present near or at the Villarrica summit (Figure 5.1, diagram 1). Many of these magmas probably extruded beneath the summit ice cap, accounting for their abundant prismatic jointing. About 0.02 km^3 of these lavas and/or domes, equivalent to a moderate-volume lava dome or flow, were fragmented at the onset of the Pucón eruption generating abundant dense prismatically-jointed (DPJ) clasts and dense ash shards that were incorporated by the subsequent Pucón products.

Prior to the Pucón eruption and following a maximum repose period of ~400 years, the volcano summit was probably marked by fumarolic activity when a violent strombolian to subplinian fallout started (0.2 km^3 of deposits, 0.1 km^3 of magma, VEI = 3 to 4) marking the onset of the Pucón eruption (Figure 5.1, diagram 2). The magma emitted under normal, open-conduit magmatic conditions was very hot and fluidal, probably ejecting abundant spatter fragments proximally. Vent erosion and conduit widening started during this phase, suggested by the sudden appearance of DPJ fragments in the upper part of the basal scoria fall deposit.

The eruptive dynamics of the volcano then evolved towards an ignimbrite-forming mechanism rapidly enough to prevent significant erosion of the fall deposit or development of a paleosol. During the first phase (P1), multiple pyroclastic flows (0.6 km^3, 20% of the total volume) covered ~180 km^2 of the western and northern flanks of the volcano up to 15 km from the present-day summit (Figure 5.1, diagram 3). First, a small phreatomagmatic explosion at the summit generated a base surge that swept down the north flank (P1aI) which was then followed by a series of about ten powerful vulcanian explosions (0.14 km^3 of magma, 20% of the total volume). Each explosion (0.014 km^3) emptied the conduit and tapped into the main reservoir at depth. Following each discharge event, magma would have partially refilled the conduit prior to the next explosion. A progressive deepening of the fragmentation level during P1 increased the supply of altered fragments and decrease of fresh volcanics upwards through P1. As the magma level dropped during each explosion, abundant external water poured into the conduit probably from melting of the summit glacier and snow. Explosive expansion of water from the melting of the ice cap, caused erosion and pulverization on wall rock, progressively widening the conduit and generating quantities of lithic debris that were incorporated into the pyroclastic flows. The first lithic-rich deposits (P1aII-III) were laid down by highly concentrated pyroclastic flows, being deposited in valleys and

depressions. Lithic clasts too coarse or too dense to be transported by the pyroclastic flows were left proximally, generating lag breccias. Subordinate pyroclastic surges were deposited mostly in proximal slope environments, probably by the upper, more dilute levels of the pyroclastic flows. Spatter fragments, emitted either during the initial fallout phase or during eruption of P1a, were transported by the pyroclastic flows. Some vegetation was burned by the passage of the pyroclastic flows. The eruption intensity then declined with the emission of at least two brown juvenile-rich pyroclastic flows with a restricted distribution (P1aIV). A lower amount of available external water could explain the lithic-poor character of these pyroclastic flows because most of the summit glacier and snow had by then melted. The P1a phase left a deposit of multiple stacked, well-defined flow units. Available water mobilised and transported some pyroclastic debris.

The P1a phase was followed by the emission of at least three black, juvenile-rich pyroclastic flows that were emitted across the western to northern flanks of the volcano (P1b). These highly concentrated scoria flows overspilled the topography, depositing strongly thinned veneers on proximal valley margins. The flows were very hot, causing strong charcoalization of wood and forming abundant degassing pipes. While wood in P1b was still being charcoalised, at least three less juvenile-rich pyroclastic flows were discharged into valleys on the western and northwestern flanks of the volcano (P1c).

During a pause in explosive activity following the phase P1 which was probably several weeks to months long, the P1 deposits cooled below the temperature necessary for charcoalization of wood (~200°C) and changes took place in the plumbing system of the volcano (Figure 5.1, diagram 4). Reservoir replenishment by a more primitive new magma batch enriched in incompatible elements from depth and/or slight contamination by basement granitoids, occurred in the plumbing system. Vent erosion and widening all around the volcano, or at least in different and more extensive areas than during P1 phase, provided the P2 pyroclastic density currents of a new assemblage of basaltic-andesitic to rhyolitic lava fragments (at least 0.03 km^3).

During the second eruptive phase (P2) which probably lasted no more than a few days, voluminous pyroclastic flows and minor surges (2.5 km^3 of deposits, 0.8 km^3 DRE magma, 80% of the total volume) were deposited all around the volcano, covering ~530 km^2 and extending up to 21 km from the present-day summit probably up to the present town of Pucón. These P2 flows left thick sequences in valleys (<70 m thick) with an important deposition on interfluves (<5 m thick). The climactic phase (P2a) represents an increase in the eruptive intensity and is characterised by the abrupt appeareance of a significant proportion of free clasts of basement granitoids, suggesting that very rapidly after the start of this phase the magma level dropped to within the granitoid basement, at a level lower than that during phase P1 (Figure 5.1, diagram 5). This is probably explained by the high magma discharge rate, causing the fragmentation level

of the magma to fall rapidly, probably accompanied by the climactic phase of caldera collapse. Dispersal of granitoid fragments in P2 scoria must record either vigorous inmixing of shattered wall rock into the magma near the fragmentation surface, and/or stoping of roof material into a magma reservoir residing within granitoid basement. Granitoid fragments in P2 scoria include vesicle-bearing, actively disaggregating, partially melted examples, but also many angular, non-melted ones, showing that the granitoid was being actively mixed into the magma during eruption.

The turbulent, blast-like leading edge of these flows arrived first, eroding, shearing and deforming the substrate during its path, and representing the most energetic and violent pulse of all the pyroclastic currents of P2 (Figure 5.1, diagram 5). It travelled further than the rest of P2, leaving a fines-depleted deposit up to 5 m thick along the valleys with important interfluve deposition. Three or more high-energy P2a pyroclastic flows followed in rapid succession, forming thick and commonly amalgamated valley ponds that locally thicken downstream. Some of the coarser-grained interfluve facies of P2a are veneers left where the entire pyroclastic flow swept over the landscape; finer-grained beds probably record deposition from the dilute upper part or margins of density-stratified flows, which formed an almost completely record of the deposits on interfluves. The P2a flows were highly erosive, forming angular unconformities, shearing and thrusting the underlying strata. The flows were unsteady and of high- to intermediate-concentration, deduced from their dominantly diffusely stratified aspect and from the presence of huge bed forms. Old big trees partly buried, but not felled by the less energetic P1 flows were now knocked over by the arrival of the more violent flows of P2a. However, in some sectors of the northern and western flanks, little vegetation was probably available by this time, because it had already been buried by the P1 flows. In places, the initial fines-depleted facies was eroded or sheared off, leaving isolated pockets preserved in channels and depressions. Channels were carved into P1 deposits of the northern flank.

The P2 phase then continued with the emission of juvenile-rich pyroclastic flows (P2b), extending up to ~11 km from the summit in a restricted sector from the south to east of the volcano (Figure 5.1, diagram 6). Similar than in P1 phase, a possible explanation of the passage from lithic- to juvenile-rich deposits (P2a to P2b) is that the external water was greatest during the early stages of P2 phase, then decreased because most of the summit glacier and snow had by then melted. These high-concentration pyroclastic flows formed thick deposits in the valleys and thinner ones on interfluves; they burned much of the available wood due to their high temperature. At least two rapidly emplaced lithic-rich pyroclastic surges then covered the previous hot deposits with charcoal still burning (degassing pipes traverse the contact). This represents a major surge-forming phase, the product of which is distributed all around the volcano with an important deposition on slope environments (P2c; Figure 5.1, diagram 7).

The Pucón eruption terminated with a low-intensity waning phase consistent with greatly decreased reservoir pressure, during which three high-concentration lithic-rich pyroclastic flows were emitted on the northern flank up to 10 km from the present-day crater (P2d; Figure 5.1, diagram 8). Immediately after the eruption, the ignimbrite surface was inundated by several lahar waves (Figure 5.1, diagram 9).

A new cycle of explosive activity characterised by vigorous strombolian to subplinian eruptions and phreatic/phreatomagmatic explosions, started no more than a few rain seasons after the discharge of the final pyroclastic flow (Figure 5.1, diagram 10). The porphyric magma of the Chaimilla scoria fall deposit is tentatively interpreted as residual cumulates from Pucón magma, containing geochemical signals of both P1 and P2 components, indication that the magmatic chamber was not completely emptied during the Pucón eruption.

If the 2-km-diameter caldera was associated with the Pucón eruption at all, the evidence of a few time elapse between the Pucón and Chaimilla eruptions, suggest that the construction of the modern cone started very short after the caldera collapse associated with the Pucón eruption (Figure 5.1, diagram 11).

Pucón magma was probably sufficiently rich in volatiles at depth to exsolve and drive magmatic fragmentation and we lack evidence to support premature phreatomagmatic quenching of juvenile clasts. Low-pressure degassing and associated rapid microlite crystallization could explain the origin of the density clasts, rather than by quenching by water. External water may, on the other hand, have played an important role in pulverizing large quantities of rock from the conduit margins progressively eroding and widening the conduit. This effect could have been the greatest early on each phase (P1 and P2) and then decreased because most of the summit glacier and snow had then melted. These fluctuations in the amount of water involved could account for the observed lithic-rich nature of much of the P1 and P2 sequences and the highly variable lithic contents, which produced the characteristic brown to black colour variations of the Pucón Ignimbrite on the field.

Villarrica volcano is one of the most historically active volcanoes in South America, with a past tendency for large-scale explosive activity and the generation of pyroclastic currents highly destructive to life and the environment. Even infrequent on a human timescale, if a Pucón-sized eruption (VEI = 5) occurred today, approximately 15,000 - 40,000 people would be directly threatened by pyroclastic currents and even more by associated lahars and ash falls.

The Pucón eruption started with a fallout phase that quickly evolved towards an ignimbrite-forming eruptive mechanism. This may have implications for hazards at Villarrica, because the possible occurrence of a violent strombolian or subplinian eruption may quickly evolve towards the generation of voluminous pyroclastic flows of much higher volcanic hazard.

The evolution of the Pucón eruption shows that a violent ignimbrite-type episode (such as P2), of short duration but large magnitude, catastrophic on a regional scale affecting all the flanks with the generation of very violent pyroclastic currents, can occur after a pause of several weeks to months following a period of already important pyroclastic activity (P1). This pause at the end of P1 marked a prolonged adjustment phase of the plumbing system, rather than the end of the eruption, as could be assumed during monitoring of a similar event today.

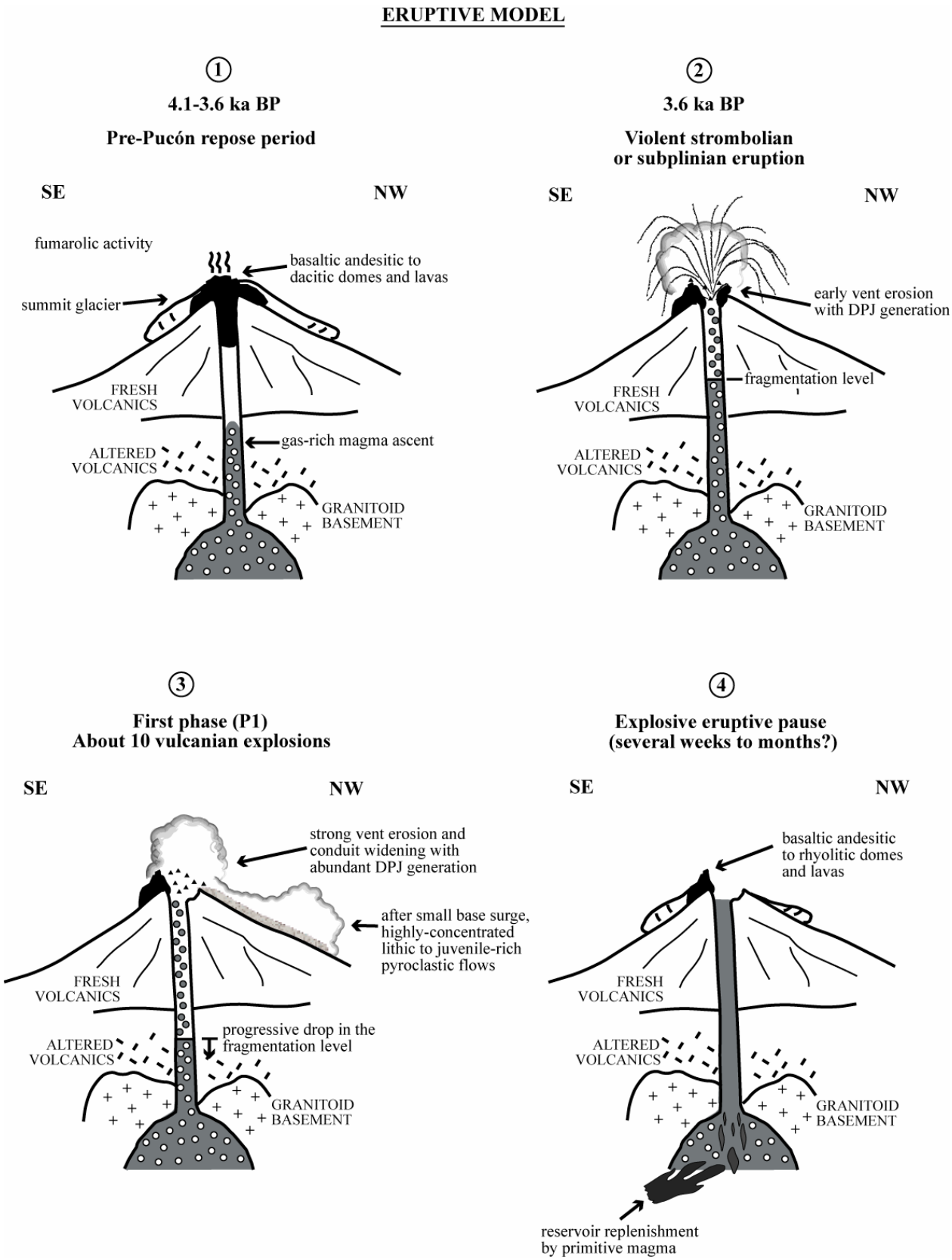

Figure 5.1: Eruptive model of the Pucón eruption (schematic, not to scale)

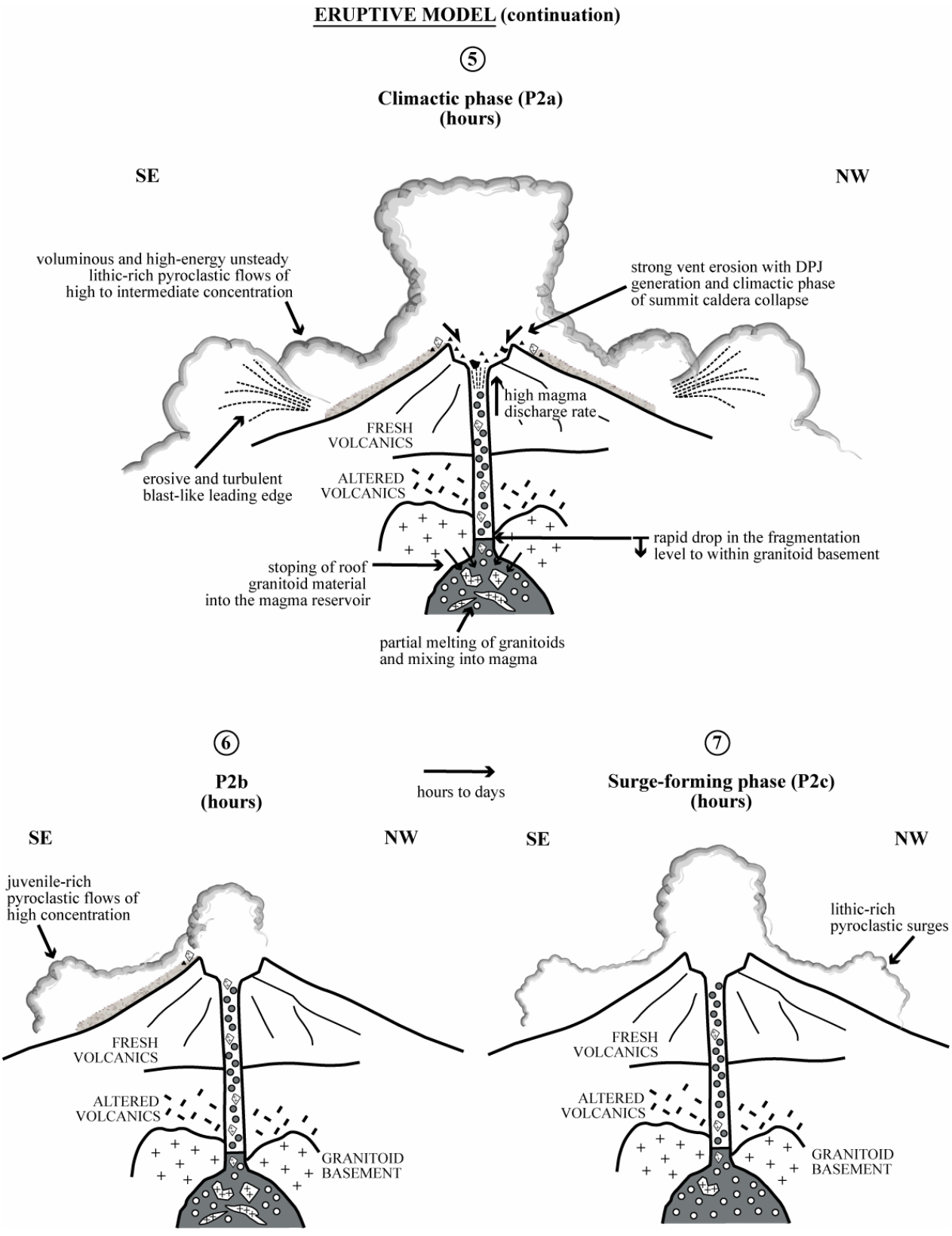

Figure 5.1: Eruptive model of the Pucón eruption (continuation)

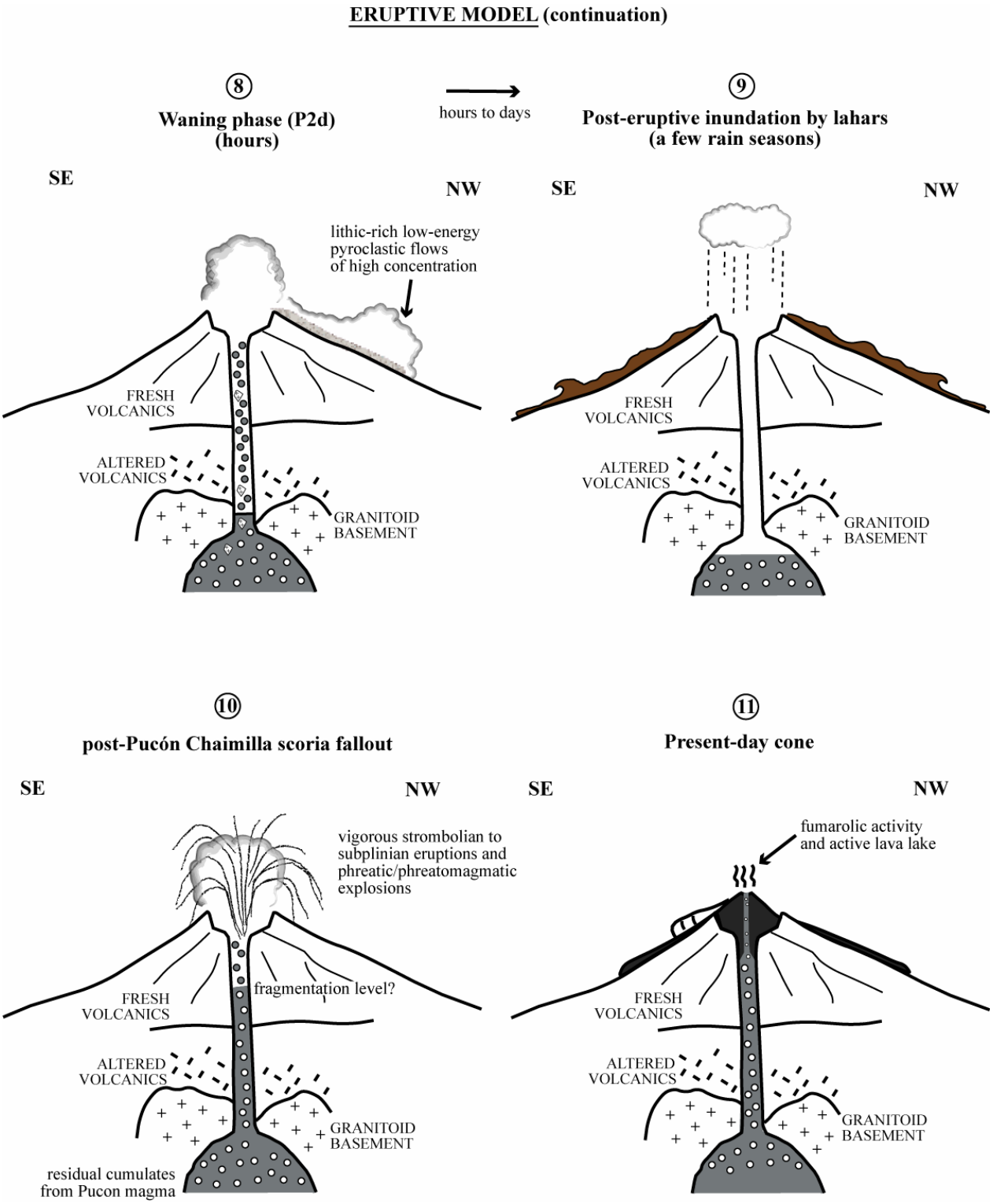

Figure 5.1: Eruptive model of the Pucón eruption (continuation)

REFERENCES

Aguirre, L. & Levi, B., 1964. Geología de la Cordillera de los Andes de las provincias de Cautín, Valdivia, Osorno y Llanquihue. *Instituto de Investigaciones Geológicas, Boletín, N°17, 37 p., 1 mapa escala 1:500.000, Santiago.*

Allen, S.R. & Cas, R.A.F., 1998. Lateral variations within coarse co-ignimbrite lithic breccias of the Kos Plateau Tuff, Greece. *Bulletin of Volcanology, Vol.59, pp.356-377.*

Alvarado & Soto, 2002. Pyroclastic flow generated by crater-wall collapse and outpouring of the lava pool of Arenal Volcano, Costa Rica. *Bulletin of Volcanology, Vol.63, pp.557-568.*

Ancey, M., Bastenaire, F. & Tixier, R., 1978. Applications des méthodes statistiques en microanalyse. *In: Maurice, F., Meny, L. & Tixier, R., 1978. Microanalyse et Microscopie Electronique à Balayage. Les éditions de Physique.*

Arguden, A. & Rodolfo, K., 1990. Sedimentologic and dynamics differences between hot and cold laharic debris flows of Mayon Volcano, Philippines. *Geological Society of America Bulletin, Vol.102, pp.865-876.*

Blong, R.J., 1996. Volcanic hazards risk assessment. In: *Scarpa, R. & Tillling, R.I. (Editors). 1996. Monitoring and Mitigation of Volcano Hazards, Springer, 841 p.*

Blundy, J. & Cashman, K., 2005. Rapid decompression-driven crystallization recorded by melt inclusions from Mount St. Helens volcano. *Geology, Vol. 33, Issue 10, pp. 793-796.*

Bohm, M., Lüth, S., Echtler, H., Asch, G., Bataille, K., Bruhn, C., Rietbrock, A. & Wigger, P., 2002. The Southern Andes between 36° and 40°S latitude: seismicity and average seismic velocities. *Tectonophysics, N°356, p.275-289.*

Bowman, S., 1990. Radiocarbon dating. Interpreting the past. *British Museum Publications, 64 pp.*

Branney, M.J & Kokelaar, B.P., 1992. A reappraisal of ignimbrite emplacement: progressive aggradation and changes from particulate to non-particulate flow during emplacement of high-grade ignimbrite. *Bulletin of Volcanology, Vol.54, pp.504-520.*

Branney, M.J. & Kokelaar, P., 2002. Pyroclastic density currents and the sedimentation of ignimbrites. *Geological Society Memoir N°27, 143 pp.*

Brown, R.J. & Branney, M.J., 2004. Bypassing and diachronous deposition from density currents: Evidence from a giant regressive bed form in the Poris Ignimbrite, Tenerife, Canary Islands. *Geology, Vol.32, N°5, pp.445-448.*

Calder, E.S., Harris, A.J.L., Peña, P., Pilger, E., Flynn, L.P., Fuentealba, G. & Moreno, H., 2004. Combined thermal and seismic analysis of the Villarrica volcano lava lake, Chile. *Revista Geológica de Chile, Vol.31, N°2, p.259-272.*

Carey, S. & Sigurdsson, H., 1987. Temporal variations in column height and magma discharge rate during the 79 A.D. eruption of Vesuvius. *Geological Society of America Bulletin, Vol. 99, pp. 303-314.*

Carey, S.N. & Sparks, R.S.J., 1986. Experimental studies of particle-laden plumes. *Journal of Geophysical Research, Vol.93, pp.15314-15328.*

Cas, R.A.F. & Wright, J.V., 1987. Volcanic Successions modern and ancient. A geological approach to processes, products and successions. *London Allen & Unwin Boston Sydney Wellington, 528 p.*

Casassa, G., Acuña, C., Zamora, R., Schliermann, E. & Rivera, A., 2004. Ice thickness and glacier retreat at Villarrica Volcano. In: *Lara, L.E.; Clavero, J. (Editors). 2004. Villarrica Volcano (39.5°S), Southern Andes, Chile. Servicio Nacional de Geología y Minería, Boletín, N°61, pp.53-60.*

Casertano, L., 1963a. Actividad del volcán Villarrica en el curso de este siglo. *Universidad de Chile, Boletín, N°40, Santiago.*

Casertano, L., 1963b. Actividad del volcán Villarrica en el curso de este siglo (II y final). *Universidad de Chile, Boletín, N°41, Santiago.*

Cashman, K.V., 1992. Groundmass crystallization of Mount St. Helens dacite, 1980-1986: a tool for interpreting shallow magmatic processes. *Contributions to Mineralogy and Petrology, Vol. 109, pp. 431-449.*

Castruccio, A. 2008. Comparación y modelación numérica de lahares calientes en el volcán Calbuco (41,3ºS) y lahares fríos en el volcán Villarrica (39,5ºS), Andes del Sur. *Tesis para optar al grado de Magister en Ciencias Mención Geología, Departamento de Geología, Universidad de Chile (Inédito), 177 p.*

Castruccio, A., 2005. Análisis de facies de los lahares de la erupción de 1971 del volcán Villarrica, Andes del Sur. *Inédito, Memoria de título, Universidad de Chile, Santiago, 112p.*

Castruccio, A., Clavero J. & Rivera, A., 2005. Lahares de la erupción de 1971 en el flanco occidental del volcán Villarrica, Andes del Sur. *XVI Congreso Geológico Argentino, La Plata, Argentina.*

Castruccio, A., Clavero, J. & Rivera, A., 2006. Nuevos antecedentes sobre los lahares generados por la erupción de 1971, en el flanco occidental del volcán Villarrica (39,5°S). *XI Congreso Geológico Chileno, Antofagasta, Chile.*

Cembrano, J. & Moreno, H., 1994. Geometría y naturaleza contrastante del volcanismo cuaternario entre los 38°S y 46°S: Dominios compresionales y tensionales en un régimen transcurrente? *Actas VII Congreso Geológico Chileno, Vol.I, pp.240-244.*

Cembrano, J., Hervé, F. & Lavenu, A., 1996. The Liquiñe-Ofqui fault zone: a long-lived intra-arc fault system in southern Chile. *Tectonophysics, Vol. 259, p. 55-66.*

Cembrano, J., Schermer, E., Lavenu, A. & Sanhueza, A., 2000. Contrasting nature of deformation along an intra-arc shear zone, the Liquiñe-Ofqui fault zone, Southern Chilean Andes. *Tectonopyhsics 319, p. 129-149.*

Chmeleff, J., 2005. Les déséquilibres radioactifs ^{238}U-^{230}Th-^{226}Ra : discussions sur les sources et processus responsables du volcanisme de la Cordillère des Andes et sur la déglaciation en Islande. *Thèse Docteur d'Université (Inédit), Clermont-Ferrand, Université Blaise Pascal, 209 p.*

Clavero, J. & Moreno, H., 1994. Ignimbritas Licán y Pucón: Evidencias de erupciones explosivas andesítico-basálticas postglaciales del Volcán Villarrica, Andes del Sur, 39°25'S. *Actas VII Congreso Geológico Chileno, Vol.I, pp.250-254, Concepción.*

Clavero, J. & Moreno, H., 2004a. Evolution of Villarrica Volcano. In: Lara, L.E.; Clavero, J. (Editors). 2004. Villarrica Volcano (39.5°S), Southern Andes, Chile. *Servicio Nacional de Geología y Minería, Boletín*, N°61, pp.17-27.

Clavero, J. & Moreno, H., 2004b. Intra meeting field trip guide-B1: Pucón-Villarrica Volcano Sky Center. *IAVCEI General Assembly 2004, Pucón, Chile. 12 p.*

Clavero, J. & Moreno, H., 2004c. Intra meeting field trip guide-B2: Pucón-Coñaripe. Leaders: J. Clavero & C.Silva. *IAVCEI General Assembly 2004, Pucón, Chile. 12 p.*

Clavero, J., 1996. Ignimbritas andesítico-basálticas postglaciales del Volcán Villarrica, Andes del Sur (39°25'S). *Tesis para optar al grado de Magister en Ciencias Mención Geología y al título de geólogo, Departamento de Geología, Universidad de Chile (Inédito), 112 p.*

Clavero, J., Moreno, H. & Silva, C., 2004. Field trip guide-C3 Villarrica Volcano explosive activity. Leaders: J. Clavero & C.Silva. *IAVCEI General Assembly 2004, Pucón, Chile. 13 p.*

Cole, P.D., Calder, E.S., Sparks, R.S.J., Clarke, A.B., Druitt, T.H., Young, S.R., Herd, R.A., Harford, C.L. & Norton, G.E., 2002. Deposits from dome-collapse and fountain-collapse pyroclastic flows at Soufrière Hills Volcano, Montserrat. In: *Druitt, T.H. & Kokelaar, B.P. (eds) 2002. The Eruption of Soufrière Hills Volcano, Montserrat, from 1995 to 1999. Geological Society, London, Memoirs, 21, pp.231-262.*

Cotten, J., Le Dez, A., Bau, M., Caroff, M., Maury, R., Dulski, P., Fourcade, S., Bohn, M. & Brousse, R., 1995. Origin of anomalous rare-earth element and yttrium enrichments in subaerially exposed basalts: Evidence from French Polynesia. *Chemical Geology 119, p.115-138.*

D'Oriano, C., Poggianti, E., Bertagnini, A., Cioni, R., Landi, P., Polacci, M. & Rosi, M., 2005. Changes in eruptive style during the A.D. 1538 Monte Nuovo eruption (Phlegrean Fields, Italy): the role of syn-eruptive crystallization. *Bulletin of Volcanology 67, pp. 601-621.*

Dalla Salda, L., Cingolani, C. & Varela, R., 1991. El basamento pre-andino ígneo metamórfico de San Martín de los Andes, Neuquén. *Revista de la Asociación Geológica Argentina, Vol.46, N°3-4, p.223-234.*

Denton, G.H., Heusser, C.J., Lowell, T.V., Moreno, P.I., Andersen, B.G., Heusser, L.E., Schlüchter, C. & Marchant, D.R., 1999. Interhemispheric linkage of paleoclimate during the last glaciation. *Geografiska Annaler 81A, 2, pp. 107-153.*

Druitt, T., 1998. Pyroclastic density currents. In: *Gilbert, J.S. & Sparks, R.S.J. (eds) The Physics of Explosive Volcanic Eruptions. Geological Society, London, Special Publications, 145, 145-182.*

Druitt, T., Calder, E.S., Cole, P.D., Norton, G.E., Ritchie, L.J., Sparks, R.S.J. & Voight, B., 2002. Small-volume, highly mobile pyroclastic flows formed by rapid sedimentation from pyroclastic surges at Soufrière Hills Volcano, Montserrat: an important volcanic hazard. In: *Druitt, T.H. & Kokelaar, B.P. (eds) The Eruption of Soufrière Hills Volcano, Montserrat, from 1995 to 1999. Geological Society, London, Memoirs, 21, pp.263-281.*

Druitt, T.H. & Bacon, C.R., 1986. Lithic breccia and ignimbrite erupted during the collapse of Crater Lake caldera, Oregon. *Journal of Volcanology and Geothermal Research, 29, pp. 1-32.*

Druitt, T.H. & Kokelaar, B.P. (eds), 2002. The Eruption of Soufrière Hills Volcano, Montserrat, from 1995 to 1999. *Geological Society, London, Memoirs, 21, pp.231-262.*

Druitt, T.H. & Sparks, R.S.J., 1982. A proximal ignimbrite breccia facies on Santorini volcano, Greece. *Journal of Volcanology and Geothermal Research, 13, pp. 147-171.*

Druitt, T.H. & Sparks, R.S.J., 1985. On the formation of calderas during ignimbrite eruptions. *Nature, 310, pp. 679-681.*

Druitt, T.H., 1985. Vent evolution and lag breccia formation during the Cape Riva eruption of Santorini, Greece. *Journal of Geology, 93, pp. 439-454.*

Druitt, T.H., Avard, G., Bruni, G., Lettieri, P. & Maez, F., 2007. Gas retention in fine-grained pyroclastic flow materials at high temperatures. *Bulletin of Volcanology, Vol.69, N°8, pp.881-901.*

Druitt, T.H., Bruni, G., Lettieri, P. & Yates, J.G., 2004. The fludization behaviour of ignimbrite at high temperature and with mechanical agitation. *Geophysical Research Letters, Vol.31, pp.1-5.*

Eichelberger, J.C., Carrigan, C.R., Westrich, H.R. & Price, R.H., 1986. Non-explosive silicic volcanism. *Nature 323, pp. 598-602.*

Fierstein, J. & Hildreth, W., 1992. The plinian eruptions of 1912 at Novarupta, Katmai National Park, Alaska. *Bulletin of Volcanology, Vol.54, pp.646-684.*

Fierstein, J. & Nathenson, M., 1992. Another look at the calcaulation of fallout tephra volumes. *Bulletin of Volcanology, Vol.54, pp.156-167.*

Fisher, R.V. & Schminke, H.-U., 1984. Pyroclastic rocks. Springer-Verlag Berlin Heidelberg New York Tokyo, 472 p.

Fisher, R.V., 1966. Mechanism of deposition from pyroclastic flows. *American Journal Science, 264, p.350-363.*

Freundt, A., Wilson, C.J.N. & Carey, S.N., 2000. Ignimbrites and block-and-ash flow deposits. In: Sigurdsson, H., Houghton, B., Rymer, H., Stix, J. & McNutt, S. (editors) *Encyclopedia of Volcanoes. Academic Press, pp: 581-599.*

Gardner, J.E., Sigurdsson, H. & Carey, S.N., 1991. Eruption dynamics and magma withdrawal during the Plinian phase of the Bishop tuff eruption, Long Valley caldera. *Journal of Geophysical Research, 96, pp. 8097-8111.*

Gardner, J.E., Thomas, R. & Jaupart, C., 1996. Fragmentation of magma during Plinian volcanic eruptions. *Bulletin of Volcanology 58, pp. 144-162.*

Gaytán, D., 2006. Volcanismo explosivo intraglacial del volcán Villarrica, Andes del Sur, durante la glaciación Llanquihue. *Memoria de título de geólogo, Universidad de Chile.*

Gaytán, D., Clavero, J. & Rivera, A., 2005. Actividad explosiva del Volcán Villarrica, Andes del Sur (39.5°S), durante la Glaciación Llanquihue. *XVI Congreso Geológico Argentino, La Plata, Argentina.*

Gaytán, D., Clavero, J. & Rivera, A., 2006. Volcanismo explosivo intra Glaciación Llanquihue en el Volcán Villarrica, Andes del Sur. (39,5°S). *XI Congreso Geológico Chileno, Antofagasta, Chile.*

Geshi, N., Shimano, T., Chiba, T. & Nakada, S., 2002. Caldera collapse during the 2000 eruption of Miyakeyima Volcano, Japan. *Bulletin of Volcanology, Vol.64, pp.55-68.*

Gonnermann, H.M. & Manga, M., 2003. Explosive volcanism may not be an inevitable consequence of magma fragmentation. *Nature 426, pp. 432-435.*

Hammer, J.E., Cashman, K.V., Hoblitt, R.P. & Newman, S., 1999. Degassing and microlite crystallization during pre-climactic events of the 1991 eruption of Mt. Pinatubo, Philippines. *Bulletin of Volcanology 60, pp. 355-380.*

Haughton, D., Roeder, P. & Skinner, B., 1974. Solubility of sulphur in mafic magmas. *Economic Geology and the Bulletin of the Society of Economic Geologists, Vol. 69, N°4, pp. 451-462.*

Heiken, G. & McCoy, F., 1984. Caldera development during the Minoan eruption, Thira, Cyclades, Greece. *Journal of Geophysical Research, Vol. 89, N°B10, pp. 8441-8462.*

Hervé, F., 1994. The southern Andes between 39º and 44ºS latitude: the geological signature of a transpressive tectonic regime related to a magmatic arc. *Tectonics of the Southern Central Andes, K.J. Reutter et al. (Eds.), Springer-Verlag, Berlin.*

Hervé, F., Araya, E., Fuenzalida, J.L. & Solano, A., 1979. Edades radiométricas y tectónica neógena en el sector costero de Chiloé continental, X región. *Actas II Congreso Geológico Chileno, Vol. 1, p. F1-F8.*

Hervé, F., Moreno, H. & Parada, M.A., 1974. Granitoids of the Andean Range of Valdivia Province, Chile. *Pacific Geology, Vol.8, p. 39-45.*

Hervé, M., 1976. Estudio geológico de la falla Liquiñe-Reloncaví en el área de Liquiñe: Antecedentes de un movimiento transcurrente (Provincia de Valdivia). *Actas I Congreso Geológico Chileno, Vol. 1, p. B39-B56.*

Hickey-Vargas, R., López-Escobar, L, Moreno, H., Clavero, J., Lara, L. & Sun, M., 2004. Magmatic evolution of the Villarrica volcano. In: *Lara, L.E.; Clavero, J. (Editors). 2004. Villarrica Volcano (39.5°S), Southern Andes, Chile. Servicio Nacional de Geología y Minería, Boletín, N°61, pp.39-45.*

Hickey-Vargas, R., Moreno, H., López-Escobar, L. & Frey, F., 1989. Geochemical variations in Andean basaltic and silicic lavas from the Villarrica-Lanín volcanic chain (39°25'S): An evaluation of source heterogeneity, fractional crystallization, and crustal assimilation. *Contributions to Mineralogy and Petrology, Vol.103, pp.361-386.*

Hickey-Vargas, R., Sun, M., López-Escobar, L., Moreno, H., Reagan, M.K., Morris, J.D. & Ryan, J. G., 2002. Multiple subduction components in the mantle wedge: evidence from eruptive centers in the Central Southern volcanic zone, Chile. *Geology, Vol.30, N°3, pp.199-202.*

Hoblitt, R.P., Reynolds, R.L., & Larson, E.E., 1985. Suitability of nonwelded pyroclastic-flow deposits for studies of magnetic secular variation: A test based on deposits emplaced at Mount St. Helens, Washington, in 1980. *Geology, Volume 13, Issue 4, pp. 242–245.*

Hoblitt, R.P., Reynolds, R.L., & Larson, E.E., 1985. Suitability of nonwelded pyroclastic-flow deposits for studies of magnetic secular variation: A test based on deposits emplaced at Mount St. Helens, Washington, in 1980. *Geology, Volume 13, Issue 4, pp. 242–245.*

Houghton, B. & Wilson, C., 1989. A vesicularity index for pyroclastic flows. *Bulletin of Volcanology 51, pp. 451-462.*

Houghton, B., Wilson, C.J.N., Fierstein, J. & Hildreth, W., 2004. Complex proximal deposition during the Plinian eruptions of 1912 at Novarupta, Alaska. *Bulletin of Volcanology, vol.66, pp.95-133.*

Hunt, J. & Hill, P., 2001. Tephrological implications of beam size – sample-size effects in electron microprobe analysis of glass shards. *Journal of Quaternary Science 16, pp.105-117.*

Inman, D.L., 1952. Measures for describing the size distribution of sediments. *Journal of Sedimentary Petrology, 22, pp. 125-145.*

Kaminsky, E. & Jaupart, C., 1997. Expansion and quenching of vesicular magma fragments in Plinian eruptions. *Journal of Geophysical Research, Vol. 102, N°B6, pp. 12187-12203.*

Klug, C. & Cashman, K.W., 1994. Vesiculation of May 18, 1980, Mount St. Helens magma. *Geology, Vol. 22, pp. 468-472.*

Klug, C. & Cashman, K.W., 1996. Permeability development in vesiculating magmas: implications for fragmentation. *Bulletin of Volcanology 58, pp. 87-100.*

Klug, C., Cashman, K.W. & Bacon, C.R., 2002. Structure and physical characteristics of pumice from the climactic eruption of Mount Mazama (Crater Lake), Oregon. *Bulletin of Volcanology 64, pp. 486-501.*

Kueppers, U., Scheu, B., Spieler, O. & Dingwell, D., 2005. Field-based density measurements as tool to identify preeruption dome structure: set-up and first results from Unzen volcano, Japan. *Journal of Volcanology and Geothermal Research, Vol. 141, pp. 65-75.*

Lara, L.E. & Clavero, J. (Editors), 2004. Villarrica Volcano (39.5°S), Southern Andes, Chile. *Servicio Nacional de Geología y Minería, Boletín, N°61, 73 p.*

Lara, L.E. & Moreno, H., 2004. Geología del área Liquiñe-Neltume. *Servicio Nacional de Geología y Minería, Carta Geológica de Chile, Serie Geología Básica, 1 mapa escala 1:50.000, 1 anexo.*

Lara, L.E., 2004a. Overview of Villarrica Volcano. In: *Lara, L.E.; Clavero, J. (Editors). 2004. Villarrica Volcano (39.5°S), Southern Andes, Chile. Servicio Nacional de Geología y Minería, Boletín, N°61, pp.5-12.*

Lara, L.E., 2004b. Villarrica-Lanín chain: tectonic constraints for volcanism in a tranversal alignment. In: *Lara, L.E.; Clavero, J. (Editors). 2004. Villarrica Volcano (39.5°S), Southern Andes, Chile. Servicio Nacional de Geología y Minería, Boletín, N°61, pp.13-16.*

Lavenu, A. & Cembrano, J., 1999. Compressional and transpressional-stress pattern for Pliocene and Quaternary brittle deformation in fore arc and intra-arc zones (Andes of Central and Southern Chile). *Journal of Structural Geology, Vol.21, p. 1669-1691.*

Le Maitre, R.W., Bateman, P., Dudek, A., Keller, J., Lameyre, J., Le Bas, M.J., Sabine, P.A., Schmid, R., Sorensen, H., Streckeisen, A., Woolley, A.R. & Zanettin, B., 1989. A classification of igneous rocks and glossary of terms. Recommendations of the Intenational Union of Geological Sciences, Subcommission on the Systematics of Igneous Rocks. *Blackwell Scientific Publications, 191 p.*

Legendre, C., Maury, R., Savanier, D., Cotten, J., Chauvel, C., Hémond, C., Bollinger, C., Guille, G., Blais, S. & Rossi, P., 2005. The origin of intermediate and evolved lavas in the Marquesas archipelago: an example from Nuku Hiva island (French Polynesia). *Journal of Volcanology and Geothermal Research 143, p.293-317.*

Lirer, L., Munno, R., Petrosino, P. & Vinci, A., 1993. Tephrostratigraphy of the A.D. 79 pyroclastic deposits in perivolcanic areas of Mt. Vesuvio (Italy). *Journal of Volcanology and Geothermal Research, Vol. 58, pp. 133-149.*

Lohmar, S., 2008. Petrología de las ignimbritas Licán y Pucón (Volcán Villarrica) y Curacautín (Volcán Llaima) en los Andes del sur de Chile. Tesis de Doctorado (Inédito). Cotutela entre la Universidad de Chile (Santiago, Chile) y la Université Blaise Pascal (Clermont-Ferrand, Francia), 327 p.

Lohmar, S., Robin, C., Gourgaud, A., Clavero, J., Parada, M.A., Moreno, H., Ersoy, O., López-Escobar, L., & Naranjo, J.A., 2007. Evidence of magma-water interaction during the 13,800 years BP explosive cycle of the Licán ignimbrite, Villarrica volcano (Southern Chile). *Revista Geológica de Chile, Vol.34, No.2, p.233-247.*

Lohmar, S., Parada, M.A., Robin, C., Gerbe, M.C., Deniel, C., Gourgaud, A., López-Escobar, L., Moreno, H. & Naranjo, J.A., 2006. Origin of postglacial "mafic" ignimbrites at Llaima and Villarrica volcanoes (Southern Andes, Chile): Assimilation of plutonic rocks as one of the triggering factors? *V Simposio Sudamericano de Geología Isotópica (SSAGI), Punta del Este, Uruguay.*

Lohmar, S., Robin, C., Parada, M. A., Gourgaud, A., López-Escobar, L., Moreno, H. & Naranjo, J.A., 2005. The two major postglacial (13-14,000 BP) pyroclastic eruptions of Llaima and Villarrica volcanoes (Southern Andes): A comparison. *6th International Symposium on Andean Geodynamics (ISAG), p.442-445, Barcelona, Spain.*

Lohmar, S., Silva, C., Moreno, H., Clavero, J., Naranjo, J.A., López-Escobar, L., Robin, C., Druitt, T. & Gourgaud, A., 2004a. The problematic origin of voluminous mafic pyroclastic flows at Villarrica volcano (Southern Andes). *Abstracts IAVCEI General Assembly 2004, Pucón, Chile.*

Lohmar, S., Vennat, J., Gourgaud, A., Robin, C., Höskuldsson, A., Silva, C., Clavero, J., Moreno, H., Naranjo, J.A. & López-Escobar, L., 2004b. Features of voluminous mafic pyroclastic flow deposits: The Licán ignimbrite (Villarrica volcano, Chile). *Abstracts IAVCEI General Assembly 2004, Pucón, Chile.*

López-Escobar, L. & Moreno, H., 1994. Contribution to the knowledge of the postglacial geochemical evolution of the Villarrica volcano (Southern Andes, 39°25'S), Chile. *Actas VII Congreso Geológico Chileno, Vol.II, pp.1091-1094, Concepción.*

López-Escobar, L., Cembrano, J. & Moreno, H., 1995. Geochemistry and tectonics of the Chilean Southern Andes basaltic Quaternary volcanism (37-46°S). *Revista Geológica de Chile, Vol.22, N°2, pp.219-234.*

Manning, S., 1999. A test of time. The volcano of Thera and the chronology and history of the Aegean and east Mediterranean in the mid second millenium BC. *Oxbow Books, Park End Place, Oxford OX1 1HN, 494 p.*

Marshall, P., 1935. Acid rocks of the Taupo-Rotorua volcanic district. *Transactions of the Royal Society of New Zealand, 64, pp.323-366.*

Mason, B.G., Pyle, D.M. & Oppenheimer, C., 2004. The size and frequency of the largest explosive eruptions on Earth. *Bulletin of Volcanology, Published online: 7 May 2004.*

Mastrolorenzo, G. & Pappalardo, L., 2006. Magma degassing and crystallization processes during eruptions of high-risk Neapolitan-volcanoes: Evidence of common equilibrium rising processes in alkaline magmas. *Earth and Planetary Science Letters, Vol. 250, pp. 164-181.*

Maurice, F., 1978. Emission X. *In: Maurice, F., Meny, L. & Tixier, R., 1978. Microanalyse et Microscopie Electronique à Balayage. Les éditions de Physique.*

Mayfield, J.D. & Schiffman, P., 1998. Measuring the density of porous volcanic rocks in the field using a saran coating. *J. Geosci. Educ. 46, pp. 460-464.*

McCurry, M. & Schmidt, K., 2001. Petrology and oxygen isotope geochemistry of the Pucón Ignimbrite-Southern Andean Volcanic Zone, Chile: implications for genesis of mafic ignimbrites. *Extended Abstract III Simposio Sudamericano de Geología Isotópica SSAGI, Pucón, Chile.*

McCurry, M., Chadwick, J., Wright, K., Smith, R. & Ford, M., 2004. Preliminary LA/ICP-MS and EPMA examination of dacite enclaves and melt inclusions in phenocrysts from basaltic andesite pyroclasts from the Pucón Ignimbrite, Volcán Villarrica, Southern Andean Volcanic Zone: implications for mafic ignimbrite volcanism. *Abstracts IAVCEI General Assembly 2004, Pucón, Chile.*

Mellors, R.A. & Sparks, R.S.J., 1991. Spatter-rich pyroclastic flow deposits on Santorini, Greece. *Bulletin of Volcanology, Vol. 53, N°5, pp. 327-342.*

Métrich, N. & Clocchiatti, R., 1989. Melt inclusion investigation of the volatile behaviour in historic alkali basaltic magmas of Etna. *Bulletin of Volcanology, Vol. 51, pp. 185-198.*

Métrich, N. & Clocchiatti, R., 1996. Sulfur abundance and its speciation in oxydized alkaline melts. *Geochimica et Cosmochimica Acta, Vol. 60, pp. 4151-4160.*

Michaut, C. & Jaupart, C., 2006. Ultra-rapid formation of large volumes of evolved magma. *Earth and Planetary Science Letters, Vol.250, pp.38-52.*

Moreno, H. & Clavero, J., 2006. Geología del área del volcán Villarrica, Regiones de la Araucanía y de los Lagos. *Servicio Nacional de Geología y Minería, Carta Geológica de Chile, Serie Geología Básica*, No., p.21, 1 mapa escala 1:50.000, Santiago.

Moreno, H. & Parada, M., 1974. Geología del área de Liquiñe, Neltume y Pirihueico, Proyecto Hidroeléctrico Neltume. *Inédito, IIG, Santiago.*

Moreno, H., 1974. Airplane flight over active volcanoes of central-south Chile. International Symposium on Andean and Antarctic Volcanology Problems, IAVCEI. Universidad de Chile, Departamento de Geología, Guide Book, N°D-3, 56 p.

Moreno, H., 1976. The Upper Cenozoic volcanism in the Andes of Southern Chile (from 40°00' to 41°30'S.L.). *Symposium of Andean and Antarctic Volcanology Problems, IAVCEI Proceedings, p. 143-173.*

Moreno, H., 1993. Volcán Villarrica: Geología y evaluación del riesgo volcánico, regiones IX y X, 39°25'S. *Informe final Proyecto FONDECYT 1247 (Inédito) 112 p.*

Moreno, H., 2000. Mapa de Peligros del Volcán Villarrica, Regiones de la Araucanía y de Los Lagos. *Servicio Nacional de Geología y Minería, Documento de Trabajo, N°17, 1 mapa escala 1:75.000. Santiago.*

Moreno, H., Clavero, J. & Lara, L., 1994a. Actividad explosiva postglacial del Volcán Villarrica, Andes del Sur (39°25'S). *Actas VII Congreso Geológico Chileno, Vol.I, pp.329-333, Concepción.*

Moreno, H., López-Escobar, L. & Cembrano, J., 1994b. The Villarrica-Quetrupillán-Lanín volcanic chain: a review and probable significance in the southern Andes, 39.4°S, Chile. *Actas VII Congreso Geológico Chileno, Vol.I, pp.339-341, Concepción.*

Morris, J.D., Leeman, W.P. & Tera, F., 1990. The subducted component in island arc lavas: constraints from Be isotopes and B-Be systematics. *Nature, N°344, pp.31-36.*

Moune, S., 2005. Volatils mineurs (S, Cl, F) et éléments traces dans les magmas pré-éruptifs et les gaz volcaniques. Etude des processus de dégazage magmatique sur les volcans Hekla (Islande) et Masaya (Nicaragua). *Thèse de Doctorat, Université Blaise Pascal, 278 p.*

Munizaga, F., Hervé, F., Drake, R., Pankhurst, R.J., Brook, M. & Snelling, N., 1988. Geochronology of the Lake region of south-central Chile (39°-42°S): Preliminary results. *Journal of South American Earth Sciences, Vol.1, N°3, p.309-316.*

Naranjo, J.A. & Moreno, H., 2004. Laharic debris-flows from Villarrica Volcano. In: *Lara, L.E.; Clavero, J. (Editors). 2004. Villarrica Volcano (39.5°S), Southern Andes, Chile. Servicio Nacional de Geología y Minería, Boletín, N°61, pp.28-38.*

Newhall, C.G. & Punongbayan, R.S., 1996. Fire and mud: eruptions and lahars of Mount Pinatubo, Philippines. *University of Washington Press, Seattle, pp.1-1126.*

Newhall, C.G. & Self, S., 1982. The Volcanic Explosivity Index (VEI): an estimate of explosive magnitude for historical volcanism. *Journal of Geophysical Research 87, 1231-1238.*

Noguchi, S., Toramaru, A. & Shimano, T., 2006. Crystallization of microlites and degassing during magma ascent: Constraints on the fluid mechanical behaviour of magma during the Tenjo Eruption on Koozu Island, Japan. *Bulletin of Volcanology 68, pp. 432-449.*

Pallister, J.S., Hoblitt, R.P., Meeker, G.P., Knight, R.J. & Siems, D.F., 1996. Magma mixing at Mount Pinatubo: Petrographic and Chemical Evidence from the 1991 Deposits. In: Newhall, C.G. & Punongbayan, R.S. (editors) *Fire And Mud: Eruptions and Lahars of Mount Pinatubo, Philippines. University of Washington Press, pp. 687-732.*

Palma, J.L., 2001. Facies de la Ignimbria Pucón al noroeste del volcán Villarrica: un analisis estratigrafico y granulometrico para la interpretación de los mecanismos de transporte y depositacion. *Inédito, Memoria de título, Universidad de Chile, Santiago.*

Papale, P., 1999. Strain-induced magma fragmentation in explosive eruptions. *Nature, Vol. 397, pp. 425-428.*

Papale, P., 2001. Dynamics of magma flow in volcanic conduits with variable fragmentation efficiency and nonequilibrium pumice degassing. *Journal of Geophysical Research, Vol. 106, N°B6, pp. 11043-11066.*

Paquereau-Lebti, P., 2006. Corrélations des ignimbrites néogènes du sud du Pérou – Apports des propriétés physiques et magnétiques à la comprensión des processus de mise en place et de soudure. *Thèse Docteur d'Université (Inédit), Clermont-Ferrand, Université Blaise Pascal, 341 p.*

Petit-Breuilh, M.E. & Lobato, J., 1994. Análisis comparativo de la cronología eruptiva histórica de los volcanes Llaima y Villarrica (38°-39°L.S.). *Actas VII Congreso Geológico Chileno,Vol.I, pp.366-370, Concepción.*

Petit-Breuilh, M.E., 1994. Contribución al conocimiento de la cronología eruptiva histórica del volcán Villarrica (39°25'S), 1558-1985. *Universidad de la Frontera, Revista Frontera, Vol.13, pp. 71-99, Temuco, Chile.*

Pino, M., Adán, L. & Seguel, O., 2004. Geoarchaeology of the Area of Calafquén Lake, Southwestern Flank of Villarrica Volcano. In: *Lara, L.E.; Clavero, J. (Editors). 2004. Villarrica Volcano (39.5°S), Southern Andes, Chile. Servicio Nacional de Geología y Minería, Boletín, N°61, pp.61-67.*

Piochi, M., Mastrolorenzo, G. & Pappalardo, L., 2005. Magma ascent and eruptive processes from textural and compositional features of Monte Nuovo pyroclastic products, Campi Flegrei, Italy. *Bulletin of Volcanology 67, pp. 663-678.*

Polacci, M., Papale, P. & Rosi, M., 2001. Textural heterogeneities in pumices from the climactic eruption of Mount Pinatubo, 15 June 1991, and implications for magma ascent dynamics. *Bulletin of Volcanology 63, pp. 83-97.*

Polacci, M., Pioli, L.& Rosi, M., 2003. The Plinian phase of the Campanian Ignimbrite eruption (Phlegrean Fields, Italy): evidence from density measurements and textural characterization of pumice. *Bulletin of Volcanology 65, pp. 418-432.*

Polanco, E. & Clavero, J., 2003. Análisis estadístico de erupciones del Volcán Villarrica (39°25'S), Andes del Sur, Chile. *10° Congreso Geológico Chileno, Universidad de Concepción, 7 p.*

Poussineau, S., 2005. Dynamique des magmas andésitiques: approche expérimentale et pétrostructurale; application à la Soufrière de Guadeloupe et à la Montagne Pelée. *Thèse de Doctorat, Université d'Orléans, 300 p.*

Pyle, D., 1989. The thickness, volume and grainsize of tephra fall deposits. *Bulletin of Volcanology, Vol.51, pp.1-15.*

Reagan, M., Tepley III, F.J., Gill, J.B., Wortel, M. & Hartman, B., 2005. Rapid time scales of basalt to andesite differentiation at Anatahan volcano, Mariana Islands. *Journal of Volcanology and Geothermal Research, Vol.146, pp.171-183.*

Rivera, A., Bown, F., Mella, R., Wendt, J., Casassa, G., Acuña, C., Rignot, E., Clavero, J. & Brock, B., 2006. Ice volumetric changes on active volcanoes in southern Chile. *Annals of Glaciology, 43, 111–122.*

Robertson, E. & Peck, D., 1974. Thermal conductivity of vesicular basalt from Hawaii. *Journal of Geophysical Research, Vol. 79, N°32, pp. 4875-4888.*

Roche, O., Gilbertson, M.A., Phillips, J.C. & Sparks, R.S.J., 2005. Inviscid behaviour of fines-rich pyroclastic flows inferred from experiments on gas–particle mixtures. *Earth and Planetary Science Letters, Vol.240, pp.401–414.*

Roche, O., Gilbertson, M.A., Phillips, J.C. & Sparks, R.S.J., 2002. Experiments on deaerating granular flows and implications for pyroclastic flow mobility. *Geophysical Research Letters, Vol.29.*

Roche, O., Gilbertson, M.A., Phillips, J.C. & Sparks, R.S.J., 2004. Experimental study of gras-fluidized granular flows with implications for pyroclastic flow emplacement. *Journal of Geophysical Research, Vol.109.*

Rosi, M., Landi, P., Polacci, M., Di Muro, A. & Zandomeneghi, D., 2004. Role of conduit shear on ascent of the crystal-rich magma feeding the 800-year-B.P. Plinian eruption of Quilotoa Volcano (Ecuador). *Bulletin of Volcanology 66, pp. 307-321.*

Rosi, M., Vezzoli, L., Aleotti, P. & De Censi, M., 1996. Interaction between caldera collapse and eruptive dynamics during the Campanian Ignimbrite eruption, Phlegrean Fields, Italy. *Bulletin of Volcanology, Vol. 57, pp. 541-554.*

Rust, A., 1998. Mapping of modern pyroclastic deposits with ground penetrating radar: experimental, theoretical and field results. *M.Sc. Thesis, University of British Columbia.*

Ruste, J., 1978. Spectrométrie de rayons X. *In: Maurice, F., Meny, L. & Tixier, R., 1978. Microanalyse et Microscopie Electronique à Balayage. Les éditions de Physique.*

Ryan, M.P. & Sammis, Ch.A., 1981. The glass transition in basalt. Journal of Geophysical Research, 86, 9519-9535.

Rymer, H., van Wyk de Vries, B., Stix, J. & Williams-Jones, G., 1998. Pit crater structure and processes governing persistent activity at Masaya Volcano, Nicaragua. *Bulletin of Volcanology, Vol.59, pp.345-355.*

Sahagian, D., 2005. Volcanic eruption mechanisms: Insights from intercomparison of models of conduit processes. *Journal of Volcanology and Geothermal Research, Vol. 143, pp. 1-15.*

Scott, A.C. & Glasspool, I.J, 2005. Charcoal reflectance as a proxy for the emplacement temperature of pyroclastic flow deposits. Geology, Volume 33, Issue 7, pp. 589–592.

Scott, W.E., Hoblitt, R.P., Torres, R.C., Self, S., Martinez, M.L. & Nillos Jr., T., 1996. Pyroclastic flows of the June 15, 1991, Climactic Eruption of Mount Pinatubo. In: Newhall, C.G. & Punongbayan, R.S. (editors) *Fire And Mud: Eruptions and Lahars of Mount Pinatubo, Philippines. University of Washington Press, pp: 545-570.*

Self, S., Rampino, M.R. & Barbera, J.J., 1981. The possible effects of large 19th and 20th century volcanic eruptions on zonal and hemispheric surface temperatures. *Journal of Volcanology and Geothermal Research, Vol.11, pp.41-60.*

SERNAGEOMIN, 2002. Mapa Geológico de Chile, escala 1:1.000.000. *Servicio Nacional de Geología y Minería, Carta Geológica de Chile, Serie Geología Básica, N°75, 1 mapa en 3 h..*

Sigmarsson, O., Chmeleff, J., Morris, J. & López-Escobar, L., 2002. Origin of ^{226}Ra-^{230}Th disequilibria in arc lavas from southern Chile and implications for magma transfer time. *Earth and Planetary Science Letters, N°196, pp.189-196.*

Sigmarsson, O., Condomines, M., Morris, J.D. & Harmon, R.S., 1990. Uranium and ^{10}Be enrichments by fluids in Andean arc magmas. *Nature, N°346, pp.163-165.*

Sigurdsson, H., Cashdollar, S. & Sparks, S., 1982. The eruption of Vesuvius in A.D. 79: Reconstruction from historical and volcanological evidence. *American Journal of Archeology, 86, pp.39-57.*

Silva, C., Druitt, T.H., Robin C., Moreno H. & Naranjo J.A., 2008. The 3.6 ka BP Pucón eruption of Villarrica Volcano, Chile. Deposit architecture and eruption chronology (*Bulletin of Volcanology, submitted*).

Silva, C., Robin, C. & Druitt, T., 2005. Architectural characteristics and deposition of the 3635±50 yr BP Pucón Ignimbrite of the Villarrica Volcano, Southern Andes, Chile. *6th International Symposium on Andean Geodynamics (ISAG 2005, Barcelona), Extended Abstracts: 666-669.*

Silva, C., Druitt, T., Robin, C., Lohmar, S., Clavero, J., Moreno, H. & Naranjo, J.A., 2004. The 3700-yr Pucón eruption of Villarrica volcano, 39°S Southern Andes, Chile. *Abstracts IAVCEI General Assembly 2004, Pucón, Chile.*

Simkin, T., 1993. Terrestrial volcanism in space and time. *Ann Rev Earth Plane Sci, 21, pp.427-452.*

Smith, G. & Lowe, D., 1991. Lahars: volcano-hydrologic events and deposition in the debris flow-hyperconcentrated flow continuum. In: *Sedimentation in volcanic settings, SEPM Special Publication No. 45, pp.59-70.*

Sparks, R.S.J., 1976. Grain size variations in ignimbrites and implications for the transport of pyroclastic flows. *Sedimentology, 23, pp.147-188.*

Sparks, R.S.J., 1978. The dynamics of bubble formation and growth in magmas: a review and analysis. *Journal of Volcanology and Geothermal Research, Vol. 3, pp. 1-37.*

Sparks, R.S.J., Bursik, M.I., Carey, S.N., Gilbert, J.S., Glaze, L.S., Sigurdsson, H. & Woods, A.W., 1997. Volcanic plumes. *John Wiley & Sons Ltd. (eds) England, 574 p.*

Sparks, R.S.J., Self, S. & Walker, G.P.L., 1973. Products of ignimbrite eruptions. *Geology, 1, pp. 115-118.*

Stuiver, M., Reimer, P., Bard, E., Beck, J., Burr, G., Hughen, K., Kromer, B., McCormac, G., Van der Plicht, J. & Spurk, M., 1998. INTCAL98 Radiocarbon Age Calibration, 24,000-0 calBP. *Radiocarbon, Vol.40, N°3, p.1041.*

Sun, 2001. Geochemical variations among small eruptive centres in the Central SVZ of the Andes: An evaluation of subduction, mantle and crustal influences. Ph.D. Thesis (Unpublished), *Miami, Florida International University*, 292 p.

Szramek, L., Gardner, J.E. & Larsen, J., 2006. Degassing and microlite crystallization of basaltic andesite magma erupting at Arenal Volcano, Costa Rica. *Journal of Volcanology and Geothermal Research, Vol. 157, pp. 182-201.*

Tadeucci, J. & Wohletz, K.H., 2001. Temporal evolution of the Minoan eruption (Santorini, Greece), as recorded by its Plinian fall deposit and interlayered ash flow beds. *Journal of Volcanology and Geothermal Research, Vol. 109, Issue 4, pp. 299-317.*

Takeuchi, S. & Nakamura, M., 2001. Role of precursory less-viscous mixed magma in the eruption of phenocryst-rich magma: evidence from the Hokkaido-Komagatake 1929 eruption. *Bulletin of Volcanology 63, pp. 365-376.*

Thomas, N., Jaupart, C. & Vergniolle, S., 1994. On the vesicularity of pumice. *Journal of Geophysical Research, Vol. 99, N°B8, pp. 15633-15644.*

Thorardson, Th., Self, S., Oskarsson, N. & Hulsebosch, T., 1996. Sulphur, chlorine, and fluorine degassing and atmospheric loading by the 1783-1784 AD Laki (Skaftar Fires) eruption in Iceland. *Bulletin of Volcanology 58, pp. 205-225.*

Torres, R.C., Self, S. & Martinez, M.L., 1996. Secondary pyroclastic flows from the June 15, 1991, Ignimbrite of Mount Pinatubo. In: Newhall, C.G. & Punongbayan, R.S. (editors) *Fire And Mud: Eruptions and Lahars of Mount Pinatubo, Philippines. University of Washington Press, pp: 665-678.*

Walker, G.P.L., 1971. Grain-size characteristics of pyroclastic deposits. *Journal of Geology, 79, p.696-714.*

Walker, G.P.L., 1980. The Taupo pumice: product of the most powerful known (ultraplinian) eruption? *Journal of Volcanology and Geothermal Research, Vol.8, pp.69-94.*

Walker, G.P.L., 1981. Plinian eruptions and their products. *Bulletin of Volcanology, Vol. 44-2, pp. 223-240.*

Walker, G.P.L., Self, S. & Froggatt, P.C., 1981. The ground layer of the Taupo Ignimbrite: a striking example of sedimentation from a pyroclastic flow. *Journal of Volcanology and Geothermal Research, 10, pp.1-11.*

Wilson, C.J.N. & Hildreth, W., 1997. The Bishop Tuff: New Insights from Eruptive Stratigraphy. *The Journal of Geology, Vol. 105, pp. 407-439.*

Wilson, C.J.N., 1980. The role of fluidisation in the emplacement of pyroclastic flows: an experimental approach. *Journal of Volcanology and Geothermal Research, 8, pp.231-249.*

Witham, A.G. & Sparks, R.S.J., 1986. Pumice. *Bulletin of Volcanology 48, pp. 209-223.*

Witham, C.S., 2005. Volcanic disasters and incidents: A new database. *Journal of Volcanology and Geothermal Research, Vol.148, pp.191-233.*

Witter, J., Kress, V., Delmelle, P. & Stix, J., 2004. Volatile degassing, petrology, and magma dynamics of the Villarrica Lava Lake, Southern Chile. *Journal of Volcanology and Geothermal Research, Vol.134, pp.303-337.*

Witter, J.B. & Calder, E.S., 2004. Magma degassing at Villarrica Volcano. In: Lara, L.E.; Clavero, J. (Editors). 2004. Villarrica Volcano (39.5°S), Southern Andes, Chile. *Servicio Nacional de Geología y Minería, Boletín, N°61, pp.46-52.*

Witter, J.B. & Delmelle, P., 2004. Acid gas hazards in the crater of Villarrica volcano (Chile). *Revista Geológica de Chile, Vol.31, No.2, p.273-277.*

Wright, J.V. & Walker, G.P.L., 1977. The ignimbrite source problem: significance of a co-ignimbrite lag-fall deposit. *Geology, 5, pp. 729-732.*